THE HIGH-REDSHIFT EVOLUTION OF RADIO GALAXIES AND QUASARS

James Scott Dunlop

Presented for the Degree of Doctor of Philosophy
at the University of Edinburgh

December 1987

This thesis has been composed by myself and consists entirely of my own work except where specifically indicated in the text.

December 1987

ABSTRACT

The results of an extensive optical/infrared study of radio galaxies and quasars in the Parkes Selected Regions are presented. The data are then analysed to place new constraints on the high-redshift evolution of the radio-source population, and also to investigate the ages and star-formation histories of the galaxies in the sample.

The optical observations were undertaken with the aim of completing the identification programme commenced by Downes *et al.* (1986). CCD images (in both B and R) have been obtained for all the sources which Downes *et al.* failed to identify on sky-survey plate material. This has resulted in 71 new identifications, raising the overall identification content of the sample to 96%. In addition, new spectroscopic observations have increased the fraction of measured redshifts in the sample to 43%, while K photometry has been obtained for a complete subsample comprising ~2/3 of the sources. The infrared data is used to provide accurate redshift estimates for the faintest galaxies in the sample, as well as to compliment the optical photometry in the study of spectral evolution.

After incorporation of these new data, the Selected Regions sample is combined with the existing brighter samples at 2.7GHz to form a large, complete database which is then analysed to determine the form of the Radio Luminosity Function (RLF) at high redshift. The most important results of this study are the confirmation of the redshift cutoff in the flat-spectrum population (first discovered by Peacock 1985), and the discovery (for the first time) of a corresponding redshift cutoff for steep-spectrum sources. These results are demonstrated first using the free-form modelling technique of Peacock & Gull (1981), and subsequently by a variety of model-independent approaches. Finally it is shown that the evolution of the RLF can be described by a model of pure luminosity evolution, involving negative luminosity evolution beyond $z \sim 2$. The implications of these results are briefly discussed.

An analysis of the optical (B-R) and optical-infrared (R-K) colours of the galaxies in the sample is carried out in order to investigate their ages and star-formation histories. This is done through comparison with the predictions of theoretical models of spectral evolution. All the galaxies display at least passive evolution and a large fraction exhibit more active behaviour. It is found to be difficult, with simple models, to reproduce simultaneously both the R-K and B-R evolution - the former implying older, more passive models than the latter. However, it is shown that the addition of a small quantity of UV flux is sufficient to reconcile a simple 'Burst' model with both sets of colour data. Extremely old (~18Gyr) models are required to account for the reddest galaxies, while the blueward scatter can be successfully reproduced either by assuming a range of formation redshifts, or by superimposing small starbursts on the old 'Burst' model. The similarity between the colour evolution of the galaxies in the Selected Regions and that observed for the 3CR sources suggests that such evolution is not associated solely with the brightest radio luminosities.

The thesis concludes with a brief investigation into the high-redshift evolution of optically-selected quasars, and a discussion of some of the possible connections between radio-source and star-formation activity.

ACKNOWLEDGEMENTS

I would principally like to thank John Peacock, my supervisor, for his continual encouragement, enthusiasm and suggestion of ideas throughout the course of this project. I would also like to thank him for assistance during various observing runs, and for generously supplying the alcohol to perk up the morning fruit salad at the AAT. Most of all I would like to thank him for showing me the value of thoroughness and high standards in research.

I am obviously indebted to those who "came before me", particularly Ann Downes and Ann Savage for their extensive work on the Selected Regions sample prior to commencement of this project.

Several astronomers provided invaluable assistance at the telescopes. I would particularly like to thank Simon Lilly for introducing me to the delicate art of observing invisible objects in the infrared, Fred Watson for guiding me through my first visit to the AAT, and John MacKenty for his helpful and clear advice on instrumentation at the UH-88inch telescope (and for serving up a tasty beach barbecue).

The work described in Chapter 7 could not have been achieved without the generous collaboration of Bruno Guiderdoni, who kindly (and promptly) supplied the library of evolution models most suited to the present study. This area of the work also benefited considerably from fruitful discussions with Malcolm Longair in Edinburgh and Simon Lilly in Hawaii, which helped clarify my ideas about spectral evolution. I am also grateful to Paul Hewett for allowing me to use his high-redshift quasar data in Chapter 8, prior to publication.

Thanks are due to Lance Miller for undertaking the formidable task of reading the completed manuscript just prior to submission, and for being an informative and approachable source of advice throughout my three years at Edinburgh. I would also like to acknowledge the staff of the Photolabs unit at the Royal Observatory Edinburgh for their assistance in producing the photographic reproductions of the CCD images presented in Chapter 2.

Many other people have contributed to my post-graduate scientific education at Edinburgh, particularly Peter Brand and Alan Heavens who provided valuable insight during many Kamikaze seminars, and also my fellow students Andrew Mead and James More for their assistance in preparing material for the aforementioned suicidal sessions.

Various people outside of astronomy deserve a mention for contributing indirectly to the completion of this thesis. I would particularly like to thank the staff of the Argyle and of the "Marchmont Chippie" for providing essential sustenance at the end of many a long night of computing. Also the Warthog for cooking the sort of food that fueled my desire to "write up", and David Cooper for continual inspiration.

I would like to acknowledge the assistance of the Royal Society of Edinburgh who provided financial support for the duration of this project via the generous award of the Robert Cormack Bequest studentship.

Finally I would like to thank my Mother and Father for their constant support during three more years of student life.

CONTENTS

Chapter 1 : GENERAL INTRODUCTION

1.1 : INTRODUCTORY REMARKS

This thesis is concerned with the cosmological evolution of radio sources - both the evolution of the high energy sources themselves, and also the evolution of the stellar populations which comprise their host galaxies. The existence of such evolution is either very bad or very good depending on one's interests and point of view.

Cosmological evolution is certainly a major stumbling block in the quest to determine the large scale geometry of the Universe. The observational determination of the cosmological parameters H_o, Ω_o and Λ (see Section 1.2a) requires unchanging objects to act as cosmological probes, or at least objects which evolve sufficiently slowly to enable the subtle effects of different geometries to be distinguished. The discovery of the dramatic evolution of the radio-source population therefore came as a blow for classical cosmologists, whose hopes of utilising radio sources as cosmological probes had been raised ever since the early identification work showed that the majority of bright radio sources lay at cosmologically significant distances.

However, if one takes a broader view of Observational Cosmology, the existence of evolution can be regarded in a more cheerful light. The strong bias of the radio-source population towards high redshift has made it considerably easier to discover very distant objects than would otherwise have been the case. Radio sources therefore provide an opportunity to investigate directly the physical state of the Universe at epochs corresponding to $\sim 1/2 \rightarrow 1/4$ of its present age. Whatever one's attitude, the study of all aspects of cosmological evolution is central to modern extragalactic research - it is now clear that evolution will have to be understood in some detail before the fundamental questions of classical cosmology can be answered.

Radio sources and their evolution are generally studied for two distinct reasons:

i) Because they are interesting objects in their own right. Radio sources, along with other manifestations of the active galactic nuclei (AGN) phenomenom, are obviously of interest since they are the most powerful known objects in the Universe. At present the physics of radio source production is still very poorly understood. An understanding of the statistical evolution of the radio-source population is essential to place constraints on physical theories of AGN.

ii) As a means to an end. Radio sources provide the most convenient route to the discovery of high-redshift galaxies - at present practically all the known galaxies with measured redshifts greater than one are radio sources. Radio galaxies are therefore often the only tools available to investigate properties which are hopefully not significantly influenced by radio activity, such as the spectral evolution of galaxies or the epoch of galaxy formation.

In approach i) it is the very unusualness of radio sources which is the motivation for study, and the ultimate aim must be an understanding of the whole AGN phenomenon. In approach ii) the hope is that radio galaxies are not "too unusual" to prevent more general conclusions being drawn from their behaviour. In this case the ultimate aim is an understanding of the formation and evolution of galaxies in general.

The aim of this introductory chapter is to describe the general background to the thesis. Sections 1.2 and 1.3 provide a brief description of two subjects which underpin the study of radio source evolution, namely cosmology and the properties of the radio source population. Sections 1.4 and 1.5 are more directly relevant to the work presented in this thesis - Section 1.4 reviews the history of the study of radio source evolution, while Section 1.5 briefly introduces the subject of the spectral evolution of galaxies. In Section 1.6 the aims and layout of the thesis are described. Finally, Section 1.7 describes the radio sample on which the observational work described in this thesis was carried out - the Parkes Selected Regions - and summarizes its status prior to commencement of the present study.

1.2 : COSMOLOGY

1.2a : Friedmann Cosmology

Any study of evolution is made all the more difficult by the fact that the large-scale geometry of the Universe is unknown. Throughout this thesis the Universe will be assumed to have the geometry of the Friedmann-Robertson-Walker models of General Relativity. It is therefore worth briefly reviewing the origin of these models, and the assumptions on which they rest.

The basic observational facts which any model of the Universe must satisfy are:

i) The sky at night is dark - this rather obvious observation in fact gives rise to a paradox - Olber's paradox. If the Universe were to be simultaneously infinite, uniform, and static, the whole night sky would be expected to have the surface brightness of the sun, due to complete blanketing of the celestial sphere by an infinite number of stars.

ii) The Universe is expanding - Hubble showed that the Universe was not static, but that in fact the galaxies were receding with a velocity (as measured from the Doppler shift of their light - the redshift z) proportional to their distance, $v = H_o x$ (H_o is the constant of proportionality, Hubble's constant). This fact can resolve Olber's paradox since the recession progressively dims the light of more distant galaxies. It also was welcomed by theorists, since it removed the need for the artificial repulsive force (the Cosmological Constant, Λ) which Einstein had introduced into his theory of General Relativity in order to balance gravity and achieve a static Universe.

iii) The Universe is isotropic - on the largest scales, the Universe of galaxies appears to be isotropic in all its measured properties. More powerful evidence for isotropy is provided by the Microwave Background radiation, the measured intensity of which varies by less than one part in ten thousand on all angular scales from about 1 arcmin to 180^o (the only detectable anisotropy is the dipole

anisotropy - approx 0.2% peak to peak - which is believed to arise from the peculiar motion of the local group of galaxies relative to the "rest frame" of the Universe).

These observations thus demand that any model of the Universe must be isotropic and expanding. To go further it is necessary to invoke one assumption and one well established law of physics.

The assumption is the Cosmological Principle (basically an extension of the Copernican Principle) which simply states the belief that we are not specially privileged observers. This principle, combined with the observational fact of isotropy, demands that the Universe is Homogeneous, and also demands PURE EXPANSION because only then will all "stationary" observers view isotropic recession (pure expansion has no centre and no preferred direction).

Finally, this expanding, isotropic, homogeneous Universe must also satisfy the space-time metric of Special Relativity, ie $d\tau^2 = c^2dt^2 - dl^2$. The metric which describes such a Universe is the Robertson-Walker metric:

$$c^2d\tau^2 = c^2dt^2 - R^2(t)(dr^2 + D^2(d\theta^2 + \sin^2\theta d\phi^2)) \qquad (1.1)$$

where $d\tau$ is an invariant "interval" which all observers can agree upon, t is proper time, and the expansion of the Universe is taken care of by the scale factor R(t). This means that real distance, x, is given by $x = R(t)r$ and r is called Comoving Distance - the comoving distance to a given galaxy is thus the same for all time, although the real distance increases with the expansion. D is called "effective distance" and is a function of r, the form of which is determined by the curvature of the Universe ($D = r$ for small r, ie the Euclidean Universe).

Since R(t) is the scale factor describing the expansion of distance with time, it must also describe the expansion of the wavelength of light with time, ie the redshift $z = (\lambda_o - \lambda_e)/\lambda_e$, thus:

$$R(t) = \frac{\lambda_e}{\lambda_o} = \frac{1}{1+z} \qquad (1.2)$$

This is the best way to interpret redshift in cosmology - as a measure of the size of the Universe at the time the light was emitted.

None of the above has involved General Relativity. However, at this stage a theory of gravity has to be invoked to determine the functional form of R(t) and D(r) (ie the dynamics of the expansion and the geometry of the Universe). Of course, in an empty Universe with no matter, these two can be derived simply using Special Relativity - with no gravitational deceleration it is obvious that R(t) $\propto$ t - but otherwise it is necessary to solve the dynamical equations for dR/dt and d^2R/dt^2. This process will not be discussed in detail here - a full discussion can be found in Gunn (1978) or Longair (1984) - but the result is that R(t) and D(r) are intimately linked and both are completely determined by two parameters, Hubble's parameter H and the dimensionless deceleration parameter q (assuming zero Cosmological Constant Λ).

$$H = \frac{\dot{R}}{R} \qquad (1.3)$$

$$q = -\frac{\ddot{R}R}{\dot{R}^2} = \frac{4\pi G\rho}{3H^2} = \frac{1}{2}\Omega \qquad (1.4)$$

where Ω is the ratio of the actual density of the Universe, ρ, to a critical density, ρ_c :

$$\Omega = \frac{\rho}{\rho_c} = \frac{\rho}{(3H_o^2/8\pi G)} \qquad (1.5)$$

Ω determines both the long-term evolution of the Universe and its large-scale geometry. ρ_c is the density of matter which provides <u>just</u> enough attractive gravitational force to eventually halt the expansion. Thus if $\Omega < 1$ the Universe will continue to expand forever, but if Ω

Figure 1.1 : Time evolution of the expansion scale factor, R(t), in open ($\Omega_o < 1$), flat ($\Omega_o = 1$) and closed ($\Omega_o > 1$), Friedmann model universes with zero cosmological constant.

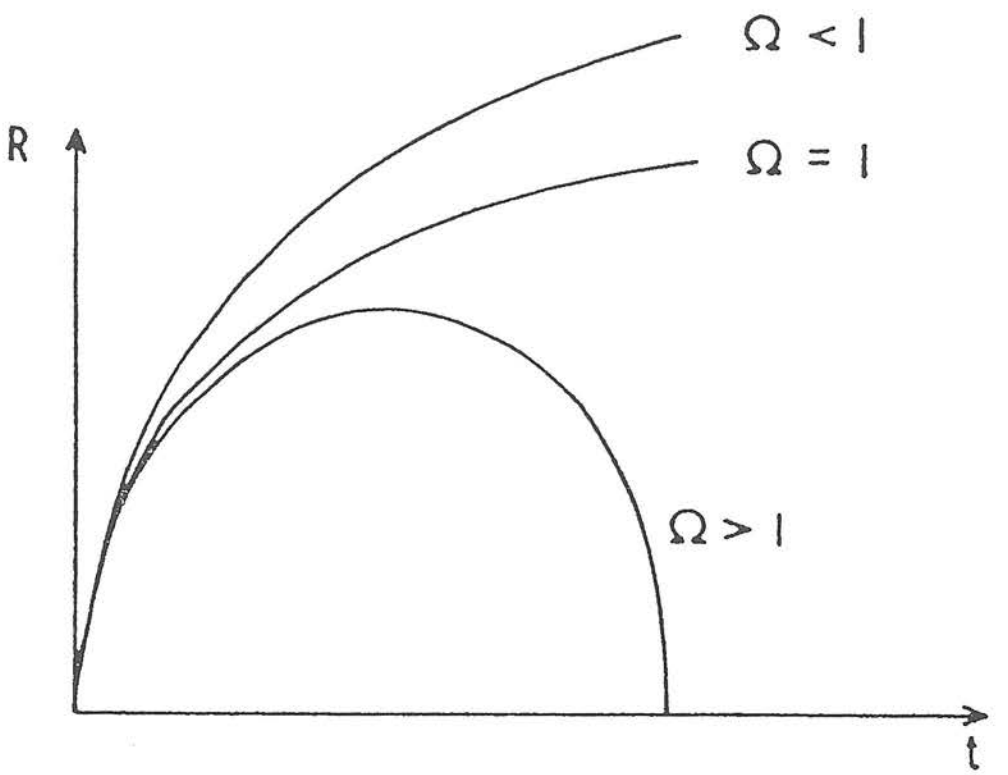

> 1 the expansion will eventually halt and then the Universe will start to contract. The variation of R(t) with Ω is illustrated in Figure 1.1. General Relativity also predicts that the curvature of the Universe is determined by Ω - if $\Omega > 1$ the geometry is spherical (+ve curvature), if $\Omega < 1$ it is hyperbolic (-ve curvature) and if $\Omega = 1$ the geometry is flat. Note that the precise relation $q = 0.5\Omega$ is unique to General Relativity and therefore its verification is a potential test of the theory on the largest scales. However, given that it has not yet proved possible been possible to perform such checks, it is important to point out that General Relativity is normally adopted as the theory of gravitation, not because there exists irrefutable evidence that it is in fact correct, but simply because it is at present the simplest available theory. The adoption of any more complex cosmological model is unjustified as long as General Relativity continues to pass every test to which it is subjected.

For the purposes of the rest of this thesis, the most important result is the expression for Effective Distance

$$D = \frac{2c}{H_o \Omega^2 (1+z)} \left\{ \Omega z + (\Omega - 2) \left[(\Omega z + 1)^{0.5} - 1 \right] \right\} \qquad (1.6)$$

This expression can then be used to calculate elements of comoving volume - in studies of density evolution it is important to consider comoving volumes since the real density evolution of interest is that which occurs in addition to the pseudo density evolution inevitably caused by the expansion of the Universe. The comoving cosmological volume enclosed between two spheres separated by a redshift increment dz is:

$$dV = 4\pi D^2 dr = 4\pi D^2 \frac{dr}{dz} dz = 4\pi D^2 \frac{cdz}{H_o (1+z)(\Omega z + 1)^{0.5}} \qquad (1.7)$$

D also enables determination of the relationship between observed flux-density and source luminosity. If luminosity is in units of sr^{-1} then the observed monochromatic flux-density is given by:

$$S(\nu_o) = \frac{L(\nu_1)R(t_1)}{D^2} = \frac{L(\nu_1)}{D^2(1+z)} = \frac{L(\nu_o)}{D^2(1+z)^{1+\alpha}} \qquad (1.8)$$

where ν_1 is the emission frequency, ν_o is the observed frequency, and $L(\nu_1)$ can be related to $L(\nu_o)$ if the spectrum has a power-law of the form $\nu^{-\alpha}$. It is worth pointing out that D, Effective distance is not the same as Angular Diameter distance, D_A, or Luminosity distance D_L which are often quoted instead. $D_A = D/(1+z)$ and is sometimes used because it makes the angular component of the Robertson-Walker metric appear like the Euclidean expression, while $D_L = D(1+z)$ is sometimes used to achieve the same illusion in the relation between bolometric flux-density and luminosity.

Even on the assumption that the Friedmann Models provide a correct description of the Universe, there remains the problem of the exact present day values of H and q, ie H_o and q_o (or equivalently Ω_o). At present, most observations appear to indicate that $H_o \simeq 50$ $kms^{-1}Mpc^{-1}$ and $q_o \simeq 0.1$, but both these values are highly uncertain, the former due to the difficulty in measuring accurate distances to galaxies, the latter due to the problems connected with determining the amount or composition of dark matter in the Universe. In addition there are theoretical reasons (from inflationary models of the early Universe) for believing that $q_o = 0.5$ (ie $\Omega = 1$). Throughout this thesis $H_o = 50$ $kms^{-1}Mpc^{-1}$ will be assumed and the dependence of the results on the value of q_o will be indicated.

1.2b : The Hot Big Bang model of the Universe

The picture of the expanding Universe inevitably leads to the conclusion that some time in the distant past the Universe must have been much denser than it is now, and that $\sim 10^{10}$ yr ago it commenced in an initial singularity - the "Big Bang". It is possible to show that, in the initial stages of expansion, the Universe would have been radiation dominated, rather than matter dominated (as it is today) and temperatures would have been very high ($\sim 10^{10}$ K after 1 minute). For this reason, this theory of the evolution of the

Universe is often called the Hot Big Bang model. In addition to the observed present day expansion of the Universe, there are two other pieces of evidence which strongly suggest that this rather radical and violent picture is indeed correct.

Firstly there is the Microwave Background Radiation (MBR), the strong isotropy of which strongly suggests that it is of cosmological, rather than local origin. Present measurements continue to indicate that the spectrum of this radiation is highly Plankian, indicating that at some time it must have been in equilibrium with matter at a particular temperature. This would indeed have been the case in the early stages of the Hot Big Bang. Secondly, there are the universally observed abundances of the light elements such as Helium-3 (^{3}He), Helium-4 (^{4}He), Deuterium D and Lithium-7 (^{7}Li). Unlike the heavier elements, these rather fragile elements cannot be produced by nuclear reactions in stars because they are rapidly destroyed or converted into heavier species. However, these elements are exactly those which are produced naturally in the very hot, but short-lived initial phase of the Hot Big Bang - only for the first ~500s of the early Universe is the temperature high enough for fusion reactions to occur, and so there is not sufficient time for the initial fusion products to be converted into heavier elements. In fact, with an appropriate choice of Ω, the exact fractions of all the light elements can be successfully produced. Even opponents of the Big Bang theory accept the existence of the light elements means that the matter in the Universe must have passed through a very hot phase.

There are thus 3 pieces of evidence - expansion, the MBR and the light elements - which lead naturally to the Hot Big Bang model of the Universe. There do of course remain problems such as:

i) The observed present—day asymmetry between matter and antimatter.

ii) The "Horizon Problem" - why is the Universe so isotropic given that it does not appear to be old enough for all regions to have communicated with each other.

iii) The "Flatness Problem" - why is Ω so close to 1 when this value is unstable. Ω must have been very nearly equal to 1 in the early Universe.

However, such has been the success of the Hot Big Bang theory that most present-day attempts to solve these problems (such as Inflationary models) are carried out within the framework of this model, and centre on particle physics in the very early stages of the expansion.

1.2c : Galaxy formation

Galaxies are generally believed to be the end-product of the evolution of density fluctuations which arose in the early universe. The dominant influence on the growth of these fluctuations is usually assumed to be gravity, with regions of overdensity gradually condensing and eventually separating from the background expansion to form isolated, bound systems. However, ordinary (baryonic) matter fluctuations would have been unable to begin this process of growth and contraction until ~ 10^5 yr after the Big Bang. Before this time the Universe was so hot that all baryonic matter was ionized and thus strongly coupled to radiation. Mass perturbations smaller than the horizon size (the distance a light ray could have travelled since the Big Bang) were therefore unable to grow because the attractive force of gravity was counteracted by the force of radiation pressure. This stalemate situation came to an end at the "epoch of recombination" ($z \approx 1300$), by which time the universe had cooled sufficiently to allow matter to exist in the form of electrically neutral atoms. After this epoch the matter perturbations were free to begin collapsing under the influence of gravity alone, and the thermal background radiation bath to which the matter had been coupled was left to cool as the universe expanded. Nowadays this radiation has cooled to ~ 3K and constitutes the Microwave Background Radiation (MBR). The MBR should thus contain information on the size of the perturbations which existed at the time of recombination.

The origin and form of the perturbations in the early universe is

at present still very poorly understood. For this reason, the approach which has normally been adopted is to assume some initial pattern of fluctuations, simulate its growth and evolution, and then compare the result with present-day observations. A general perturbation has two degrees of freedom, one for matter fluctuations and one for radiation. Different relations between these can lead to radically different pictures for galaxy formation. In practice, attention has focussed on two particular modes:

i) Isothermal fluctuations - the "bottom-up" model.

This model derives from work done in the late 1960s and early 1970s by Peebles and his colleagues at Princeton University (eg Peebles & Dicke 1968). They considered a purely baryonic universe and, for simplicity, assumed that the fluctuations in the early universe were isothermal - ie that the fluctuations were confined to the matter, with the background radiation remaining uniformly distributed. Matter perturbations cannot grow while the Universe is radiation dominated (ie prior to $z_{eq} \simeq 2.5\times10^4\Omega h^2$ where $h = H_o/100 kms^{-1}Mpc^{-1}$) because during this phase the timescale for expansion is much shorter than the timescale for gravitational collapse. After t_{eq} matter fluctuations can begin to grow but, in the case of baryonic matter, the radiation pressure keeps the Jeans mass very large (ie $M_J \sim 10^{14}M_\odot$) prior to recombination. However, after the radiation and the matter decouple at recombination, the Jeans mass drops to $M_J \sim 10^6M_\odot$ which means that, in this picture, the first structures to condense out of the smoothly expanding universe would have to be associated with globular clusters or dwarf galaxies. Galaxies could then, in principle, be formed by the gravitational clustering of these small protogalaxy building blocks, with gravity also being the origin of subsequent galaxy clustering. For obvious reasons, this model of galaxy formation is often called the "bottom-up" model - the initial small protogalaxies are formed at fairly early epochs, $z \sim 30$, while galaxy clustering occurs relatively late. The main drawback of this model is that gravitational clustering occurs <u>too late</u> to produce structures as large as superclusters. The universe is simply not old enough for such large-scale structures to have formed purely as a result of the gravitational aggregation of galaxies. It is also worth noting that,

nowadays, Isothermal perturbations are considered rather artificial since it is in fact very difficult to perturb the matter distribution in the early universe without also perturbing the radiation. Recently, however there has been considerable interest in Isocurvature fluctuations, which are in many respects very similar to the Isothermal case. Isocurvature perturbations correspond to a Universe of uniform density/curvature with a varying photon:baryon ratio (Peebles 1983), possibly depending on exactly how the matter/antimatter asymmetry was generated. The basic idea of the bottom-up model in a baryonic universe is thus still very relevant today.

ii) Adiabatic perturbations - the "top-down" model.

An alternative, and generally more popular assumption is that the fluctuations in the early universe were adiabatic. The current popularity of this type of perturbation is due to the fact that it arises naturally from quantum fluctuations associated with the phase transition at the end of the Inflationary period (eg Bardeen, Steinhardt & Turner 1983). Adiabatic fluctuations are sound waves in the strongly coupled matter/radiation medium which fills the universe prior to recombination - the distribution of radiation mimics the distribution of matter in such a way as to ensure that the ratio of the energy density of matter and that of radiation is the same in all regions of space. An important consequence of this strong coupling between the matter and radiation fluctuations is that the fluctuations are damped by photon diffusion, a process which is unimportant in the isothermal model. This means that only very large-scale density perturbations can survive until recombination ("Silk Damping"). Thus, in this model, the first structures to form are very massive and must be associated with galaxy clusters and superclusters. Individual galaxies form later as a result of subsequent fragmentation of the large-scale perturbations. This model of galaxy formation is therefore often referred to as the "top-down" model. In the purely baryonic universe this model has one major flaw. Because the fluctuations are adiabatic, the large density fluctuations necessary to produce the observed level of structure would have to be accompanied by correspondingly large fluctuations in the background radiation field.

Such large fluctuations are inconsistent with the observed level of isotropy of the MBR.

The problem of reconciling the existence of highly developed structure with the observed lack of large fluctuations in the MBR has been circumvented in recent years by discarding the assumption that the universe consists primarily of baryons (Silk 1986). The advantage of considering the universe to be dominated by non-baryonic dark matter is that, because such matter decouples from radiation earlier than the epoch of recombination, dark matter perturbations are free to begin gravitational growth after t_{eq}. Since the baryonic matter and radiation are not coupled to the dark matter, they are unaware of the growing fluctuations in the underlying medium, and can thus continue to posses a perturbation spectrum well below the level which would cause problems in the conventional picture. After recombination the baryonic matter is free to fall into the potential wells of the already well developed dark matter fluctuations, and rapidly attains a similar level of density enhancement. Non-baryonic dark matter thus gives a "head start" to the development of structure in the universe.

The problem with dark matter is that, although there are reasons for believing in its existence (eg to achieve the theoretically desirable $\Omega = 1$, eg Peebles 1986) there are, at present, relatively few constraints on its possible nature. A wide variety of possible kinds of non-baryonic matter have been proposed (Turner 1987), but generally these can be classified as either "hot" or "cold" dark matter, depending on the rest mass of the chosen particle type. Because particle mass determines the extent of fluctuation damping in the early universe, these two classes of dark matter result in two very different scenarios of galaxy formation.

i) Hot dark matter - another "top-down" model

Hot dark matter is the term used to describe light, weakly interacting particles, the best known example being massive neutrinos. It was originally proposed that neutrinos were massless, but there is no theoretical reason why this need necessarily be the

case. Stringent experimental limits have been set on the value of the electron neutrino mass, and it is probably too small to close the Universe ($m_\nu \leqslant$ 15eV, Krauss 1987). Nevertheless, masses of this order can arise naturally in Grand Unified Theories (only particles which mediate an ∞ range interaction, like photons and gravitons, have to be massless) and the limits on the μ and τ neutrino masses are not restrictive. Neutrinos do have one strong advantage over other dark matter candidates in that they are known to exist. The reason neutrinos are called "hot" dark matter is that, because of their low rest mass, they continue to move at relativistic speeds until shortly before the epoch of recombination. This means that, just as with adiabatic fluctuations in a baryonic universe, only very large-scale density fluctuations can avoid being damped out in the early universe. Hot dark matter thus results in a top-down model of galaxy formation very similar to that which arises in the original adiabatic picture considered above. At the time of writing this class of model appears to be faced with some serious difficulties. The neutrino damping scale is so huge that hot dark matter models have great difficulty in making galaxies by the present epoch without at the same time producing a Universe which is excessively inhomogeneous on large scales (10 → 100Mpc) (White 1986). It seems impossible in this picture to account for the known existence of discrete objects, such as quasars, at redshifts as large as $z \sim 4$.

ii) Cold dark matter - an improved "bottom-up" model

To avoid the problem of large scale damping in the early universe, what is needed is a form of dark matter which becomes non-relativistic at very early epochs. Cold dark matter is the term used to describe any such species of particle whose velocity dispersion in the early Universe is very small, and which has non-gravitational interactions that are much weaker than the weak interaction. Grand Unified/Supersymmetric theories predict the existence of many potential cold dark matter particles (Turner 1987). The best candidates appear to be the lightest (but still rather massive) supersymmetric partner particles, namely the photino, gravitino, scalar neutrino, Higgsino etc, (which have masses ~ few GeV), or alternatively the much lighter axion ($m \sim 10^{-5}$GeV) which,

despite its low rest mass, can provide a cold dark matter background because it is created with low thermal velocity and subsequently interacts so weakly with ordinary matter that it would never have been in thermal equilibrium with the Hot Big Bang. Despite the fact that these exotic particles have yet to be detected experimentally, cold dark matter is now generally regarded as the most promising solution to the problems faced by galaxy formation theories. A useful summary of the "standard" cold dark matter model is provided by Silk (1987). Because of the lack of large-scale damping, cold dark matter leads to a "bottom-up", or "all-at-once" picture of galaxy formation depending on the choice of the initial perturbation spectrum. This theory possesses the best features of both the isothermal and hot dark matter models. It is able to produce galaxies (or even Population III stars, eg Couchman & Rees 1986) at relatively early epochs and yet, unlike the isothermal model, does not have to rely purely on the gravitational clustering of galaxies to produce large-scale structure. With this model it is possible to reproduce the observed form of galaxy clustering but then the assumption of $\Omega = 1$ leads to excessively large peculiar velocities for individual galaxies ($\gtrsim$ 600kms^{-1} as compared with the observed value of $\sim$ 200kms^{-1}) (White 1986). There are two alternative solutions to this problem - either one must adopt a lower value of Ω (ie $\Omega \approx 0.2$), or it is necessary to assume that the luminous matter is more strongly clumped than the dark matter. The latter situation can in fact be produced fairly naturally by introducing a biassing threshold for galaxy formation (Bardeen *et al.* 1986) - ie by assuming that galaxies only form at the largest (2.5σ) density peaks. This means that, in contrast to the predictions of hot dark matter theories, the voids between galaxy clusters are not expected to be completely devoid of matter.

This biassed, adiabatic, cold dark matter theory has proved to be very successful at reproducing much of the observed structure in the Universe (eg Blumenthal *et al.* 1984), a fact which goes a long way to account for its present popularity. It may yet, however, be faced with two potentially serious difficulties. The first of these is the cluster-cluster correlation length, which has been measured (eg Bahcall & Soneira 1983) to be about 5 times larger than the galaxy-galaxy correlation length. The biassed cold dark matter model

predicts that it should only be larger by a factor ~ 2 (Barnes *et al.* 1985). The second is the discovery of large-scale streaming motions (eg Dressler *et al.* 1987) which would only be expected to arise in a top-down (eg hot dark matter) model. However, these two potentially awkward results have not yet been firmly established and so the biassed, cold dark matter model is still generally regarded as the most promising alternative.

1.3 : THE RADIO-SOURCE POPULATION

This section provides a brief description of some of the basic properties of the radio-source population, principally to introduce some of the terminology which is used throughout the thesis. At some level, all galaxies are radio emitters. However, the term "radio galaxy" is generally taken to mean an object with a radio luminosity greater than $P_{408} = 10^{24}$ $WHz^{-1}sr^{-1}$ (P_{408} being the luminosity of the source at an emission frequency of 408MHz). Most sources with luminosities lower than this are identified with normal galaxies - our own galaxy has a radio luminosity of $P_{408} \sim 10^{22}$ $WHz^{-1}sr^{-1}$ - while brighter sources are generally associated with giant elliptical galaxies or quasars (eg Cygnus A, which has a luminosity of $P_{408} \sim 10^{28}$ $WHz^{-1}sr^{-1}$). It is not clear whether there is a physical distinction between sources which are brighter or fainter then this luminosity, but this thesis is principally concerned with bright sources near the top of the radio luminosity function.

1.3a : Radio structures and luminosities

Radio sources are generally defined by their morphological structure and radio spectra. It is convenient to classify them as Double, Compact or Complex sources, although the boundaries between these categories are rather blurred with, for example, many compact sources also displaying weak extended structure or double structure if observed with sufficient angular resolution.

i) Double Sources

The early radio surveys were carried out at relatively low frequencies - ie at or below 408MHz. The best known of these is the 178MHz 3CR sample (Bennett 1962). Most of the sources found in such samples have rather steep radio spectra with spectral indices $\alpha \sim 0.8$ (radio spectra are generally roughly power-law in form - $S_\nu \propto \nu^{-\alpha}$), and consist of two lobes positioned roughly symmetrically about the associated galaxy (or quasar). The typical separation of the two radio components is ~ 100 → 500kpc, although some sources are as large as

6 Mpc in extent. Many of these double sources also possess a weak, compact, flat-spectrum, central component which is coincident with the nucleus of the optical counterpart, and in a few cases radio jets are observed extending from this core to one or both of the radio lobes. The origin of the radio emission in all these components is believed to be synchotron radiation from relativistic electrons gyrating in large-scale magnetic fields, principally because the derived brightness temperatures are extremely high and the radiation is always observed to be strongly polarized.

Generally one or both of the radio lobes contains a relatively compact ($\simeq$ 10kpc) "hotspot" of particularly intense radio emission. In powerful radio sources, such as Cygnus A, these hotspots are located near to the outer edge of the radio lobes, but in weaker sources they are either situated rather closer to the host galaxy, or completely absent. Fanaroff & Riley (1974) quantified this behaviour by introducing a classification based on the linear separation of the hotspots, relative to the overall size of the source. If this ratio is greater than 0.5, the source is classified as class II (FRII), otherwise it is class I (FRI). This division correlates well with luminosity - FRI sources generally have luminosities lower then $P_{178} = 2\times10^{25}$ $WHz^{-1}sr^{-1}$, while essentially all FRIIs are brighter than this. Sometimes a further, more qualitative subdivision is introduced within class II, with the term "classical double" being reserved for the most extreme examples in which the hotspots are found right at the leading edge of the lobes. A good review of the structure of extended radio sources is given by Miley (1980).

It is generally accepted that energy is supplied to the radio lobes from the compact nucleus via highly collimated jets, and that the hotspots are formed by the interaction of the jets with the inter-galactic medium (IGM). Because of the large amounts of energy which are apparently generated in an extremely small region, there is also general agreement over the fact that the fundamental power source is most probably a massive black hole. However, although various mechanisms for the generation and collimation of jets have been proposed (eg Blandford & Rees 1974), there is as yet no consensus as to their exact composition or method of production (see

Begelman *et al.* 1984 for a review). Nevertheless, it has been proposed that the FR division arises from jets of different Mach numbers. Jets are Kelvin-Helmholtz unstable at all Mach numbers but, above a critical value near unity, the jet is not fully disrupted. It has therefore been suggested that FRII sources are generated by stable supersonic jets, whereas FRI sources are the consequence of disruption of a sub- or trans-sonic jet by entrainment of the surrounding IGM (eg Norman *et al.* 1984, Bicknell 1985). Within this framework two different explanations have been offered for the correlation of FR class with total power - Norman *et al.* (1984) argue that total luminosity and jet Mach number will be correlated since both should increase with the total kinetic energy flux of the jet, whereas Bicknell (1985) suggests that the weakness of FRI sources reflects inefficient conversion of the jet kinetic energy, with much of this energy being lost in entrainment rather than converted into relativistic particles by shocks.

It is clear that the local Mach number is controlled by the local gas density, and so the FRI/FRII division might be expected to arise from intrinsically similar sources living in rather different environments. The environments of powerful radio sources have been investigated by Longair & Seldner (1979) and Prestage & Peacock (1987). FRI sources are typically found in regions of significantly enhanced galaxy density, whereas FRII sources are generally found in cluster environments typical of that found for the general elliptical galaxy population. However there is evidence (eg Yates *et al.* 1986) that the most powerful known FRII sources in the 3CR sample may lie in rich clusters. Qualitatively this appears to make good sense. Sources of moderate power will be able to form a supersonic jet, and hence an FRII source, in regions of low gas density, but might be unable to do so in a rich cluster environment. However, as argued by Prestage & Peacock (1987), the most powerful sources such as Cygnus A produce jets of sufficient ram pressure that the static pressure, even in rich clusters, is negligible - such beasts might well be able to produce an FRII source in any environment.

One other outstanding problem has been the origin of the one-sidedness of the jets which are seen in many powerful radio

sources - are these large kpc-scale jets genuinely one-sided or is it simply an artefact of viewing angle and relativistic beaming (an explanation which is commonly invoked to explain the apparent superluminal motions often observed in parsec-scale jets, eg Kellermann & Pauliny-Toth 1981). Recently strong evidence in favour of the latter explanation has been presented by Robert Laing, who has found that the radio emission from the lobe which lacks a jet is always more strongly depolarized than the radiation from the other radio lobe. The most natural explanation of this effect is that the lobe without a jet is being observed through a greater depth of plasma, and hence is more distant, than its jet-fed counterpart (Scheuer 1987). It therefore seems very likely that all radio jets are genuinely two-sided (as is observed in some weaker sources) and that the observed one-sidedness of powerful jets is simply an orientation effect, enhanced by the effects of relativistic beaming.

ii) Compact sources

The term "Compact" is generally used to describe radio sources which are smaller than 1 arcsec in angular size (often as low as 10^{-3} arcsec). Information on the structure of these objects is thus generally obtained from Very Long Baseline Interferometry (VLBI), or from studies of their spectra and variability. Many of these sources show variations in radio intensity whose time-scales imply structures $<$ 1pc in extent. The spectra of compact sources are usually affected by synchotron self-absorption which leads to rather flat radio spectra, $\alpha < 0.5$. Because of this fact, the existence of a large population of such objects was not discovered until radio surveys were carried out a high frequencies - the early low frequency surveys being heavily biassed towards steep-spectrum sources.

The fact that the emission in these compact objects occurs on such a drastically different scale to the emission in extended sources suggests that these two classes may be physically distinct, and so the two populations are normally considered separately. This is not to say that there exists no relation between the two types of object, but simply that there is no *a priori* reason for assuming one. It has been suggested, however, that compact sources may simply be double

sources viewed practically end-on (Orr & Browne 1982) - ie the extreme case of the orientation effect invoked above to explain the apparent one-sidedness of jets. Arguments against this type of unified scheme come principally from studies of the cluster environments of radio sources, a property which should obviously be independent of the orientation of the radio source itself. Prestage & Peacock (1987) find that compact sources do not appear to lie in regions of enhanced galaxy density. The extended sources in their sample which have total luminosities similar to their compact sources are FRIs which, as mentioned above, do appear to lie in relatively rich environments. Such a difference in environment would not be expected if the only difference between extended & compact sources were to be viewing angle. It is important to point out, however, that in this type of study it is difficult to be sure that the correct extended counterpart has been chosen for comparison - detailed knowledge of the extended luminosities of compact sources is required to determine the luminosity of their supposedly unaligned counterparts.

iii) Complex sources

Finally there are sources which possess more complex morphologies. These include 'bent doubles' in which the axis of the double source is distorted (probably by movement of the source relative to the IGM), diffuse sources with no clear axis of symmetry, and "radio-trail" sources, in which the bulk of the emission originates from a trail which extends like a wake behind the parent galaxy. Most of these sources are of low surface brightness and are classified as FRI. They are therefore not of great interest in the context of the present study.

1.3b : Division by spectral index

The bulk of the data considered in this thesis are drawn from radio surveys made at 2700MHz. The advantage of this frequency is that the surveys contain reasonable numbers of both steep-spectrum extended sources and flat-spectrum compact sources, thus facilitating

simultaneous study of both classes of object. As mentioned above, surveys at lower frequencies are dominated by sources of the former type, while at frequencies $\nu \gtrsim$ 5GHz the bulk of the sources have flat spectra. The most convenient way of separating the two classes of source is by a division based on high-frequency radio spectral index, the dividing line being set at $\alpha = 0.5$. In the remainder of this thesis the terms steep-spectrum and flat-spectrum will be assumed to mean $\alpha \gtrsim 0.5$ and $\alpha < 0.5$ respectively. This division is obviously fairly crude, but in most cases it does appear to be effective in separating compact and extended sources (see eg Peacock & Wall 1981). In fact this spectral classification is cleaner in one direction than the other - virtually all flat-spectrum sources are compact but the inverse statement is not true. Thus, the one group of sources which do not conform to the general rule that steep-spectrum=extended, flat-spectrum=compact, are the steep-spectrum compact sources. In the Northern Sky 2.7GHz sample of Peacock & Wall (1981) roughly a third of the compact sources were found to possess steep spectra. The nature of this class of source is of great interest.

Finally, in the context of radio spectral indices, it is worth noting the existence of the observed correlation between luminosity and radio spectral index for steep-spectrum sources (Laing & Peacock 1980). This P–α correlation is in the sense that the sources with steeper radio spectra are more luminous, and results in low frequency surveys like the 3CR being biassed towards very powerful sources. An understanding of this correlation is important to relate surveys which are defined at different frequencies, and is therefore discussed further in the context of multi-frequency modelling in Chapter 6.

1.3c : The optical counterparts of radio sources

All powerful radio sources have either elliptical galaxies or quasars as their optical counterparts. Quasars are only associated with the most powerful sources. For sources of a given power, the probability that the optical identification is a quasar increases as the relative strength of the compact radio component increases. The

identification trends which have been noticed (mainly from the bright 2.7 GHz samples of Peacock & Wall 1981, Wall & Peacock 1985) are summarized below.

QUASARS

i) The vast majority of compact flat-spectrum sources are identified with quasars.

ii) Very few complex or FRI sources are identified with quasars.

iii) Some FRII sources are identified with quasars. The probability of a quasar ID rises along with the relative strength of the core component, and with the overall power of the source (eg ~ 40% of all 3CR FRII sources with $z > 0.3$ are quasars).

iv) Some steep-spectrum compact sources are identified with quasars. Variability is a valuable extra indicator in this case.

GALAXIES

i) Very few compact flat-spectrum sources are identified with galaxies.

ii) Essentially all complex or FRI sources are identified with galaxies.

iii) Most moderate luminosity ($P_{408} = 10^{24} \rightarrow 10^{28}$ $WHz^{-1}sr^{-1}$) FRII sources are identified with galaxies. About half of the powerful FRII sources are identified with galaxies, particularly those with weak or undetected central components.

iv) Some steep-spectrum compact sources are identified with galaxies, but the detection of variability makes this highly unlikely.

v) Strong emission-line spectra are found much more frequently amongst powerful radio galaxies than is the case for normal galaxies. Hine & Longair (1979) found a correlation between radio luminosity and the likelihood of strong emission lines - for low radio

luminosities (ie FRI type sources), only 10 → 15% of radio galaxies exhibit strong emission-line spectra, whilst at the highest radio luminosities (ie FRII sources) this fraction reaches 70%. Some radio galaxies exhibit broad emission lines and hence may be regarded as quasar-galaxy hybrids.

Two obvious questions are, firstly, what is the relation between radio quasars and radio galaxies, and secondly, what is the difference between radio-loud and radio-quiet quasars. One of the best established, and as yet unexplained, facts about radio galaxies is that all powerful radio sources are housed in ellipticals and not spirals. This may provide a clue to the answers to these questions, since it leads naturally to the hypothesis that the host galaxies of radio-loud quasars are ellipticals, while their radio-quiet counterparts might be housed in spiral galaxies, just as Seyferts are known to be. Peacock *et al.* (1986) have shown that such a two-population model of quasars can explain the observations of samples of optically- and radio-selected quasars, and that the almost universally accepted radio-optical correlation for quasars (Schmidt 1970) is not in fact necessary to explain the data. The ultimate confirmation of this idea must of course come from imaging and spectroscopy of the host galaxies themselves - there is already preliminary evidence that radio-loud quasars lie in brighter galaxies then radio-quiet QSOs (Hutchings *et al.* 1984) and that the profiles of these galaxies suggest that they are indeed ellipticals (Smith *et al.* 1986).

1.4 THE EVOLUTION OF THE RADIO-SOURCE POPULATION

1.4a : Source counts

Given the fact that the radio sources described above are clearly violently active objects, and also the evidence presented in Section 1.2 that the Universe as a whole is evolving, it would be rather a surprise if radio sources did not display evolution with cosmic time. Evidence for the existence of evolution of the number density of bright radio sources was found as early as the 1960s, from the observed variation of radio-source counts with flux density. A recent

compilation of source counts at different frequencies from Kellermann & Wall (1987) is shown in Figure 1.2. The observations are plotted as differential counts of the number of sources n in the flux density interval ΔS as a function of flux-density S. The counts have been normalized to the prediction of a static Euclidean world model in which it is expected that, for a uniform distribution of sources, $n_o \propto S^{-2.5}\Delta S$. In the case of a Friedmann Universe (see Section 1.2a) it is expected that, for a uniform distribution of sources, the function n/n_o should be a monotonically decreasing function of decreasing flux density. The feature of these counts which is therefore inconsistent with a uniform distribution of sources in any realistic Universe is the rise in n/n_o down to flux densities ~ 1Jy. This excess of "faint" sources is model-independent evidence of evolution in the radio-source population. At lower flux densities, $S < 0.1$Jy, the counts begin to converge as expected for Friedmann models, but the rate of this decline is slower than is expected for reasonable values of H_o and q_o, thus providing further (but this time Friedmann model-dependent) evidence of an excess of faint sources. At the very lowest flux densities there is some evidence for flattening of the counts, possibly associated with a population of very weak radio galaxies associated with mildly active objects such as IRAS galaxies. Such faint radio objects will be of little importance in the present study.

The first information concerning the form of the evolution was derived by Longair (1966) who showed that, given the known wide range of radio-source luminosities, the sharpness of the peaks in Figure 1.2 could only be reproduced if the powerful sources alone changed their comoving densities - ie the evolution had to be differential in luminosity.

1.4b : The V/V_{max} test

Following this initial discovery of evolution, a more direct way of investigating the change in comoving density with redshift was devised in the form of the V/V_{max} test (developed independently by Schmidt 1968 and Rowan-Robinson 1968). V is the cosmological volume

Figure 1.2 : The normalised differential counts of radio sources at frequencies of 0.4, 1.4, 2.7 and 5 GHz (Kellermann & Wall 1987). The detailed references to the sources of the data are given in the paper by Kellermann and Wall. The normalizations of the counts are as follows: 0.4GHz, n_o = 1125 $S^{-1.5}$; 1.4GHz, n_o = 225 $S^{-1.5}$; 2.7GHz, n_o = 150 $S^{-1.5}$; 5GHz, n_o = 60 $S^{-1.5}$.

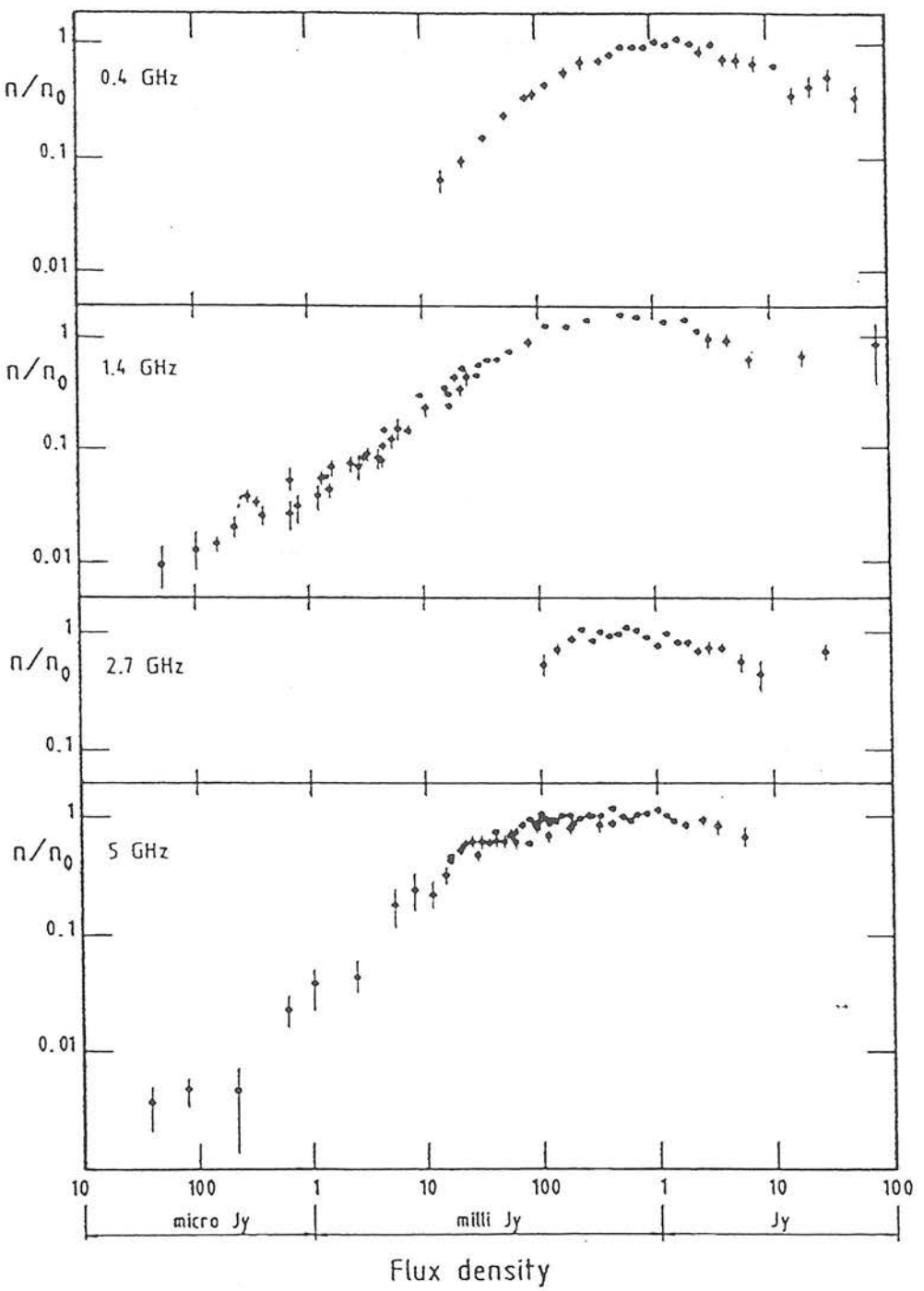

enclosed by an object and V_{max} is the volume that would be enclosed by that same object if it were pushed out to the flux density limit of its parent sample. Under the null hypothesis of uniform distribution in space, the individual values of V/V_{max} for objects in a flux-limited sample should be uniformly distributed between 0 and 1, and $\langle V/V_{max} \rangle$ should be $0.5 \pm (12N)^{-0.5}$, where N is the number of objects in the sample. Values of $\langle V/V_{max} \rangle > 0.5$ indicate a bias of objects towards the more distant regions of their accessible volumes, and hence correspond to an increase in comoving density with redshift.

The problem with the application of the V/V_{max} test is that a redshift is required for every source in the sample - only in a static Euclidean Universe can V/V_{max} be determined simply from the flux density of a source. Because of this, the V/V_{max} test has historically mainly been applied to samples of quasars (both radio- and optically-selected) for which redshifts are relatively easily obtained. In his review of the field of radio source evolution, Wall (1983) provides a useful collection of V/V_{max} results obtained from various quasar samples and one galaxy sample (from the 3CR survey). The important results can be summarized as follows:

i) In all cases the values of V/V_{max} were found to exceed 0.5, but not always by 1 sigma.

ii) Samples of optically-selected QSOs and steep-spectrum radio quasars were all found to display strong positive evolution, with $0.65 < \langle V/V_{max} \rangle < 0.75$. As demonstrated by Longair (1978) such values imply an increase in density of a factor ~1000 between the present-day and $1 < z < 3$.

iii) The one available sample of radio galaxies with complete redshift information, the 3CR galaxy sample, also displays significant positive evolution, but only at high radio luminosity - ($\langle V/V_{max} \rangle = 0.61$ for $P_{178} > 10^{26}$ WHz^{-1}sr^{-1}, $\langle V/V_{max} \rangle = 0.52$ for $P_{178} < 10^{26}$ WHz^{-1}sr^{-1}).

iv) In the case of the flat-spectrum radio quasars found in high-frequency surveys, early workers found relatively low values of V/V_{max}, compared to the values obtained for steep-spectrum surveys

of similar depth (eg Wills & Lynds 1978). It was thus originally believed that the flat-spectrum population did not evolve as strongly. However, it has since been established (eg Peacock & Gull 1981) that the flat-spectrum population does display strong, positive, differential evolution. The origin of the apparent discrepancy between this result and the early V/V_{max} results is that the flat-spectrum counts turn over at higher flux densities than the steep-spectrum counts - V/V_{max} values for brighter flat-spectrum samples reveal the evolution. This tendency for $\langle V/V_{max} \rangle$ to increase with increasing flux density is additional evidence of the need for differential evolution.

1.4c : The evolving Radio Luminosity Function

Thus, simply on the basis of the source counts and the V/V_{max} test, it is possible to conclude that both steep- and flat-spectrum radio sources display positive, differential evolution with redshift. However, a more detailed description of evolution is clearly desirable - ideally a complete description of the variation of both the numbers and properties of the different classes of object described in Section 1.3. A more realistic aim is to consider the change with epoch of the number of sources having a given radio luminosity - ie the Radio Luminosity Function (RLF). Such an approach is useful in that the luminosity of a source is often indicative of its physical type. The one direct attempt at sub-classification is to consider separately the evolution of the steep- and flat-spectrum populations (see Section 1.3). The subject of interest is therefore the evolving RLF which is often factorised as follows:

$$\rho(P,z) = \rho_o(P)E(P,z) \qquad (1.9)$$

where ρ_o is the RLF at the present epoch and the function E is called the evolution function. The latter is the important quantity, since it contains information about the creation and evolution of radio sources.

If redshifts were available for all the sources which contribute to

the counts shown in Figure 1.2, it would be possible to calculate the evolving RLF directly by simple binning in luminosity and redshift. However, because the redshift content of surveys is generally only complete at high flux densities, the coverage of the P-z plane is still rather poor. As a result of this, in order to make maximum use of all the available information, most of the recent work on the evolving RLF has concentrated on the technique of model fitting.

1.4d : Modelling of the evolving RLF

The value of using model fitting to study the RLF is that it enables maximum use to be made of all the available data. A consistent model can extrapolate the trends observed in well-defined regions of the P-z plane into less well-defined areas, and moreover the form of this extrapolation is constrained by less complete data such as source counts and identification statistics.

The early work in this field was reviewed by Peacock & Gull (1981), and generally involved fitting a parameterized analytic guess for ρ to the data. This approach culminated in the work of Wall, Pearson & Longair (1980, 1981). Wall *et al.* (1980) considered 408MHz data only, and assumed that all powerful sources displayed the same form of evolution - either $E \propto (1+z)^n$ (power-law evolution) or $E \propto \exp(m\tau)$ (exponential evolution, where τ is the normalized look-back time, $\tau = 1 - t/t_o$). Differential evolution was introduced by assuming that this evolution applied only to sources with 408MHz luminosities in the range $10^{25} \rightarrow 10^{27}$ $WHz^{-1}sr^{-1}$. The parameters n and m, and the critical luminosity range, were adjusted until the best fit was found to the available data. The exponential models were successful, but the power-law models did not achieve an acceptable fit to the data, although good qualitative agreement was obtained upon the introduction of a redshift cutoff at $z \sim 3$. Wall *et al.* (1981) extended this approach to consider source counts at 2700MHz, and the evolution of the flat-spectrum population.

Since then the most important modelling work has been carried out by Peacock (Peacock & Gull 1981, Peacock 1985) and Condon

(1984). The main drawbacks of the studies by Wall *et al.* were the poor quality of the high-frequency data, and the fact that their guessed parametric models gave no indication of the possible range of acceptable RLFs. Both these shortcomings were removed by Peacock & Gull (1981). Firstly they had at their disposal improved luminosity information at high frequencies due to extensive identification work on the 2.7 GHz Northern Sky Survey of Peacock & Wall (1981). Secondly, they introduced a truly free-form approach to modelling the RLF, which did not require any analytic guess of the form of the evolution. In addition, an ensemble of these model RLFs were considered in order to give some indication of what range of RLFs were allowed by the data. This approach to modelling the RLF is used in Chapter 6, and is thus described in detail in that chapter. The most important result of Peacock & Gull's study was the confirmation of strong, differential evolution for the flat-spectrum population, a result which had not been found by Wall *et al.* (1981), and which had hitherto been rather controversial (see Section 1.4c).

The existence of strong differential evolution in both populations was confirmed by Condon (1984), but in this case only one model was considered. Condon showed that he could construct a consistent RLF which underwent a combination of density and luminosity evolution:

$$\rho(P,z) = g(z)\rho(P/f(z)) \qquad (1.10)$$

Since neither g nor f depend on power, Condon stated that differential evolution was not required. However, because the RLF is strongly curved, simply shifting it about with redshift changes ρ by a larger amount at high power - ie differential evolution in the normal sense. This is an important point to remember since, in Section 6.5, it is shown that pure luminosity evolution is in fact an acceptable model of the evolving RLF - such a model is still consistent with differential evolution.

1.4e : Evolution at high redshift

All of the above has been concerned with the positive evolution exhibited by the radio source population out to $z \sim 2$. The question

of what happens to the RLF beyond this redshift is the main subject of this thesis. In particular the aim is to determine whether there is any definite evidence for a "redshift cutoff" at high z, which might represent the epoch of radio source, or even galaxy, formation. Until recently, as shown by Peacock & Gull (1981), it has not been possible to constrain the form of the RLF at $z > 2$, simply because no detailed redshift information was available for samples fainter than $S_{2.7} > 1.5$Jy. The first improvement in this situation was achieved by Peacock (1985) who, by the addition of a small $S_{2.7} > 0.5$Jy sample of flat-spectrum sources to the database of Peacock & Gull, found the first evidence for a decline in the flat-spectrum RLF beyond $z \sim 2$. This improvement in the flat-spectrum data was only possible because such a large fraction of flat-spectrum sources are quasars for which redshifts are relatively easily obtained. No corresponding improvement in the steep-spectrum data was available to Peacock (1985) and so the high-redshift evolution of steep-spectrum sources remained undetermined.

To constrain the high-redshift evolution of the whole RLF, redshift information is required for a radio sample which is sufficiently deep to sample the RLF out to redshifts $z \sim 4$. The observational work described in this thesis was undertaken to improve the identification and redshift content of just such a sample - the $S_{2.7} > 0.1$Jy Parkes Selected Regions. The status of this radio sample prior to commencement of the present study is summarized in Section 1.7. The new observations are described in Chapters 2, 3 and 4, and then the resultant database is assembled in Chapter 5. Then, in Chapter 6, the impact of this new information on the high-redshift form of the RLF is investigated.

1.5 : THE SPECTRAL EVOLUTION OF GALAXIES

When compared to the violence of radio sources, galaxies appear to be rather passive, unchanging systems. However, there are various pieces of observational evidence, and various lines of theoretical argument which indicate that galaxies must also evolve with cosmological time. The two most important aspects of galaxy evolution

are Dynamical evolution and Spectral evolution, although other properties such as gas content and chemical composition are also expected to change. Dynamical evolution involves the collapse and formation of the galaxy, and the resultant distribution of light and mass. At present this area is poorly understood. In particular, it is not known at which stage in its evolution the morphological type of a galaxy is determined. Spectral evolution is concerned with how the stellar population of a galaxy, and hence observable features such as galaxy spectrum, colour and luminosity change with cosmological time. It is not clear to what extent these two types of evolution are connected. For instance, it would seem very likely that dynamical evolution has a strong influence on the initial stages of star formation. In addition, the subsequent star formation history might also be influenced by interactions and mergers.

In this thesis only spectral evolution will be investigated. Good reviews of this field are given by Bruzual (1985) and Spinrad (1986). Observationally this is possibly the easier of the two aspects of evolution to investigate, since information can be gained simply from photometry (rather than imaging) of high redshift galaxies. The present study is also further restricted to the spectral evolution of only elliptical galaxies. This is an inevitable consequence of the fact that the galaxies considered here are radio galaxies. However, it is also true to say that most work on spectral evolution has concentrated on early-type galaxies because, at the present day, they seem to be relatively simple systems in comparison to the much more actively star-forming spirals (see eg King & Ellis 1985, Guiderdoni & Rocca-Volmerange 1985, for studies of the evolution of spiral galaxies).

Interest in the spectral evolution of elliptical galaxies was first aroused when it was realised that evolutionary effects could systematically bias attempts to determine q_o from the Hubble diagram (eg Gunn & Oke 1975). It is now well established (from eg spectral features) that the light of nearby ellipticals is giant-dominated throughout the visible and near-infrared regions of the spectrum. Elliptical galaxies in the past are thus expected to be both brighter and bluer, since the young galaxy must have been dominated by hot,

bright, young main-sequence stars. There are various ways of selecting distant elliptical galaxies to investigate this behaviour. These include selection of distant clusters (eg Oke 1984), faint red field galaxies (Koo 1985, Hamilton 1985) or radio galaxies (eg Lilly & Longair 1984, Lebofsky & Eisenhardt 1986, Windhorst *et al.* 1986).

Observational evidence that galaxies were indeed brighter in the past has come from various areas. Both the optical (eg Yoshii & Takahara 1987) and the infrared (Lilly & Longair 1984) Hubble diagrams give unfeasibly large values of q_o if luminosity evolution is ignored. There is also evidence of luminosity evolution in the galaxies around quasars at $z \sim 1$ (Tyson 1986) and from faint galaxy number counts (eg Tyson & Jarvis 1979, Shanks *et al.* 1984, Hall & Mackay 1984).

The question of colour evolution has been rather more controversial, partly because of the uncertainty in the form and origin of the typical UV spectrum of nearby elliptical galaxies (see Chapter 7, Section 7.2). Basically it is agreed that at least <u>some</u> ellipticals were bluer in the past (eg McLaren *et al.* 1987, Koo 1986a), but evidence has also been presented (Hamilton 1985) which indicates that there are also galaxies which still show little or no evidence of evolution by $z \sim 0.8$.

At present the only available probes of galaxy evolution at redshifts $z > 0.8$ are radio sources. This is an important point to bear in mind. Although there are good reasons for believing that the properties of these galaxies are not strongly biassed by the fact that they are radio sources, one has to be cautious in extrapolating any conclusions to elliptical galaxies in general. However it should be possible to check for the existence of any effects of radio bias by comparing the spectral evolution of the powerful 3CR radio galaxies with the evolution of galaxies of lower radio luminosity. The radio galaxies in the Parkes Selected regions provide an opportunity to do this, since they are a factor ~ 10 less luminous than 3CR galaxies at the same redshift. The colour evolution of the radio galaxies in the Parkes Selected Regions is investigated in Chapter 7, with the help of theoretical models of spectrophotometric evolution developed by

Guiderdoni & Rocca-Volmerange (1987).

1.6 : AIMS AND LAYOUT OF THE THESIS

The principle aims of this study are as follows:

i) To determine unambiguously the existence or otherwise of the high-redshift cutoff for both steep- and flat-spectrum radio sources

ii) To investigate the spectral evolution and star-formation histories of radio galaxies which have fainter radio luminosities than the extreme 3CR sources, and thus might be more representative of the general elliptical galaxy population.

These problems have been addressed by carrying out extensive optical and infrared observations of sources in the $S_{2.7} > 0.1$Jy Parkes Selected Regions radio sample. This sample was chosen for study because it is sufficiently deep to sample the bright end of the radio luminosity function out to $z \sim 4$, and also because, being a high frequency sample, it contains significant numbers of both flat- and steep-spectrum sources. The detailed study of such a sample is a long term project, and a considerable amount of work had already been carried out by other workers prior to commencement of the present study. The author is indebted to these workers for laying the foundations for this work, and the status of the sample which he inherited is reviewed in the next section, Section 1.7.

Chapters 2, 3 and 4 describe the new observations and results. Chapter 2 describes the CCD imaging which was carried out in order to discover the missing optical identifications, and to obtain B and R photometry for these faint objects. Chapter 3 is concerned with the infrared photometry of the radio source identifications, while Chapter 4 describes the spectroscopic observations which were undertaken to improve the redshift content of the sample.

In Chapter 5 the complete Selected Regions database is assembled (by combining the new data with the existing information) and its

properties discussed. Particular attention is drawn to the most distant object in the sample - PKS 1351-018.

Analysis of the data is carried out in Chapters 6 and 7. Chapter 6 investigates the impact of the new data on the high-redshift form of the RLF in an attempt to achieve aim i) above. Chapter 7 addresses aim ii) by comparing the observed colour evolution of the radio galaxies in the Parkes Selected Regions with the results of recently developed models of galaxy spectral evolution.

Finally, Chapter 8 considers some of the possible ways in which the results of Chapters 6 and 7 might be closely connected, and how the evolution of radio sources might be related to the evolution of quasars and galaxies in general.

1.7 : THE PARKES SELECTED REGIONS RADIO SAMPLE

The aim of this thesis is to investigate the high-redshift behaviour of powerful radio sources. This is best done by studying a radio sample selected at intermediate flux density, rather than a very faint survey. The reason for this is that an object at $z \sim 4$ should appear $\sim 10 \rightarrow 15$ times fainter than if it were at $z \sim 1$. An intermediate level sample is therefore capable of probing the interesting redshift range $z = 3 \rightarrow 4$ for powerful "3CR-type" sources. In contrast, very faint radio samples will inevitably be dominated by low luminosity sources because very powerful objects should be found at $z \sim 10$, by which stage the cosmological volume element is so small that, even if they existed, very few such sources would be seen.

The sample which was therefore selected for the present study is the Parkes Selected Regions. This radio sample was first defined by Wall, Shimmins & Merkelijn (1971) as consisting of 188 sources with $S \geq 0.1$Jy at 2.7GHz. The regions themselves are six 6.5^{o}-square areas of sky (each roughly the size of one Schmidt plate) providing a total sample area of 0.075sr.

The detailed study of this sample was commenced by Downes *et al.* (1986) and the present study represents an extension of their work. Downes *et al.* investigated all the sources in the sample with the VLA, and then, with the assistance of the resulting radio maps, carried out an extensive optical identification search using Schmidt-plate material. The result of this study was the rejection of 10 sources due to confusion, and the identification of 56% of the remaining 178 sources down to a limiting magnitude of V ~ 21.

A detailed description of the properties of the sample as given by Downes *et al.* is not repeated again here, since many of these are reassessed in Chapter 5 in the light of the new observations of Chapters 2, 3 and 4. However, since the present study contains no radio observations, the radio properties of the sample remain unchanged from Downes *et al.* and are therefore summarized below in Table 1.1

Table 1.1 : Radio structures in the Parkes Selected Regions. Full descriptions of the radio structure abbreviations used throughout the thesis are given in Appendix A.

	Complete sample	Steep-spectrum sources $\alpha \geq 0.5$	Flat-spectrum sources $\alpha < 0.5$
Total number of sources	178	137	41
FR class I	12 = 7%	11 = 8%	1 = 2%
FR class II	101 = 57%	94 = 69%	7 = 17%
U+Di	5 = 3%	3 = 2%	2 = 5%
U	34 = 19%	8 = 6%	26 = 63%
P	25 = 14%	20 = 15%	5 = 12%

As noted by Downes *et al.*, there are several obvious differences between the radio properties of the Selected Regions sample, and that of the brighter samples defined at the same frequency. Firstly, 41 of the 178 sources (ie 23%) in the Selected Regions have flat spectra.

This fraction is lower than that found by Peacock & Wall (1981) for their 1.5Jy sample (30% of which have flat spectra). Such a difference is expected because 0.1Jy is well below the peak of the flat-spectrum counts. Secondly, for the compact sources in the Selected Regions, the steep/flat-spectrum ratio is roughly 1:1. This ratio is nearer 1:2 in the brighter sample of Peacock & Wall. In addition, the fraction of steep-spectrum sources which are compact is also smaller in the Selected Regions (21% in Table 1.1, versus 31% from Peacock & Wall). Thus, in decreasing the flux limit from 1.5 to 0.1Jy, both flat- and steep-spectrum compact sources have become relatively less numerous. Thirdly, and most importantly, the FRII:FRI ratio has increased from 3:1 to 8:1. This large proportion of FRII sources provides direct evidence that the Selected Regions sample is dominated by powerful sources at high redshift.

The complete revised version of the Selected Regions sample (after incorporation of the new data described in the following three chapters) is given at the end of the thesis in Appendix A, Table A.1.

Chapter 2 : DEEP OPTICAL IDENTIFICATIONS AND CCD PHOTOMETRY OF SOURCES IN THE PARKES SELECTED REGIONS

2.1 : INTRODUCTION

The virtues of completeness, freedom from galactic contamination, and the power to probe high redshift space make studies of cosmological evolution in the radio rather more attractive than in other wavebands. However, because redshifts cannot be determined from the essentially featureless radio spectra of active galaxies, a somewhat arduous route must be followed to find the spatial distribution of radio sources. This route involves :

i) Selecting the radio sample

ii) Mapping each source at radio wavelengths to accurately define the expected position of its optical counterpart.

iii) Making an initial search for optical identifications using existing plate material.

iv) Taking deep CCD exposures to find those optical identifications which remain undetected at the limiting magnitudes of the plates.

v) Measuring the optical spectrum of each source and hence determining its redshift.

For any sample large enough to be statistically useful this process requires large amounts of observing time. In particular, genuine completion of step v) is rarely a feasible proposition, and some fraction of the redshifts must be estimated photometrically.

In the case of the Parkes Selected Regions, steps i) -> iii) have been completed and reported by Downes *et al.* (1986). In summary :

i) The sample consists of six 6.5^{o} - square areas of sky surveyed to a depth of 0.1 Jy at 2.7 GHz, and contains 178 sources after

correcting for confusion.

ii) All the sources were mapped with the VLA, enabling the positions of expected optical counterparts to be defined to < 1 arcsec (for sources with a central component). This greatly reduces the possibility of mis-identifications.

iii) Optical identifications for 56% of the sources were found by searching existing Schmidt plate material (with the COSMOS measuring machine), reaching a limiting magnitude of $V \approx 21$.

This chapter is concerned with the completion of the optical identification programme using deep CCD observations (ie step iv), and also with the accurate measurement of B and R magnitudes for these faint objects. The optical photometry is important for a number of reasons. Firstly, although recent work has greatly increased the redshift content of the sample (see Chapter 4), obtaining optical spectra for a significant number of the faintest identifications requires a prohibitive amount of observing time with present day technology. It is therefore necessary to resort to multi-colour photometry to determine the nature of the faintest identifications, and to estimate their redshifts. Multi-colour photometry also provides a means of studying the evolution of the stellar populations in the radio galaxies, and hence determining the ages of these objects. The multi-colour data set was achieved by combining the results of the optical photometry, described in this chapter, with the infrared data discussed in Chapter 3.

2.2 : THE OBSERVATIONS

2.2a : Acquisition of the data

The bulk of the CCD observations were made during 3 observing runs in 1985, two at the Anglo Australian Telescope (AAT) (in April 1985 and September 1985) and one at the University of Hawaii 88-inch Telescope (in August 1985). These 3 runs provided a total of 8 nights devoted to CCD imaging, essentially all of which were photometric. In

addition a small number of useful frames were obtained from two less successful runs at the same telescopes, one at the AAT in June 1984 (observations made by Dr. John Peacock and Dr. Ann Downes) which was almost completely wiped out by cloud, and half a night of imaging at the 88-inch telescope in January 1985 (observations made by John MacKenty).

2.2b : The instruments

The CCD data thus consist of exposures taken with two distinct cameras.

At the Anglo Australian Telescope the instrument used was the RGO CCD camera which is based on an RCA SID53612 chip, thinned and back illuminated. It has 320 × 512 pixels, each 30 microns square. The estimated quantum efficiency is 80% at peak (4000 → 7000Å) and about 50% at 3600 and 8000Å. Readout noise is about 70 electrons rms per pixel, while dark current at the usual operating temperature is approximately 0.1 electrons/pixel/second. The saturation level is around 1.6×10^5 electrons and digitisation of the charge results in 1 A/D level corresponding to approximately 15 electrons. The camera is mounted at the f/3.3 prime focus of the 3.9m telescope, giving an image scale of 0.49 arcsec per pixel.

At the Hawaii 88-inch Telescope the instrument used was the Galileo/Institute for Astronomy CCD camera. The detector used in the system was a Texas Instruments three-phase CCD, thinned and back illuminated. It has 500 × 500 pixels, each 15 microns square. The estimated quantum efficiency is 75% at peak (4000 → 7000Å) and about 60% at 3500 and 7500Å. Readout noise has been measured at 25 electrons rms per pixel, while dark current is approximately 0.05 electrons/pixel/second. However, in order to improve its blue response and cosmetic properties, the chip is normally flooded with UV light prior to the first night of observation, and this results in a somewhat higher initial dark current which decays exponentially over a period of several hours. The saturation level is around 40000 electrons and digitisation of the charge results in 1 DN (Data

number) corresponding to 2.5 electrons. The camera is mounted at the f/10 Cassegrain focus of the 2.2m telescope, normally resulting in a pixel scale of 0.14 arcsec. However, for the observations described in this chapter, a focal reducer (constructed by Dr. Alan Stockton of the Institute for Astronomy) was used which produces an image scale of 0.42 arcsec per pixel.

The low readout noise of the TI CCD, combined with the good seeing on Mauna Kea meant that, at least in R, both systems were comparable in their ability to detect objects at faint magnitudes, despite the smaller aperture of the Hawaii telescope. Also, the RCA chip displayed severe fringing at red wavelengths due to thin film interference, a problem which was not present in the TI detector. However, detections in B were found to be much more easily achieved at the AAT because the optics of the focal reducer used on the Hawaii 88-inch Telescope impaired the blue response of the TI CCD.

At both telescopes the observations were made through Kitt Peak National Observatory Mould interference filters (KPNO 1983). The response curves of the B and R filters are shown in Figure 7.2 in Chapter 7.

2.2c : Observational procedure

The adopted observational strategy was to take an initial set of relatively short exposures (eg 300s at the AAT) in R of all the fields which had remained empty at the level of the Sky-Survey plate material. Any identifications lying within one magnitude of the plate limit could therefore be detected with minimal waste of observing time (~ 40% of the sky-survey empty fields were identified in these short exposures). Longer exposures in R were then taken of those fields which had still not yielded a positive identification. Subsequently each field was imaged in B, with the required exposure time estimate based on the ease of the initial detection in R. All of the B frames were taken at the AAT.

To calibrate the photometry, photometric standards in the same

fields as the target objects were observed regularly throughout each night. The standard stars observed are listed below in Table 2.1. Observations of a standard were generally made approximately 3 times per hour. In addition, at the AAT a 30min exposure in R of an area of blank sky was taken during each run to provide a calibration frame for removal of the interference fringes. Flat fields at both telescopes were made by illuminating the inside of the dome with an photoflood lamp and taking a series of short exposures through the relevant filters.

Table 2.1 : Photometric standard stars used to calibrate the optical photometry of the CCD identifications.

STAR NAME	RA	Dec	B mag	R mag	Literature reference
92 263	$00^h\ 54^m\ 54^s$	$+00^\circ\ 31'\ 26''$	12.83	11.22	Landolt (1983)
93 333	01 54 19	+00 41 20	12.84	11.54	" "
104 337	12 41 42	-00 29 21	11.98	10.77	" "
104 598	12 44 31	-00 11 42	12.58	10.81	" "
105 815	13 39 18	+00 02 23	11.84	11.19	" "
115 516	23 43 29	+01 09 13	11.46	9.87	" "
E 8.07	22 02 21	-19 05 02	12.72	11.94	Tritton *et al.* (1984)

2.2d : Data reduction

Reduction of the data was carried out on the ROE Starlink Vax 11/780. The raw data were converted to the final images by the standard procedure of :

i) Subtraction of the bias level from all image and calibration frames.

ii) Subtraction of the appropriate level of dark current from all frames, generally only significant for the longer integrations.

iii) Division of each image frame by the relevant flat-field frame.

iv) Cosmetic improvement of the final image by the removal of chip defects and cosmic rays.

Also, for the R band images taken at the AAT, the interference fringes had to removed by

v) Creation of a fringe frame by flat-fielding the blank sky exposures.

vi) Subtraction of an appropriately scaled version of the fringe frame from the R band image frames.

De-biassing of the Hawaii 88-inch frames was achieved by simple subtraction of the DC level calculated from the over-readout of the chip. However, for the AAT images a smoothed version of a bias frame had to be subtracted due to the presence of structure in the bias level which was visible on the final images. Dark current was found to be essentially insignificant on all images except those taken during the first night of the 88-inch run as the current decayed from the enhanced level produced by the UV-flood procedure.

2.3 : OPTICAL IDENTIFICATIONS - METHOD

2.3a : CCD astrometry

Except for a few unusually empty fields, the field of view covered by both CCD cameras was sufficiently large to contain several stars which were also visible on the sky-survey plates. These stars were thus suitable secondary astrometric standards, particularly since accurate positions for many of them had already been measured during the original Schmidt-plate search of Downes *et al.* (1986). Because the pixel scale was a known parameter, and because the CCD field of view was very small compared to that of a Schmidt plate, only the correct rotation and translation were required to match the

coordinate frame on the CCD to that of the appropriate region on the plate. Thus two adequately bright stars were sufficient to perform the astrometry, although in most cases several more were available (and were used). Using this procedure the positions of candidate identifications could be measured to an rms accuracy of < 0.6 arcsec.

For each field, astrometry was performed on the deepest available R frame, and also the deepest available B frame. Astrometry was also performed on both R frames whenever duplicate exposures had been taken at the two telescopes, a procedure useful for confirming the reality of the faintest identifications. In the few cases where a satisfactory identification was not found on the deepest available frame, all the exposures taken of that field were stacked together in an effort to reach still fainter magnitudes. Two further identifications were discovered in this way. Measurements were also made of a few additional CCD images which had been taken of fields in which there was reason to doubt the validity of the existing sky-survey identification.

2.3b : Selection of candidates

Once fitting of the coordinate frame had been achieved, calculation of the positions of any number of candidate identifications was a trivial process, and so positions were always measured for every optical object within roughly 30 arcsec of the radio position. This deliberately extravagant procedure ensured that the position of every possible candidate was measured. The problem then becomes one of selecting the best candidate and deciding if that object is in fact the correct identification.

For compact radio sources and extended sources where a compact core has been detected this is simple - the position of the correct identification and the compact component should coincide to within the measurement errors. As stated above, the measurement errors in the optical positions are < 0.6 arcsec, and in comparison with this the errors in the VLA positions are negligible. Therefore for this class of source a positional discrepancy of < 2.5 arcsec was required (allowing

~ 0.5 arcsec for systematic errors) for an acceptable identification, and, with such a small search area, the problem of multiple candidates did not arise.

Double sources with no central core present a more difficult problem. For Fanaroff-Riley class II sources, Laing *et al.* (1983) have shown that 96% of their optical identifications lie within 0.2θ of the midpoint of the line joining the two hotspots (where θ is the angular separation of the two hotspots). In the present study there is no need to consider the case of the other major class of extended source, Fanaroff-Riley class I, since all such sources in the sample were successfully identified at plate level by Downes *et al.* (1986). The above 0.2θ criterion was therefore taken as defining the expected position of the optical counterpart of all the extended sources of interest here (with an assigned r.m.s. deviation of 0.1θ). However, a large fraction (~ 1/3) of these double sources which escaped plate identification have very small angular sizes ($\theta \approx 4$ arcsec) so that the selection and measurement errors are comparable. In such cases the selection criterion is less important and, just as for the compact sources, the correct identification is usually both obvious and unambiguous.

2.3c : Probability of mis-identifications

To calculate the probability that each of the new identifications was in fact correct, and not merely a chance positional coincidence, it was decided to follow the method used by Downes *et al.* (1986). This decision was made for two reasons. Firstly there was the obvious advantage of continuity with the earlier work. Secondly, in contrast to the frequently used likelihood ratio method, this technique avoids the awkward problem of calculating unknown *a priori* probabilities. A brief recap the details of this method, and its application in the present context, is given below.

For a given candidate one wishes to calculate the probability that it could in fact be a member of the random background population. Consider a candidate of magnitude m, found a distance r from the

radio position. Then the expected number of objects brighter than the chosen one and lying within r of the radio source is simply

$$\mu = \pi r^2 N \qquad (2.1)$$

where N is the surface density of objects on the optical image brighter than m. The Poisson probability of there being at least one object is given by

$$P = 1 - \text{probability of no objects}$$

$$= 1 - \exp(-\mu)$$

which for $\mu << 1$ simplifies to

$$P \approx \mu \qquad (2.2)$$

It is important to be clear about what this means. Suppose we calculate such a probability for a chosen candidate and call it P^* ($\approx \pi r_*^2 N_*$). P^* is then the *a posteriori* probability of finding an object brighter than the observed one within the radius r_* of the radio source. However, P^* is not the same as the *a priori* probability of finding an object on the optical image with $P \leq P^*$. In fact many such objects could be present on the frame, each individually satisfying this criterion, and so we cannot simply say that the probability of our chosen candidate being the correct identification is $(1 - P^*)$.

The range of r within which $P \leq P^*$ is a function of magnitude, ie of surface density N, and so the expected number of objects on the frame with $P \leq P^*$ is

$$E = \int_0^{N_T} \pi r^2(N)\, dN \qquad (2.3)$$

where N_T = surface density at the magnitude limit of the optical image. For $P^* << 1$, we have $\pi r^2(N) = P^*/N$ and so E diverges logarithmically. However, in the present case there is an upper limit

to r in the form of the search radius r_s, and so r grows as $1/\sqrt{N}$ (as we reduce the magnitude from the limit of the image) until it becomes equal to r_s, after which it remains constant for all brighter magnitudes. The magnitude at which $r = r_s$ can be described in terms of a critical surface density N_c, where $P^* = \pi r_s^2 N_c = \pi r_*^2 N_*$ and so the integral becomes

$$E = \int_0^{N_c} \pi r_s^2 \, dN + \int_{N_c}^{N_T} \frac{P^*}{N} \, dN$$

$$= P^* \left(1 + \ln\left(\frac{P_c}{P^*} \right) \right) \qquad (2.4)$$

where $P_c = \pi r_s^2 N_T$. One can then calculate the Poisson probability $(1 - \exp(-E))$ that the object is in fact a chance coincidence.

For the sky-survey identifications of Downes *et al.* (1986) the correction factor $(\ln(P_c/P^*))$ was unimportant since P_c was generally small (~ 0.001). However, this is not always true for the deeper CCD identifications considered here, particularly for those sources with a large search radius ($P_c \approx 0.5$ for a search radius of 6 arcsec on a CCD image reaching a limiting R magnitude of ≈ 24).

In the present study it was only necessary to consider galaxy counts (whereas Downes *et al.* 1986 had to consider both galaxy and star counts) to estimate the surface density of background objects at various limiting magnitudes (ie N(m)). This is because, at the magnitudes of interest here, the stellar contribution to the total counts is negligible. The integrated galaxy counts in both B and R (from 19.5 to 25) were estimated using the data from Koo (1986a), Hall & MacKay (1984) and Shanks *et al.* (1984).

The final results of this probability analysis are included in the next section.

2.4 : OPTICAL IDENTIFICATIONS - RESULTS

Of the 178 sources in the complete selected regions sample, 78 remained unidentified following the plate search to V ≈ 21 by Downes *et al.* (1986). The new CCD imaging of these empty fields to R ≈ 24 has resulted in 70 new identifications, thus effectively completing (>95%) the optical identification of the sample. In addition a new identification has been discovered for one source, 1214-029A, which had previously been listed as a sky-survey identification. This single revision resulted from the CCD imaging of 8 fields in which there was reason to doubt the validity of the sky-survey identification - in the other 7 cases (0059+017, 0101+023, 0223+018, 0230-027, 0239-016, 2150-202 & 2155-202) the original identification was confirmed as correct, and the CCD data used to provide improved photometry (See section 2.6).

Of the 8 remaining empty fields, one (0240-027) is contaminated by a bright star which made deep exposures impossible. This leaves 7 radio sources whose optical counterparts must lie below the threshold of the present optical material (R ≈ 24, B ≈ 25). These sources (listed below in Table 2.2) are evenly distributed throughout the 6 selected regions and are all either partially resolved or small doubles. Note however that, as described in Chapter 3, four of these optical empty fields (0105+025, 0225+002, 2158-170, 2357-006) were in fact detected in the infrared.

Table 2.2 : The remaining optically unidentified sources (see Appendix A for a full description of the radio structure abbreviations).

SOURCE NAME	RADIO STRUCTURE	ANGULAR DIAMETER, θ
0043-003	Do,II	2 arcsec
0105+025	Do,II/D2?	2
0225+002	Do,II	4
1159-023	P	
1349-019	Do,II	2
2158-170	D2	2
2357-006	P	

For convenience, the results of all the observational work described in Chapters 2, 3 and 4 have been combined with the data from Downes *et al.* (1986) to form a single table (Table A.1, Appendix A) which summarizes all the available data on the selected regions. The positions of all the optical identifications (old and new) are presented in columns 7 and 8 of this table, while CCD finding charts for the new identifications (including 1214-029A) are shown in Plate 2.1. CCD images of the fields of the 7 remaining unidentified sources are presented in Plate 2.2. Also, for all the extended radio sources in the sample, Fig. 2.1 indicates the position of each optical identification (new and old) superimposed on the VLA map of its radio counterpart.

An attempt was made to classify each new identification as a "galaxy" or "quasar" on the basis of its optical morphology. However, in practice this could only be done reliably for the brighter CCD identifications. Thus, for many of the faint objects, the classification listed in column 10 of Table A.1 is based on the multi-colour data (see Chapter 5, Section 5.2a).

Additional notes on individual sources now follow:

0059+017

For this large double source the sky survey identification was confirmed as the best candidate and remains listed as the identification in Table A.1. However, this object appears to be stellar in appearance and if subsequent spectroscopy should reveal it to be a star we note here the existence of an alternative much fainter galaxy identification 18 arcsec South, 5 arcsec East of the existing identification.

0100+023

The radio-optical positional offset of 4.3 arcsec is larger than the adopted search radius for compact sources, but the object is still listed as an identification. This is because it is extended and possibly interacting with a nearby galaxy, and the positional discrepancy arises from ambiguity concerning the true centre of such a distorted object.

0223-018

The CCD imaging confirmed the two alternative sky-survey identifications as the only conceivable candidates. However, the NW object was found to be stellar in appearance, while the SE object is now listed as a probable galaxy.

1154-019

Two alternative identifications are listed in Table A.1. The confusion arises from the ambiguous nature of the upper radio component (see Fig 2.1). If this is in fact a core component rather than a radio lobe, then the first optical object is the correct identification.

1157+026

The radio-optical positional offset of 3.4 arcsec is larger than the compact source search radius, but the object is listed as an identification, in this case because of doubt over the accuracy of the astrometry. However, the object was only visible on the blue image, and this must be considered a potential mis-identification.

1214-029A

This is the one sky survey identification which was revealed to be incorrect as a result of CCD imaging. In fact the original identification proved to be a plate flaw as it was not present on either the blue or red CCD image (the original identification was found at the limit of the red plate, but was not seen on the corresponding blue plate). However, the CCD image did provide a new identification, whose position is given in Table A.1, and whose finding chart is included in Plate 2.1.

2150-202

The CCD image confirmed the sky survey identification, but its position has been revised by +2 arcsec in declination.

2158-177

The identification is the lower of two objects separated by only 2 arcsec in declination.

2355-024

The third compact source with an abnormally large radio-optical offset (4.6 arcsec) for which an identification is claimed. The discrepancy is due to difficulty in achieving accurate astrometry in

this field.

Finally, to determine the reliability of the CCD identifications, it is necessary to consider the results of the chance coincidence probability analysis described in section 2.3c. Because of the greatly increased background counts at faint magnitudes, it might have been expected that the predicted fraction of mis-identifications among the new deep CCD identifications would be considerably greater than the result found by Downes *et al.* (1986) for their sky-survey identifications. In fact this is not the case, with the total number of expected spurious objects among the 70 new IDs being $\Sigma E_i = 3$ (Downes *et al.* predicted 3 mis-identifications out of their 100 sky-survey IDs). The reason for this is that most of the radio sources which escaped plate identification have small angular sizes (the majority of large doubles in the sample are relatively nearby objects) and so the increase in background surface density is offset by a decrease in the average search area. Combining the ΣE_i for the new IDs with the ΣE_i deduced by Downes *et al.* for the brighter IDs leads to a prediction that ~ 6 mis-identifications are expected in the sample as a whole. However, the true figure is undoubtedly less than this since the CCD imaging of the sky-survey IDs which possessed the largest E values failed to reveal any other candidate identifications (with the possible exception of 0059+017).

Of the 70 new candidates, 64 are essentially certain identifications with $E \leq 0.05$. As expected, the 6 sources with high values of E (0245+013, 1154-019, 1345+008, 2204-182, 2353+010 & 2354+008) are all large double sources with no central component, and it is likely that any genuine mis-identification is associated with one of these. Since large double sources are unlikely to have $z >> 1$ these sources are not very important in the context of the study of high-redshift evolution.

Plate 2.1 : CCD images of the new optical identifications of radio sources in the Parkes Selected Regions. Each field is 2 arcmin square with north at the top and east to the left, and the identification is indicated by two bars.

0000-022

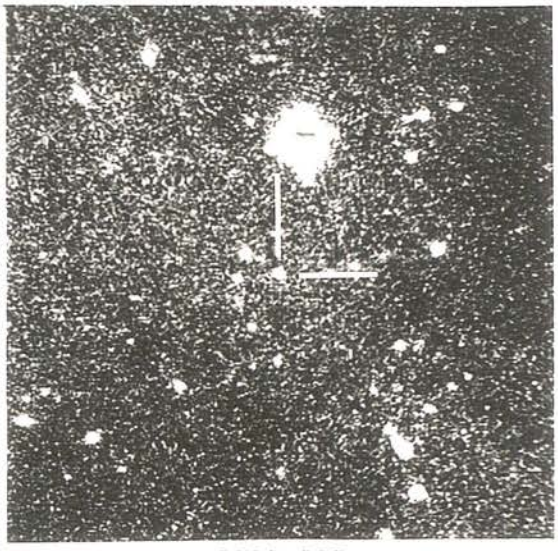

0000+035

0003+006

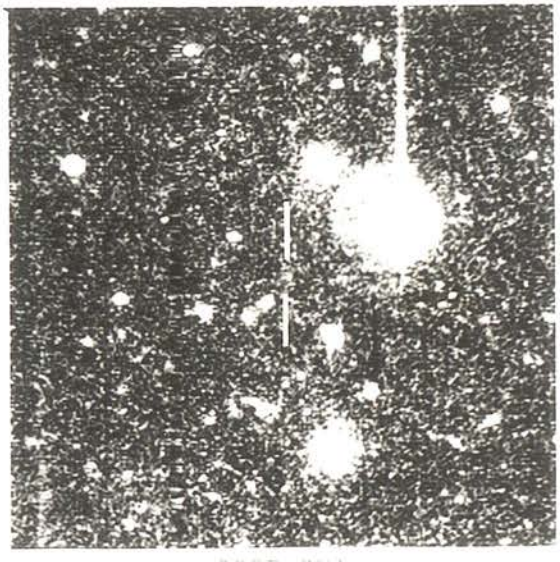

0005+021

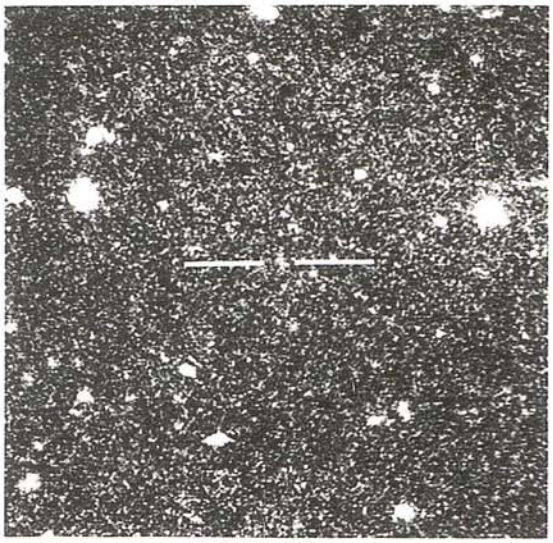

0008-006

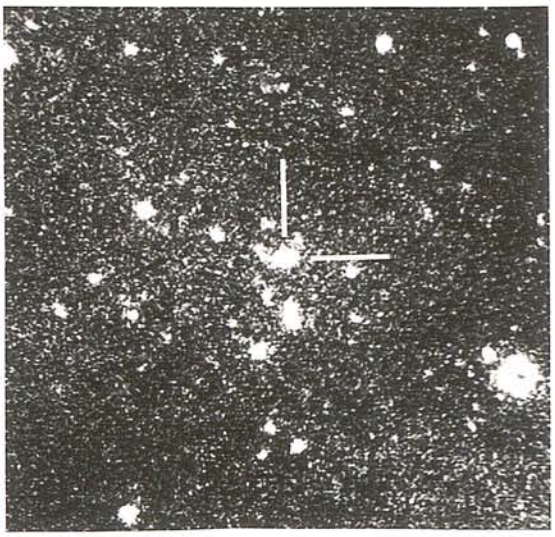

0010+005

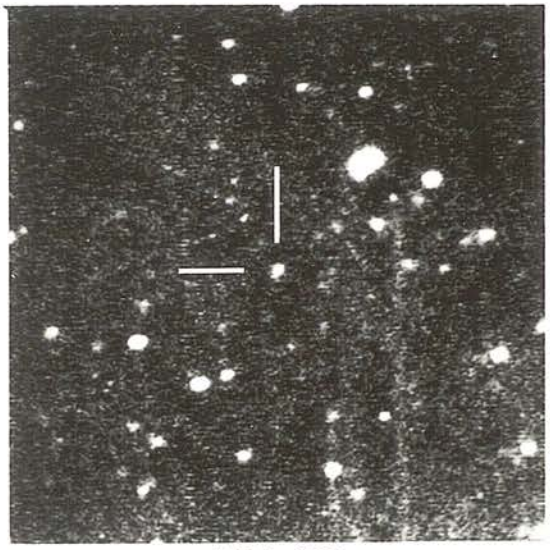

0011-023

0017+026

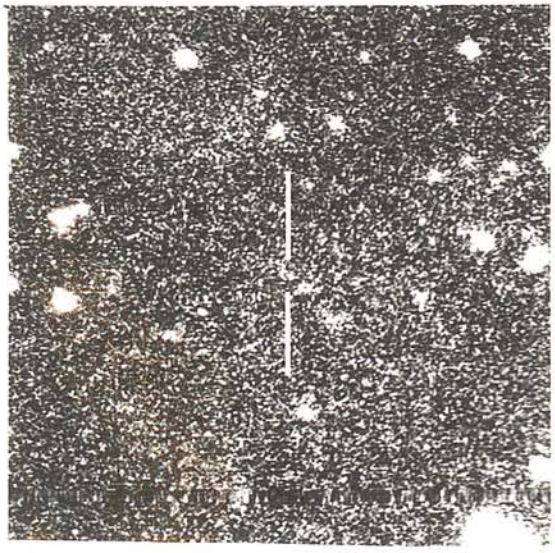

0043-010

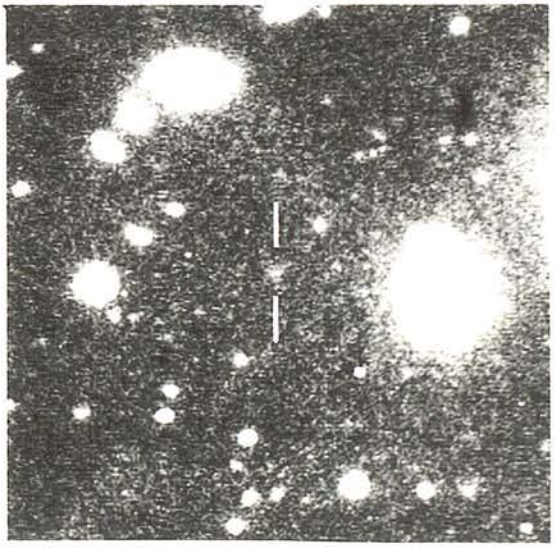

0043+000

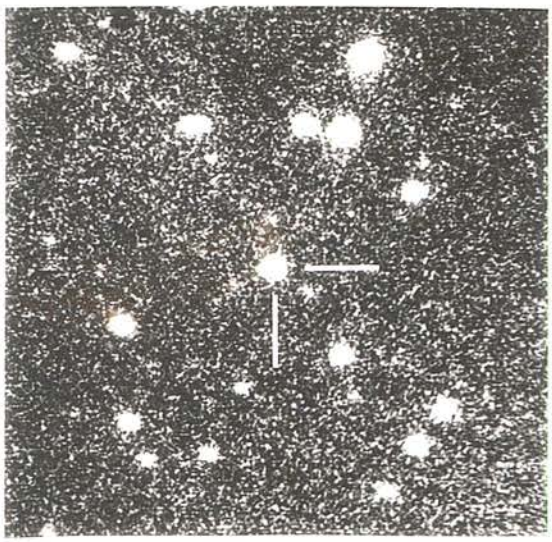

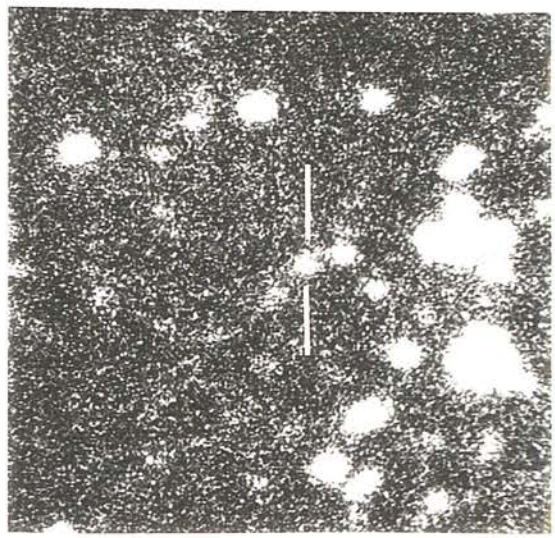

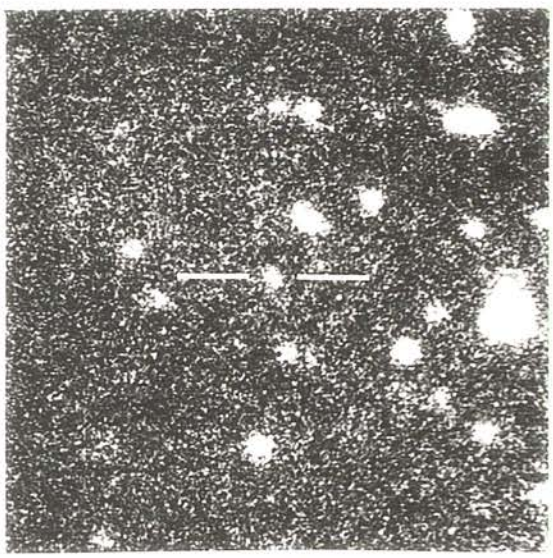

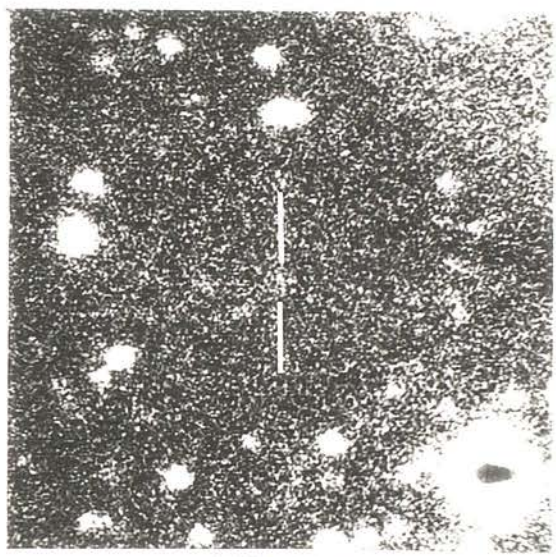

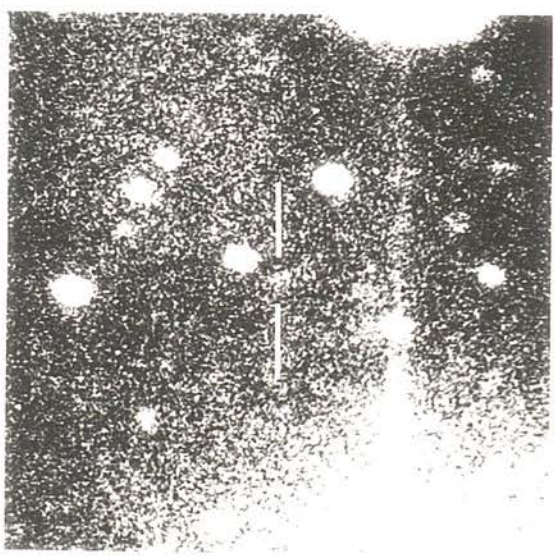

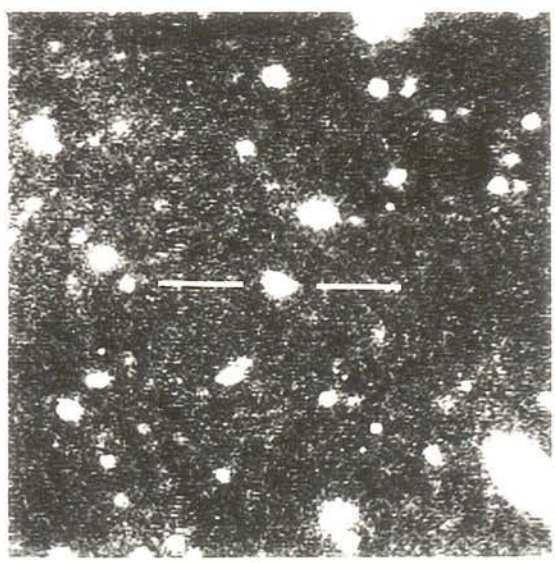

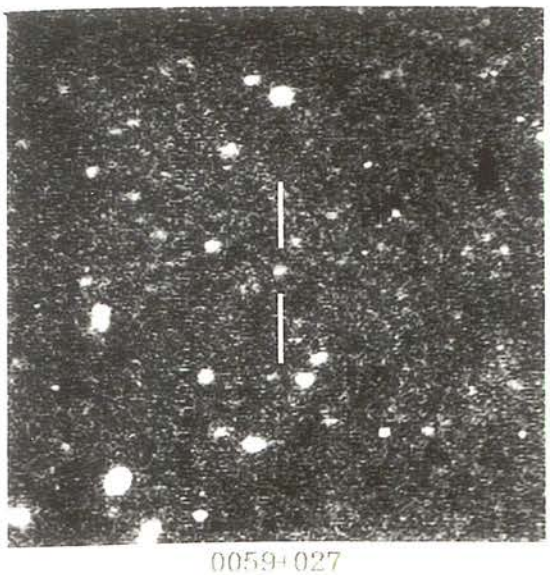

0059+027

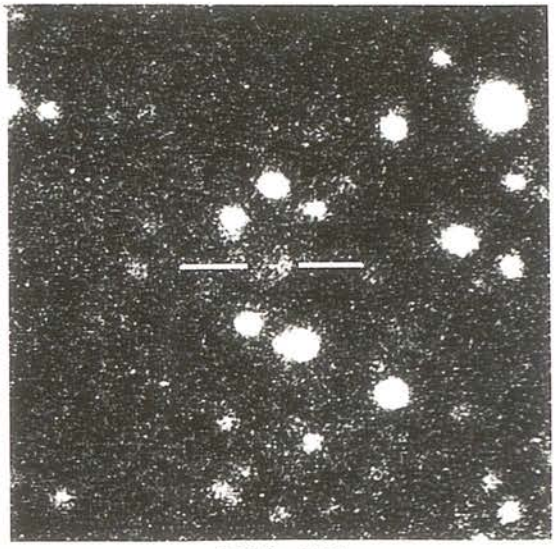

0100+023

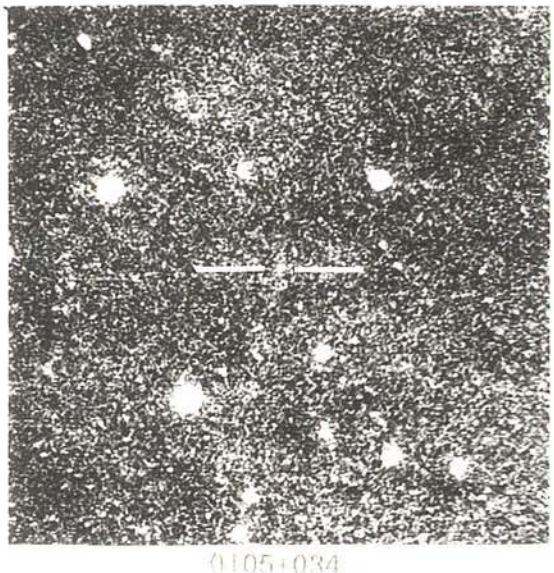

0105+034

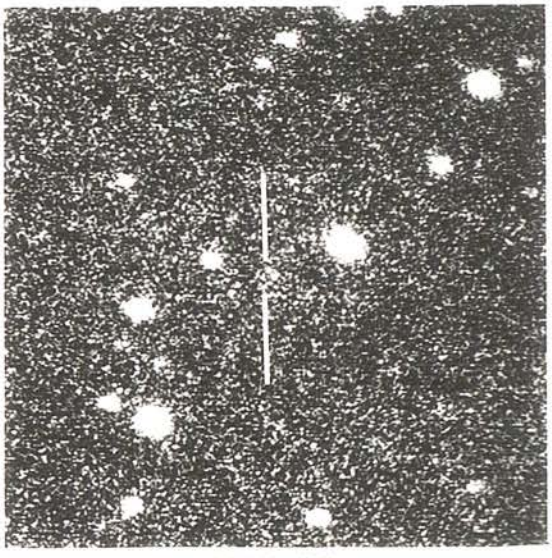

0220 023

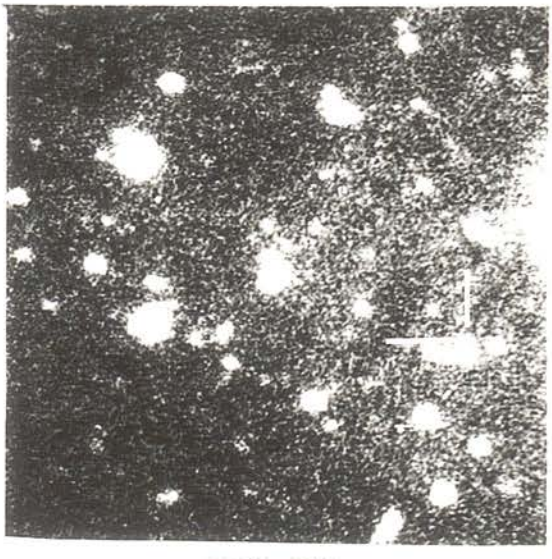

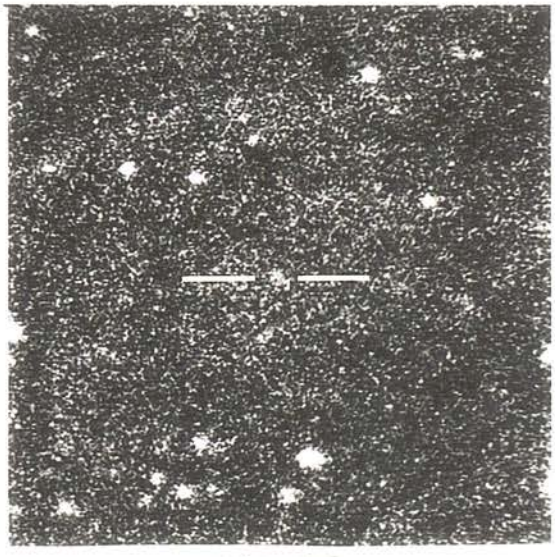

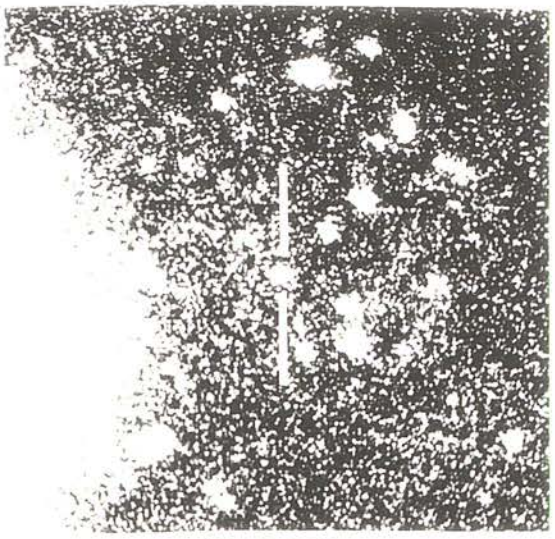

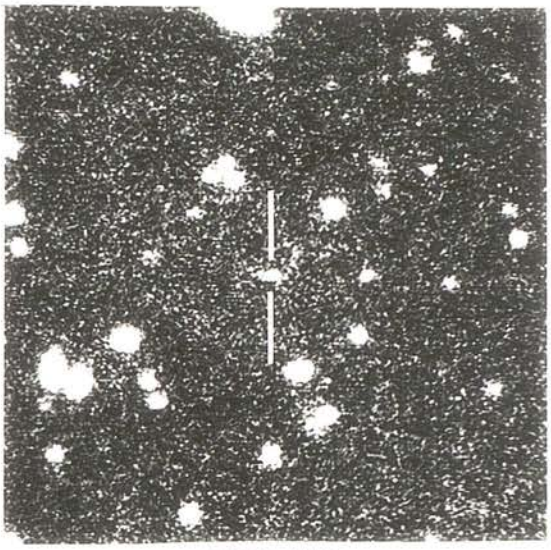

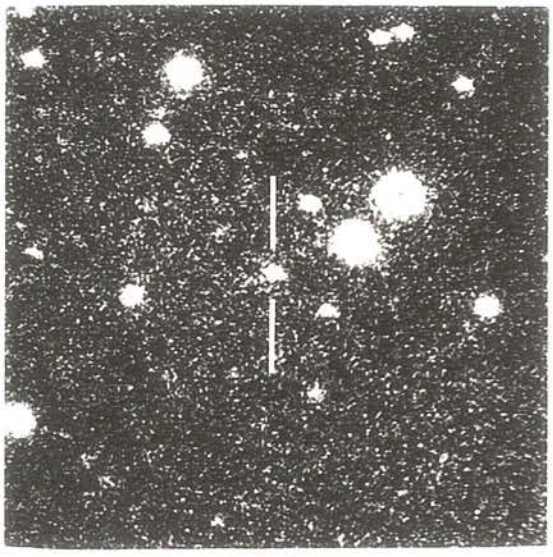

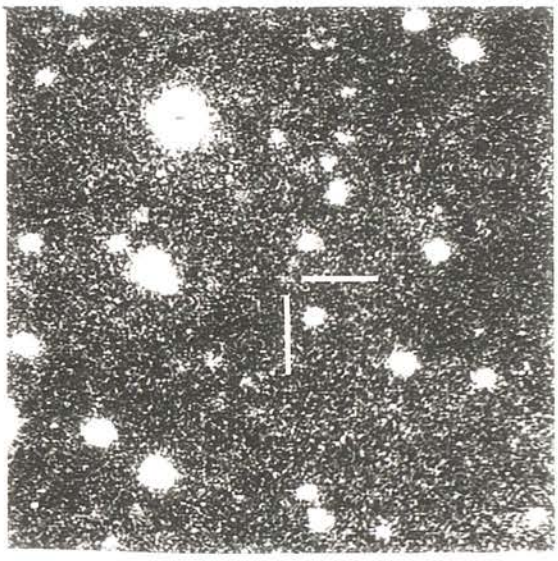

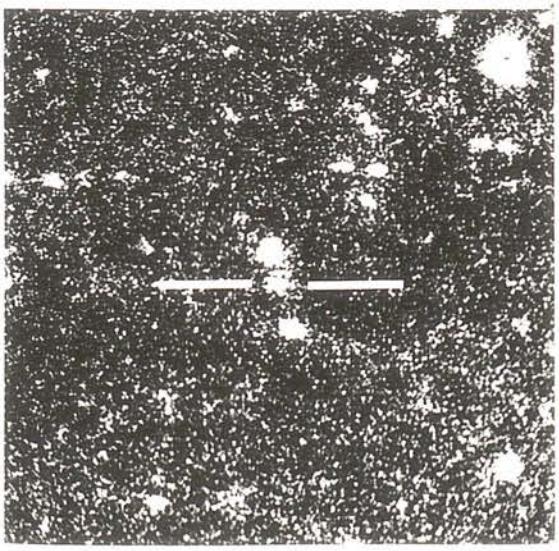

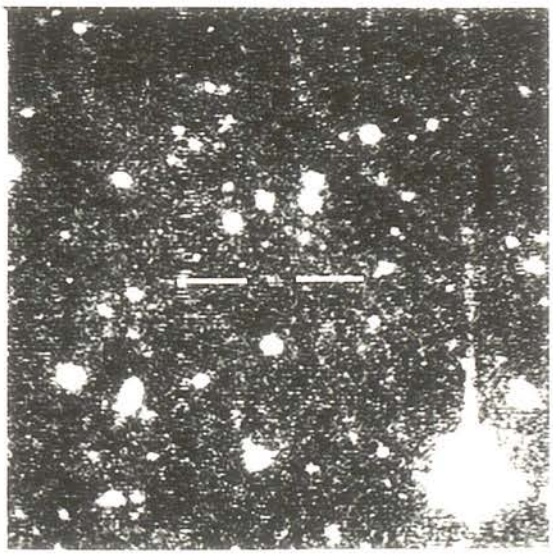

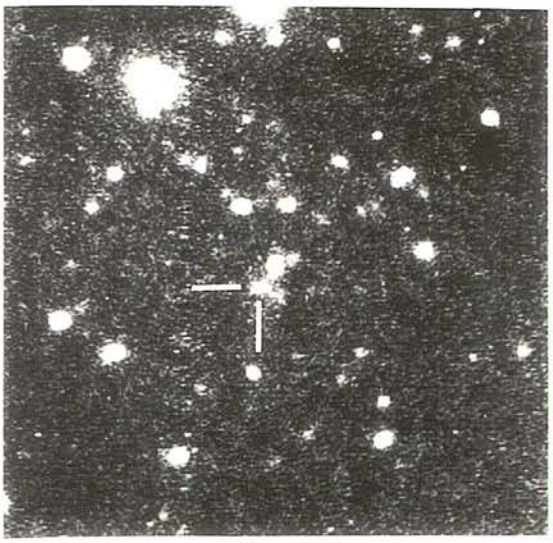

1154-010

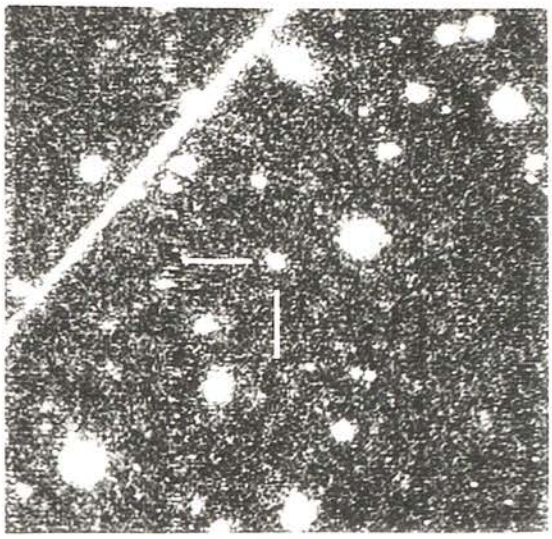

1154-011

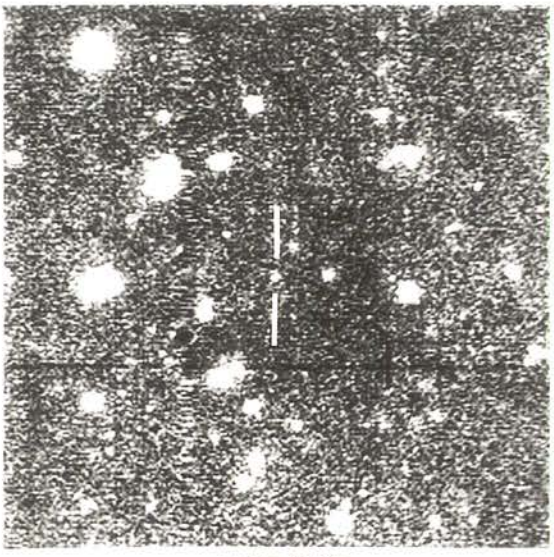

1157-026

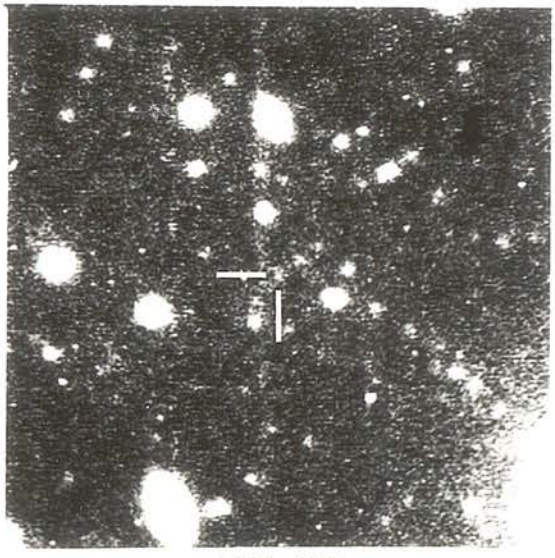

1201-026

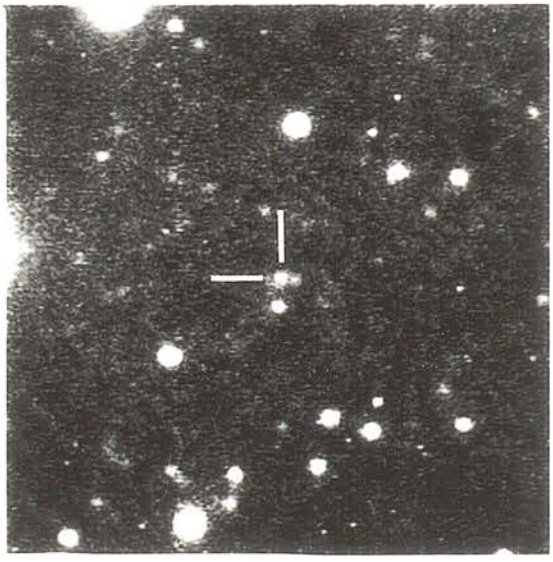

1205-011

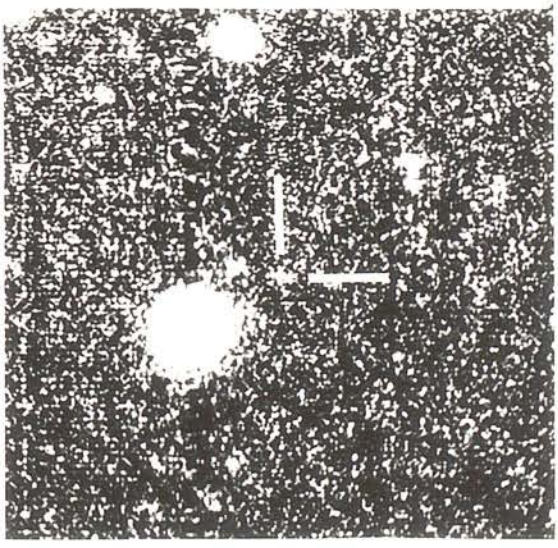

1212-007

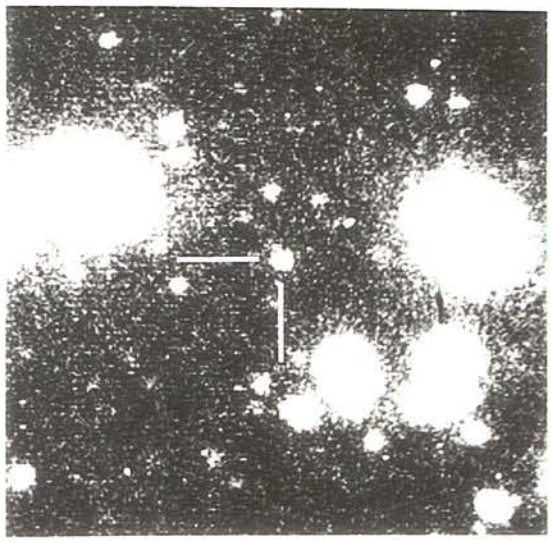

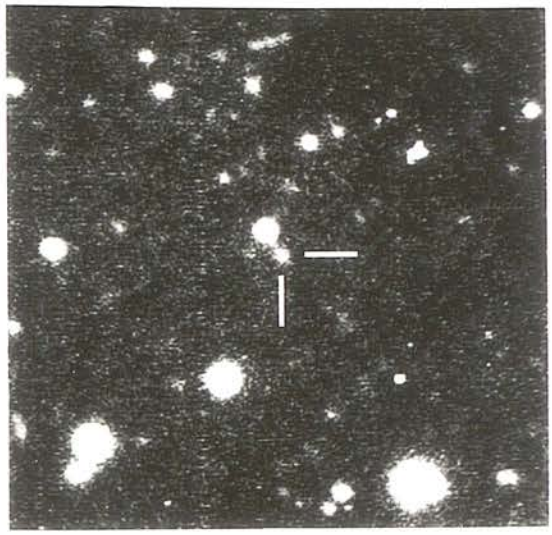

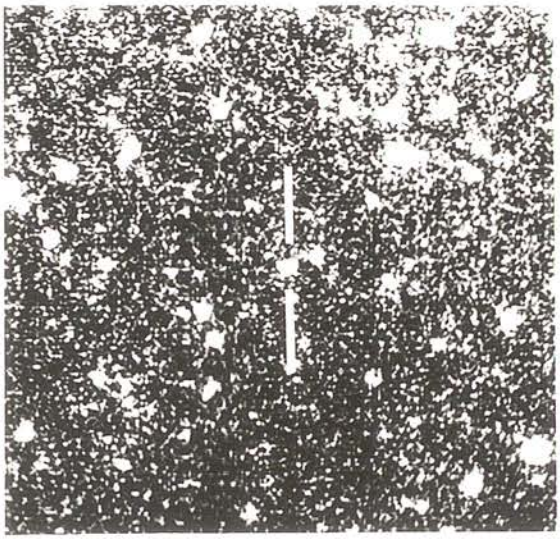

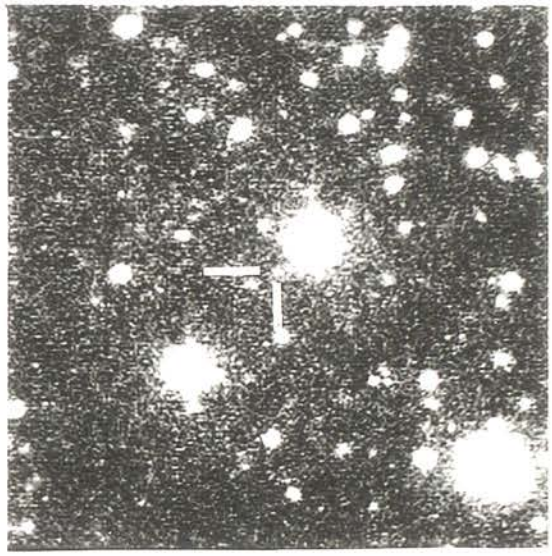

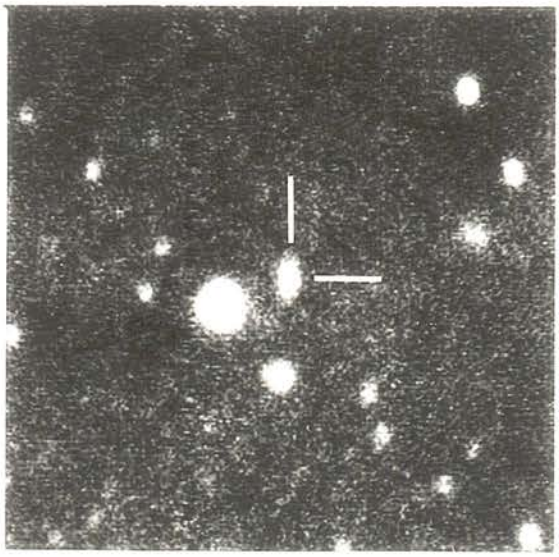

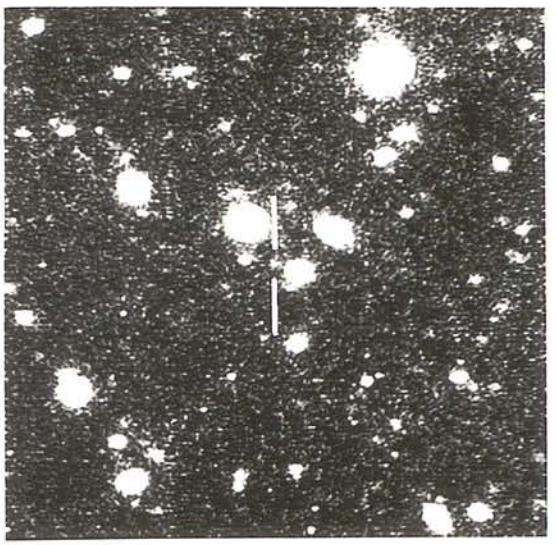

1339+015

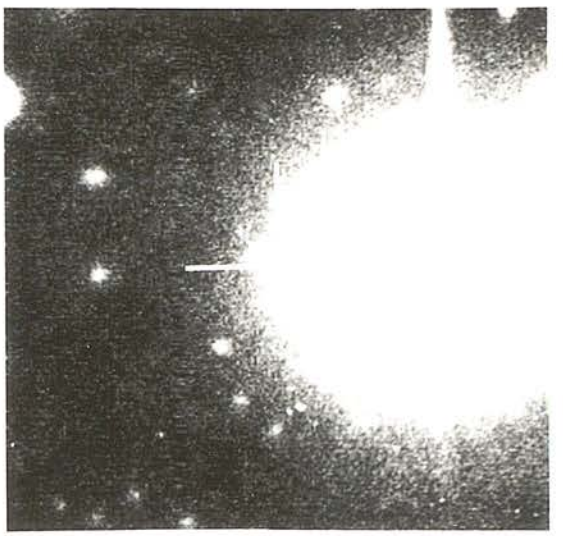

1340+022

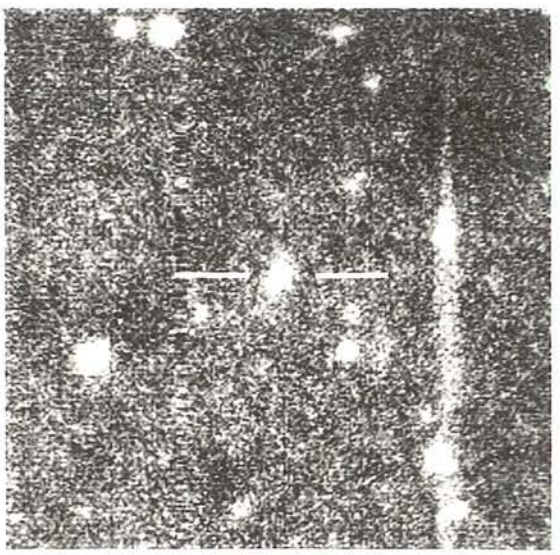

1343-007

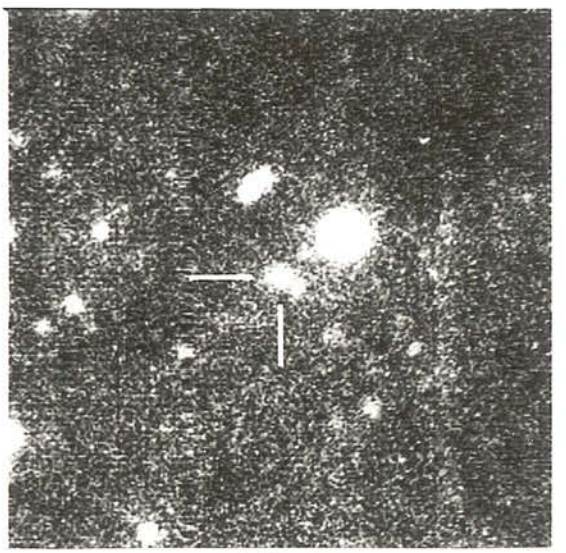

1343+011

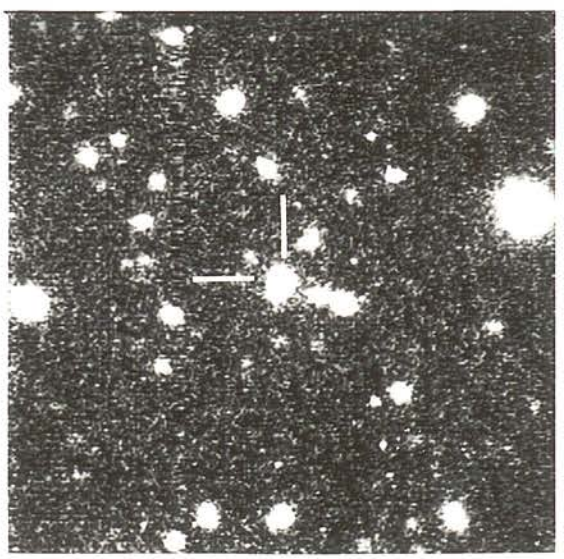

1345+002

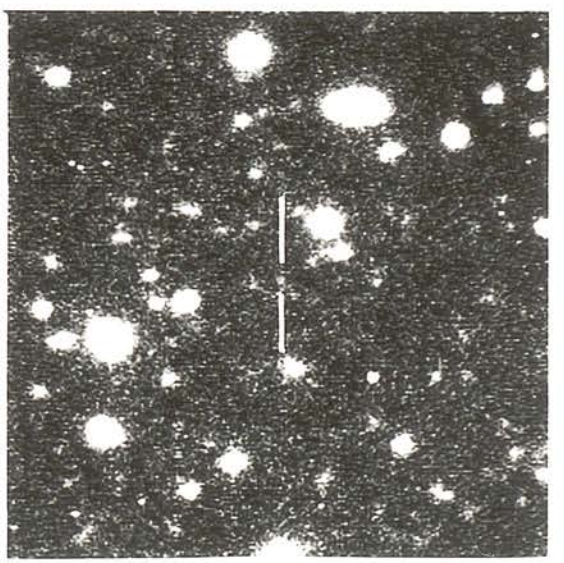

1345+008

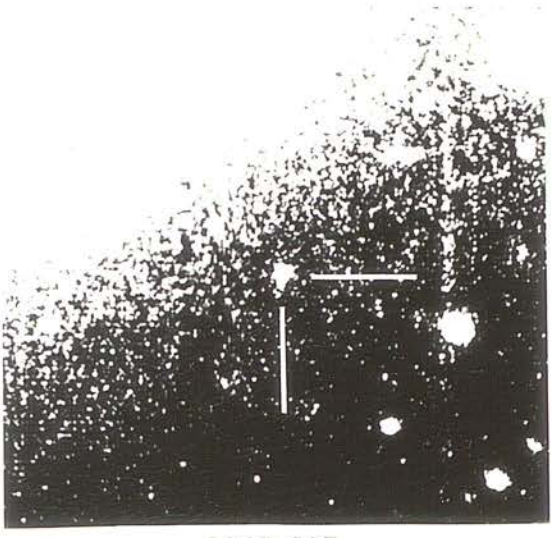

1348+007

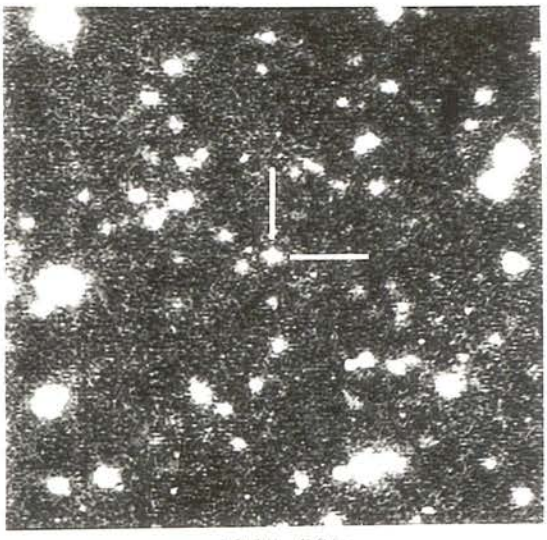

1349+008

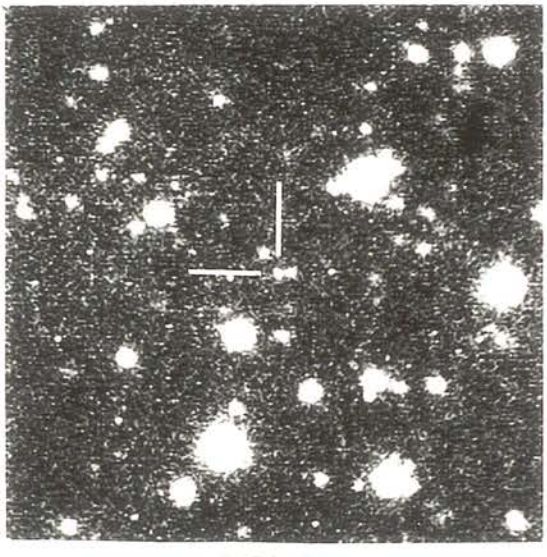

1352+008

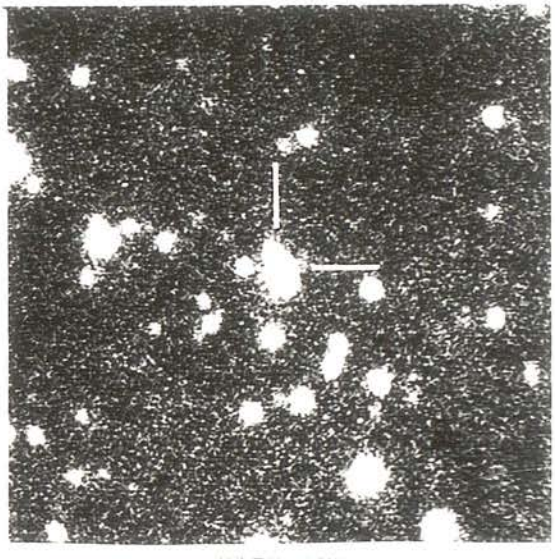

2153+188

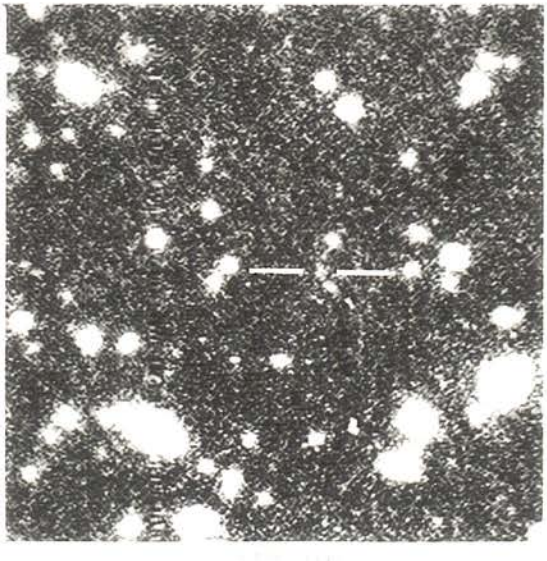

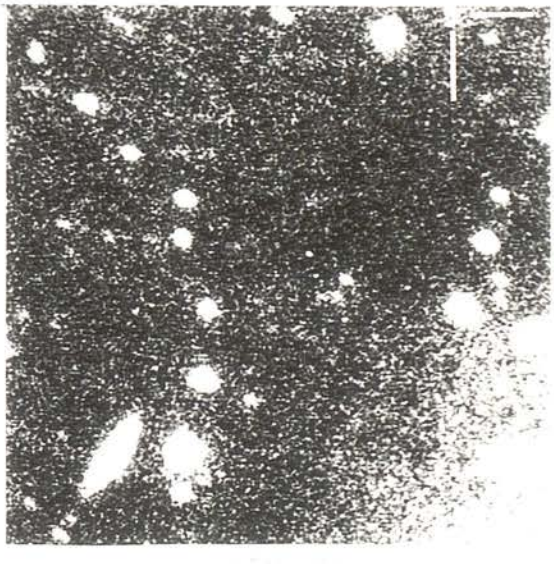

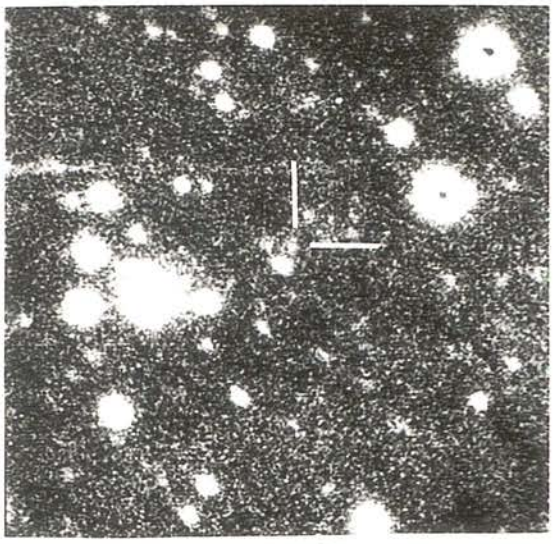

2158-160

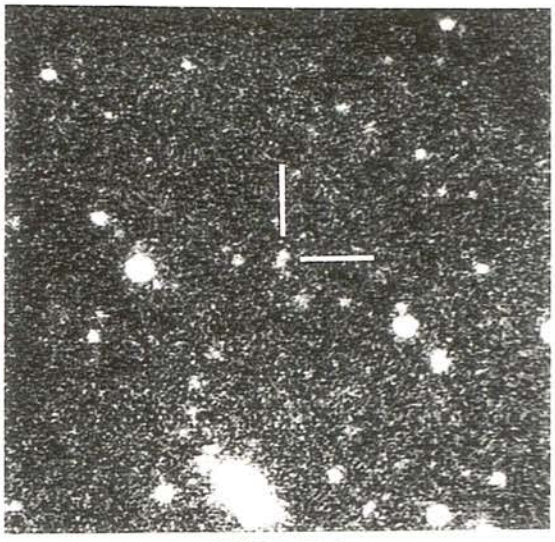

2159-215

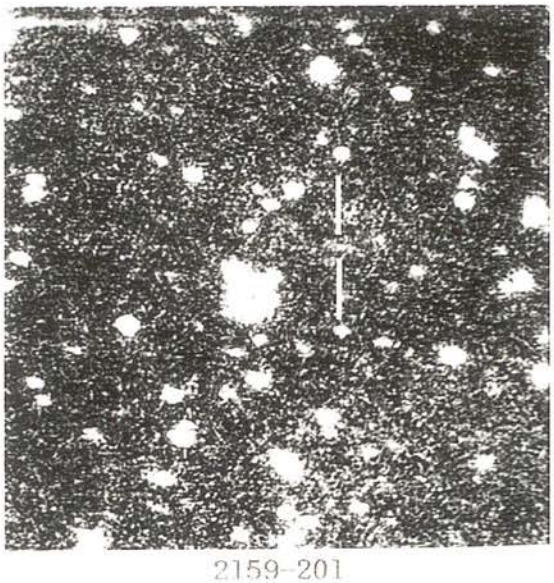

2159-201

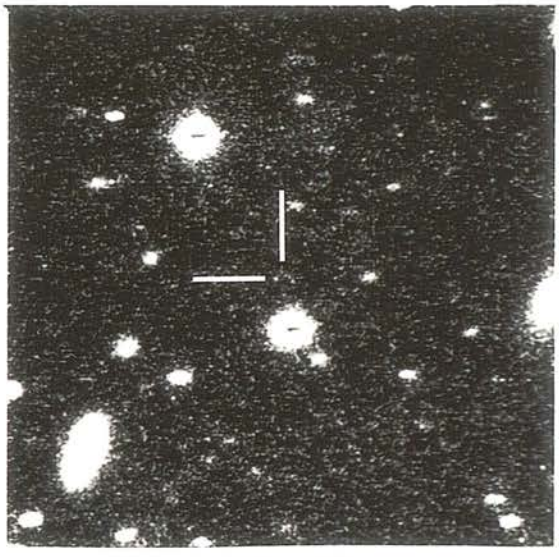

2159-192

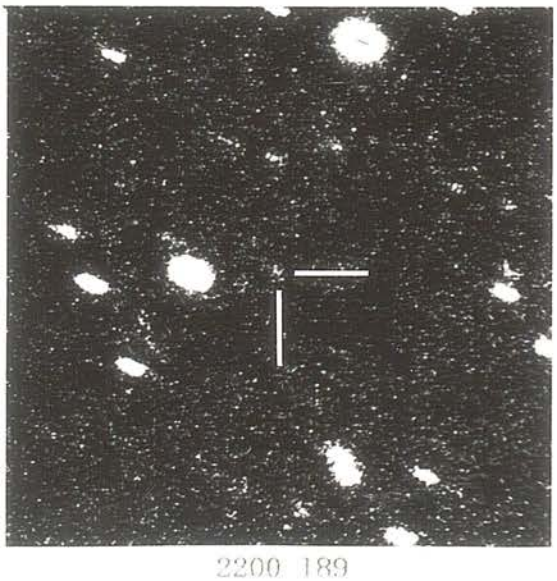

2200-189

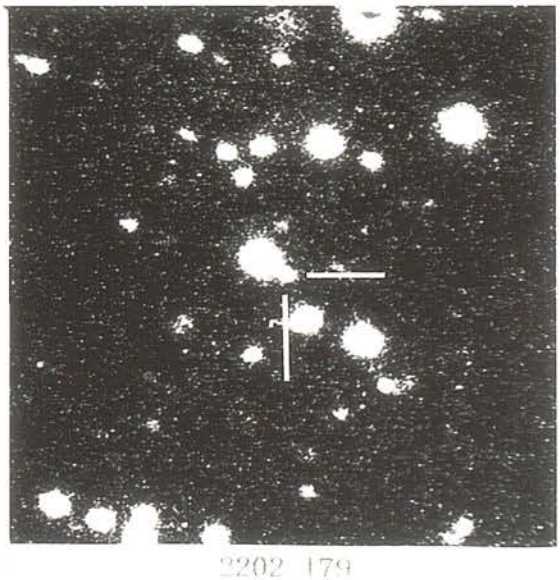

2202-179

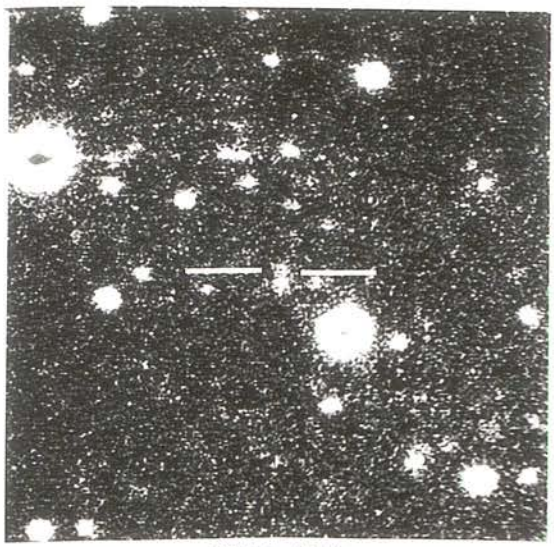

2204 203

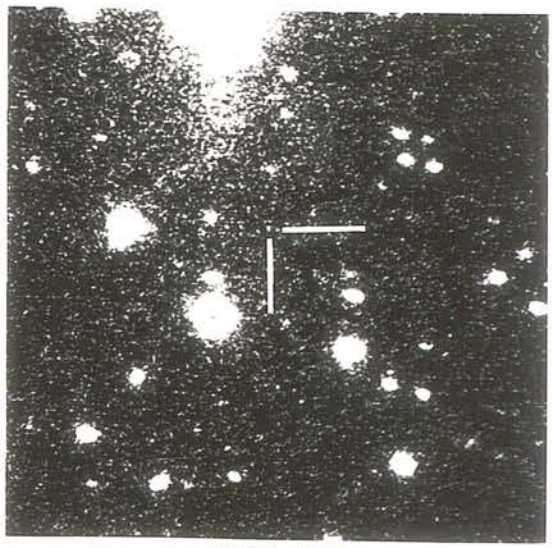

2204 182

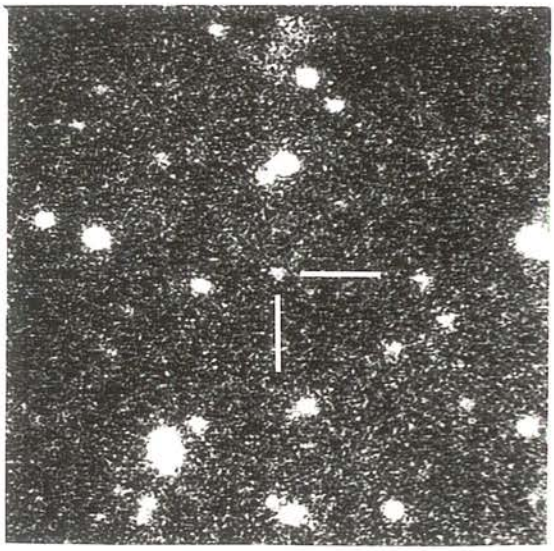

2205 178

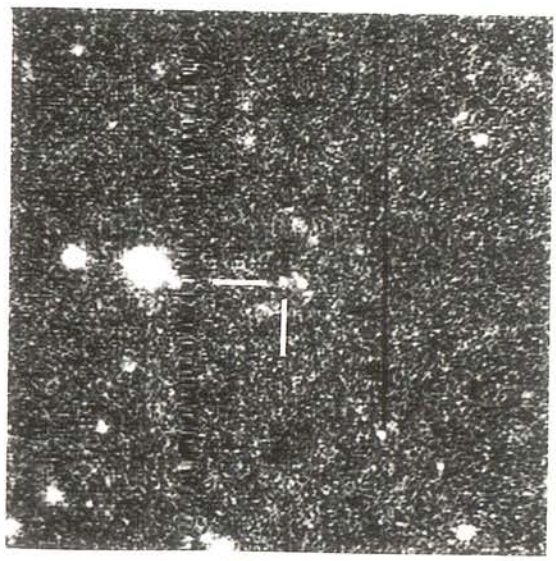

2207 203

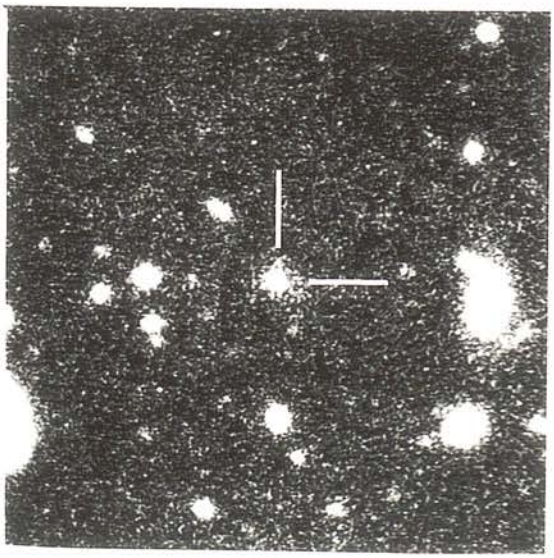

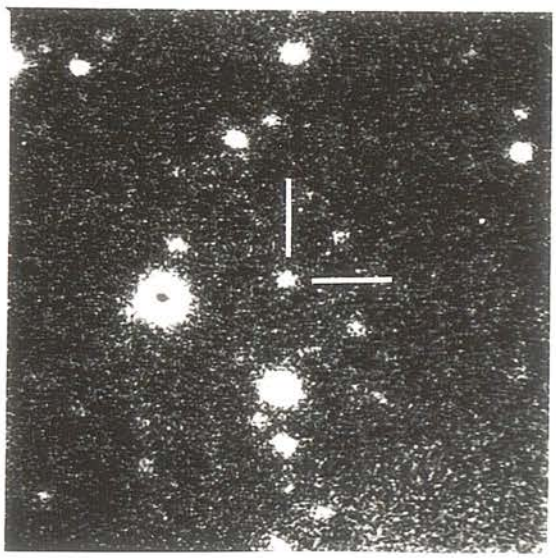

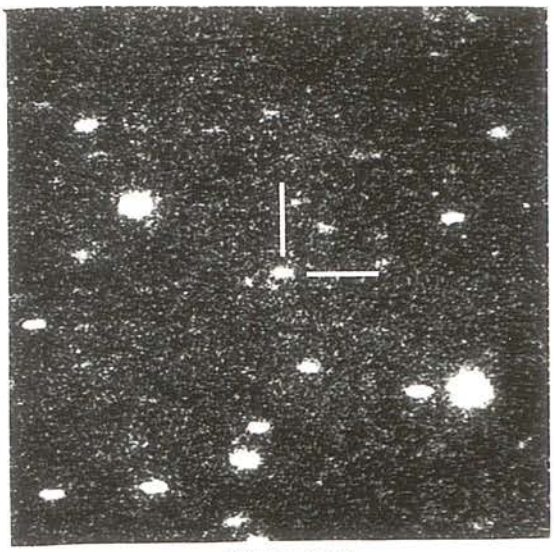

2353+010

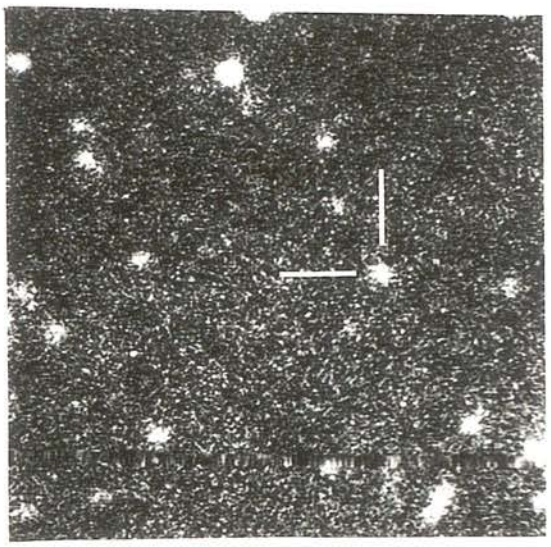

2354+008

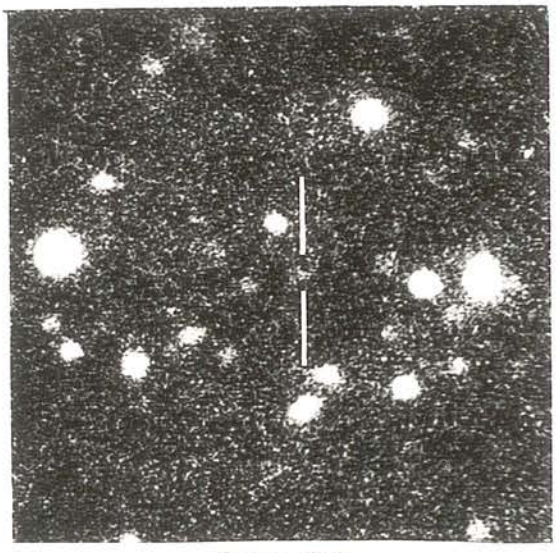

2355-024

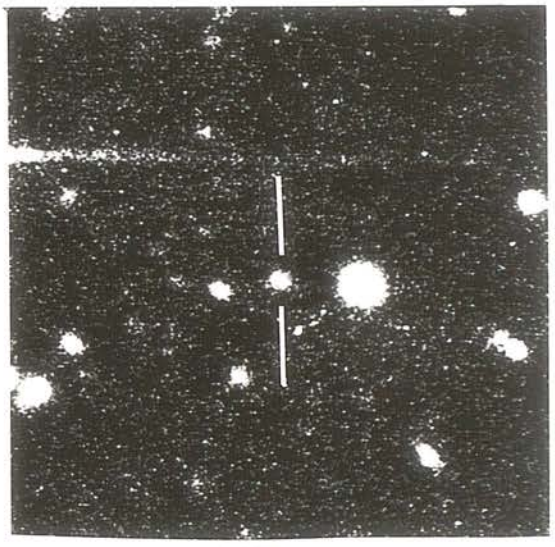

2355-010

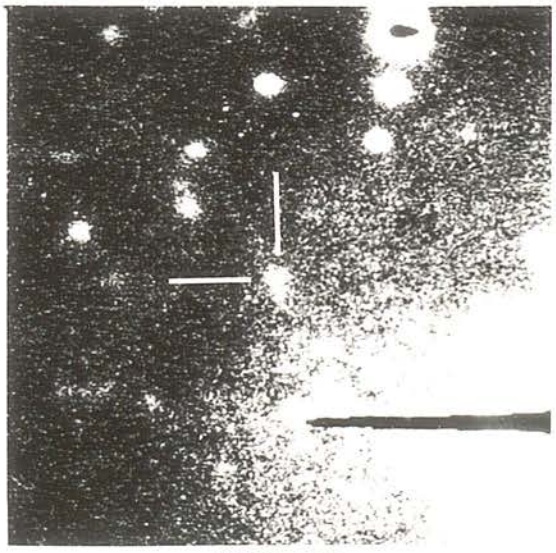

2356+033

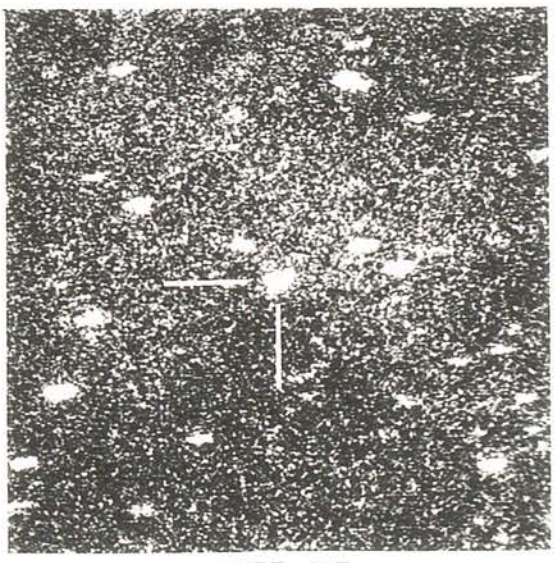

2357-007

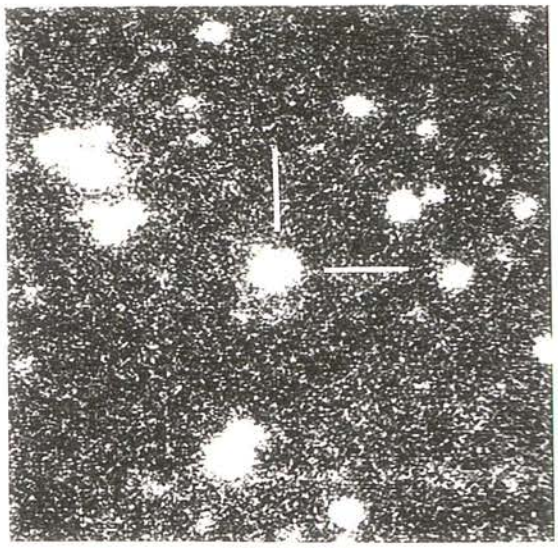

Plate 2.2 : CCD images of the fields of the remaining optically unidentified sources in the Parkes Selected Regions. Each field is 2 arcmin square with north at the top and east to the left, and the expected position of the (as yet undiscovered) optical identification is indicated by a circle.

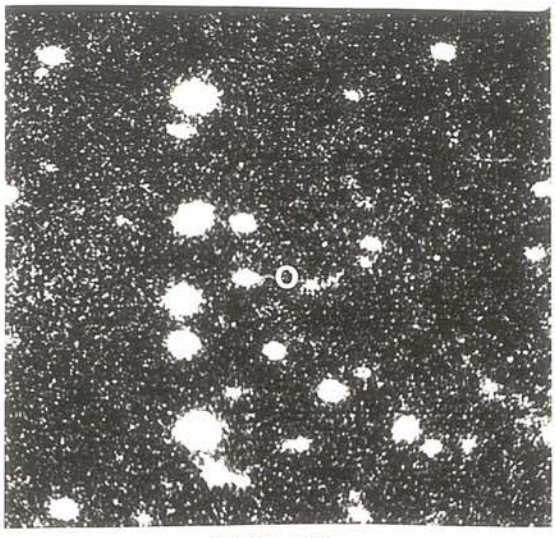

0043−003

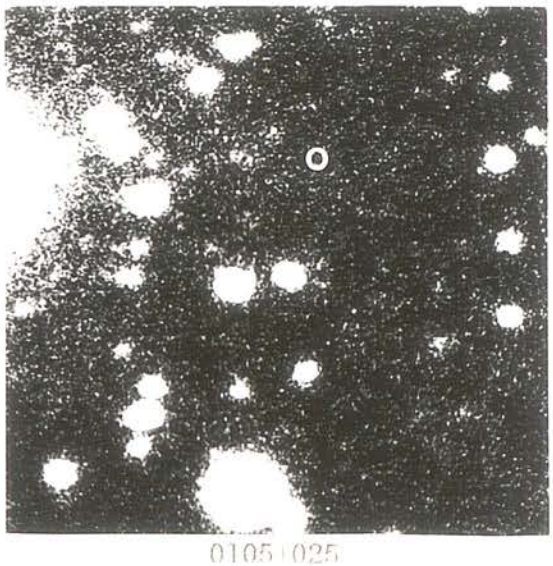

0105+025

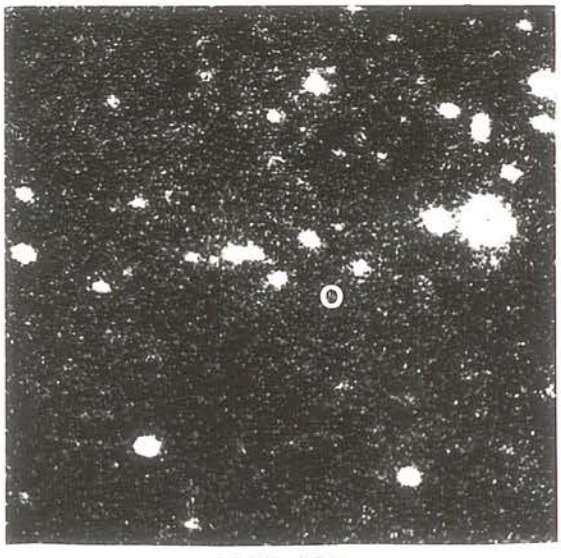

0235+003

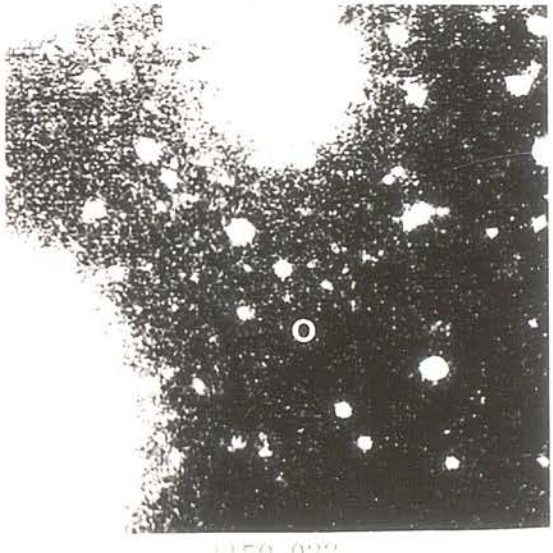

1159+023

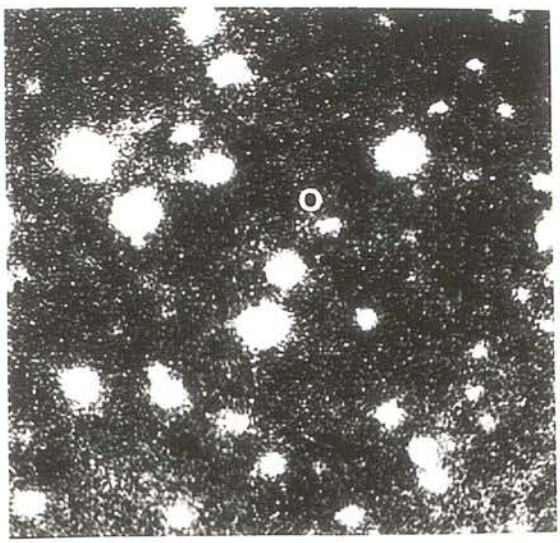

1349-019

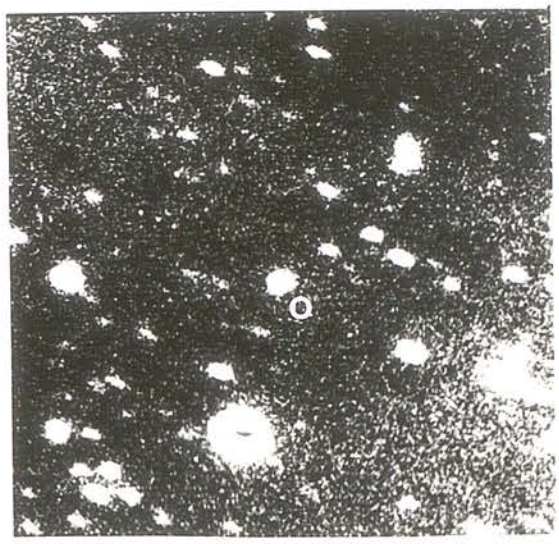

2158-170

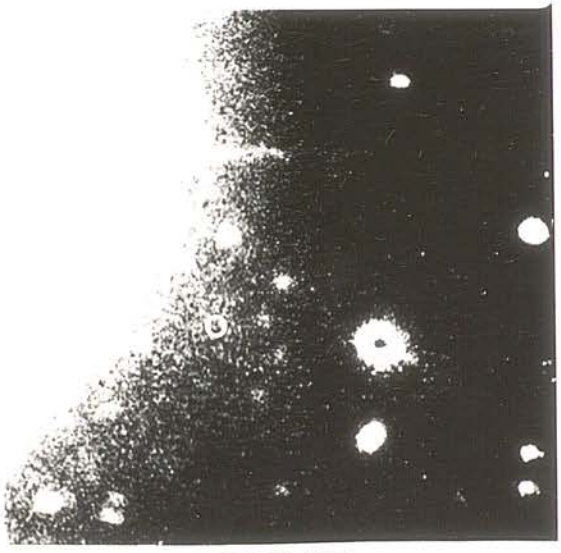

2357-006

Figure 2.1 : Positions of the optical identifications relative to the radio structure of all the extended sources in the Selected Regions sample. The position of each identification is marked by a cross. (The original version of this figure was obtained from Downes *et al.* 1986)

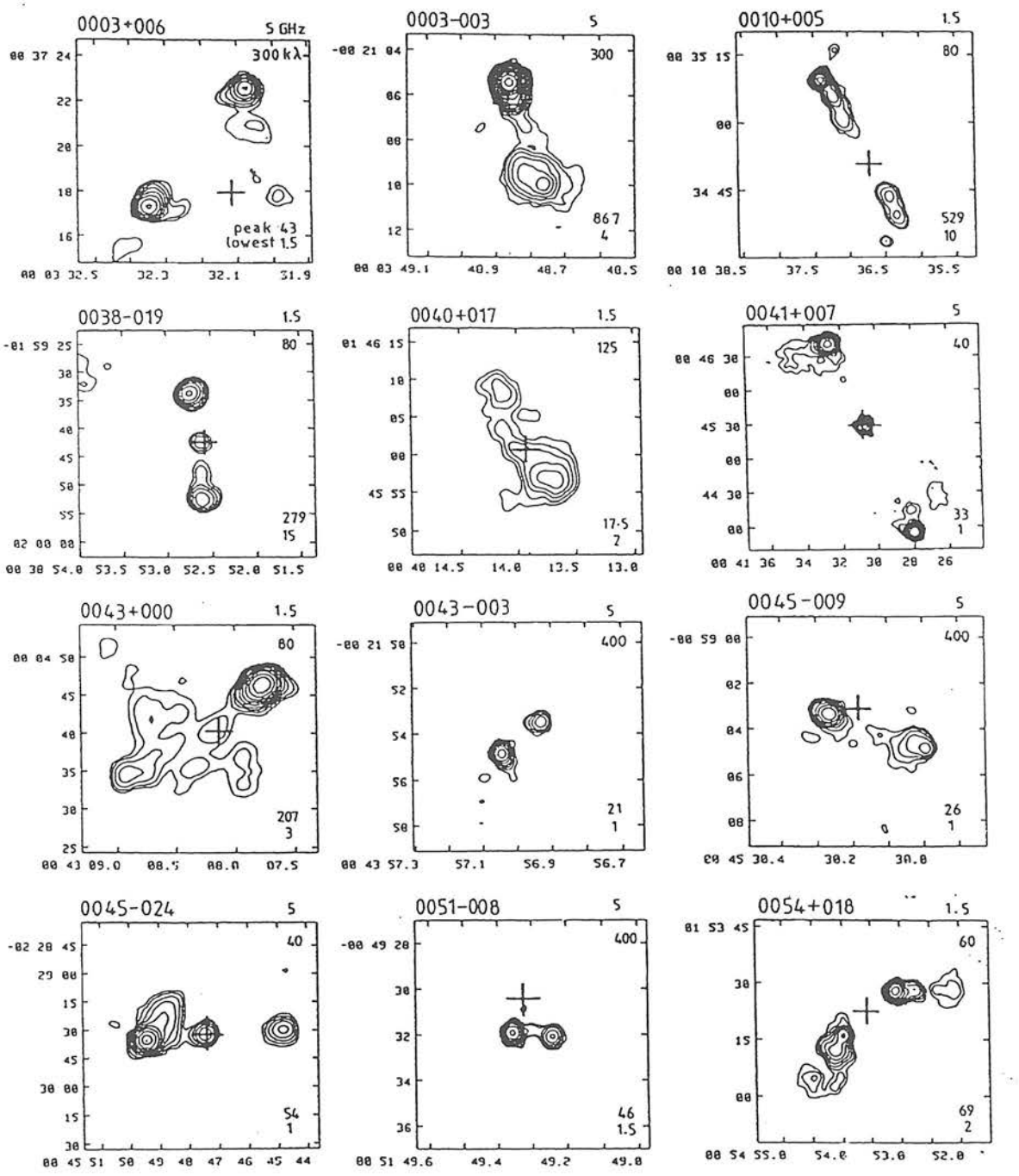

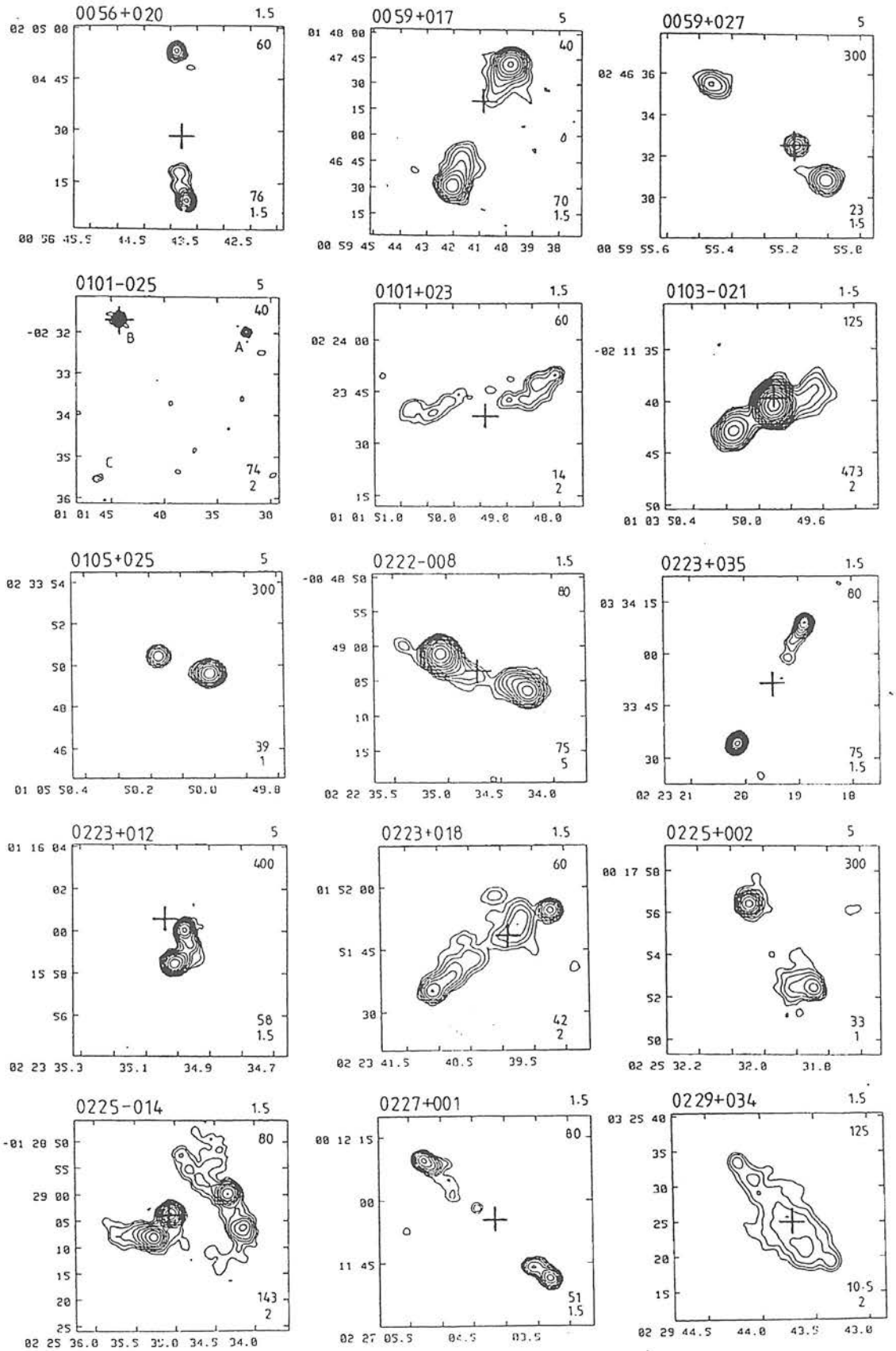
0056+020
1.5
60
76
1.5
0059+017
5
40
70
1.5
0059+027
5
300
23
1.5
0101-025
5
B
A
C
40
74
2
0101+023
1.5
60
14
2
0103-021
1.5
125
473
2
0105+025
5
300
39
1
0222-008
1.5
80
75
5
0223+035
1.5
80
75
1.5
0223+012
5
400
58
1.5
0223+018
1.5
60
42
2
0225+002
5
300
33
1
0225-014
1.5
80
143
2
0227+001
1.5
80
51
1.5
0229+034
1.5
125
10.5
2

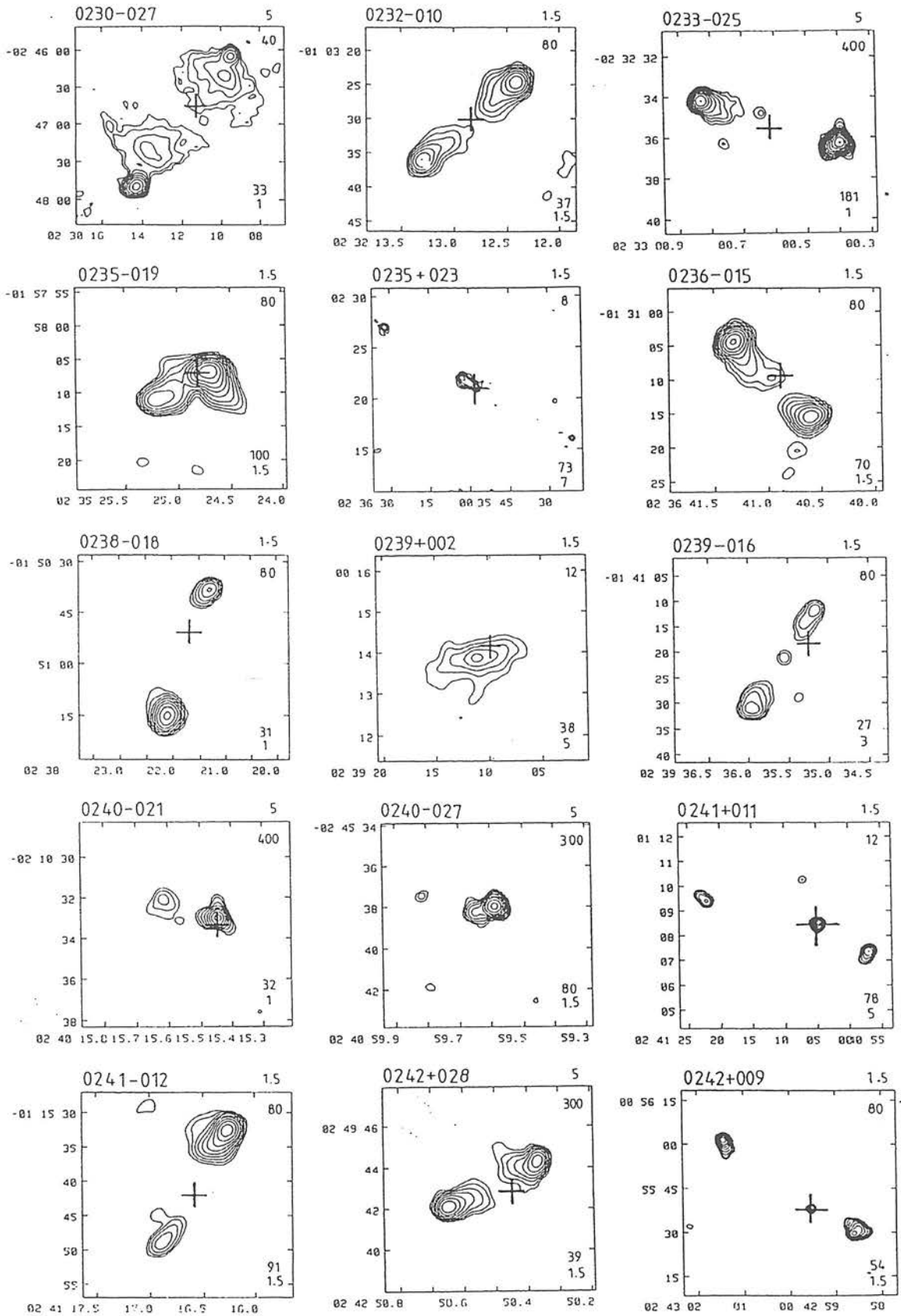
0230-027
5
40
33
1
0232-010
1.5
80
37
1.5
0233-025
5
400
181
1
0235-019
1.5
80
100
1.5
0235+023
1.5
8
73
7
0236-015
1.5
80
70
1.5
0238-018
1.5
80
31
1
0239+002
1.5
12
38
5
0239-016
1.5
80
27
3
0240-021
5
400
32
1
0240-027
5
300
80
1.5
0241+011
1.5
12
78
5
0241-012
1.5
80
91
1.5
0242+028
5
300
39
1.5
0242+009
1.5
80
54
1.5

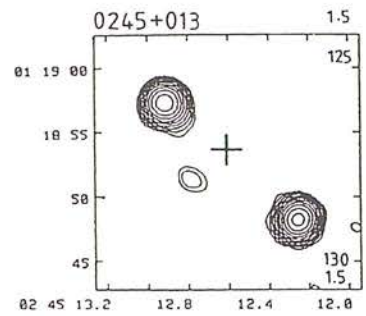
0245+013
1.5
125
130
1.5

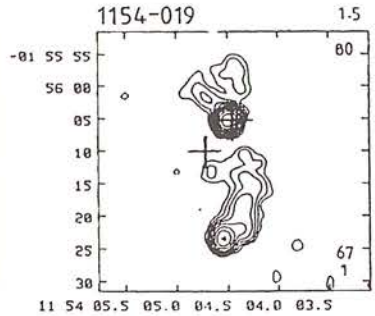
1154-019
1.5
80
67
1

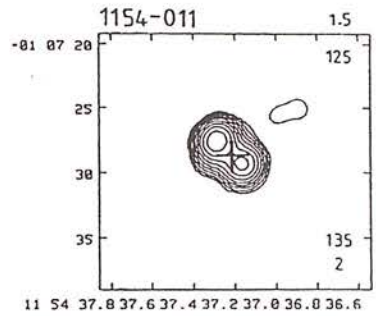
1154-011
1.5
125
135
2

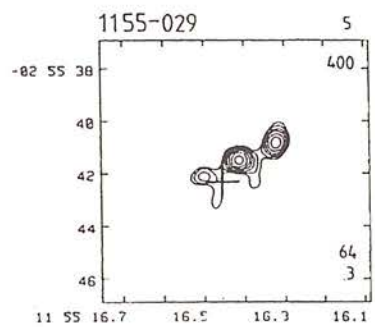
1155-029
5
400
64
3

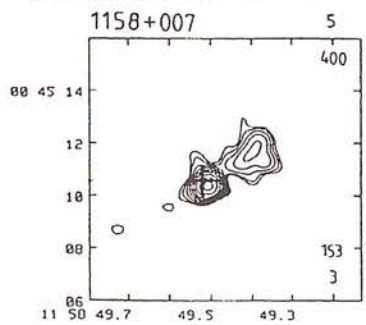
1158+007
5
400
153
3

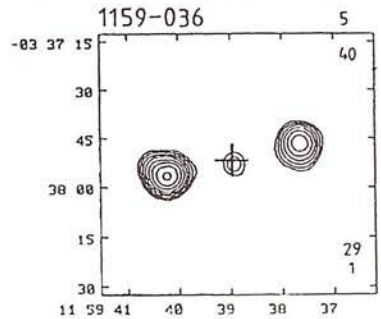
1159-036
5
40
29
1

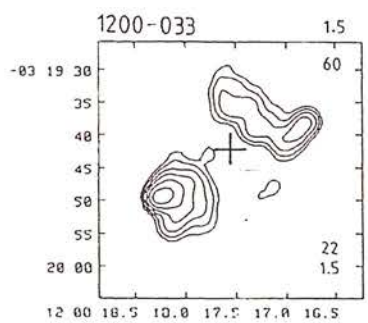
1200-033
1.5
60
22
1.5

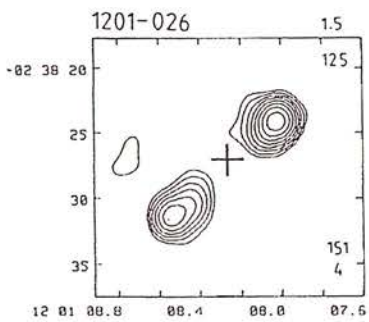
1201-026
1.5
125
151
4

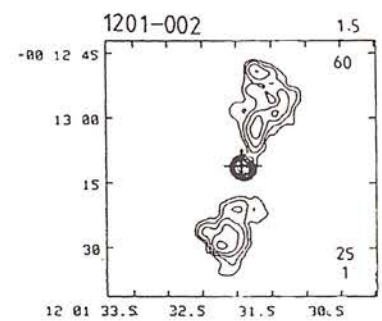
1201-002
1.5
60
25
1

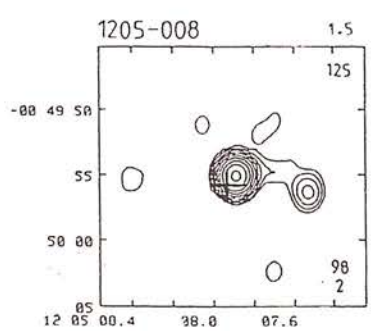
1205-008
1.5
125
98
2

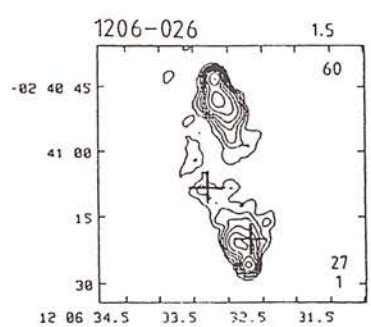
1206-026
1.5
60
27
1

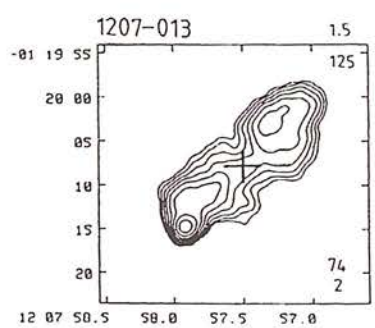
1207-013
1.5
125
74
2

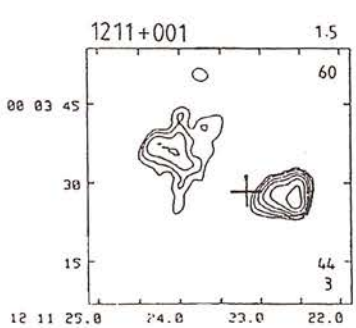
1211+001
1.5
60
44
3

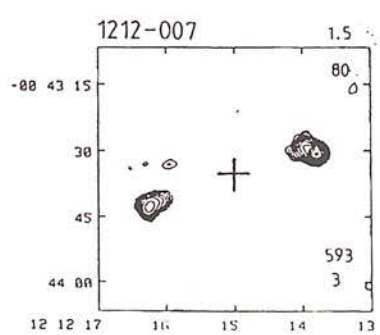
1212-007
1.5
80
593
3

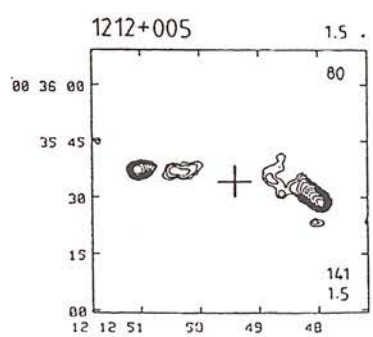
1212+005
1.5
80
141
1.5

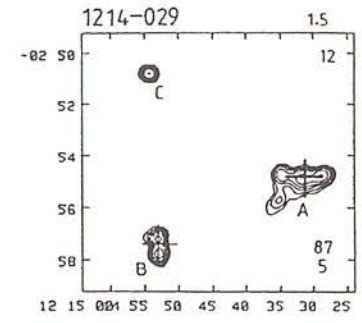
1214-029
1.5
12
C
A
B
87
5
-02 50
52
54
56
58
12 15 00m 55s 50 45 40 35 30 25

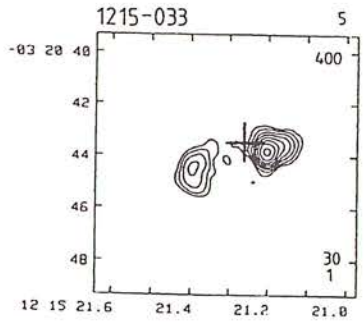
1215-033
5
400
30
1
-03 20 40
42
44
46
48
12 15 21.6 21.4 21.2 21.0

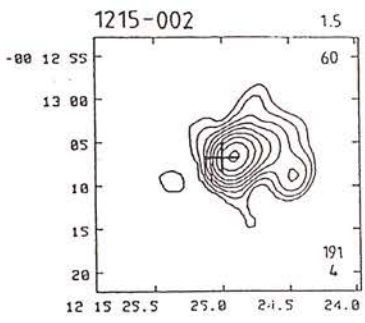
1215-002
1.5
60
191
4
-00 12 55
13 00
05
10
15
20
12 15 25.5 25.0 24.5 24.0

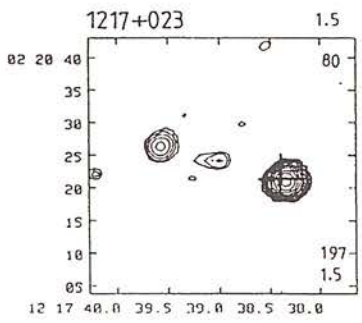
1217+023
1.5
80
197
1.5
02 20 40
35
30
25
20
15
10
05
12 17 40.0 39.5 39.0 30.5 30.0

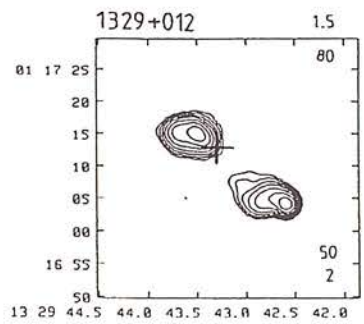
1329+012
1.5
80
50
2
01 17 25
20
15
10
05
00
16 55
50
13 29 44.5 44.0 43.5 43.0 42.5 42.0

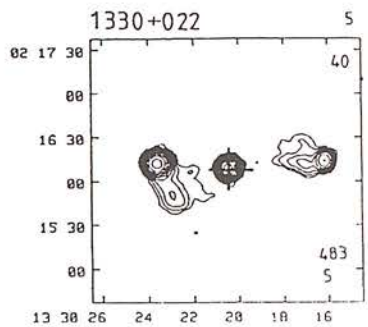
1330+022
5
40
483
5
02 17 30
00
16 30
00
15 30
00
13 30 26 24 22 20 18 16

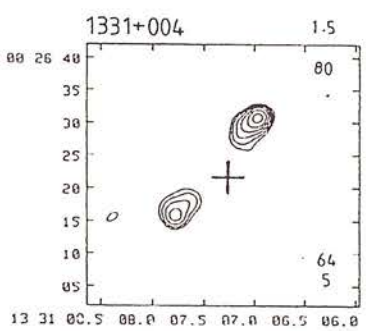
1331+004
1.5
80
64
5
00 26 40
35
30
25
20
15
10
05
13 31 00.5 00.0 07.5 07.0 06.5 06.0

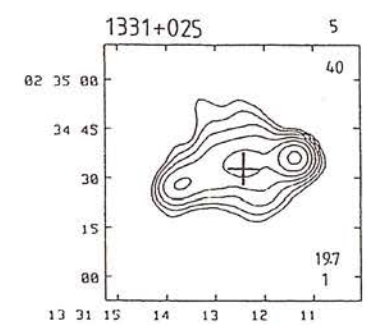
1331+025
5
40
197
1
02 35 00
34 45
30
15
00
13 31 15 14 13 12 11

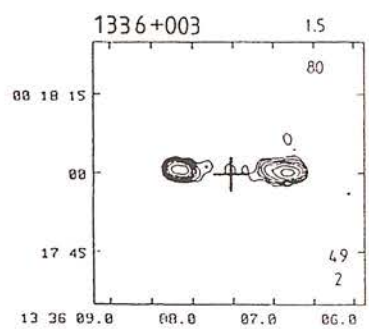
1336+003
1.5
80
49
2
00 18 15
00
17 45
13 36 09.0 08.0 07.0 06.0

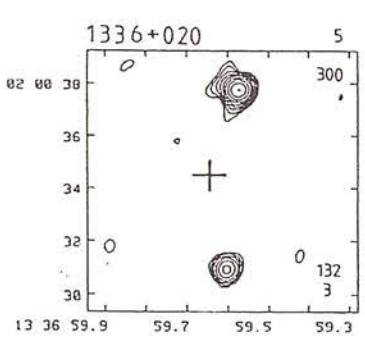
1336+020
5
300
132
3
02 00 38
36
34
32
30
13 36 59.9 59.7 59.5 59.3

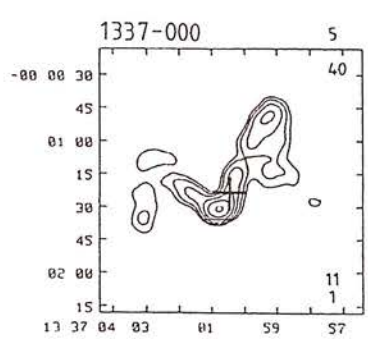
1337-000
5
40
11
1
-00 00 30
45
01 00
15
30
45
02 00
15
13 37 04 03 01 59 57

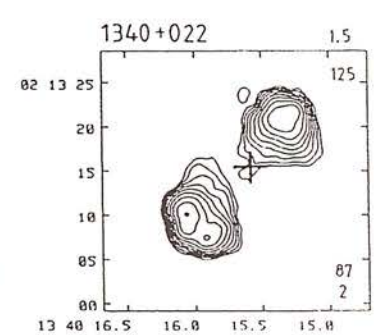
1340+022
1.5
125
87
2
02 13 25
20
15
10
05
00
13 40 16.5 16.0 15.5 15.0

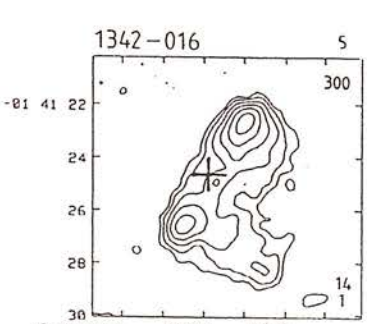
1342-016
5
300
14
1
-01 41 22
24
26
28
30
13 42 42.4 42.2 42.0

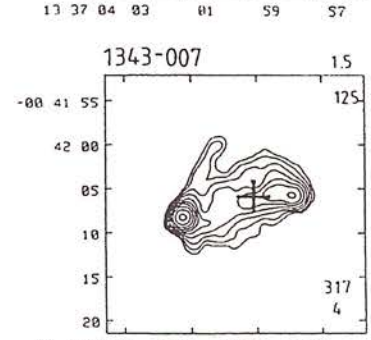
1343-007
1.5
125
317
4
-00 41 55
42 00
05
10
15
20
13 43 04.0 03.5 03.0 02.5

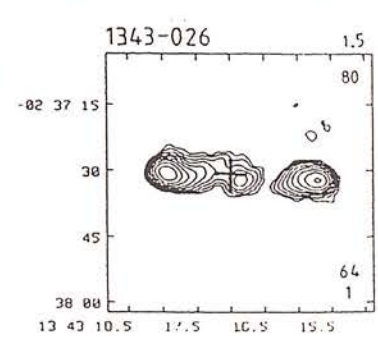
1343-026
1.5
80
64
1
-02 37 15
30
45
38 00
13 43 10.5 10.0 09.5 09.0

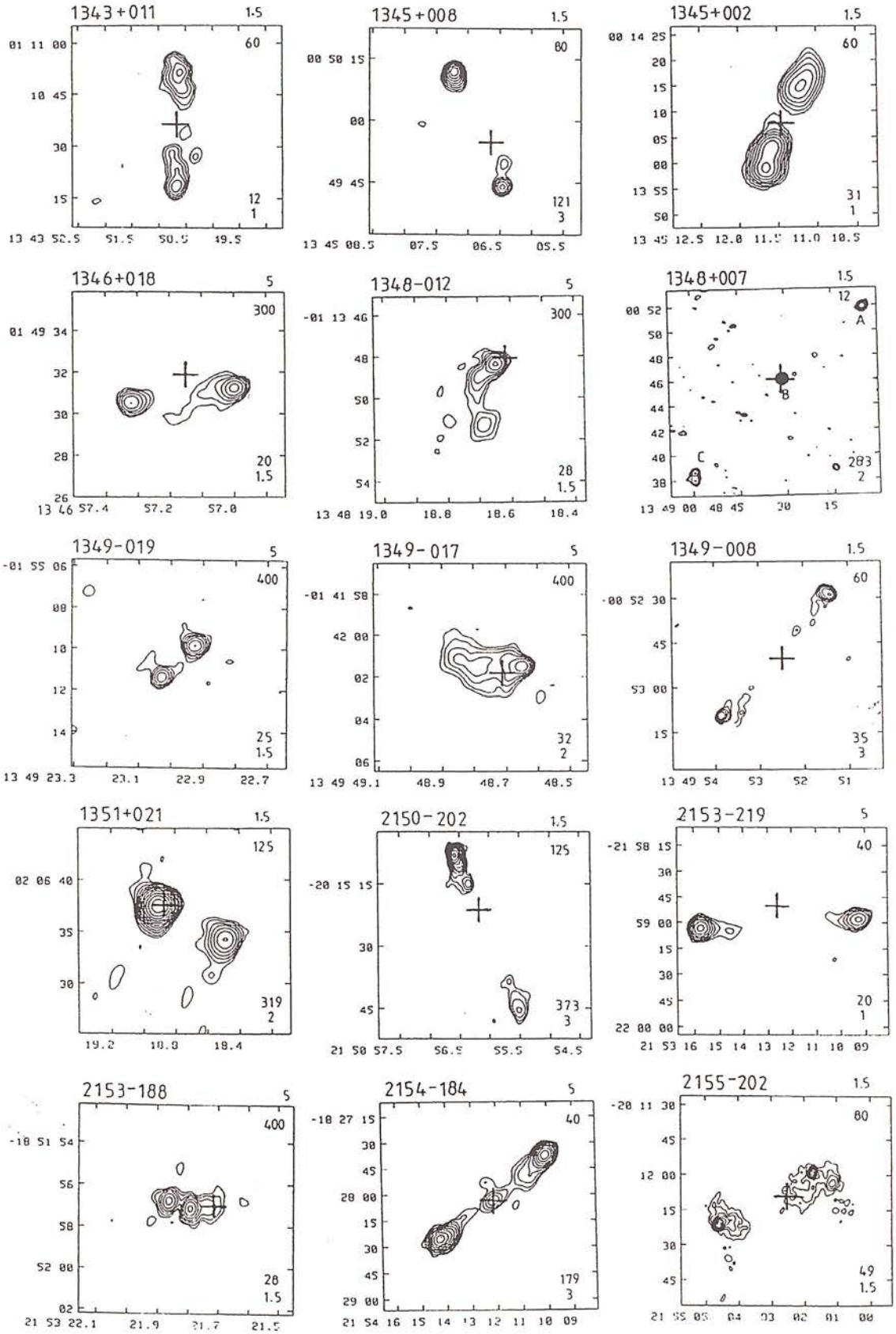
1343+011
1345+008
1345+002
1346+018
1348-012
1348+007
1349-019
1349-017
1349-008
1351+021
2150-202
2153-219
2153-188
2154-184
2155-202

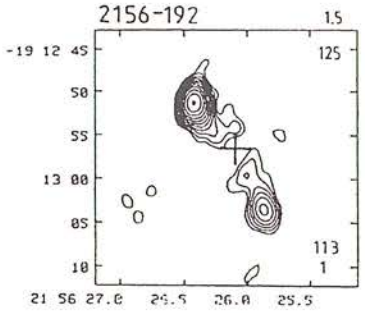
2156-192
1.5
125
113
1

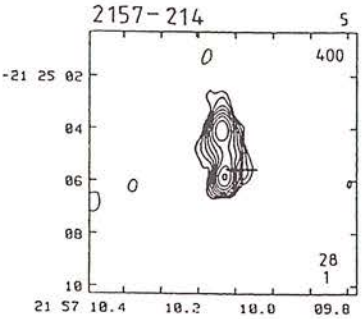
2157-214
5
400
28
1

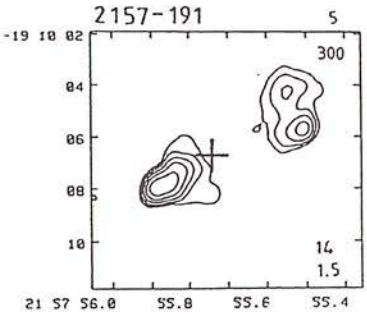
2157-191
5
300
14
1.5

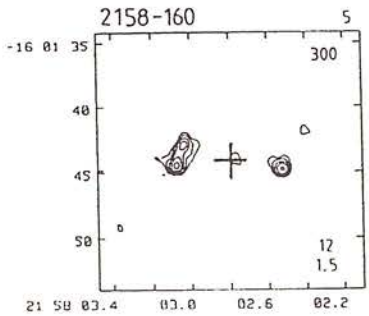
2158-160
5
300
12
1.5

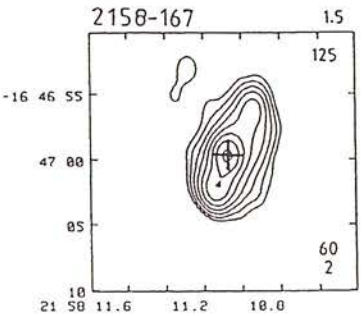
2158-167
1.5
125
60
2

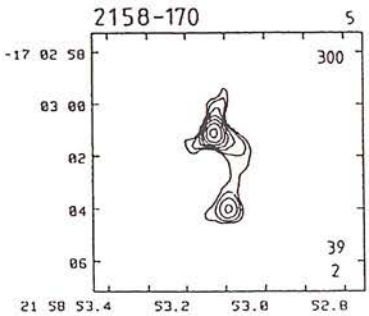
2158-170
5
300
39
2

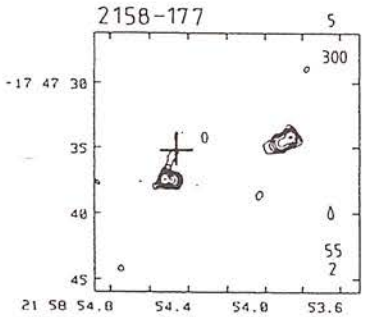
2158-177
5
300
55
2

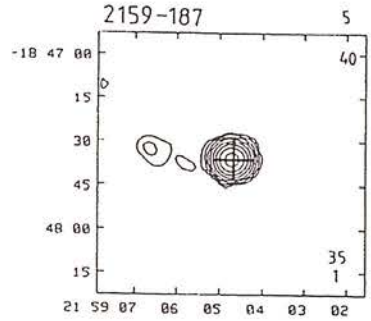
2159-187
5
40
35
1

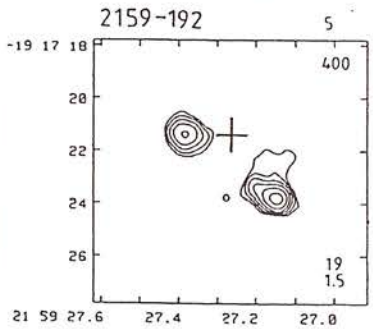
2159-192
5
400
19
1.5

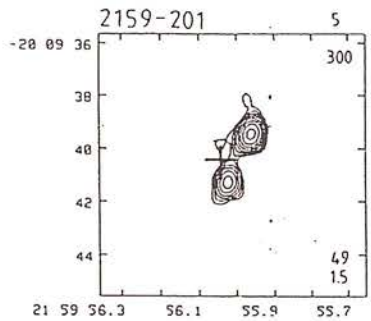
2159-201
5
300
49
1.5

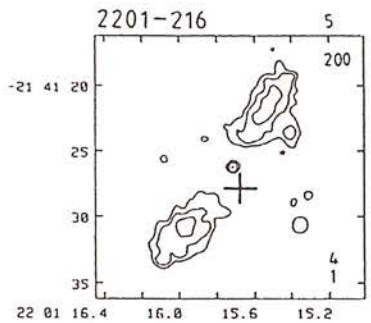
2201-216
5
200
4
1

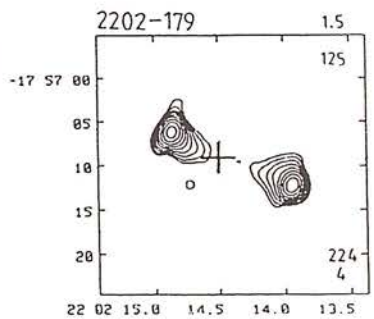
2202-179
1.5
125
224
4

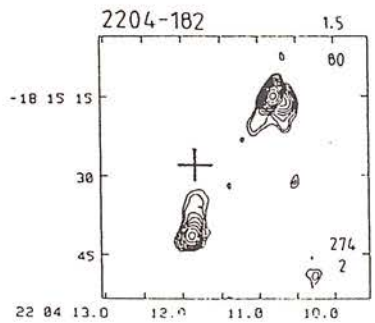
2204-182
1.5
60
274
2

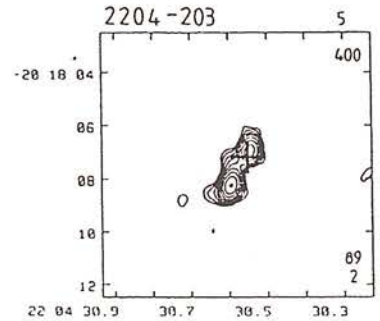
2204-203
5
400
89
2

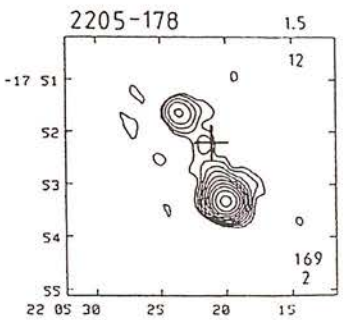
2205-178
1.5
12
169
2

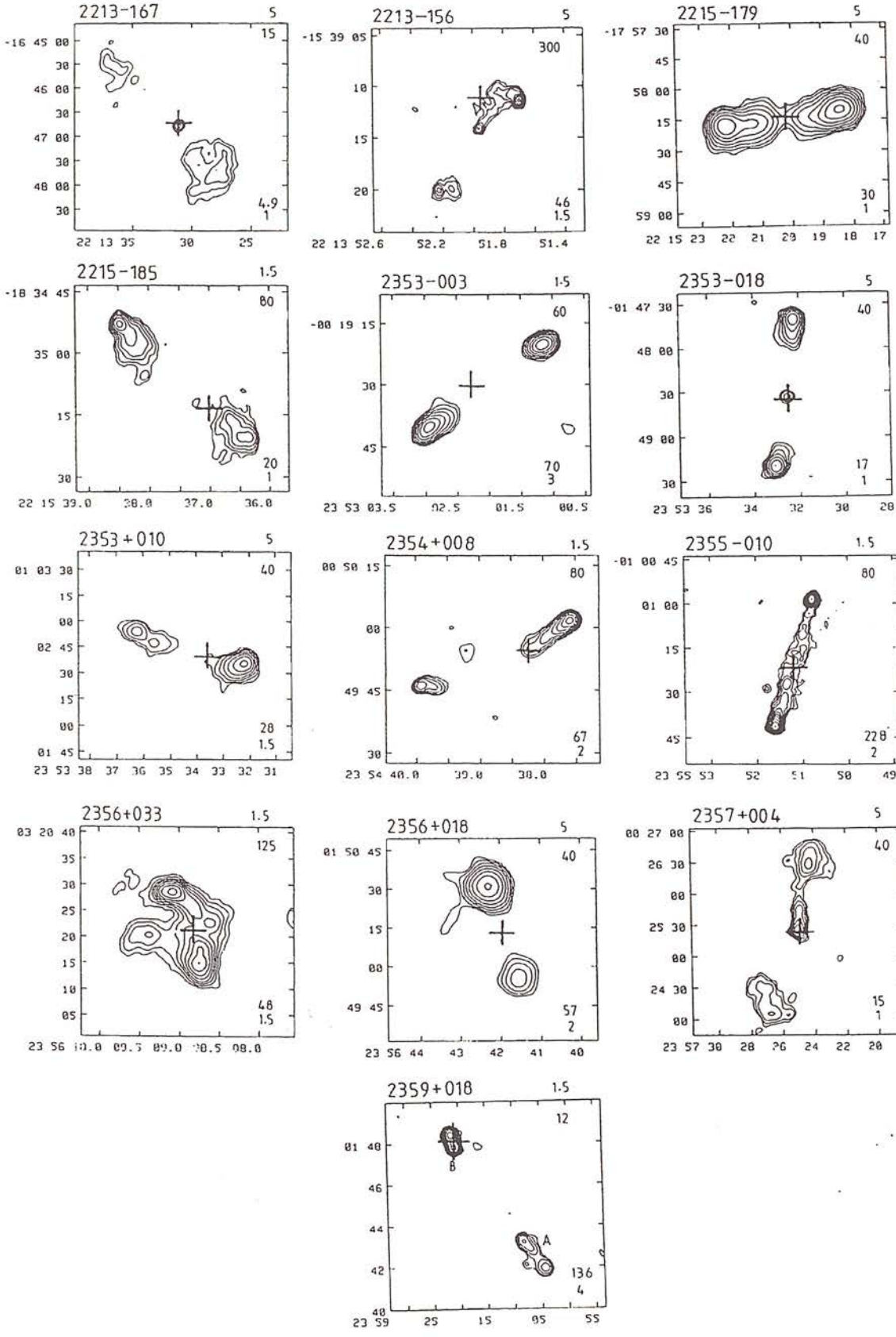
2213-167
5
15
4.9
1
2213-156
5
300
46
1.5
2215-179
5
40
30
1
2215-185
1.5
80
20
1
2353-003
1.5
60
70
3
2353-018
5
40
17
1
2353+010
5
40
28
1.5
2354+008
1.5
80
67
2
2355-010
1.5
80
228
2
2356+033
1.5
125
48
1.5
2356+018
5
40
57
2
2357+004
5
40
15
1
2359+018
1.5
12
A
B
136
4

2.5 : OPTICAL PHOTOMETRY - METHOD

2.5a : General approach

In measuring the magnitudes of the CCD identifications, it was clearly desirable to employ a consistent, meaningful and reproducible magnitude system. Two types of magnitude are most commonly quoted, isophotal magnitudes and aperture magnitudes. Measurement of an isophotal magnitude involves counting all the visible flux above a chosen practical surface brightness. The results of this method are highly sensitive to the seeing and signal/noise level of the image and are therefore difficult to reproduce. They are also difficult to interpret, particularly for faint galaxies for which the region of the object sampled inevitably varies depending on the surface brightness profile and redshift of the galaxy. Attempts to define "intrinsic" isophotal magnitudes for faint galaxies (eg Koo 1986a) also lead to problems of reproducibility and involve somewhat ad hoc assumptions concerning the effective size of the galaxies. Alternative methods of measuring integrated magnitudes involve the somewhat subjective procedure of profile fitting. Aperture magnitudes are more objective but, for small apertures, are dependent on the seeing at the time of observation. For extremely faint objects signal/noise is at a premium and small apertures must be used to minimise the effect of sky noise.

Because of the above problems it was decided to try to measure seeing-independent aperture magnitudes. This required the deconvolution of the seeing profile from the image prior to the aperture magnitude measurement. To achieve the deconvolution, a computer program was written to perform an optical analogue of the CLEAN procedure commonly used by radio astronomers to deconvolve complex beam patterns.

2.5b : CLEAN

The CLEAN procedure is one of the most widely used methods of image reconstruction in radio astronomy (Pearson and Readhead 1984). Developed by Hogbom in the early 1970s (Hogbom 1974) it attempts to

decompose a radio map of a region of sky into a number of components, each of which has the shape (often very complex) of the beam profile of the telescope. The algorithm searches the raw map for the pixel with the largest absolute value $|F_{max}|$ and subtracts a beam pattern centred on this point with amplitude λF_{max} (the factor λ is called the "loop gain"). The residual map is then searched for the next largest pixel and a second beam pattern is subtracted and so on. The iteration continues until the largest remaining pixel value is consistent with the expected noise level. The outcome of this iterative procedure is a residual map containing noise plus contributions from very weak sources, and a list of the amplitudes and positions of the components which have been removed (ie a set of delta functions). To produce the final map the delta functions are usually convolved with a chosen "clean" beam (eg an elliptical Gaussian the same size as the central lobe of the "dirty" beam) and added back onto the residuals. This final step is somewhat subjective since there are no theoretical criteria for choosing the shape of the clean beam. However, this drawback is not important in the present context, since the aim here is simply to exploit the ability of the CLEAN method to deconvolve a beam profile from an image.

2.5c : Design and testing of the optical CLEAN program

i) Method

Initially, both CLEANING with an analytical profile and CLEANING with a bright star on the frame of interest were explored. However, the latter technique was found to be much more satisfactory, largely because the analytical CLEAN was very sensitive to the seeing estimate. Also, CLEANING with a bright star on the same frame made it relatively easy to deal with the asymmetric beam profiles which resulted from slight trailing of the images on some of the Hawaii 88inch telescope frames.

The procedure adopted was therefore the following. On each frame the brightest available unsaturated star was chosen to provide the relevant beam profile. A large (30 × 30 arcsec) and a small (14 × 14

arcsec) square sub-image were then extracted, both centred on the chosen star. Two similar sub-images centred on the object of interest were also extracted. For both the CLEANING star and the object, the large sub-image was used to determine the local median sky value (which was re-assessed after a 3 sigma cut to eliminate any bias caused by objects). The actual CLEAN was then performed using the two small sub-images, after the appropriate sky subtraction. Finally aperture magnitudes were measured for both the CLEANED and unCLEANED object, through apertures ranging from 15 to 2 arcsec in diameter.

ii) Tests and choice of parameters

Initial tests were carried out on bright stars and bright simulated galaxies. These simulated galaxies (of chosen, known magnitude) were convolved with one star on an image, and then CLEANED using another in order to test the ability of the procedure to reclaim the true result. An example of the results of one of these tests is shown in Fig 2.2. The instrumental magnitude is plotted as a function of aperture diameter in arcsec for i) the unconvolved simulated galaxy, ii) the galaxy convolved with a star to simulate the effects of seeing, and iii) the CLEANED galaxy. The procedure was found to be effective down to an aperture diameter $\simeq$ 3 times the seeing width. With smaller apertures problems arose because of the effect of sampling in the beam profile.

The sensitivity of the results to the chosen CLEANING star was investigated by CLEANING a simulated galaxy with several different stars from the same frame. Provided the chosen star was "reasonably" bright but unsaturated, the results were essentially unaffected by the choice of CLEANING star and so in practice only one such star on each frame was selected to provide the beam profile.

Various values of the loop gain λ were investigated. Provided λ was reasonably small (ie < 0.2) the results were not very sensitive to the particular value chosen (for extended sources a low value is desirable to prevent the image profile being "chopped up"). The

value of the loop gain was fixed at $\lambda = 0.1$ for all subsequent CLEANING.

The sky noise level at which to terminate the iteration had also to be considered. Initially this was chosen as 2σ, but in some cases the procedure started to diverge before the image had been successfully CLEANED down to this level. This behaviour results from the fact that, unlike the situation in the radio, the noise on an optical CCD frame is not convolved with the beam profile and so, particularly when the seeing is poor, the beam profile and the noise have very different scale lengths. Cleaning into the noise is therefore to be avoided and so the CLEAN threshold had to be raised to 2.5σ.

iii) Effectiveness of the optical CLEAN procedure.

Tests on a variety of simulated galaxies of different brightnesses and profiles, and also on various stellar images, showed that the random error introduced by the CLEAN procedure was ≤ 0.04 magnitudes until the measurement aperture was reduced to < 3 times the seeing width (eg see Figure 2.2). These tests also demonstrated the significant fractions of flux which are recovered by the procedure - for example, in seeing of ≈ 1 arcsec CLEANING of one bright star by another on the same frame reclaims 0.2 magnitudes within a 4 arcsec aperture.

Having confirmed the advantages and feasibility of the technique, tests were next carried out on very faint objects. It was found that for the very faintest identifications the procedure became less effective because very few pixels contained flux $> 2.5\sigma$ of the sky noise. Therefore, for the very faintest objects a "single-step" CLEAN (with a loop gain of $\lambda = 1$) was adopted as the best way of reclaiming the flux.

iv) Error estimation

Measurements made on identical faint objects placed at different sites on the same image demonstrated that the dominant source of error was variation of the background level due to the limitations of

flat-fielding (although the Poisson noise was also non-negligible). An estimate was therefore made of the rms variation in the background level of each frame. This was then added in quadrature to the independent Poisson noise to arrive at a value for the error in the magnitude measurement.

Fig 2.2 : Example of a test of the optical CLEAN program

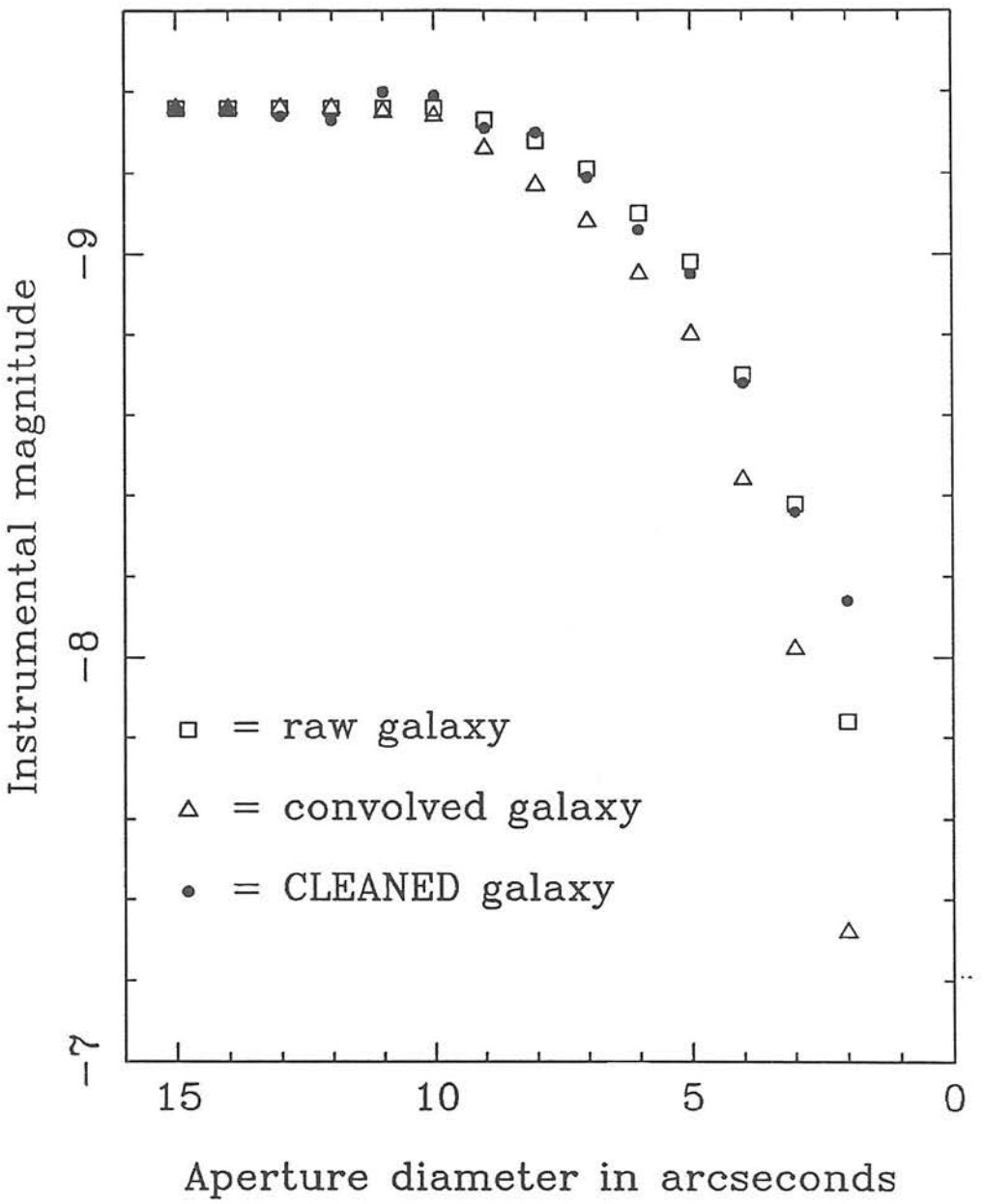

2.5d : Measurement of images

An aperture of 5 arcsec diameter was used for all the measurements. This was chosen as the smallest possible aperture consistent with the small scale limitations of the CLEAN procedure described above.

B and R magnitudes were determined for the new CCD identifications by measuring the deepest available B and R images of each object. As in the astrometry, measurements were made of both R frames for those fields where duplicate exposures had been taken at the two telescopes. These measurements confirmed that the error estimates described above were realistic measures of the uncertainty in the photometry.

In addition to the photometry of the new identifications, CCD magnitudes were also measured for several of the existing sky-survey identifications. Images of these objects had been taken with the specific aim of improving the accuracy of the optical photometry for a subset of the sky-survey identifications.

2.6: OPTICAL PHOTOMETRY - RESULTS

The results of the optical photometry are included in columns 11 → 13 of Table A.1. The quoted magnitudes are 5 arcsec aperture magnitudes of the seeing-deconvolved objects. The R and B magnitudes refer to the Mould interference filter system.

For those sources where improved CCD photometry has been obtained for the existing sky-survey identification, Table A.1 has been revised to show the new result. This subset of sources is also listed below in Table 2.3 which contains the results of both the new CCD photometry and the original eye-estimated magnitudes. CCD images of these objects are shown in Plate 2.3.

Table 2.3 : CCD photometry of existing sky-survey identifications.

Source Name	Optical type	CCD photometry R mag	CCD photometry B mag	Original plate photometry R mag	Original plate photometry B mag
1157+014	Q	17.20 ±0.03	18.07 ±0.03	16.5	17.7
1158+007	Q	18.33 ±0.04	18.94 ±0.04	17.8	18.4
1211+001	G	18.56 ±0.04	21.06 ±0.08	17.8	21.7
1212+005	G	19.54 ±0.05	21.84 ±0.12	19.4	21.3
1215-033	G	17.90 ±0.03	19.87 ±0.05	17.7	19.8
1215+013	G	17.21 ±0.03	19.03 ±0.04	16.0	18.3
1330+022	G	17.82 ±0.03	19.42 ±0.05	16.6	18.2
1331+025	G	18.97 ±0.05	21.29 ±0.09	18.6	20.9
1334+008	G	18.39 ±0.04	20.25 ±0.05	17.6	19.3
1343-026	G	19.81 ±0.06	21.84 ±0.13	19.9	21.4
1346+018	G	20.37 ±0.07	21.73 ±0.11	20.3	21.9
1349-017	G	18.39 ±0.04	19.54 ±0.05	17.4	19.3
1351-018	Q	19.30 ±0.10	20.89 ±0.03	19.2	>21.0
2150-202	G?	22.45 ±0.40	22.96 ±0.30	>20.0	>22.5
2152-218	Q?	19.16 ±0.05		19.1	20.6
2154-184	Q?	19.43 ±0.08		19.2	19.8
2154-183	Q	21.41 ±0.25		19.1	20.6
2155-202	G	19.67 ±0.05	21.86 ±0.15	19.5	21.0
2156-192	G	19.96 ±0.08		19.5	20.9
2157-214	Q?	20.51 ±0.10		20.0	21.2
2158-167	Q?	20.64 ±0.10		19.9	20.7
2204-208	Q	19.81 ±0.05	20.26 ±0.05	20.0	21.4
2211-172	G	17.69 ±0.04		16.6	19.7
2213-156	?	21.22 ±0.13	21.20 ±0.07	19.8	21.3
2214-206	Q	20.16 ±0.09		19.9	20.6
2215-185	G	17.81 ±0.03	18.62 ±0.03	17.1	18.7
2354-021	Q?	20.20 ±0.10	21.16 ±0.08	19.5	20.5
2356+018	G?	19.59 ±0.08		19.5	20.8
0012-008	G	17.15 ±0.03		15.5	18.4
0059+017	Q?	18.30 ±0.04	20.49 ±0.06	18.3	20.4
0101+023	G	19.42 ±0.06	22.06 ±0.13	19.9	21.7
0223+018 i)	Q?	21.11 ±0.20	21.68 ±0.10	22.0	>20.0
ii)	G	20.81 ±0.12	22.81 ±0.22	22.0	>20.0
0230-027	G	18.18 ±0.04	20.41 ±0.05	18.7	20.0
0239-016	G	20.75 ±0.11	22.81 ±0.25	>20.0	>22.5
0240-021	Q?	18.87 ±0.05	19.69 ±0.04	19.4	19.2

Additional notes on individual sources now follow:

1334+008

The nucleus of this bright, extended object appears to be stellar.

2211-172

The CCD image revealed that this distorted galaxy has a double nucleus.

Plate 2.3 : CCD images of existing sky-survey plate identifications in the Parkes Selected Regions. Each field is 2 arcmin square with north at the top and east to the left, and the identification is indicated by two bars.

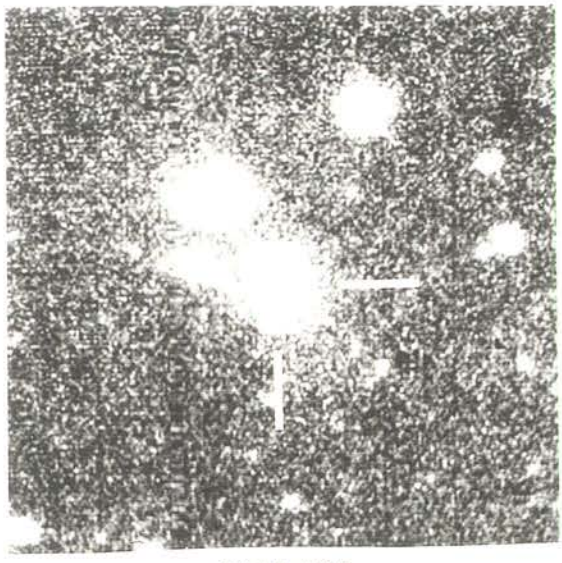

0012−008

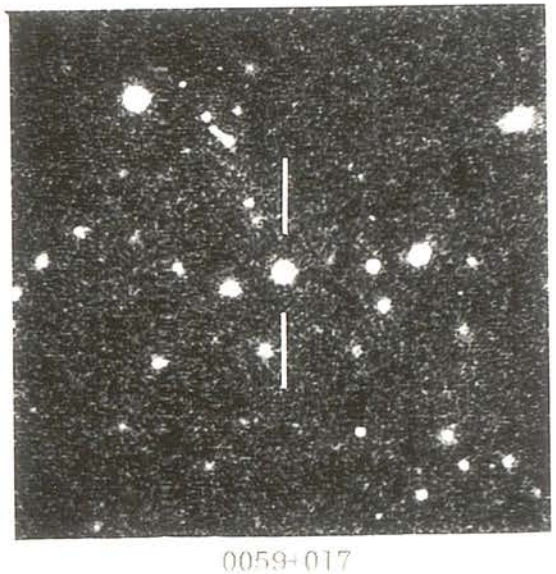

0059+017

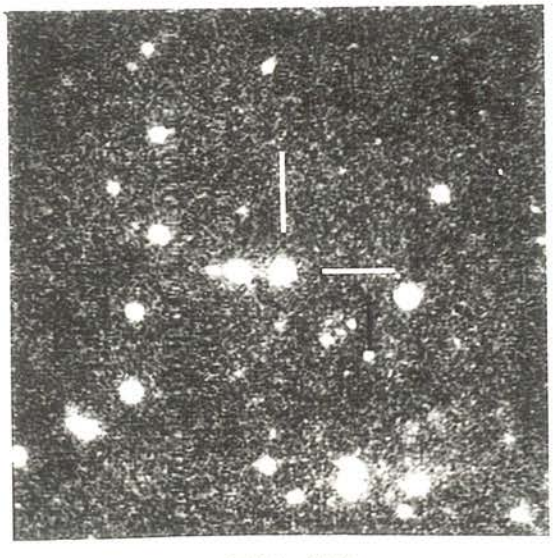

0101+023

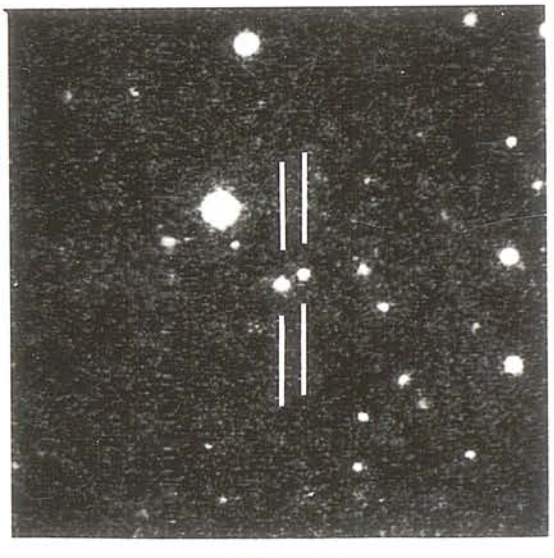

0223+018

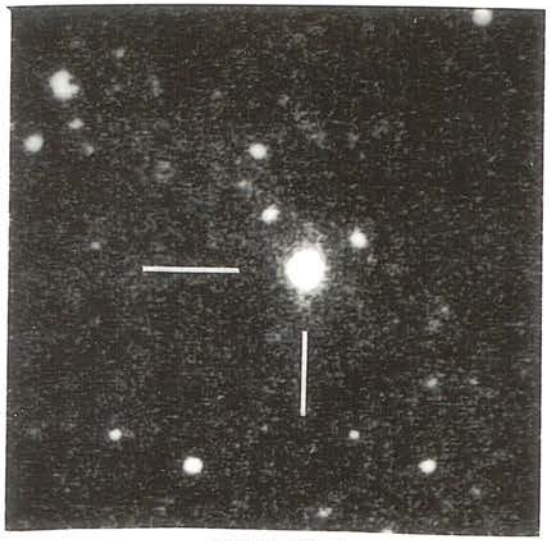

0230−027

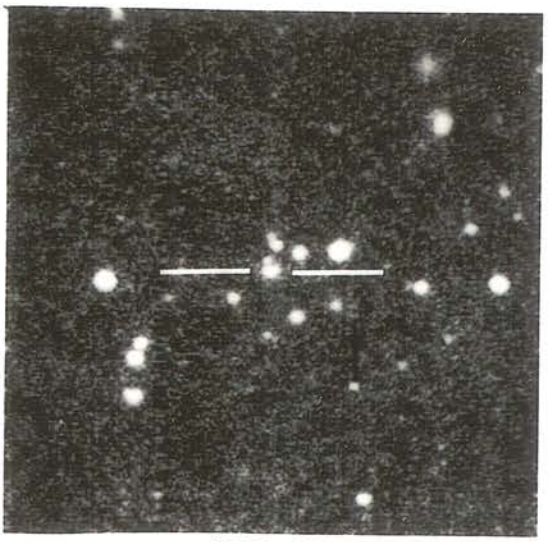

0239−016

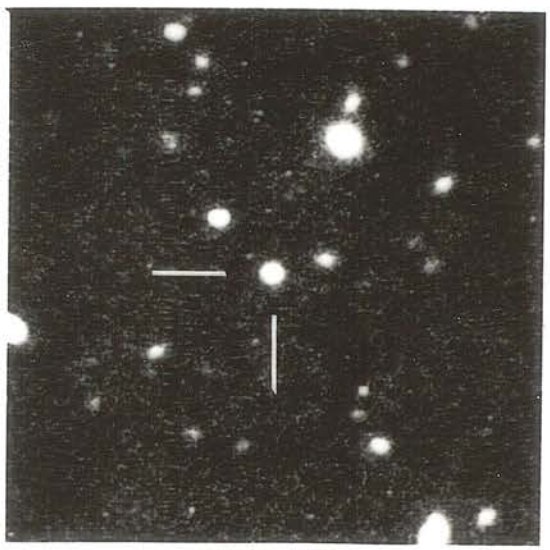

0240−021

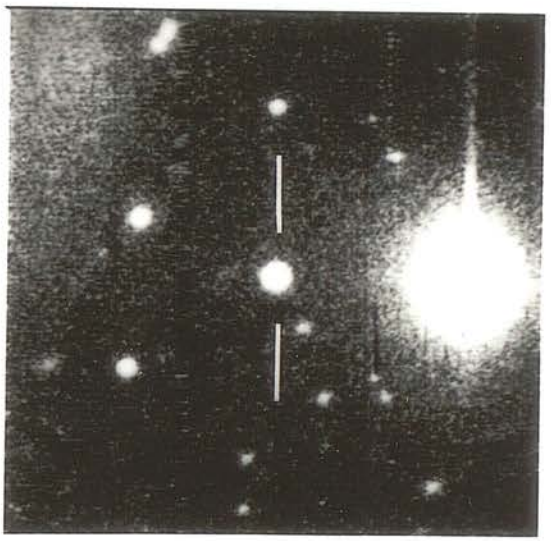

1157+014

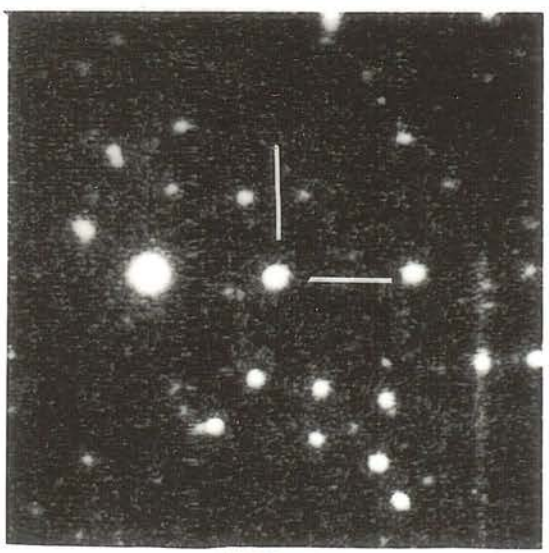

1158+007

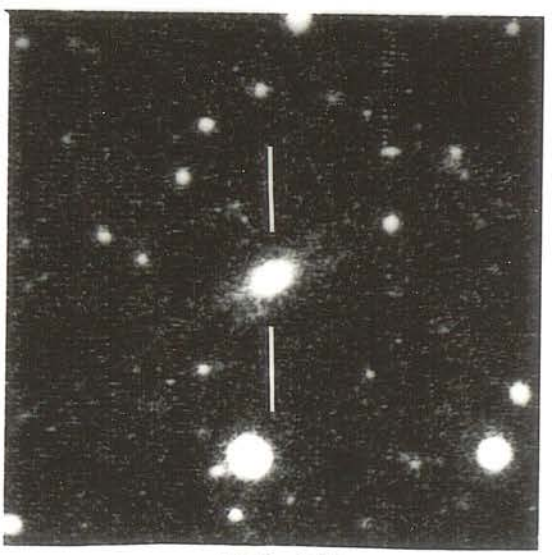

1211+000

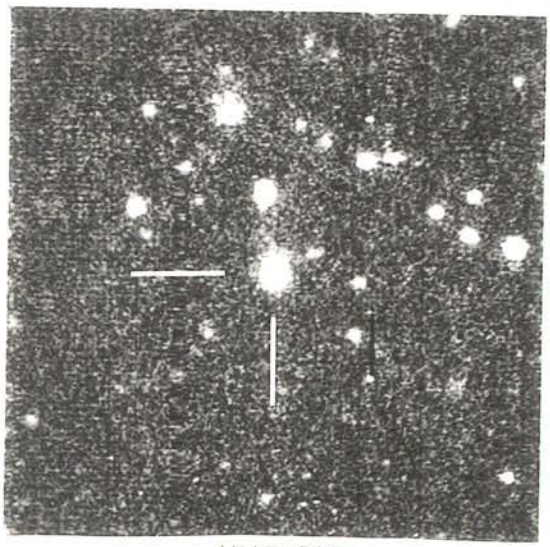

1212+005

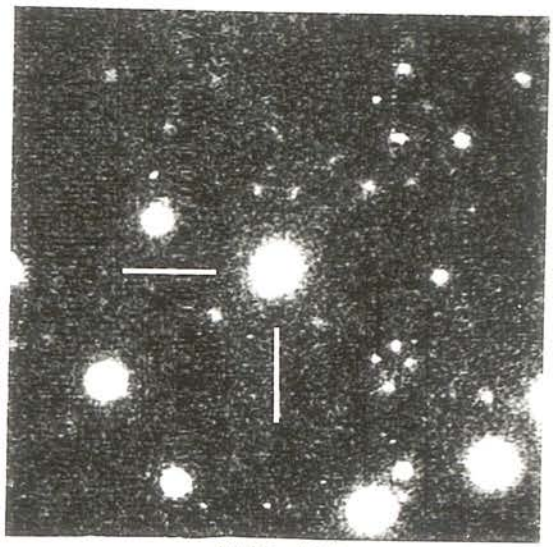

1215+033

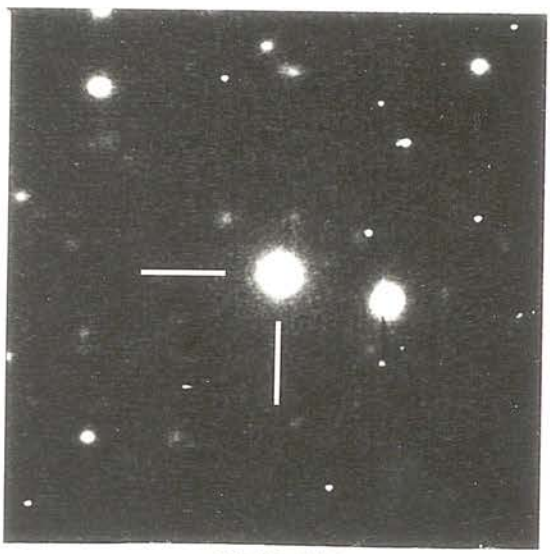

1215+013

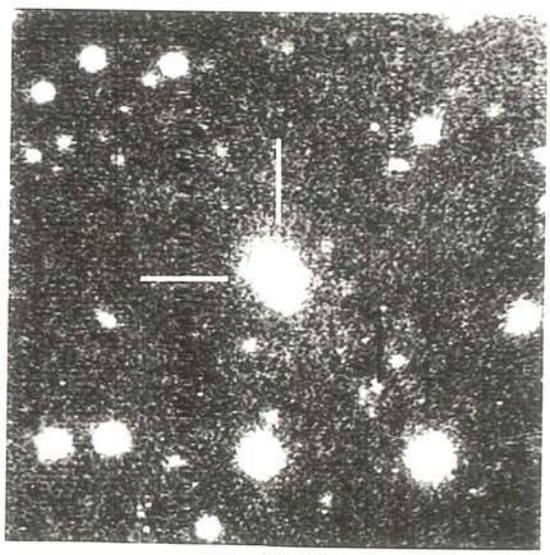

1330+022

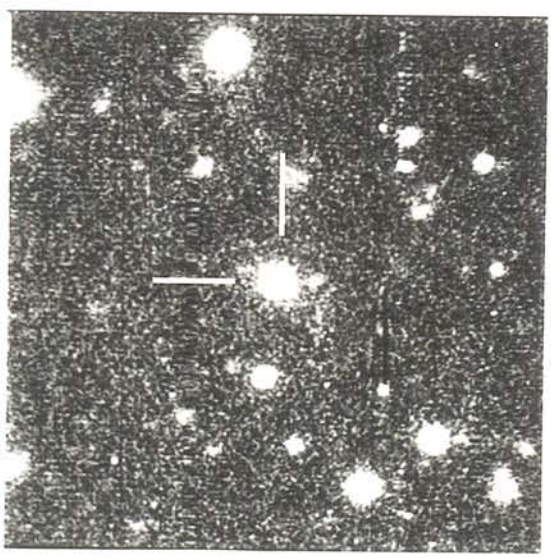

1331+025

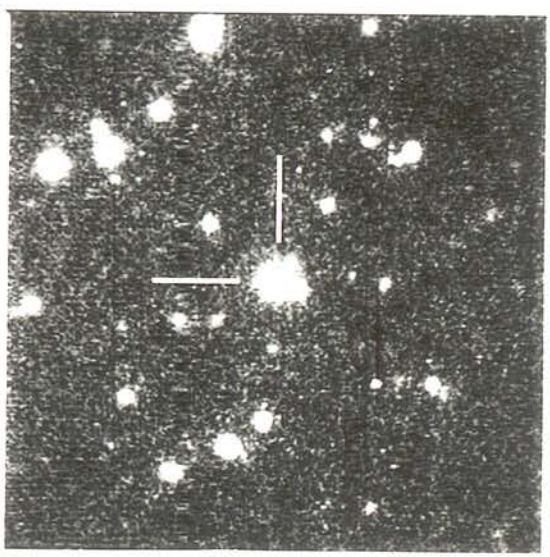

1331+005

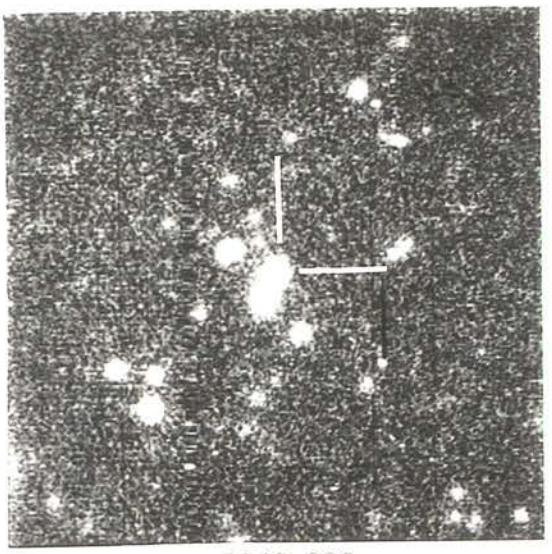

1343-026

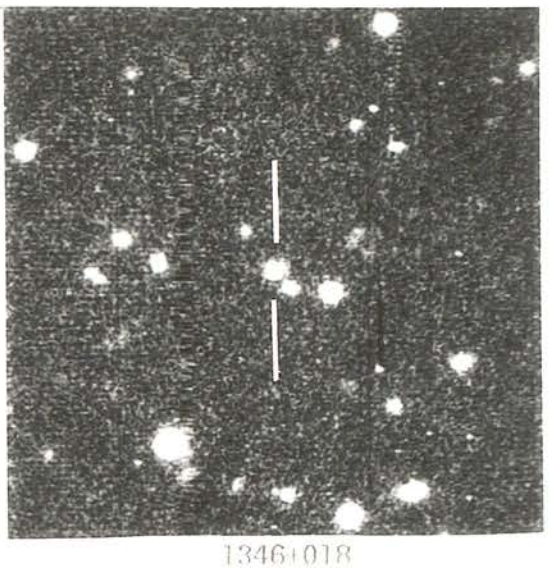

1346+018

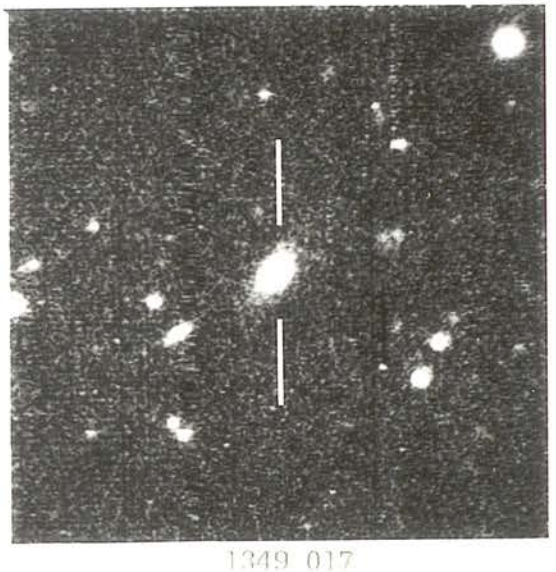

1349-017

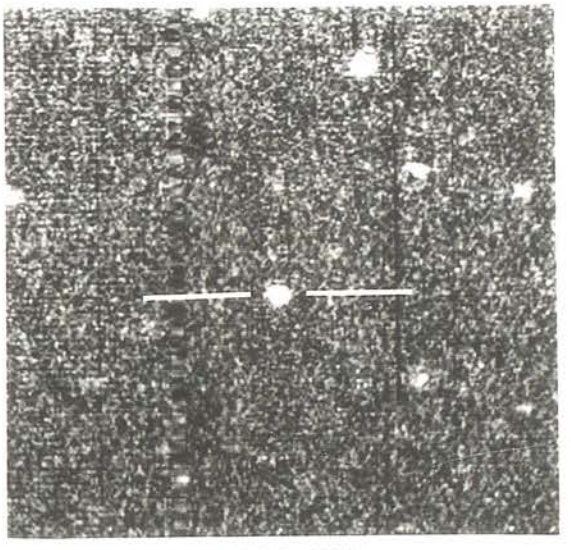

1351-018

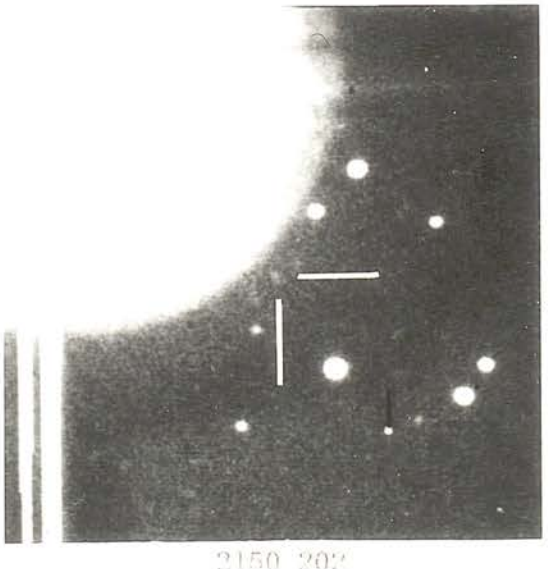

2150-202

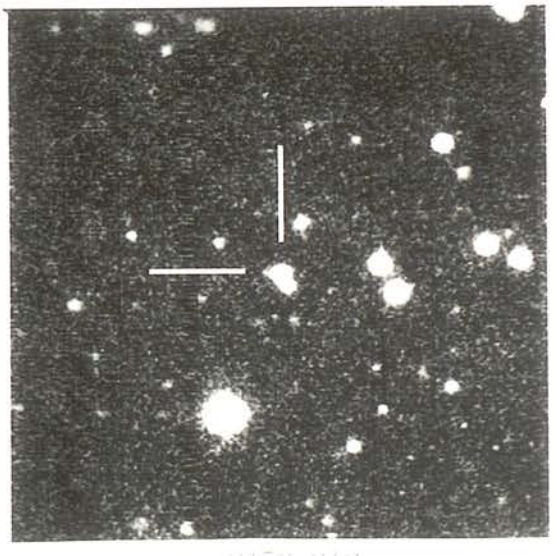

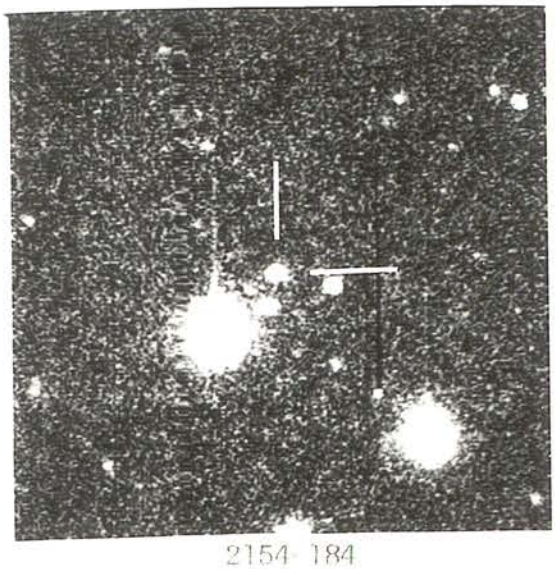

2154-184

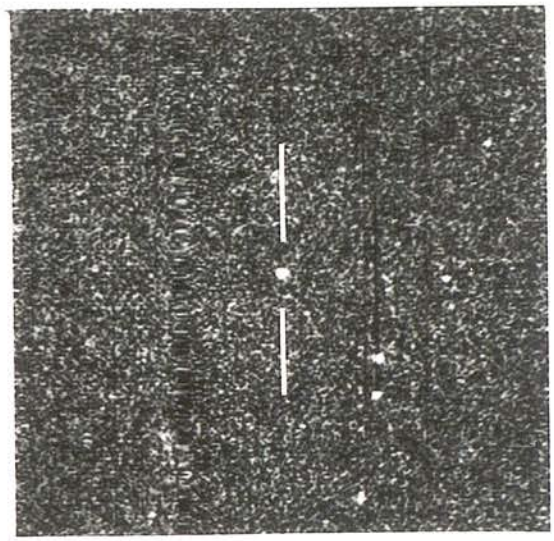

2154-183

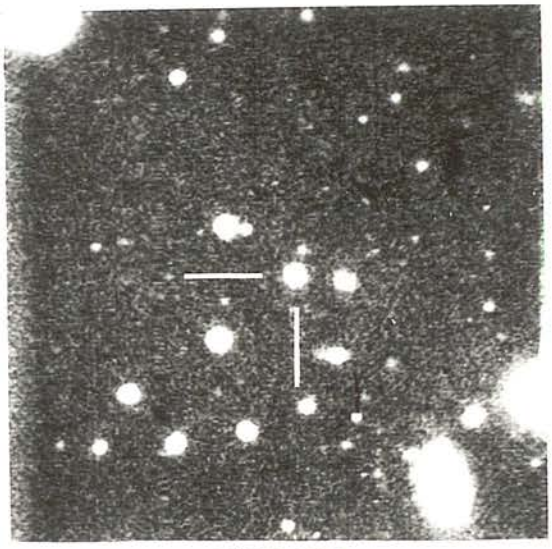

2155-202

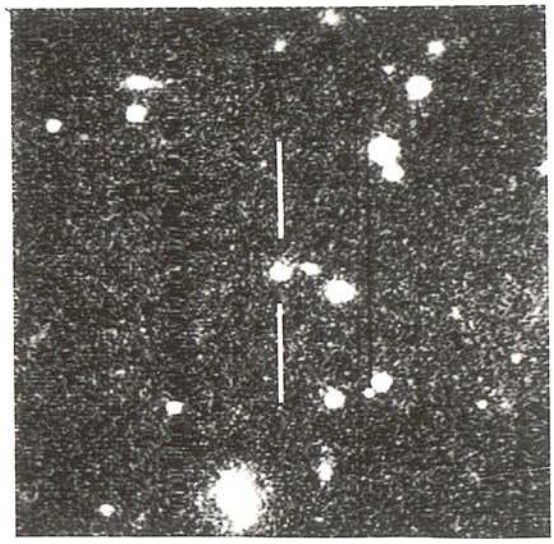

2156-192

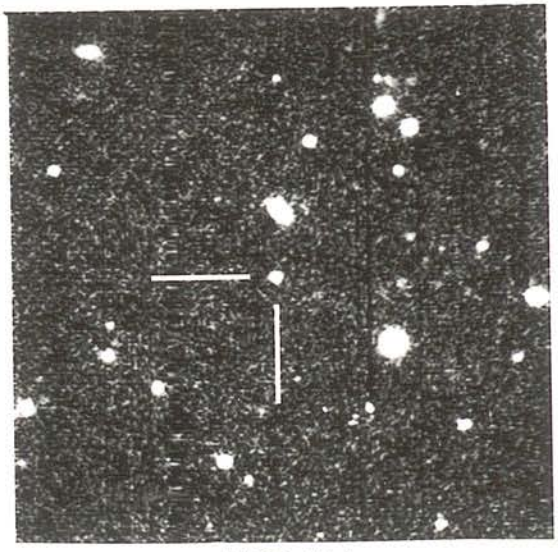

2157-214

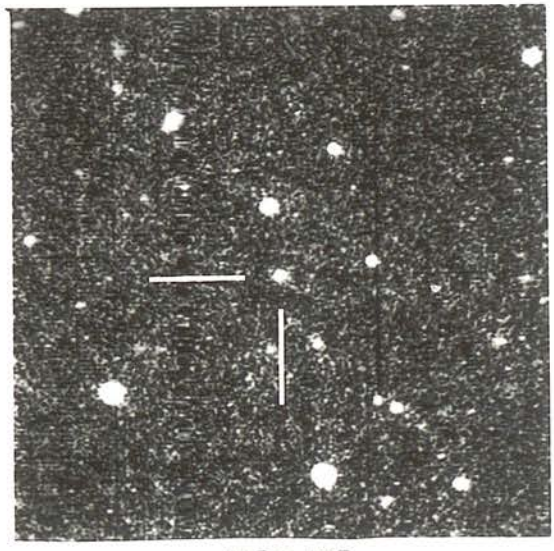

2158-167

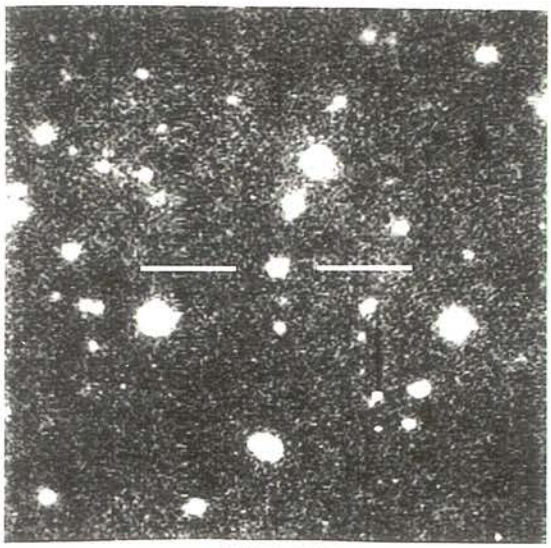

2204 208

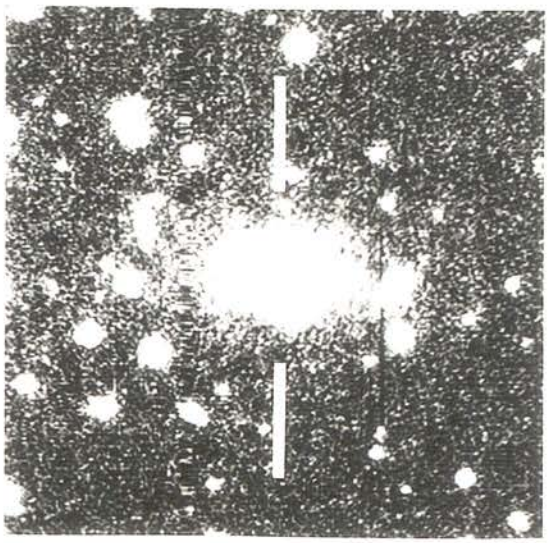

2211 172

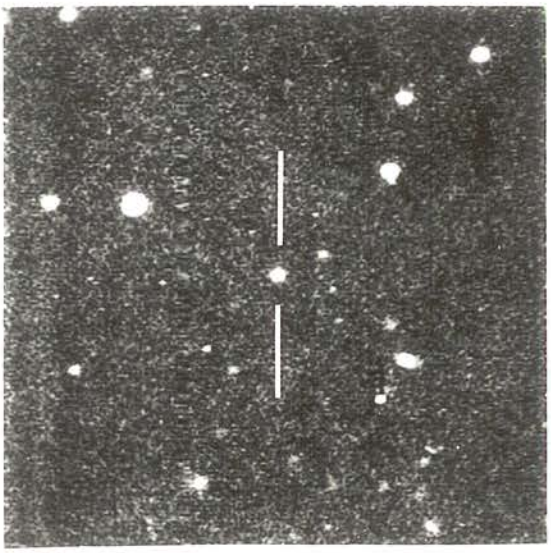

2212 156

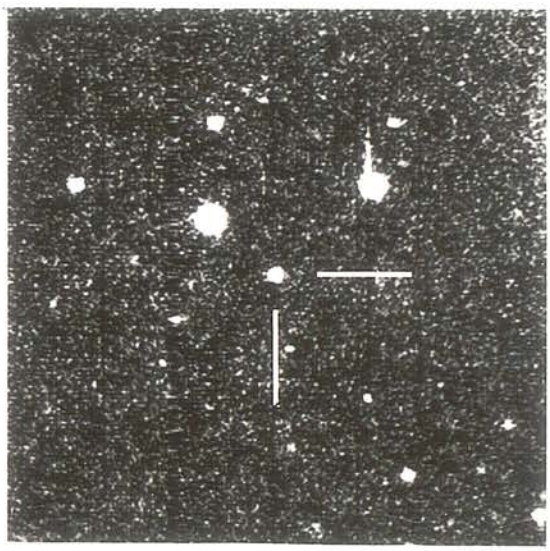

2214 206

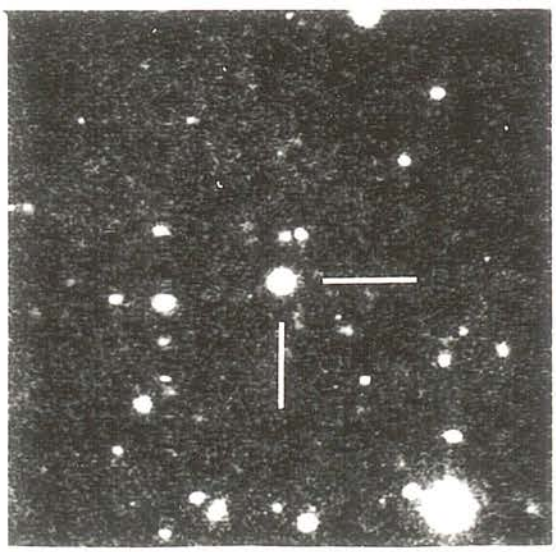

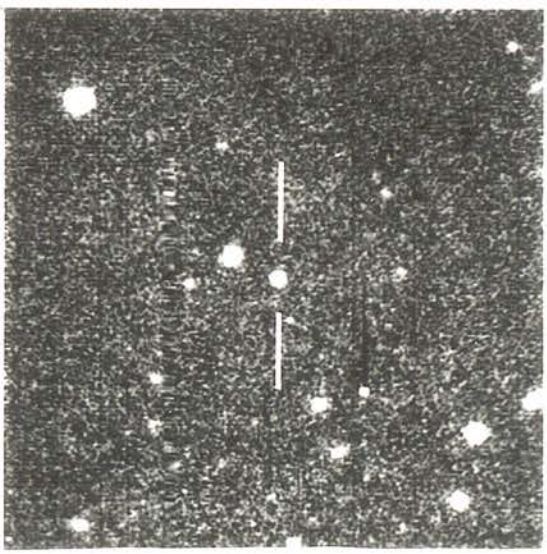

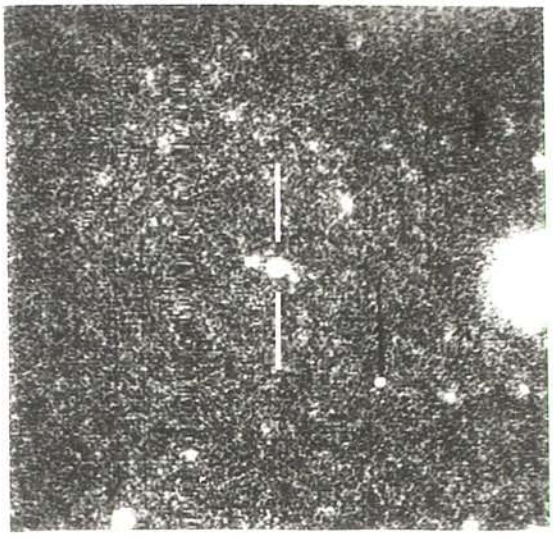

Chapter 3 : INFRARED PHOTOMETRY OF SOURCES IN THE PARKES SELECTED REGIONS

3.1 : INTRODUCTION

The value of infrared photometry in the study of distant galaxies has been convincingly demonstrated in recent years (eg Lilly and Longair 1984, Lilly *et al.* 1985, Lilly and Gunn 1985, Lebofsky and Eisenhardt 1986, Eisenhardt and Lebofsky 1987). When such infrared data can be combined with optical colour data its value is greatly increased. As described in the previous chapter, for the Parkes Selected Regions essentially complete photometry has now been obtained in both B and R wavebands. The addition of infrared photometry to this database can provide information in the following three basic areas:

i) Classification of the faint optical identifications.

It is obviously important for any subsequent analysis to determine which of the faint CCD identifications described in Chapter 2 are galaxies and which are quasars. A brief examination of Plate 2.1 demonstrates the difficulty of such a classification on purely morphological grounds, and, since spectroscopy of a large fraction of these objects is not feasible at present, classification cannot be attempted on the basis of emission lines. It is therefore necessary to use colour information to determine the nature of the faintest objects. This is possible because multi-waveband photometry, being in effect a form of very low resolution spectroscopy, is sensitive to the shape of the the optical continuum. One can therefore hope to distinguish the thermal spectrum of a galaxy from the non-thermal, power-law spectrum of a quasar. Obviously this is more easily achieved by sampling over a long baseline in wavelength, and so optical-infrared colours are a particularly powerful diagnostic.

ii) Stellar evolution.

To relate the macroscopic evolution of the radio source population

to the formation and evolution of galaxies it is necessary to study the evolution of the stellar populations in the galaxy identifications. To do this one requires multi-colour data and it is vital to have infrared data to complement the optical photometry described in Chapter 2. This is because the optical observations are sensitive to even small populations of very young stars, while the infrared light (even at redshifts $z \sim 1$) is dominated by the older Giant Branch stars. Therefore by combining measurements in the two wavebands one can hope to distinguish whether any star-formation activity indicated by the optical measurements is associated with the whole galaxy (ie galaxy formation), or merely some subset of the general population experiencing a starburst, possibly induced by interactions. Over the past few years Lilly & Longair have used this multi-waveband photometry approach to study the evolution of radio galaxies found in bright, low frequency radio samples (Lilly and Longair 1984, Lilly *et al.* 1985). However there are several reasons why it is important to extend this work to the Parkes Selected Regions sample. Firstly, in studies based on flux limited samples it is always difficult to disentangle the effects of redshift and luminosity dependence - to investigate a range of luminosities at a given redshift it is necessary to compare sources from bright and faint complete samples. There is evidence that the most radio-powerful 3CR galaxies may be anomalously bright in K (Yates *et al.* 1986) and the study of the Selected Regions can be used to investigate the possible existence of such a radio-power effect. Secondly, because of the high selection frequency (2.7GHz), the Selected Regions sample contains a relatively large fraction of compact, flat-spectrum radio sources. Many of these are identified with quasars, but those that have been identified with galaxies represent a class of source whose infrared properties have not previously been investigated. It is important to determine if these objects display similar colour evolution to the host galaxies of extended radio sources which have been studied by Lilly & Longair. Thirdly, for the present sample there now exists deeper and more extensive optical information than has been available for any radio sample previously studied in the infrared. Thus the Parkes Selected Regions provide the opportunity to investigate the star formation activity in more detail than has previously been possible.

iii) Redshift estimation

Redshift information is clearly important for the stellar evolution studies described above. It is also vital to constrain the redshift content of the Selected Regions in order to improve our knowledge of the high z evolution of the radio source population. Even with the addition of the spectroscopic data described in Chapter 4, at present the redshift content of the Selected Regions sample stands at only 40%, and so it is important to utilise the best possible method to estimate the remaining redshifts. As described above, the infrared magnitudes of galaxies are insensitive to small amounts of star-forming activity. A consequence of this is that, as demonstrated by Lilly & Longair (1984), the dispersion of the infrared Hubble diagram for galaxies does not increase significantly with redshift and the K-z relation continues to rise fairly linearly down to quite faint magnitudes (K ~ 18). In contrast, the scatter in the optical Hubble diagram rises drastically as the ultraviolet flux from young stars is redshifted into the optical passbands, and the effects of evolution cause the Hubble relation to turn over at lower redshifts than in the infrared. K photometry therefore provides the best method for estimating the redshifts of the faint galaxies in the sample.

This chapter describes the infrared observations and the resulting dataset. To address the problems described above the infrared data must be analysed in conjunction with the optical results, and therefore such analysis has been postponed until Chapters 5, 6 and 7.

3.2 : THE OBSERVATIONS

3.2a : Acquisition of the data

All of the infrared observations were made with the 3.8m United Kingdom Infrared Telescope (UKIRT) on Mauna Kea in Hawaii, during 5 observing runs between March 1985 and March 1987. These provided a total of 19 observing nights, but 12 of these were lost due to bad weather. The resulting limited amount of clear time meant that the

original aim of obtaining complete infrared colour data for the whole sample had to be revised, and the observing programme had to be restricted to trying to obtain K (2.2μm) photometry for the complete sample (K is the most sensitive waveband at UKIRT for objects as red as high redshift galaxies). This was in fact achieved for 4 of the 6 Selected Regions (see Section 3.3) but the persistently bad conditions each spring prevented completion of the entire sample. Infrared colours were obtained for only a small number of sources during the first observing run (see Section 3.3).

3.2b : The instrument

Infrared array cameras are only just becoming available at the time of writing, and so all of the observations described in this chapter were made with a single element detector. The photometer used was the common-user instrument UKT9, which uses an Indium Antimonide (InSb) photovoltaic device as a detector. This instrument is mounted at the Cassegrain focus, with the telescope in f/35 configuration. The chopping secondary mirror provides a reference beam throw which is adjustable in both position angle and size. A range of aperture sizes is available, but all of the present observations were made through either the 12.4 arcsec or 7.8 arcsec diameter aperture. The reasoning behind the choice of aperture is described in Section 3.2c below.

3.2c : Observational procedure

i) Telescope pointing and tracking

The majority of the optical identifications are too faint to be visible on the UKIRT TV even when the maximum available memory integration is used. It was therefore necessary to use accurate offsetting from the position of a nearby star to the position of the target object. For each source the brightest star within $\approx$ 1 arcmin of the object position was selected as a suitable offset star and its position measured. In fact, in most cases an accurate position had

already been measured for a suitable offset star during the original identification search. The positions of many of these stars were measured on recently taken UK Schmidt telescope plates, but in some cases they were measured on Palomar Schmidt plates taken over 30 years ago. However, although these offset stars obviously had to be bright enough to be visible on the UKIRT TV, they were also generally faint enough for their proper motions to be extremely small over a 30 year interval. In the case of the CCD identifications an adequately bright star was usually present among the secondary astrometric standards which had been used to determine the position of the optical identification (see Section 2.3a), thus ensuring the contemporary accuracy of the calculated offset.

This "blind" offsetting technique is thus believed to be extremely reliable, since the positions of both target objects and offset stars have been measured to an accuracy of $\leqslant$ 0.6 arcsec, and the telescope offsetting procedure is known to be extremely accurate over distances as small as a few arcmin. The only target objects for which accurate optical positions were not available were of course the 7 CCD empty fields (see Chapter 2). However, each of these radio sources is sufficiently compact (see Table 2.1) that one can be confident the radio position is within $\approx$ 1 arcsec of the position of the (as yet undiscovered) optical counterpart.

At the end of each observation the offset was inverted to check the accuracy of the telescope tracking during the integration, and long integrations were paused at intervals to make this check. At no time was a drift $>$ 1 arcsec detected, and indeed in many fields it was possible to monitor the accuracy of the tracking directly by marking the position of a nearby object which was visible on the TV screen

ii) Placement of the chop

The techniques of chopping and nodding are now well established in infrared astronomy as a means of coping with the problems posed by a high background. Chopping provides a reference beam which is accessed at high frequency (5-10Hz) to overcome the problem of

rapid variation in the background, and is achieved at UKIRT by hydraulic oscillation of the secondary mirror. Nodding involves movement of the whole telescope (at intervals of a few seconds) to shift the target object from the main beam into the reference beam. What was originally the reference beam then becomes the main beam for the next section of the integration, and the new reference beam is located diametrically opposite the previous reference beam position. This is done to eliminate the effects of any asymmetry between the two beam paths, and also cancels out the effect of a uniform gradient in the background. During the observations of the radio identifications the telescope was nodded every 15 seconds and so each integration consisted of a series of 30 second pairs.

The length and direction of the chop are easily adjusted and must be selected so that the reference beam does not contain any contaminating objects. An optical image of each field must therefore be used to locate a region of apparently blank sky which is larger than the chosen aperture size. This region must be far enough away from the target object to avoid any overlap of the main and reference beams (ie >10 arcsec for the present work), but not so remote as to be beyond the limit of the chopping system (the technical upper limit to the chop length is $\approx$ 100 arcsec, but in practice all the observations were made with a chop length of < 50 arcsec).

In fact, as a result of the nodding procedure, one must find find two such object-free regions, symmetrically placed about the target object. For observations of bright objects this is fairly simple, since the surface density of background objects bright enough to influence the result is not high. However, the problem becomes more serious at faint magnitudes since the background density of confusing objects is expected to increase. Lilly *et al.* (1985) estimated that by K = 18 the background density of objects in the infrared is sufficiently large for confusion to be a potential problem. However they also found that although practically none of these potential contaminants would be visible on sky survey material, 90% of them would be brighter than R $\approx$ 23, and could therefore be avoided by reference to an appropriately deep, red CCD image of the field. Such deep optical

material was available for all of the faint identifications in the present sample and so the chop was always carefully selected to avoid all objects visible on the CCD image. We are therefore confident that the infrared observations have not been significantly affected by the presence of spurious objects in the reference beam.

iii) Aperture selection

In single element aperture photometry the choice of aperture size obviously has to be made prior to each observation. This choice therefore required some consideration.

The advantages of a small aperture are better sensitivity and the reduced probability of contamination of either the reference or main beam. At K the dominant source of noise is the background - ie the sky and the telescope etc. This noise is proportional to the diameter of the aperture and so for faint, unresolved objects the sensitivity of the system will vary accordingly. As discussed in the previous section (ii) above) deep optical data can be used to ensure that the reference beam is uncontaminated. However, in a crowded field this is considerably easier to achieve with a small aperture. A more important advantage of the smaller aperture is the reduced chance of contamination of the main beam, since for obvious reasons this cannot be moved.

The main advantage of a larger aperture is increased tolerance to positional errors resulting from the offsetting procedure described above in i). Although the offsetting procedure is believed to be accurate to $\approx$ 1 arcsec, the larger aperture is obviously preferable in cases where signal/noise or potential contamination are not important problems, such as in the observations of bright galaxies.

For these reasons most of the observations of the "bright" sky-survey radio identifications were made through a "large" 12.4 arcsec diameter aperture, except in cases where contamination of the main beam was obviously going to be a problem. The majority of the faint CCD identifications were observed through the smaller 7.8 arcsec aperture. The limiting magnitude at K is about 0.3 magnitudes

fainter through the 7.8 arcsec aperture than the 12.4 arcsec one. Even larger and smaller apertures are available at UKIRT, but the positional tolerance of the next smallest aperture (5.4 arcsec diameter) was judged to be too small for safety, while there was no benefit to be gained from using apertures larger than 12.4 arcsec. During each observing run the beam profiles of each aperture were regularly checked. These were always found to be very symmetric and sufficiently square for the quoted aperture diameters to be regarded as correct.

Even with the 7.8 arcsec aperture there are a few objects for which contamination of the main beam by a close companion was unavoidable. A list of the objects for which this is probably the case is given in Table 3.7 in Section 3.3. However, in almost all of these cases the contaminating object appears very similar to the target object and so the affect on the observation is unlikely to be severe. Indeed, many of these close companions seem to be interacting with the radio identifications, in which case the two objects could be regarded as components of a single system.

iv) Photometric calibration

To calibrate the photometry, near-infrared flux standards were observed regularly throughout each observing session. The list of flux standards which have been observed at UKIRT is now extensive enough that it was possible to select a "faint" standard star in close proximity (ie ~ few degrees distant) to each of the six selected regions. The standards observed during this programme are listed below in Table 3.1. The infrared magnitudes quoted in Section 3.3 therefore refer to the UKIRT system rather than the CTIO system used by Lilly. Note, however that at K the difference between the two systems is negligible and so the present K magnitudes are directly comparable with the earlier results.

As a result of observing such nearby standards, systematic corrections due to the effects of atmospheric extinction were rendered unimportant. The normal extinction corrections at Mauna Kea are 0.05 per airmass for H and K, and 0.08 for J (an airmass of 1.25

corresponds to a zenith angle of ≈ 35 degrees). Therefore, for photometry calibrated with standards within a few degrees of each target object, these effects are clearly insignificant (ie < 1%).

Because the Selected Regions are located at high galactic latitude ($|b| > 50^{o}$) the effect of galactic extinction caused by dust near to the plane of the galaxy is also unimportant, and so no further corrections need be applied to the photometry. Since this chapter is only concerned with the presentation of the raw data, the problem of aperture corrections is not considered here but is postponed until Chapter 5, Section 5.2b.

Table 3.1 : Near-infrared flux standards used to calibrate the photometry of the Selected Regions identifications.

STAR NAME	RA	Dec	J (1.2μm)	H (1.6μm)	K (2.2μm)
HD 1160	00 13 23.1	+03 58 24.0	7.06	7.05	7.04
GL 105.5	02 38 07.6	+00 58 57.0	7.30	6.64	6.53
HD 106965	12 15 24.0	+01 51 10.0	7.38	7.34	7.32
HD 129655	14 41 11.0	-02 17 38.0	6.82	6.72	6.69
GL 811.1	20 54 04.0	-10 37 36.0	7.81	7.16	6.93

v) Signal/noise

As already mentioned in the discussion of chop placement, because of the nodding procedure each integration consists of the sum of a series of "pairs". During the observations of the radio identifications the telescope was nodded every 15 seconds and so each pair consisted of 30 seconds of integration (for very bright objects, such as the flux standards, which only require very short integrations the telescope is nodded more frequently). At the end of each pair, the instrument computer calculates and outputs the running mean, associated instrumental magnitude, and the standard deviation of the integrated signal derived from all the previous pairs. Provided that

there are several pairs, this uncertainty estimate is therefore the minimum statistical uncertainty in the data, and it is this uncertainty which was used to derive the quoted errors in the measured magnitudes (see Section 3.3). For each object the length of integration was decided upon after a sufficient number of pairs had been taken for the approximate brightness of the object to become apparent. In general the objective was to achieve a measurement accuracy of $\approx$ 10%, but for many of the fainter objects this would have necessitated unjustifiably long exposure times given the large number of target objects. Therefore for the faint objects a compromise had to be made between signal/noise and exposure time, and in such cases the exposure time estimate was aimed at achieving a magnitude error $\approx$ 0.2.

3.3 : RESULTS

3.3a : General

The measured K magnitudes and the associated errors are presented in columns 15 and 16 of Table A.1. The diameter of the aperture used for each measurement has been indicated by flagging (with an asterisk) those K magnitudes which refer to the 7.8 arcsec diameter aperture.

As can be seen from Table A.1, essentially complete K photometry has been obtained for 4 of the 6 selected regions - the regions centered on 0 hrs, 1 hr, 2 hrs and 22 hrs. The level of this completeness is discussed below in Section 3.3d. In the other 2 regions (12 hrs and 13 hrs) the infrared data are relatively sparse. Certain areas of the subsequent analysis are therefore, by necessity, confined to the complete 4-region subsample.

For a few objects (all in the 12 hr or 13 hr regions) photometry was obtained in more than a single infrared waveband. However, the number of sources which possess this additional infrared data is so small that it was decided not to include their J and H magnitudes in Table A.1. Instead, the complete infrared data for these sources are

presented below in Table 3.2.

Table 3.2 : Sources possessing multi-waveband infrared photometry

SOURCE NAME	J (1.2μm)	H (1.6μm)	K (2.2μm)
1157+014	15.93 ± 0.02	15.51 ± 0.04	14.79 ± 0.04
1201-002	16.11 ± 0.03		14.62 ± 0.05
1211+000	16.40 ± 0.20		14.80 ± 0.20
1212-007	19.20 ± 0.17		17.87 ± 0.19
1212+005	17.10 ± 0.20		15.40 ± 0.20
1215-033	15.65 ± 0.01	14.98 ± 0.03	14.35 ± 0.01
1215+013	14.91 ± 0.01	14.13 ± 0.05	13.65 ± 0.03
1330+022	15.70 ± 0.01		14.00 ± 0.10
1331+025	17.00 ± 0.10		15.40 ± 0.10
1334+008	16.08 ± 0.02	15.22 ± 0.02	14.52 ± 0.03
1336+020	17.94 ± 0.09	17.36 ± 0.13	16.72 ± 0.10
1340+022	17.80 ± 0.09	16.90 ± 0.09	15.91 ± 0.08
1342-016	14.96 ± 0.04		13.62 ± 0.03
1343-007	17.32 ± 0.04		15.71 ± 0.04
1343-026	16.83 ± 0.02		15.19 ± 0.05
1346+028	17.99 ± 0.11		16.29 ± 0.09
1348+007	18.26 ± 0.11	17.09 ± 0.08	16.12 ± 0.07
1349-017	15.80 ± 0.10		14.50 ± 0.10
1351-018	18.32 ± 0.18		17.26 ± 0.19

3.3b : Infrared observations of the optical empty fields

As described in Section 2.4 of Chapter 2, 7 radio sources in the Parkes Selected regions remained unidentified following the CCD investigation to R ~ 24, B ~ 25. Despite the obvious lack of an optical position for these objects, it was still possible to observe them in the infrared by centring the measurement aperture on the radio position. Clearly this procedure can only be relied upon when one is sure that

the position of the as yet undiscovered optical identification is very nearly coincident with the position of the radio source. One can be confident that this is indeed the case for the 7 Selected region empty fields because of the small diameters of the radio sources (see Table 2.2)

Four out of the seven optical empty fields were observed in K and all were detected at reasonable significance levels. The data on these 4 objects are presented below in Table 3.3. The other 3 optical empty fields were not observed due to lack of observing time, and only one of these, 0043-003, is part of the complete 4-region subsample.

Table 3.3 : Infrared photometry of the optical empty fields (see Appendix A for a full description of the radio structure abbreviations).

SOURCE NAME	RADIO STRUCTURE	K (2.2μm)	R-K
0105+025	Do,II / D2 ?	17.26 ± 0.22	> 6.24 ± 0.22
0225+002	Do,II	18.54 ± 0.36	> 5.46 ± 0.36
2158-170	D2	18.44 ± 0.28	> 5.56 ± 0.28
2357-006	P	17.97 ± 0.23	> 5.53 ± 0.23

The limits on the optical-infrared colours of these 4 objects strongly suggest that they are high-redshift galaxies rather than quasars (See Chapter 5, Section 5.2a).

These infrared detections mean that now only 4 of the 178 sources in the Selected Regions sample still lack an identification.

3.3c : Infrared empty fields

There are 4 sources in the sample which were not detected in the infrared, although all of them had been successfully detected at optical wavelengths. The photometric data on these objects are

presented below in Table 3.4. All 4 sources were observed on at least two separate occasions and with at least two different chops. Because of the limited amount of available observing time it was decided to terminate an integration after ~ 20 minutes if no significant amount of flux had been detected by that time. This means that no extremely deep infrared integrations have been obtained for these objects and the assigned lower limits to their K magnitudes of 19.0 may be regarded as conservative.

Table 3.4 : The infrared empty fields (see Appendix A for a full description of the radio structure abbreviations).

SOURCE NAME	RADIO STRUCTURE	K (2.2μm)	R-K	B-R
0000+035	P	> 19.0	< 2.27	1.74
2204-182	Do,II	> 19.0	< 4.82	> 0.18
2205-178	Do+CC,II	> 19.0	< 3.30	1.33
2355-024	P,V	> 19.0	< 3.37	0.56

The last of the 4 sources listed above, 2355-024, was one of the objects which was noted in Chapter 2 to have a rather large radio-optical positional discrepancy. To allow for the potential problem of poor astrometry in this field, or the possibility of a mis-identification, this object was therefore observed twice, first with the measurement aperture centred on the optical position, and then with the aperture centred on the radio position. However in neither case was any significant flux detected.

A brief note on the probable nature of each of these 4 undetected sources now follows. By necessity this involves reference to classification on the basis of colour information, a full description of which is not given until Section 5.2a.

0000+035

On the basis of its colours this object was originally classified as a

quasar - the low upper limit to the optical-infrared colour (R-K) places it firmly in the natural extension of the quasar locus on the R-K/K diagram, in which case its high optical (B-R) colour would suggest a high redshift (See Figure 5.1, Section 5.2a). However, recent spectroscopy by Jeremy Allington-Smith at the William Herschel Telescope has revealed that this object is in fact a galaxy with z = 0.363. In retrospect it is clear that the reason for the incorrect colour classification is that, for z = 0.363, this galaxy is anomalously faint, both in the optical and infrared.

2204-182

The nature of this object is unclear. It was one of the faintest of the CCD identifications and no morphological information can be gained from the CCD image. Because of the relatively large value of R-K it is the best candidate among the 4 infrared empty fields for a very distant galaxy.

2205-178

This object is probably a quasar, since the radio source has a strong compact core and also the R-K colour of the identification is fairly blue.

2355-024

This object is also probably a quasar. The radio source has been classified as variable and again the R-K value is relatively small.

3.3d : Completeness of the 4-region subsample

At the beginning of Section 3.3 it was noted that essentially complete K photometry has now been obtained for 4 out of the 6 selected regions. This section briefly discusses the level of this

completeness and the potential importance of the omissions.

The 4-region subsample comprises the regions centered on 0 hrs, 1 hr, 2 hrs and 22 hrs RA and contains a total of 123 sources. Only 16 of these were not observed in the infrared, but examination of the radio and optical data on these sources reveals that only ~ 4 of these omissions are relevant to the subsequent analysis of the data. The 16 unobserved sources are listed below in Table 3.5 along with the relevant optical and radio information.

Table 3.5 : Objects in the 'complete' 4-region subsample which were not observed in the infrared (see Appendix A for a full description of the radio structure abbreviations).

SOURCE NAME	RADIO STRUCTURE	OPTICAL TYPE	B	R	z
0005+021	U,V		24.4	>23.0	
0013-005	U	Q?	20.2	18.4	0.100
0043-003	Do,II		>23.5	>23.0	
0101-025	P	Q	18.8	18.7	2.050
0103-021	D2	Q	19.0	19.0	2.201
0223+018	Do,II	Q?	21.68	21.11	
0235+017	U+Di	G	10.9	10.5	
0239+002	U+Di	G	11.4	12.2	0.003
0240-002	I	G	9.5	8.8	0.004
0241+011	Do+CC,II	Q	19.0	19.5	1.400
0241-012	Do,II		>23.5	23.58	
2150-202	Do,II	G?	22.96	22.45	
2157-200	U,V	Q	19.4	18.9	1.198
2159-201	Do,II / D2?		>24.5	23.2	
2204-208	U,V	Q	20.26	19.81	1.900
2357-006	Do+CC,I	G	15.6	14.3	0.084

Examination of the above table makes it clear that 10 of these 16 objects are either quasars of known redshift or extremely bright,

nearby galaxies, several of which also possess a known redshift. Two further sources, 0005+021 and 0223+018 are also very probably quasars - 0005+021 is an unresolved, variable radio source with a very blue optical identification, while the optical identification of 0223+018 is also blue and stellar in appearance.

There are thus only 4 omissions (0043-003, 0241-012, 2150-202 and 2159-201) which are relevant to the study of galaxy evolution at high redshift. It is important to stress here that observations of these objects were not attempted purely because of the lack of observing time and so their omission is not expected to seriously bias the infrared properties of the sample.

3.3e : Repeatability of the infrared photometry

A few objects which had been observed in the October 1985 run were re-observed during the October 1986 run. The measurements of these objects therefore provide some evidence of the reproducibility of the K photometry, and the relevant data are presented below in Table 3.6.

Table 3.6 : Objects with repeated K photometry

SOURCE NAME	OCT 85 MEASUREMENT		OCT 86 MEASUREMENT	
	K (2.2μm)	Aperture	K (2.2μm)	Aperture
0047+023	18.00 ± 0.32	12.4"	17.78 ± 0.25	12.4"
0056+020	15.88 ± 0.11	12.4"	15.82 ± 0.07	7.8"
0059+017	15.50 ± 0.15	12.4"	15.62 ± 0.04	7.8"
0101+023	15.73 ± 0.11	12.4"	16.01 ± 0.09	12.4"
0242+009	16.14 ± 0.15	12.4"	16.16 ± 0.07	12.4"
2153-188	15.24 ± 0.09	12.4"	15.21 ± 0.05	7.8"
2153-204	15.32 ± 0.06	12.4"	15.23 ± 0.09	12.4"
2215-179	16.05 ± 0.10	12.4"	15.93 ± 0.08	7.8"

For all of these sources the two measured K magnitudes are consistent to within the statistical uncertainty, providing evidence of the repeatability of the measurements. The value of χ^2 for these 8 comparison results is 6.7, which indicates that the quoted statistical errors are indeed accurate measures of the uncertainty in the results.

3.3f : Contamination of the measuring aperture

The vast majority of the faintest identifications were observed through the smaller of the two apertures (ie the 7.8 arcsec aperture). This aperture was also used for observations of brighter identifications whenever there was a danger of contamination of the main beam by a nearby object. In some cases, however, the companion is so close to the target object that, even in the 7.8 arcsec aperture, contamination at some level was unavoidable.

The objects whose measured K magnitudes may have been affected by contamination of the main beam are listed below in Table 3.7. Contamination of the main beam will obviously always result in an overestimate of the true brightness of the object. However in most of these cases the effect on the result is unlikely to be severe and is probably often negligible in comparison with the errors in the photometry. The potential contaminants fall into two categories:

i) Very nearby (~ 4 → 5 arcsec distant), often interacting companions which appear very similar to the target object

ii) Nearby stars which, although not so close to the target object, are considerably brighter than it and may therefore influence the result, particularly if the seeing is poor at the time of observation.

For only two of the objects listed below are the contaminants of the latter type. These are 1329+012 and 2202-179 which are both ~ 8 arcsec distant from a nearby star.

In all of the other nine cases the companion is a faint object ~ 5

arcsec from the radio identification. In fact, for several of these sources it is not clear whether the companion object should be regarded as a genuinely undesirable contaminent since often the target and companion appear to be components of a single interacting system.

Table 3.7 : Sources for which the K magnitude may have been affected by contamination of the measurement aperture by a nearby object.

SOURCE NAME	K (2.2μm)
0100+023	17.22 ± 0.25
0223-023	17.32 ± 0.14
1205+011	17.20 ± 0.20
1329+012	17.10 ± 0.30
1352+006	17.00 ± 0.50
2152-018	16.08 ± 0.09
2157-191	17.63 ± 0.20
2158-160	17.39 ± 0.12
2202-179	16.79 ± 0.10
2207-203	17.40 ± 0.18
2356+033	16.24 ± 0.12

Chapter 4 : SPECTROSCOPY OF RADIO IDENTIFICATIONS IN THE PARKES SELECTED REGIONS AND BRIGHTER 2.7GHz RADIO SURVEYS

4.1 : INTRODUCTION

Redshift information is the vital ingredient in any study of cosmological evolution. The more complete the redshift information, the more secure the resulting conclusions. In principle the ultimate goal of the optical study of a radio survey is the measurement of an optical spectrum, and hence a redshift, for every source in the sample. However, in practice this is rarely feasible.

Prior to the introduction of CCD detectors, extensive deep imaging of the sort described in Chapter 2 would have required prohibitive amounts of observing time. Nowadays the technology/telescope-time barrier is encountered when one wishes to measure the optical spectra of large numbers of very faint objects ($R > 21$). This is demonstrated by the existence, at the time of writing, of only one 'large' radio sample with complete redshift information - the 3CR (Laing *et al.* 1983), despite the fact that many radio galaxies, and certainly most radio quasars, possess emission lines which greatly ease the problem of redshift determination from low signal/noise spectra (eg Hine & Longair 1979). With detectors now approaching efficiencies ~ 1 we must await the next generation of optical telescopes before complete spectroscopy of large, faint samples becomes anything other than a long-term, multi-group proposition.

It was clear, therefore, that, in the timescale of the present study, completion of the redshift content of the Parkes Selected Regions could not possibly be achieved. Nevertheless, it was still important to try to increase the fraction of spectroscopically measured redshifts in the sample, which, at the start of the present work, stood at only 22%. In particular it was hoped to complete the redshift content of the quasar subsample. This was important because photometric redshift estimation is not as reliable for quasars as it is for galaxies. It was also a feasible proposition because, as described in Chapter 5, >80% of the quasar identifications in the sample are

brighter then the sky-survey limit of R ~ 20.

The spectroscopic observations described in this chapter were therefore principally aimed at obtaining redshifts for all the quasi-stellar identifications in the Parkes Selected Regions for which redshifts did not already exist in the literature. Observations were also made of some identifications whose nature was ambiguous, as well as several sky-survey galaxy identifications. In addition to these observations of Selected Region sources, spectra were also measured of some radio identifications from the brighter 2.7GHz samples (Peacock & Wall 1981, Wall & Peacock 1985, Peacock 1985) as part of the long-term programme to improve the redshift content of the complete sample database at 2.7GHz.

4.2 : THE OBSERVATIONS

4.2a : Acquisition of the data

The majority of the spectroscopic observations were made at the 3.9m Anglo Australian Telescope (AAT) during two observing runs in April and September of 1985. These two runs provided a total of 3 nights devoted to spectroscopy, of which approximately 1 night was lost due to bad weather. Some additional data were also obtained from ~ 1 clear night of spectroscopy at the 2.5m Isaac Newton Telescope (INT) at La Palma in January 1986. Also included are some INT spectra kindly taken in May 1985 by Alan Purvis (0213-13, 0528+13, 1741-03) and in January 1986 by Jeremy Allington-Smith (0229+034, 0230-022, 1225+36).

4.2b : The instruments

i) The FORS/IPCS

At the 3.9m AAT the observations were made with the Faint Object Red Spectrograph (FORS) in tandem with the Image Photon Counting System (IPCS)/RGO Spectrograph mounted at the f/8 Cassegrain focus

of the telescope. This two-instrument combination is achieved by dichroic splitting of the beam at 5300Å. All wavelengths longer than this are directed to the FORS while the IPCS receives the blue light. The resulting spectra thus consist of two distinct halves which must later be joined at 5300Å.

The Faint Object Red Spectrograph is a fixed-format, low-dispersion spectrograph which uses a GEC CCD as a detector. As its name implies, this instrument is optimized for low resolution, red spectroscopy of faint objects and has been designed with a minimum number of optical components to ensure high efficiency. The CCD has a readout noise of about 6.7 electrons and has a good red response; saturation occurs at 245750 electrons, or 65535 counts. The chip has 385 by 576 elements with the larger dimension in the dispersion direction; each pixel is 22μm square. The dispersing element is a grism which produces a CCD pixel scale of 10Å by 1 arcsec. The normal wavelength range is fixed at 5200 → 10900Å with peak response at ~ 7000Å.

The Image Photon Counting System is the main detector of the RGO Spectrograph. This is a 2-dimensional detector which counts individual photon events. The maximum number of pixels available is 2044 in the spectral and 514 in the spatial direction. The detector is mainly useful between 3500 and 6000Å with a maximum quantum efficiency of about 20% at 4000Å. This wavelength range is therefore complementary to the wavelength range covered by the FORS. The RGO Spectrograph has a variety of gratings available as dispersing elements. The 250B grating, which has the lowest dispersion, was used for the present observations. The resulting dispersion is ~ 150Å per mm, or ~ 2Å per pixel, although this dispersion varies somewhat over the wavelength range.

The combination of these two detectors provides low resolution spectroscopy over a wide wavelength range (3500 → 10000Å), which is obviously ideally suited to the determination of emission-line redshifts for faint objects. As well as extending the wavelength coverage below the 5000Å limit of the FORS, use of the IPCS provides the additional benefit of real-time readout - because the detector of

the FORS is a CCD, it is not possible to examine the level of signal/noise achieved until the chip is read out at the end of an integration. By monitoring the build-up of the IPCS portion of the spectrum, one can make an on-line decision as to how much integration will be required to enable an unambiguous determination of the redshift.

ii) The FOS

At the 2.5m INT the observations were made with the Durham-RGO Faint Object Spectrograph (FOS) mounted at the f/15 Cassegrain focus of the telescope. Like the FORS at the AAT, this instrument is a fixed-format, low resolution (15 → 20Å FWHM) device of high throughput, specifically designed for faint object work. It also uses the same type of detector, a low readout noise, 385 × 576 GEC CCD. Dispersion is provided by a transmission grating and a cross-dispersing prism (ie a grism) which together give a two-order format covering the wavelength range 4000 → 10500Å. The first-order spectrum covers the wavelength range 4000 → 10500Å with a dispersion of 10.7Å per pixel. The second-order spectrum covers the range 4000 → 5500Å with a dispersion of 5.4Å per pixel. The pixel scale in the spatial direction is 1.25 arcsec (each pixel is 22μm square).

Although the wavelength coverage of this instrument is nominally almost as great as that of the FORS/IPCS combination at the AAT, the poor sensitivity of the GEC chip at wavelengths shortward of 5000Å results in a relatively poor blue response. The second-order spectrum of the FOS spectra was therefore not as effective as the IPCS portion of the AAT spectra in extending the wavelength coverage to the blue. This fact, combined with the smaller aperture of the INT, makes the FOS a somewhat less effective instrument for faint object redshift determination than the FORS/IPCS combination. Obviously the advantage of real-time readout offered by the IPCS at the AAT is also absent at the INT. The optical design of the FOS is described in detail by Wynne (1982).

4.2c : Observational procedure

i) The AAT observations

The observations were made through a single long slit, the width of which was adjusted to be compatible with the seeing at the time of observation (eg 2 arcsec in seeing of 1.5 arcsec). The slit was always set perpendicular to the horizon to eliminate the effects of atmospheric dispersion. Many of the target objects were bright enough to be visible on the aquisition TV, in which case accurate centring of the slit over the target object was achieved by manual adjustment of the telescope pointing. For the fainter objects accurate positional offsetting from nearby stars was used.

To remove any asymmetry in the 2-D spectra a beam-switching technique analogous to the infrared procedure of nodding was used, and each integration was divided in half. During the first half of the integration the target object object was positioned at a chosen location along the slit. Then, for the second half, the telescope was slewed to move the object along the slit to a second location so that the spectrum of the object fell onto a different region of the 2-D detectors. This technique enables the sky subtraction to be carried out in a symmetric manner (see Section 4.2d) and allows the reality of dubious features in a spectrum to be checked by comparison of the two halves.

To maximise observing efficiency, each integration was terminated as soon as it became clear that a redshift could be determined unambiguously from the final spectrum. An initial estimate of the required exposure time was made on the basis of apparent magnitude, but this estimate was often revised as a result of monitoring the real-time buildup of the IPCS portion of the spectrum.

For calibration purposes the following observations were made during each run.

i) Wavelength calibration was achieved by observing a CuAr arc lamp at regular intervals throughout each night.

ii) Smooth spectrum stars were observed (in FORS only) to facilitate removal of the atmospheric absorption features which are prevalent in the red region of the spectrum.

iii) Finally, spectrophotometric standards were observed to enable flux calibration of the final spectra. Flux calibration is often regarded as superfluous when the main aim of the observations is simply redshift determination. However, for these particular observations such calibration was valuable for two reasons. Firstly, relative flux calibration is necessary to enable the IPCS and FORS sections of the spectrum to be smoothly joined at 5300Å. Secondly, the shape of the continuum is often an important source of information, particularly if the spectrum has no strong emission features (eg low redshift galaxies can be identified by the presence of the 4000Å break, even in spectra of poor signal/noise). The spectrophotometric standards which were observed to flux calibrate the AAT spectra are included in Table 4.1 below. In Figure 4.1 the flux calibrated spectra of these standard stars are shown along with the corresponding literature data. Of course, because a narrow slit was used, the flux calibration cannot be absolute but the relative calibration should be approximately correct.

ii) The INT observations

The observations were made through a single slit of projected length 25 arcsec. This short slit was used to prevent overlap of the 2nd-order object spectrum and the 1st-order spectrum of the sky. Again the width of the slit was adjusted to be compatible with the seeing at the time of observation, and the slit was always adjusted to be aligned perpendicular to the horizon. Almost all of the objects observed were too faint to be visible on the aquisition TV at the INT, and so accurate offsetting from nearby stars was used to position the target object on the slit.

For each object an initial exposure of 10 or 15 minutes was taken, and the chip read out. The resulting spectrum was then inspected to decide how much additional integration would be required to achieve a satisfactory level of signal/noise.

For calibration purposes the following observations were made.

i) A CuAr arc lamp was observed several times during each night to enable wavelength calibration of the spectra.

ii) Smooth spectrum stars were observed to facilitate removal of the atmospheric absorption features.

iii) Spectrophotometric standards were observed to flux calibrate the spectra. The standards which were observed at the INT are included in Table 4.1 below.

Table 4.1 : Spectrophotometric standards observed for flux calibration

STAR NAME	LITERATURE REFERENCE	OBSERVING RUN
W485A	Oke (1974)	AAT, April 1985
VMa2	Oke (1974)	AAT, Sept 1985
GD248	Fillipenko & Greenstein (1984)	INT, Jan 1986
W1346	Oke (1974)	INT, May 1985

4.2d : Data reduction

i) The AAT spectra

Reduction of the data was carried out on the ROE Starlink Vax 11/780. Because each integration had been divided in two, the raw spectrum of each object consisted of 4 2-dimensional spectra - ie 2 FORS spectra and 2 IPCS spectra. After removal of cosmic rays, extraction of the spectra from the 2-D image, sky subtraction, smooth star division (of the FORS section only) and addition of the two halves of integration were carried out with the SPICA package. Sky subtraction for the first half of each integration was achieved by

extracting the sky spectrum from the channels which contained the object spectrum during the second half, and vice versa.

Wavelength calibration, flux calibration and the joining of the IPCS and FORS sections were carried out using software which was specifically written for the purpose. The procedure adopted was as follows.

i) The IPCS and FORS sections were separately wavelength calibrated and re-binned. A fifth order polynomial was required to wavelength calibrate the IPCS spectra, while a linear fit was adequate to calibrate the FORS. The coefficients of these polynomials were obtained using the ARC procedure in SPICA. The error in the wavelength calibration is < 1Å over both sections of the spectra.

ii) The IPCS and FORS sections were flux calibrated using the spectrum of the photometric standard (ie either W485A or VMa2, depending on the observing run). The absolute accuracy of this calibration is probably only ~ 50%, but the relative accuracy, which is more important, is ~ 10%.

iii) Finally the IPCS and FORS spectra were joined by averaging the data values over the region 5290 → 5320Å, and the IPCS portion was median smoothed into 10Å bins to be consistent with the resolution of the FORS.

ii) The INT spectra

The FOS spectra were initially processed using software provided by Ian Parry (Durham): the curved 1^{st} and 2^{nd} order spectra were straightened and extracted from the 2-dimensional data. Several problems can arise at this stage: i) sometimes the 2^{nd} order spectrum was so faint that the object could not be extracted; ii) the FOS chip has a charge transfer efficiency that is less than ideal, so that the usual process of sky subtraction by interpolation from the channels on either side of the object leaves the long-wavelength end of the spectrum looking rather messy. From this stage, the extracted

spectra were processed using the FIGARO package. Linear wavelength calibration was accurate to ≤ 1Å. Atmospheric absorption removal and flux calibration were carried out in the normal manner. The 1^{st} and 2^{nd} order spectra were then convolved by a Gaussian with σ = 10Å, before being joined by averaging over the overlap region 5000 → 5300Å (usually with a relative scaling of a factor ≤ 1.5)

Figure 4.1 : The observed spectra of W485A and VMa2 after flux calibration, compared to the spectra in the literature (Oke 1974).

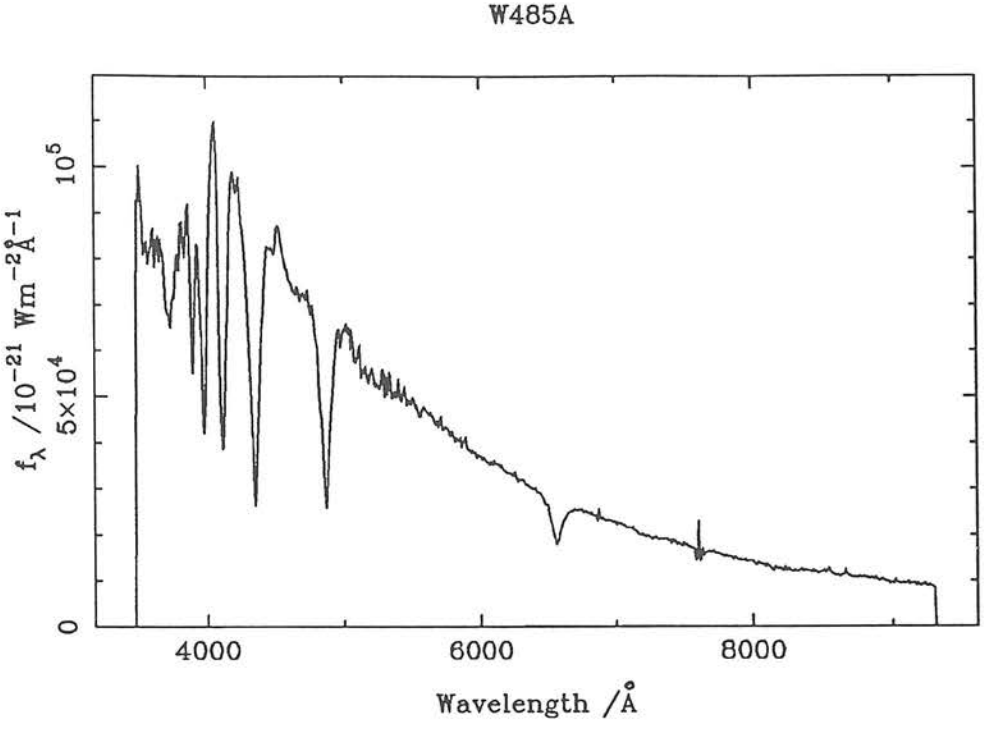

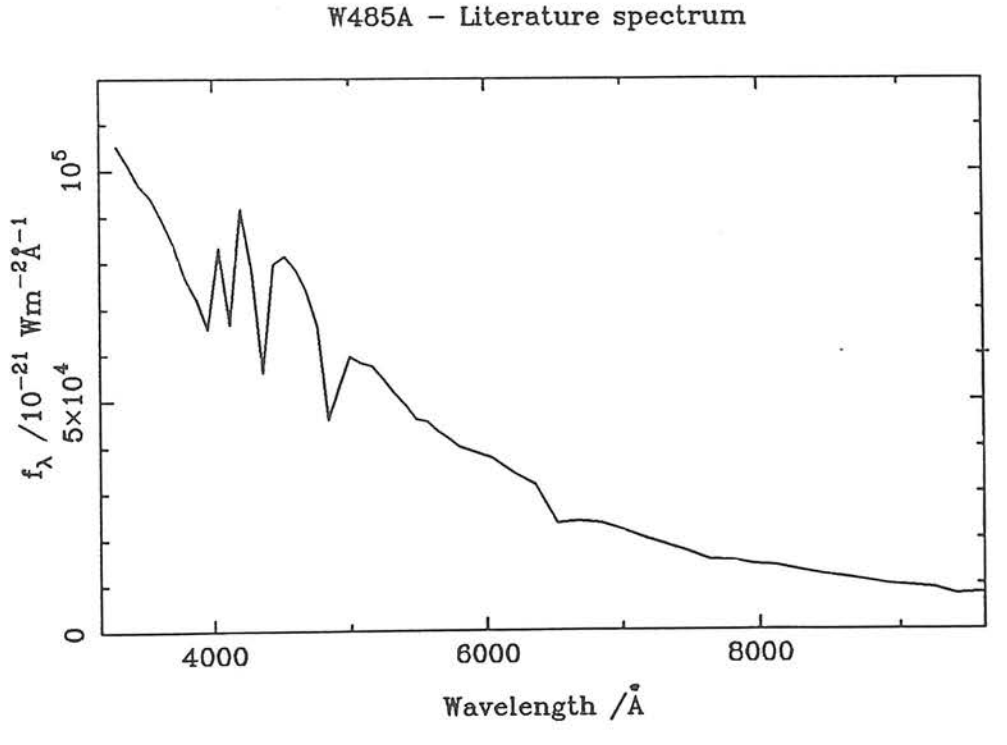

VMa2

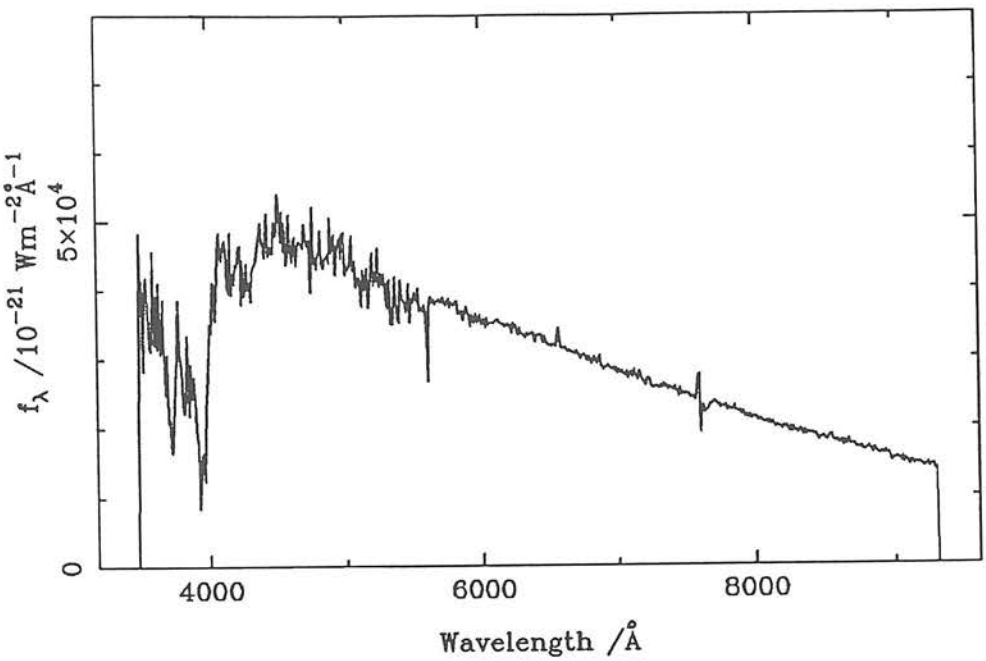

VMa2 – Literature spectrum

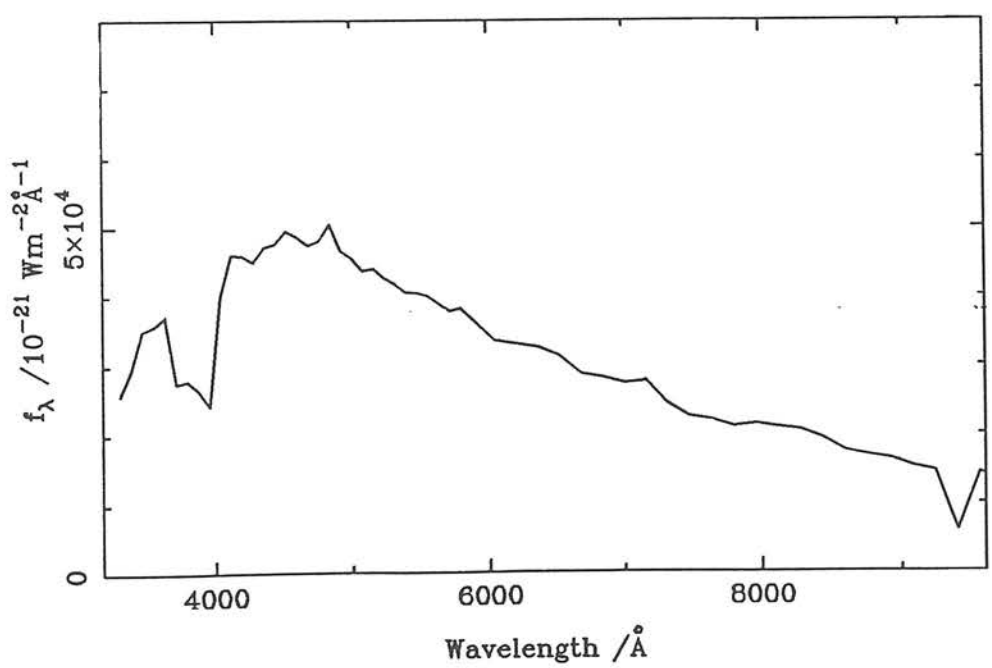

4.3 : RESULTS

The final reduced spectra are presented below in Figure 4.2, while the line identifications and the resulting redshift determinations are given in Table 4.2. Finally a summary of the results of the spectroscopic observations is given in Table 4.3. The new redshifts have been incorporated into the appropriate sample tables which are given in Appendix A (Tables A.1 → A.4).

The success rate of redshift determination is fairly high (particularly for the AAT observations, >75%), despite the fact that many of the objects turned out to be galaxies rather than quasars. This success is largely attributable to the now well established frequent appearance of emission line features in the spectra of radio galaxies (eg Hine & Longair 1979, Perryman *et al.* 1984, Spinrad & Djorgovski 1984). In fact, most of the objects for which a redshift could not be determined appear to have non-thermal power-law continua and are therefore probably weak-lined quasars or BLlacs. White *et al.* (1987) have also noted the frequent occurrence of such objects in their spectroscopy of quasar identifications from the Parkes survey. Table 4.3 would seem to suggest that these weak-lined quasars occur rather more frequently in the brighter 2.7GHz samples than in the Selected Regions. However, it is not clear to what extent this simply reflects the fact that most of the non-Selected Region objects were observed at the INT, and thus possess poorer quality spectra making the determination of a redshift less likely.

The most spectacular result of these spectroscopic observations was the discovery of a redshift of $z = 3.709$ for PKS 1351-018 (Dunlop *et al.* 1986). This is by far the largest redshift measured for any source in the Selected Regions and indeed, at the time of its discovery, was the second largest ever measured (second only to PKS 2000-330, $z = 3.78$, Peterson *et al.* 1982). PKS 1351-018 is also notable for being one of the optically faintest high-redshift quasars, although interestingly it is one of the most radio luminous sources in the Selected Regions ($S_{2.7} = 1.0$Jy). It was also the first high-redshift quasar to be identified as such on the basis of its

optical-infrared colour (see Chapter 5, Section 5.2). The properties of this object are discussed in more detail in Chapter 5.

Figure 4.2 : The spectra. In the cases where it has proved possible to determine a redshift from the spectrum, the value of z is shown in the figure. Individual line wavelengths and identifications can be found in Table 4.2. The spectra which do not extend blueward of 5000Å are INT spectra in which the second-order spectra have been discarded because they contained no significant flux.

PKS 0000−006

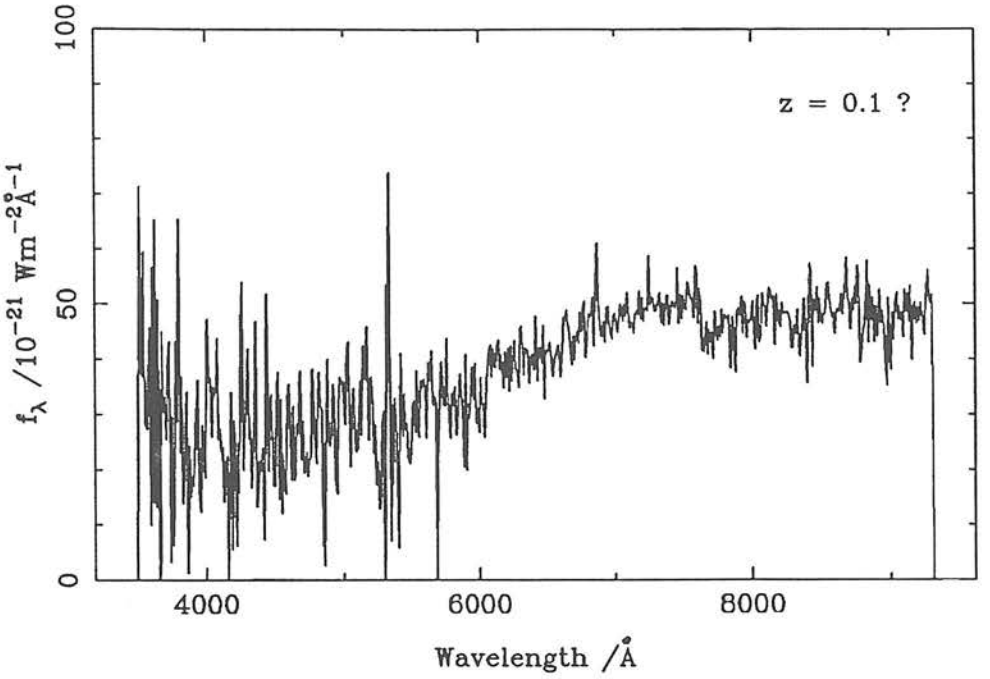

PKS 0013−005

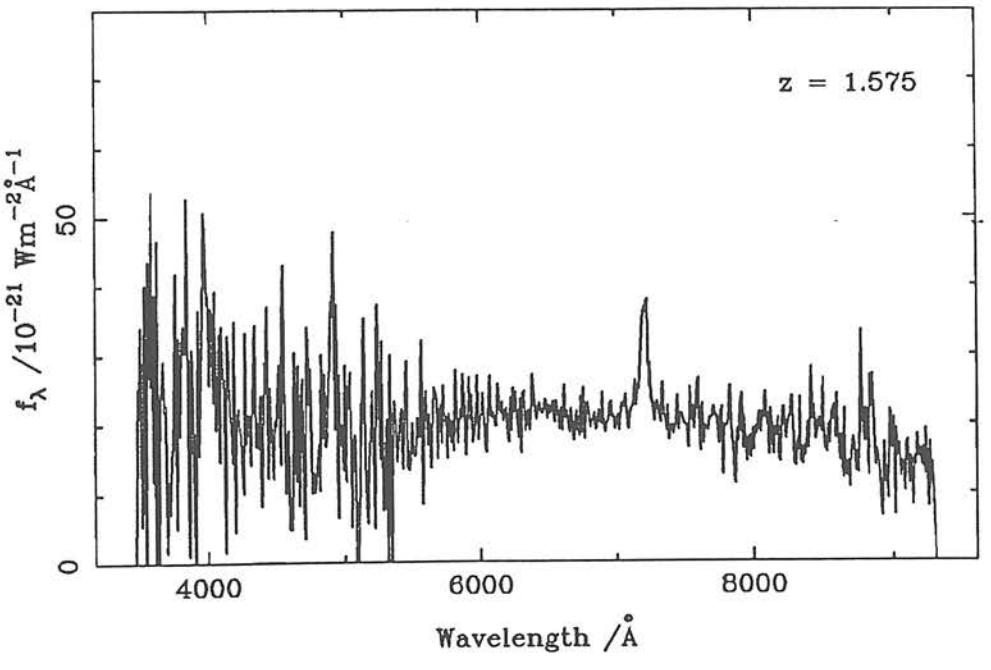

PKS 0040+017

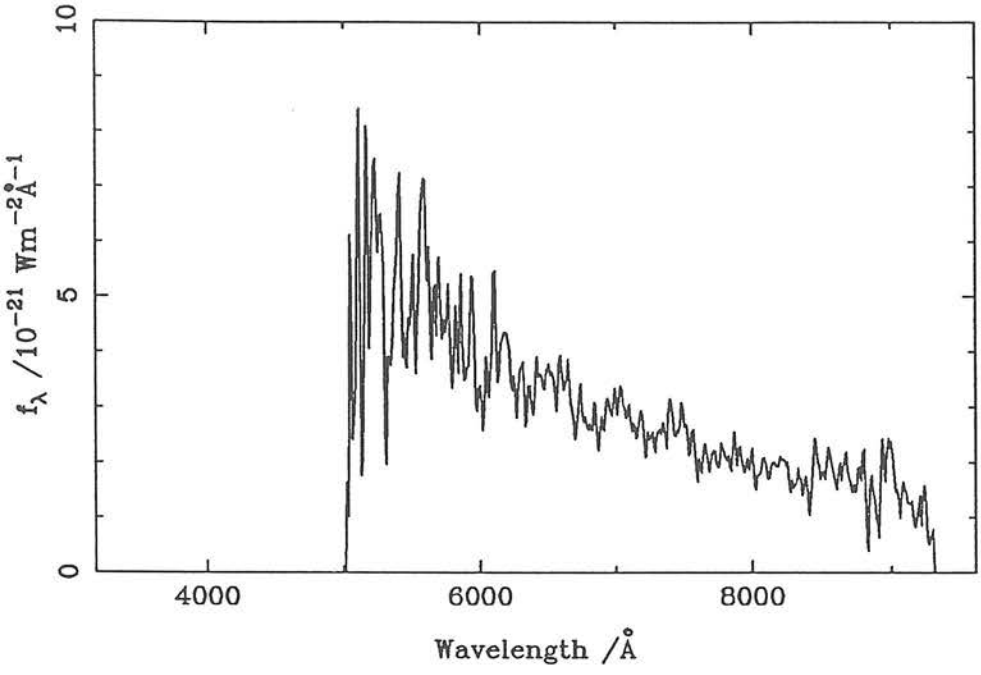

PKS 0041+007

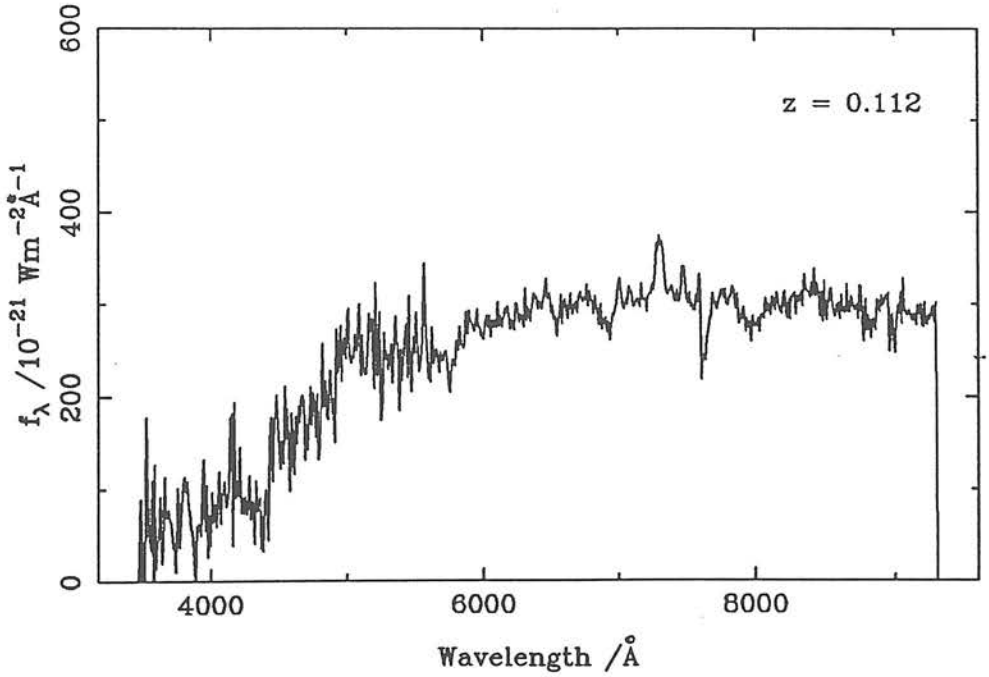

PKS 0047+023

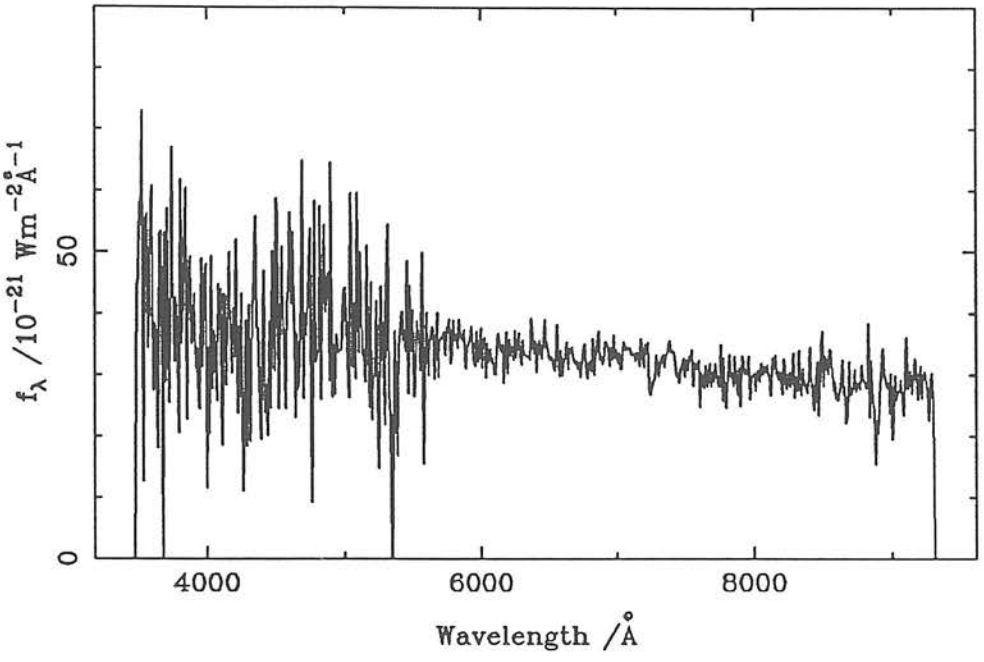

PKS 0213−13

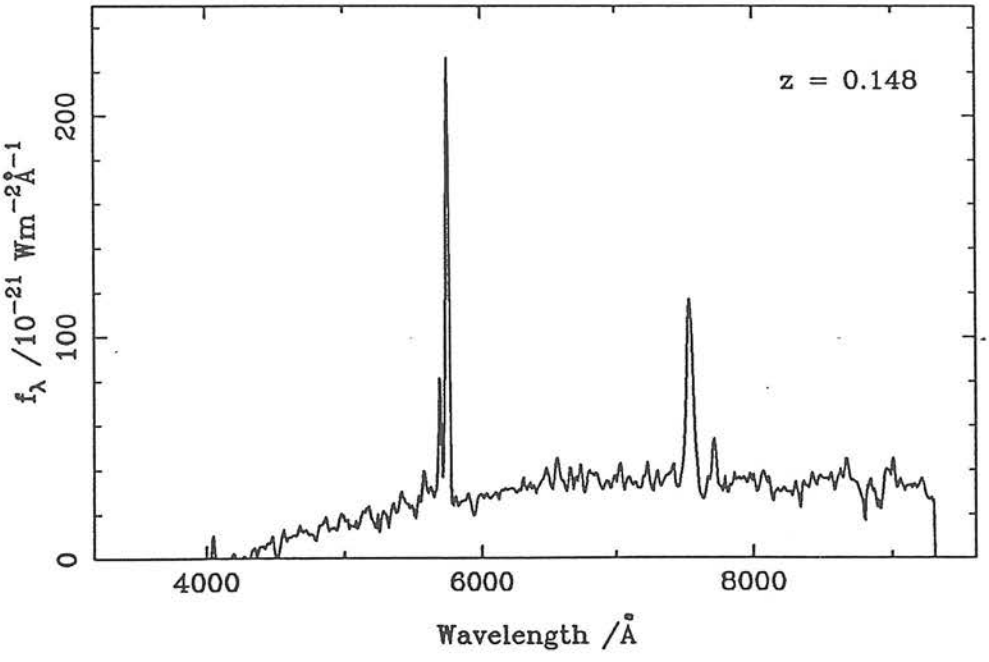

PKS 0215+015

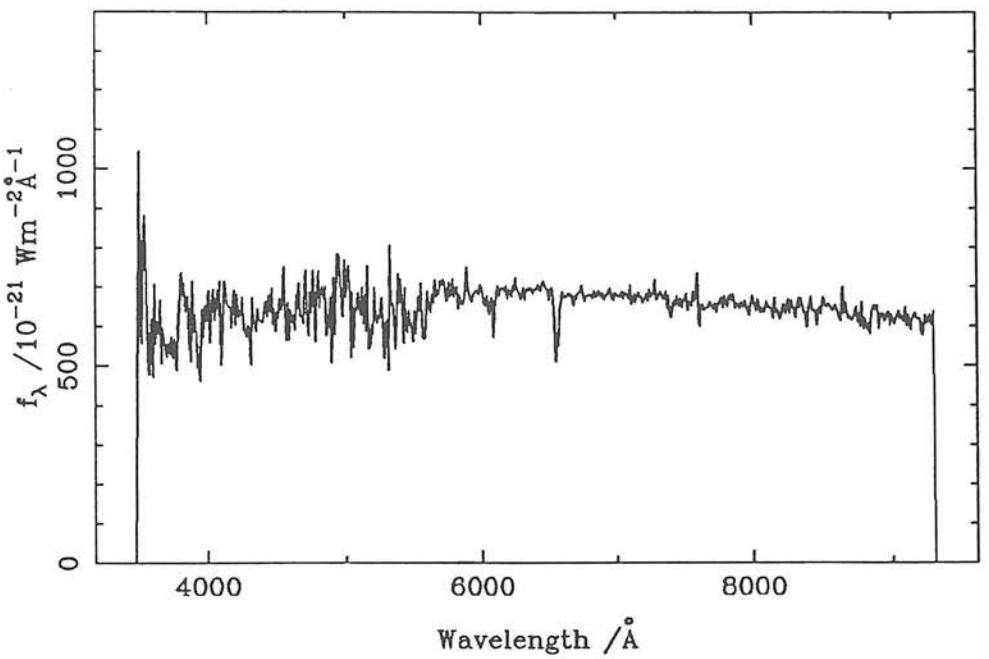

PKS 0223+012

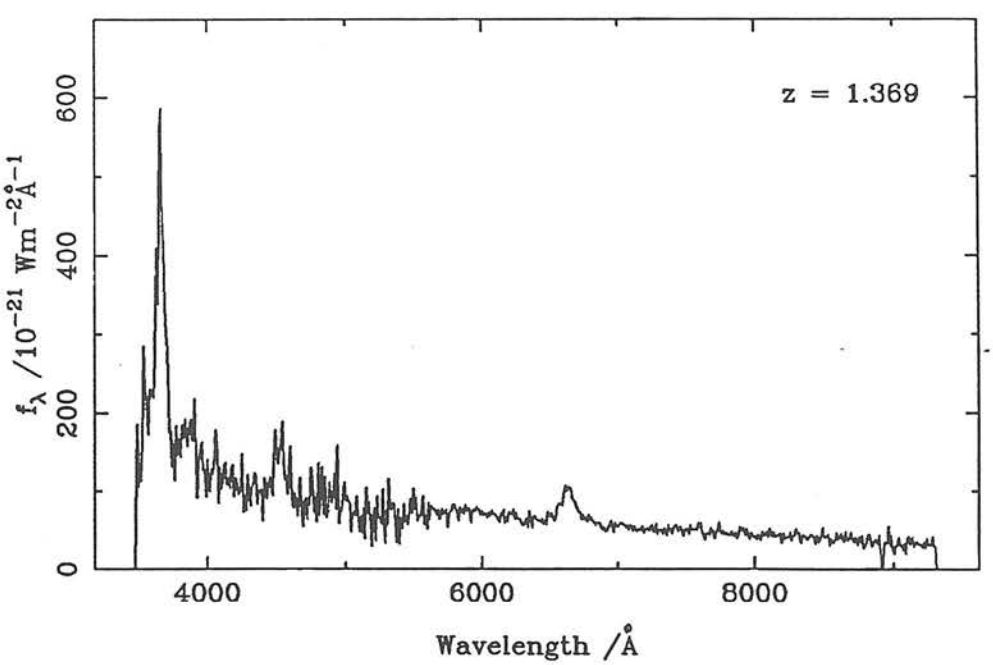

PKS 0229+034

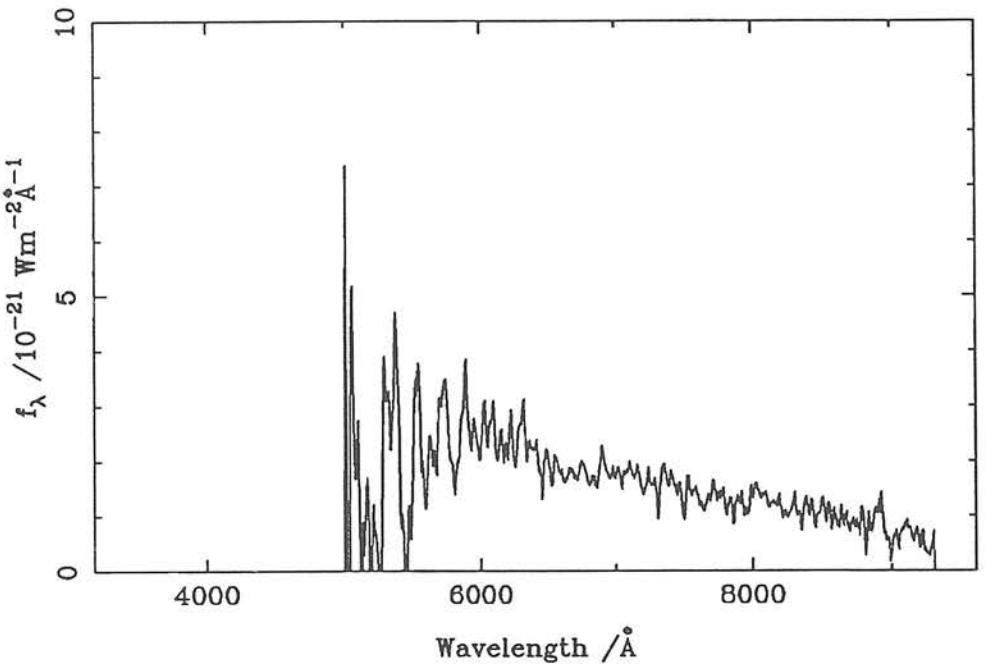

PKS 0230−027

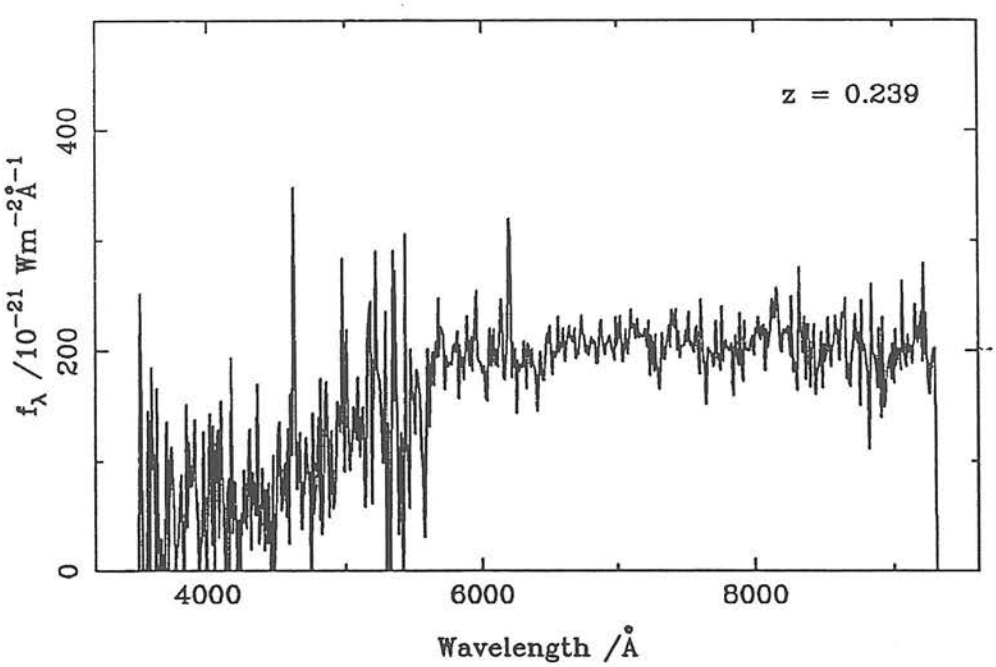

PKS 0230−022

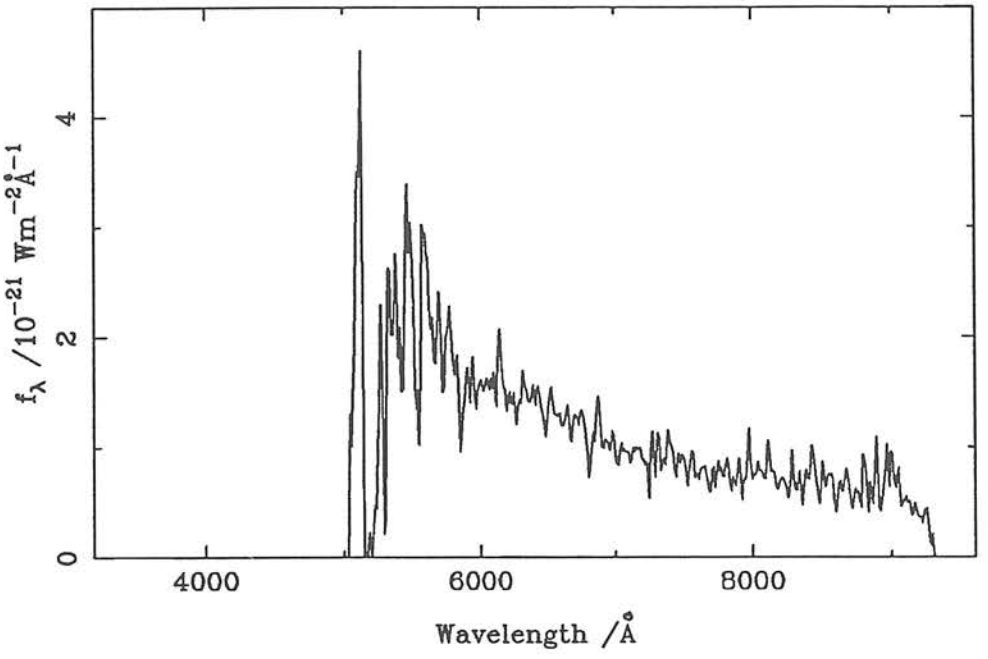

PKS 0235+023

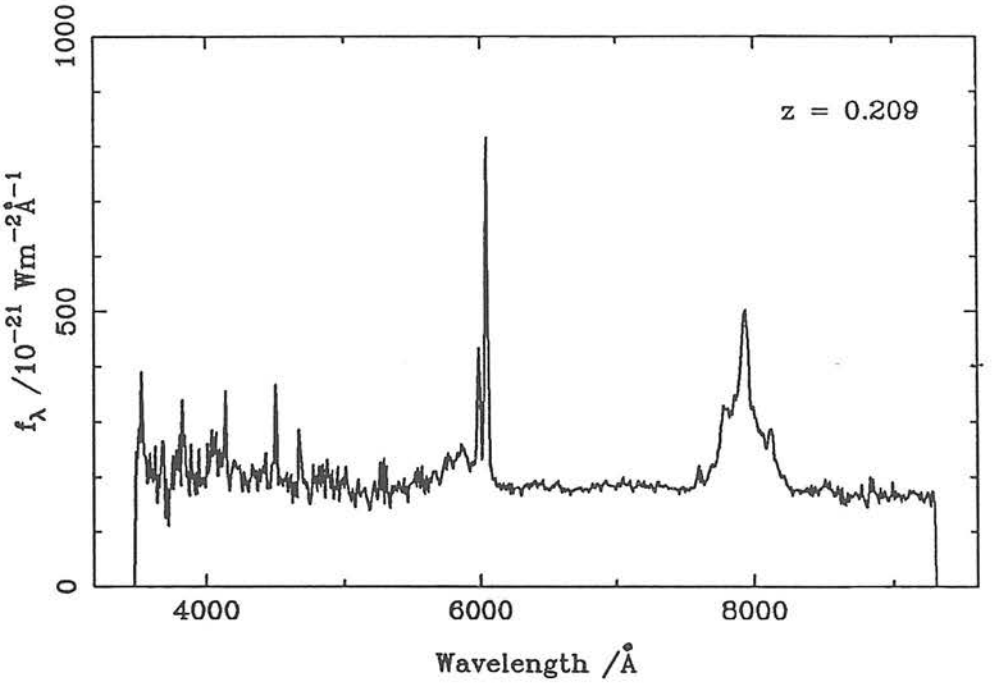

PKS 0236−015

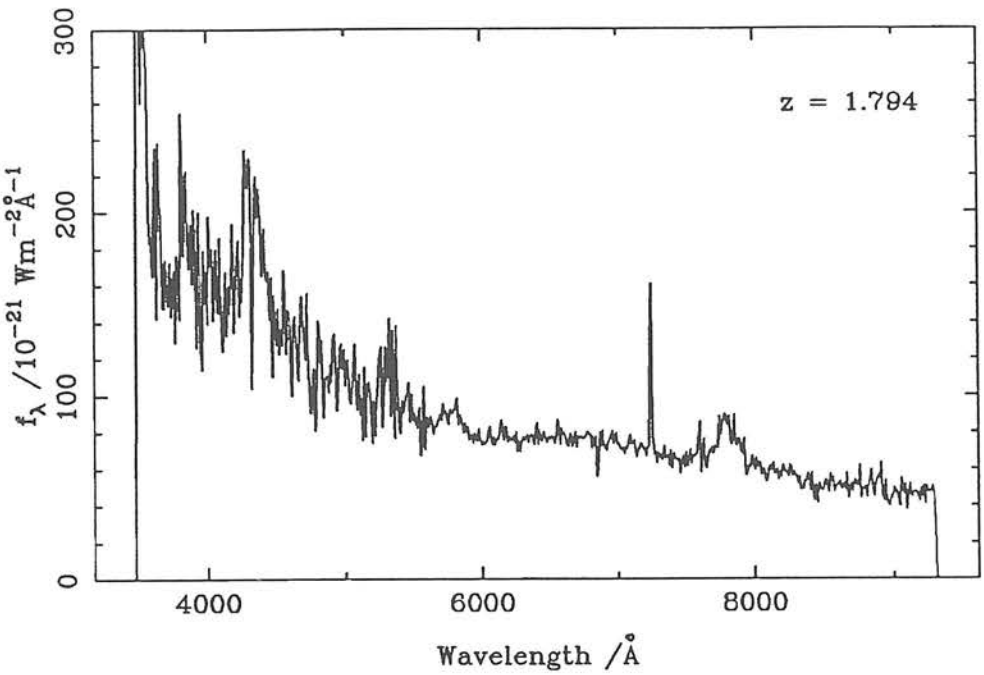

PKS 0238−018

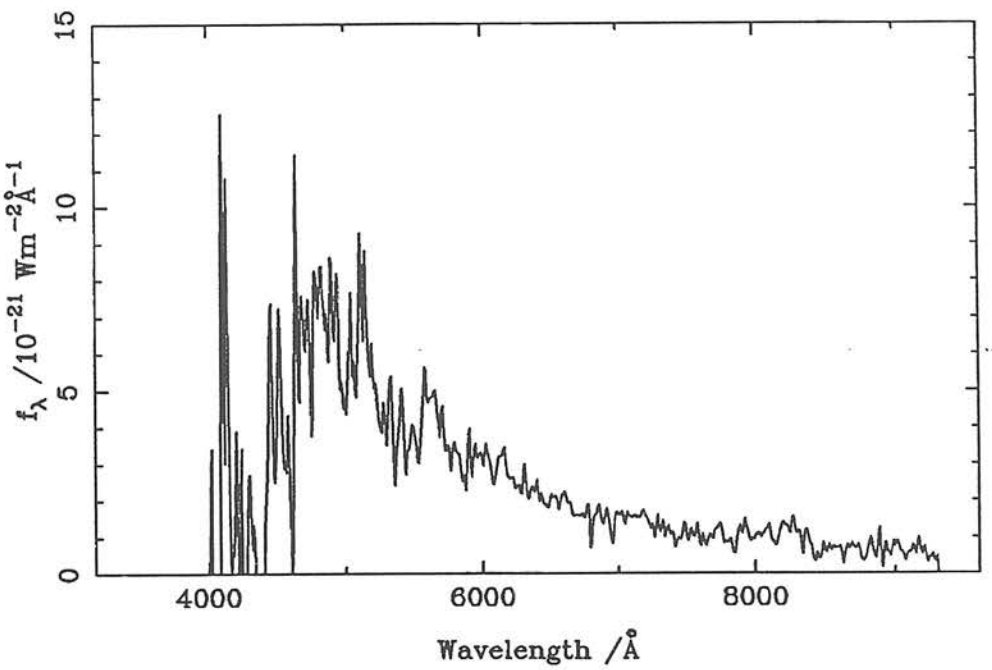

PKS 0240−021

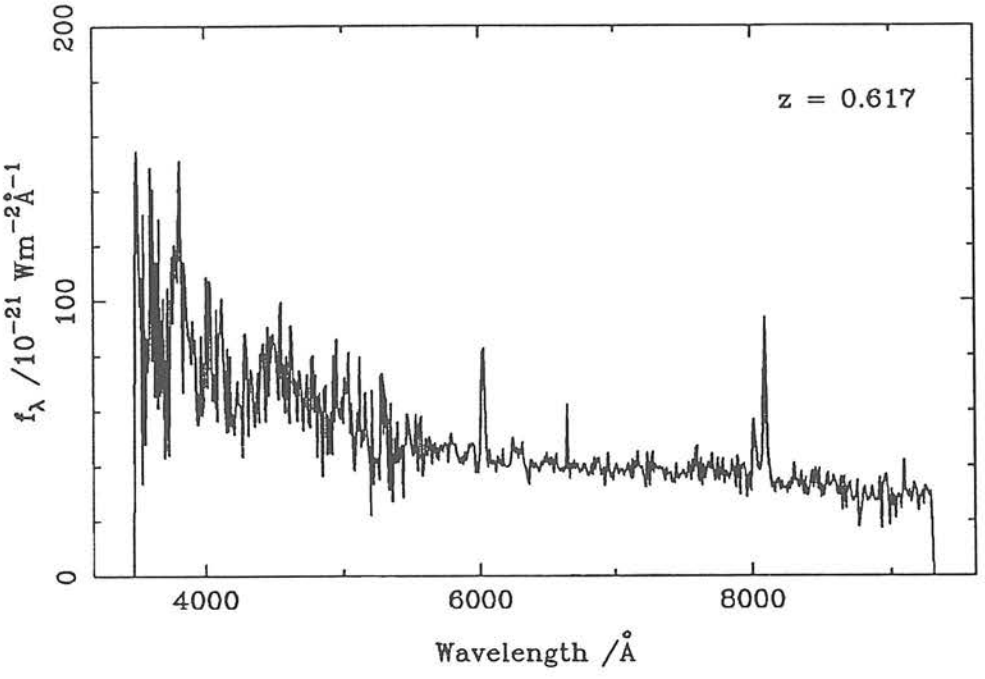

PKS 0242+009

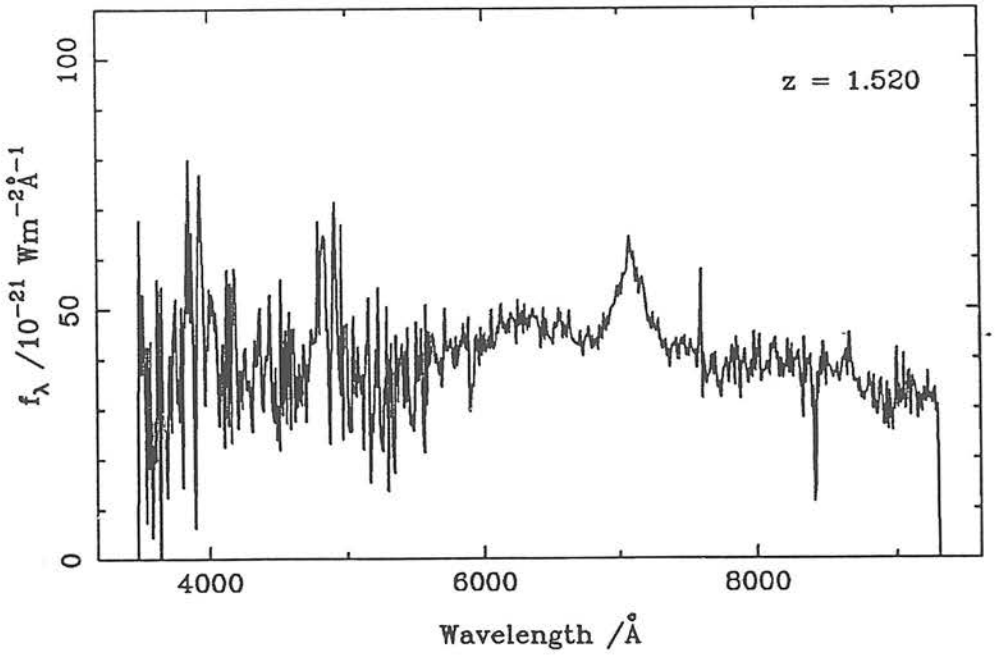

PKS 0422+004

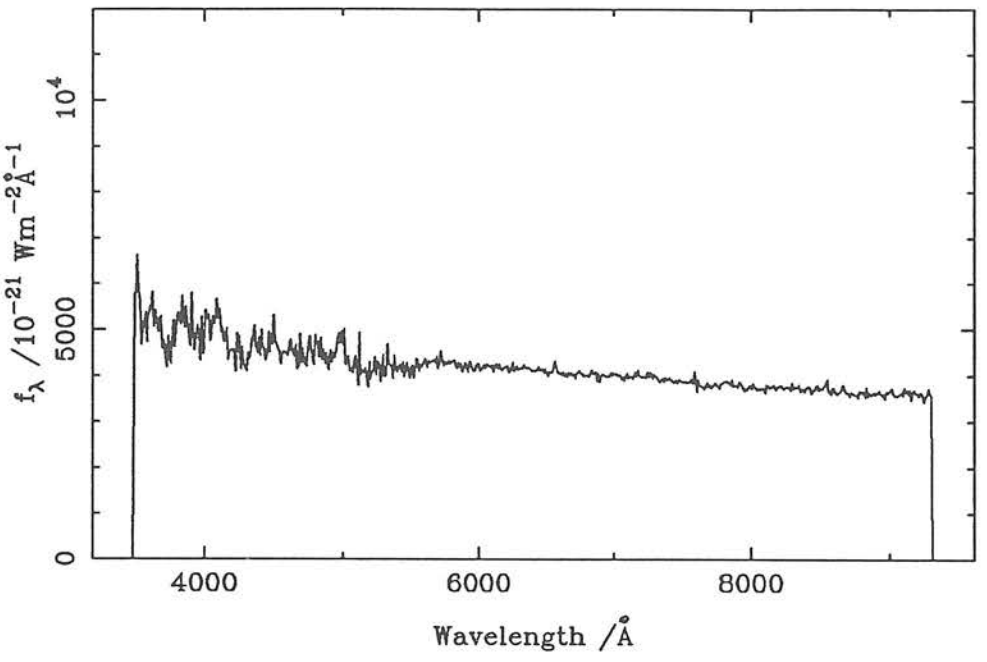

PKS 0528+13

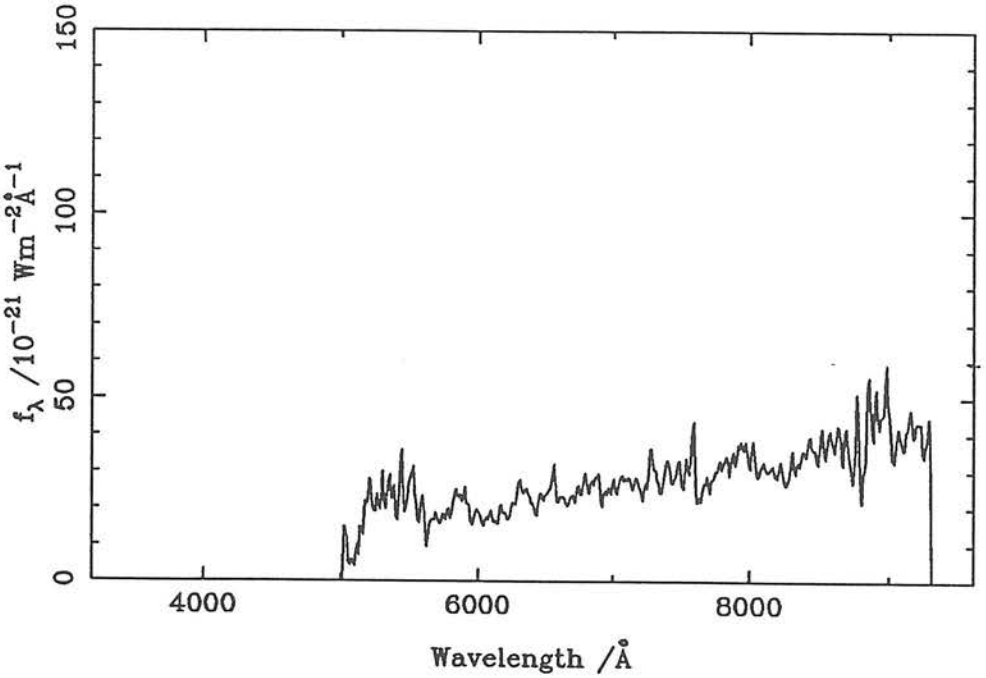

PKS 0804+49

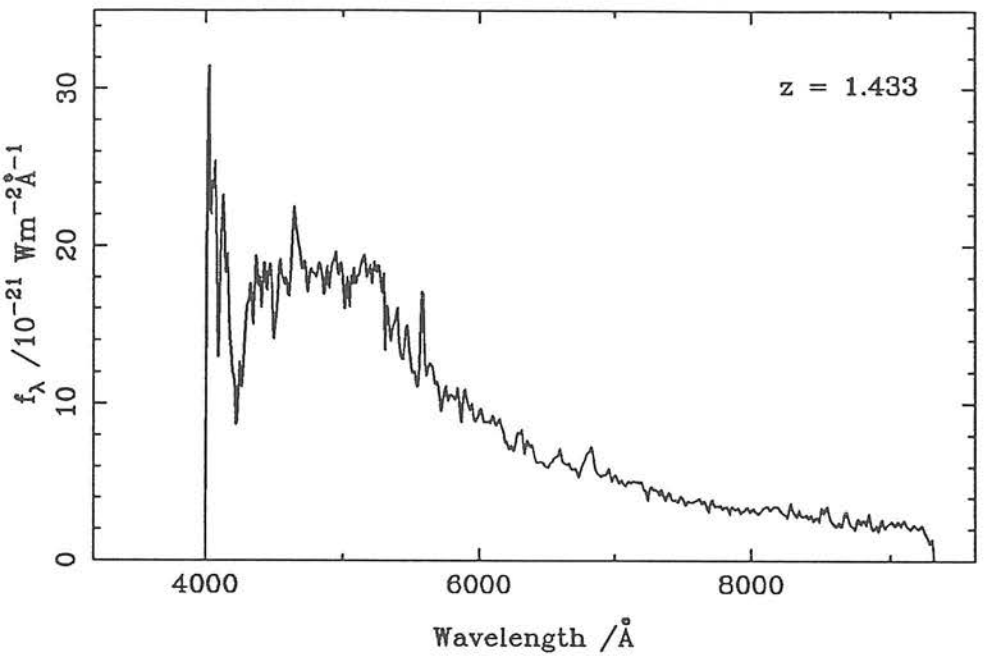

PKS 0814+42

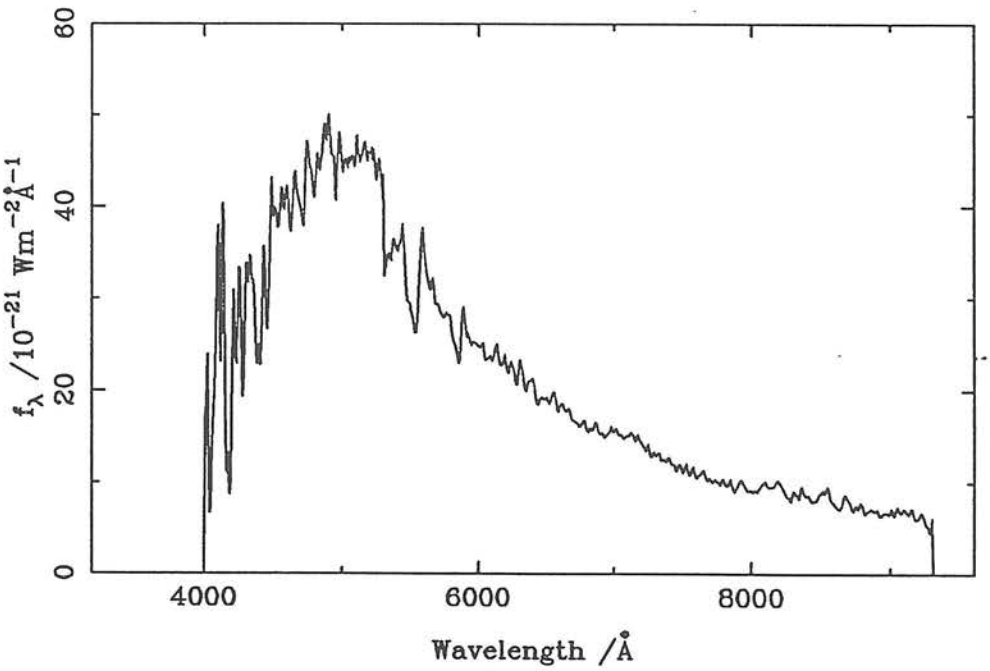

PKS 0823+033

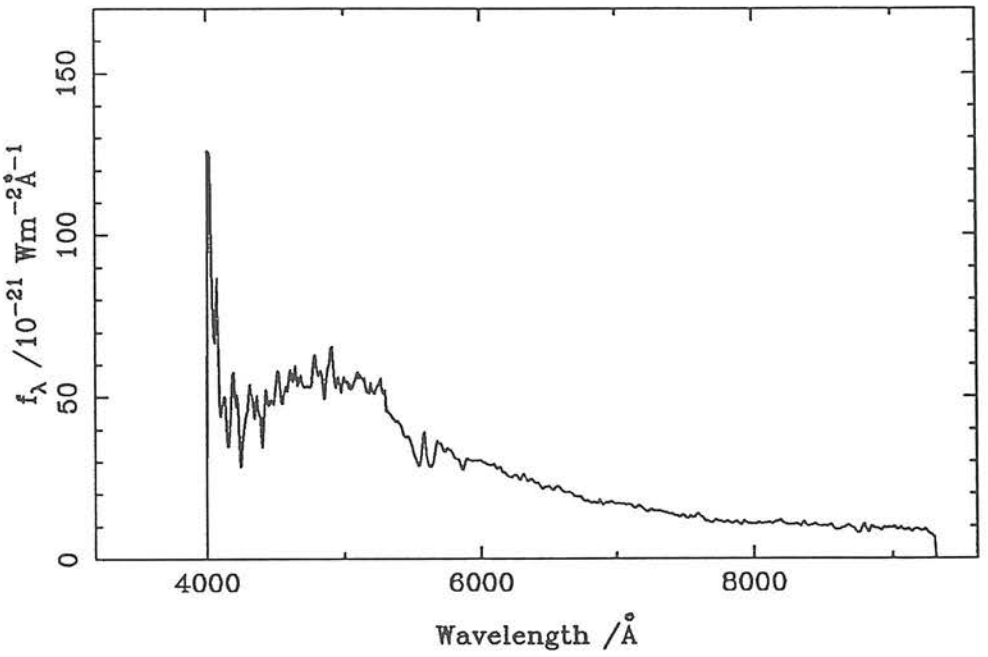

PKS 0837+035

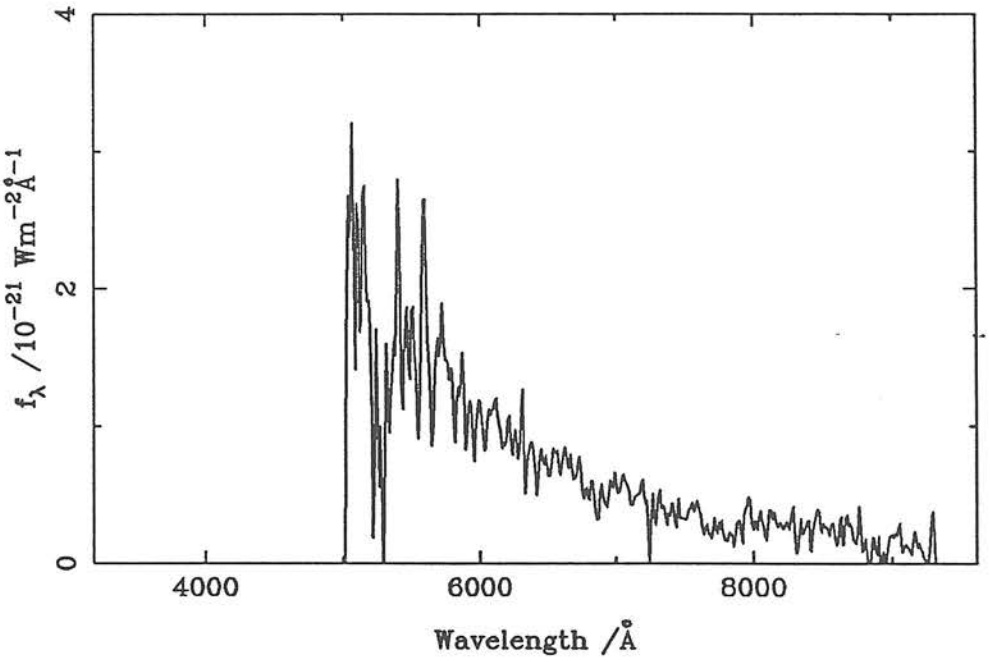

PKS 1031+56

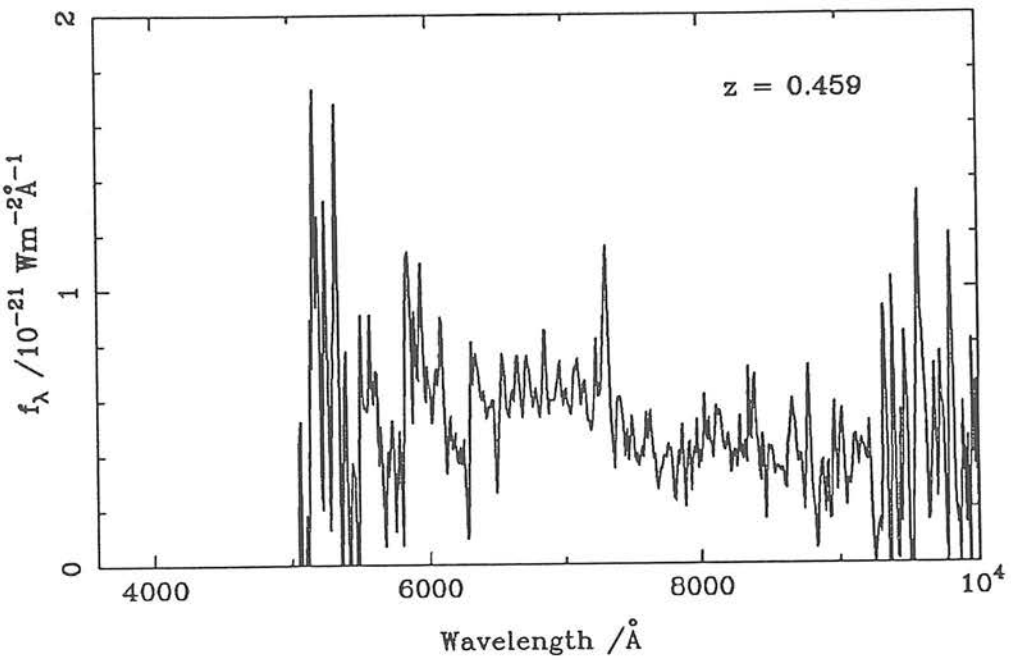

PKS 1206−026

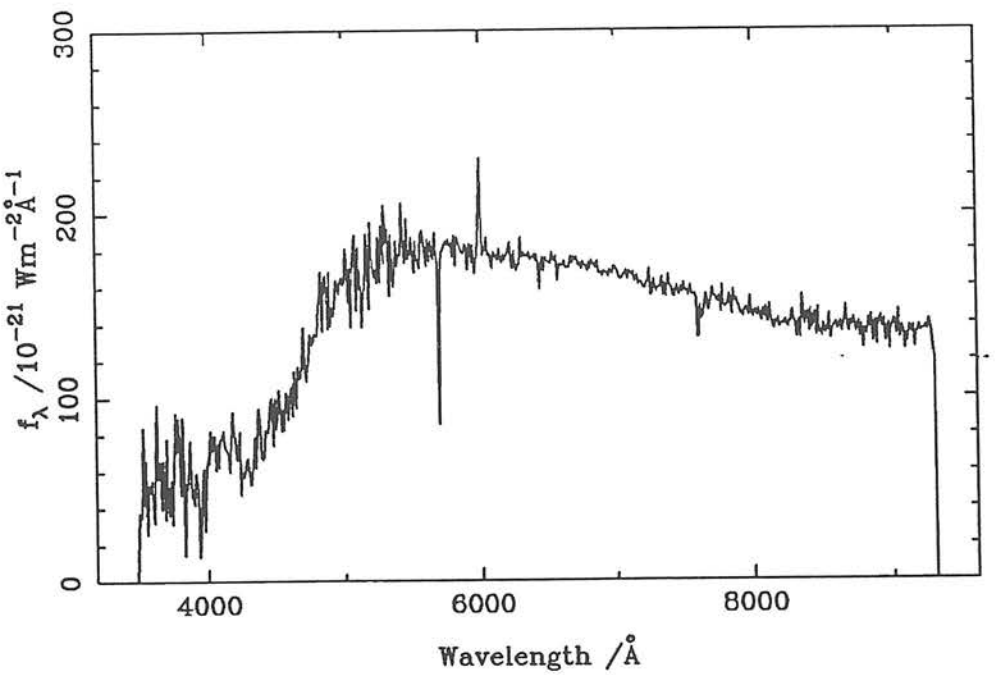

PKS 1215−033

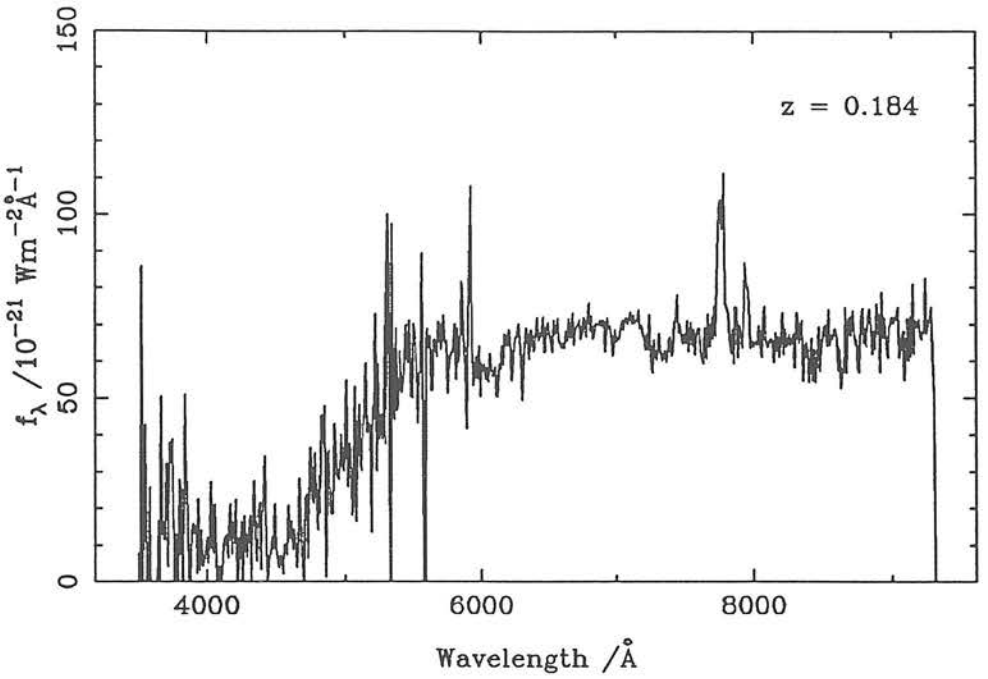

PKS 1215−002

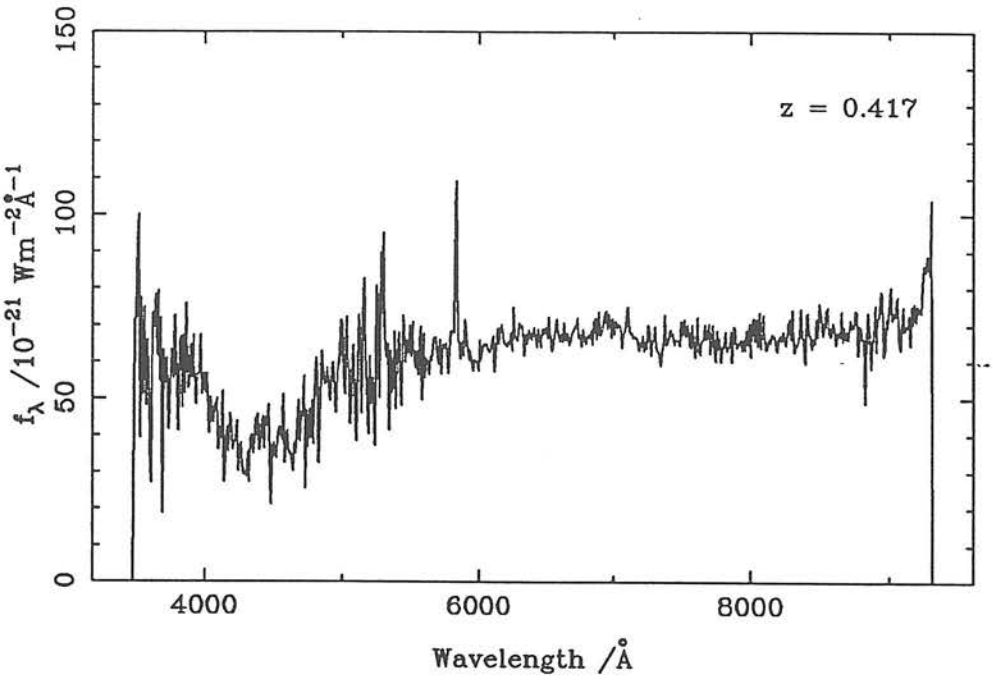

PKS 1225+36

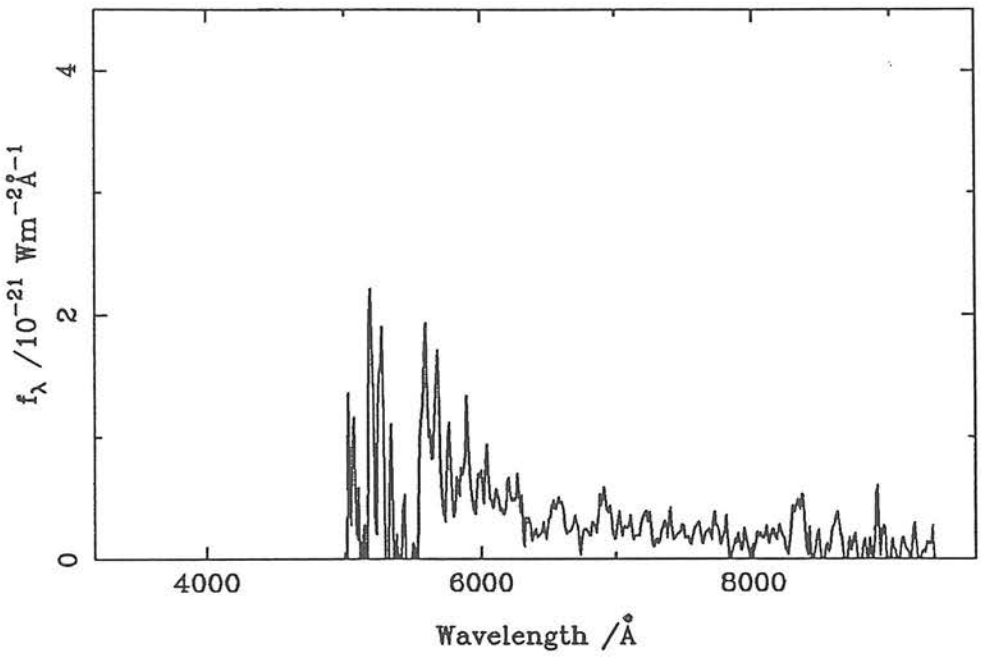

PKS 1317+019

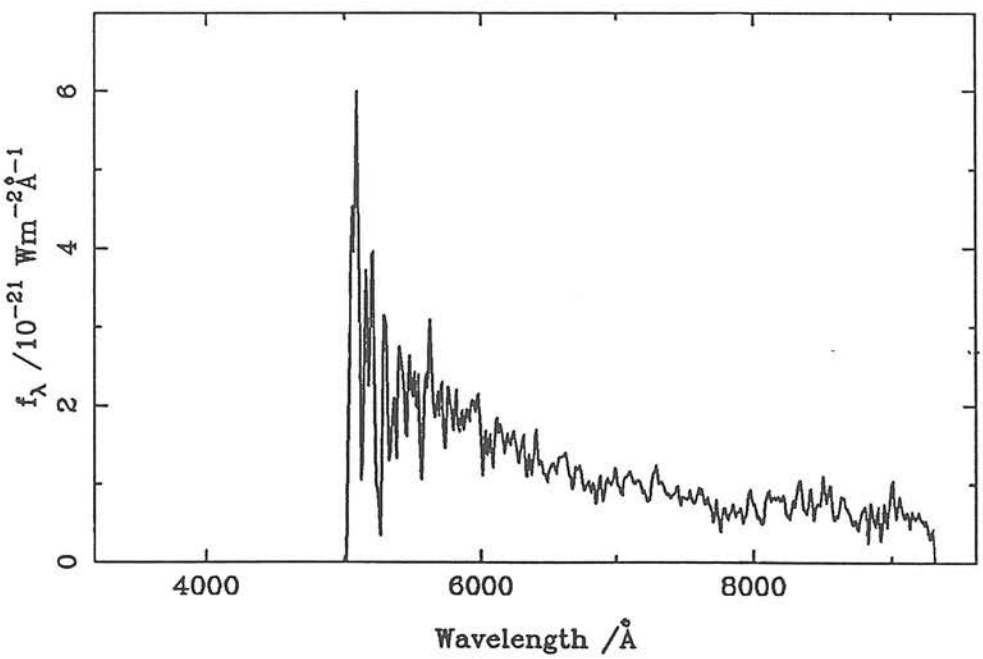

PKS 1323+32

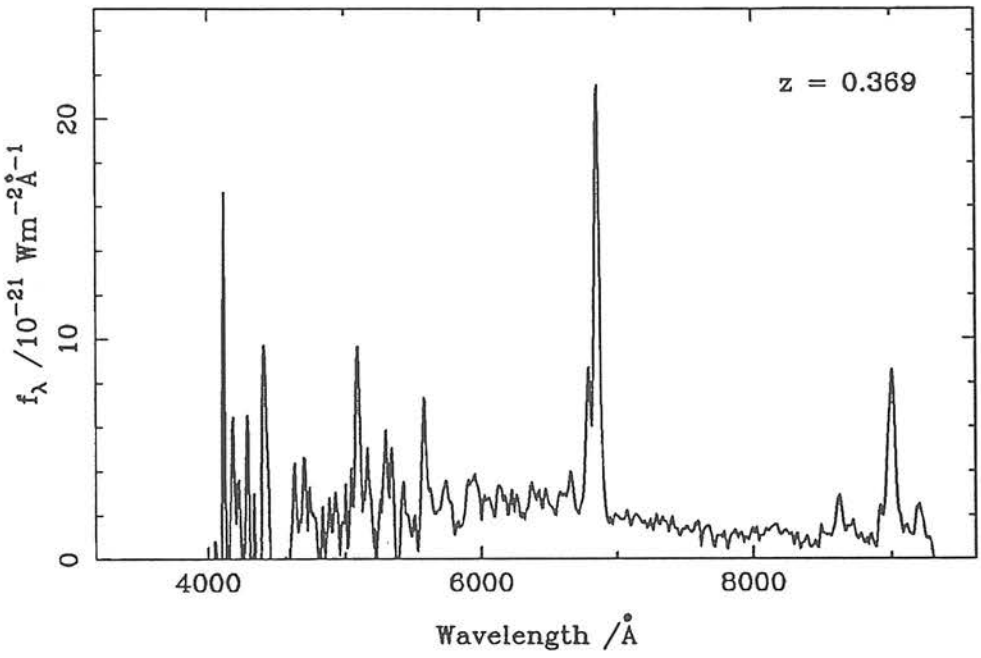

PKS 1334+008

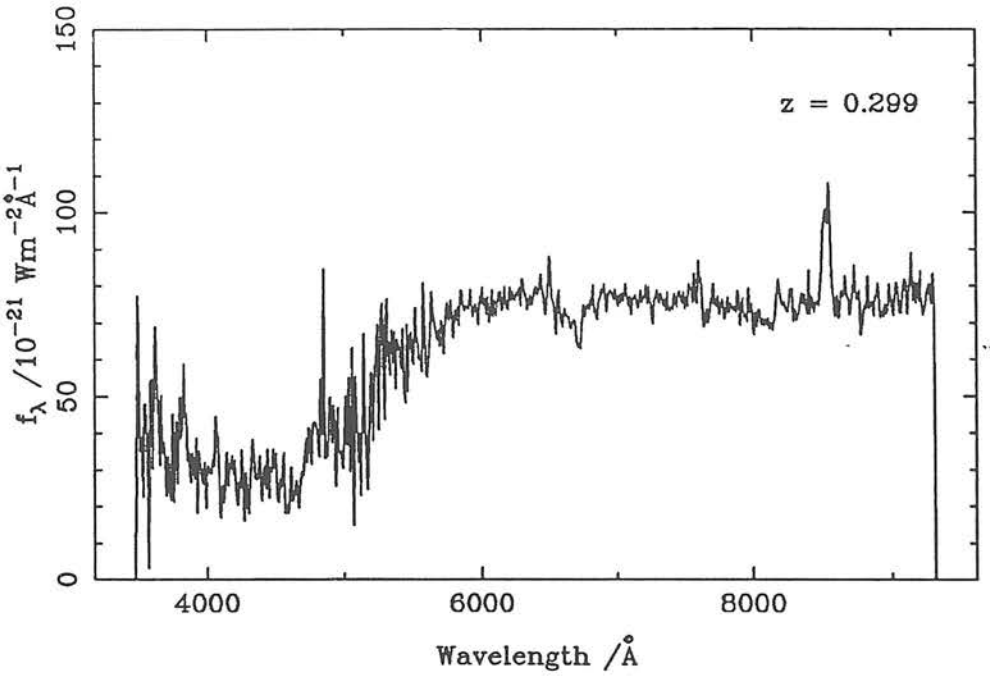

PKS 1336−030

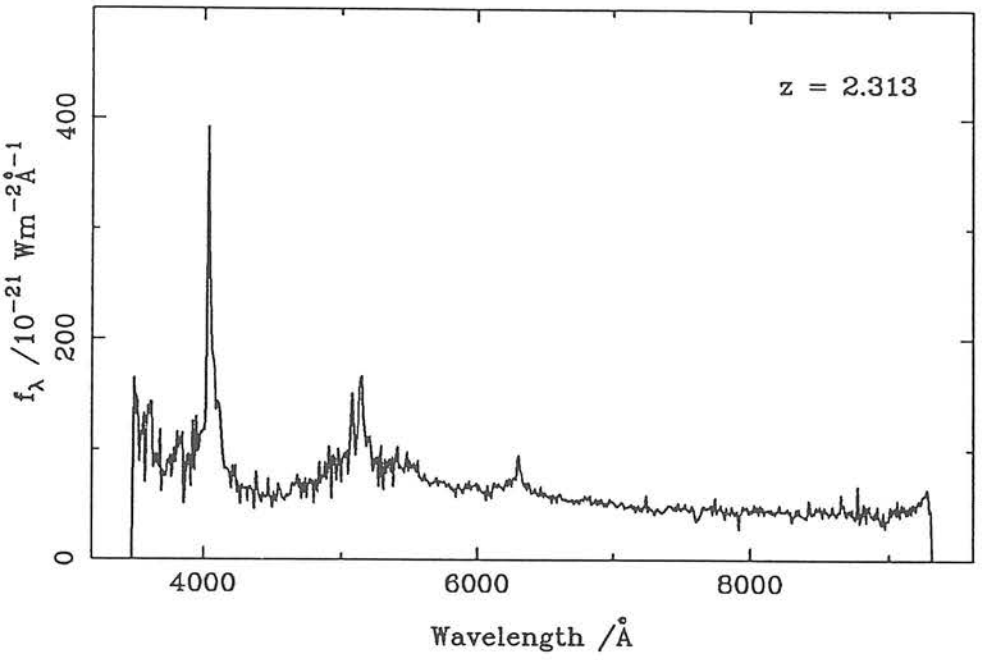

PKS 1342−016

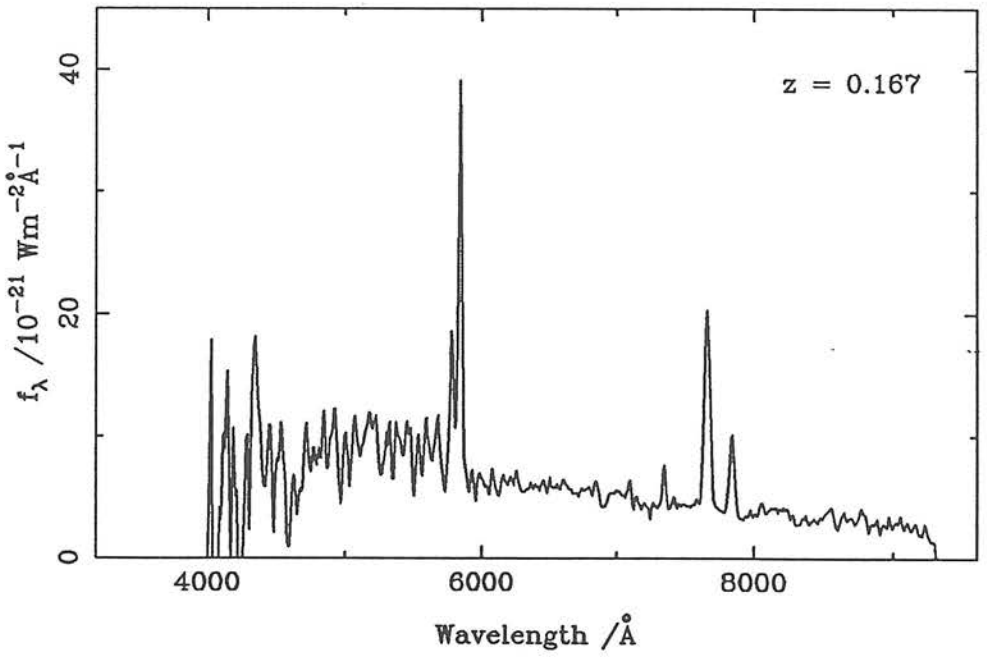

PKS 1345+12

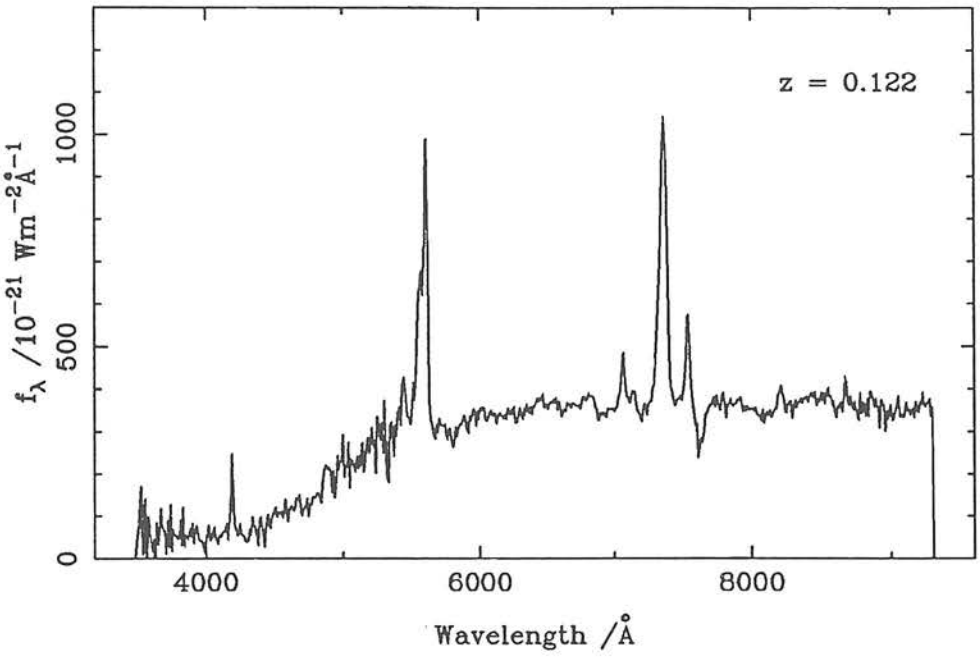

PKS 1348−012

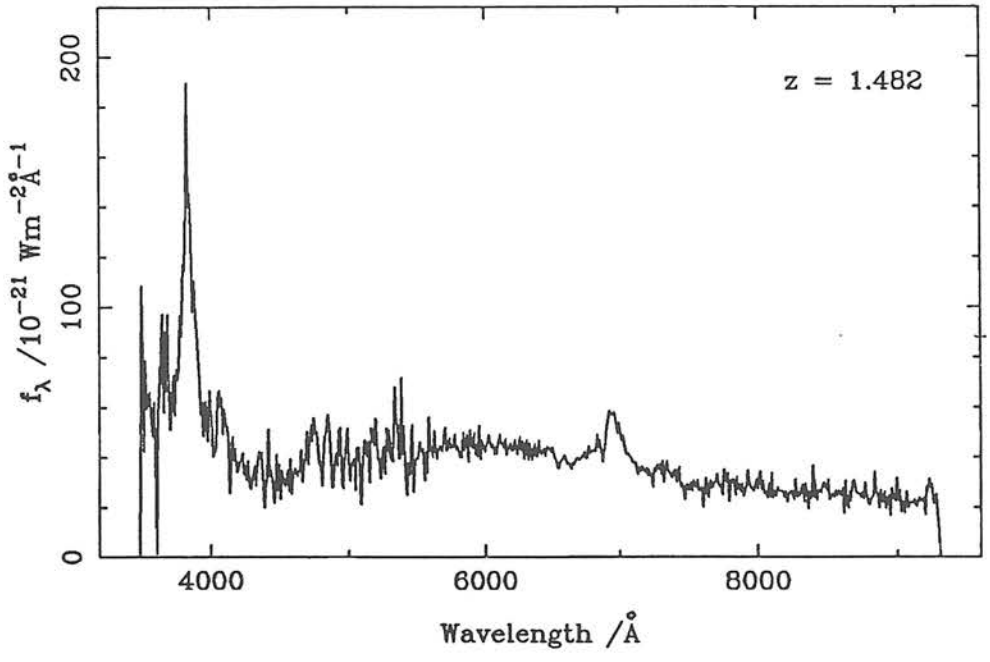

PKS 1348+007

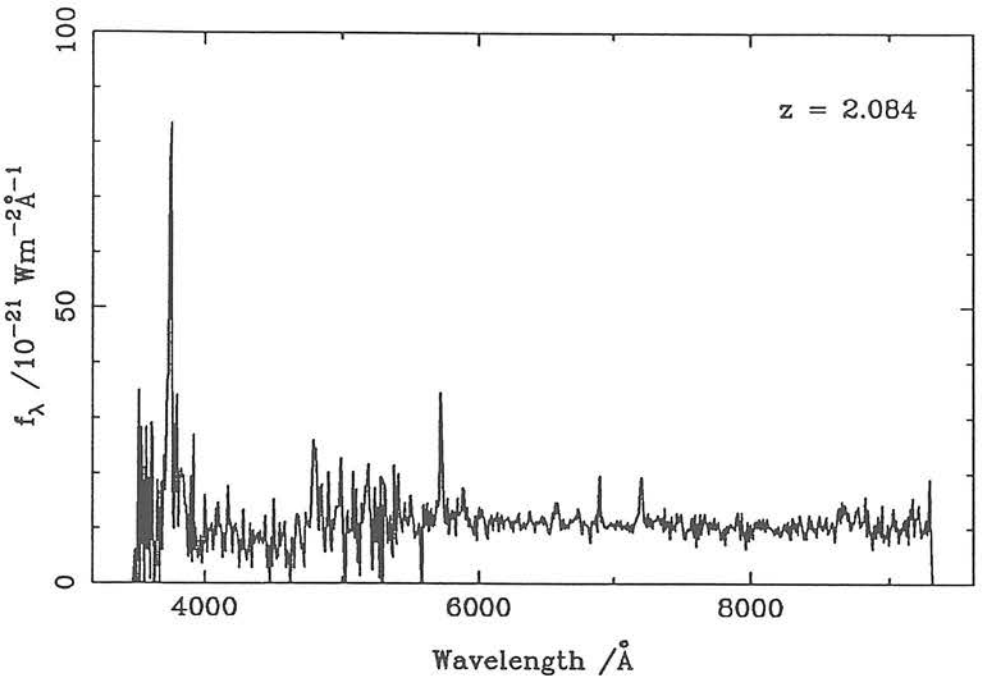

PKS 1351−018

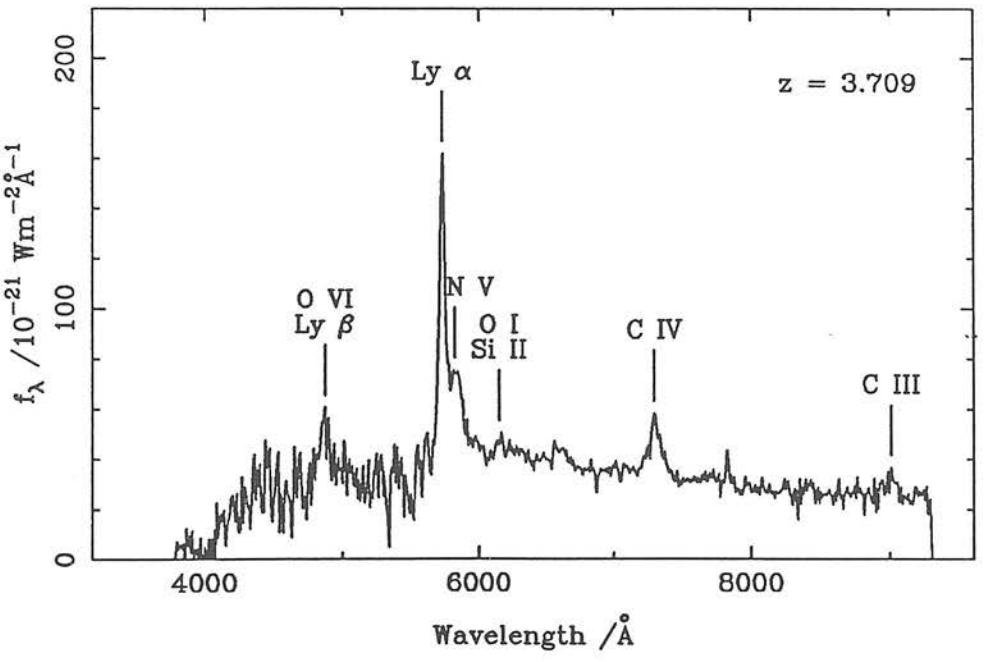

PKS 1538+14

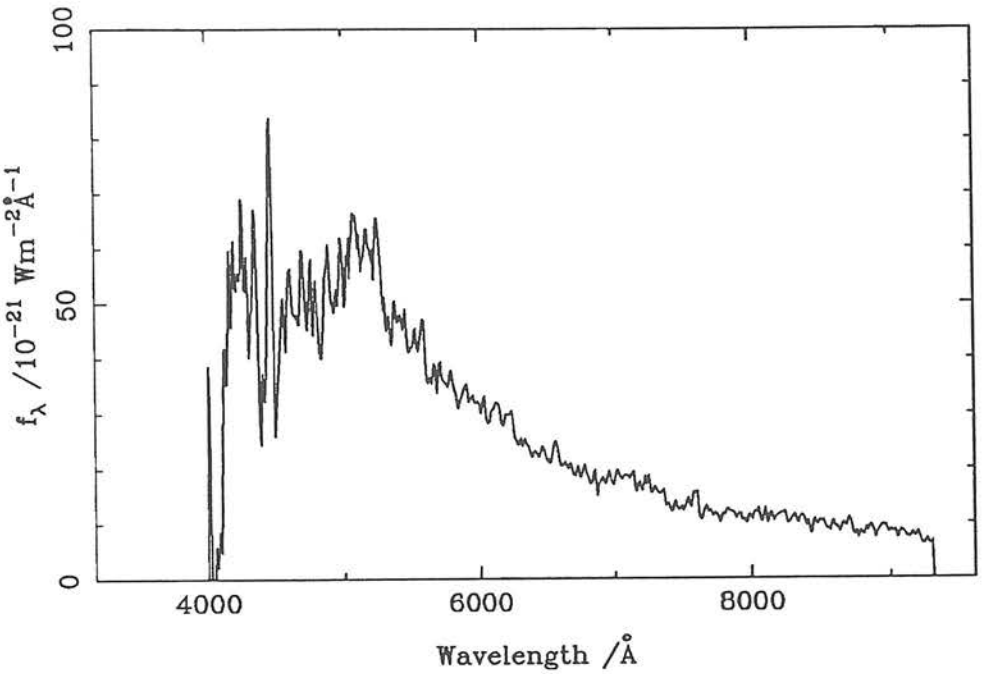

PKS 1741−03

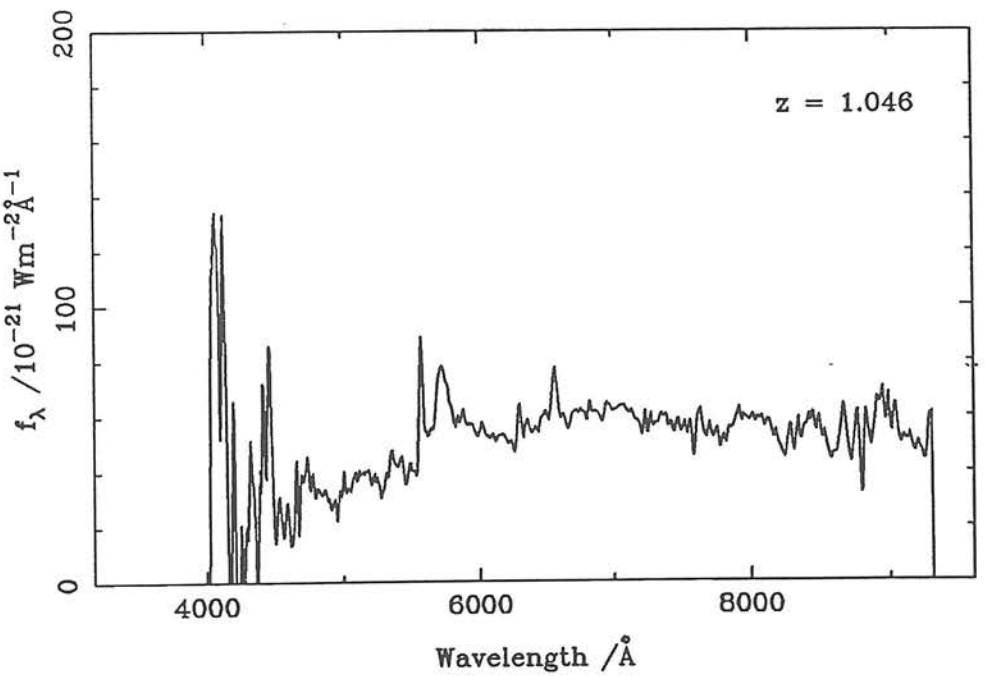

PKS 2012−017

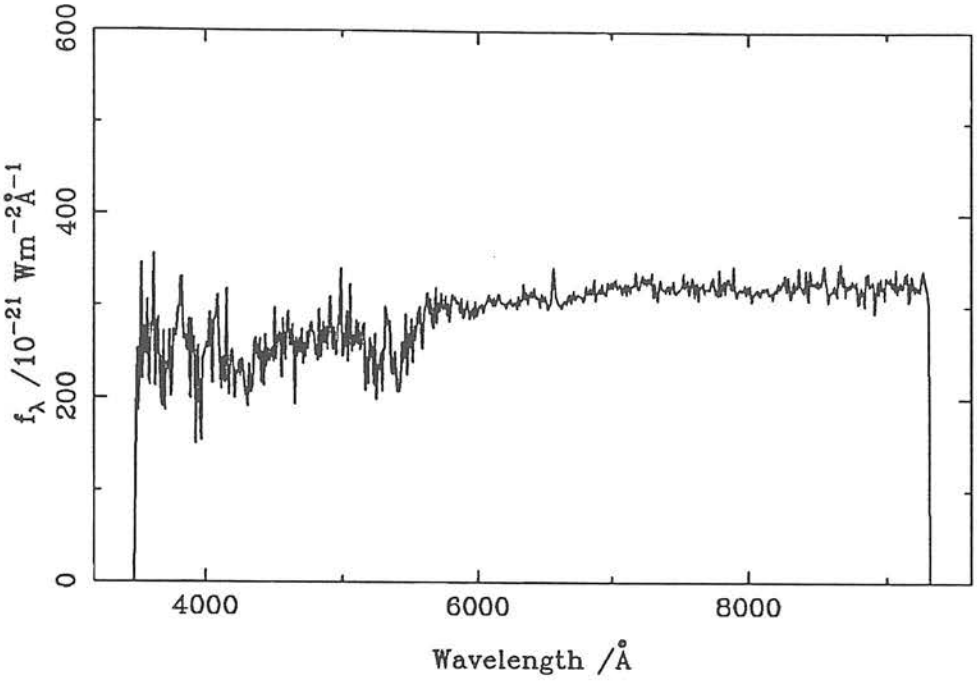

PKS 2047+039

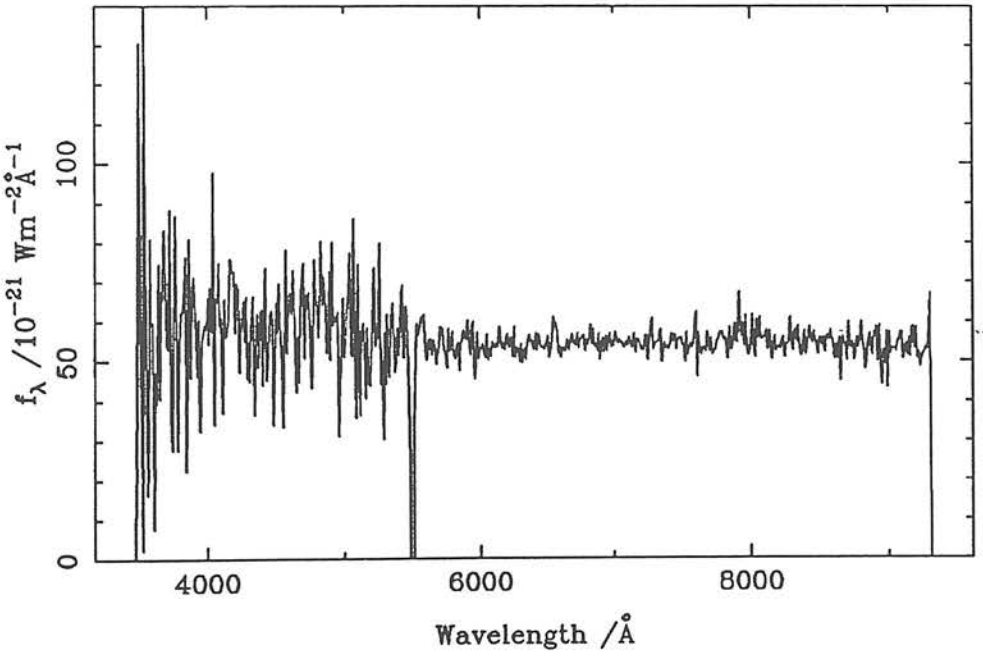

PKS 2106-413

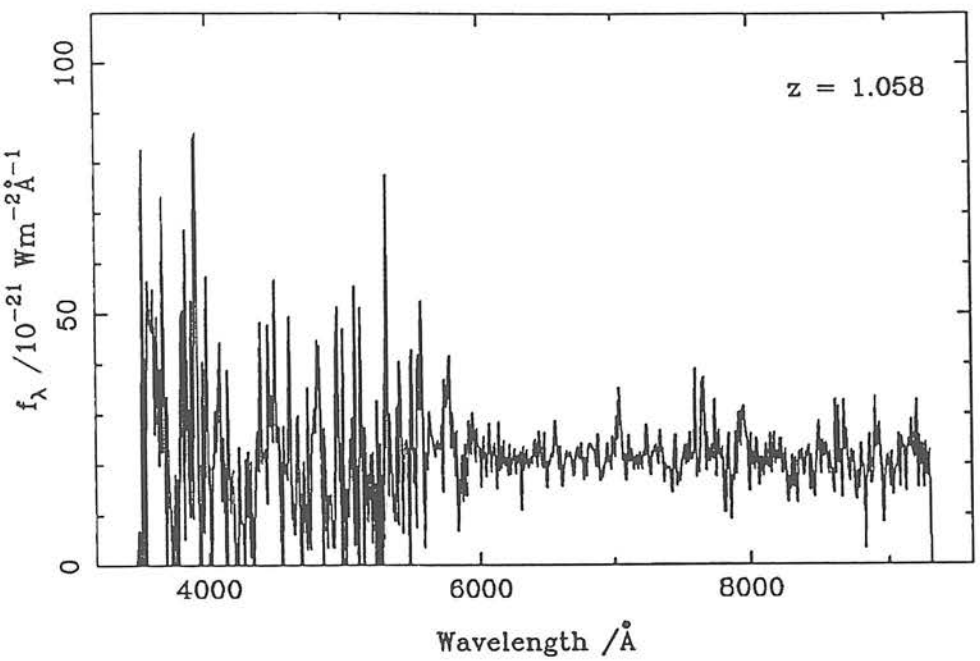

PKS 2152-218

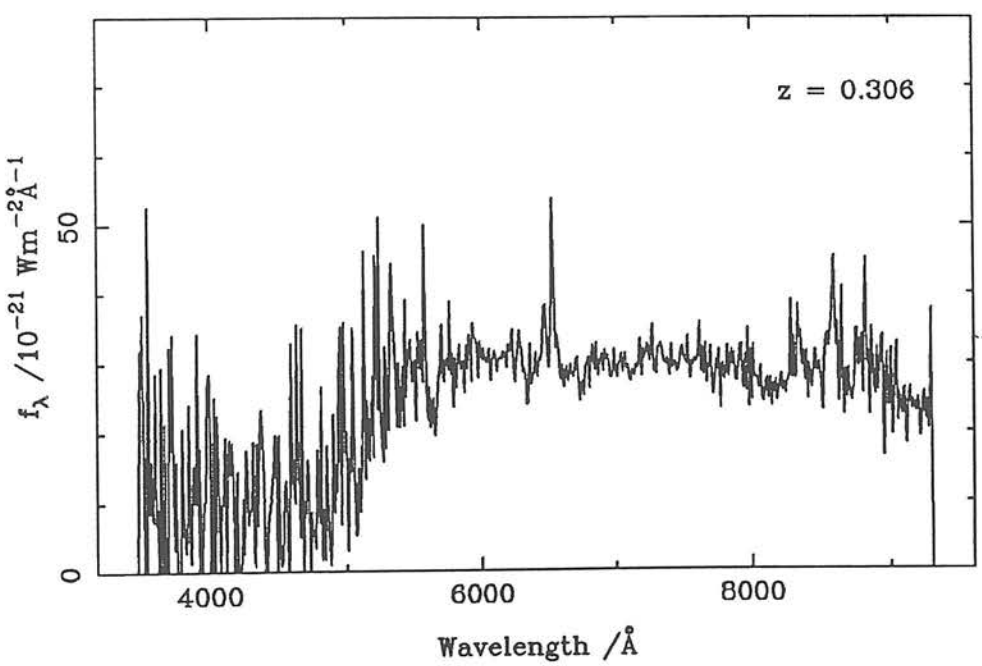

PKS 2153−219

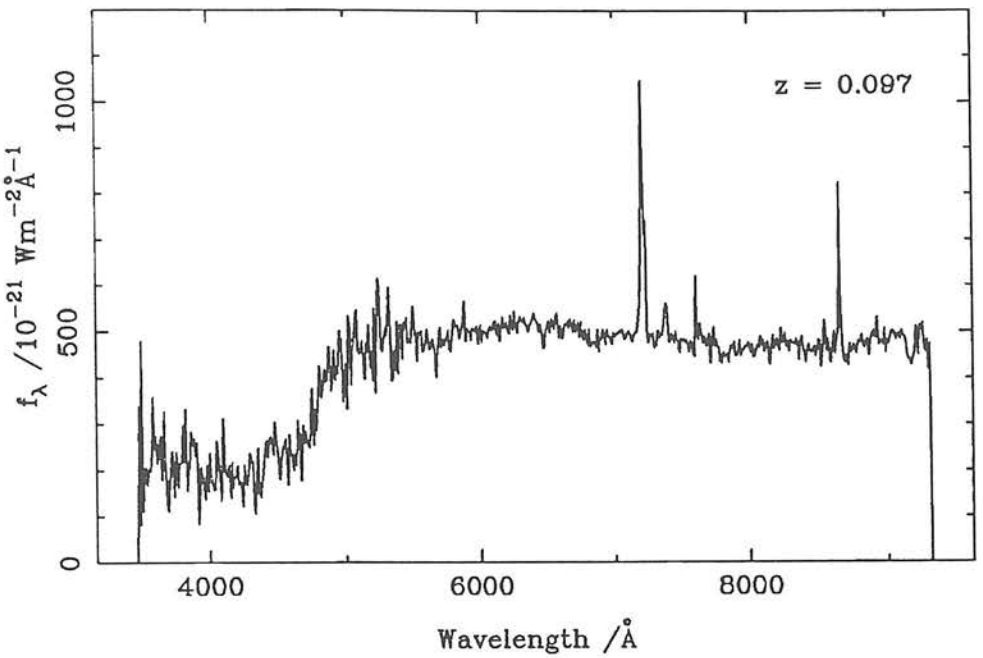

PKS 2154−184

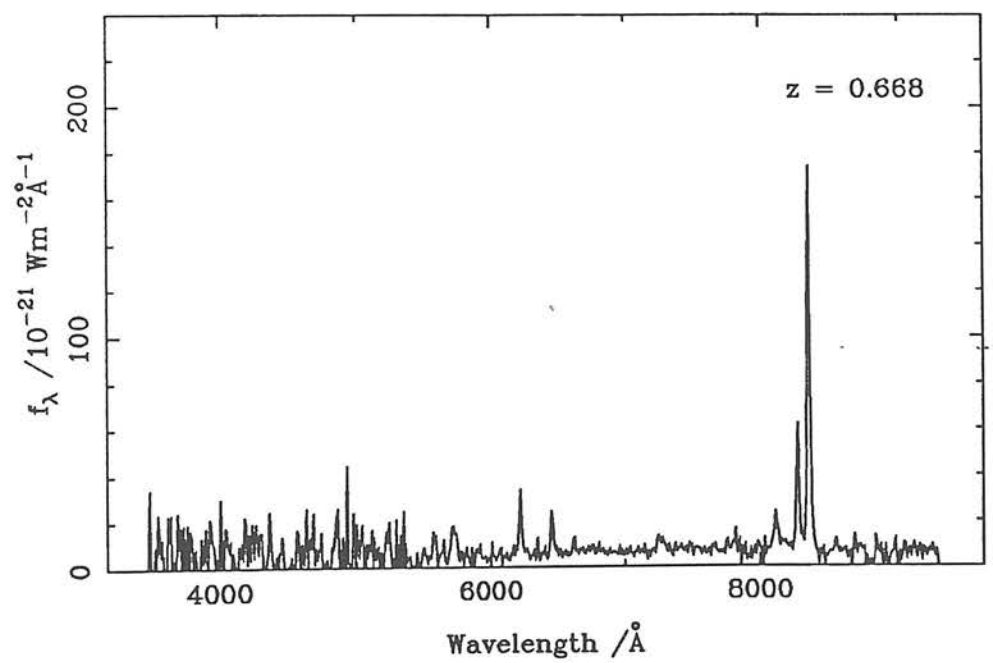

PKS 2154−183

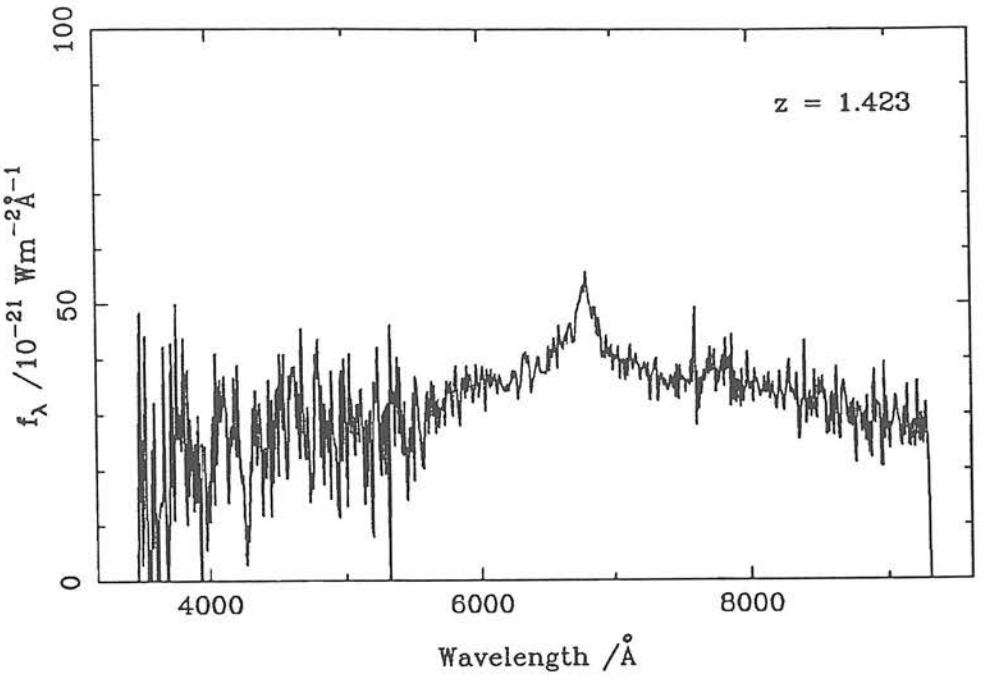

PKS 2159−187

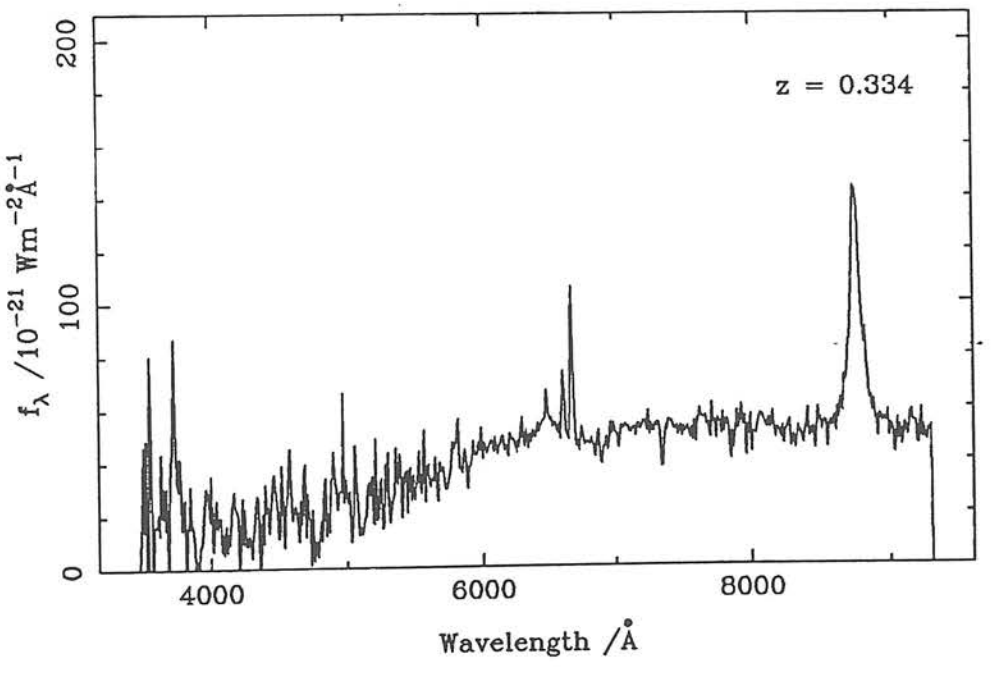

PKS 2203−215

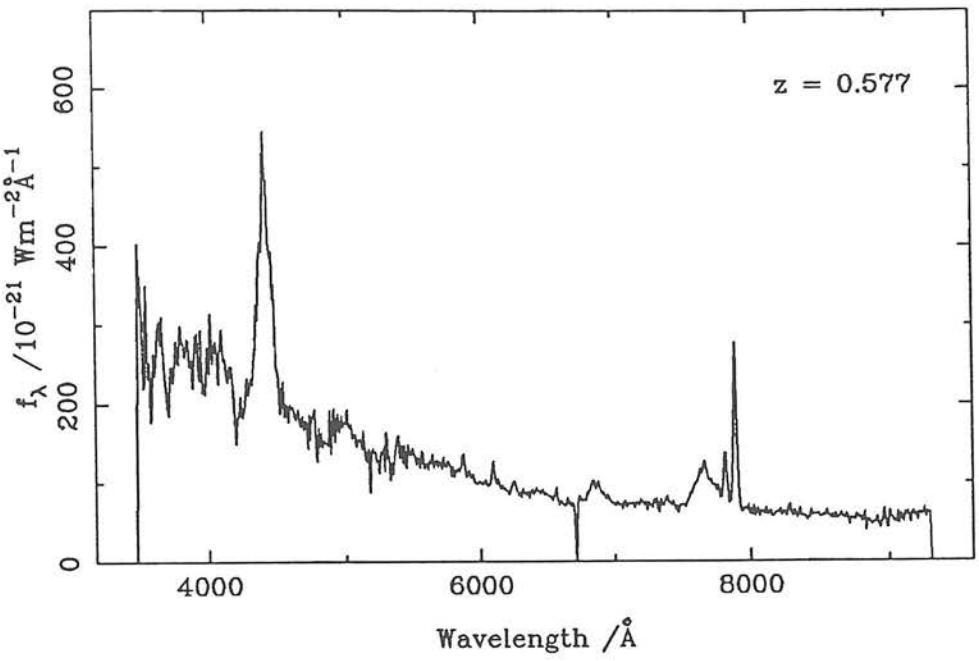

PKS 2204−208

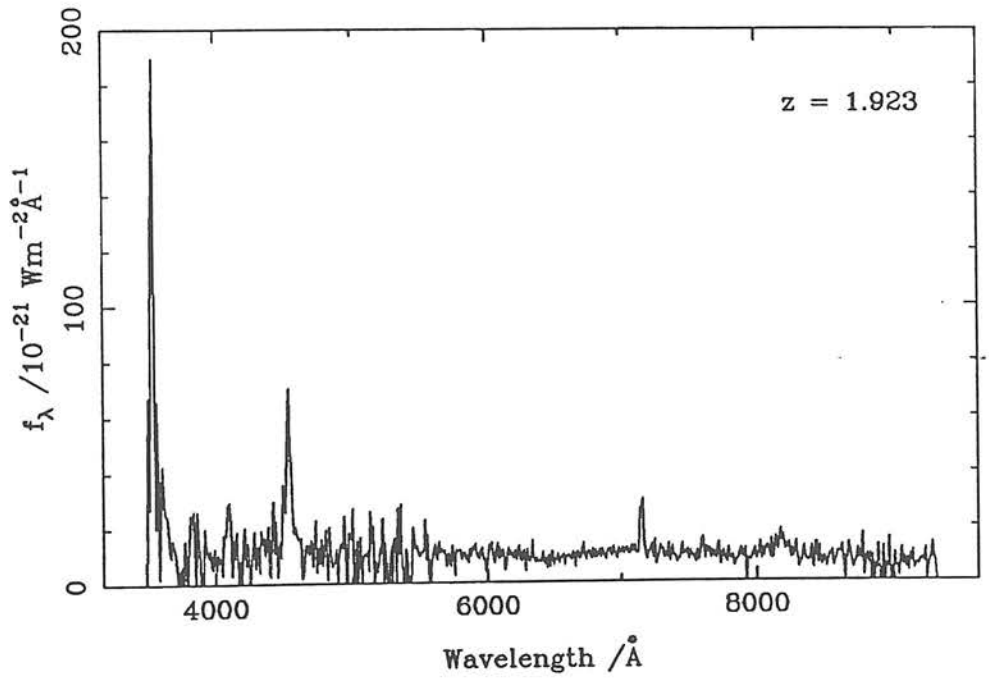

PKS 2213−167

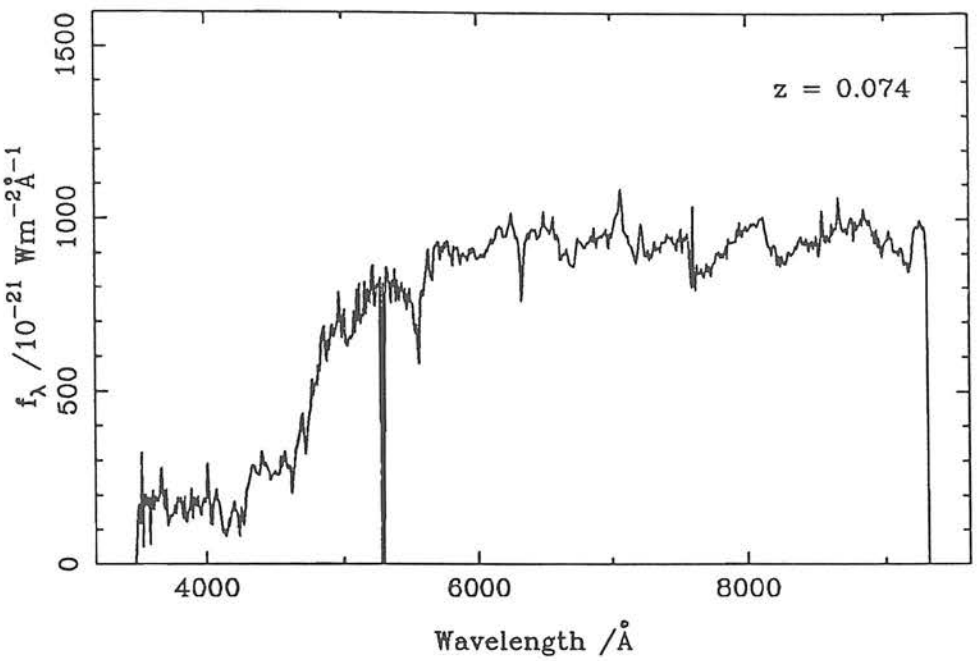

PKS 2214−206

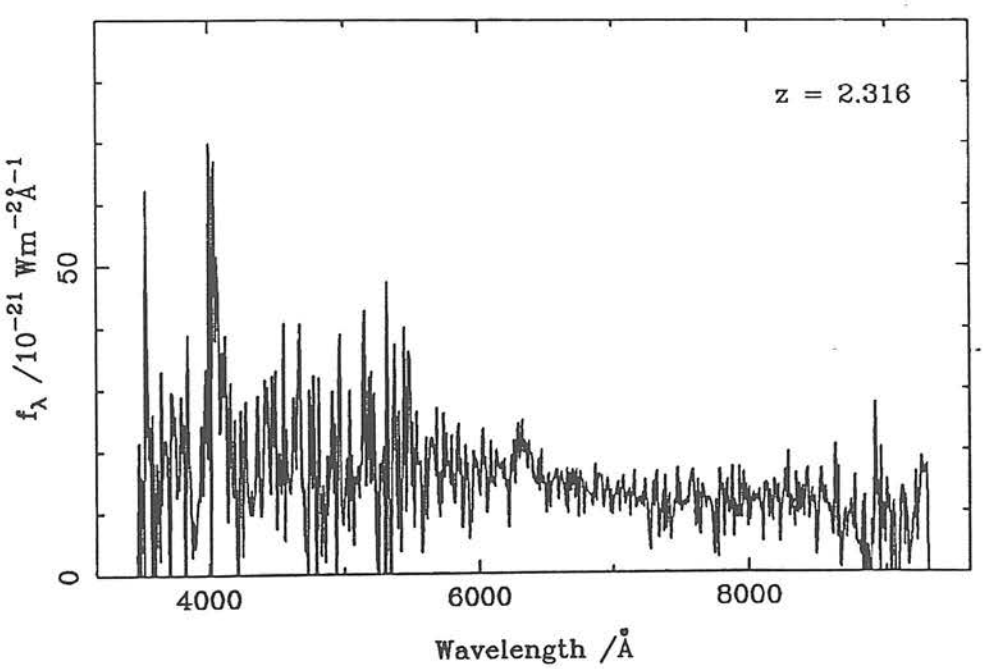

PKS 2215−185

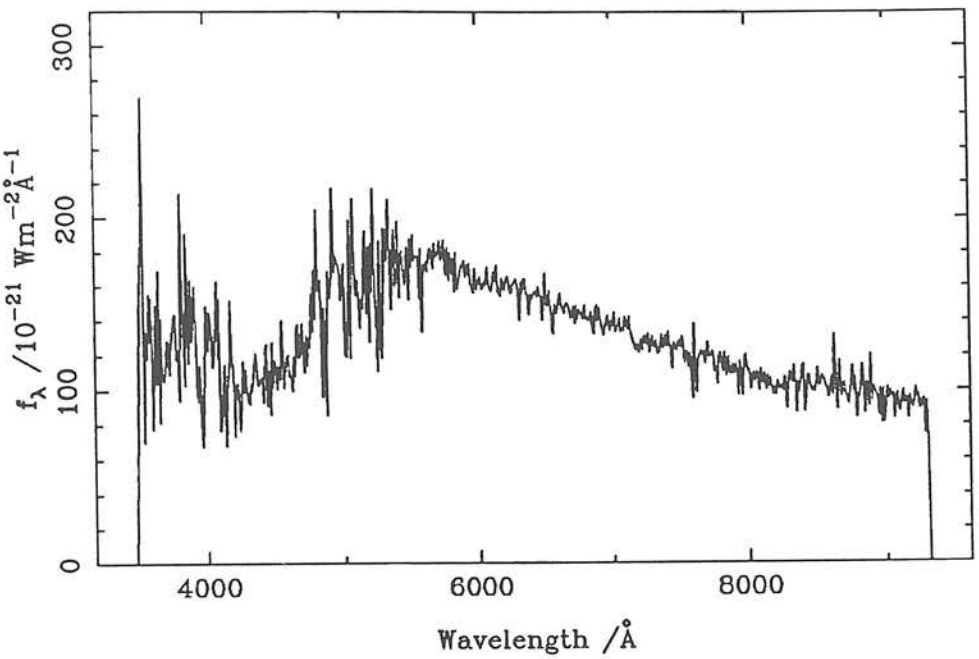

PKS 2354−021

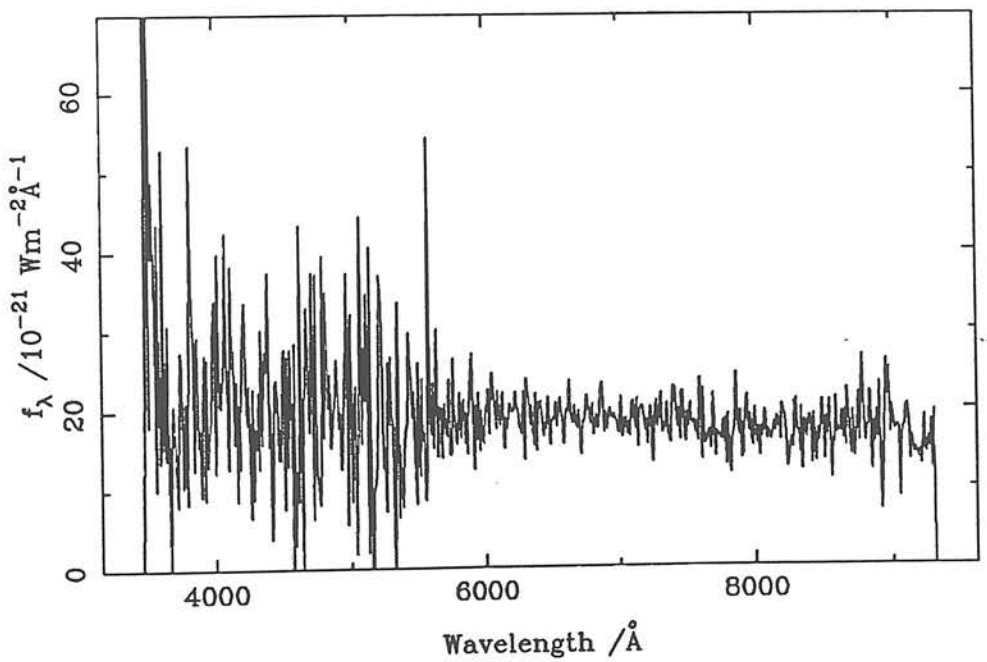

Notes on the individual spectra

0000-006

There are no obvious emission lines (the spike at 5300Å has been caused by the joining of the IPCS and FORS sections of the spectrum), but the broad absorption feature at ~ 7700Å has a shape characteristic of the TiO absorption feature (seen longward of Hα in the spectrum of 2213-167). The object therefore appears to be a galaxy with $z \simeq 0.07$. If this redshift is correct the Na D absorption feature must be fairly weak and the galaxy must be optically very sub-luminous.

0013-005

The identification of the prominent line at 7200Å as MgII is confirmed by the presence of CIII and CIV in the rather noisy IPCS portion of the spectrum. The object is therefore a quasar with $z = 1.575$. This redshift has been confirmed by White *et al.* (1987) who quote a value of $z = 1.574 \pm 0.002$

0040+017

The continuum has been clearly detected but the signal/noise is too poor to enable a redshift determination. However, the lack of blue flux in the second-order section of the INT spectrum suggests that the object is probably galaxy.

0041+007

A galaxy at $z = 0.112$. The spectrum shows fairly weak oxygen and Hα emission along with prominent absorption features and an obvious 4000Å break.

0047+023

The continuum has been clearly detected and appears to be non-thermal, but there are no obvious emission features from which to determine a redshift. However the signal/noise ratio, particularly at the blue end, is not sufficiently high to be sure that the continuum is genuinely featureless.

0213+013

A low-redshift ($z = 0.148$) radio galaxy with very strong oxygen lines.

0215+015

Like 0047+023, the spectrum appears to be a featureless, non-thermal continuum (the apparent absorption feature at ~ 6600Å is caused by imperfect sky subtraction). However, in this case the signal/noise ratio is considerably greater and the object is indeed a famous BLlac. A redshift has in fact recently been measured for this object - $z = 1.715$ (Foltz & Chaffee 1987).

0223+012

A quasar with strong emission lines (CIV, CIII and MgII) which give a redshift of $z = 1.369$.

0229+034

A low signal/noise INT spectrum from which no redshift determination has been possible. Like 0040+007, the lack of signal in the second-order spectrum suggests that the object is probably a galaxy. Since this spectrum was taken a redshift has been successfully measured for this object by Jeremy-Allington Smith at the INT. This confirms that the object is indeed a galaxy, with $z = 0.278$.

0230-027

A galaxy at z = 0.239. The spectrum shows Oxygen and Hα emission, along with absorption features and a clear 4000Å break.

0230-002

Another low signal/noise INT spectrum from which it has not been possible to determine a redshift. Again, like 0040+017 and 0229+034, the lack of blue continuum suggests that the objects is a galaxy rather than a quasar. Like 0229+034, a redshift has been recently measured for this object by Jeremy Allington-Smith at the INT. The result is z = 0.794, and in retrospect one might tentatively identify the emission feature at ~9000Å in the present spectrum with the [OIII] doublet.

0235+023

A quasar at z = 0.209. The continuum is clearly non-thermal and the Hydrogen and Oxygen lines are very strong. The Hα line is extremely broad and is blended with the [SII] line at 6724Å.

0236-015

A quasar at z = 1.794. Like 0013-005 the identification of the broad line in the FORS section as MgII is confirmed by the detection of CIII and CIV in the IPCS portion. The feature at ~ 7200Å is not real.

0238-018

The signal/noise ratio is too low to enable a redshift to be determined. It is also difficult to make any statement regarding the shape of the continuum.

0240-021

A quasar at z = 0.617. The continuum is clearly non-thermal and the broad CII and MgII lines are seen in the IPCS section. The forbidden oxygen and Neon lines are clearly seen in the FORS portion.

0242+009

Another quasar (see 0013-005 and 0236-015) for which the identification of the broad line at ~ 7000Å as MgII is confirmed by the Carbon features in the IPCS spectrum. The CII line is possibly just visible at 5860A, as is [NeV] at 8662Å. The redshift (derived from the Carbon lines) is z = 1.520.

0422+004

This object is a well known BLlac. The continuum is clearly non-thermal and has been detected at high signal/noise. There are no obvious emission features from which to attempt a redshift determination.

0528+13

There are no clear emission-line features on which to base a redshift, but the continuum appears non-thermal. This object is therefore a possible BLlac or weak-lined quasar. A redshift of z = 2.060 has recently been measured for this object by Kuhr (private communication).

0804+49

A rather weak-lined quasar at z = 1.433. The identification of the broad line at ~ 6800Å as MgII is confirmed by the presence of CIII at 4650Å.

0814+42

There are no obvious features from which to determine a redshift, but the similarity of the continuum shape with that of the previous object suggests that this is also a weak-lined quasar or BLlac.

0823+033

Like the above object the spectrum appears to be featureless and non-thermal - another BLlac candidate.

0837+035

Yet another possible BLlac, but this time the signal/noise ratio is rather poorer.

1031+56

A moderate-redshift ($z = 0.459$) radio galaxy. [OIII] and Hα are visible despite the fact that the spectrum is rather noisy.

1206-026

The object appears to be a star (the two features either side of 6000Å are not real) and the identification, which was originally one of three alternative candidates has since been revised (this identification is in fact not the one marked on the finding chart given by Downes *et al.* 1986).

1215-033

A low-redshift galaxy ($z = 0.184$) with strong Oxygen and Hα emission. The Na D and Mg b absorption features are also clear, as is the

4000Å break.

1215-002

A galaxy at z = 0.417. Hα is just visible at the red end of the spectrum and a strong [OII] line is present at 5265Å (the feature at ~ 5900Å is not real). The redshift determination is confirmed by Mg b and Na D absorption. Also the 4000Å break, although not very strong, is clearly visible.

1225+36

A spectrum with very poor signal/noise in which the continuum has barely been detected.

1317+019

The signal/noise ratio is slightly higher than in the previous spectrum, but again no redshift determination is possible.

1323+32

A moderate-redshift (z = 0.369) radio galaxy with very strong [OIII] emission.

1334+008

Another low redshift galaxy (z = 0.299) with clear Hydrogen and Oxygen emission lines. The Mg b and Na D absorption features are also visible, as is the 4000Å break.

1336-030

A quasar with z = 2.313. The most prominent line is Lyα, the red wing of which is blended with NV. The blue wing of the MgII line is just visible at the extreme red end of the spectrum.

1342-016

A low-redshift galaxy (z = 0.167) with very strong [OIII] and Hα emission lines.

1345+12

A low redshift galaxy (z = 0.122) with very strong emission lines. The Oxygen and Hydrogen emission lines are very strong, but the Mg b and Na D absorption features and 4000Å break are also clearly seen.

1348-012

A quasar at z = 1.482. Once again the identification of the single broad line in FORS as MgII is confirmed by the Carbon lines in the IPCS.

1348+007

A quasar at z = 2.084 with relatively narrow emission lines. The feature just below 5800Å is not real.

1351-018

The largest redshift measured in the present sample (z = 3.709). The centroid of the Lyα emission line is biassed towards long wavelengths because of absorption in the blue wing, and so this line was not

used in the redshift determination. Attention is drawn to the properties of this extreme object in Chapter 5.

1538+14

There are no obvious features on which to base a redshift, despite the fact that the continuum has been clearly detected. In fact, this object is a known BLlac.

1741-03

A quasar at z = 1.046. The identification of the broad line at 5724Å as MgII is confirmed by the presence of [OII] at 7630Å. A redshift for this object has also been measured by White *et al.* (1987), who quote a value of z = 1.054 ± 0.002.

2012-017

There are no obvious features from which to determine a redshift (the apparent feature around 5300Å is an artefact of the joining process) although the continuum is detected at fairly good signal/noise and appears to be non-thermal.

2047+039

Another object for which a redshift determination has not been possible. Again the continuum appears non-thermal although the signal/noise in the IPCS section is too poor for us to be sure that it is genuinely featureless.

2106-413

A quasar at z = 1.058. Despite the poor signal/noise in the IPCS

section the presence of CII at 4795Å confirms the line at 5766Å as MgII. The presence of the narrow Neon and Oxygen lines in the FORS section confirm the redshift. A redshift for this object has also been measured by White *et al.* (1987) who quote z = 1.0547 ± 0.0003.

2152-218

A low-redshift galaxy (z = 0.306) with strong Oxygen and Hα emission. Mg b absorption is just visible and the 4000Å break is clearly seen

2153-219

A very low-redshift galaxy (z = 0.097) with strong narrow Hα emission but no detectable Oxygen lines. Mg b abs, Na D abs and the 4000Å break are clearly present (the feature ~ 8600Å is not real).

2154-184

A quasar at z = 0.668. The continuum is very weak but there are a large number of strong narrow Oxygen and Neon lines.

2154-183

A quasar at z = 1.423. The identification of the single broad line at ~ 7000Å as MgII is once again confirmed by the presence of the CIII line in the relatively noisy IPCS section of the spectrum.

2159-187

A broad-line radio galaxy at z = 0.334. The Mg b and Na D absorption features are also present as is a fairly weak 4000Å break.

2203-215

A strong-lined quasar at z = 0.577.

2204-208

A quasar at z = 1.923. The spectrum appears very similar to that of 1348+007 with its fairly narrow emission lines.

2213-167

A bright low-redshift galaxy (z = 0.074) with fairly weak Hα emission and possible detection of the [OII] 3727Å line at 4000Å. The Mg b and Na D absorption features are very strong, as is the 4000Å break and the TiO band at ~ 7500Å (see discussion of 0000-006)

2214-206

A quasar at z = 2.316. Despite the poor signal/noise, Lyα/NV is clearly seen at ~ 4000Å.

2215-185

This appears to be a galactic star (Ca H & K and Telluric O_2 at 7594Å are visible - compare with 1206-026). The correct identification must be a galaxy below the sky-survey limit.

2354-021

The continuum appears flat and non-thermal but, because of the poor signal/noise ratio, no redshift determination has been possible.

Table 4.2 : Line measurements and identifications

SOURCE NAME	TYPE	MEAN REDSHIFT	OBSERVED λ	IDENTIFICATION		z
0000-006	G	0.07 ?				
0013-005	Q	1.575 ± 0.003	3997Å	CIV	1549Å	1.580
			4905	CIII	1909	1.569
			7206	MgII	2799	1.575
0040+017	G?					
0041+007	G	0.112 ± 0.001	4153	[OII]	3727	0.114
			5562	[OIII]	5007	0.111
			5766	Mg b abs	5174	0.114
			6549	Na D abs	5892	0.111
			7300	Hα	6563	0.112
			7472	[SII]	6724	0.111
0047+023	BLlac?					
0213-13	G	0.1483 ± 0.0003	5692	[OIII]	4959	0.1478
			5747	[OIII]	5007	0.1478
			5942	Mg b abs	5174	0.1493
			7542	Hα	6563	0.1492
			7719	[SII]	6724	0.1480
0215+015	BLlac					
0223+012	Q	1.369 ± 0.003	3668	CIV	1549	1.368
			4529	CIII	1909	1.373
			6627	MgII	2799	1.368

0229+034	G					
0230-027	G	0.239 ± 0.001	4623	[OII]	3727	0.240
			6141	[OIII]	4959	0.238
			6204	[OIII]	5007	0.239
			6408	Mg b abs	5174	0.238
			7300	Na D abs	5892	0.239
			8146	Hα	6563	0.241
0230-022	G					
0235+023	Q	0.209 ± 0.001	4044	[NeV]	3346	0.209
			4138	[NeV]	3426	0.208
			4498	[OII]	3727	0.207
			4686	[NeIII]	3869	0.211
			5281	[OIII]	4363	0.210
				(Hγ	4340	0.217)
			5860	Hβ	4861	0.205
			6016	[OIII]	4959	0.213
			6048	[OIII]	5007	0.208
			7926	Hα	6563	0.208
			8114	[SII]	6724	0.207
0236-015	Q	1.794 ± 0.003	4341	CIV	1549	1.803
			5328	CIII	1909	1.791
			7801	MgII	2799	1.788
0238-018	?					
0240-021	Q	0.617 ± 0.001	3793	CII	2326	0.631
			4498	MgII	2799	0.607
			6032	[OII]	3727	0.618
			6251	[NeIII]	3869	0.616
			8020	[OIII]	4959	0.617
			8067	[OIII]	5007	0.611

0242+009	Q	1.520 ± 0.003	3903	CIV	1549	1.520
			4811	CIII	1909	1.520
			5860	CII	2326	1.519
			(7081	MgII	2799	1.530)
			(8662	[NeV]	3426	1.528)
0422+004	BLlac					
0528+13	BLlac?					
0804+49	Q	1.433 ± 0.004	4647	CIII	1909	1.434
			6822	MgII	2799	1.437
0814+42	BLlac?					
0823+033	BLlac?					
0837+035	BLlac?					
1031+56	G	0.4590 ± 0.0001	7304	[OIII]	5007	0.4588
			9576	Hα	6563	0.4591
			9806	[SII]	6724	0.4584
1206-026	Star					
1215-033	G	0.184 ± 0.001	4592	[NeIII]	3869	0.187
			5860	[OIII]	4959	0.182
			5923	[OIII]	5007	0.183
			6126	Mg b abs	5174	0.184
			6987	Na D abs	5892	0.186
			7770	Hα	6563	0.184
			7958	[SII]	6724	0.184

1215-002	G	0.417 ± 0.001	5265	[OII]	3727	0.413
			7332	Mg b abs	5174	0.417
			8380	Na D abs	5892	0.422
			9288	Hα	6563	0.415
1225+36	?					
1317+019	?					
1323+32	G	0.369 ± 0.001	5093	[OII]	3727	0.367
			6796	[OIII]	4959	0.370
			6857	[OIII]	5007	0.369
			8623	[OI]	6300	0.369
			9002	Hα	6563	0.372
			9193	[SII]	6724	0.367
1334+008	G	0.299 ± 0.001	4842	[OII]	3727	0.299
			6298	Hβ	4861	0.296
			6439	[OIII]	4959	0.298
			6502	[OIII]	5007	0.299
			6721	Mg b abs	5174	0.299
			7660	Na D abs	5892	0.300
			8537	Hα	6563	0.301
			8725	[SII]	6724	0.298
1336-030	Q	2.313 ± 0.003	4028	Ly α	1216	2.313
			4106	NV	1240	2.312
			5140	CIV	1549	2.318
			6314	CIII	1909	2.307
			9273	MgII	2799	2.313

1342-016	G	0.1675 ± 0.0005	4344	[OII]	3727	0.1655
			5783	[OIII]	4959	0.1662
			5841	[OIII]	5007	0.1666
			7350	[OI]	6300	0.1667
			7664	Hα	6563	0.1678
			7846	[SII]	6724	0.1669
1345+12	G	0.122 ± 0.001	4200	[OII]	3727	0.127
			4889	[OIII]	4363	0.121
				(Hγ	4340	0.127)
			5453	Hβ	4861	0.122
			5562	[OIII]	4959	0.122
			5609	[OIII]	5007	0.120
			5797	Mg b abs	5174	0.120
			6627	Na D abs	5892	0.125
			7065	[OI]	6300	0.121
			7363	Hα	6563	0.122
			7551	[SII]	6724	0.123
1348-012	Q	1.482 ± 0.003	3840	CIV	1549	1.479
			4748	CIII	1909	1.487
			6940	MgII	2799	1.479
1348+007	Q	2.084 ± 0.002	3746	Lα	1216	2.081
			3793	NV	1240	2.059
			4795	CIV	1549	2.096
			5876	CIII	1909	2.078
			7206	CII	2326	2.098
			8662	MgII	2799	2.095
1351-018	Q	3.709 ± 0.003	4870	(Lβ	1026	3.748)
				[OVI]	1034	3.711
			5735	Lα	1216	3.717
			5830	NV	1240	3.701
			6155	([OI]	1304	3.722)
				SiII	1308	3.707
			7295	CIV	1549	3.709
			9005	CIII	1909	3.717

1538+14	BLlac					
1741-03	Q	1.046 ± 0.001	5724	MgII	2799	1.045
			7630	[OII]	3727	1.047
2012-017	BLlac?					
2047+039	BLlac?					
2106-413	Q	1.058 ± 0.002	4795	CII	2326	1.062
			5766	MgII	2799	1.060
			7034	[NeV]	3426	1.053
			7660	[OII]	3727	1.055
2152-218	G	0.306 ± 0.001	6470	[OIII]	4959	0.305
			6533	[OIII]	5007	0.305
			6752	Mg b abs	5174	0.305
			8333	[OI]	6363	0.310
			8584	Hα	6563	0.308
			8756	[SII]	6724	0.302
2153-219	G	0.097 ± 0.001	5672	Mg b abs	5174	0.0963
			6470	Na D abs	5892	0.0982
			7206	Hα	6563	0.0980
			7378	[SII]	6724	0.0973
2154-184	Q	0.668 ± 0.001	5578	[NeV]	3346	0.667
			5719	[NeV]	3426	0.669
			6220	[OII]	3727	0.669
			6455	[NeIII]	3869	0.668
			7269	[OIII]	4363	0.666
			8114	Hβ	4861	0.669
			8271	[OIII]	4959	0.668
			8349	[OIII]	5007	0.667

2154-183	Q	1.423 ± 0.003	4623	CIII	1909	1.422
			6784	MgII	2799	1.424
2159-187	G	0.334 ± 0.001	3746	MgII	2799	0.338
			4576	[NeV]	3426	0.336
			4968	[OII]	3727	0.333
			5797	Hγ	4340	0.336
				([OIII]	4363	0.329)
			6470	Hβ	4861	0.331
			6611	[OIII]	4959	0.333
			6673	[OIII]	5007	0.333
			6893	Mg b abs	5174	0.332
			7864	Na D abs	5892	0.335
			8756	Hα	6563	0.334
2203-215	Q	0.577 ± 0.001	4420	MgII	2799	0.579
			5876	[OII]	3727	0.576
			6095	[NeIII]	3869	0.575
			6846	Hγ	4340	0.577
				([OIII]	4363	0.569)
			7660	Hβ	4861	0.576
			7817	[OIII]	4959	0.576
			7895	[OIII]	5007	0.577
2204-208	Q	1.923 ± 0.003	3559	Lα	1216	1.926
			3621	NV	1240	1.920
			4529	CIV	1549	1.924
			8177	MgII	2799	1.921
2213-167	G	0.074 ± 0.001	3997	[OII]	3727	0.0724
			5547	Mg b abs	5174	0.0720
			6330	Na D abs	5892	0.0743
			7065	Hα	6563	0.0765
			7221	[SII]	6717	0.0739

2214-206	Q	2.316 ± 0.003	4028	Lα	1216	2.313
			4122	NV	1240	2.324
			5140	CIV	1549	2.318
			6314	CIII	1909	2.307
2215-185	Star					
2354-021	BLlac?					

Table 4.3 : Summary of the spectroscopy results (see Appendix A for a full description of the radio structure abbreviations)

i) Selected Region Sources

SOURCE NAME	RADIO SPECTRAL INDEX α	RADIO STRUCTURE	SPECTRAL TYPE	R mag	z
0000-006	0.34	U+Di	G	18.90	0.07?
0013-005	0.21	U	Q	18.40	1.575
0040+017	0.66	Do+CC,II	G?	16.50	
0041+007	1.24	Do+CC,II	G	16.00	0.112
0047+023	0.23	U,V	BLlac?	18.20	
0223+012	0.76	Do+CC,II	Q	18.80	1.369
0229+034	0.66	Do+CC,II	G	18.00	
0230-027	0.83	Do,II	G	18.18	0.239
0230-022	0.75	P	G	19.50	
0235+023	0.72	Do+CC,II	Q	17.10	0.209
0236-015	1.08	Do,II	Q	18.90	1.794
0238-018	1.19	Do,II	?	19.60	
0240-021	0.95	U+Di	Q	18.87	0.617
0242+009	0.91	Do+CC,II	Q	18.20	1.520
1206-026	0.87	Do,II	Star	Wrong Object	
1215-033	0.88	D2	G	17.90	0.184
1215-002	0.33	U+H,V?/HT	G	17.50	0.417
1334+008	-0.10	U	G	18.39	0.299
1336-030	0.51	P	Q	18.00	2.313
1342-016	0.87	Do+CC,II	G	15.80	0.1665
1348-012	0.57	D2?	Q	19.20	1.482
1348+007	0.37	U	Q	21.40	2.084
1351-018	-0.08	U	Q	19.30	3.709
2152-218	1.48	U,V?	G	19.16	0.306
2153-219	1.24	Do,II	G	14.10	0.097
2154-184	1.17	Do+CC,II	Q	19.43	0.668
2154-183	0.79	U	Q	21.41	1.423
2159-187	1.33	D2	G	18.30	0.334
2203-215	-0.19	U	Q	17.90	0.577
2204-208	0.05	U,V	Q	19.81	1.923

2213-167	0.85	Do+CC,II	G	14.10	0.074
2214-206	0.97	P	Q	20.10	2.316
2215-185	1.10	Do,II+CC?	Star	17.81	
2354-021	0.07	P,V	BLlac?	20.20	

ii) Sources from the brighter 2.7GHz samples

SOURCE NAME	RADIO SPECTRAL INDEX α	SPECTRAL TYPE	V mag	z	SAMPLE REF.
0213-13	0.74	G	18.0	0.1483	3
0215+015	-0.61	BLlac	18.5		1
0422+004	-0.36	BLlac	16.0		1
0528+13	-0.43	BLlac?	19.5		2,3
0804+49	-0.49	Q	19.0	1.433	2
0814+42	0.47	BLlac?	16.9		2,3
0823+033	0.15	BLlac?	18.5		1
0837+035	0.28	BLlac?	20.0		1
1031+56	0.30	G	19.5	0.4590	2
1225+36	1.17	?	21.9		2
1317+019	0.00	?	19.5		1
1323+32	0.60	G	19.0	0.3693	2,3
1345+12	0.44	G	17.0	0.122	2,3
1538+14	0.01	BLlac	16.4		2
1741-03	-0.28	Q	18.5	1.046	3
2012-017	0.35	BLlac?	17.5		1
2047+039	-0.16	BLlac?	18.5		1
2106-413	-0.13	Q	20.0	1.058	3

Sample references

1 = The $S_{2.7}$ > 0.5Jy equatorial flat-spectrum sample (Peacock 1986, updated version given in Appendix A, Table A.2)

2 = The $S_{2.7}$ > 1.5Jy Northern-Sky survey (Peacock & Wall 1981, updated version given in Appendix A, Table A.3)

3 = The $S_{2.7}$ > 2Jy All-Sky survey (Wall & Peacock 1985, updated version given in Appendix A, Table A.4)

Chapter 5 : PROPERTIES OF THE PARKES SELECTED REGIONS SAMPLE AND THE EXTREME EXAMPLE OF PKS 1351-018

5.1 : INTRODUCTION

The purpose of this chapter is to gather together the results presented in the previous three chapters and discuss the properties of the final complete Selected Regions sample which is formed by incorporating the new data into the original dataset of Downes *et al.* (1986). Table 5.1 below summarizes the status of the sample at the time of writing (1987) as compared to its status at the start of the present work (1985).

Table 5.1 : The complete sample of sources with flux density S ≥ 0.1Jy at 2.7GHz in the Parkes Selected Regions : status of the sample.

FIELD	Field centre (1950.0)		Status at the start of the present work (1985)			Status now (1987)		
	RA	Dec	No. of sources	No. of IDs	No. of redshifts	No. of IDs	No. of redshifts	No. of K mags
1	$00^h04^m51^s$	$00^\circ32'$	26	9	3	25	11	23
2	00 52 55	00 31	29	16	10	27	14	26
3	02 32 31	00 25	31	20	8	29	17	24
4	12 04 50	-00 31	25	18	8	24	10	11
5	13 40 48	-00 29	30	15	6	29	11	14
6	22 03 26	-18 50	37	22	5	36	14	33
Total			178	100 (56%)	40 (22%)	170 (96%)	77 (43%)	131 (74%)

The identification statistics given above include only the optical identifications - if the 4 additional IR detections are included the identification content rises to 98%. In the 4-region subsample

comprising fields 1,2,3 and 6 the K photometry is 86% complete.

Also discussed in this chapter are the properties of one particular object in the sample, PKS 1351-018. The measurement of a redshift of 3.709 for this object was the most spectacular result of the spectroscopic observations described in Chapter 4 (Dunlop *et al.* 1986). This redshift is by far the largest of those measured in the Selected Regions to date (the next largest z in the sample is 2.795 for 0054-006) and indeed, at the time of observation, it was the second largest ever discovered (second only to PKS 2000-330, z = 3.78, Peterson *et al.* 1982). In the two intervening years several more high redshift quasars have been discovered, including several with z > 4 (eg Warren *et al.* 1987, Schmidt *et al.* 1987b). Nevertheless, PKS 1351-018 remains the 3rd most distant radio quasar and is very important in the context of the present study, firstly because it confirms the ability of the Selected Regions to probe high-redshift space, and secondly because it provides direct evidence of how certain properties, such as quasar colours, may be expected to behave at high redshift.

Firstly, however, it is necessary to consider the final additions and corrections which had to be made to the dataset.

5.2 : COMPLETION OF THE DATASET

5.2a : Classification of the faint optical identifications

As discussed earlier in Chapter 2, the extreme faintness of many of the new optical identifications meant that it was impractical to attempt to classify them solely on the basis of their optical morphology. Instead it was decided to use a combination of optical morphology, optical colour and optical-infrared colour.

Colour classification involves deciding whether an object lies in the quasar locus, or the galaxy locus on the relevant colour diagram. These loci must therefore be delineated using objects of known optical type. Figure 5.1 shows the positions of known radio galaxies

and quasars on the (B-R)/K and (R-K)/K colour-magnitude diagrams. All of the quasars on these diagrams were taken from the Selected Regions. The Selected Region galaxies have been supplemented with some additional points from the brighter 1Jy and 3CR samples to help delineate the extension of the galaxy locus to large values of K (Lilly *et al.* 1985, Lilly & Longair 1984).

On both these diagrams the galaxy and quasar loci are well defined and, although there are regions of overlap, there clearly exist large areas of colour space in which an unambiguous classification can be made. An important feature of these two diagrams is that they provide effective quasar/galaxy separation over complementary ranges in K magnitude ($\cong$ complementary ranges in z). In the (B-R)/K diagram the two loci are most distinct over the range $K \simeq 14 \rightarrow 16$, but at fainter K magnitudes they inevitably become intermeshed - the B-R colour of quasars begins to increase at high redshift ($z > 2.5$) as Lyα moves longward of the B filter (see Figure 5.7), while for galaxies it decreases once the 4000 Å break has been redshifted out of the optical region. This is in sharp contrast to the situation in the (R-K)/K diagram where the two loci appear to diverge as K increases. The location of PKS 1351-018 on these diagrams illustrates the power of the R-K colour to isolate high-redshift quasars which are inevitably indistinguishable from galaxies on the basis of optical colours. In fact, PKS 1351-018 was identified as a potential high-redshift quasar, prior to spectroscopy, precisely because of this important combination of red optical colour and blue optical-infrared colour.

It is worth noting that at sufficiently high redshift the R-K colour of a quasar will also start to increase as Lyα moves longward of the R filter. However, this will not occur until $z > 5$, by which stage the object should be very red in the optical ($B-R > 3$, see Section 5.4).

Figure 5.1 : Positions of established radio galaxies and quasars on the (B-R)/K and (R-K)/K colour-magnitude diagrams.

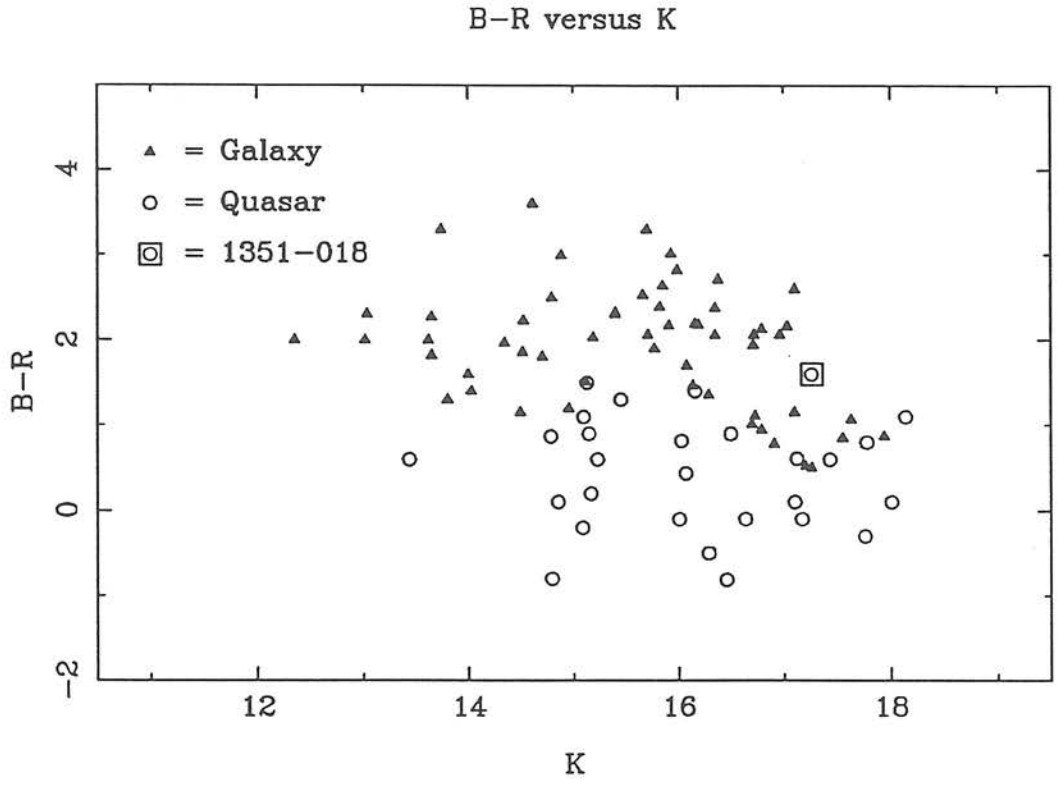

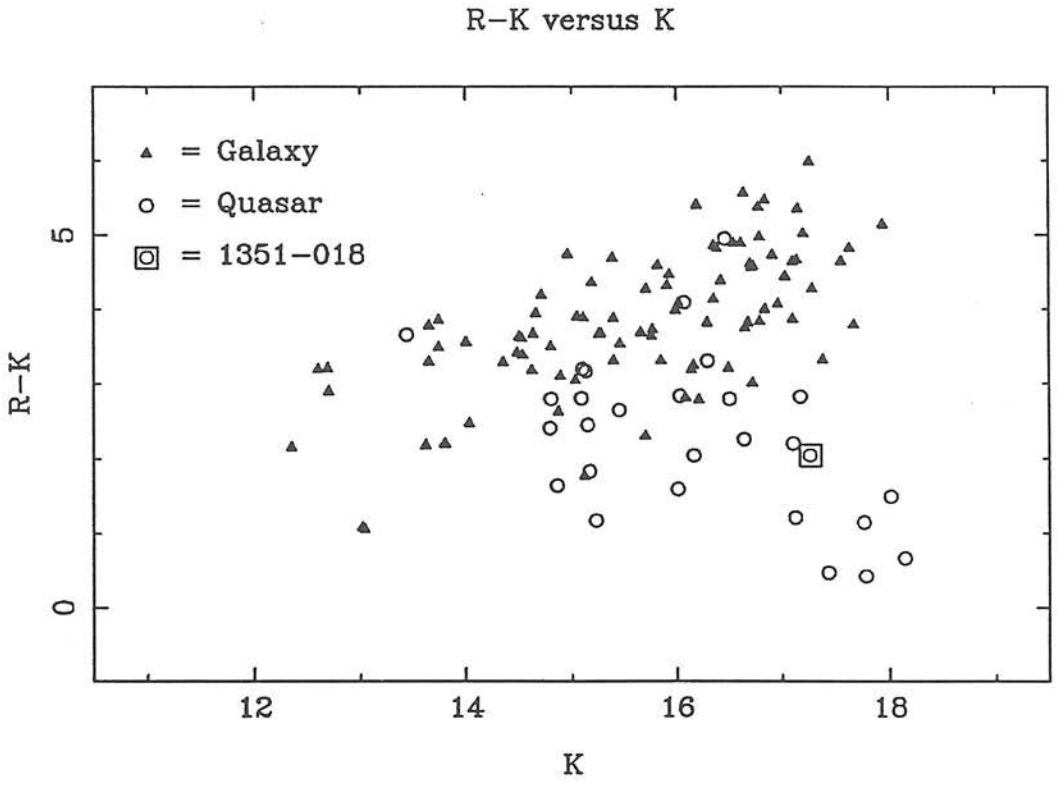

For each of the new identifications 3 independent classifications were attempted - first on the basis of optical morphology (on the CCD image), second by location on the (B-R)/K diagram, and third by position on the (R-K)/K diagram. The classification finally adopted was then based on the majority decision, with a ? added whenever this was not unanimous.

The result of this procedure was that of the 71 new CCD identifications, 59 were classified as G or G?, 6 as Q or Q? and 6 as simply ?. The predominance of galaxy identifications is consistent with expectations based on extrapolating the magnitude distributions of the brighter sky-survey quasar and galaxy identifications (see Section 5.3c). An attempt was also made to classify the 4 optical empty fields which were observed in the infrared (see Section 3.3b) on the basis of the lower limits to their R-K colours. All 4 of these sources have R-K > 5.5 and have therefore been classified as G?.

5.2b : Aperture corrections

The optical-infrared database consists of measurements made through 3 different apertures - the infrared photometry is a mixture of 7.8" and 12.4" aperture magnitudes (see Chapter 3), while the CCD optical magnitudes were all measured through a 5" aperture after deconvolution of the seeing profile (see Chapter 2). This mixed aperture data is not a problem for the quasar identifications since all 3 apertures should contain essentially all the light from a stellar object (this is only true for the 5" aperture because of the seeing deconvolution procedure). However for the galaxies it was necessary to consider what, if any, aperture corrections should be applied. In general it was considered desirable to avoid any complex and subjective alteration of the raw photometry, but at the same time it was important to consider whether any simple corrections could be applied to improve the homogeneity of the data.

In the end it was decided <u>not</u> to apply any aperture corrections to the infrared data, the reasoning being as follows. Since essentially all of the sky-survey identifications were observed through the 12.4"

aperture, the mixed aperture IR data is confined to the fainter CCD identifications. As described above (see Section 5.2a) the bulk of these CCD identifications are faint galaxies, most of which should be sufficiently distant ($z \sim 1$) for effectively all their light to be contained within a 7.8" aperture. The difference between a 12.4" and 7.8" aperture magnitude is therefore expected to be very small for these objects, and so no aperture correction is justified. Empirical evidence that this is indeed the case is provided by the results of the repeated infrared measurements listed in Table 3.6. Some of these repeated observations were made through a different aperture on each occasion, and yet the systematic difference between the results appears to be negligible.

The CCD optical photometry is internally homogeneous (ie all 5" seeing-deconvolved aperture magnitudes). It therefore only remained to consider whether any correction should be applied to the optical photometry to assist comparison with the infrared data. For this purpose it was decided to correct all the galaxy 5" aperture magnitudes to a 7.8" aperture. This decision was made for several reasons. Firstly it was clear that some sort of correction was justified since, even at $z \simeq 2$, the light of a giant elliptical galaxy is not fully contained within a 5" aperture. Secondly, extrapolation to even larger apertures was considered to involve a dangerously large modification to the raw data, and in any case is not justified for the distant galaxies (see above). Thirdly this correction is uniform and simple, involving merely the application of a constant offset to the CCD photometry.

The only assumption involved in this aperture correction is the Structure Parameter, α, introduced by Gunn & Oke (1975), where $L \propto R^{\alpha}$. α is itself a function of R and it is common (eg Gunn & Oke 1975, Lilly *et al.* 1984) to consider a sampling radius of $19.2h^{-1}$kpc where $H_o = h \times 50 kms^{-1}Mpc^{-1}$. At $z \sim 1$ (which should be a reasonable approximation for the faint CCD galaxy identifications) an aperture radius of 2.5" corresponds to a metric radius of $\sim$ 20kpc (for $H_o = 50 kms^{-1}Mpc^{-1}$, $\Omega = 1$) and so it is reasonable to use the quoted values of α to aperture-correct the 5" diameter aperture magnitudes in the present study. The value of α adopted here was 0.5. This

represents a compromise between the value of 0.7 found by Schneider *et al.* (1983) for Abell cluster galaxies, and the lower value of 0.4 found by Lilly *et al.* (1984) for 3C radio galaxies (Because α is < 1, the exact value is not too important for the present study). With this assumed brightness distribution, the aperture correction from 5" to 7.8" is $\Delta m = -0.24$. This offset was therefore applied to the results of the CCD galaxy photometry prior to the subsequent analysis.

Without more detailed information concerning the surface brightness distributions and redshifts of the galaxy identifications, no more complex procedure than the above is justified. This simple correction should assist in achieving the important aim of meaningful optical-infrared colours for the high-redshift galaxies.

5.2c : Estimation of the uncertainty in the sky-survey eye-estimated magnitudes

As described in Chapter 2, CCD observations were made of several of the original sky-survey plate identifications, either to obtain improved photometry or to check the validity of the identification. The results of the CCD photometry of these objects were compared with the original eye-estimated values in Table 2.1 of Chapter 2. This data can be used to obtain an estimate of the uncertainty in the eye-estimated magnitudes. The region of overlap covers the magnitude range R = 16.5 → 20, B = 18 → 21.5. As expected, the 5 arcsec CCD aperture magnitudes are systematically fainter than the plate values - by 0.37 in R, and 0.36 in B. Application of the above aperture correction to the CCD galaxy magnitudes reduces these offsets to 0.19 and 0.18 respectively. After taking account of these remaining systematics the rms deviation was found to be 0.55 in R, and 0.45 in B. For simplicity an error of ± 0.5 has therefore been assigned to all the sky-survey plate, eye-estimated magnitudes. This value agrees well with the original error estimates of Downes *et al.* (1986).

No attempt has been made to apply any systematic correction to the plate magnitudes, since any such correction will be magnitude

dependent. Also, the systematic offset in the overlap region is small compared with the random errors and should be negligible for objects near the plate limit.

5.3 : STATISTICS

5.3a : Identification statistics

Figure 5.2 shows the distribution of radio spectral indices in the sample (shown separately for extended and compact sources, compact being those with U or P radio structure) along with the type of optical identification associated with each source. This figure illustrates the fact that, whereas the compact subsample contains roughly equal numbers of flat- and steep-spectrum objects, almost all of the extended sources have steep radio spectra. The bulk of these extended, steep-spectrum sources have FRII structures and remained unidentified following the original identification search of Downes *et al.* (1986), a fact which demonstrates that the sample is dominated by distant, high-luminosity objects. Figure 5.2 illustrates that, as a result of the deep CCD observations, most of these distant FRII sources have now been identified with faint galaxies. The figure also shows that the 4 remaining unidentified objects (unidentified in optical or infrared) all possess very steep radio spectra.

The identification statistics are considered in more detail in Table 5.2, with the radio sources first divided by spectral index, and then further subdivided on the basis of radio structure. The important points in this table are summarized below.

i) Flat-spectrum sources.

All of the flat-spectrum sources have now been identified. 73% are quasars (Q or Q?) while only 25% are galaxies. This dominance of quasar identifications explains why 75% of the flat-spectrum sources were successfully identified by Downes *et al.* (1986) on sky-survey plate material. There are very few extended flat-spectrum sources, but of these the majority are D2 sources which, as expected, have

been identified with quasars. Most of the compact flat-spectrum sources are unresolved (U) (rather then partially resolved, P) and, as would have been anticipated, have also been mostly identified with quasars.

ii) Steep-spectrum sources

There are 4 unidentified steep-spectrum sources. These are the 3 optical empty fields which were not observed in the infrared, plus the one source which is obscured by a bright star, 0240-027. The other 4 optical empty fields are listed as G? because of their IR identification and subsequent colour classification (see Section 5.2a). The steep-spectrum sources are therefore now 97% identified, with the vast majority of these identifications being galaxies (~72%). Only 50% of the steep-spectrum sources were identified on the sky-survey plates, and the main impact of the CCD imaging has been to convert EFs into Gs and G?s in this table. There are relatively few FRI sources in the sample and essentially all of these (10 out of 11) were successfully identified by Downes *et al.* with low redshift galaxies, a fact which is consistent with the known low radio power of this class of source (Fanaroff & Riley 1974). Table 5.2 shows that the bulk of the FRII sources have been identified with galaxies. However, as mentioned in Chapter 1, the probability of a quasar identification is expected to increase with the relative strength of the central radio component. This is investigated in Table 5.3. This table shows that, as expected, most of the radio galaxies do not possess a detected radio core component, while most of the quasars do. Rather surprising, however, is the fairly large number (15) of galaxies which do have a central component. Also, there are a few (5) quasars without a radio core, and the possibility must be considered that some of these sources might have been mis-identified with stars. Finally there are the compact steep-spectrum sources. Unlike the corresponding flat-spectrum objects, most of these are partially resolved (P), and the identifications divide between galaxies and quasars in the ratio roughly 2:1. These objects are considered in more detail in the next section.

Figure 5.2 : The distribution of spectral indices for the complete sample of 178 sources with S > 0.1Jy at 2.7GHz. The spectral index α is defined in the sense $S(\nu) \propto \nu^{-\alpha}$. The lower plot for compact sources includes all those with unresolved, U, or partially resolved, P, structure. The type of the identifications is also given.

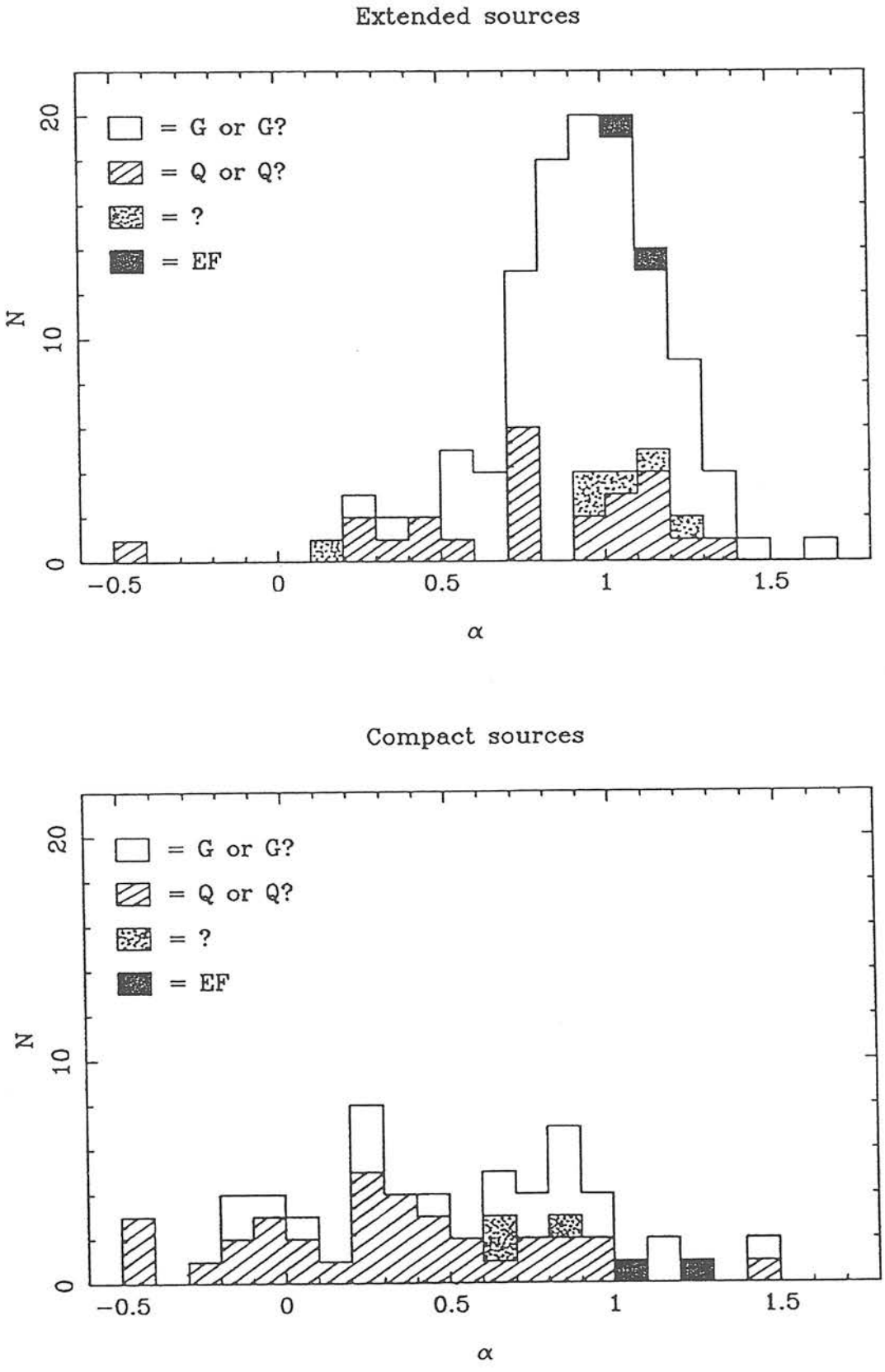

Table 5.2 : Identification statistics for sources in the Parkes Selected Regions.

a) Steep-spectrum sources ($\alpha \geq 0.5$)

	Q	Q?	G+G?	?	EF	TOTAL
FRI	0	0	10	1	0	11 = 8%
FRII and D2	14	3	71	5	2	95 = 70%
P and U+Di	7	0	12	0	2	23 = 17%
U	2	0	3	3	0	8 = 6%
TOTAL	23	5	96	9	4	137

b) Flat-spectrum sources ($\alpha < 0.5$)

	Q	Q?	G+G?	?	EF	TOTAL
FRI	0	0	0	1	0	1 = 2%
FRII and D2	5	1	1	0	0	7 = 17%
P and U+Di	4	1	2	0	0	7 = 17%
U	17	2	7	0	0	26 = 63%
TOTAL	26	4	10	1	0	41

Table 5.3 : The identification of FRII sources - relation to the detection of a central component

	Q+Q?	G+G?	?	EF	TOTAL
With central component	9	15	3	0	27
Without central component	5	54	2	2	63
TOTAL	14	69	5	2	90

5.3b : The nature of the steep-spectrum compact sources

As illustrated in Figure 5.2, there are very few extended sources in the sample which possess flat radio spectra. The spectral division is not however so clear for the compact sources, for which the steep:flat-spectrum ratio is roughly 1:1. The steep-spectrum compacts thus form an interesting class of source which does not conform to the normal steep-spectrum = extended, flat-spectrum = compact classification (This does not of course imply that the $\alpha = 0.5$ division has been ineffective since the steep-spectrum class as a whole is still dominated by extended sources).

It has been suggested (Savage & Peterson 1983) that these steep-spectrum compact sources could be the high-redshift counterparts of the flat-spectrum compacts, since a flat spectrum will eventually become steep at high frequency due to the effect of spectral curvature. If true, this could have important implications for the redshift cutoff for radio quasars since the high-redshift decline in the flat-spectrum population might then be an artefact caused by the classification procedure. In fact Peacock (1985) demonstrated that the scale of spectral curvature in most flat-spectrum sources is sufficiently broad that this effect should be statistically unimportant until $z > 10$. Nevertheless, the optical properties of faint, steep-spectrum, compact sources are still of interest. For brighter examples of this type of source (such as those found in the 1.5Jy sample of Peacock & Wall 1981) the ratio of quasar:galaxy identifications is roughly 1:1. Since less than half of the steep-spectrum compacts in the Selected Regions were identified on sky-survey material, the deep CCD images might therefore have been expected to reveal a significant number of faint quasar identifications. In fact, the result of the classification procedure described in Section 5.2a was that almost all of the faint CCD identifications of these objects turned out to be galaxies, and <u>not</u> high-redshift quasars. Much of the evidence for this comes from the position of these compact identifications on the (R-K)/K diagram, shown in Figure 5.3. All of the objects on this diagram are from the 4-region Selected Regions subsample for which complete K photometry was obtained. The "galaxies" comprise the sky-survey galaxy

identifications and the CCD identifications of Do,II sources which were expected, and confirmed (see Section 5.2a) to be galaxies. It is clear from this diagram that the vast majority of the compact CCD IDs lie in the galaxy, rather than the quasar locus, and therefore do not constitute a population of distant quasars. The result of this is that, as can be seen from Table 5.2, the ratio of quasar:galaxy identifications for compact steep-spectrum sources in the Selected Regions is nearer 1:2 rather than the 1:1 found in the brighter samples.

A clue as to the origin of this increase in the number of steep-spectrum compacts identified with galaxies is to be found among the compact CCD IDs which are very faint in the infrared. There are 4 compact CCD IDs in Figure 5.3 with $K > 18.5$. Because it is unclear whether or not they lie in an extension of the galaxy locus on this diagram, these objects were among the very few compact sources which were not classified as galaxies. One of them, 0000+035 ($K > 19.0$, $R-K < 2.27$, $B-R = 1.74$), appears to lie in a natural extension of the quasar locus and therefore, because of its large value of B-R, appeared to be a strong candidate for a high-redshift quasar. The other 3 lie in a somewhat ambiguous region of the diagram. 2355-024 ($K > 19.0$, $R-K < 3.37$, $B-R = 0.56$) and 0008-006 ($K = 18.94$, $R-K = 3.96$, $B-R = 1.07$) are radio variables and have been classified as Q?, but their optical colours make it unlikely that they are at $z > \sim 3$ (see Section 5.4). Finally, 2200-187 ($K = 18.55$, $R-K = 3.52$, $B-R > 0.93$) has been classified as a ?. The important point is that, at the time of writing (Oct 87), a redshift has just been measured for one of these sources - 0000+035 - by Jeremy Allington-Smith at the William Herschel Telescope on La Palma. This object turns out to be a galaxy with $z = 0.363$, a result clearly at odds with the above expectation of a very high-redshift quasar. However, it is important to note that the radio structure of this object is P, rather than U and that no radio variability has been reported. Thus, from a radio point of view, it was not a strong quasar candidate. In retrospect, it becomes clear that the reason for the incorrect colour classification is that, for $z = 0.363$, this object is anomalously faint, both in the optical and infrared. Thus (although in this particular case the object was originally classified as Q?) the

measurement of such a low-redshift for such a faint object suggests the possibility that a significant fraction of the steep-spectrum P sources in the Selected Regions which have been identified as galaxies might be drawn from a population of low-luminosity, nearby galaxies which was not detected in the brighter 2.7GHz samples.

Figure 5.3 : The (R-K) versus K diagram illustrating the classification of the bulk of the steep-spectrum compact CCD IDs as galaxies.

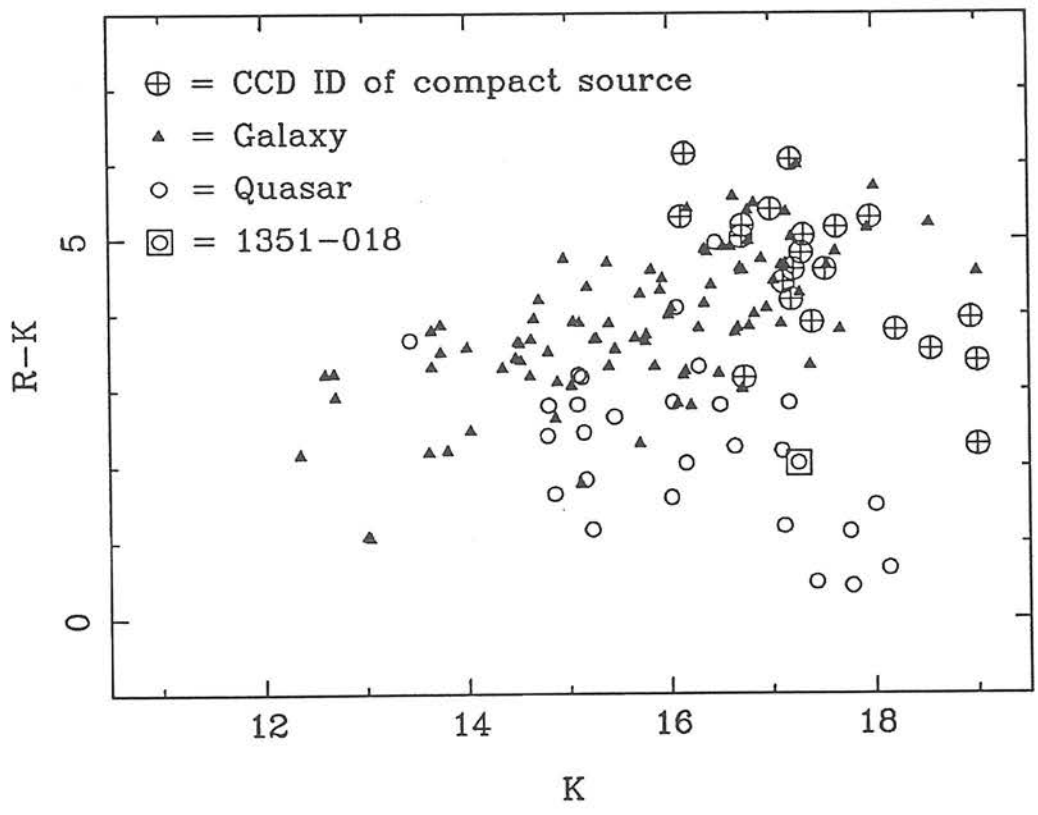

5.3c : Magnitude distributions

Figure 5.4 shows the magnitude distributions of the identifications in all 3 wavebands. The K-magnitude histograms have been restricted to the complete 4-region subsample. Since the 4 optical empty fields which were observed and detected in K were classified in Section 5.2a as G?, they are included in the galaxy distributions. The other 3 optical empty fields appear as lower limits in the B & R ? distributions. These 3 objects are obviously omitted completely from the K distributions, but in any case only one of them is part of the 4-region subsample.

The shapes of these histograms are consistent with expectations based on the sky-survey magnitude distributions; the quasars tend to be much brighter than the galaxies, and their magnitude distribution, having peaked at B ~ 19, R ~ 18, continues to decline beyond the plate limit. In contrast the galaxy distribution continues to rise until a peak at B ~ 23, R ~ 22, beyond which it declines fairly rapidly. In K the galaxy distribution peaks at K ~ 17, while the quasar distribution shows no well-defined peak, reflecting the large dispersion in quasar infrared magnitudes. An interesting feature of the K-magnitude distributions is that, unlike the situation in B and R, the faintest quasars and galaxies have comparable magnitudes. The implications of this are discussed in Section 5.4.

Figure 5.5 compares the K-magnitude distributions for the galaxy identifications in the present sample ($S_{2700} > 0.1$Jy, 4-region subsample only), the 1Jy sample ($S_{408} > 1$Jy, Lilly *et al.* 1985) and the 3CR sample ($S_{178} > 10$Jy, Lilly & Longair 1984). At 408MHz these 3 samples correspond to flux limits of ~ 0.6Jy, 1Jy and ~ 5Jy respectively (assuming $\alpha \simeq 1$ for steep-spectrum sources). Although the statistics for the 1Jy galaxies are relatively poor, it is clear that the 1Jy K-magnitude distribution is biassed towards larger values of K than the 3CR distribution. However, despite the further reduction in radio flux limit, a similar shift is not evident between the 1Jy and Selected Regions galaxy distributions. On the basis that K magnitude is a good redshift estimator for radio galaxies (see Chapter 6) this would imply that the 1Jy galaxies are the high-redshift counterparts

of the powerful 3CR sources, but that the Selected Regions sample is dominated by sources of lower radio luminosity at similar redshifts to the 1Jy galaxies. It is important to note, however, that the 3 1Jy galaxies with K > 17.5 for which redshifts have now been measured all lie close to the upper envelope of the 3CR K–z diagram (see Chapter 6, Section 6.2b). This suggests that the very faintest 1Jy and Selected Regions galaxies (ie K ~ 18) may not be extreme high-redshift counterparts of the 3CR galaxies, but simply intrinsically fainter galaxies at z ~ 1.5. This important point is considered in more detail in Chapters 6 and 7.

Figure 5.4 : The distribution of apparent magnitudes in B, R and K for the identifications in the Selected Regions. The K distributions include only objects from the 0, 1, 2 & 22hr regions in order to ensure a reasonable level of completeness. Sources with measured redshifts are shaded.

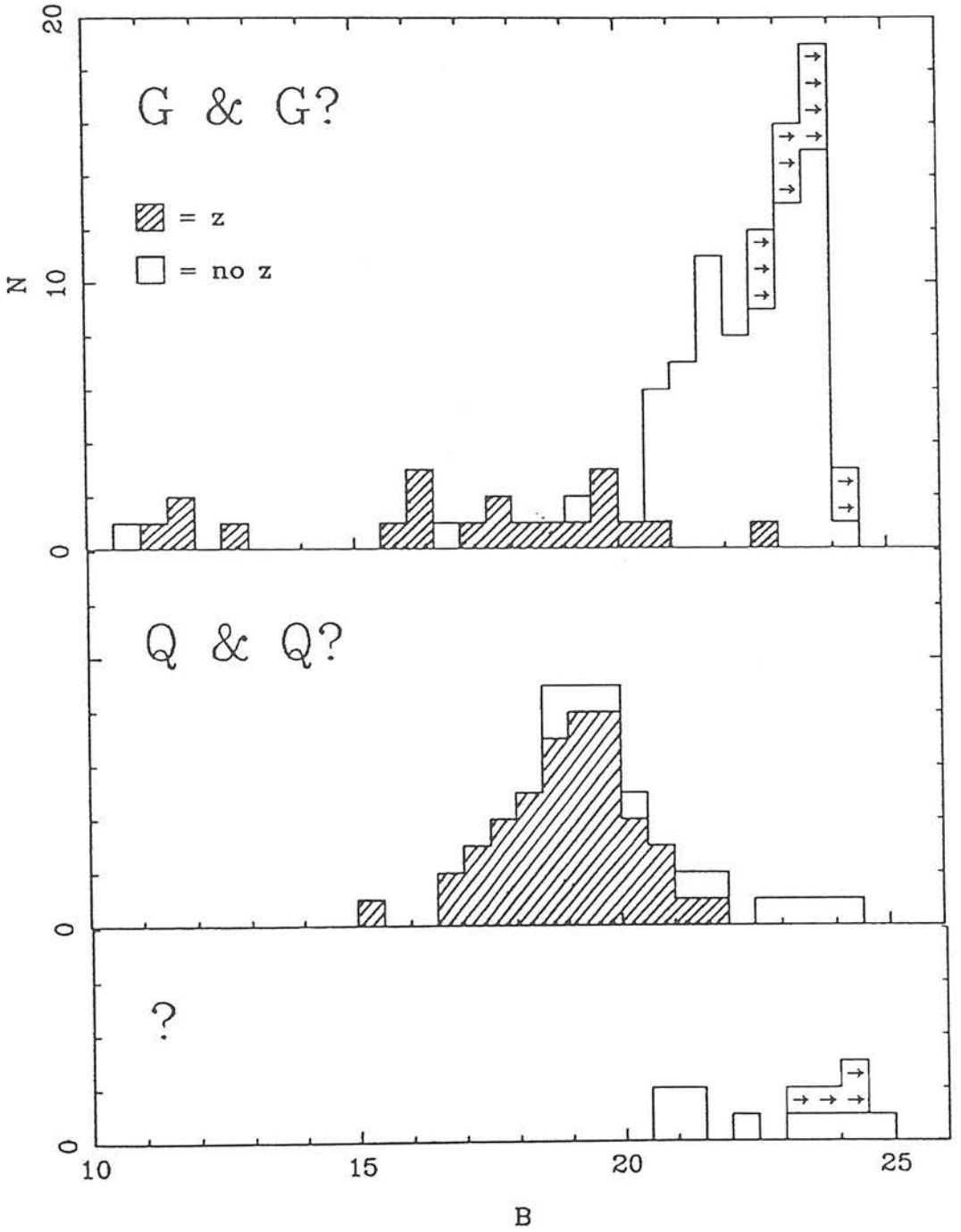

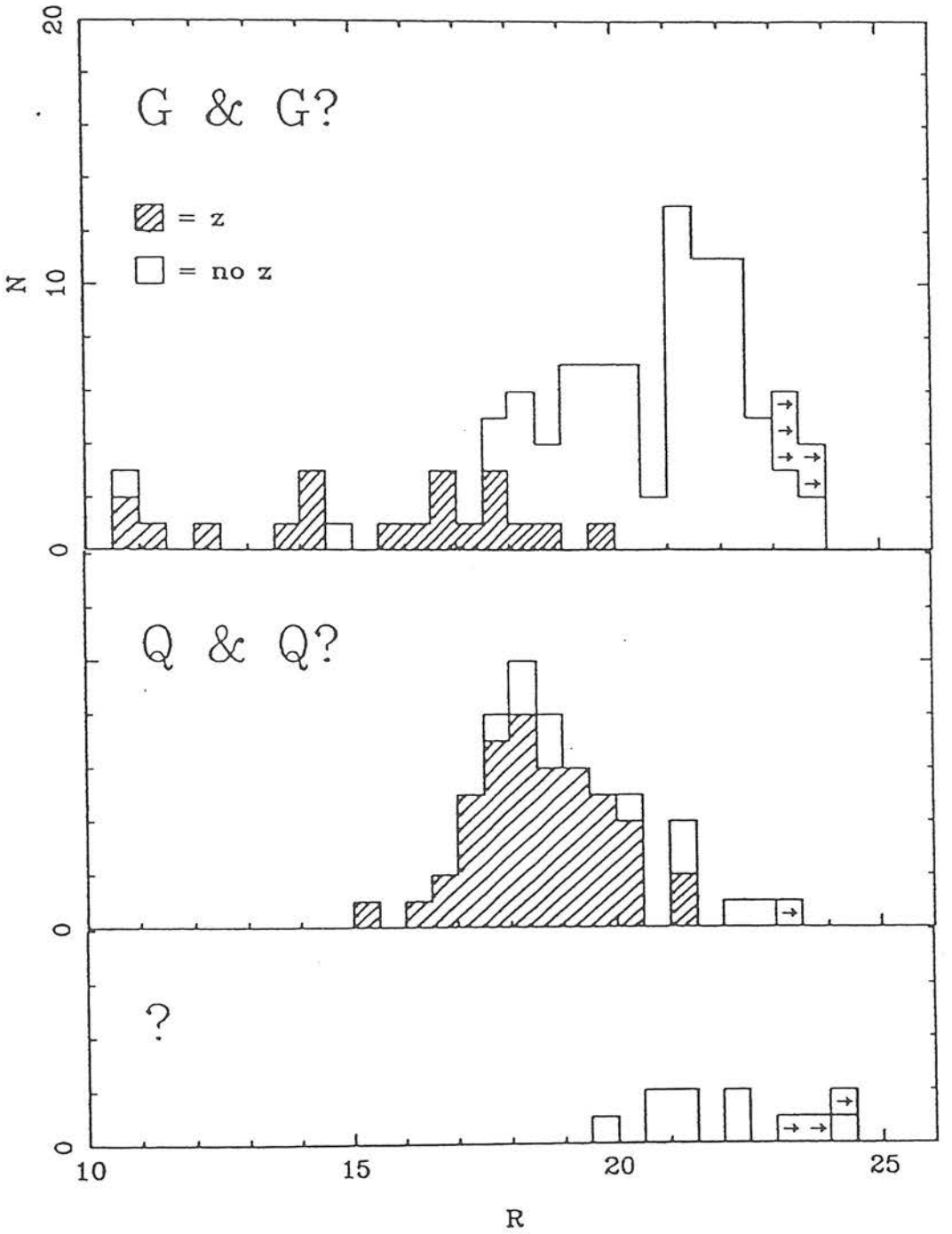
G & G?
= z
= no z
Q & Q?
?
N
R
0
10
20
0
10
20
0
10
15
20
25

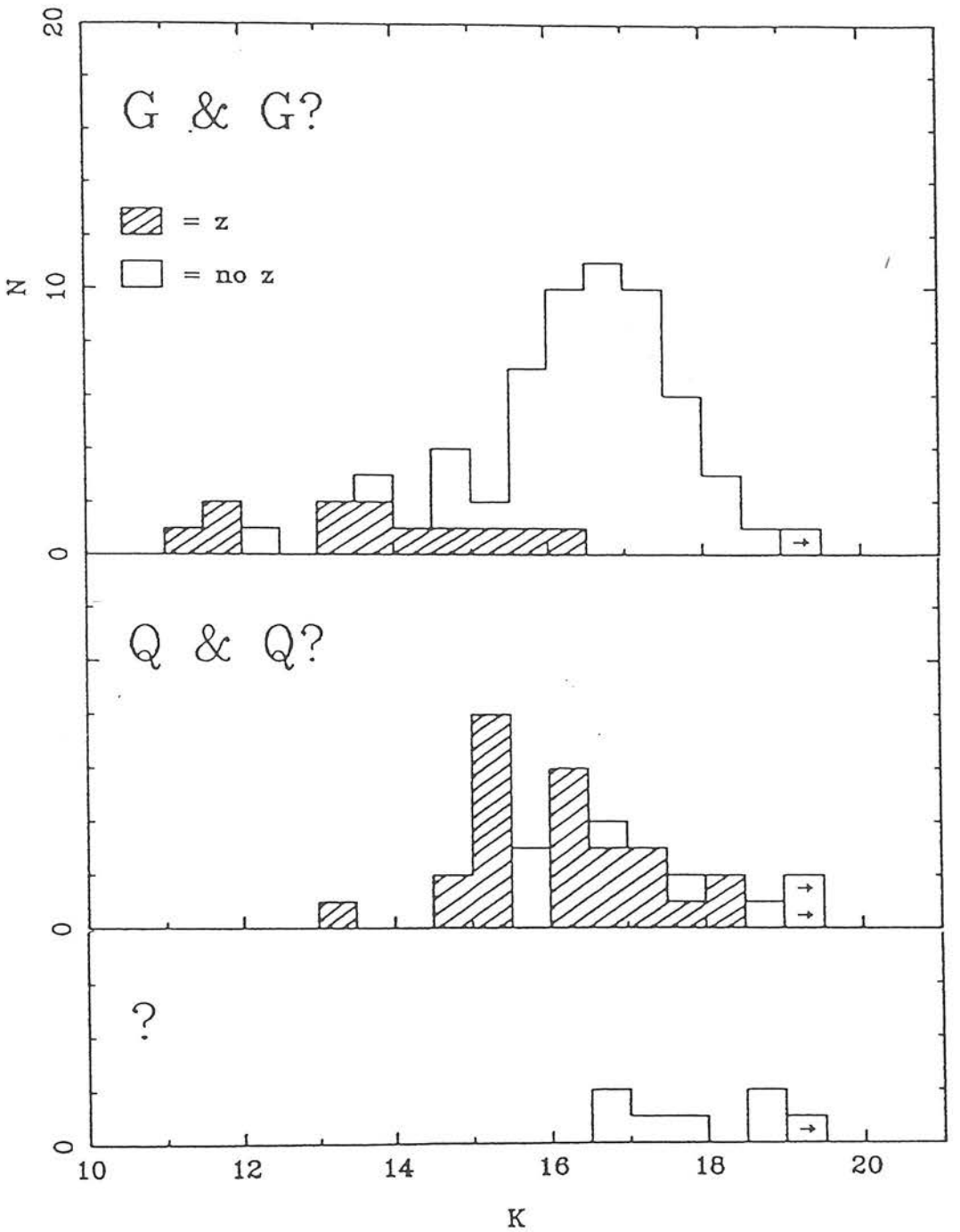
G & G?
= z
= no z
Q & Q?
?
N
K
0
10
20
10
12
14
16
18
20

Figure 5.5 : Comparison of the distribution of apparent K magnitudes for galaxies from the present sample, the 1Jy sample, and the 3CR sample (Longair & Lilly 1984). Again the Selected Regions data is only taken from the 4-region subsample. All 3 histograms include Gs, G?s and ?s, with only quasars being excluded. Optical empty fields in each sample are shown shaded.

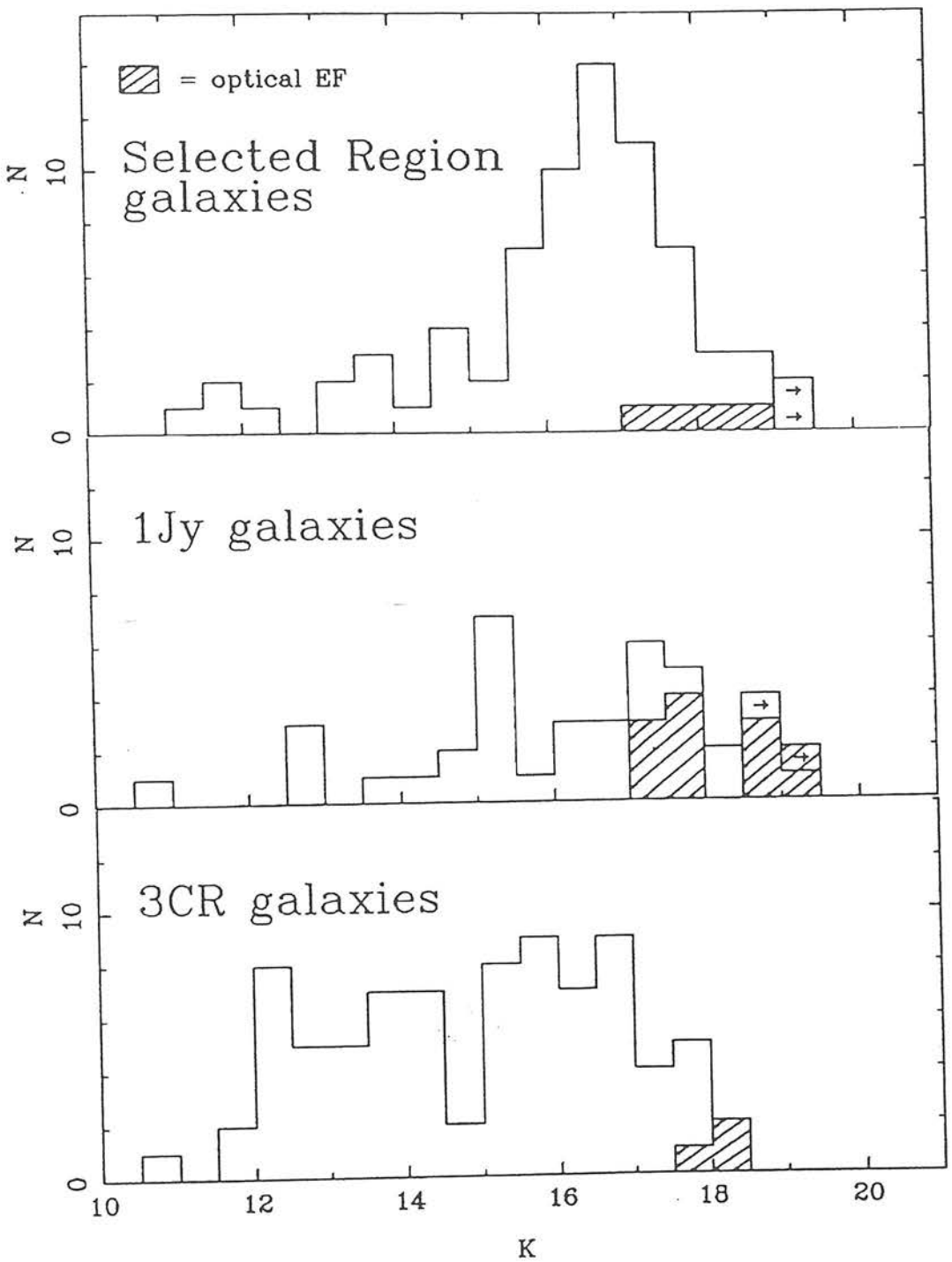

5.4 : QUASARS

5.4a : The quasar Hubble diagram and the estimation of quasar redshifts

It has been known for some time that, whereas the Hubble diagram for optically selected QSOs is a scatter diagram, radio quasars display a significant m-z correlation (eg Wills & Lynds 1978, Wall & Peacock 1985, Wampler 1987). It is not yet understood why such a Hubble relation for radio quasars should exist. The m-z correlation for radio galaxies is 'understood' in the sense that the host galaxies of powerful radio sources are known to be among the most luminous ellipticals, and hence might be expected to act as standard candles. However, there is no evidence that radio emission selects out the most optically luminous quasars in a similar fashion. Indeed, the most luminous optically-selected quasars are $\geq$ 2 magnitudes more luminous than the brightest radio quasars.

In the context of evolution studies, the radio-quasar Hubble diagram can be used to estimate crudely small numbers of missing redshifts in complete radio-quasar samples (eg Wall & Peacock 1985, Peacock 1985). This procedure is justified provided the quasar identifications which lack redshifts are representative of the total quasar sample. Wall & Peacock found the following m-z relation for quasars in the All-Sky $S_{2.7} > 2Jy$ sample,

$$\mathrm{Log}_{10}(z) = 0.23V - 4.2 \qquad (5.1)$$

and concluded that, using this relation, it was possible to estimate the missing quasar redshifts to within a factor of ~ 3.

Figure 5.6 shows the z versus R magnitude diagram for the quasars in the Selected Regions with measured redshifts. The correlation is clear. The spectroscopic observations of Chapter 4 (plus the recent observations of Jeremy Allington-Smith) have contributed 17 new quasar redshifts in the Selected Regions and in Table 5.4 these new results are compared with the original predicted values.

Figure 5.6 : The redshift-magnitude (z-R) diagram for quasar identifications in the Selected Regions sample.

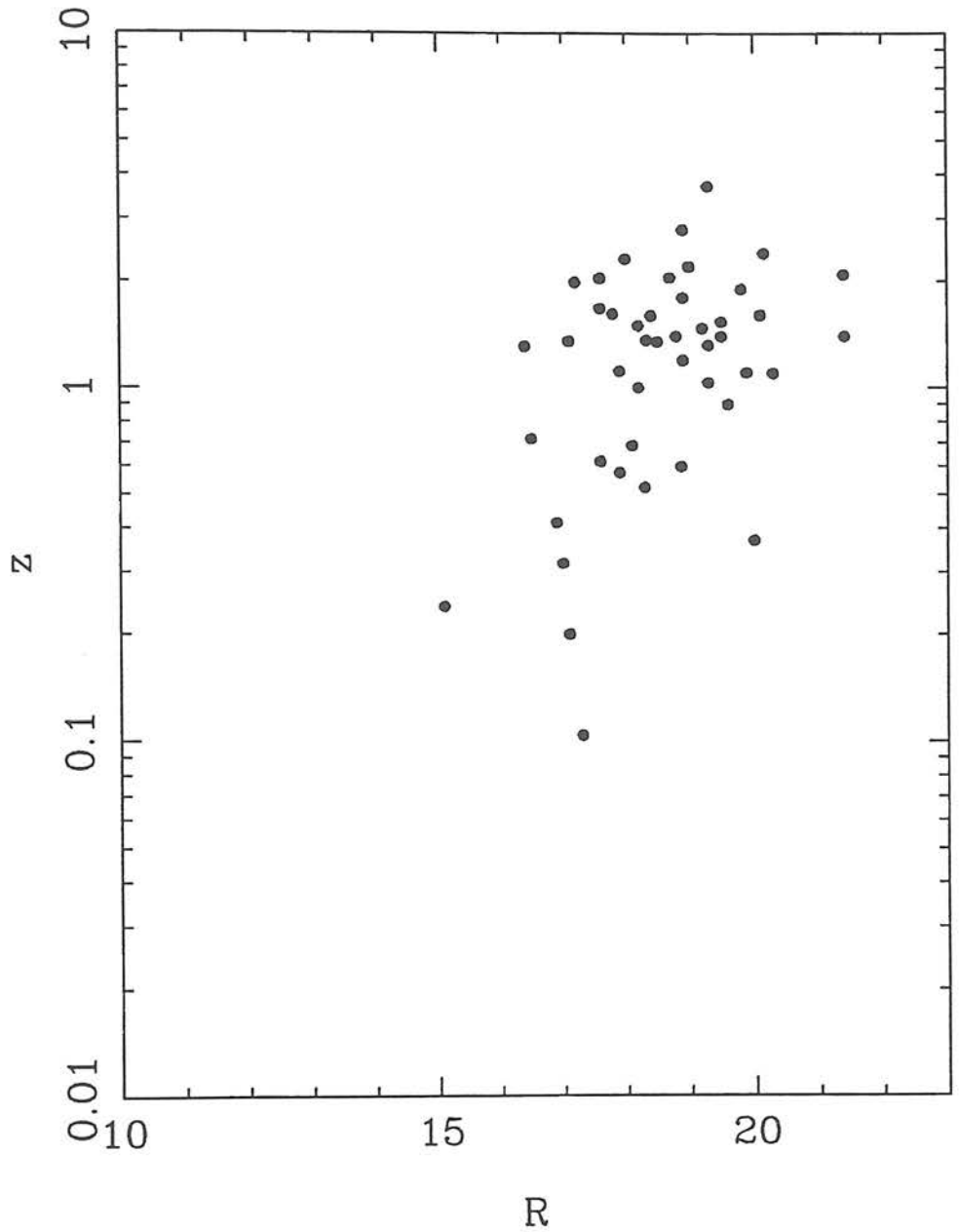

Table 5.4 : Comparison of new quasar redshifts in the Selected Regions with the values predicted using the radio quasar Hubble relation.

SOURCE NAME	Measured z	Estimated z	V mag
0007+016	2.9	1.5	19.1
0013-005	1.575	1.7	19.3
0223+012	1.369	1.7	19.3
0235+023	0.209	0.6	17.4
0236-015	1.794	1.4	18.9
0240-021	0.617	1.7	19.3
0242+009	1.520	1.4	18.9
1336-030	2.313	1.1	18.5
1348-012	1.482	1.7	19.3
1348+007	2.084	5.9	21.6
1351-018	3.709	3.3	20.5
2154-184	0.668	1.8	19.5
2154-183	1.423	4.3	21.0
2203-215	0.577	0.9	17.8
2204-208	1.923	2.5	20.0
2214-206	2.316	3.1	20.4
2357-007	1.107	3.5	20.6

The estimating procedure appears to be reasonably successful down to V ~ 20.5 (ie the magnitude limit of the sky-survey), and indeed was fairly successful at predicting the redshift of PKS 1351-018. Although spectra have been obtained for only 3 objects fainter than this (ie 1348+007, 2154-183 and 2357-007) it is clear that the Hubble relation based on sky-survey quasar results seriously overestimates the redshifts of these faint quasars. This of course is not surprising since there are already strong indications that the comoving space density of radio quasars starts to decline beyond z ~ 2 (Peacock 1985) - at a certain magnitude limit one must inevitably start to sample quasars of lower optical luminosity rather than continuing to find bright quasars at still higher redshifts. However

this fact does mean that the Hubble relation cannot be used to estimate the redshifts of quasar candidates which are CCD identifications.

It is possible to at least set upper limits to the redshifts of the faint quasar candidates using their optical (B-R) colours. At low z the B-R colour is a somewhat ambiguous redshift estimator, but for z > 2 it increases monotonically with redshift. This fact is demonstrated by the simulated colour evolution of PKS 1351-018 shown in Figure 5.7. The evolution track has been synthesized from the flux-calibrated spectrum of PKS 1351-018 (presented in Chapter 4) using the profiles of the Kitt Peak Mould interference filters combined with the spectral response of the RCA CCD. At z = 3.7 the synthesised B-R colour agrees with the photometrically measured value of 1.6 to within 0.1 magnitudes, which suggests that using the spectrum in this manner is satisfactory.

8 of the 57 quasar candidates in the Selected Regions do not have a measured redshift. Of these 8, 5 are sky-survey identifications for which the relevant redshifts can be estimated using the m-z relation. This leaves only 3 faint quasars for which an upper limit has to be assigned on the basis of optical colour. The results of the redshift estimation for these objects are presented below in Table 5.5.

Table 5.5 : Estimation of quasar redshifts in the Selected Regions.

a) Sky-survey quasar candidates

SOURCE NAME	ESTIMATED z
0047+023	1.1
0059+017	1.5
0223+018	2.5
2215-185	0.8
2354-021	2.5

b) CCD quasar candidates

SOURCE NAME	ESTIMATED z
0005+021	< 3.5
0008-006	< 3.0
2355-024	< 2.5

It is, of course, important to note that high-redshift quasars do show considerable variation in optical colour, and so the B-R versus z track shown in Figure 5.7 must not be regarded as definitive. Nevertheless the basic point remains that, at a high enough redshift, any quasar will begin to look very red in B-R, and, since only 3 quasars in the sample require redshift estimates based on colour, the exact values are not too important. Note that, in the subsequent analysis of the redshift data, the 3 objects in Table 5.5 with upper-limit redshift estimates are assumed to possess these maximum possible values.

5.4b : Comparison of the infrared Hubble diagrams of radio quasars and radio galaxies.

In Section 5.3b attention was drawn to the fact that the K-magnitude distribution for quasars in the Selected Regions extends out to magnitudes comparable with the faintest galaxies. This is quite unlike the situation in the optical and raises the possibility that some radio quasars have absolute infrared magnitudes comparable to those of elliptical galaxies. The best way to check this is to compare the radio-galaxy and radio-quasar infrared Hubble diagrams. Figure 5.8 shows the K-z relation for the Selected Regions quasars, superimposed on the K-z relation for 3CR and 1Jy radio galaxies (Lilly & Longair 1984, Lilly *et al.* 1985). This figure demonstrates that there are indeed several spectroscopically confirmed quasars in the present sample whose absolute infrared magnitudes are comparable to those of radio galaxies. If, as is commonly believed, the host galaxies of all radio quasars are giant ellipticals, this would suggest that at infrared wavelengths the light of these objects is dominated by starlight rather than the non-thermal continuum which dominates in the optical/ultraviolet. This interpretation can be checked by infrared imaging of the objects in question, which should reveal them to appear non-stellar at K. The alternative explanation is that some radio quasars are housed in much fainter galaxies.

Figure 5.7 : The simulated evolution of B–R (Mould filters × response of RCA CCD) colour with redshift for PKS 1351–018.

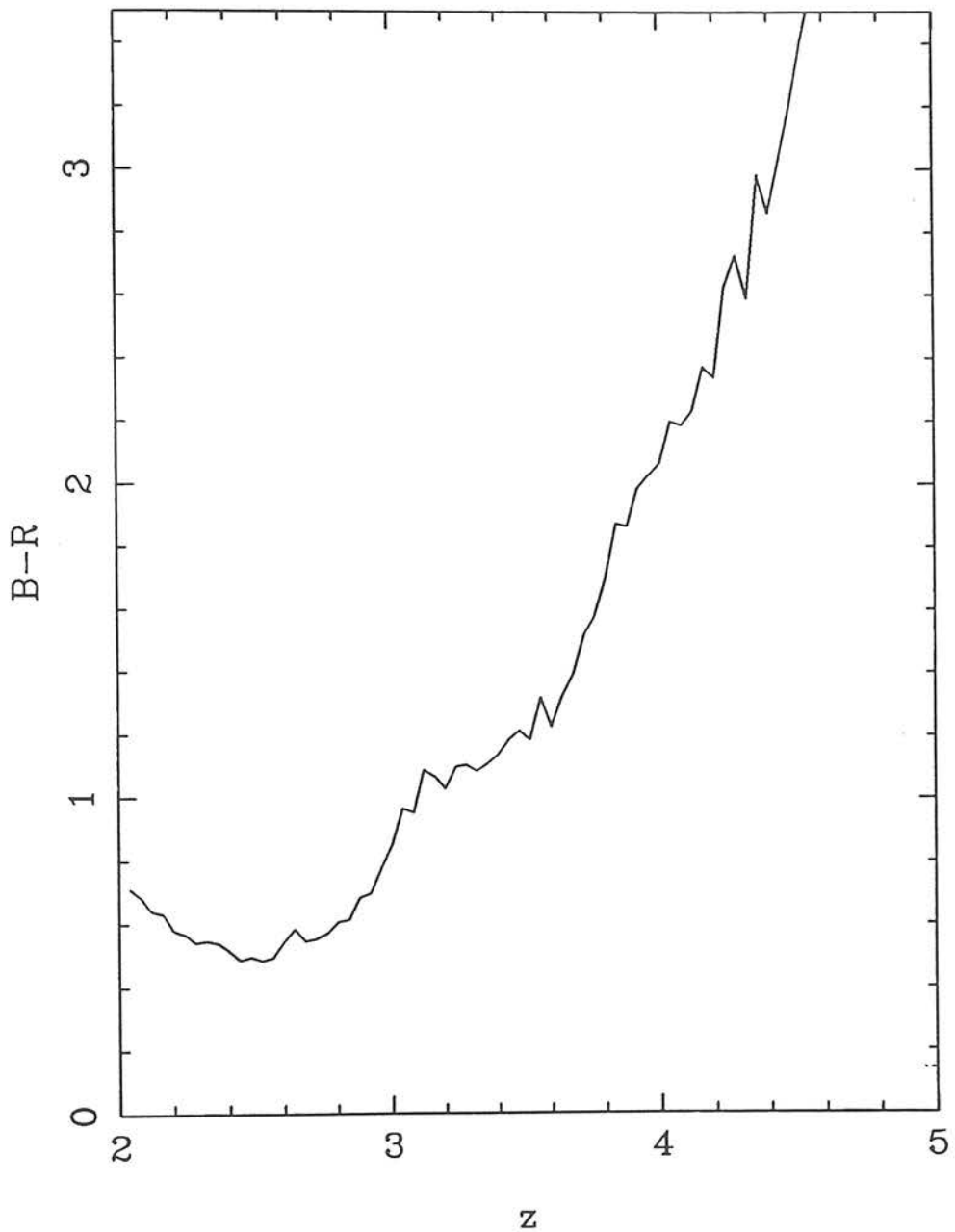

Figure 5.8 : Comparison of the K-z relation for radio quasars from the Selected Regions sample (open circles) with the K-z relation for 3CR and 1Jy radio galaxies (filled circles - Lilly & Longair 1984, Lilly *et al.* 1985). The line is the empirical fit to the galaxy data given by Lilly *et al.* - see Chapter 6 for details.

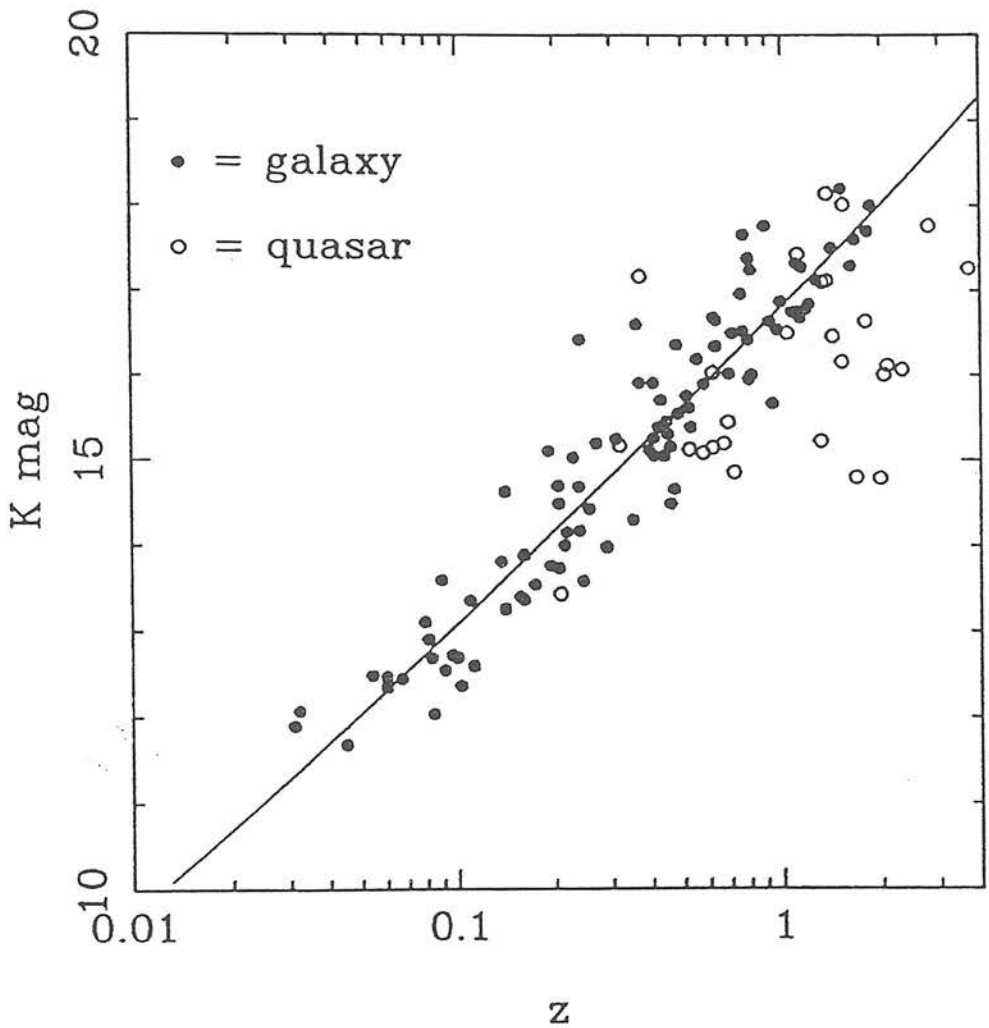

5.4c : The implications of PKS 1351-018 for optical studies of high-redshift quasars

The majority of known very high-redshift quasars have relatively bright apparent magnitudes ($R \leq 18$) (eg Peterson *et al.* 1982, Hazard & McMahon 1985, Hazard *et al.* 1986). This has led to suggestions that searches deeper than R = 18 would be unlikely to result in the discovery of high-redshift objects (Wright 1983, Hazard & McMahon 1985). The important question is whether this effect reflects a genuine change in the quasar optical luminosity function at high z, or whether it is simply the result of selection effects which hinder the discovery of fainter high-redshift objects. For this reason the discovery of PKS 1351-018 with R = 19.3, B = 20.9 was of particular interest.

The radio quasar PKS 2000-330 (Peterson *et al.* 1982) with $z = 3.78$ remained for 4 years the most distant known object. PKS 1351-018 is 2.3 magnitudes fainter than PKS 2000-330 and with an optical absolute magnitude of $M_B = -26.8$ (assuming $H_o = 50 kms^{-1}Mpc^{-1}$, $\Omega_o = 1$ and $f_\nu \propto \nu^{-0.5}$ beyond 9000Å) has an absolute magnitude typical of low-redshift, radio-loud quasars. However, the radio-quasar Hubble diagram (see Figure 5.6) suggests that the magnitude of 1351-018 is typical of that expected for a quasar at $z \sim 4$ (as demonstrated by the accuracy of the z prediction in Table 5.4), and that PKS 2000-330 is anomalously bright (a fact which explains its relatively early discovery).

The discovery of an object like PKS 1351-018 in the relatively selection-effect free domain of radio astronomy makes it interesting to ask whether similar objects could be found using purely optical selection criteria. In particular, comparison of the spectra of high-redshift quasars reveals 1351-018 (along with other radio quasars such as the much brighter PKS 2000-330) to have systematically weaker emission lines than their optical counterparts and it is therefore questionable whether even a brighter version of PKS 1351-018 would have been found in the UK Schmidt prism-plate searches. An estimate of the rest frame equivalent width (W_o) of Ly α in 1351-018 yields $W_o = 35 \pm 8$Å, compared to $W_o \simeq 88$Å in 0055-2659

(Hazard & McMahon 1985) and W_o = 55 ± 10Å in 0046-293 (z = 4.01, Warren *et al.* 1987). The bias of limiting magnitude can obviously be countered by using deeper optical material and indeed, since the discovery of PKS 1351-018, several more quasars with R > 18 have been found using deep-grism plate surveys (eg 1409+732, z = 3.56, B ≥ 21, R ~ 19 Anderson & Margon 1987) and CCD spectroscopic surveys (Schmidt *et al.* 1986a,1986b & 1987a). The first redshift 4 quasar, 0046-293, which was discovered by colour selection is also fairly faint (R = 19.2, Warren *et al.* 1987). However, the bias of emission-line strength is not so easily avoided since, as well as obviously being a problem in prism or grism surveys, this may also affect colour-based studies such as those of Koo (eg Koo 1983, Koo *et al.* 1986). Using the flux-calibrated spectrum of 1351-018 it is possible to synthesise the colours of this object for various filter systems, and also the variation of these colours with redshift. This was done for B-R in the previous section. Using Koo's UJF filter system gives synthesised U-J and J-F colours of 2.7 ± 0.5 and 1.4 ± 0.1 respectively, the relatively large uncertainty in U-J being due to the very small flux in the U band. We have also synthesized the locus followed by 1351-018 on the (U-J)/(J-F) colour magnitude diagram as it varies in redshift between z = 2 and z = 4. This locus is shown in Figure 5.9 superimposed on Koo's (U-J)/(J-F) diagram for stellar images in the magnitude range 21 < J < 22 in his Selected Area 57 (Koo *et al.* 1986). The circled objects are those selected by Koo as quasar candidates. The dotted line takes into account the effect of redshift-dependent blanketing of the Lyman continuum, assuming that the number density of Lyα clouds varies as $(1+z)^2$ (Peterson 1987) and that by z = 3.71 the Lyman continuum of 1351-018 has already been dampened by a factor ~2/3. The dashed line demonstrates the effect of doubling the strength of the Lyα emission line.

The (U-J,J-F) colours are (0.4,0.5) at z = 3 and (1.8,1.2) at z = 3.5, which would be unlikely to be classed as significantly non-stellar. Between z = 3 and z = 3.5, the track of 1351-018 departs from the stellar locus, but beyond z = 3.5 it starts to return to it again. Thus for z > 3.5 and 2.7 < z < 3, faint quasars similar to 1351-018 would not have been detected. Furthermore, the spectrum of 1351-018 falls rapidly just blueward of the Lyman limit, whereas many high-redshift

quasars retain significant flux at this point (eg 0055-2659). Adding a significant fraction of ultraviolet flux to 1351-018 would make its (U-J,J-F) colours stellar at all $z > 2.5$. Conversely it is clear from the diagram how increasing the strength of the Lyα emission line moves the quasar track further from the stellar locus , at least until $z \sim 3.5$.

It therefore seems feasible that <u>both</u> slitless spectroscopy, and colour selection of high-redshift quasars may be biassed towards bright, strong-lined objects. It is interesting to note here the recent results of Schmidt and his collaborators who, over the past ~ 2 years, have been attempting to quantify the high-redshift evolution of the quasar optical luminosity function via deep CCD slitless spectroscopic surveys (Schmidt *et al.* 1986a, 1986b, 1987a & 1987b). Schmidt *et al.* (1986a) reported their failure to find any quasars with $z > 2.66$ in $0.91 deg^2$ of sky, and then in a subsequent similar survey Schmidt *et al.* (1986b) failed to find any redshifts greater than 2.76. The contrast between this result and the relatively high success rate of bright large-area surveys was taken as further evidence for a luminosity-dependent cutoff (Schmidt *et al.* concluded that quasars with $M_B \approx -25$ suffer a redshift cutoff at $z \leq 3$). However, Schmidt *et al.* (1987a, 1987b) have since reported preliminary results from a more sensitive, larger area survey in which they have already discovered 10 quasars in the redshift range $z = 3.0 \rightarrow 3.8$ with R magnitudes ranging from $18.5 \rightarrow 21.7$. This result indicates that although the picture in which quasars were "brighter but fewer" in the past (Koo 1986b) may indeed be correct, the issue cannot yet be regarded as settled (there may be evidence for behaviour of this sort in the radio - PKS 1351-018 is one of the brightest radio sources in the Selected Regions, see Chapter 6) Also, since the average rest frame equivalent width of Lyα for these 9 quasars is 90Å, the question of emission-line bias still remains (although Schmidt *et al.* 1986a state observed equivalent widths of $W > 50$Å as a selection criterion).

The high-redshift evolution of optically-selected quasars is discussed further in Chapter 8 where attention is drawn to the recent results of a new multi-colour (UBVRI) survey by Warren, Osmer and Hewett at Cambridge. In conclusion it is worth noting that

this survey, and the multi-dimensional colour selection technique on which it is based, represent a considerable improvement over the earlier colour-based studies of Koo discussed above. It seems probable that the above criticisms concerning the colour-selection of high-redshift quasars are not so applicable to this new, more sophisticated approach, particularly since it has already succeeded in detecting weak-lined objects at high redshift.

Figure 5.9 : The locus followed by PKS 1351-018 on the (U-J)/(J-F) colour diagram between z = 2 and 4. The dotted line takes account of redshift dependent blanketing of the Lyman continuum, while the dashed line demonstrates the effect of doubling the strength of the Lyα emission line. The stellar points are from Koo's 21 < J < 22 magnitude bin in Selected Area 57 (Koo *et al.* 1986). The circled points are those which were selected by Koo as quasar candidates.

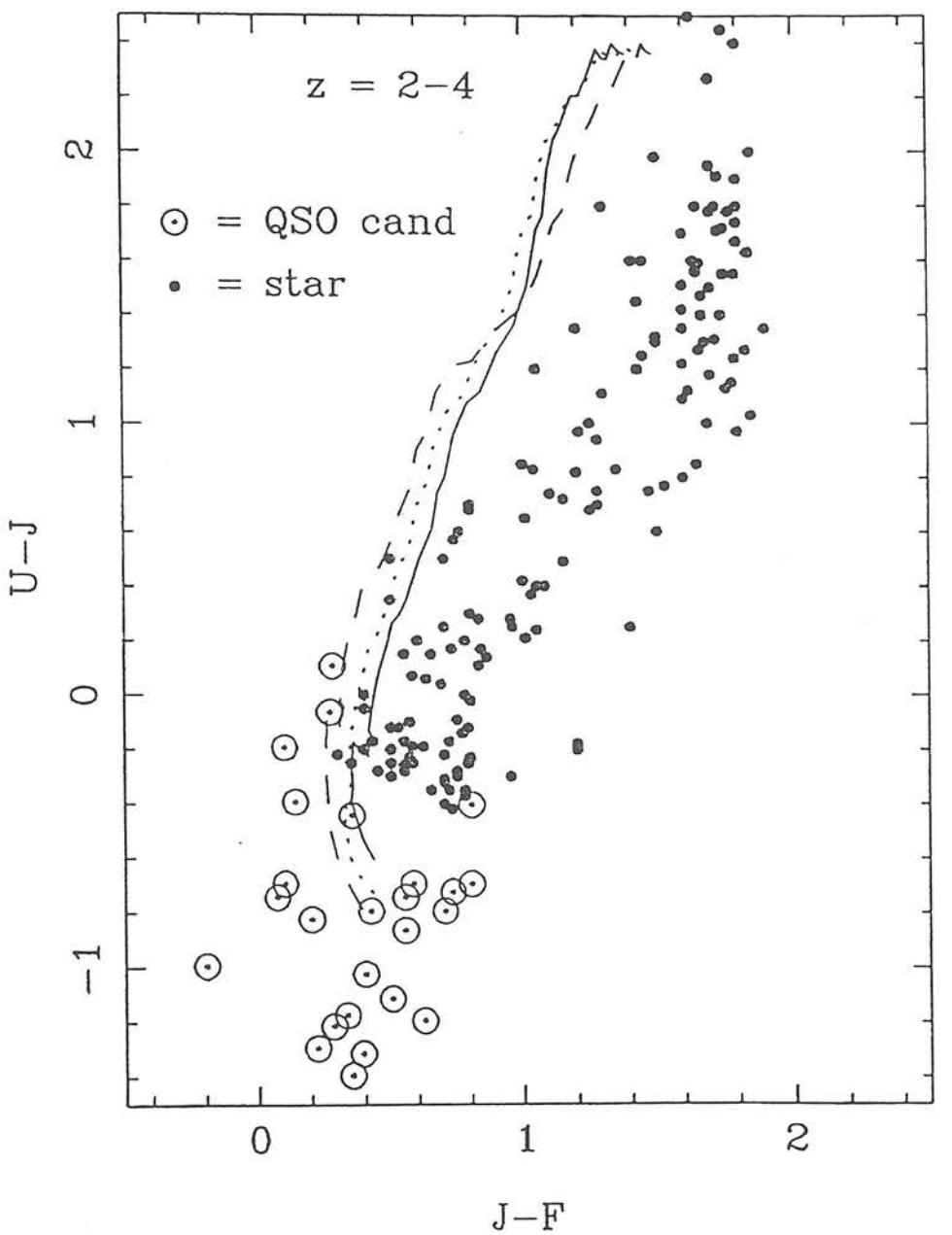

Chapter 6 : THE HIGH-REDSHIFT EVOLUTION OF THE RADIO LUMINOSITY FUNCTION

6.1 : INTRODUCTION

The purpose of this chapter is to investigate what new information can be gained on the evolving RLF from the new optical and infrared data obtained on the Selected Regions. Previous studies of radio source evolution were reviewed in Chapter 1. The important results established before commencement of the present study can be summarized as follows:

i) Out to $z \sim 2$, both steep- and flat-spectrum populations exhibit strong, positive, differential evolution (eg Peacock & Gull 1981).

ii) The form of this evolution is consistent with a mixture of luminosity and density evolution (Condon 1984).

iii) Beyond $z \sim 2$ there is evidence for a decline in the comoving density of flat-spectrum sources, but no such evidence exists for a corresponding cutoff in the steep-spectrum RLF (Peacock 1985).

The main concern of the present study is to investigate whether the new Selected Regions database can settle the issue of the redshift cutoff for steep-spectrum sources.

Section 6.2 describes the role of the Selected Regions sample as part of the complete S-z database at 2.7 GHz, and also discusses in detail the method of redshift estimation for the faint galaxies. In Section 6.3 the free-form modelling technique of Peacock & Gull (1981) and Peacock (1985) is applied to the new database. Section 6.4 attempts to confirm the main results of Section 6.3 in a model-independent manner. Finally, in Section 6.5 a model of pure luminosity evolution is investigated.

6.2 : THE SELECTED REGIONS AS PART OF THE COMPLETE SAMPLE DATABASE AT 2.7GHz

6.2a : The 2.7GHz complete sample database

The Selected Regions sample is important because it provides a low flux density extension (ie 0.1Jy) to the existing complete sample database at 2.7GHz. Previously the flux limits of the complete S-z data were 0.5Jy for flat-spectrum sources and 1.5Jy for steep-spectrum sources. The database at 2.7GHz now consists of data taken from 4 complete samples

i) The $S_{2.7} > 0.1$Jy Parkes Selected Regions sample.

ii) The $S_{2.7} > 0.5$Jy flat-spectrum sample selected by Peacock (1985) from the Parkes ±4° zone (Wright *et al.* 1982).

iii) The $S_{2.7} > 1.5$Jy 'Northern-Sky' survey of Peacock & Wall (1981).

iv) The $S_{2.7} > 2$Jy 'All-Sky' survey of Wall & Peacock (1985).

Since these samples first appeared in print many new redshifts have been obtained - from the spectroscopic work described in Chapter 4, from recent publications, and by private communication from various other workers. The revised versions of these 4 samples are therefore provided in Appendix A, Tables A.1 → A.4, and their properties are summarized below in Table 6.1.

Table 6.1 : The complete sample data at 2.7GHz

Sample	Area	No. of sources	No. of sources unidentified	No. of sources without z
$S_{2.7} > 0.1$Jy	0.075sr	178	8	96 (54%)
$S_{2.7} > 0.5$Jy	0.584sr	41	2	12 (29%)
$S_{2.7} > 1.5$Jy	4.05sr	171	5	18 (11%)
$S_{2.7} > 2$Jy	9.81sr	233	5	51 (22%)

To make maximum use of these data they must be combined into a single sample. After allowing for overlap between the surveys, the resulting combined dataset consists of 522 sources (172 flat-spectrum and 350 steep-spectrum) of which only 3% are unidentified and a further 14% are identified but lack either a measured or securely estimated redshift (estimated from galaxy photometry - see Section 6.2b). The objects with uncertain redshifts are either quasar candidates or objects for which the classification of the optical identification is uncertain.

6.2b : Redshift estimation in the Parkes Selected Regions sample

There are two reasons why the problem of redshift estimation is particularly important in the Selected Regions sample. Firstly, in this sample estimated redshifts are required for a relatively large number of sources - Table 6.1 demonstrates how low the redshift content of the Selected Regions is in comparison with that of the 3 brighter samples. Secondly, because it is the deepest of the 4 samples, the Selected Regions sample provides the strongest probe of high-redshift space and so the redshift estimates for the fainter objects in this sample will strongly influence conclusions about the evolution and shape of the radio luminosity function (RLF) at high z.

Redshift estimation is much more important in the study of the steep-spectrum RLF than the flat. Of the 35 new flat-spectrum sources provided by the Selected Regions in the flux-density range $0.5Jy > S_{2.7} > 0.1Jy$, 23 (66%) have measured redshifts. This relatively high fraction results from the fact that the bulk of the flat-spectrum identifications are quasars rather than galaxies (see Section 5.3a). In contrast, of the 133 new steep-spectrum sources added to the database in the flux-density range $2Jy > S_{2.7} > 0.1Jy$, only 45 (34%) have a measured redshift.

In both the flat- and steep-spectrum samples the bulk of the objects without redshifts are galaxies rather than quasars. The problem of quasar redshift estimation is therefore not very serious in the present study (the method of redshift estimation for this small

number of quasar candidates, and the adopted values are described in Section 5.4).

The crucial issue is therefore the estimation of redshifts for the faint galaxy identifications. For most of these objects K photometry had been obtained and so their redshifts could be estimated via the K-z relation for radio galaxies which was investigated by Lilly & Longair (1984). At high z, infrared photometry provides the most accurate method of redshift estimation because, in contrast to the optical Hubble diagram, the K-z diagram is unaffected by the UV-flux from small numbers of young stars. Lilly & Longair have demonstrated empirically that for the 3CR radio galaxies the dispersion in the K-z diagram does not increase significantly with z.

For galaxies with K magnitudes in the range $13 < K \leqslant 17$ the empirical relation $\log_{10}z = -5.368 + 0.384K - 0.00385K^2$ was adopted for redshift estimation. This relation is given by Lilly *et al.* (1985) as a good approximation to the K-z relation exhibited by the 3CR and 1Jy radio galaxies. At $K > 17$ the relation is not well defined empirically and the expected high-redshift extrapolation depends on the assumed model for galaxy evolution. To enable investigation of the sensitivity of the subsequent results to the assumed high-redshift extrapolation, 3 different redshift distributions were constructed on the basis of 3 different extrapolations of the infrared Hubble relation beyond K = 17. These 3 K-z relations are shown in Figure 6.1 along with the 3CR and 1Jy data which define the K-z relation at lower redshifts. The central curve is simply the continuation of the empirical relation given above, while the other 2 curves represent extreme departures from this relation which might be expected on the basis of reasonable models of galaxy evolution. The low and high curves on the diagram represent the K-z relations expected to result from a very young (ie Bruzual C-model with formation redshift, $z_f = 3.5$) or very old ($z_f \sim 20$) galaxy respectively. In fact the modelling situation is complex and a variety of combinations of model parameters could produce such curves (see Chapter 7 for the more recent models of Guiderdoni). The origin of these curves should not therefore be regarded as definitive, but for the present purpose they provide a reasonable range of possible

extrapolations from which to estimate redshifts for the faintest galaxies (eg K=18 ≃ z~1.8 in the case of the old galaxy, or z~3.5 for the young model).

Figure 6.1 : The K–z relations used to estimate the redshifts of faint galaxies in the selected regions. The 3 curves represent the range of feasible extrapolations of the Hubble relation beyond K ≃ 17, based on reasonable models of galaxy evolution. The solid circles are galaxies taken from the 3CR radio sample (Lilly & Longair 1984) while the open circles are galaxies from the 1Jy radio sample (Lilly *et al.* 1985).

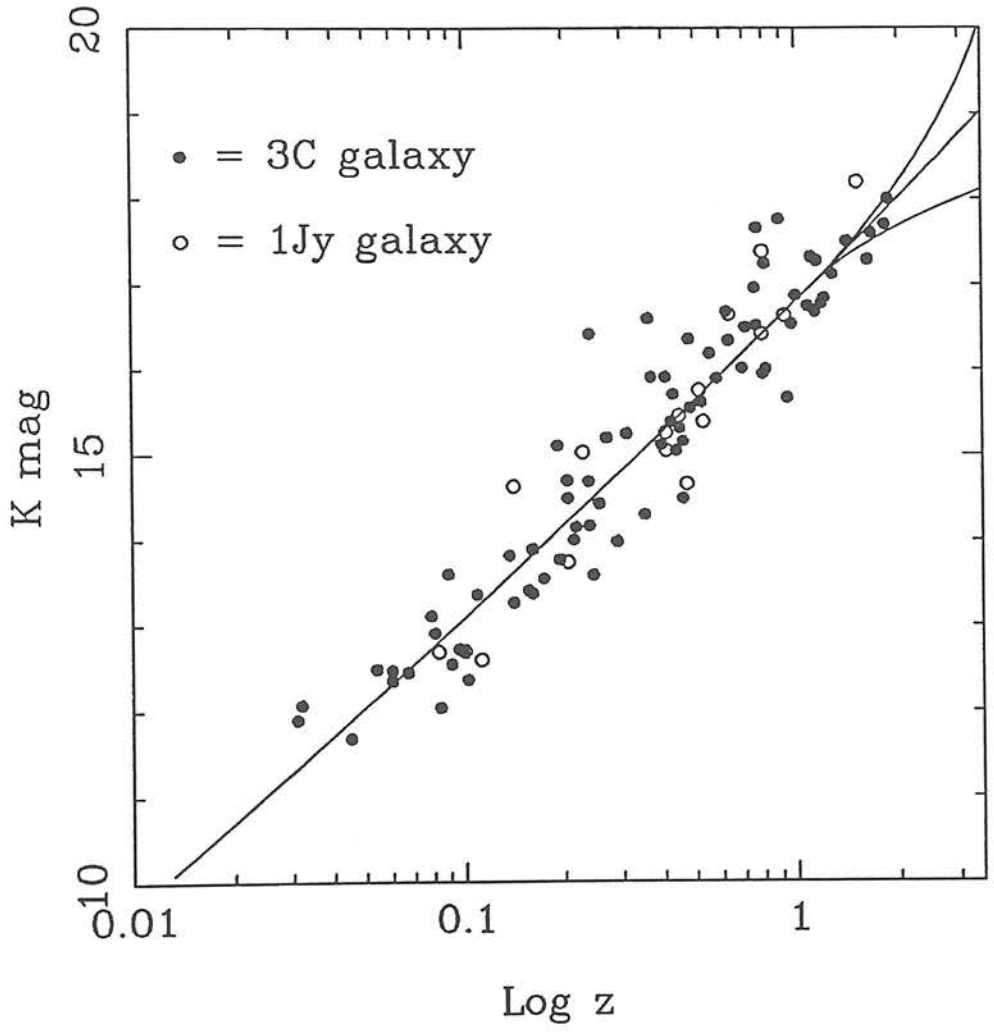

The resulting 3 redshift distributions for the steep-spectrum sources in the Selected Regions are shown in Figure 6.2 (the flat-spectrum redshift distributions are essentially unchanged). These 3 distributions will hereafter be referred to as the MEAN-z, LOW-z and HIGH-z distributions respectively (the HIGH-z distribution has a peak at $z = 3.5$ because the model on which it is based involves galaxy formation at that redshift; it is inconsistent to assign larger redshifts than this). For the small number of faint galaxies without K photometry (17 in total, 14 of them in the 12^h and 13^h regions), redshifts were estimated from the K-estimated redshifts of other galaxies in the sample of similar optical magnitude and colour. The 3 optical empty fields which had not been observed in the infrared (ie 0043-003, 1159-023 & 1349-019) were assigned similar redshifts to the 4 optical empty fields which had been observed (and were all successfully detected) at K.

There is relatively little difference between the LOW-z distribution (which results from the upper curve in Fig. 6.1) and the MEAN-z distribution, and there are several reasons for believing that they are more representative of the true distribution than the HIGH-z one is. Firstly, the shape of the HIGH-z distribution appears to be unrealistic - galaxies with $K \geq 18$ are required to be at $z \sim 3.5$ whereas the small number of galaxies with $K \sim 18$ whose redshifts are known have $z \sim 1.5$ (see Figure 6.1). Secondly the K-z extrapolation which produces the HIGH-z distribution results in galaxies never growing fainter than $K \simeq 18$, whereas radio galaxies are known with $K > 18.5$. Thirdly, Yates *et al.* (1986) have found evidence for a correlation between radio power and absolute magnitude in the most powerful 3CR radio galaxies. This would mean that the high redshift galaxies in fainter samples such as the Selected Regions should have fainter absolute magnitudes than their 3CR counterparts, in which case their redshifts would be overestimated on the basis of the 3CR Hubble diagram. An effect of this kind favours a redshift distribution biassed towards low z for reasons unrelated to model assumptions. Further support for this view comes from the fact that some of the very faint ($K > 18$) galaxies in the 1Jy sample (Lilly *et al.* 1985) have recently had their redshifts measured, and none has been found to have $z > 1.5$.

It therefore seems probable that the HIGH-z distribution is unrealistic, but much of the modelling described in this Chapter was still performed using all 3 redshift distributions in order to test the robustness of the results.

Figure 6.2 : The MEAN, LOW and HIGH redshift distributions for the steep-spectrum sources in the Selected Regions sample which result from redshift estimation based on the middle, upper and lower (respectively) K-z relations shown in Figure 6.1.

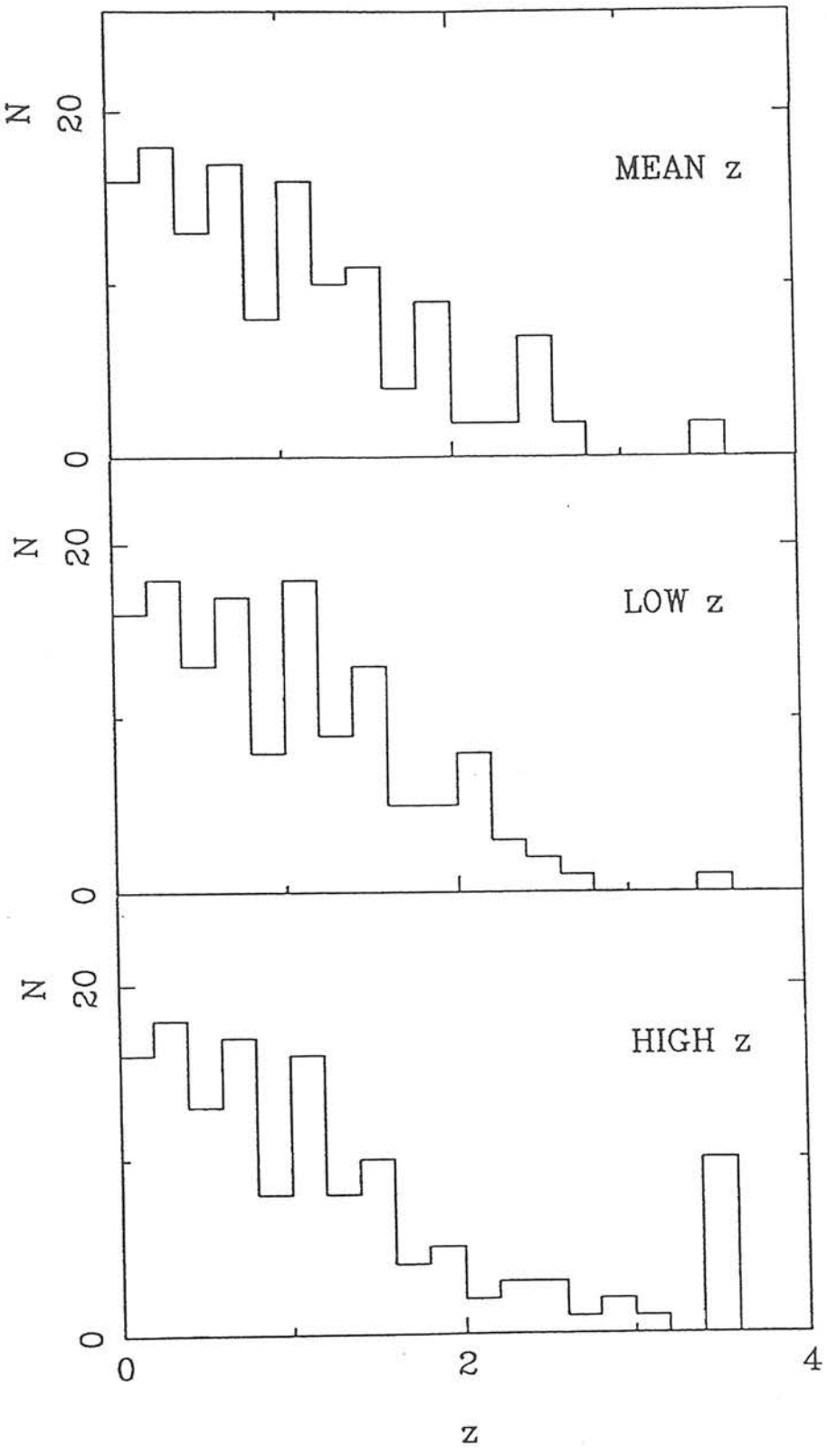

6.3 : FREE-FORM MODELLING OF THE RADIO LUMINOSITY FUNCTION, AND THE QUESTION OF THE REDSHIFT CUTOFF

6.3a : Background

This section is concerned with free-form modelling of the radio luminosity function (RLF). The aim of the modelling is to determine what possible range of evolving luminosity functions is allowed by the data. This approach was first introduced by Peacock & Gull (1981) and was further developed by Peacock (1985). The work described here represents an extension of this previous work in the light of the newly acquired data. Of particular interest is the impact of the Selected Regions on the form of the high-redshift evolution.

Model fitting has proved to be a very valuable approach to the study of the radio luminosity function, chiefly because of the incomplete redshift information available in radio surveys. Since the redshift content of such surveys is generally only well defined at higher flux densities, the form of the RLF is well constrained only in the corresponding region of the P-z plane. A consistent model is of value however because it can extrapolate the trends which are observed in this region into less well-defined areas. Moreover, the form of this extrapolation is constrained by less complete data such as source counts and identification statistics. The model fitting approach therefore allows maximum use to be made of all the available data.

The benefits of the free-form technique have been discussed by Peacock & Gull (1981) and Peacock (1985). Earlier attempts to model the RLF (eg Wall, Pearson & Longair 1980,1981, Robertson 1978,1980) all involved preconceived assumptions as to the form of the evolution, and gave no indication as to how well the models were constrained by the data. In contrast, the aim of the free-form approach is to find an ensemble of different smooth functions which are consistent with the data. These models should agree in regions of the P-z plane where they are strongly constrained by high-quality data. However, the extrapolations of the various models into the ill-constrained regions will in general differ, and the hope is that the model

ensemble will span approximately the uncertainty in smooth extrapolation of the existing data.

There is of course no guarantee that the model ensemble will describe the full range of possible extrapolations. However, where the models strongly diverge it is clear that the data are inadequate to constrain the form of the RLF. This information can then be used to decide which datasets should be regarded as high priority for more detailed study. Considerations of this sort led to the choice of the Selected Regions as the most suitable sample capable of resolving the issue of the redshift cutoff for powerful radio sources.

In the regions where the models agree, such agreement may be fortuitous but it is more likely that it may represent some genuine feature in the RLF. This possibility can then be checked by using the models to make falsifiable predictions which can be tested using a model-independent approach.

6.3b : Construction of the model RLFs

The technical aspects of model building are unchanged since Peacock (1985) and so a detailed description is not included here. The important features are:

i) The model RLFs are dual-population models. The steep-spectrum ($\alpha \geqslant 0.5$) and flat-spectrum ($\alpha < 0.5$) populations are treated as distinct and hence the corresponding RLFs are modelled independently.

ii) The models are multi-frequency models. Although the derived model RLFs are defined at 2.7GHz, data at other frequencies are used to help constrain them. To relate data at different frequencies it is necessary to incorporate the known correlation between spectral index and luminosity for steep-spectrum sources. The form used in the present work (unchanged from Peacock 1985) is:

$$\begin{aligned} \alpha &= 0.75 && P_{2.7} < 10^{24} \mathrm{WHz^{-1}sr^{-1}} \\ \alpha &= 0.75 + 0.015(\log_{10}P - 24) && P_{2.7} > 10^{24} \mathrm{WHz^{-1}sr^{-1}} \end{aligned} \qquad (6.1)$$

For flat-spectrum sources $\langle\alpha\rangle = 0$ was assumed.

iii) The overall goodness of fit of each model was assessed via the W statistic (Peacock 1985)

$$W = \prod_{i=1}^{n} p_i \qquad (6.2)$$

where p_i is the significance level of the ith dataset (ie the probability that the misfit statistic for the ith dataset would be larger than the observed value by chance). On the null hypothesis, the distribution of -lnW for large n will be normal with mean n and variance n. This statistic is effective at detecting low values of p_i and hence ensures that no individual dataset is very poorly reproduced by the model. The individual p_is are calculated using the χ^2 statistic in the case of the binned datasets (ie source counts, identification data, local RLF - see Section 6.3c) and using the 2-dimensional Kolmogorov-Smirnov (KS) test (Peacock 1983) in the case of the S-z distributions described in Section 6.2. Note however that the W statistic is not used to optimise the model, but merely to assess the final figure of merit. This is because the K-S statistic does not vary sufficiently smoothly to be suitable for use in optimization, and so, in practice, the actual fitting of the S-z distributions is better achieved using the maximum likelihood technique (see Peacock 1985 for details of method of optimization).

iv) All the models were constructed assuming a Friedmann cosmology with $q_o = 0.5$. However, as pointed out by Peacock (1985), it is not necessary to repeat the modelling for other cosmologies since the RLFs for two different geometries, ρ_1 and ρ_2 are related by

$$\rho_1(P_1,z)\frac{dV_1}{dz} = \rho_2(P_2,z)\frac{dV_2}{dz} \qquad (6.3)$$

where P_1 and P_2 are the luminosities derived from (S,z) using the corresponding effective distances in the two cosmologies, D_1 and D_2. The only complication is the variation of spectral index due to the P-α relation, since $P_1/P_2 = (D_1/D_2)^2$ which is a function of redshift

(ie $\alpha = \alpha(P_1)$ implies $\alpha(P_2,z)$ in the new geometry). However, as argued by Peacock, this redshift effect is unimportant unless P_1/P_2 becomes several orders of magnitude and in fact, for reasonable values of z and q_o, $0.5 \leq P_1/P_2 \leq 2$.

6.3c : Data

The most important component of the database used to construct the model RLFs is the complete sample data at 2.7GHz described in Section 6.2, and the incorporation of the Selected Regions sample therefore represents the most important alteration to the dataset used by Peacock (1985). The additional data which was used to help constrain the models falls into 3 main classes:

i) Source Counts

The source count data used were the same as those used by Peacock (1985), except that the counts at 408MHz had to be discarded in order to obtain satisfactory model fits. Because of the necessarily simple assumptions concerning the radio spectral index α (see Section 6.3b) multi-frequency modelling is only feasible over a restricted range of frequencies set by the scale of spectral curvature. For this reason Peacock (1985) was forced to reject 3C data from his database because 178MHz was found to be too remote from the model frequency of 2.7GHz. The problem may be expected to increase as the database (and hence the RLF) at 2.7GHz becomes more precisely defined. Hence it was not altogether surprising that, with the improvement in the complete sample data at 2.7GHz, it was found to be no longer possible to relate the high-frequency RLF to the detailed counts at 408MHz (the problem arises largely because the 408MHz counts are so well defined; the models here predict the correct numbers to better than 5%, but this small discrepancy cannot be tolerated statistically). The remaining source count data used in the present study are summarized below in Table 6.2a.

ii) Estimated redshift distributions

These data are unchanged from Peacock (1985) and are constructed from 5 faint surveys which possess partial identification data but essentially no redshift information. Peacock attempted to evaluate a single statistic for each of these samples - the fraction of sources lying within a redshift z_o (this results in 5 datasets, each consisting of 2 bins). This number was obtained essentially from the fraction of sources identified with galaxies. A full discussion of the reliability of these datasets is given by Peacock (1985). Their main role is to rule out obviously incorrect redshift distributions for faint radio sources (eg a situation in which all faint sources without measured redshifts are presumed to be at $z \sim 10$). These data are summarized below in Table 6.2b.

iii) The local RLF

In recent years there have been several new determinations of the local radio luminosity function. Both the steep- and flat-spectrum local RLFs have therefore been re-evaluated by Peacock using the data from Toffolati *et al.* (1987) and Subrahmanya & Harnett (1987), which provided 2 new independent determinations of the steep-spectrum local RLF at 2.7GHz, and 1 new determination of the flat-spectrum local RLF. These new data were incorporated into the database along with the existing local RLF data used by Peacock (1985) which has now been corrected for the counting error in the data of Cameron (1971) pointed out by Toffolati *et al.* (1987). The updated local RLF data are given in Table 6.2c and illustrated in Figure 6.3. These 3 determinations are in good qualitative agreement, but there are some regions of statistical disagreement (particularly around $\log_{10}P_{2.7} \approx 21 \mathrm{WHz^{-1}sr^{-1}}$, despite the above corrections to Cameron's data). These reflect residual systematic errors, probably due to correction from different selection frequencies and incompleteness. To represent these an error of 0.15 in $\log_{10}\rho$ has been added in quadrature to the formal errors given in Table 6.2c ; a single polynomial is then consistent with all 3 sets of data.

Peacock (1985) constrained his model RLFs to be consistent with

the local RLF out to $z = 0.2$. However, with the improved accuracy of the new local RLF determination it was found necessary to relax the formal errors by 0.1 (in $\log_{10}\rho$) and by 0.2 at $z = 0.1$ and $z = 0.2$ respectively (in addition to the initial 0.15 at $z = 0$ - see above) in order to achieve acceptable model fits. This is not unreasonable, since studies which indicate no evolution out to $z = 0.2$ have errors on ρ of this order (Windhorst 1984).

Table 6.2 : Source counts, estimated redshift distributions, and local RLF data used to derive the model RLFs.

a) SOURCE COUNTS

Frequency	Flux-density range	Spectral Separation?	References
1.4GHz	>0.5Jy	No	Bridle *et al.* (1972)
1.4GHz	0.6→500mJy	No	Van der Laan & Windhorst (1982)
2.7GHz	>0.1Jy	Yes	Wall *et al.* (1981)
5.0GHz	>0.015Jy	Yes	Kuhr (1980); Condon & Ledden (1982)
5.0GHz	>0.07mJy	Yes	Kellermann & Wall (1983); Fomalont *et al.* (1984)

b) ESTIMATED REDSHIFT DISTRIBUTIONS

Frequency	Flux-density range	Spectral type	N	z_o	$f(z<z_o)$	Reference of origin.
408MHz	1→2Jy	All	59	1.25	0.51±0.07	Allington-Smith (1984)
408MHz	0.1→1Jy	Steep	83	0.8	0.20±0.04	Benn *et al.* (1984)
408MHz	0.01→0.1Jy	Steep	60	0.5	0.22±0.05	Benn *et al.* (1984)
5GHz	0.015→0.1Jy	Flat	35	0.6	0.46±0.08	Condon & Ledden (1982)
1.4GHz	>0.58mJy	All	302	0.5	0.43±0.03	Windhorst (1984)

c) THE LOCAL RADIO LUMINOSITY FUNCTION AT 2.7GHz

STEEP-SPECTRUM

Determination 1 (modified from Peacock 1985)		Determination 2 (Toffolati *et al.* 1987)		Determination 3 (Subrahmanya & Harnett 1987)	
$\log_{10}(P_{2.7})$	$\log_{10}\rho$	$\log_{10}(P_{2.7})$	$\log_{10}\rho$	$\log_{10}(P_{2.7})$	$\log_{10}\rho$
18.3	-1.11 ± 0.85	19.38	-2.00 ± 0.73	18.53	-2.05 ± 0.31
18.7	-0.46 ± 0.85	20.13	-2.80 ± 0.07	18.93	-2.42 ± 0.25
19.1	-1.46 ± 0.85	20.63	-3.06 ± 0.09	19.33	-2.57 ± 0.31
19.5	-1.56 ± 0.85	21.13	-3.45 ± 0.05	19.73	-2.53 ± 0.11
19.7	-1.71 ± 0.85	21.63	-4.14 ± 0.05	20.13	-2.76 ± 0.10
19.9	-2.11 ± 0.85	22.13	-4.67 ± 0.09	20.53	-2.70 ± 0.08
20.1	-2.30 ± 0.85	22.63	-5.28 ± 0.10	20.93	-2.93 ± 0.08
20.4	-2.60 ± 0.11	23.13	-5.50 ± 0.08	21.33	-3.58 ± 0.13
20.8	-2.57 ± 0.08	23.63	-5.82 ± 0.08	21.73	-4.43 ± 0.26
21.2	-2.91 ± 0.08	24.13	-6.18 ± 0.07	22.13	-5.53 ± 0.25
21.6	-4.07 ± 0.22	24.63	-6.96 ± 0.10		
22.0	-4.45 ± 0.31	25.13	-7.43 ± 0.22		
22.8	-5.51 ± 0.25				
23.3	-5.92 ± 0.11				
23.8	-6.06 ± 0.11				
24.3	-6.74 ± 0.15				
24.7	-7.01 ± 0.18				
25.1	-7.35 ± 0.31				

FLAT-SPECTRUM

Determination 1 (Peacock 1985)		Determination 2 (Toffolati *et al.* 1987)	
$\log_{10}(P_{2.7})$	$\log_{10}\rho$	$\log_{10}(P_{2.7})$	$\log_{10}\rho$
19.4	-3.10 ± 0.31	20.0	-4.10 ± 0.43
20.9	-4.12 ± 0.22	20.75	-4.46 ± 0.31
22.1	-5.48 ± 0.31	21.25	-4.82 ± 0.19
22.85	-5.83 ± 0.18	21.75	-5.26 ± 0.19
23.60	-6.73 ± 0.31	22.25	-5.46 ± 0.22
		22.75	-6.06 ± 0.31
		23.25	-6.90 ± 0.22
		23.75	-7.38 ± 0.43
		24.25	-7.05 ± 0.19

Figure 6.3 : The local radio luminosity function at 2.7GHz. The open circles are the (corrected) data used by Peacock (1985) (see references therein). The filled circles are the new determinations from the data of Toffolati *et al.* (1987), while the stars are the new steep-spectrum LRLF determined from the data of Subrahmanya & Harnett (1987). The curves shown are best-fitting polynomials of order 1 and 5 respectively.

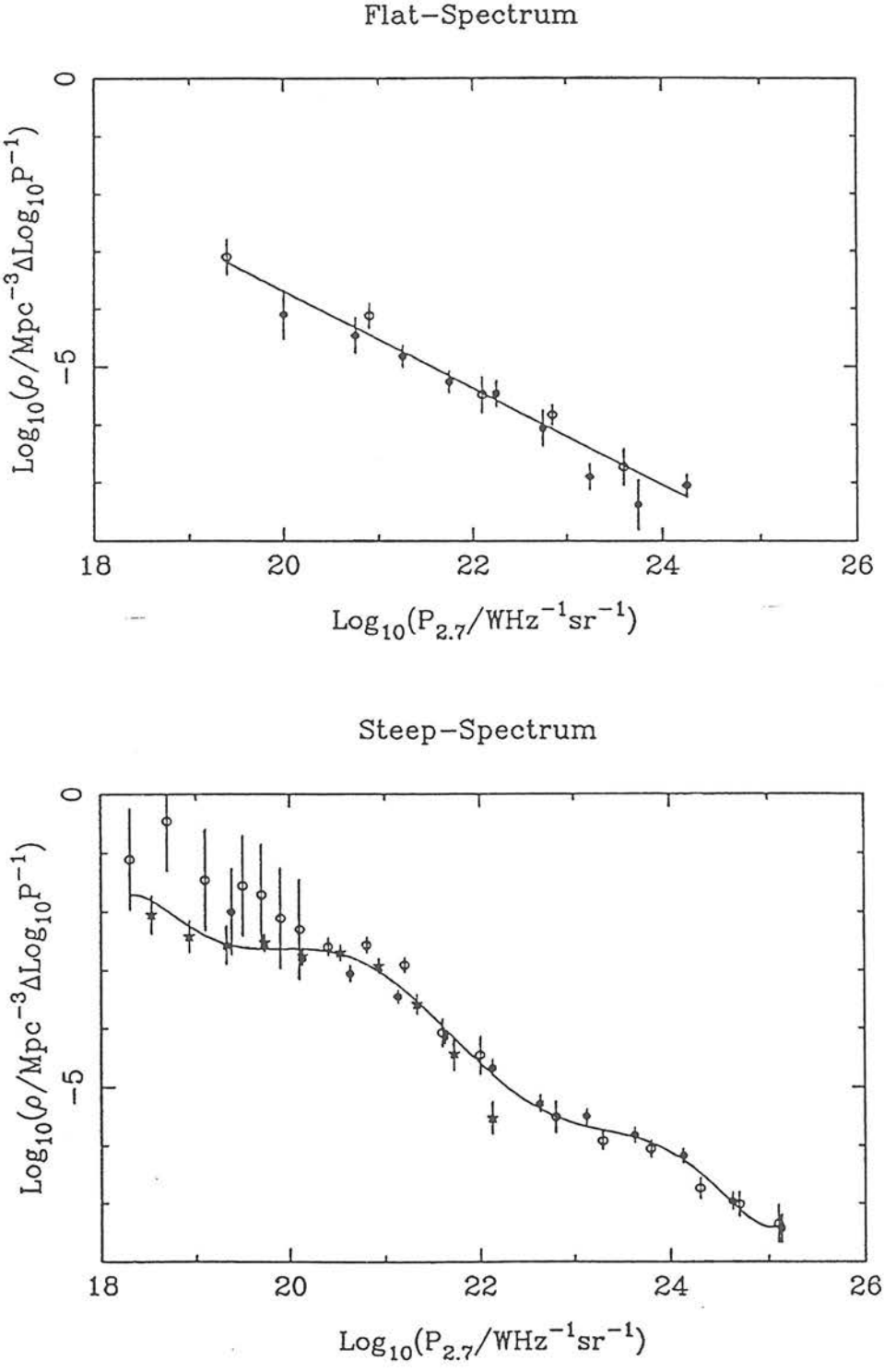

6.3d : The model RLF ensemble

The RLF ensemble consists of 7 differently formulated models which were found to be consistent with the data. Models number 1 → 5 are genuinely free-form models constructed in a similar manner to the model ensemble of Peacock (1985). Models number 6 and 7 resulted from the attempt to fit luminosity and luminosity/density evolution to the data, a topic which is discussed in Section 6.5. These two additional models thus involve fewer free parameters than models 1 → 5, but are included here to further boost the size of the ensemble.

Models 1 → 5 were all constructed using a series expansion

$$\log\rho = \sum_{i=0}^{n} \sum_{j=0}^{n-i} A_{ij}\, x^i(P)\, y^j(z) \qquad (6.4)$$

where x and y are transformed axes of the P-z plane, and the series was truncated at the lowest expansion order consistent with the data. Model number 1 may be regarded as the fundamental model: the (P,z) coordinates are $(0.1(\log_{10}P-20),\ 0.1z)$ and integration of the RLF is carried out over the redshift range $z = 0 \rightarrow 10$, and over the luminosity range $P_{2.7} = 10^{18} \rightarrow 10^{30}$. The expansion orders are 5th order (21 terms) for the steep-spectrum RLF (plus one extra term in $(\log_{10}P)^6$ to assist in fitting the sharp kink in the local RLF) and 4th order (15 terms) for the flat-spectrum RLF.

Models 2 → 5 vary successively one aspect of this:

RLF2: An exponential cutoff is added at high luminosity. The form adopted was $\rho \rightarrow \rho\exp(-P/P_c)$ where $P_c = 10^{28}\mathrm{WHz^{-1}sr^{-1}}$.

RLF3: The redshift coordinate used is $\log_{10}(1+z)$ instead of 0.1z.

RLF4: Integration of the RLF is terminated at $z = 5$ instead of $z = 10$.

RLF5: A cutoff at high redshift is added such that the RLF decays sinusoidally from $z = 2$ to a value of zero at $z \geqslant 4$ - ie for $2 \leqslant z < 4$,

$\rho \rightarrow \rho(1 + \cos\Phi)/2$ where $\Phi = (z-2)\pi/2$, and for $z \geqslant 4$, $\rho = 0$.

Models number 1 → 4 are directly comparable with models 1 → 4 of Peacock (1985). Peacock's model 5 involved enforcing zero evolution of the RLF out to $z = 0.4$. In view of the difficulty experienced in the present work in fitting the new local RLF at $z = 0.2$ (see Section 6.3c) this model was not re-attempted. The construction of models 6 and 7 is given in Section 6.5.

These 7 models were each derived 3 times, using 3 different versions of the database. The 3 versions of the database differed in the redshifts which were assigned to the faint galaxies in the Selected Regions sample: ie the MEAN-z, LOW-z and HIGH-z estimates described in Section 6.2b. This was done in order to test the sensitivity of the models to these estimated redshifts.

After rejection of the 408MHz counts (see Section 6.3c, i) and progressive relaxation of the LRLF errors at $z = 0.1$ and 0.2 (see Section 6.3c) it was found that all of the 21 models could achieve acceptable fits (at better than the 1% level) over all the datasets. The variations between the 7 model RLFs in each ensemble therefore give a lower bound to the 99% confidence limits on $\rho(P,z)$.

The expansion parameters for models 1 → 5 derived on the basis of the MEAN-z, LOW-z, and HIGH-z datasets are given in Appendix B, Tables B.1, B.2 and B.3 respectively. The parameters for models 6 and 7 are given in Section 6.5. All these models assume a density parameter $\Omega = 1$, but as explained in Section 6.3b, translation to other values is straightforward.

6.3e : Results - the high-redshift cutoff in the RLF

i) The first evidence of a high-redshift cutoff in the steep-spectrum RLF

In Figure 6.4 the results of the new model RLF ensemble are compared with those of Peacock (1985). These plots show the limits on ρ (allowed by the 7 model RLFs) viewed at 3 different cuts of constant luminosity ($P_{2.7}$ = 10^{27}, 10^{26} & 10^{25}WHz^{-1}sr^{-1}) over the luminosity range in which the high-redshift RLF is reasonably well defined. The redshift coordinate is look-back time τ, normalized to the age of the universe. The new RLFs shown are those derived using the MEAN-z dataset (see Section 6.3d).

The most important feature of these diagrams is that the new model RLFs show a turn-over at high-redshift in the steep-spectrum population which is not exhibited by the model RLFs of Peacock (1985). These new constraints on the high-redshift form of the steep-spectrum RLF are a direct consequence of the improvement in the steep-spectrum database provided by the addition of the Parkes Selected Regions sample. The new models also provide improved constraints on the form of the flat-spectrum redshift cutoff which was discovered by Peacock (1985).

Of particular interest is the similarity between the form of the new steep- and flat-spectrum RLFs. In both cases the comoving density of sources peaks at a redshift of about 2 and declines thereafter. At all 3 sampling luminosities the density of the flat-spectrum sources declines by a factor $\simeq$ 10 between z = 2 and z = 4. The constraints in the steep-spectrum case are somewhat more luminosity dependent (at present), but a density decline of similar magnitude is certainly exhibited at $P_{2.7}$ = 10^{27}WHz^{-1}sr^{-1}.

It therefore now seems likely that the WHOLE radio population (ie both flat- and steep-spectrum sources) suffers a gradual high-redshift decline over the redshift range z = 2 $\rightarrow$ 4.

Figure 6.4 : The limits to ρ at constant $P_{2.7}$ allowed by the new model RLFs (MEAN-z dataset) compared to the limits allowed by the corresponding models of Peacock (1985). $Log_{10}\rho$ is plotted against normalized look-back time τ (Ω=1) at 3 different luminosities $P_{2.7}$ = 10^{27}, 10^{26} & 10^{25}WHz^{-1}sr^{-1}. The steep-spectrum RLF is indicated by the solid lines, the flat-spectrum by dashed. Units of ρ are Mpc^{-3}(log$_{10}$P$_{2.7}$)$^{-1}$.

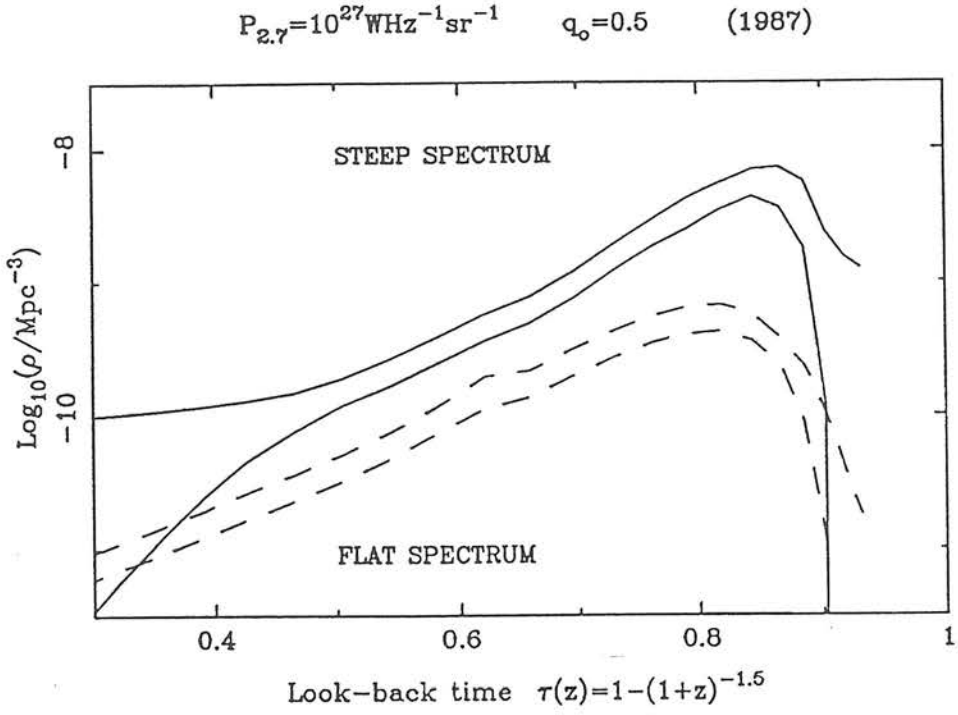

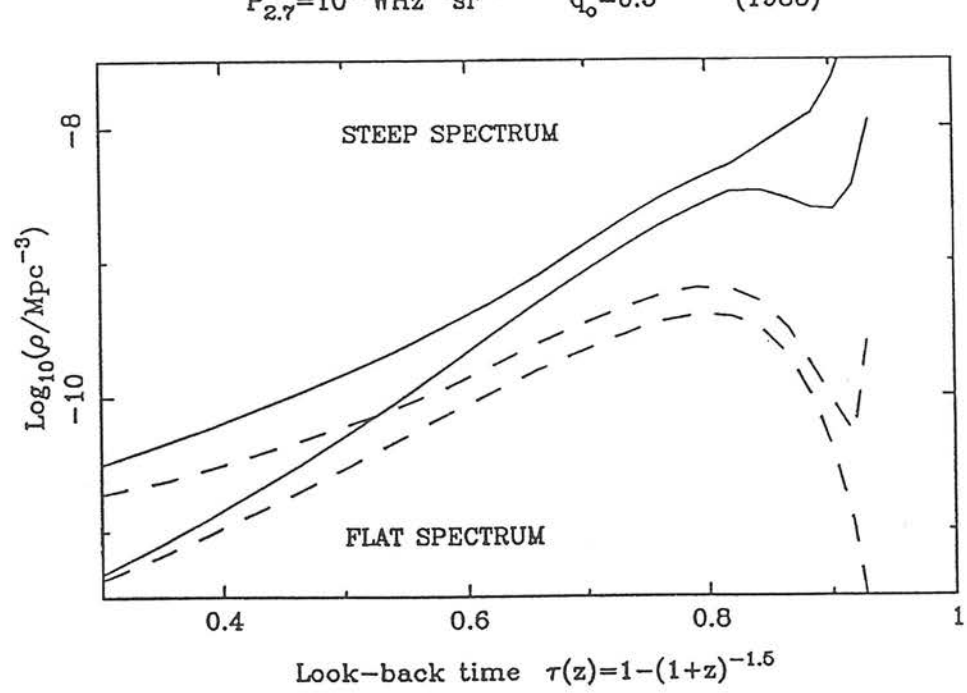

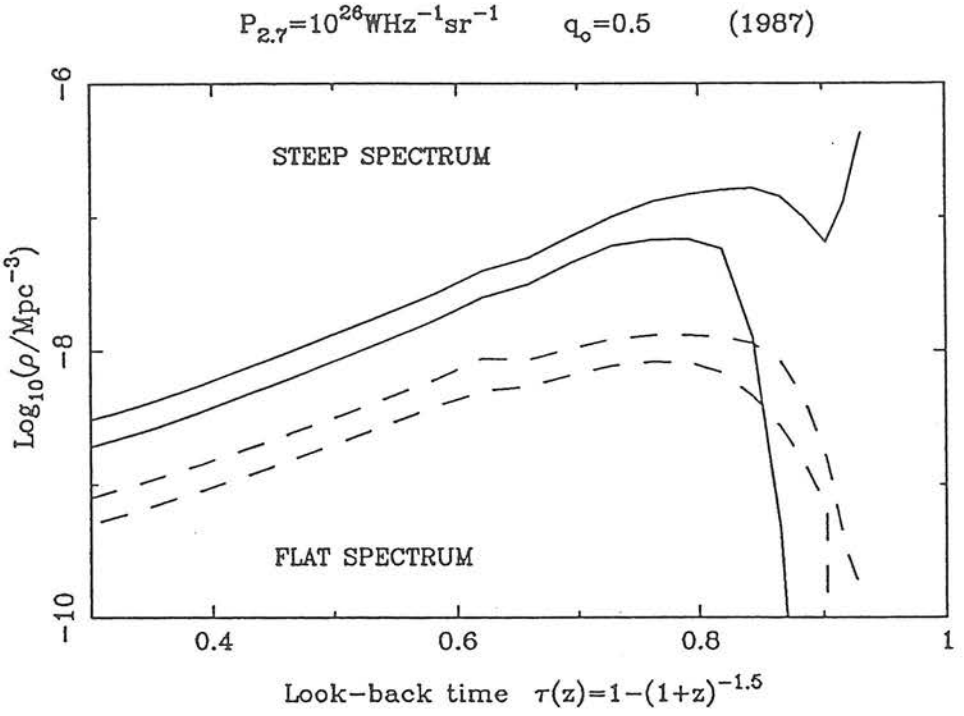
$P_{2.7}=10^{26}WHz^{-1}sr^{-1}$ $q_o=0.5$ (1987)
STEEP SPECTRUM
FLAT SPECTRUM
$Log_{10}(\rho/Mpc^{-3})$
-6
-8
-10
0.4
0.6
0.8
1
Look-back time $\tau(z)=1-(1+z)^{-1.5}$

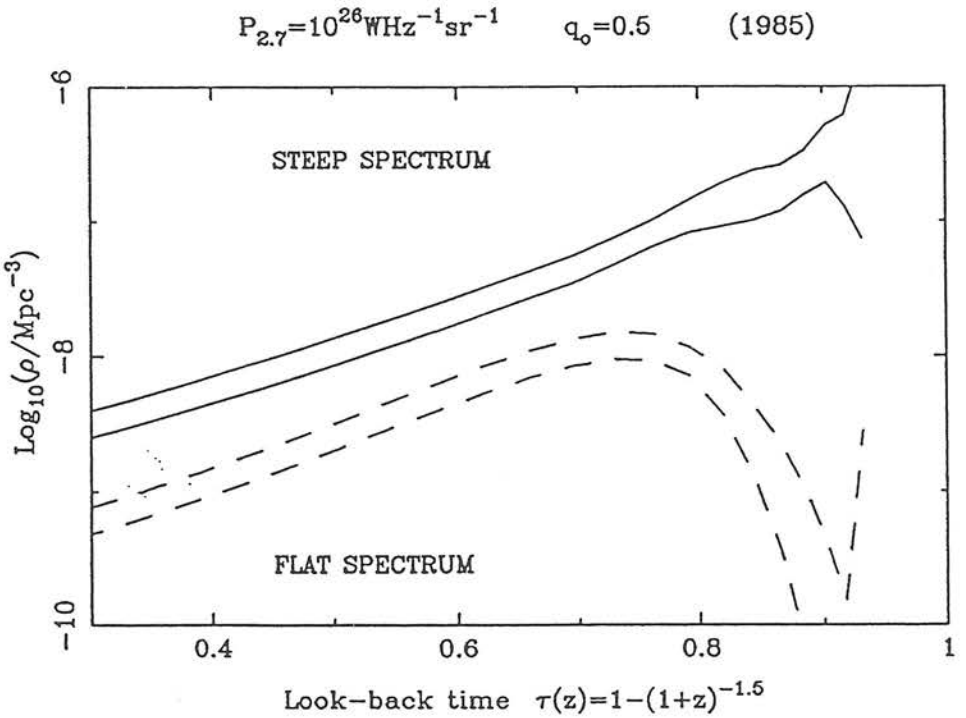
$P_{2.7}=10^{26}WHz^{-1}sr^{-1}$ $q_o=0.5$ (1985)
STEEP SPECTRUM
FLAT SPECTRUM
$Log_{10}(\rho/Mpc^{-3})$
-6
-8
-10
0.4
0.6
0.8
1
Look-back time $\tau(z)=1-(1+z)^{-1.5}$

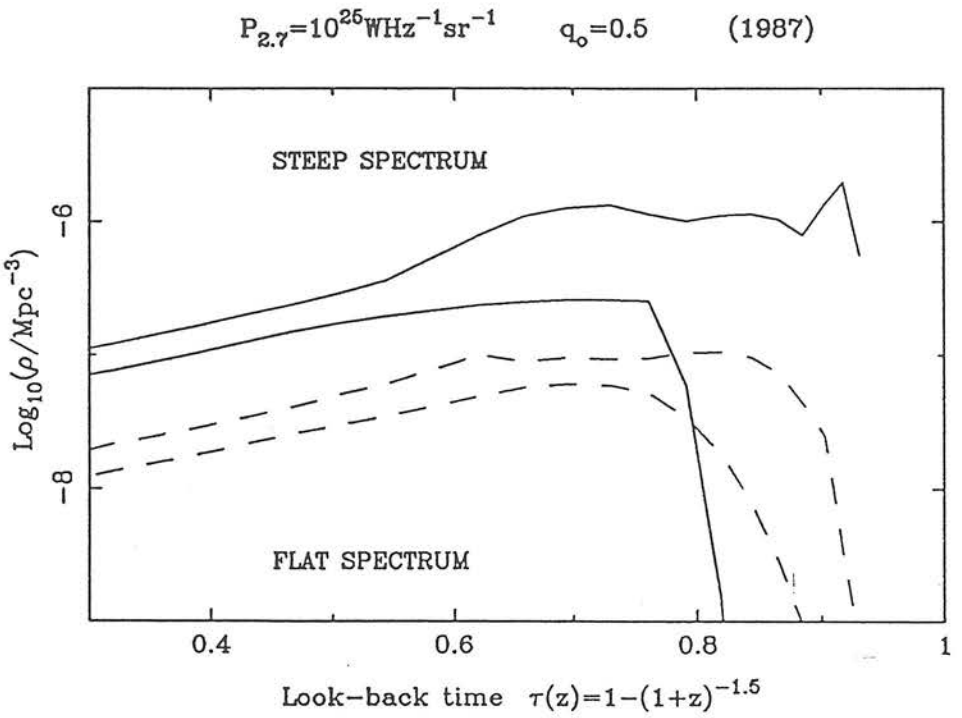
$P_{2.7}=10^{25}WHz^{-1}sr^{-1}$ $q_o=0.5$ (1987)
STEEP SPECTRUM
FLAT SPECTRUM
$Log_{10}(\rho/Mpc^{-3})$
-6
-8
0.4
0.6
0.8
1
Look-back time $\tau(z)=1-(1+z)^{-1.5}$

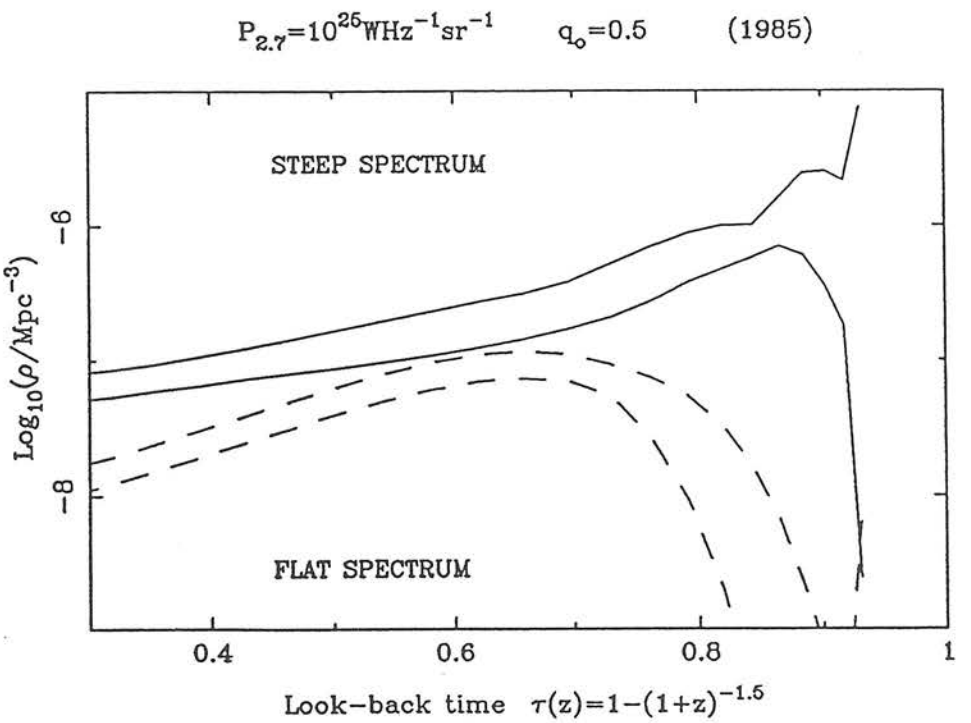
$P_{2.7}=10^{25}WHz^{-1}sr^{-1}$ $q_o=0.5$ (1985)
STEEP SPECTRUM
FLAT SPECTRUM
$Log_{10}(\rho/Mpc^{-3})$
-6
-8
0.4
0.6
0.8
1
Look-back time $\tau(z)=1-(1+z)^{-1.5}$

It is interesting to calculate the redshift distributions of the flat- and steep-spectrum sources in the Selected Regions which are predicted by the new model RLFs. This was carried out using RLF1 since this model was found to represent roughly the average of the allowed range of RLFs. The method of calculation was as follows.

The redshift range $z = 0 \rightarrow 4$ was divided into bins of width 0.1. At each redshift the limiting luminosity P_L corresponding to the Selected Regions flux limit of $S_{2.7} = 0.1$Jy was calculated (To do this one must assume a value for the radio spectral index α. Values of $\alpha = 0.95$ and $\alpha = 0.12$ were chosen for steep- and flat-spectrum sources respectively, since these are the relevant averages of the observed values in the Selected Regions). Then, at each redshift point, the RLF was evaluated between $P_{2.7} = 10^{18}$ and $P_{2.7} = 10^{30}$WHz^{-1}sr^{-1} at intervals of 0.1 in $\log_{10}P_{2.7}$, and the resulting values were summed over the range $10^{18} \leq P_{2.7} \leq P_L$. Finally this "luminosity-integrated" RLF was multiplied by the cosmological volume of the redshift bin and the solid angle (0.075sr) subtended by the Selected Regions survey.

In Figure 6.5 the predicted flat- and steep-spectrum redshift distributions are shown along with the corresponding observed redshift distributions which were used to derive the model RLF (MEAN-z distribution). This comparison demonstrates the good agreement between model and data. The predicted distributions also illustrate the form of smooth redshift distributions which are consistent with a similar form of high-redshift cutoff in both populations.

Figure 6.5 : The steep- and flat-spectrum redshift distributions for sources in the Selected Regions predicted by RLF model 1, compared to the actual distributions on which the model was based (the MEAN-z distributions described in Section 6.2b).

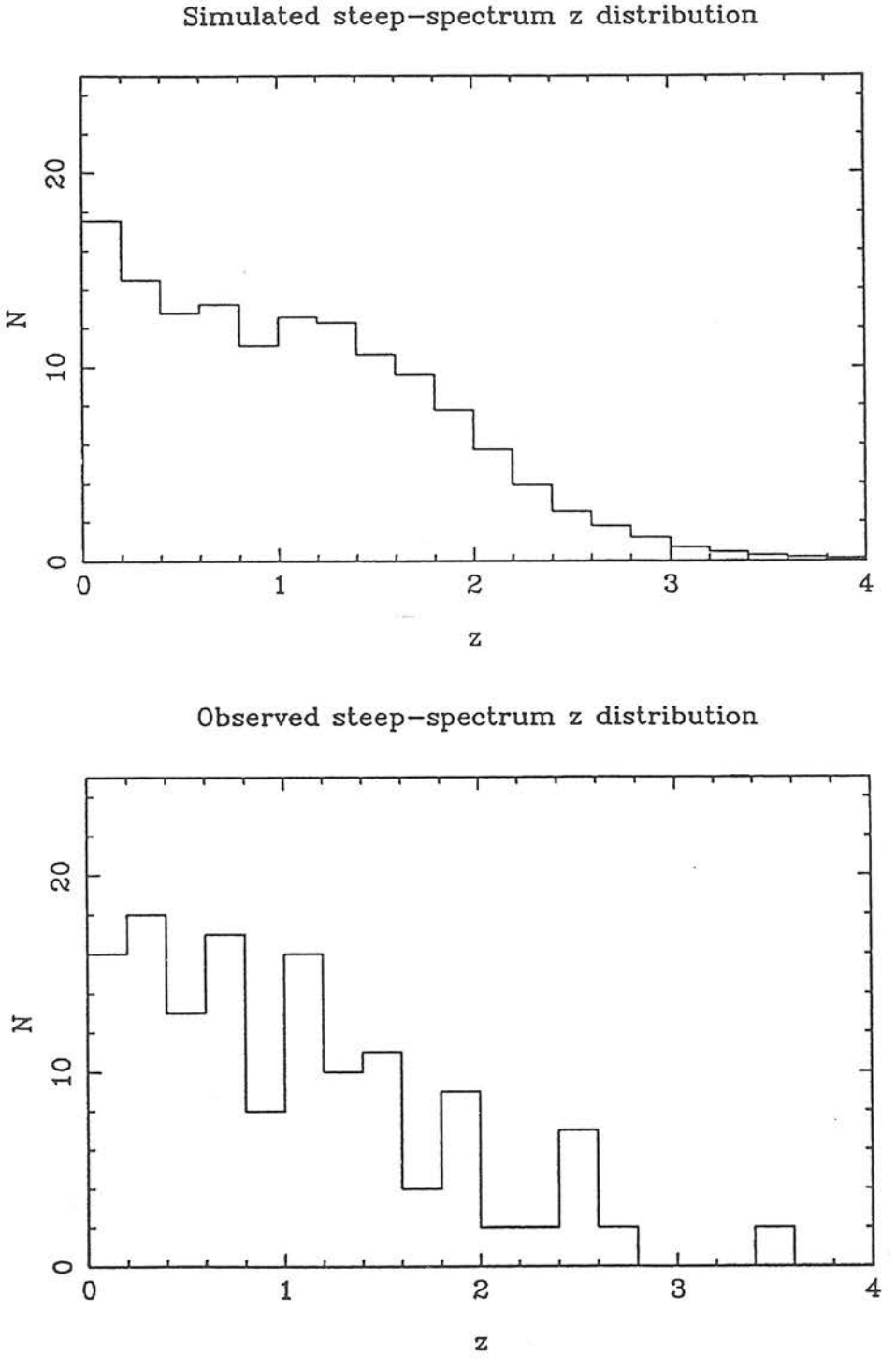

Simulated flat−spectrum z distribution

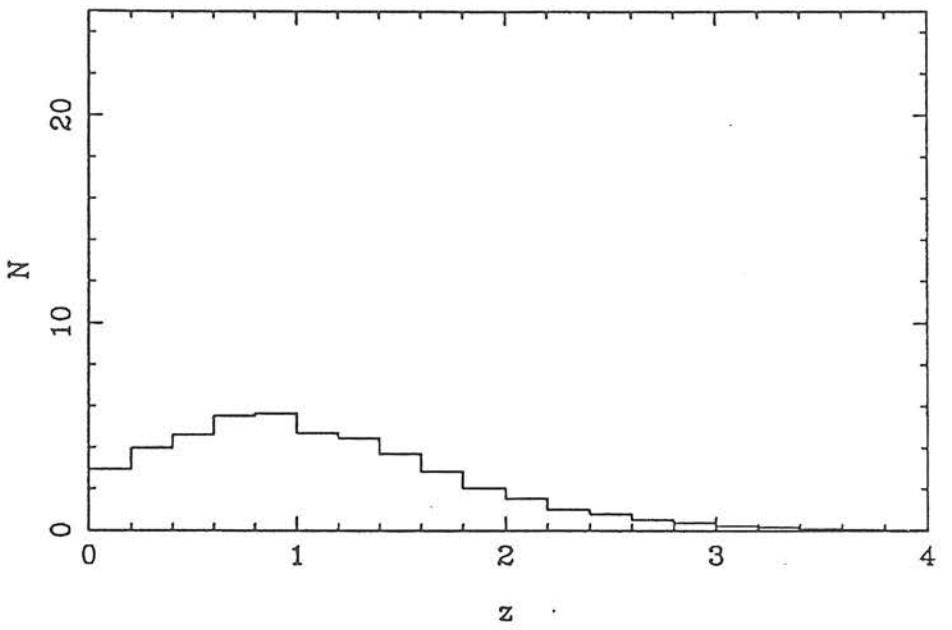

Observed flat−spectrum z distribution

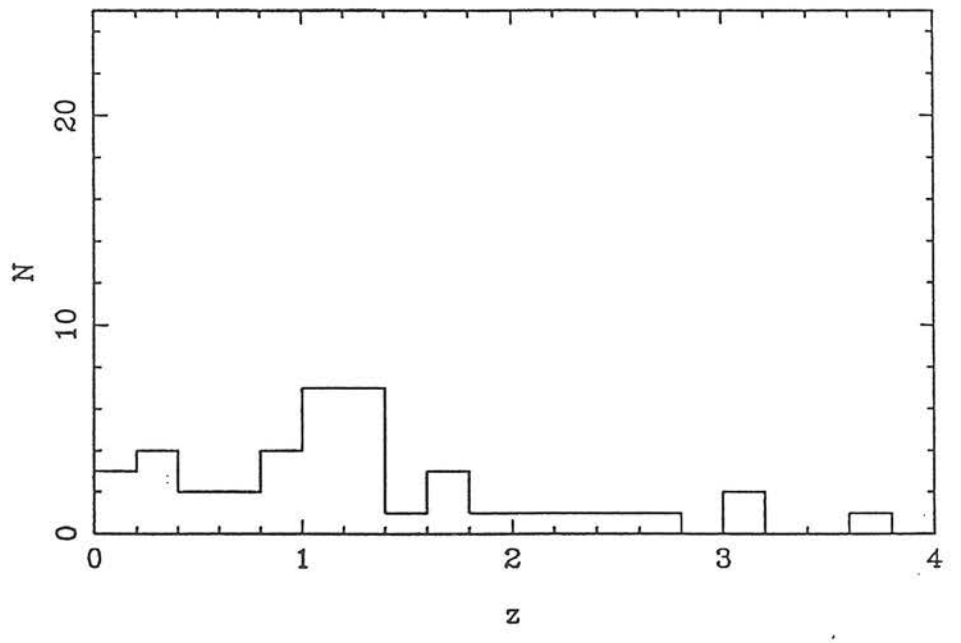

ii) Reliability of the result

Having found evidence for a high-redshift cutoff in the steep-spectrum RLF, it is important to consider the robustness of this result. Figure 6.6 shows the results of the RLF models derived on the basis of the LOW-z and HIGH-z datasets, for comparison with the MEAN-z results which were presented in Figure 6.4.

As expected, the form of the flat-spectrum RLF is essentially unchanged because of the small fraction of sources in the Selected Regions which are identified with faint galaxies.

The steep-spectrum RLFs derived using the LOW galaxy estimated redshifts are very similar to those derived using the MEAN-z values. However, the range of steep-spectrum RLFs allowed by the HIGH-z models is rather different, and no longer displays the turnover at z ~ 2. It therefore seems feasible that a redshift cutoff in the steep-spectrum RLF would not be in fact required IF the true redshift distribution of the Selected Regions were to be represented by the HIGH-z distribution discussed in Section 6.2. However, as argued in that section, there are several good reasons for believing that the HIGH redshift estimates are unrealistic. In fact, only one of the 7 model RLFs based on the HIGH-z dataset fails to decline at high redshift. This is RLF2, and so it is this model which is responsible for the upper limit of ρ failing to turn-over in the lower diagrams of Figure 6.6. This model RLF (ie model 2 based on the HIGH-z data) can therefore be used to predict what redshift distribution of steep-spectrum sources in the Selected Regions would be consistent with no redshift cutoff. The resulting predicted distribution is shown in Figure 6.7, along with the HIGH-z distribution which was used to derive the model. The shape of the predicted distribution is somewhat different from the observed one, but this is simply the result of the rather crude way in which the HIGH-z distribution was constructed (ie scattering all galaxies with $K > 18$ out to $z \approx 3.5$). It is interesting to compare this predicted distribution with the corresponding distribution in Figure 6.5 in order to see the difference between redshift distributions which are inconsistent or consistent with a density decline over the redshift range $z = 2 \rightarrow 4$.

From these distributions it is possible to deduce what fraction of steep-spectrum Selected Regions sources must lie beyond a given redshift z_o to be consistent with the two scenarios (ie no cutoff, or a cutoff similar in form to that of the flat-spectrum RLF). The results are given below in Table 6.3 for z_o = 2.0, 2.5 and 3.5.

Table 6.3 : The number of steep-spectrum sources (out of the total number of 137) in the Selected Regions which are predicted to lie beyond a redshift z_o on the basis of model RLFs which do and do not exhibit a redshift cutoff.

With cutoff		Without cutoff	
z_o	number ($>z_o$)	z_o	number ($>z_o$)
2.0	15	2.0	28
2.5	5	2.5	18
3.0	1	3.0	12

Even assuming the HIGH-z K-z relation, the maximum possible number of steep-spectrum sources in the Selected Regions which could possibly have $z > 2$ is 24, and so it is clearly almost impossible to force the data to be consistent with no redshift cutoff. Measurement of redshifts for even a few of the faint sources should put the issue beyond any doubt - it seems likely that many of these will turn out to be low-redshift, low-luminosity galaxies, as was found to be the case for 0000+035 (see Chapter 5, Section 5.3b).

Figure 6.6 : The limits to ρ at constant $P_{2.7}$ allowed by the new model RLFs derived using the LOW and HIGH redshift distributions for the Selected Regions. $Log_{10}\rho$ is plotted against normalised look-back time τ (Ω=1) at 3 different luminosities $P_{2.7}$ = 10^{27}, 10^{26} & 10^{25} $WHz^{-1}sr^{-1}$. The steep-spectrum RLF is indicated by the solid lines, the flat-spectrum by dashed. Units of ρ are $Mpc^{-3}(\log_{10}P_{2.7})^{-1}$.

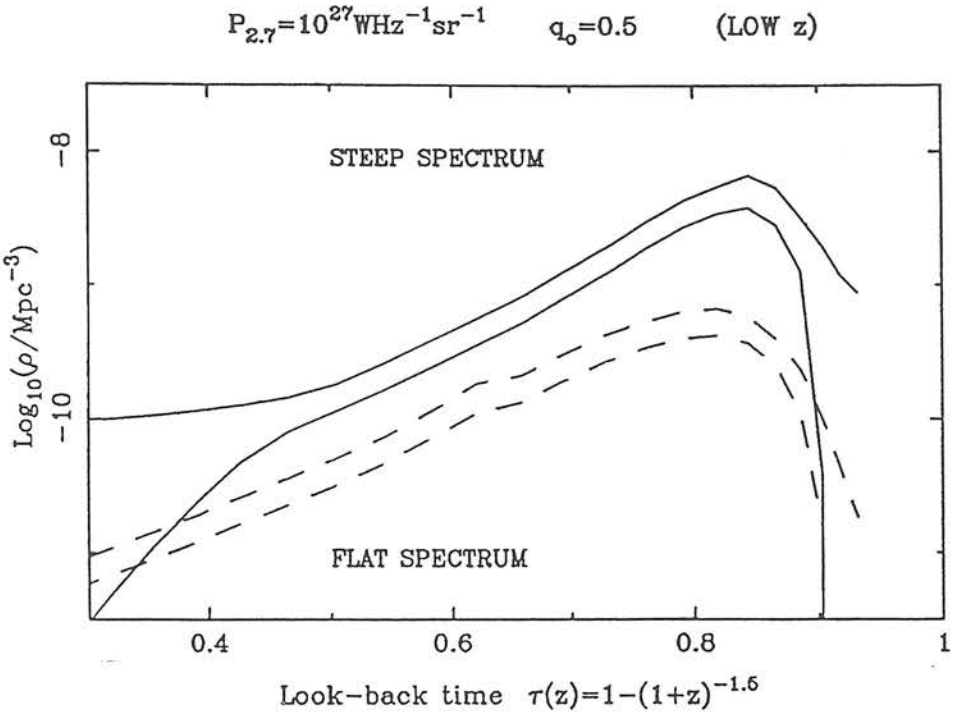

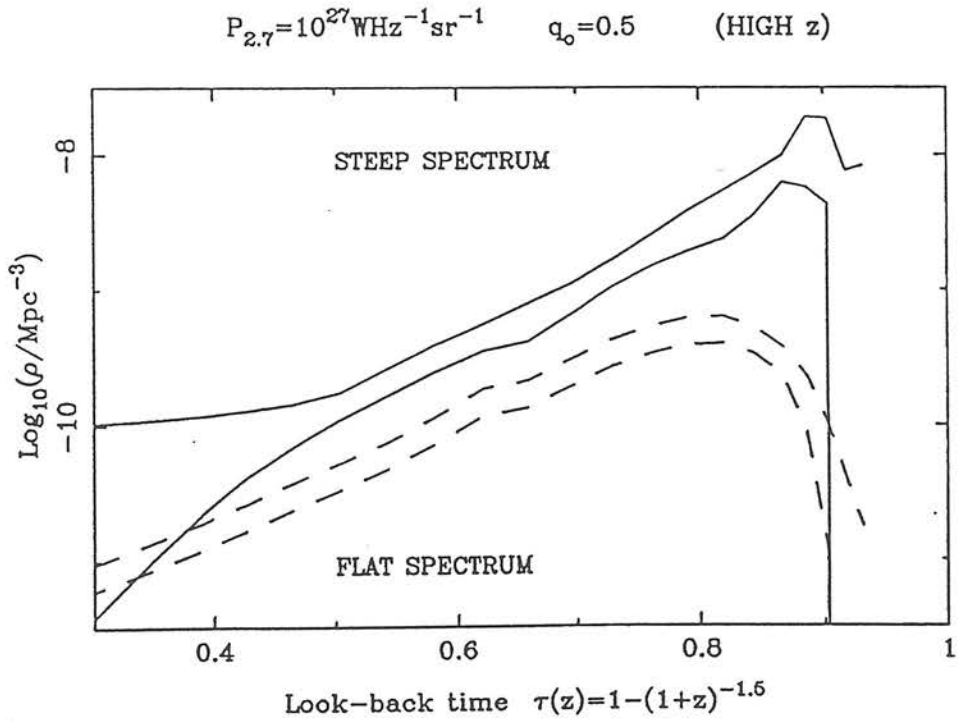

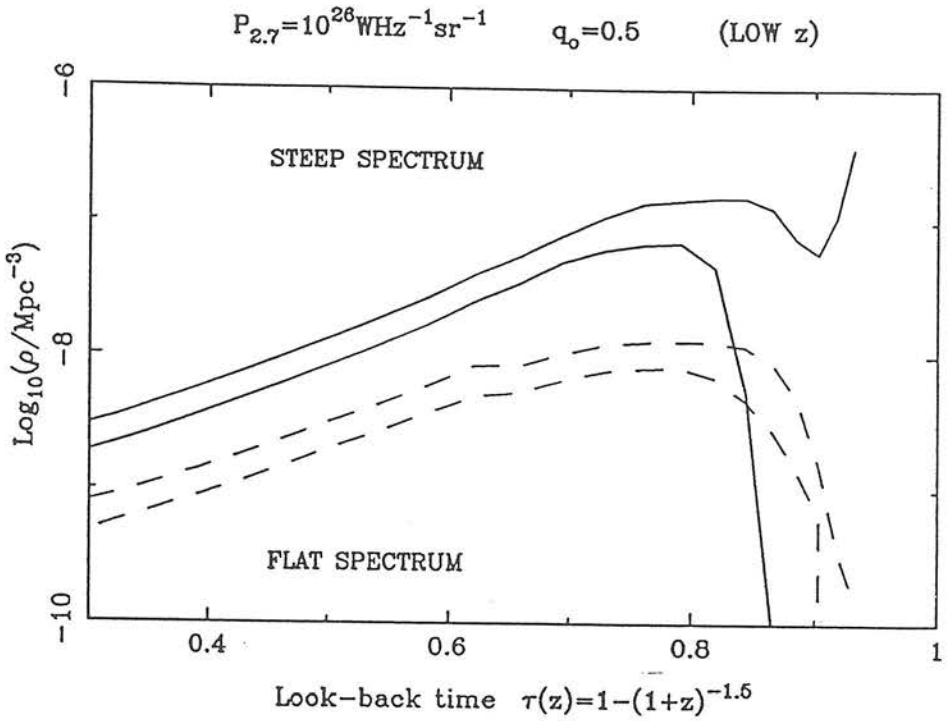
$P_{2.7}=10^{26}WHz^{-1}sr^{-1}$ $q_o=0.5$ (LOW z)
STEEP SPECTRUM
FLAT SPECTRUM
$Log_{10}(\rho/Mpc^{-3})$
-6
-8
-10
0.4
0.6
0.8
1
Look-back time $\tau(z)=1-(1+z)^{-1.5}$

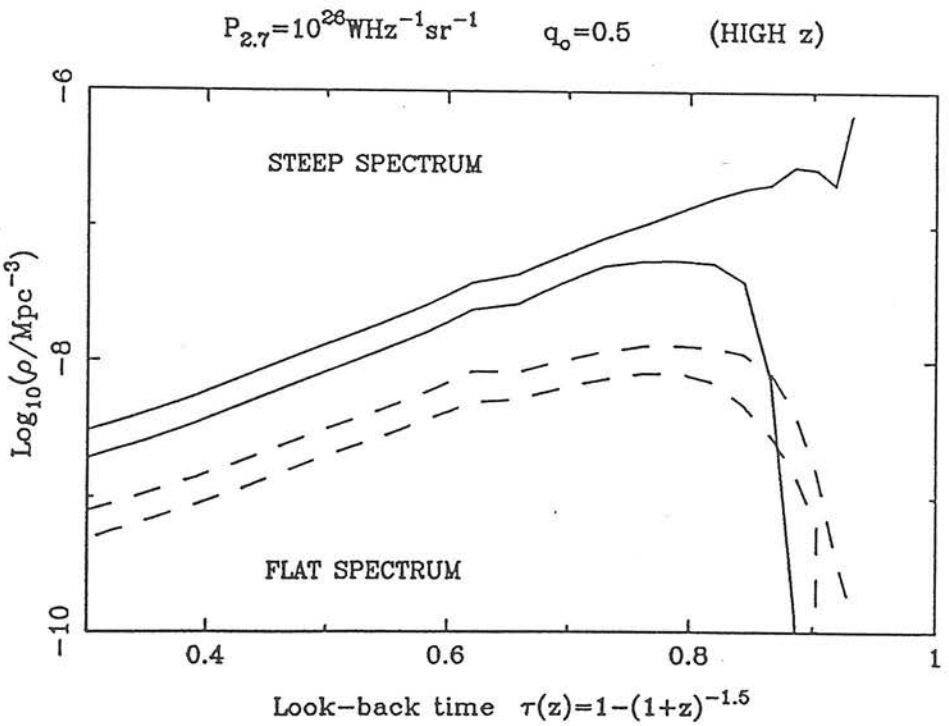
$P_{2.7}=10^{26}WHz^{-1}sr^{-1}$ $q_o=0.5$ (HIGH z)
STEEP SPECTRUM
FLAT SPECTRUM
$Log_{10}(\rho/Mpc^{-3})$
-6
-8
-10
0.4
0.6
0.8
1
Look-back time $\tau(z)=1-(1+z)^{-1.5}$

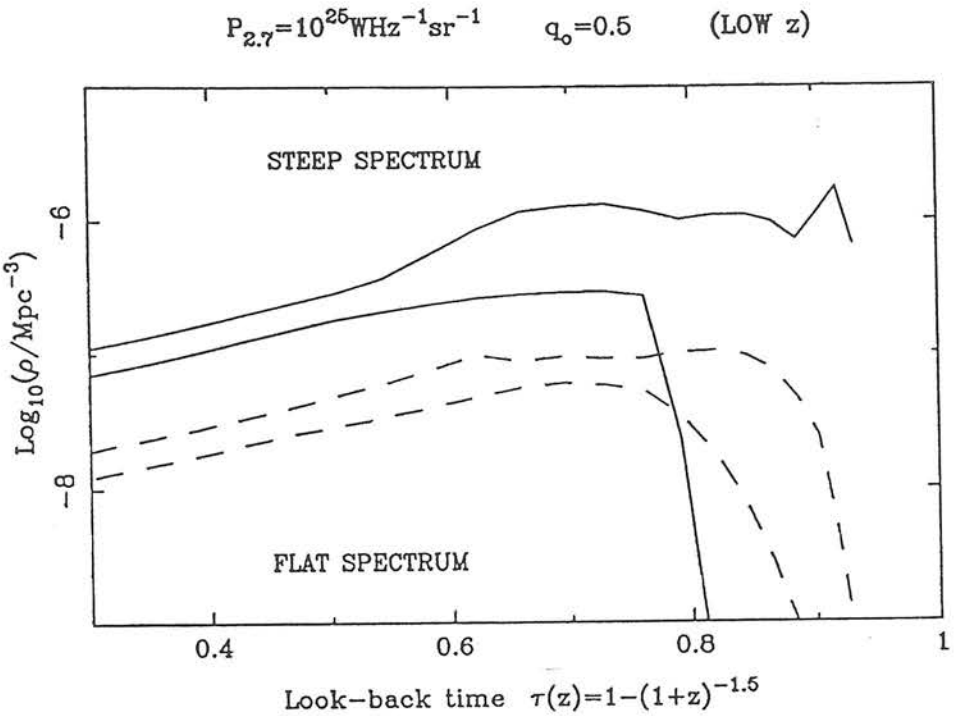
$P_{2.7}=10^{25}WHz^{-1}sr^{-1}$ $q_o=0.5$ (LOW z)
STEEP SPECTRUM
FLAT SPECTRUM
$Log_{10}(\rho/Mpc^{-3})$
-6
-8
0.4
0.6
0.8
1
Look-back time $\tau(z)=1-(1+z)^{-1.5}$

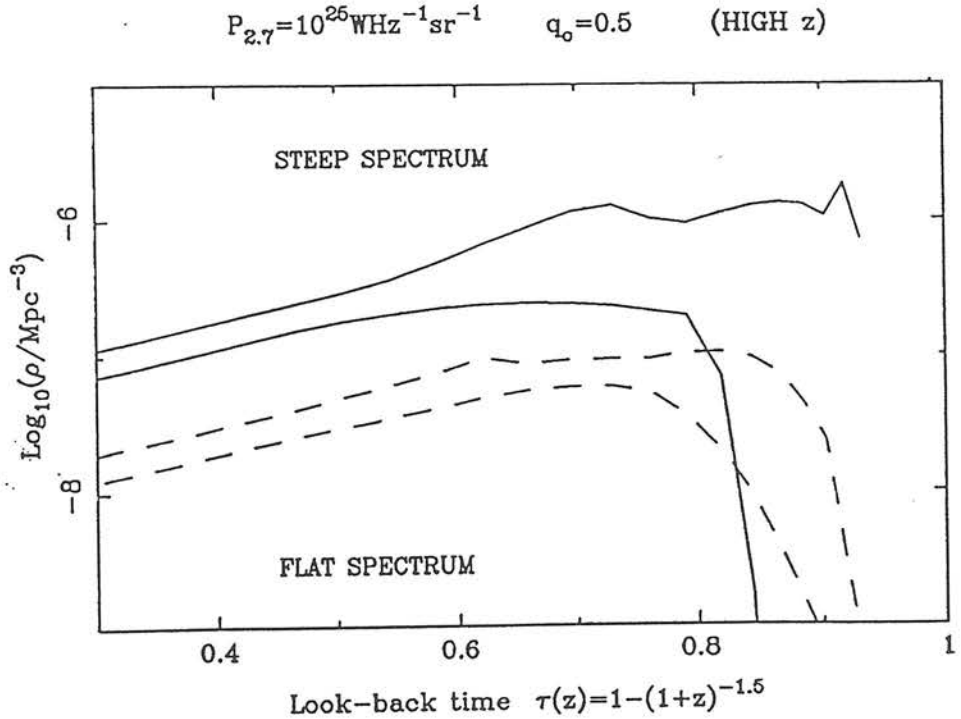
$P_{2.7}=10^{25}WHz^{-1}sr^{-1}$ $q_o=0.5$ (HIGH z)
STEEP SPECTRUM
FLAT SPECTRUM
$Log_{10}(\rho/Mpc^{-3})$
-6
-8
0.4
0.6
0.8
1
Look-back time $\tau(z)=1-(1+z)^{-1.5}$

Figure 6.7 : The steep-spectrum redshift distribution for sources in Selected Regions predicted by the HIGH-z version of RLF model 2, compared to the distribution on which the model was based.

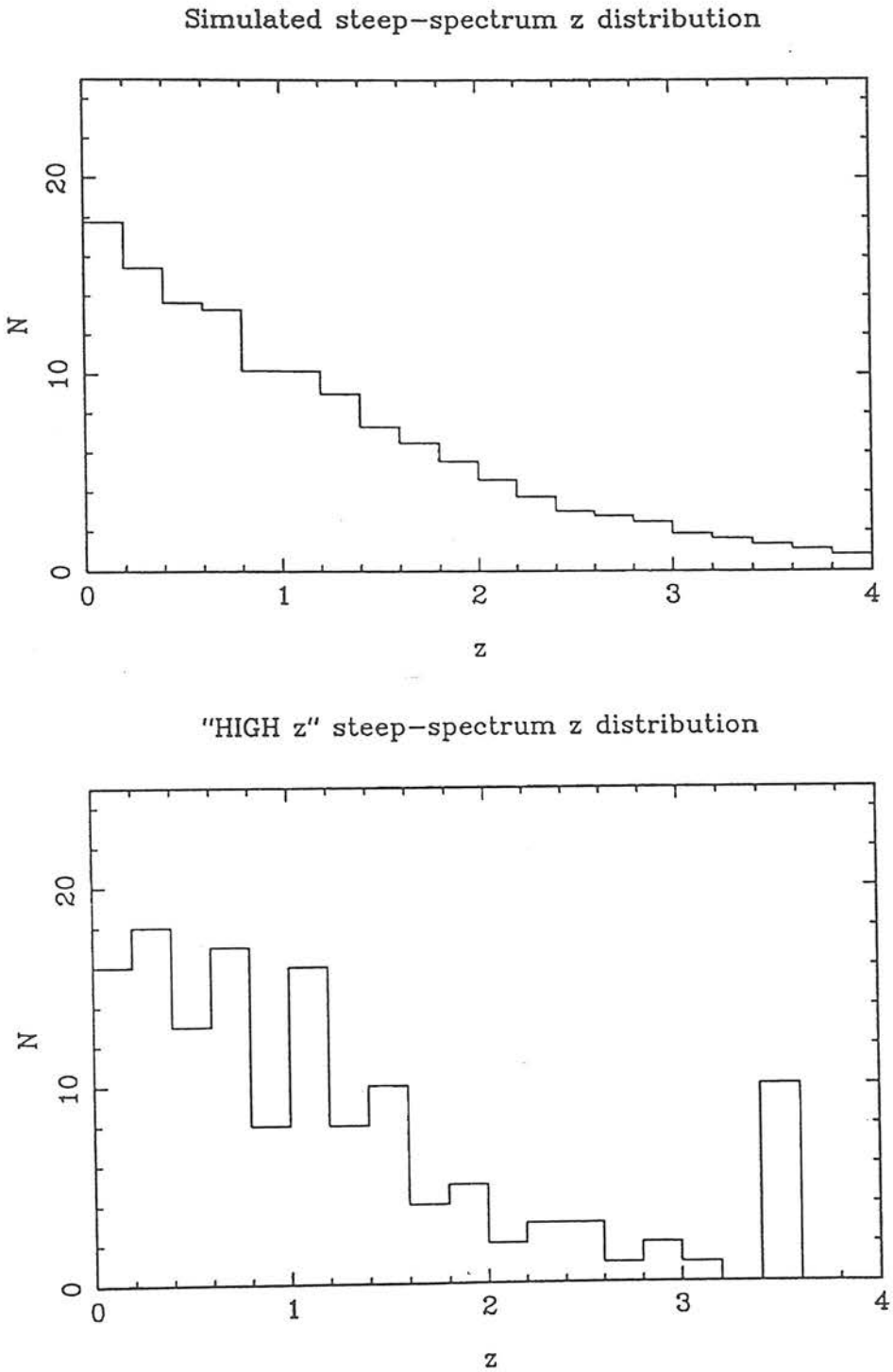

6.4 : DIRECT INVESTIGATION OF HIGH-REDSHIFT EVOLUTION

6.4a : Illustration of the redshift cutoff

The evidence for the high-redshift cutoff presented in the previous section was based on model fitting. However, as stressed in the introduction to that section, it is important to try to investigate in a model-independent manner the features which are displayed by the model RLFs. We cannot be sure of the reality of the redshift cutoff unless its existence can be deduced directly from the data. Figure 6.8 illustrates the complete sample data at 2.7GHz in the form of plots of luminosity against flux density. The estimated redshifts used to derive the luminosities are the MEAN-z estimates (see Section 6.2). Figure 6.8a shows all the flat- and steep-spectrum data. In Figures 6.8b and 6.8c the corresponding plots for the quasar and galaxy subsets are shown separately, and the sources with estimated redshifts are indicated.

These diagrams make it clear why it is necessary to study samples at flux densities as low as 0.1Jy in order to distinguish a redshift limit from a cutoff in luminosity at the upper end of the RLF. The diagonal line in these figures represents a redshift $z = 4$, and so it is apparent that the powerful sources (with luminosities $P_{2.7} \sim 10^{27}WHz^{-1}sr^{-1}$) which are present on these diagrams at high flux densities would lie at $z > 4$ if detected near the flux limit of the Selected Regions (ie $S_{2.7} > 0.1Jy$). The diagrams illustrate the lack of such sources in the Selected Regions and hence demonstrate pictorially the existence of the redshift cutoff for both flat- and steep-spectrum sources. Figure 6.8 also shows the range of luminosities for which the Selected Regions sample allows us to reach such a conclusion - fainter samples are necessary before any statement can be made concerning the behaviour of sources with $P_{2.7} \leq 10^{25}WHz^{-1}sr^{-1}$ at $z > 2$.

Figure 6.8 : The complete sample data at 2.7GHz plotted on the $P(q_o=0.5)$ - S plane. The lines indicate the flux density limits of the various samples and the area of the P - z plane in which an object with z > 4 would lie. The estimate redshifts for the Selected Region galaxies are the MEAN-z estimates discussed in Section 6.2.

a) ALL DATA

Flat-Spectrum

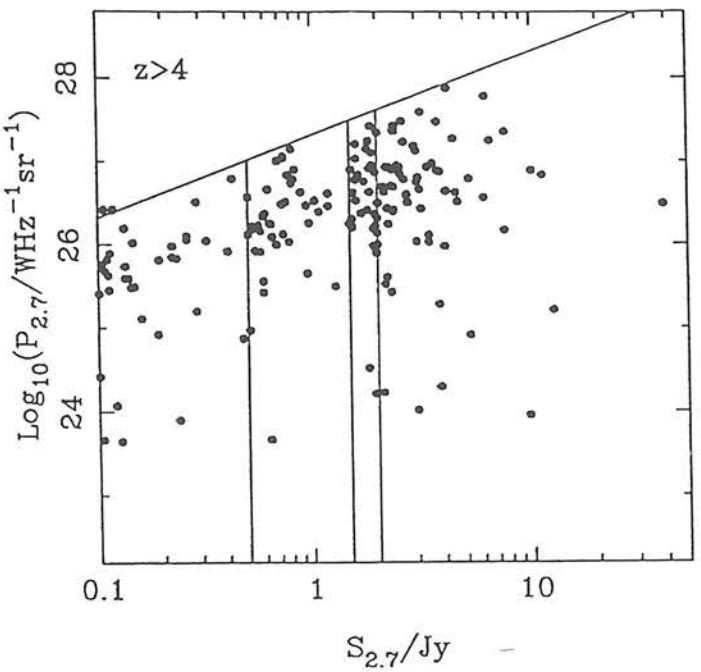

Steep-Spectrum

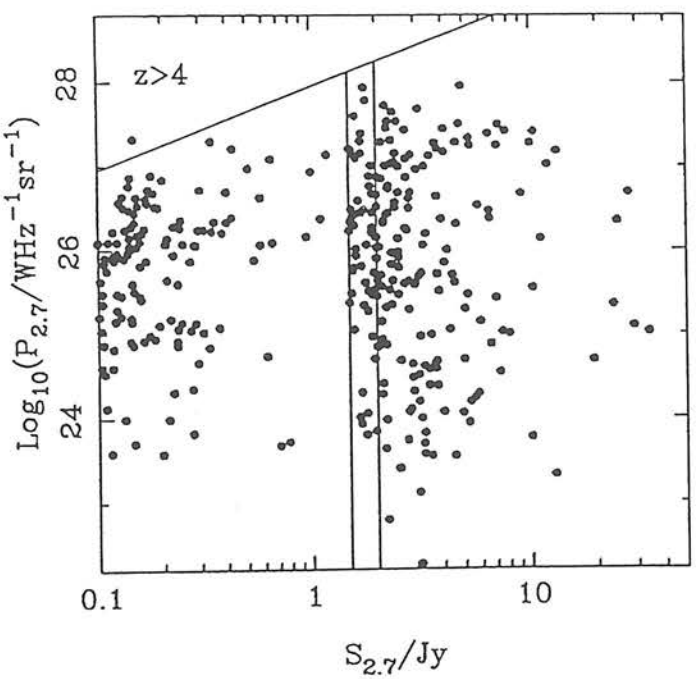

b) QUASARS ONLY - sources with estimated redshifts are shown as open circles.

Flat-Spectrum Quasars

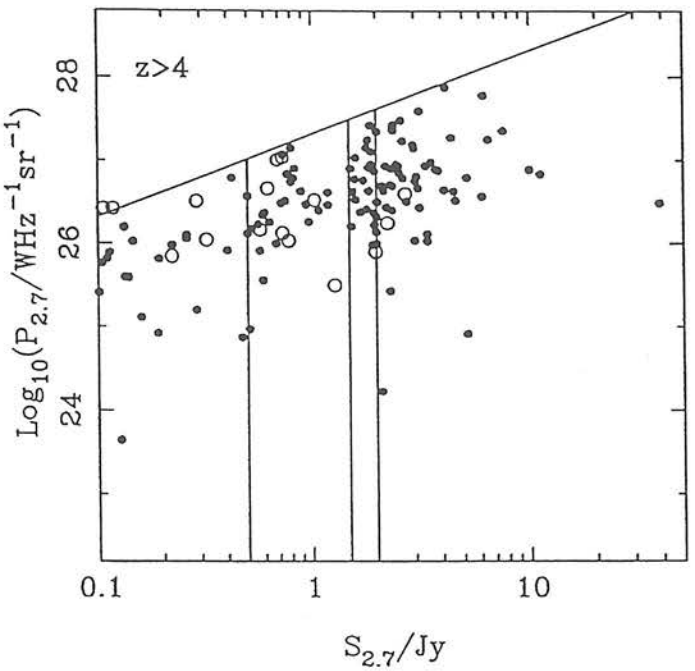

Steep-Spectrum Quasars

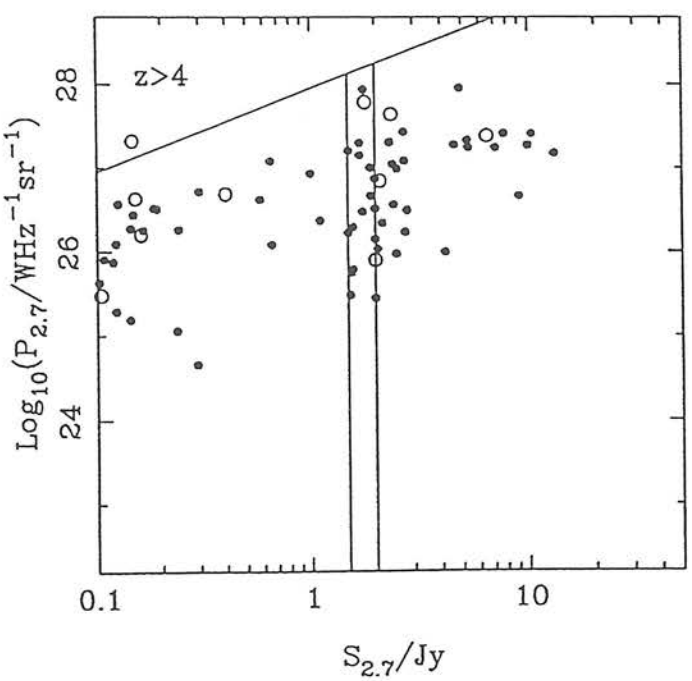

c) GALAXIES ONLY - sources with estimated redshifts are shown as open circles.

Flat-Spectrum Galaxies

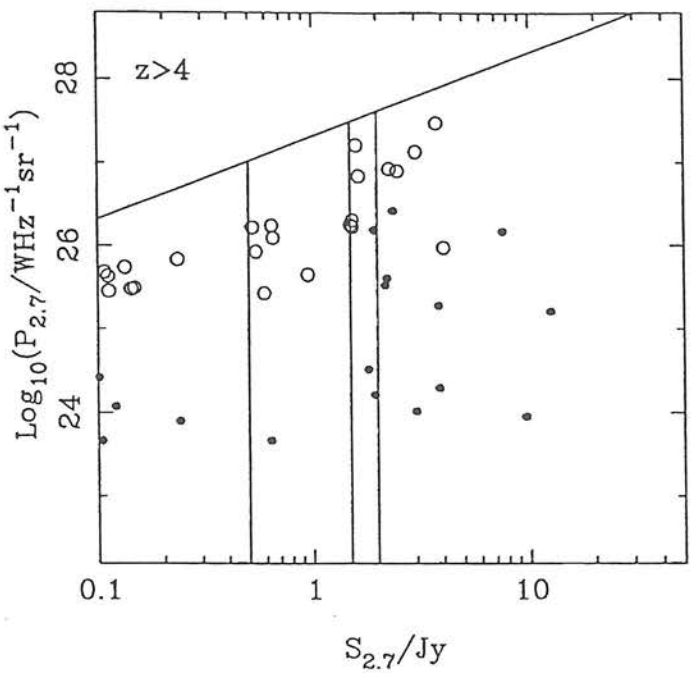

Steep-Spectrum Galaxies

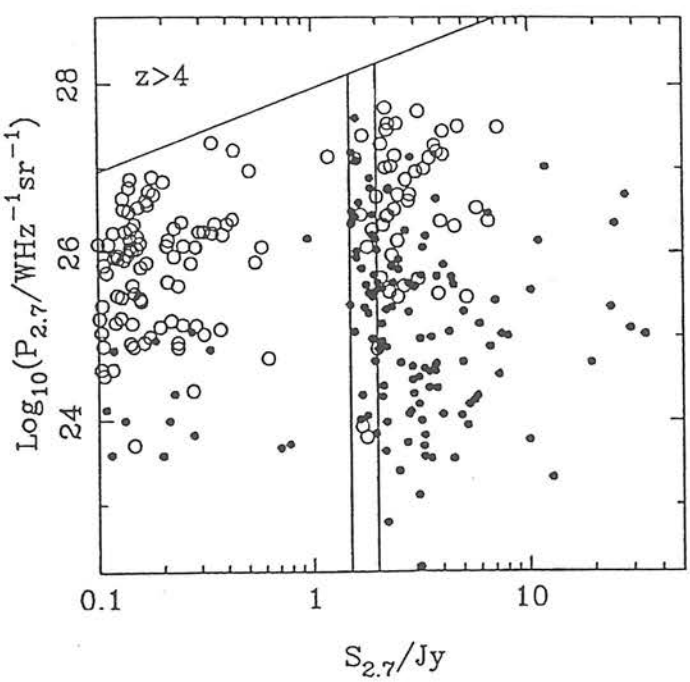

6.4b : Quantifying the cutoff via the V/V_{max} test

A useful model-independent way of quantifying the high-redshift deficit illustrated in Figure 6.8 is the V/V_{max} test (developed independently by Schmidt 1968, and Rowan-Robinson 1968). V is the cosmological volume enclosed by an object and V_{max} is the volume that would be enclosed by the same object if it were pushed out to the flux density limit of its parent sample. Under the null hypothesis of uniform distribution in space, the individual values of V/V_{max} for objects in a flux-limited sample should be uniformly distributed between 0 and 1, and $\langle V/V_{max} \rangle$ should be $0.5 \pm (12N)^{-0.5}$, where N is the number of objects in the sample. Values of $\langle V/V_{max} \rangle > 0.5$ indicate a bias of objects towards the more distant regions of their accessible volumes, and hence correspond to an increase in comoving density with redshift. Conversely, values < 0.5 indicate a deficit of high-redshift objects. This test has been applied to many radio samples over the years in order to demonstrate the strong positive evolution of radio sources between $z = 0$ and $z \sim 2$. Generally values in the range $0.6 \rightarrow 0.7$ have been found (eg Wills & Lynds 1978, Peacock *et al.* 1981) - as demonstrated by Longair (1978), $\langle V/V_{max} \rangle = 0.7$ implies a density increase over present day numbers at $1 < z < 3$ of ~ 1000.

The V/V_{max} test can therefore also be used to quantify the existence or otherwise of negative evolution beyond $z \sim 2$. For the present study the basic test had to be modified in two ways. Firstly, in order to apply the test to the complete combined 2.7GHz sample (discussed in Section 6.2a) the coherent V_e/V_a statistic of Avni & Bahcall (1980) was used. This is a generalization of the classical test which enables analysis of a combined sample in which V_e (volume enclosed) and V_a (volume available) are volumes which depend on the survey depth as a function of sky area. Secondly, in order to avoid any high-redshift negative evolution being masked by the known strong, positive, low-redshift evolution described above, a banded version of the test was required (Osmer & Smith 1980, Avni & Schiller 1983) ie

$$\left\langle \frac{V_e - V_o}{V_a - V_o} \right\rangle \qquad (6.5)$$

where V_o is the cosmological volume enclosed by a redshift z_o.

The results of the banded V_e/V_a calculation are shown in Table 6.4 (for the MEAN-z data). The most important feature of these results is that the value of $\langle V_e-V_o/V_a-V_o \rangle$ is less than 0.5 for both flat- and steep-spectrum sources, irrespective of geometry. Also, in both cases the value becomes progressively smaller as z_o is increased. This result is also individually true for both quasar and galaxy subsets of the two spectral classes.

This, therefore, is model-independent confirmation of the results of Section 6.3, ie that the comoving density of both flat- and steep-spectrum sources declines beyond $z \sim 2$. The flat-spectrum result is dominated by the quasar contribution (as is clear from Table 6.4) and hence is essentially secure. This quasar domination also results in the very poor statistics for high-redshift flat-spectrum galaxies in Table 6.4, but the values of $\langle V_e/V_a \rangle$ are still significantly less than 0.5.

The steep-spectrum quasars exhibit the same high-redshift trend as their flat-spectrum counterparts, although the statistics are rather poorer. This may be taken as evidence that the cutoff for flat-spectrum quasars is genuine, and not simply caused by re-classification as steep-spectrum at high z (as suggested by Savage & Peterson 1983).

Finally, it is interesting to explore the sensitivity of the new steep-spectrum results to the estimated redshifts, as was done with the models in Section 6.3. In Table 6.5 the steep-spectrum $\langle V_e/V_a \rangle$ results based on the MEAN-z estimates are compared with those derived from the HIGH-z distribution (see Section 6.2b). As was found with the modelling, the HIGH-z results do not require the steep-spectrum RLF to turn over at $z \sim 2$. However, it is evident from Table 6.5 that the HIGH redshift estimates have not removed the redshift cutoff, but merely postponed it to $z \sim 2.5$. Several of the galaxies which were assigned $z = 3.5$ in the HIGH-z distribution would

therefore in fact have to be at still higher redshift to be consistent with no turnover in the steep-spectrum RLF. Such a prospect seems highly unlikely.

Table 6.4 : $\langle V_e/V_a \rangle$ results (MEAN-z estimated galaxy redshifts)

i) ALL SOURCES

	Flat-spectrum			Steep-spectrum		
		$\langle V_e/V_a \rangle$			$\langle V_e/V_a \rangle$	
Redshift range	n	Ω=1	Ω=0	n	Ω=1	Ω=0
> 1.8	31	0.393	0.433	32	0.428	0.460
> 1.9	29	0.357	0.386	28	0.409	0.442
> 2.0	25	0.328	0.359	23	0.395	0.423
> 2.1	20	0.332	0.360	17	0.475	0.495
> 2.3	14	0.307	0.348	15	0.386	0.408
> 2.5	12	0.226	0.271	13	0.279	0.286

ii) QUASARS ONLY

	Flat-spectrum			Steep-spectrum		
		$\langle V_e/V_a \rangle$			$\langle V_e/V_a \rangle$	
Redshift range	n	Ω=1	Ω=0	n	Ω=1	Ω=0
> 1.8	29	0.403	0.460	11	0.509	0.525
> 1.9	27	0.372	0.403	11	0.452	0.470
> 2.0	24	0.342	0.374	10	0.417	0.431
> 2.1	20	0.332	0.360			
> 2.3	14	0.307	0.348			
> 2.5	12	0.226	0.271			

iii) GALAXIES ONLY

	Flat-spectrum			Steep-spectrum		
		$\langle V_e/V_a \rangle$			$\langle V_e/V_a \rangle$	
Redshift range	n	Ω=1	Ω=0	n	Ω=1	Ω=0
> 1.8	2	0.246	0.276	21	0.386	0.426
> 1.9	2	0.143	0.157	17	0.382	0.424
> 2.0				13	0.377	0.418
> 2.1				10	0.439	0.471
> 2.3				9	0.336	0.365
> 2.5				9	0.146	0.155

Table 6.5 : Effect of redshift estimation on the steep-spectrum $\langle V_e/V_a \rangle$ results

	MEAN-z estimates			HIGH-z estimates		
		$\langle V_e/V_a \rangle$			$\langle V_e/V_a \rangle$	
Redshift range	n	Ω=1	Ω=0	n	Ω=1	Ω=0
> 1.9	28	0.409	0.442	33	0.501	0.527
> 2.1	17	0.475	0.495	24	0.549	0.588
> 2.3	15	0.386	0.408	23	0.471	0.495
> 2.5	13	0.279	0.286	19	0.484	0.501
> 2.7				16	0.459	0.486
> 2.9				13	0.442	0.476
> 3.1				12	0.352	0.399
> 3.3				11	0.218	0.264

6.4c : Direct determination of the RLF

None of the approaches considered earlier in this chapter (eg modelling, V/V_{max} tests etc) would be necessary if it were possible to determine directly the evolution of the RLF by simple binning in luminosity and redshift. This straightforward approach has been used to determine the evolution of the luminosity function of optically-selected quasars (eg Boyle *et al.* 1987a, 1987b). The reason it has not previously been used to determine the evolving RLF is the same as the one given earlier (in Section 6.3a) for the value of the modelling approach - ie poor coverage of the P-z plane. However, in view of the recent extension of the complete 2.7GHz data to 0.1Jy, it was decided to attempt this type of direct evaluation.

The coverage of the P-z plane provided by the combined 2.7GHz sample is shown in Figure 6.9 (for Ω = 1, MEAN-z estimates). The diagonal curves are the flux-density limits of the various contributing samples, and demonstrate the importance of the flux-density extension provided by the Selected Regions. The data shown in this figure were binned into bins of width 0.5 in $\log_{10}P$,

Figure 6.9 : The coverage of the P-z plane provided by the complete sample database at 2.7GHz (see Section 6.2a). The open circles are sources with estimated redshifts (MEAN-z estimates for galaxies) and the diagonal curves are the flux density limits of the individual samples.

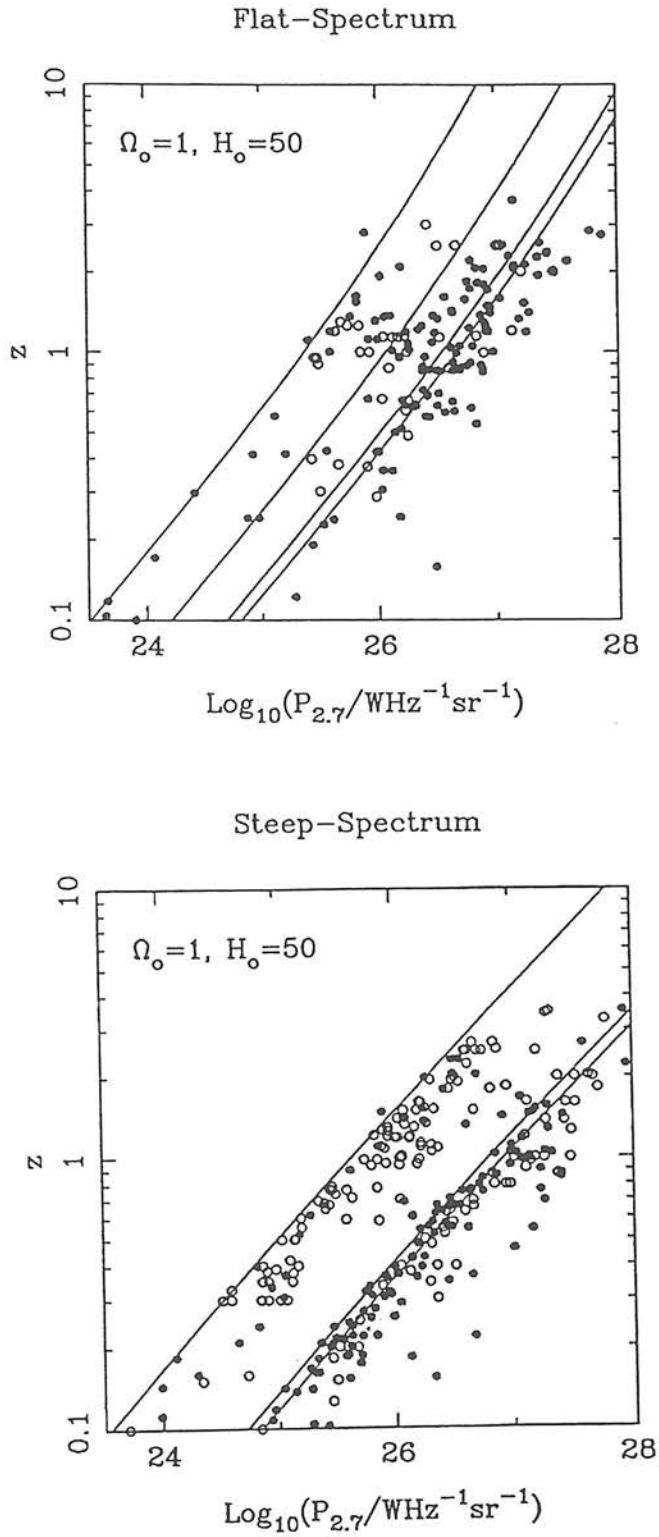

and 0.2 in $\log_{10}z$. The value of the luminosity function at each sampling point was then determined from the sum of the inverse of the volumes available (in the combined sample) to each source in the bin - ie

$$\sum_{i=1}^{n} (1/V_a)_i \qquad (6.6)$$

For bins crossed by the absolute sample limit of 0.1Jy this procedure simply results in a biassing of the true centroid of the bin to higher powers and lower redshifts.

The results of this calculation are presented in Figures 6.10 and 6.11. In Figure 6.10 the RLF is plotted at various redshifts. The evolution of the RLF out to $z \sim 2$ is clearly seen in both the flat- and steep-spectrum cases. Unfortunately, the data do not extend to low enough powers to enable the basic form of this evolution to be distinguished as density or luminosity evolution (see Section 6.5). At $z \sim 3$ the luminosity baseline is inevitably restricted and the statistics rather poor, and we pay a price for the inefficient use that is made of the data by binning. However it is clear that the evolution has certainly stopped and very probably reversed (except possibly at the very highest luminosities). In Figure 6.11 the results of the direct determination are shown superimposed on the range of RLFs allowed by the model ensemble (see Section 6.3e). Here the width of the luminosity bins have been doubled to improve the statistics. This figure provides further evidence of the validity of the model RLFs, and demonstrates that evidence for the existence of the redshift cutoff is indeed present in the raw data.

Figure 6.10 : The evolution of the flat- and steep-spectrum RLF as determined from simple binning of the 2.7GHz data illustrated in Figure 6.9.

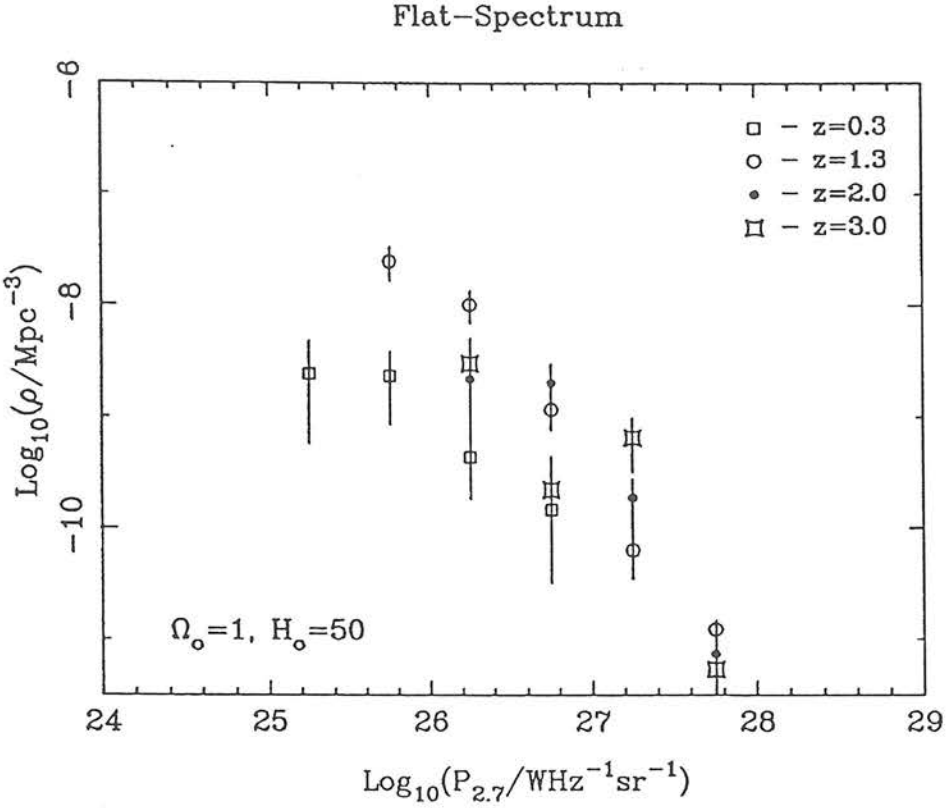

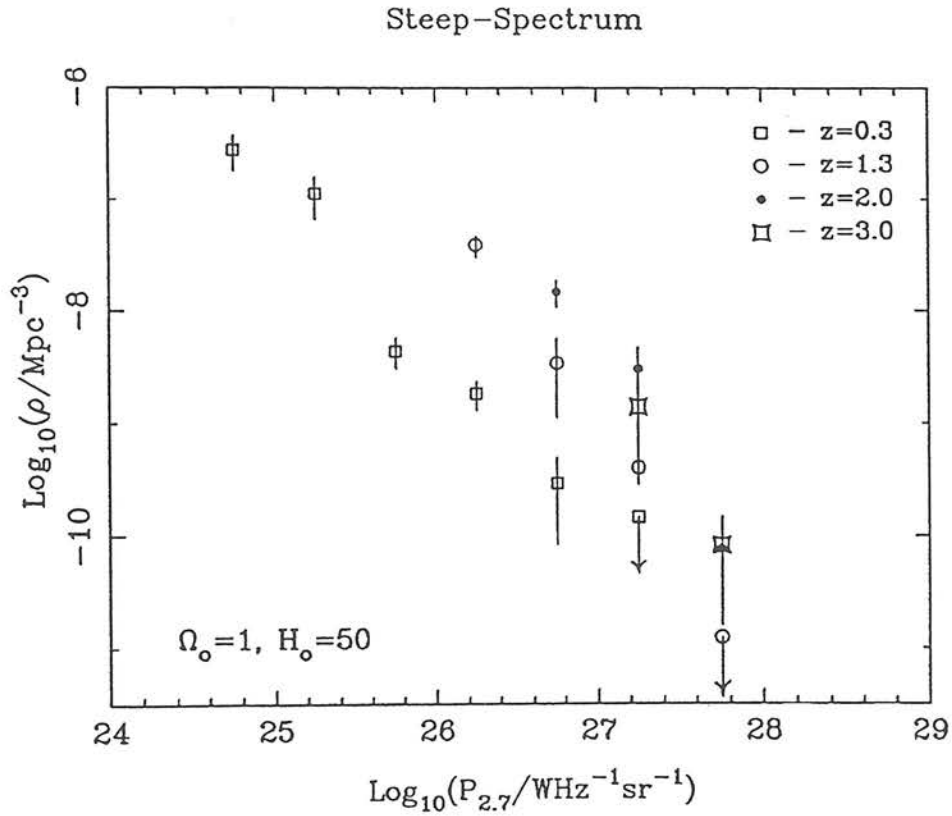

Figure 6.11 : The results of the direct determination of the RLF superimposed on the limits to ρ allowed by the model RLF ensemble (see Section 6.3e). Two slices at constant luminosity are shown, $P_{2.7} = 10^{27}$ & 10^{26} $WHz^{-1}sr^{-1}$. The flat-spectrum RLF is indicated by dashed lines and open circles, the steep-spectrum RLF by solid lines and filled circles.

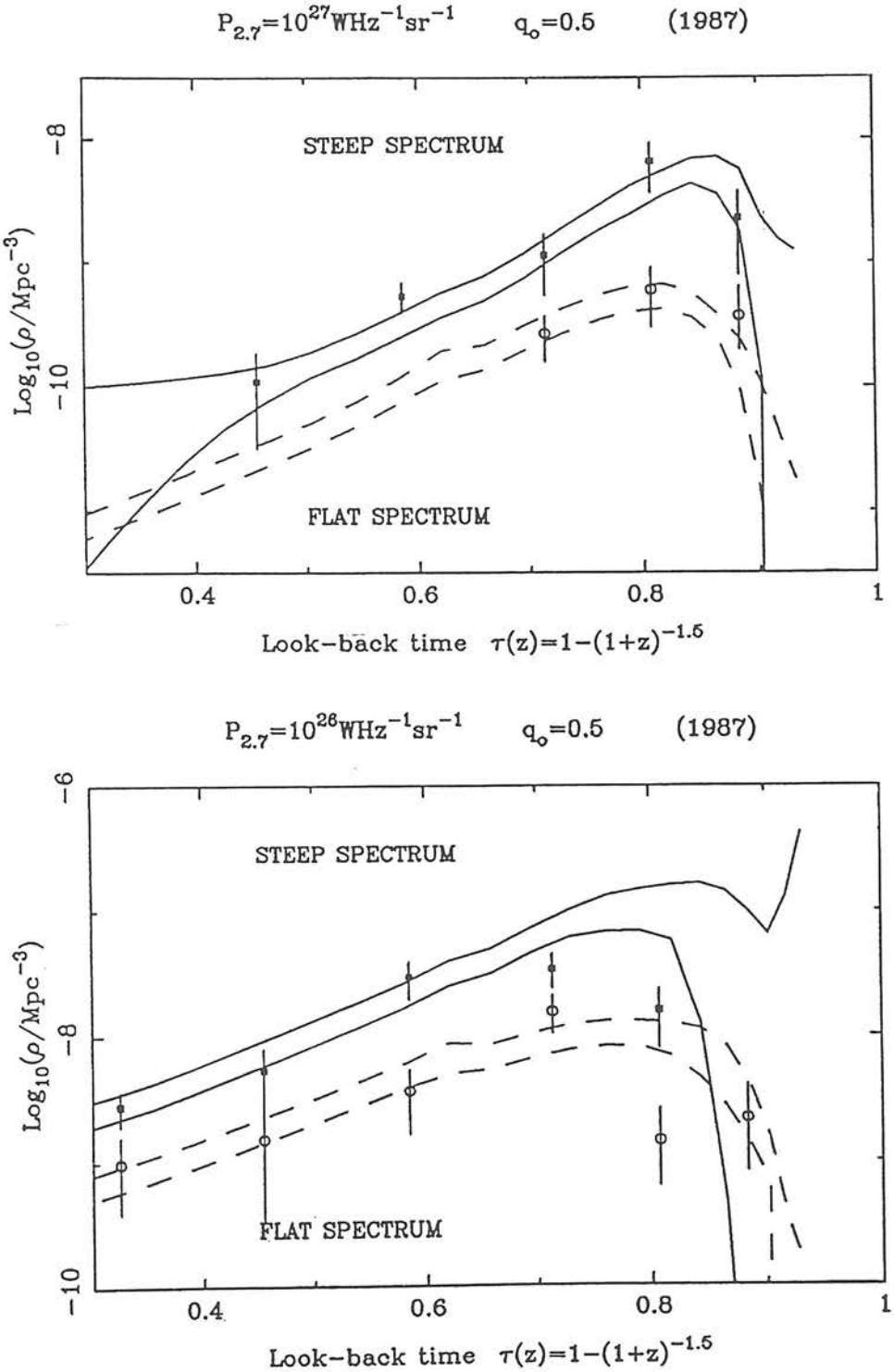

6.5 : PURE LUMINOSITY EVOLUTION AS A MODEL OF THE EVOLVING RLF

6.5a : Background

So far in this Chapter no attempt has been made to describe the evolution of the RLF by a simple parametric form, such as pure luminosity evolution, pure density evolution, or some combination of the two. Indeed one of the objectives of the free-form modelling was to avoid any such preconceived assumptions concerning the form of evolution. However, given the recent interest in pure luminosity evolution as a model for the evolution of optically-selected quasars (Koo 1986b, Shanks *et al.* 1986, Marshall 1986, Boyle *et al.* 1987a, 1987b), it is interesting to explore whether this simple form is also an acceptable description of the evolving RLF.

For the two extreme possibilities of pure luminosity evolution and pure density evolution to be distinguished, the luminosity function must contain some feature whose progress with redshift can be monitored. Only then is it possible to determine whether the luminosity function shifts horizontally in the (ρ,P) plane with redshift (ie luminosity evolution) or vertically (ie density evolution). In the case of optically-selected quasars such a feature is indeed present in the form of a "break" in the optical luminosity function - at low luminosities the luminosity function is well described by a power law of relatively shallow slope ($P^{-0.25}$), but above some critical power ($P_c \equiv M_B=-21.8$) a steeper slope is required ($P^{-2.6}$). To investigate the movement of this feature with redshift it is necessary to study large samples of quasars which are faint enough to sample luminosities below the "break", even at large redshifts. The recent results of Boyle *et al.* (1987a) suggest that the luminosity function shifts horizontally in the (ρ,P) plane (parameterized by $P \propto (1+z)^k$, $k = 3.5 \pm 0.3$ for $\Omega = 1$), consistent with the picture of pure luminosity evolution.

In the case of the RLF, comparison of the direct determination of the RLF at $z = 0.3$ (shown in Figure 6.10) with the local RLF (shown in Figure 6.3) suggests that the RLF may also be well described by a

two power-law form (with a "break" luminosity of $P \sim 10^{25} WHz^{-1}sr^{-1}$ at $z \sim 0$), with possibly the addition of a non-evolving low-power component (representing the spiral/irregular radio galaxy population) to account for the features in the local RLF. Such a form is also indicated by the mean values of the free-form models of Section 6.3. Unfortunately, as is clear from Figure 6.10, the complete sample data do not extend to low enough luminosities to enable the movement of this "break" to be followed, and hence determine unambiguously the form of the evolution. It is possible however to investigate whether pure luminosity evolution is consistent with the radio database which was used to construct the free-form models in Section 6.3.

It is also interesting to consider the implications of pure luminosity evolution at high redshift. Because most of the optical studies are largely based on UVX quasars, the evolution of the quasar optical luminosity function has only been investigated out to $z \sim 2$. As stated above, this evolution can be parameterized by $(1+z)^k$ and so is consistent with continuing POSITIVE luminosity evolution out to $z \sim 2$ (although it is clear that such evolution cannot continue at higher redshift - see Chapter 8, Section 8.2) However since, as established earlier in this Chapter, the RLF is constrained to decline at high redshift, a pure luminosity evolution model of the RLF cannot continue to evolve in the same direction beyond $z \sim 2$. Either the direction of luminosity evolution must reverse, or a depression in comoving density must occur at high redshift. These possibilities are investigated below.

6.5b : A model of pure luminosity evolution

i) Formulation

The model of luminosity evolution was formulated as follows. The RLF was considered to be the sum of two components, a high-power evolving component ϱ_h, and a low-power non-evolving component ϱ_l. Physically, the idea here is to try to fit Pure Luminosity Evolution to the powerful Elliptical radio galaxy population (described by ϱ_h), while assuming no evolution for the Spiral/Irregular galaxy

population (described by ρ_l) which dominates at the lowest radio powers) ie

$$\rho_t(P,z) = \rho_l(P) + \rho_h(P,z) \qquad (6.7)$$

ρ_h is the evolving two power-law RLF, analogous to the evolving quasar optical luminosity function.

$$\rho_h = \rho_o\left[\left[\frac{P}{P_c(z)}\right]^{\alpha} + \left[\frac{P}{P_c(z)}\right]^{\beta}\right]^{-1} \qquad (6.8)$$

where α and β are the two power-law slopes, $P_c(z)$ is the evolving "break" luminosity, and ρ_o is determined by normalization at $z = 0$. The redshift dependence of P_c was parameterized as a quadratic in order to permit the possibility of negative luminosity evolution at high redshift. ie

$$\log_{10}(P_c(z)) = a_o + a_1 z + a_2 z^2 \qquad (6.9)$$

ρ_l was parameterized as a power-law expansion in luminosity (terminated after the same number of terms as in the case of the free-form modelling) ie

$$\log_{10}(\rho_l) = b_o + b_1(PP) + b_2(PP^2) + b_3(PP^3) + b_4(PP^4) + b_5(PP^5) + b_6(PP^6) \qquad (6.10)$$

where $PP = 0.1(\log_{10}P - 20)$.

ii) Results

As in the free-form modelling, the flat- and steep-spectrum RLFs were modelled independently and a density parameter of $\Omega = 1$ was assumed. An acceptable fit was achieved at the same level (ie ~ 1%) as that achieved by the free-form models (see Section 6.3). Moreover, in the case of the flat-spectrum RLF, ρ_l was found to be superfluous since the fitted low-power section of ρ_h (ie $\rho \propto P^{-0.88}$) is itself consistent with the flat-spectrum local RLF. This fact is illustrated in Fig 6.12 which shows the local RLF predicted by the luminosity

evolution model after rejection of the flat-spectrum ρ_l. Comparison with the local RLF data shown in Figure 6.3 makes it clear that no extra low-power component is required in the flat-spectrum RLF, but in the steep-spectrum case, ρ_l is necessary to model the structure seen at lower powers. This empirical result may be understood as reflecting the known fact that, whereas the flat-spectrum local RLF continues to be dominated by elliptical galaxies down to low powers, the steep-spectrum local RLF contains additional spiral and irregular galaxy components at low power. ρ_h could therefore be interpreted as the luminosity function of elliptical radio galaxies.

As with the free-form models, the model was derived for each of the 3 datasets, MEAN-z, LOW-z and HIGH-z, and an acceptable fit achieved in all 3 cases. The best fitting model parameters are given in Table 6.6. This model was incorporated into the model ensemble of Section 6.3 as RLF6.

The results of the luminosity evolution model are presented in Figure 6.13 in which the model RLF is shown at various redshifts (these results are for the MEAN-z model, but, as is apparent from Table 6.6, the properties of the model are not significantly altered by the change of datasets). Both flat- and steep-spectrum RLFs display positive luminosity evolution out to $z \sim 2$, but by $z \sim 3$ the evolution has reversed, and at $z \sim 4$ the RLF is approaching the local value once again (the flat-spectrum behaviour is remarkably symmetric in redshift space). These results are therefore consistent with a decline in comoving density at a given luminosity beyond $z \sim 2$. It is interesting that this simple model, with its much smaller number of free parameters, provides as good a fit to the data as was achieved by the truly free-form models of Section 6.3.

Following this successful fitting of pure luminosity evolution with $\Omega = 1$, the model was re-attempted assuming $\Omega = 0$. A successful fit (ie $p > 0.1$) was not achieved in the new geometry (in fact $p < 10^{-5}$). This result is sensible because it is clear that pure luminosity evolution should not be able to work for all values of Ω. Note that in contrast to this, Boyle *et al.* (1987a) claimed to be able to fit pure luminosity evolution to the quasar optical luminosity function in both

critical and empty universes. This fact would seem to indicate that the form of the evolving RLF is better constrained at present than the form of its optical quasar counterpart. Alternatively it might simply reflect the extra sensitivity to cosmology which results from probing out to redshifts $z > 2$.

Figure 6.12 : The flat- and steep-spectrum local RLF predicted by the model of pure luminosity evolution (cf Figure 6.3). In addition to the two power-law RLF, a non-evolving low-power component is required to fit the structure in the steep-spectrum local RLF (these two components are shown separately by dashed and dotted lines respectively). No such extra component is required in the flat-spectrum case.

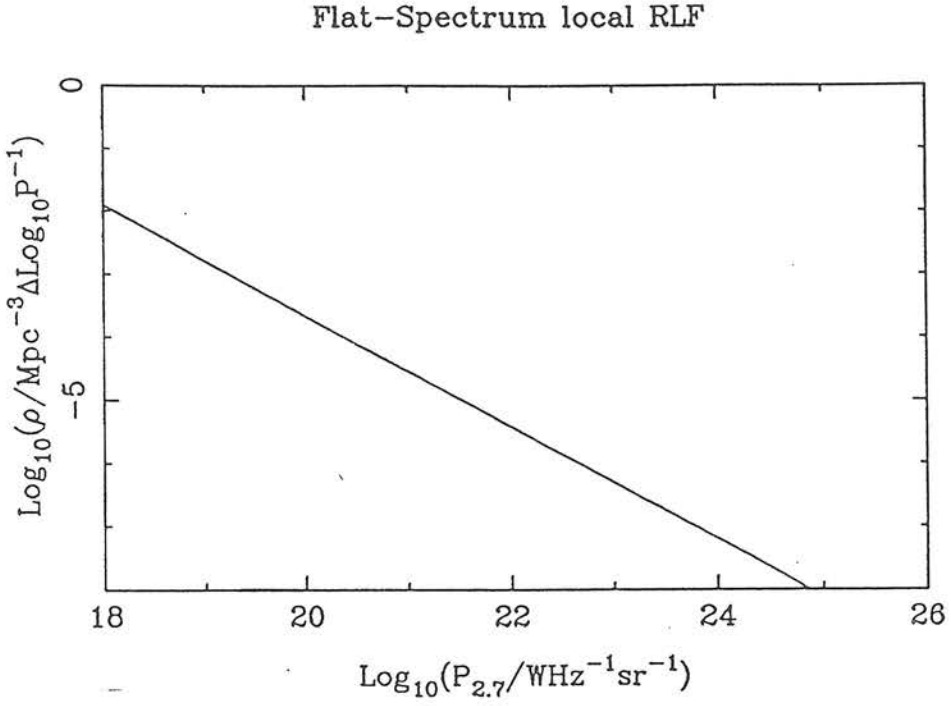

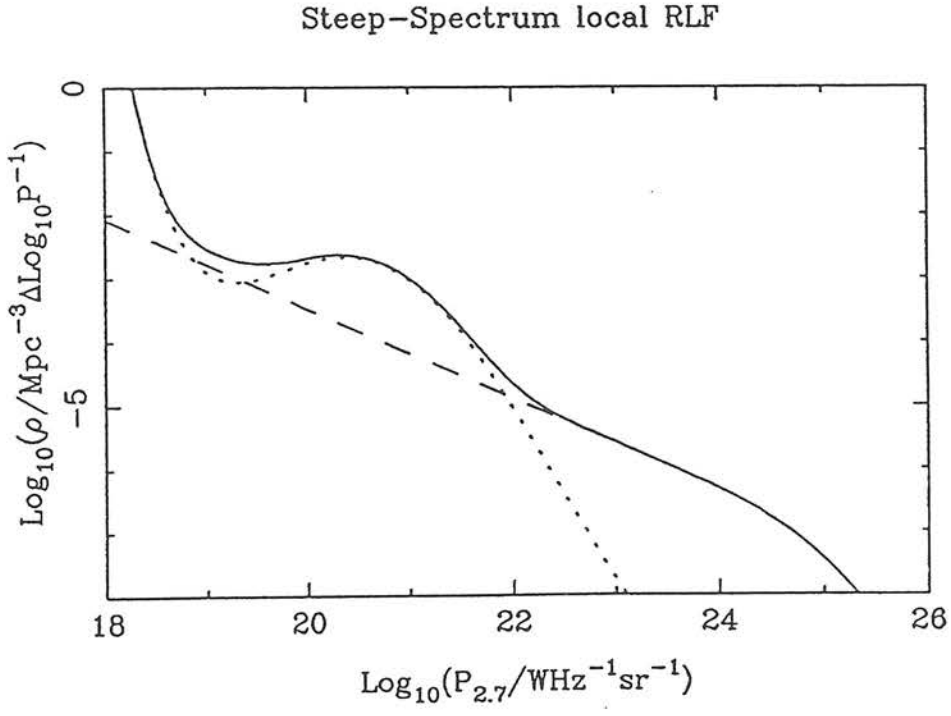

Table 6.6 : Best fit model parameters for pure luminosity evolution (Ω = 1).

i) STEEP-SPECTRUM

parameter	MEAN-z	LOW-z	HIGH-z
ρ_o	-6.84	-6.82	-7.04
α	0.70	0.70	0.75
β	2.06	2.07	2.14
a_o	24.80	24.79	25.00
a_1	1.27	1.28	1.09
a_2	-0.27	-0.28	-0.19
b_o	-2.76	-2.76	-2.94
b_1	4.60	4.57	7.50
b_2	-40.73	-40.60	-22.99
b_3	-503.00	-503.15	-706.87
b_4	1987.85	1985.78	1520.62
b_5	-2439.93	-2434.13	-231.59
b_6	975.16	971.08	-721.13

ii) FLAT-SPECTRUM

parameter	MEAN-z	LOW-z	HIGH-z
ρ_o	-8.52	-8.55	-8.52
α	0.88	0.88	0.88
β	2.21	2.24	2.19
a_o	25.52	25.55	25.52
a_1	1.22	1.20	1.22
a_2	-0.30	-0.29	-0.30

Figure 6.13 : The evolving RLF predicted by the pure luminosity evolution model. $Log_{10}\rho$ is plotted against $Log_{10}P$ at z = 0,1,2,3,4.

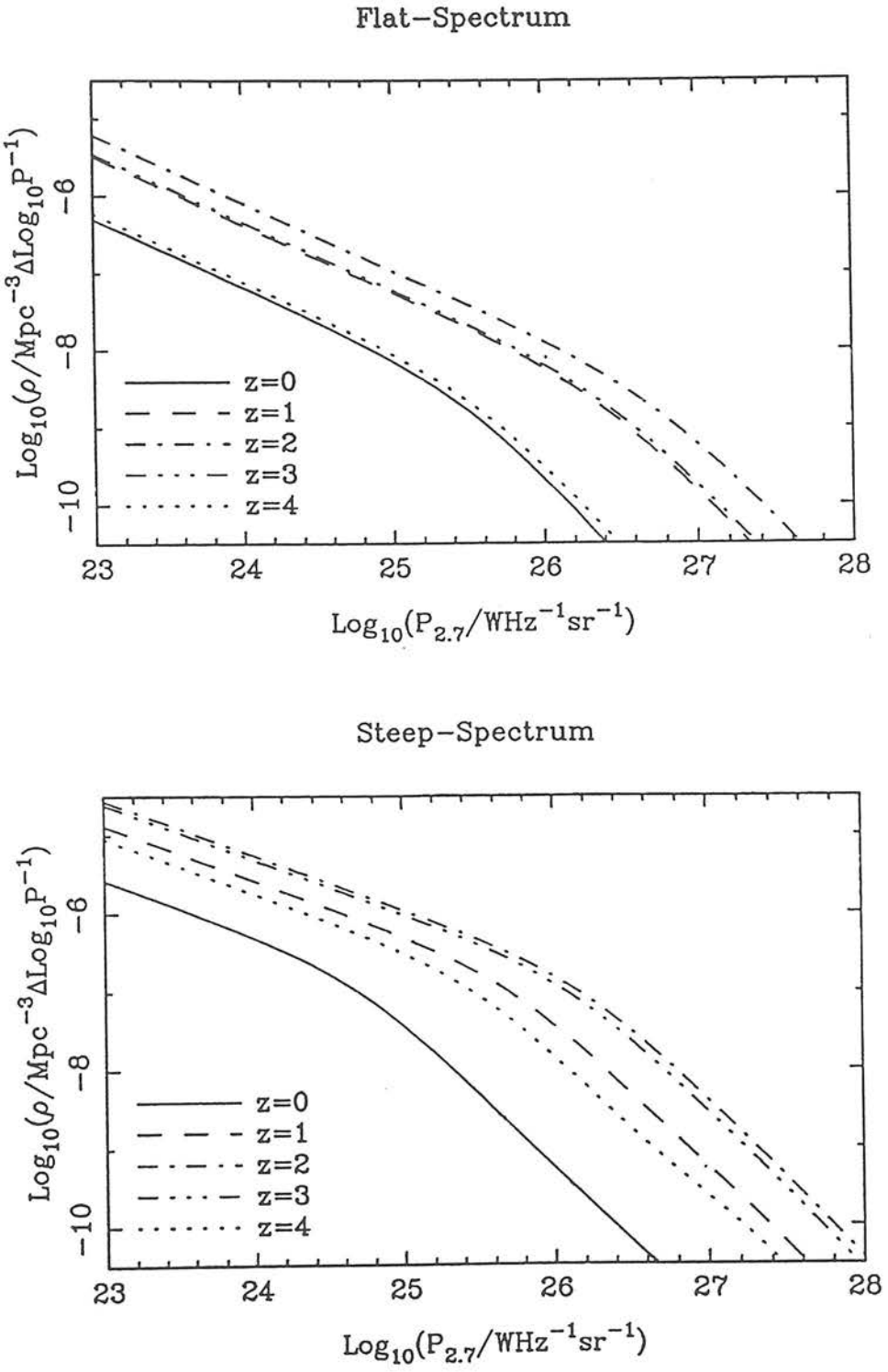

6.5c : Alternative forms of evolution at high redshift

Because of the restriction of pure luminosity evolution, the model described in the previous section is obliged to display negative luminosity evolution beyond $z \sim 2$ in order to conform with the high z cutoff. However, continuing positive luminosity evolution beyond $z \sim 2$ could possibly be reconciled with the redshift cutoff, if it were combined with negative density evolution. The motivation for considering this form of high-redshift evolution is that it naturally results in a redshift cutoff which is differential in radio power, and hence predicts that any radio sources discovered at very high redshifts (ie $z \sim 3$–4) are likely to be extremely luminous. Such an effect would explain why PKS 1351-018, which is the most distant known object in the Selected Regions, has a radio flux density a factor of 10 higher than the limit of the survey. There have also been claims of a similar effect in the studies of optically-selected QSOs at high redshift (see Chapter 5, Section 5.4b).

To investigate the possibility of such luminosity/density evolution at high z, the pure luminosity evolution model of Section 6.5b was modified to allow ρ_o to vary with z at redshifts $z > 1$. The adopted form was simply a quadratic function:

$$\log_{10}(\rho_o(z)) = c_o + c_1(z-1) + c_2(z-1)^2 \qquad \text{for } z > 1 \qquad (6.11)$$
$$\log_{10}(\rho_o) = c_o \qquad \text{for } z \leqslant 1$$

Once again $\Omega = 1$ was assumed and the model was derived using MEAN-z, LOW-z and HIGH-z datasets. An acceptable fit was achieved in all 3 cases and the best fit parameters are given in Table 6.7. This model was incorporated into the model ensemble of Section 6.3 as RLF7.

The results of this model are presented in Figure 6.14. Comparison of this figure with Figure 6.13 shows that, despite the introduction of the option of density evolution at $z > 1$, the new model has still chosen negative luminosity evolution as the dominant effect in modelling the high-redshift cutoff. It is of course possible that the particular parameterization of the high-redshift density decline used

here is not appropriate. A fuller investigation of the range of acceptable forms is obviously needed.

Table 6.7 : Best fit model parameters for luminosity/density evolution (Ω = 1).

i) STEEP-SPECTRUM

parameters	MEAN-z	LOW-z	HIGH-z
c_o	-6.80	-6.81	-6.77
c_1	-0.45	-0.42	-0.61
c_2	0.18	0.17	0.19
α	0.72	0.73	0.72
β	2.07	2.08	2.06
a_o	24.76	24.77	24.75
a_1	1.34	1.36	1.28
a_2	-0.28	-0.29	-0.23
b_o	-2.90	-2.90	-2.89
b_1	6.63	6.69	6.58
b_2	-21.86	-22.28	-22.84
b_3	-674.48	-675.02	-669.28
b_4	1465.42	1479.67	1485.80
b_5	-272.39	-304.89	-344.74
b_6	-646.43	-626.11	-595.15

ii) FLAT-SPECTRUM

parameters	MEAN-z	LOW-z	HIGH-z
c_o	-8.08	-8.12	-8.03
c_1	-1.11	-1.15	-1.09
c_2	0.44	0.44	0.43
α	0.86	0.86	0.85
β	2.05	2.07	2.02
a_o	25.03	25.07	25.00
a_1	1.61	1.60	1.61
a_2	-0.37	-0.36	-0.37

Figure 6.14 : The evolving RLF predicted by the luminosity/density evolution model. $Log_{10}\rho$ is plotted against $Log_{10}P$ at z = 0,1,2,3,4.

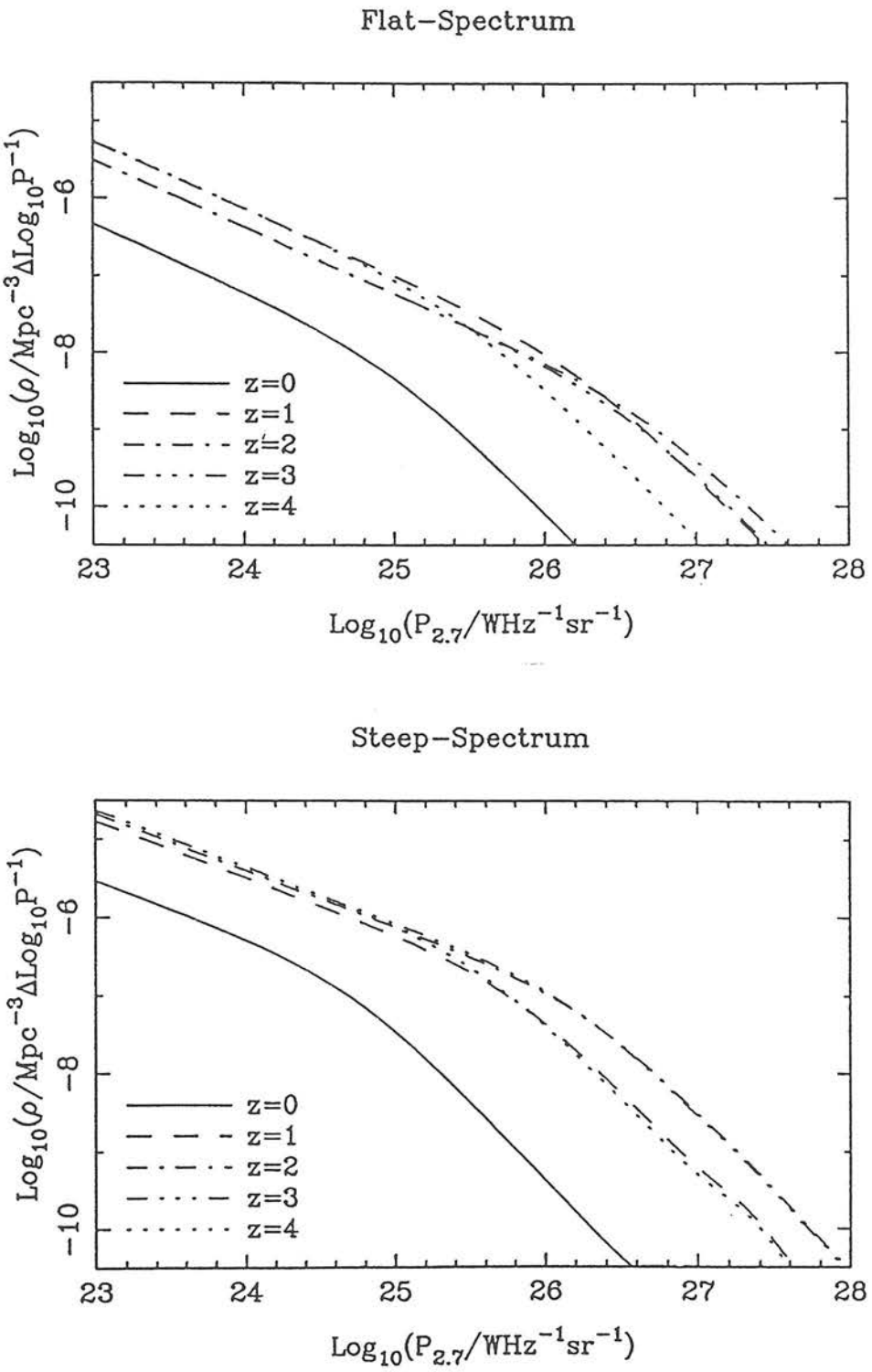

6.6 : CONCLUSIONS

The main conclusions from the work described in this chapter may be summarized as follows:

i) Modelling of the RLF shows that, unless highly unreasonable redshifts are assigned to the faintest galaxies in the Selected Regions, both steep- and flat-spectrum RLFs suffer a gradual redshift cutoff beyond $z \approx 2$. The comoving density of both classes of source declines by a factor ~ 10 between $z = 2$ and $z = 4$.

ii) The above result is confirmed directly by banded versions of the V/V_{max} test. All 4 classes of source - steep/galaxy, steep/quasar, flat/galaxy, flat/quasar - exhibit a density decline at high redshift, thus demonstrating that the cutoff is not due to problems with classification. Also, use of the HIGH-z estimates does not in fact remove the cutoff in the steep-spectrum RLF, but merely postpones it until $z \sim 3$.

iii) An attempt was made at direct calculation (via simple binning) of the RLF. This showed that, although such inefficient use of the data is possibly rather premature, the P-z data are in agreement with the models - evidence for a cutoff at $z > 2$ does exist in the raw data.

iv) A model of pure luminosity evolution can provide an adequate description of both the steep- and flat-spectrum RLFs, provided a high value of Ω is assumed. Negative luminosity evolution is required beyond $z \sim 2$. An additional, low-power, non-evolving component is required in the steep-spectrum case, but is superfluous for the flat-spectrum RLF. An attempt to fit a luminosity/density evolution model to the data was also successful, but no evidence was found in support of the idea that positive luminosity evolution continues at high redshift.

These results would seem to suggest that, at least as far as evolution is concerned, both flat- and steep-spectrum sources behave very similarly. The traditional, cautious, two-population approach may

therefore not in fact be necessary, and so, at least for powerful sources, it may now be sensible to talk about a SINGLE evolving RLF. Whether this can be taken as evidence in favour of unified beaming models (Orr & Browne 1982) is not so clear.

It is interesting to consider some of the possible interpretations of the redshift cutoff. The first question is whether such an effect could simply be an illusion - the result of obscuration at high redshift. The main process which might affect cm-wavelength radio emission is Thomson scattering due to an ionized intergalactic medium (IGM). However, as discussed by Peacock (1985), even if all the matter in the Universe is considered to be ionized, an optical depth of only $\tau = 0.2$ is achieved by $z \sim 4$. This can only reduce ρ by 0.2 in $\log_{10}\rho$, and the effect is even smaller between $z = 2$ and $z = 4$. It is therefore clear that, at radio wavelengths, obscuration cannot possibly account for the observed cutoff. However, at optical wavelengths Ostriker & Heisler (1984) demonstrated that obscuration by dust was capable of producing an apparent high-redshift cutoff. They also noted that, if this dust was unevenly distributed (eg associated with galaxies), the few visible high redshift objects could be seen through "holes", and need not therefore be heavily reddened. However, if dust obscuration was in fact a significant effect at optical wavelengths, then a considerable fraction of the Selected Regions radio sources should have remained unidentified. The fact that this is not the case gives confidence that studies of optically-selected quasars should also not be significantly influenced by obscuration.

It thus seems likely that the redshift cutoff for powerful radio sources is indeed real. It is possible to envisage a variety of scenarios which could give rise to this situation. The evolution of luminosity functions is governed by the conservation equation

$$\dot{\rho} + \frac{\partial}{\partial P}(\dot{P}\rho) = Q \qquad (6.12)$$

where Q is the rate of source creation. Possibly the most obvious interpretation of the cutoff is to envisage that radio sources were

formed during the era $z = 2 \rightarrow 4$, after which Q fell to zero and sources simply dimmed to the present day. However, the fact that radio sources are known to be short-lived (ie $\sim 10^8$ yr) relative to the age of the Universe indicates that $Q \neq 0$ at $z < 2$, and also means that one should be careful in interpreting the success of the pure luminosity evolution model in Section 6.5. The short lifetimes of radio sources has often led to the interpretation that the evolution of the RLF simply reflects the time variation of the source birth rate - ie Q rises from $z = 4$ to a peak at $z = 2$. Alternatively, Q could in fact be constant, provided $\partial P/\partial t$ increases between $z = 2$ and $z = 4$ - ie the redshift cutoff might be the consequence of sources having shorter lifetimes at high redshift.

A complicating factor is the evolution of environment with redshift. Compton snuffing by the microwave background (MWB) has been cited as a possible cause of a high-redshift cutoff, since the energy density of the MWB increases as $(1+z)^4$ (eg Rees & Setti 1968). However, this mechanism can only affect extended sources, and can thus be discounted since the cutoff is observed for both extended and compact sources. The effect of the IGM is a more difficult problem. Indeed, without detailed information on the cluster environments of the sources in question, it is difficult to decide whether the relevant IGM density increases or decreases with redshift. Kapahi (1987) has shown that double radio sources observed at high redshift are smaller than low-redshift sources of the same intrinsic luminosity, and it is interesting to note that most of the remaining unidentified sources in the Selected Regions are small doubles (see Chapter 2). However, it is not clear whether this smallness in size is a consequence of a denser surrounding medium, or whether it simply reflects the youth of the expanding source. Evidence of very distorted radio structures at high redshift (Barthel 1986, Miley 1987) supports the former explanation. At first sight increased confinement might be expected to produce more efficient sources by reducing adiabatic losses. However, the opposite result can be envisaged, as indicated by the proposed physical explanation of the difference between FRI and FRII sources (see Chapter 1, Section 1.3).

Clearly, therefore, a large number of effects could give rise to a reduction in the comoving density of powerful radio sources at high redshift. It seems likely, however, that the birth of radio sources (Q) plays an important role in producing the observed statistical evolution. This leads naturally on to the more fundamental problem of the physical process of radio source formation. The birth of a radio source might be closely related to the formation of the central black hole, and hence maybe to the formation of the host galaxy. Alternatively it might simply reflect the arrival of a new source of fuel (via interaction or merger) which triggers into action a long dormant central engine. These, inevitably rather speculative ideas, are discussed further in Chapter 8.

Chapter 7 : THE SPECTRAL EVOLUTION OF RADIO GALAXIES

7.1 : INTRODUCTION

This chapter is concerned with the study of the optical and optical-infrared colours of radio galaxies in the Parkes Selected Regions, and the interpretation of these data in terms of the spectral evolution of stellar populations. The general field of spectral evolution was briefly reviewed in Chapter 1. However, in a sense the present study is a natural extension of the study of galaxies in the brighter 3CR and 1Jy radio samples carried out by Lilly & Longair (1984) and Lilly *et al.* (1985), and so it is worth summarizing their conclusions here.

From the study of the 3CR radio galaxies, Lilly & Longair (1984) concluded:

i) There is no intrinsic change in the infrared colour out to $z \sim 1.2$, thus implying that the Giant Branch in these galaxies is essentially unchanged, and therefore that, even at $z \sim 1$, these galaxies are relatively old.

ii) A scatter in optical-infrared colours is seen at high redshift. All galaxies are significantly bluer than the colours predicted by no evolution, and the red envelope is well matched by a model of passive evolution. The additional UV flux found in many of the galaxies was interpreted as arising from young starbursts. The UV excess is often found to be distributed throughout the galaxy and is related to the strength of the [OII] 3727Å emission line, indicating that both might be a measure of the gaseous content of the galaxy.

iii) The K-z relation is well defined with approximately constant dispersion out to redshifts well in excess of unity, and indicates luminosity evolution of about a magnitude at $z \sim 1$ if $q_o \leq 0.5$. This luminosity evolution can be accounted for simply by passive evolution of the Main Sequence Turnoff Mass.

Lilly *et al.* (1985) then studied the 1Jy sample in an attempt to investigate the possible effects of radio luminosity on the above conclusions. The 1Jy sample contains galaxies whose radio luminosity is a factor ~ 5 lower than that of the 3CR galaxies. Lilly *et al.* concluded that all the above conclusions are also valid for the 1Jy galaxies. However the 1Jy sample was rather small and lacked the detailed redshift information of the 3CR.

The present study provides an extension to still lower radio luminosities. Also, unlike the above studies, optical photometry has been obtained at two different wavebands - B and R. It is therefore possible to carry out simultaneous analysis of the optical and optical-infrared colours of the galaxies. This means that the star formation histories of the galaxies can be investigated in much more detail because, at z ~ 1, the three wavebands B, R, and K sample respectively the very young, intermediate-age, and very old components of the stellar population.

The interpretation of these new data is carried out using the models of spectrophotometric evolution developed by Guiderdoni & Rocca-Volmerange (1987). Section 7.2 discusses these models, and describes the simulation of observable quantities. Section 7.3 is concerned with the selection of a suitable galaxy subsample for comparison with the theoretical models. In Section 7.4 these data are compared with the models, and the results discussed. Finally Section 7.5 summarizes the conclusions of the work described in this Chapter.

7.2 : THEORETICAL MODELLING OF THE COLOUR EVOLUTION OF GALAXIES

7.2a : Introduction to the modelling of spectrophotometric evolution

The interpretation of the results of the photometry of high-redshift galaxies relies on comparison of the data with the predictions of theoretical models of galaxy spectral evolution. The first complete models of spectrophotometric evolution to be developed were those of Bruzual (1983a, 1983b and references therein). These

were based on the technique of evolutionary synthesis first introduced by Tinsley (1967, 1972). In this approach, analytical expressions are assumed for both the star-formation rate and the initial mass function. Together, these two functions determine the number of stars of a given mass which are born during a given time interval. Theoretical evolutionary tracks are then used to deduce the amount of time spent by stars of different masses at different positions in the H-R diagram. Models for a single generation of star-formation or a continuous star-formation rate can therefore be built, and the stellar population content of the model galaxy determined at any moment in time. Once the stellar content has been determined, the predicted galaxy spectrum is synthesized from a library of observed stellar spectra of different stellar types. The simulation of observable properties such as galaxy colours at high redshift can then be achieved by integrating the spectrum under the relevant broad-band filters after the appropriate redshifting.

Progress in the development of these evolutionary synthesis models is obviously intimately linked to the quality of available spectroscopic data on galaxies and stars of all stellar types, as well as to progress in theories of stellar evolution. Because of the lack of high-quality data outside the optical region, the work prior to Bruzual (eg Huchra 1977, Tinsley 1980) was limited to predictions of the time dependence of optical magnitudes and colours. It was the new availability of ultraviolet (UV) and infrared (IR) data which prompted Bruzual to construct the first evolutionary synthesis models which covered the complete UV → IR spectral range. It is clear that a model which extends into the UV is required in order to make predictions in the optical domain at high redshift.

Since the pioneering work of Bruzual, further improvements in the relevant data and theory have occurred but, until very recently, no attempt has been made to develop more sophisticated models (although there have been attempts to add corrections to Bruzual's models, eg Chokshi & Wright 1987). This is undoubtedly largely because the development of these evolutionary synthesis models is a complex and time consuming process. Now, however, new models of spectrophotometric evolution have recently been developed in Paris

by Dr. Bruno Guiderdoni and Dr. Brigitte Rocca-Volmerange. It was therefore decided to use the results of these new models to interpret the new multicolour photometry of the Selected Regions radio galaxies. The new models are described in detail in Guiderdoni & Rocca-Volmerange (1987) and the results will be published in the form of K- and e-corrections in Rocca-Volmerange & Guiderdoni (1987b). To enable exact simulation of the photometric observations described in Chapters 2 & 3, Guiderdoni & Rocca-Volmerange kindly provided the results of their models (in advance of publication) in the form of a library of evolving synthetic galaxy spectra. In Section 7.2b a brief description of the new models is given, along with a discussion of the main differences between the new models and those of Bruzual. Section 7.2c provides a detailed description of the particular galaxy models which are most relevant to the study of radio galaxies, while Section 7.2d describes how tracks of colour evolution were constructed from the library of evolving model spectra.

7.2b : The new models of spectrophotometric evolution

Details of the model construction can be found in Guiderdoni & Rocca-Volmerange (1987), while the basic principles are described by Rocca-Volmerange *et al.* (1981). The main features are as follows:

i) Star-formation

The number of stars of mass m which form at time t from the gaseous component of the galaxy is

$$d^2N(m,t) = \Phi(m)\tau(t)d(\ln m)dt \qquad (7.1)$$

where $\Phi(m)$ is the initial mass function, and $\tau(t)$ is the rate of star-formation in units of $M_\odot Gyr^{-1}$. The adopted IMF is basically that of Scalo (1986) and has the form $\Phi(m) \propto m^{-x}$ with slopes $x = 0.25$, 1.35, 1.7 for the respective mass ranges $0.1 < m < 1$, $1 < m < 2$, $2 < m < 80M_\odot$. The normalization of the IMF is given by

$$\int_{0.1}^{80} \Phi(m)dm = 0.5 \qquad (7.2)$$

in order to reproduce the observed mass/luminosity ratios.

ii) Stellar evolution

The stars thus formed are placed on the Main Sequence in the H-R diagram and at each time step, $\Delta t = 2.5 \times 10^7$ yr, they evolve along theoretical stellar tracks. These tracks correspond to a helium fraction of $Y = 0.28 \rightarrow 3.0$ and an assumed uniform metallicity of $Z = 0.02$ (the effect of variation in metallicity is discussed below). The tracks include four evolutionary stages - Main Sequence (MS), Giant Branch (GB), "red" Horizontal Branch (HB) (around $\log_{10}T_{eff} = 3.68$) and Asymptotic Giant Branch (AGB). The sources of these tracks are given in Guiderdoni & Rocca-Volmerange (1987). The input tracks are interpolated in mass along each evolutionary stage, in order to get differences in lifetimes lower than 1Gyr for successive masses. For the very short phases, an average luminosity during time step Δt is computed from the total energy released during the phase. Mass loss of massive stars was taken into account according to case B of Maeder (1981). No mass loss during the GB stage was considered for $m < 9M_{\odot}$.

iii) Synthesis of the galaxy spectrum.

At each time step, the synthetic spectrum of the stellar population is computed from the distribution of stars in the H-R diagram, $\log_{10}T_{eff}$ - M_V. This is done using a library of 30 stellar spectra which spans the range of spectral types O5 → M8, and 2 luminosity classes, V and III (ie dwarfs and giants). These spectra cover the spectral range 220Å → 10680Å with an average spectral resolution of 10Å. At wavelengths $\lambda > 1220$Å the spectra are observational (IUE data in the wavelength range 1220Å → 3170Å) but the extreme UV range (ie 220Å $\leqslant \lambda \leqslant$ 1220Å) is constructed from theoretical models (Mihalas 1972, Borsenberger & Gross 1978). Details of the library are given by Guiderdoni & Rocca-Volmerange (1987) - the most important

improvements are the relatively high resolution, and the improved coverage of the UV domain.

The H-R diagram is divided into bins of size $\Delta M_V = 0.1$, $\Delta \log_{10} T_{eff} = 0.05$. A spectrum $F_j(\lambda)$ is then assigned to each bin j according to its T_{eff}, its M_V and its luminosity class. At time t bin j contains $N_j(t)$ stars, and so the spectrum of the stellar population is given by

$$F_*(\lambda, t) = \sum_j N_j(t) F_j(\lambda) \qquad (7.3)$$

iv) Evolution of the gaseous content of the galaxy

The evolution of the total mass of gas in the galaxy is given by the equation

$$\frac{dM_g(t)}{dt} = -\tau(t) + \int_{m_l}^{m_u} E(m)\Phi(m)\tau(t-t_m)dm \qquad (7.4)$$

where E(m) is the gas rejection rate (from Vigroux *et al.* 1976), t_m is the lifetime of a star with mass m, and m_u and m_l are the upper and lower limits of the stellar masses. The boundary condition is simply $M_g(t=0) = M_{tot}$, ie conservation of the total mass of the galaxy.

v) Nebular emission and internal extinction

An attempt is made to incorporate the effects of nebular emission and extinction in disks. This sophistication (described in detail by Guiderdoni and Rocca-Volmerange 1987) is only significant in the modelling of gas-rich late-type galaxies, and therefore is not very important for the present study of radio galaxies (which are known to be ellipticals).

The main differences between this new model and that of Bruzual may be summarized as follows (again see Guiderdoni & Rocca-Volmerange 1987 for a full discussion).

i) The new stellar library has a greater resolution (~10Å) than that used by Bruzual (20→50Å) and extends further into the UV.

ii) Bruzual's model did not include post-GB stages of stellar evolution, in particular the AGB. Also, Bruzual used a unique GB taken from Tinsley & Gunn (1976), whereas the new model incorporates a mass dependent GB from Yale tracks computed by Sweigart & Gross (1978). The GB in Bruzual's model is stronger and hence produces REDDER colours at late epochs when it is well developed. This also results in Bruzual's model galaxies being fainter at early epochs because normalisation of the galaxy is carried out at the present day.

iii) The new model adopts the observationally-determined IMF of Scalo (1986) in contrast to the single-slope Salpeter (1955) IMF which was used in the original Bruzual models. It is worth noting however that Bruzual's models have also been re-run using the multi-slope IMF of Miller & Scalo (1979) - see, for example Bruzual (1985) - with very little change in the colour evolution.

iv) Bruzual's models did not attempt to account for nebular emission or disk extinction, although as already mentioned these sophistications have an insignificant impact on models of elliptical galaxies, except possibly at very high redshift.

v) Finally, one of the most important differences concerns the approach taken to the origin of the UV light in elliptical galaxies. It is now well established that the UV flux observed in elliptical galaxies is in excess of the contribution expected from the old Population I that dominates the spectrum in the visible region. The origin of this UV-excess has been a subject of considerable dispute. Bruzual (1985) lists several possible explanations for its origin - the main contenders appear to be young massive main-sequence stars (eg Rocca-Volmerange & Guiderdoni 1987a), hot HB stars (eg Wu *et al.* 1980), or post AGB stars (eg Renzini & Buzzoni 1986). Other possible sources of UV flux include blue stragglers, white dwarfs or interacting binaries, but in general it is estimated that the contribution of these objects is below the detected flux level (Wu *et*

al. 1980, Renzini 1981). In Bruzual's models the UV light of ellipticals was obtained by 'adding in' a population of hot HB stars. In contrast, the new models account for the UV excess by young stars. The main piece of evidence usually cited in favour of HB stars is that the UV excess appears to be spread evenly throughout the elliptical galaxy. Such a light distribution might be expected to arise more naturally from an evolved population than from young stars. However recent spectral synthesis studies argue strongly in favour of young main sequence stars. Rocca-Volmerange & Guiderdoni (1987a) have carried out a detailed analysis of the UV spectra of E/S0 galaxies with the help of the IUE stellar atlases and conclude that the absence of flux between 1900Å and 2500Å indicates that the contribution of HB stars to the UV light is very low. They also show that, for all the galaxies they analysed, the spectrum in the range $2500Å < \lambda < 3100Å$ has a mean spectral type of F8 to G2 indicating relatively recent star-formation (~5 → 10Gyr ago). An additional far-UV excess (ie over and above that contributed by the most recent turn-off population) was only found in a subset of their galaxy sample. This fact suggests the origin of any far UV excess is more likely to be young main-sequence stars, rather than some evolved population which one would expect to find in ALL elliptical galaxies. Kjaegaard (1987) also concludes, from his spectral analysis of Virgo elliptical galaxies, that the most likely explanation for the UV light seems to be bursts of young stars. It should also be noted that an explanation in terms of young stars has the appeal of simplicity and continuity. As will become apparent in Section 7.4, the bulk of galaxies at $z \sim 1$ show more UV flux than at the present day. The origin of this light must be young stars since the contribution of an evolved population such as HB stars should DECREASE with look-back time. It therefore seems more natural to also attribute the UV flux seen at the present day to recently formed main-sequence stars.

Based on this interpretation that the level of galaxy UV light is determined by the amount of ongoing star-formation activity, Guiderdoni & Rocca-Volmerange (1987) have proposed a scheme in which the range of colours of galaxies in the Hubble sequence are reproduced by models with a corresponding range of star-formation laws. A uniform epoch of formation is assumed for all Hubble types,

and a galaxy of a given colour is produced by simply selecting the value of the timescale t_* for conversion of gas into stars which results in the required level of star-formation at the present day. The star-formation laws which are required to produce the colours of the Hubble sequence after ~12 → 16Gyr of evolution are listed below in Table 7.1. For the present study, only the elliptical models are of interest - these are discussed in detail in the next section (Section 7.2c).

Table 7.1 : The star-formation laws, $\tau(t)$, which are used by Guiderdoni & Rocca-Volmerange (1987) to model the range of colours observed in the Hubble sequence at the present day ($g(t) = M_{gas}(t)/M_{tot}$), and the corresponding timescales t_* for gas consumption. Units of t are Gyr.

Colour class	SFR, $\tau(t)$	t_* (Gyr)
UV-Cold elliptical	$\exp(-t)$	1.0
UV-Hot elliptical	$0.37\exp(-0.37t)$	2.7
S0/a	$0.4g(t)$	2.3
Sa	$0.3g(t)$	3.0
Sb	$0.2g(t)$	4.5
Sc	$0.1g(t)$	9.1
Sd	0.048	13.2
Im	$4.0\times10^{-4}t^2$	16.8

In concluding this description of these new models, it is important to point out that there remain of course many limitations. Firstly there is the problem of metallicity. The models assume uniform solar metallicity, (justified on the basis that the metallicity is expected to rapidly approach this value) and therefore ignore the effects of chemical evolution (such an assumption has to be made because at present the amount and quality of available data do not allow the

effects of spectral and chemical evolution to be disentangled). Lower values of metallicity are not expected to change the optical colours significantly, but the position of the giant branches is altered and redder R-K colours are expected (See Section 7.4). Guiderdoni & Rocca-Volmerange are at present modifying their models to investigate this effect. Secondly, at present the stellar library does not extend to wavelengths > 10680Å, and so the infrared section of each stellar spectrum is constructed by matching a black-body curve at the effective temperature of the star to the optical spectrum at 10680Å. Work is also in progress to improve this aspect of the models by the addition of IR stellar data, but the early indications are that the resulting modifications of the synthetic spectra are insignificant. Thirdly, star-formation continues to be represented by a simple parametric expression which is assumed to be valid throughout the life of the galaxy (see Table 7.1 above) and there is no clear way at present of disentangling continuous star formation from isolated bursts.

7.2c : Models of interest in the study of radio galaxies

The 8 model galaxies listed in Table 7.1, plus an additional model comprising a single initial 1Gyr burst of star formation, were kindly supplied by Guiderdoni and Rocca-Volmerange in the form of a library of evolving galaxy spectra. Each model consisted of 16 synthetic galaxy spectra (from 220Å → 5μm) computed at time intervals of Δt_{gal} = 1Gyr, from t_{gal} = 0.47Gyr to 15.47Gyr. The simulation of colour evolution from these spectra is described below in Section 7.2d.

Since the host galaxies of radio sources are known to be ellipticals, the models of interest for the present study are the UV-Hot elliptical, the UV-Cold elliptical, and the 1Gyr "Burst" model. All the other models in Table 7.1 result in more star-formation activity at the present epoch than is observed in any nearby elliptical galaxy. The terms UV-Hot and UV-Cold refer to the two extremes of the range of UV spectra which is observed in ellipticals at the present day - an example of a UV-Hot elliptical galaxy is M87,

while an example of a UV-Cold elliptical is provided by M32 (see Rocca-Volmerange & Guiderdoni 1987a). The models of the same names have therefore been designed to produce, via the appropriate rate of exponentially decreasing star-formation throughout their evolution, the observed extremes of UV-Hot and UV-Cold spectra at the present epoch (ie after $t \gtrsim 13$ Gyr of evolution). In terms of the μ parameter introduced by Bruzual, the Hot- and Cold-elliptical models correspond to $\mu = 0.3$ and 0.6 respectively. The μ-parameter represents the fraction of the initially purely gaseous galaxy which is converted into stars during the first Gyr of its existence, ie

$$\mu = \frac{1}{M_{tot}} \int_0^{1Gyr} \tau(t)dt \qquad (7.5)$$

where $\tau(t)$ is the adopted law of star-formation. The third model of interest, the 1Gyr Burst model, therefore corresponds to $\mu = 1$ (this model is the equivalent of Bruzual's C-model). The burst model is important because it represents the simplest null hypothesis scenario of galaxy formation and evolution - ie a single epoch of star formation followed by only passive stellar evolution thereafter. This model can also be used to construct models of galaxy evolution involving a series of distinct starbursts etc.

Since the subsequent analysis of the radio-galaxy photometry centres on the comparison of the data with these 3 models of elliptical galaxy evolution, a sample of the evolving stellar spectra is shown in Figure 7.1. The Burst, UV-Cold and UV-Hot models are illustrated in Figures 7.1 a), b) and c) respectively. In each case the synthetic spectrum is shown at 6 equally spaced epochs in the life of the galaxy, 0.5, 3.5, 6.5, 9.5, 12.5 and 15.5Gyr after the epoch of galaxy formation. The flux units are 5.32×10^{29} ergs s^{-1} $Å^{-1}$ $M_{\odot}^{-1}$. These figures demonstrate clearly the important differences between the 3 alternative models. The Burst model, because it possesses the largest initial burst of star-formation, begins life as the brightest of the three models, but decays rapidly in the UV thereafter. The UV-Cold model starts out slightly less spectacularly, but maintains significant UV flux at later times because the exponentially-decaying

law of star-formation results in young massive stars still arriving on the main sequence after the initial epoch of formation. However, by t_{gal} ~ 10Gyr the flux shortward of 2500Å has decayed essentially to zero. Finally, the UV-Hot model, with its more gently declining exponential law of star-formation, begins even less spectacularly, but is still displaying enough star-formation activity after 15.5Gyr to simulate the largest UV-excess seen in elliptical galaxies today.

All three models clearly show the evolution of the 4000Å break with time, and also the increase in "red" flux (ie ~ 1μm) at late epochs which is caused by the development of the Giant Branch. This latter effect is more pronounced in the Burst and UV-Cold models, than in the UV-Hot one because larger fractions of the stellar population are well evolved.

Figure 7.1 : The time evolution of the model elliptical galaxy spectra.

a) The Burst model.

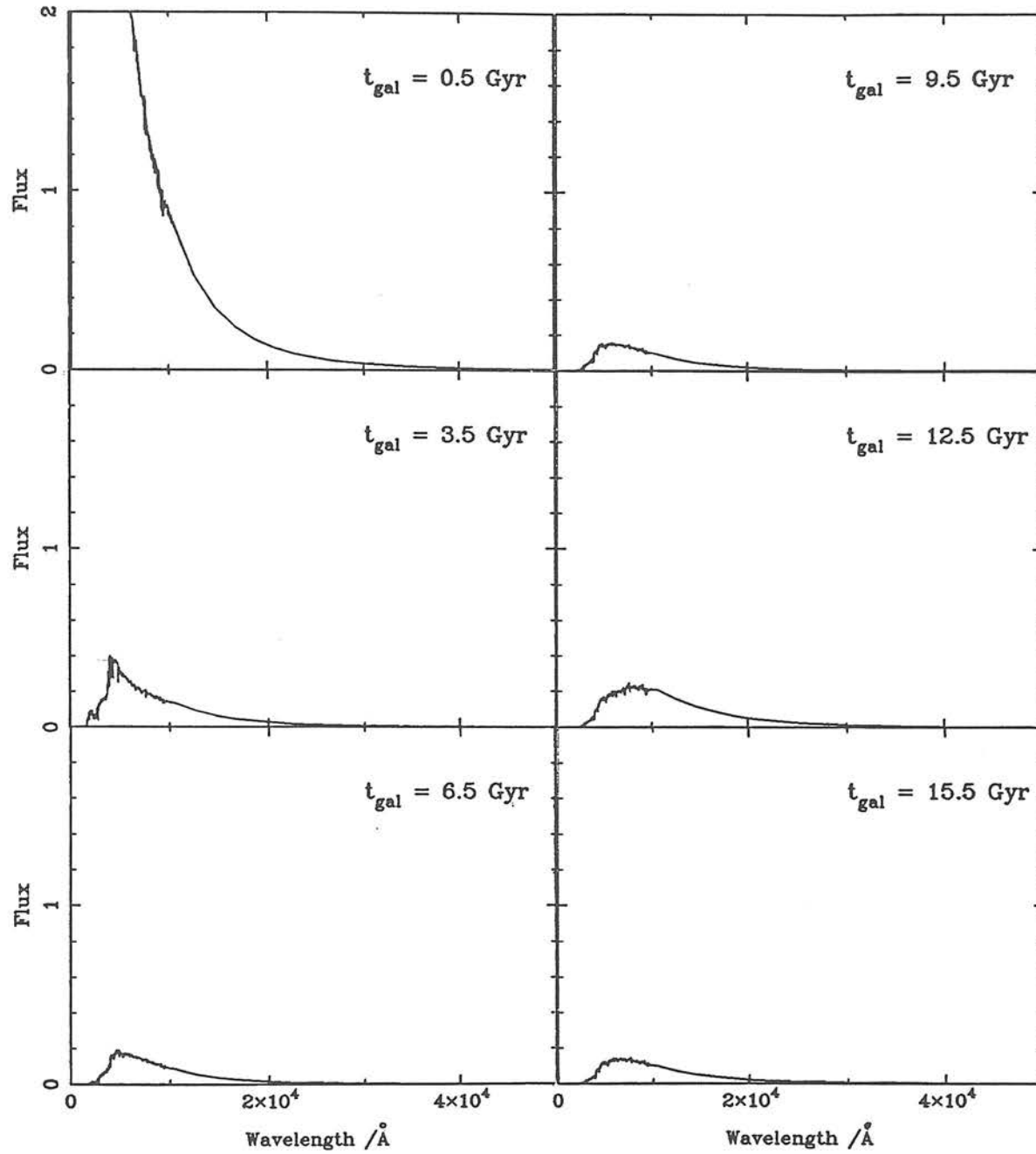

b) The UV-Cold model

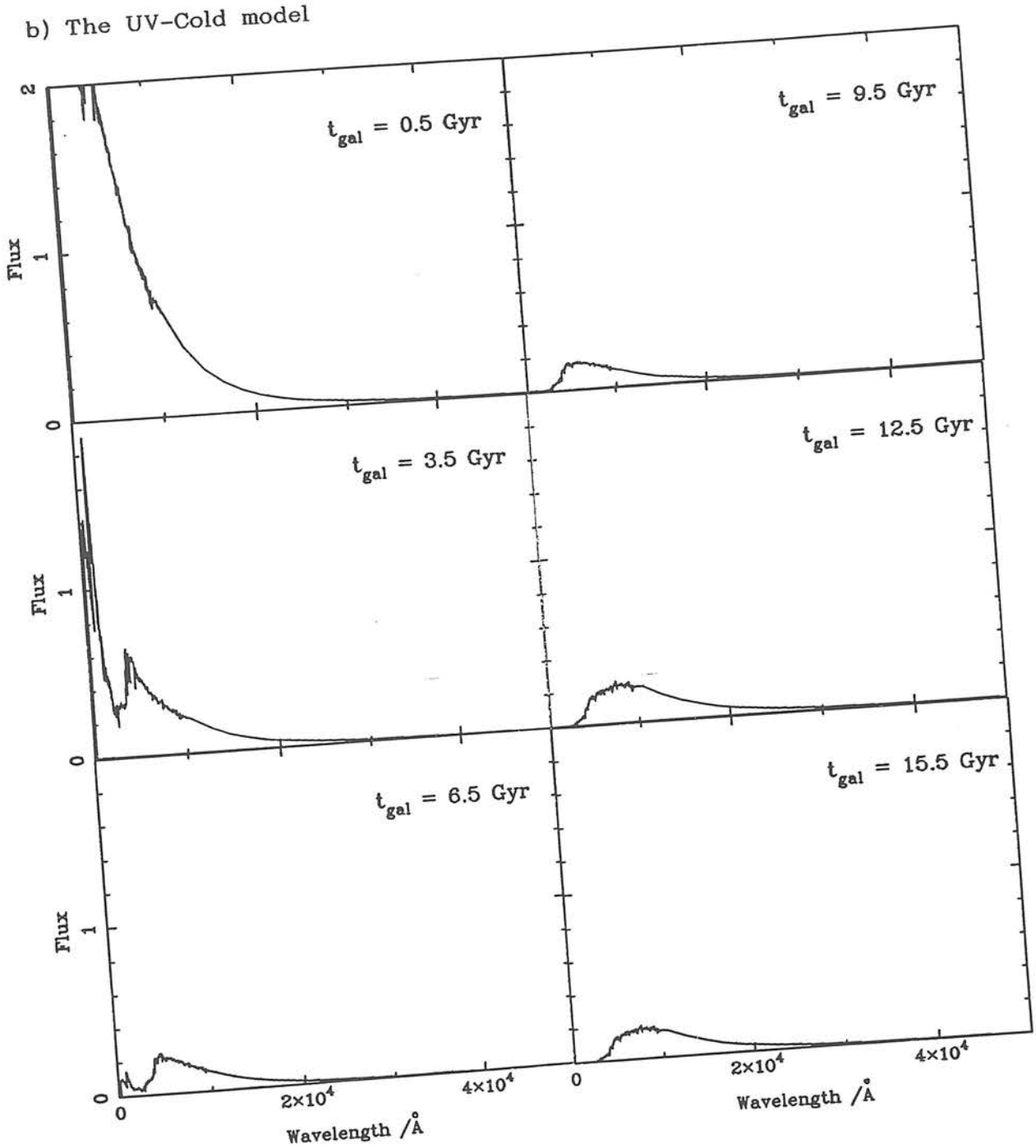

c) The UV-Hot model

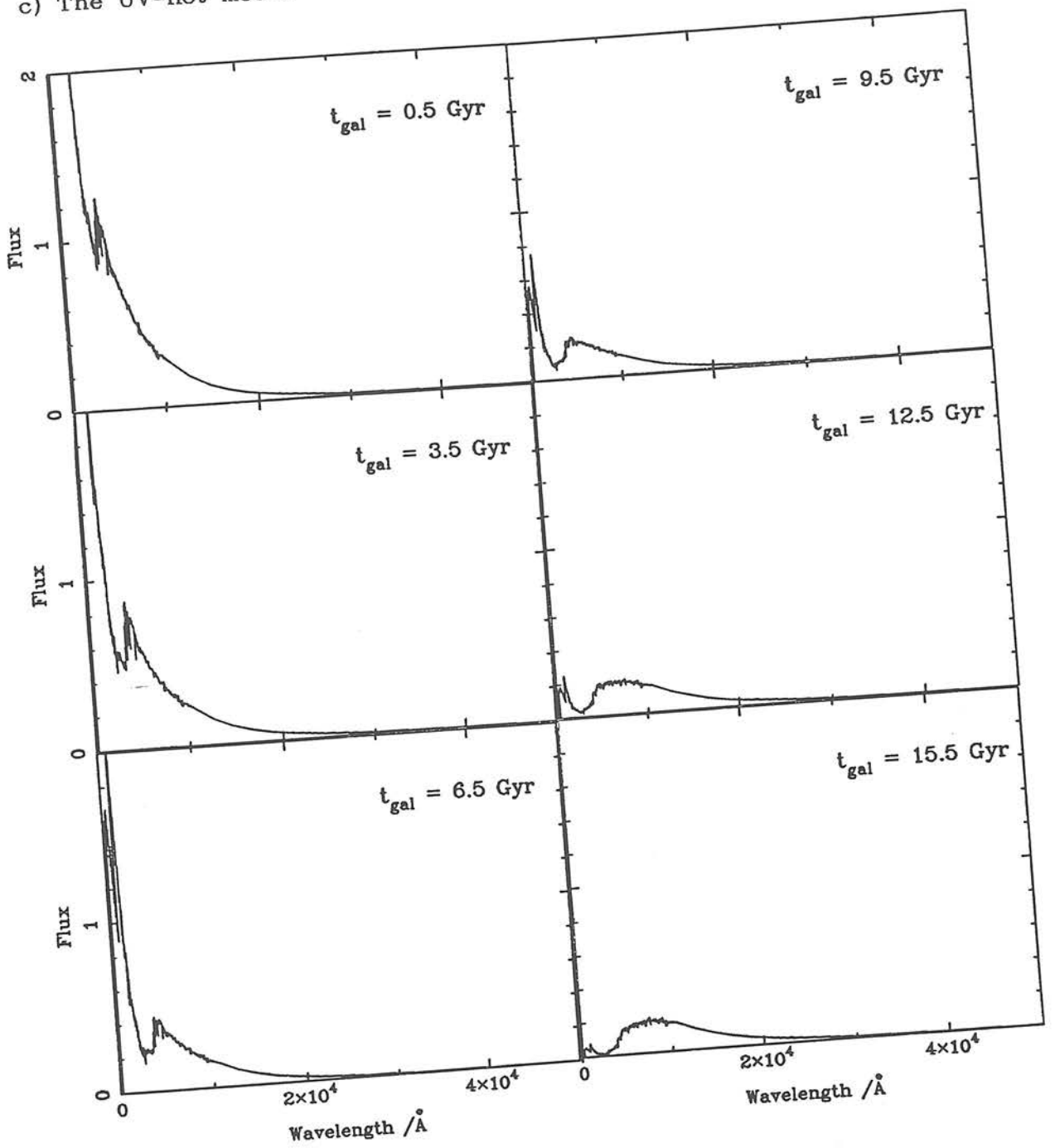

7.2d : The synthesis of colour evolution from the library of evolving model spectra

This section describes the details of how tracks of apparent magnitude and colour evolution, suitable for direct comparison with the data, were constructed from the library of evolving model spectra.

i) Filters

The response profiles of broad-band filters show considerable variation from one filter system to another. It is important therefore, when aiming to simulate the results of broad-band photometry, that the integration of the model spectrum is carried out using the exact profiles of the filters through which the observations were made. In the present study, the B and R photometry of the radio identifications was obtained through Kitt Peak Mould interference filters (see Chapter 2), while the observations at K were made through the UKIRT K filter (see Chapter 3). The response profiles of these 3 filters were obtained from the RGO over the UK Starlink computer network - the resolution of these filter data was ~ 25Å. In the case of the optical photometry it was also necessary to take into account the spectral response of the CCD chip which had been used as the detector. The Mould B and R filter profiles were therefore combined with the spectral response profile of the RCA CCD (also obtained from the RGO) which had been used to make the observations at the AAT - the fact that some of the R photometry was obtained using a TI CCD at the UH 88-inch telescope is not a problem since the spectral responses of the two CCDs are in fact very similar (partly because both chips are thinned and back-illuminated). Figure 7.2 shows the response profiles of the 3 filters (B, R & K) and also illustrates the impact of the spectral response of the RCA on the B and R profiles - the main effect is the degradation of the blue wing of the B filter.

ii) Calculation of apparent magnitudes

The integrated broad-band fluxes were converted into magnitudes

Figure 7.2 : The broad-band filter profiles used to simulate evolution of apparent magnitudes and colours from the model spectra.

a) The Kitt Peak Mould B and R interference filters.

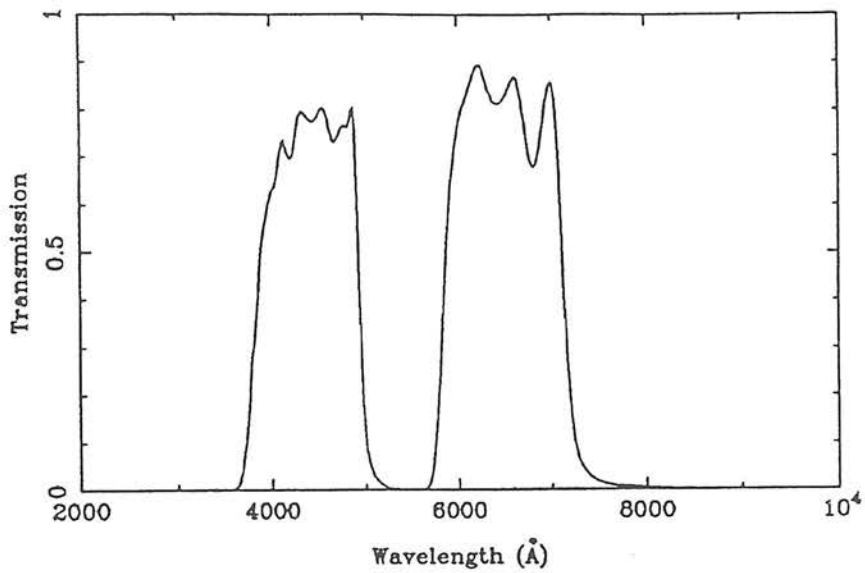

b) The effect on the R and B filter profiles of the spectral response of the RCA CCD.

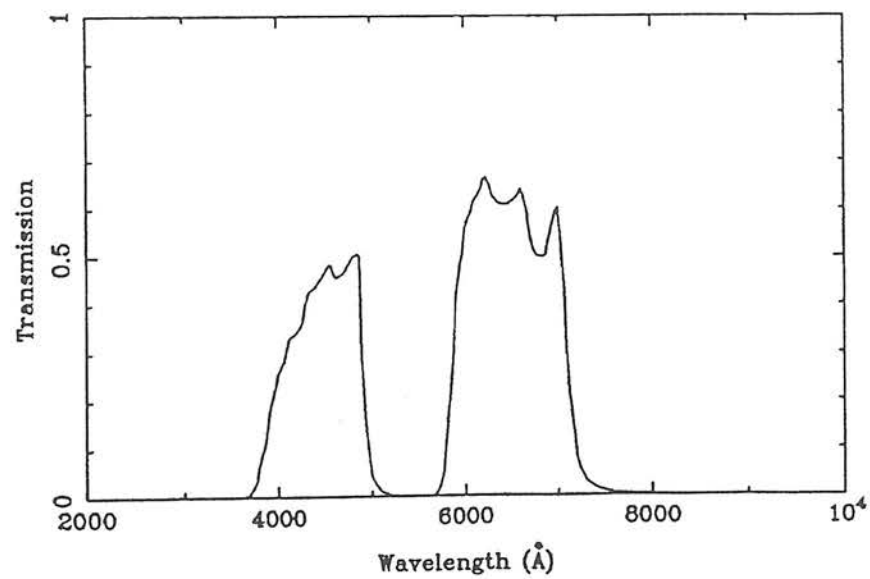

c) The UKIRT K filter.

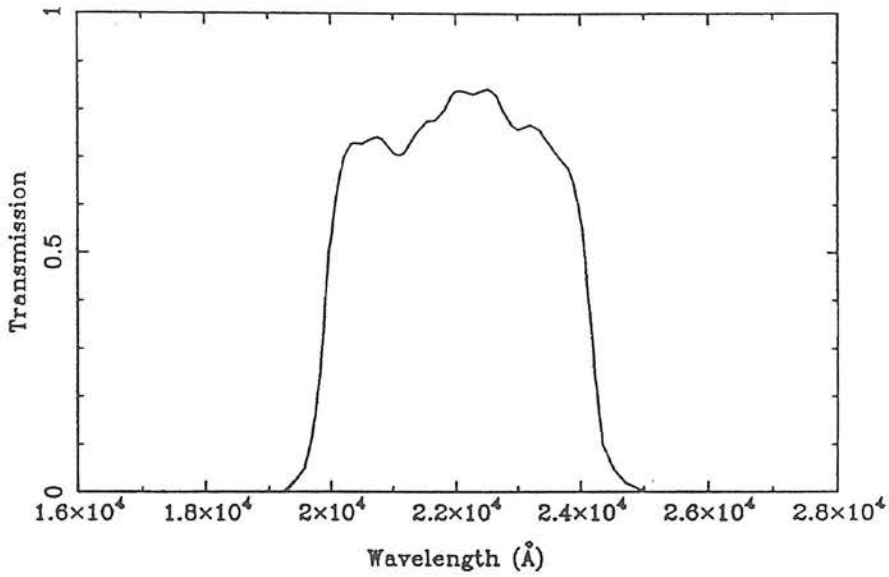

d) The B, R and K filter profiles.

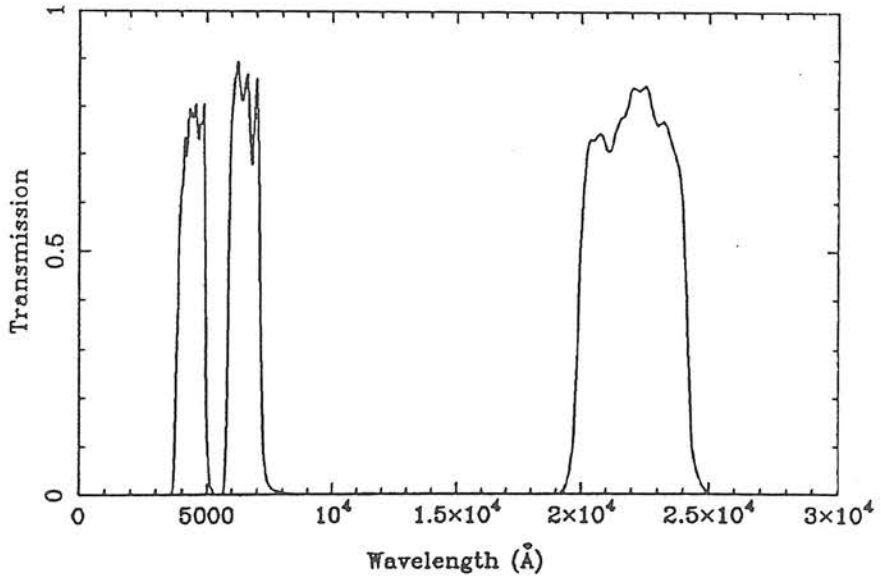

using a flux-calibrated spectrum of Vega which was constructed from the optical calibration of Hayes & Latham (1975) and the infrared measurements of Mountain *et al.* (1985). The effect of wavelength dependent atmospheric extinction was also incorporated into the calculation, although the addition of this correction was found to have a negligible effect on the computed magnitudes.

iii) Cosmology

It was decided to carry out the magnitude calculations at equal intervals in cosmological time, since the evolving model galaxy spectra had been provided in that form. Firstly, however, in order to produce smooth evolutionary tracks, the time resolution of the spectral evolution was improved from the original Δt = 1Gyr to Δt = 0.1Gyr by exponential interpolation between adjacent model spectra. Each sampling point in time was then associated with a redshift z, cosmological look-back time τ, and effective distance D, the values of which were dictated by the choice of cosmology (ie density parameter Ω), Hubble's constant H_o, and the assumed redshift of galaxy formation z_f. Then, at each evolutionary step of 0.1Gyr, the broad-band integration was carried out after the appropriate redshifting and K-dimming of the model galaxy spectrum. The absolute normalization of the resulting apparent magnitudes was determined by comparison with the magnitudes of the low-redshift radio galaxies in the sample.

The initial calculations successfully produced smooth tracks describing the evolution of B and R magnitudes with redshift. However, the K-z evolutionary track was found to oscillate at low redshift. The origin of these oscillations was traced to sudden surges in the "red" (ie ~ 1μm) flux of the model spectrum at ages of 8.5 and 12.5Gyr. It transpired that these flux oscillations were the result of sampling problems in the original modelling code. For cpu-time considerations, the difference in lifetime between successive stellar tracks had been chosen to be ~ 1Gyr. However, the duration of some of the later stages of stellar evolution can be as low as 0.2Gyr. The model does not therefore have sufficient resolution to correctly describe the smooth progress of the stellar population through these

short-lived phases, but instead causes packs of stars to suddenly arrive on the giant branches and then depart again in a single 1Gyr step. Because these late phases contribute mainly "red" light to the galaxy spectrum, the oscillations do not have a significant effect on the synthesized optical magnitudes, particularly after redshifting of the spectrum. They do however have a considerable impact in the infrared, and the effect is especially noticeable for the older galaxy models (ie Burst & UV-Cold) in which a large fraction of the stellar population is at a well developed stage (the sampling problem is a general one, also encountered with Bruzual's C-model, and noted earlier by Tinsley & Gunn 1976). The solution to the problem is to run models with stellar tracks, the lifetimes of which do not differ by more than 0.2 or 0.1Gyr. This is being carried out by Guiderdoni and Rocca-Volmerange at the time of writing. An alternative solution, and the one adopted here, is simply to smooth the latter stages of the model spectrum evolution in time - ie replace each synthetic spectrum with the mean of itself and the two adjacent spectra (from 1Gyr before and after). Implementation of this smoothing procedure successfully damped the oscillations in the K-z diagram without affecting the evolution of B or R magnitude. A recent comparison of these smoothed evolutionary tracks with those produced by the new higher resolution models of Guiderdoni & Rocca-Volmerange has shown that the results produced by the two alternative methods are essentially identical.

7.3 : DATA - SELECTION OF THE GALAXY SAMPLE FOR COMPARISON WITH THE MODELS OF SPECTROPHOTOMETRIC EVOLUTION

For comparison with the models of spectral evolution described above, a suitable galaxy subsample had to be selected from the complete Selected Regions sample. In order that a reasonably complete 3-colour sample could be constructed, attention was confined to the 4 regions for which "complete" K photometry had been obtained (ie the regions centred on 0hr, 1hr, 2hr & 22hr - see Chapter 3). The galaxy subsample was then selected to consist of all sources in these 4 regions which were classified as G or G? (see Chapter 5, Section 5.2) and which possessed a measured K magnitude (to ensure reliable

redshift estimation). As discussed in Chapter 3, Section 3.3d, the fraction of faint galaxies in the 4-region subsample which lack K photometry is very small (4 out of 70), and so the galaxy subsample thus selected may be regarded as complete.

It remained to consider whether the galaxies associated with compact radio sources should be rejected from the sample because of the worry that the colours of these objects might be influenced by the presence of a non-thermal component. The data are illustrated in Figure 7.3 in the form of plots of optical-infrared (R-K) and optical (B-R) colour versus redshift (measured, or estimated from the MEAN K-z relation - see Chapter 6, Section 6.2). Galaxies associated with extended double radio sources are shown as filled circles, those associated with compact sources (U or P in Table A.1) as open circles. There are 66 galaxies in the sample, but 6 of these (0003+006, 0017+026, 0105+025, 0225+002, 2158-170, 2357-006) are not present on the B-R/z diagram, either because of lack of B photometry, or because both B and R magnitudes are lower limits (ie optical EFs which were detected in the infrared). For clarity the redshift scale in Figure 7.3 has been restricted to $z = 3$, which results in the omission of one object (2204-182) which has a MEAN-z estimate of $z = 3.45$. The large error bars at low redshift belong to those galaxies for which only eye-estimated optical magnitudes from Schmidt plates have been obtained.

It is clear from Figure 7.3 that 3 of the most obvious outlying datapoints are compact sources - 2 compact galaxies (2159-215 at $z = 2.2$, and 2207-203 at $z = 1.4$) have very blue optical-infrared colours but very red optical colours, while 1 compact galaxy (0055+015 at $z = 0.679$) is very red in R-K but very blue in B-R. These 3 sources are therefore obvious candidates for non-thermal contamination. In general the other compact sources lie in regions of the diagram which are also occupied by extended sources, particularly in R-K. However, in the B-R diagram there appears to be a possible trend for the compact sources to be rather blue at low redshift, and rather red at high redshift (particularly considering that many of the B-R colours at $z \sim 1.3$ are lower limits). For consistency it was therefore decided to remove all the compact

sources (U and P radio structures) from the galaxy sample. The sample used throughout the remainder of this chapter thus consists of 50 galaxies (46 with B-R information) all of which are the hosts of extended double radio sources. This should help to ensure that the observed colours genuinely reflect the stellar populations of the galaxies, and also enables direct comparison with the results of the earlier work on low-frequency radio samples (eg Lilly & Longair 1984).

Figure 7.3 : The optical-infrared (R-K) and optical (B-R) colour versus redshift diagrams for galaxies in the 4-region subsample of the Selected Regions. Galaxies associated with extended sources are shown as filled circles, those associated with compact sources as open circles.

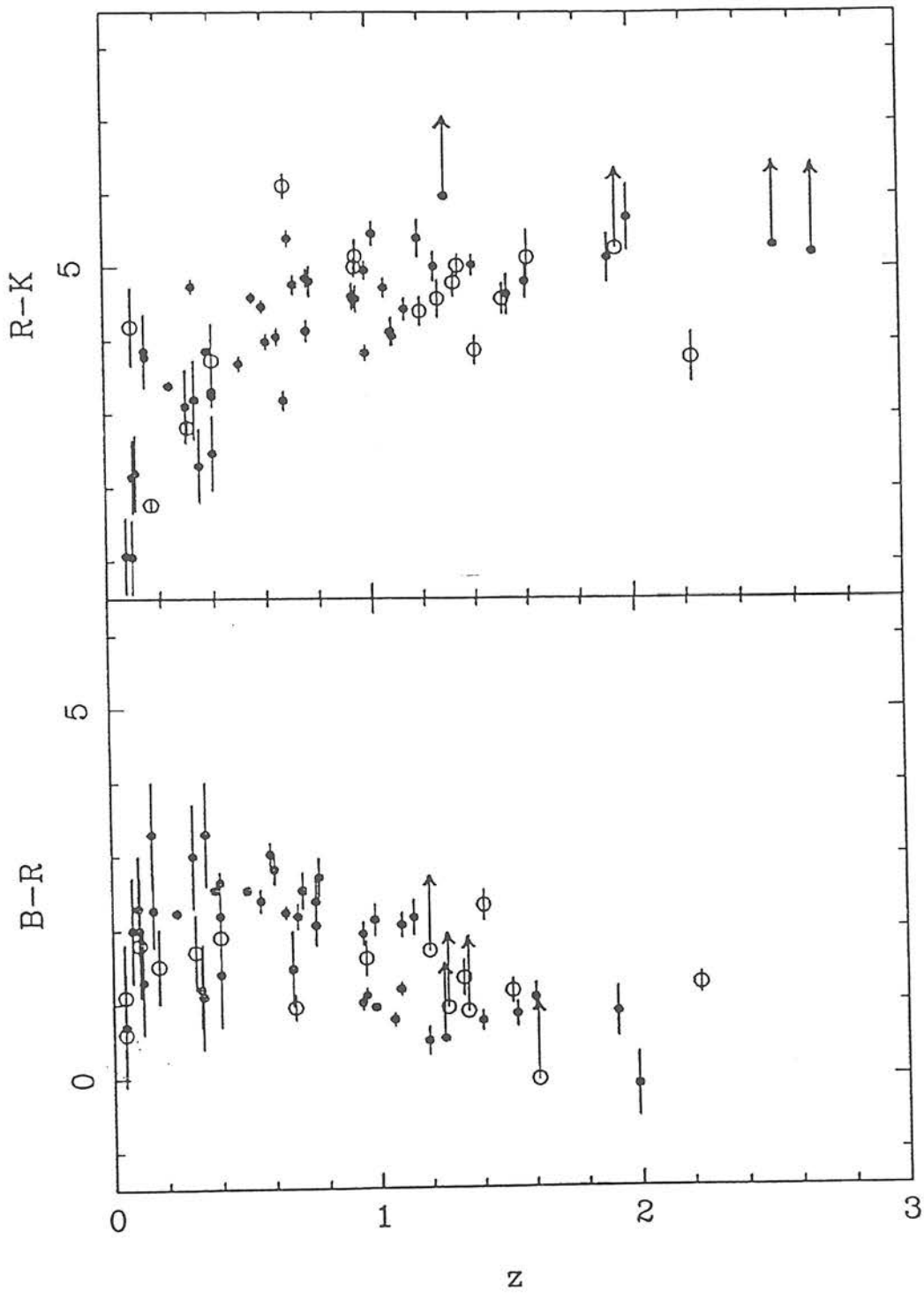

7.4 : COMPARISON OF MODELS AND DATA - RESULTS AND DISCUSSION

The results of the comparison of the models and the data are presented in this section in the form of plots of optical-infrared (R-K) and optical (B-R) colour versus redshift. This is a particularly instructive approach since it facilitates simultaneous study of both the old and young stellar populations in the galaxies. It is also the best way to analyse the photometric data given that the fraction of estimated redshifts is so large - the interpretation of colour evolution is less sensitive to exact values of z than is the analysis of Hubble diagrams. A further advantage of colour-redshift diagrams is that they are less affected by aperture and seeing corrections and possible luminosity selection effects than are diagrams of apparent magnitude versus z.

The estimated redshifts shown in the following figures are those derived from the MEAN K-z relation described in Section 6.2. The sensitivity of the results to errors in these redshifts is discussed in Section 7.4d. However it is important to stress that most of the important conclusions are drawn from the colours of galaxies at $z \sim 1$, for which the redshift estimates are reasonably secure (since the K-z relation is well defined empirically out to $z \sim 1.5$).

7.4a : Evidence of evolution

The obvious first question to address is whether it can be stated unambiguously that all the radio galaxies in the sample exhibit spectral evolution. The null hypothesis of no evolution (NE) can be easily checked by simply redshifting (ie K-correcting) the present day UV-Cold and UV-Hot elliptical spectra (ie the 15.5Gyr end points of the UV-Cold and Hot models shown in Figure 7.1). Since these two spectra are known to bracket the observed range of UV spectra observed in nearby ellipticals, the corresponding K-corrections should map out the locus of possible colour-redshift tracks which could be regarded as consistent with zero evolution. These UV-Cold and UV-Hot NE tracks are shown in Figure 7.4. The important conclusion to be drawn from this figure is that ALL the radio

galaxies show significant colour evolution above z ~ 0.6. It is important to note, however, that it is the R-K diagram which establishes this result, and that no such conclusion could have been reached solely on the basis of the optical data. On the R-K diagram BOTH UV-Cold and UV-Hot NE models are too red to fit the upper envelope of the data above z ~ 0.6, thus demonstrating that all the galaxies in the sample display some evolution beyond this redshift. In contrast, on the B-R diagram, although the UV-Cold NE model is clearly too red at z ~ 0.6, the UV-Hot NE model provides a reasonable description of the data at all epochs, and from this diagram it could only be concluded that a subset of galaxies (ie those bluer than the UV-Hot NE model) display evolution. This feature of the B-R diagram is consistent with the conclusions of other workers who have considered only optical data - in his review of spectral evolution, Bruzual (1985) concludes that "*the only safe conclusion that has been established is that some distant galaxies are brighter in the UV than most nearby elliptical galaxies*". The problem with the optical data is that any conclusion concerning the existence of evolution depends on what is taken as the present-day UV spectrum - it is clear from Figure 7.4 that the UV colours of a large fraction of the galaxies in the sample can be adequately described, at all epochs, by the UV-Hot elliptical spectrum observed today in, for example, M87. In contrast, at least up to z ~ 1, the K-corrections in R-K are relatively unaffected by the chosen level of present-day far-UV light.

The superior ability of the R-K diagram to demonstrate unambiguously the presence of at least passive evolution was first demonstrated by Lilly & Longair (1984). They showed that the upper envelope of the r-K colours of the 3C radio galaxies was inconsistent with an NE model. However, their NE model was constructed by K-correcting the final 16Gyr step of Bruzual's C-model (ie 1Gyr burst model), which is known to be a poor representation of observed present-day elliptical spectra. This NE model was therefore open to criticism as being an unreasonable null hypothesis. It is therefore significant that Figure 7.4 demonstrates the existence of evolution using NE models which are based on realistic present-day spectra.

In conclusion, all the radio galaxies show at least the effects of

Figure 7.4 : The R-K and B-R colour versus redshift diagrams showing the data compared to the colour evolution tracks produced by simply redshifting the present-day UV-Cold (solid line) and UV-Hot (dashed line) elliptical spectra.

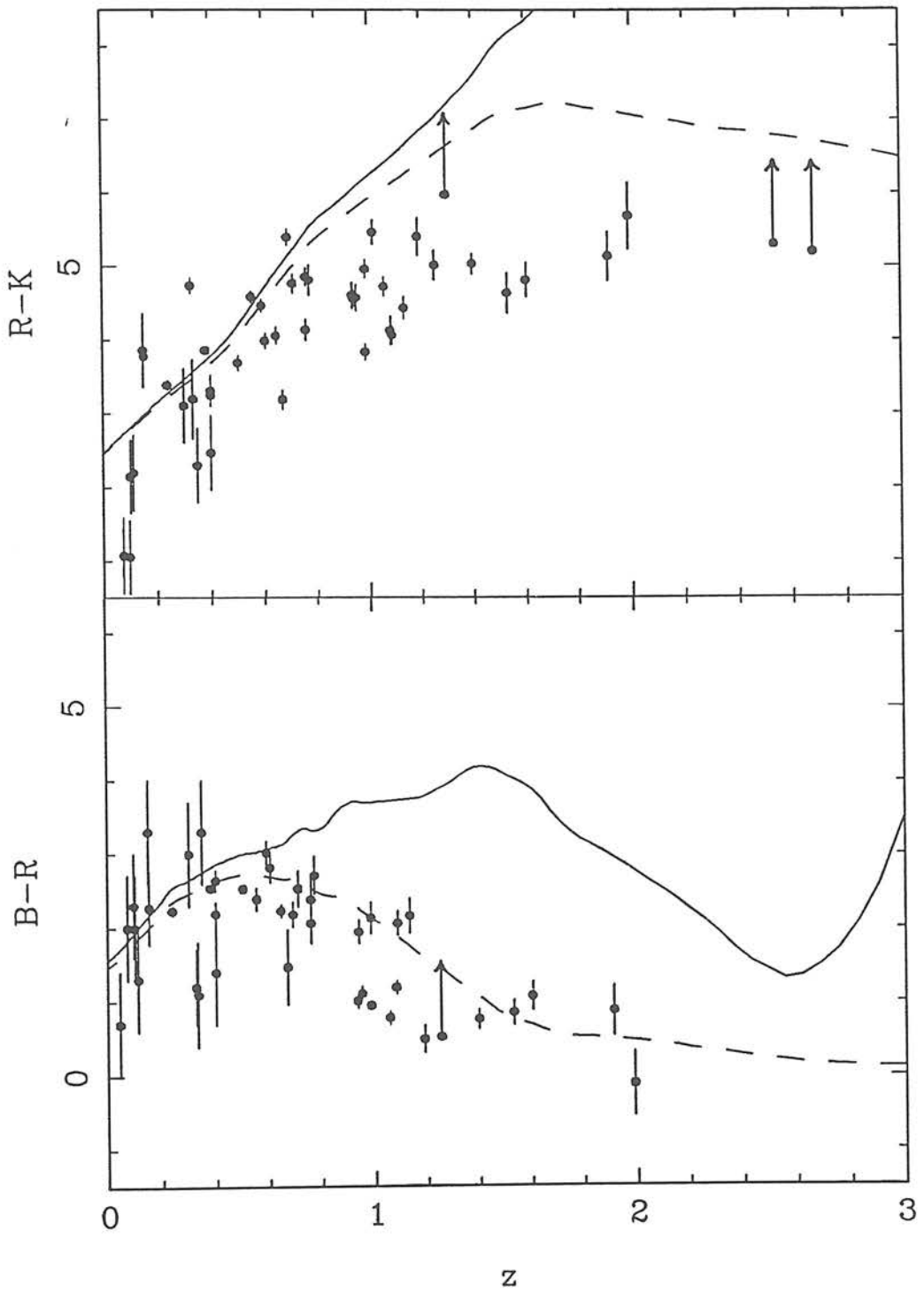

passive evolution on the R-K/z diagram, and many show considerably more dramatic evolution. No such unambiguous conclusion could have been reached on the basis of the optical colours alone - the sensitivity of the optical colours to small amounts of UV-flux is already apparent.

7.4b : Modelling the colour evolution of the radio galaxies

i) The conflict between the R-K and B-R colour diagrams

When an attempt is made to describe simultaneously the R-K/z and B-R/z data by a simple model of galaxy evolution, it is found that the two colour diagrams tend to fight against each other. This feature is illustrated in Figure 7.5. In this figure the data are compared with the colour evolution tracks produced by the UV-Cold ($\mu \sim 0.6$) and UV-Hot ($\mu \sim 0.3$) <u>evolving</u> models, assuming $\Omega = 0$, $H_o = 50$, and a formation redshift of $z_f = 5$. It is seen that the two models bracket nicely the locus of points on the B-R/z diagram, but that the same two models are completely unable to describe the R-K/z data. Older models with weaker evolution - either higher values of μ, or larger formation redshifts - are needed to fit the optical-infrared colours. Spinrad & Djorgovski (1987) noted similar behaviour in a comparison of the colours of 3C radio galaxies with the models of Bruzual - "*the data in the visual regime indicate the more active models, $\mu \sim 0.6$ but the data in the near-IR are consistent with the quieter models, $\mu \sim 0.8$ or even the passive C-models*". Spinrad conjectures that this may indicate some problem with the models. It is interesting that the same behaviour is found in the present study using both new models and a new independent set of data (although it must be remembered of course that the two models have many features in common). It is also interesting to note the similarity of the model which fits the upper envelope of the B-R data in Figure 7.5, with the Bruzual model which describes the upper envelope of the optical colours of the 3C galaxies - a $\mu = 0.7$ Bruzual model with $\Omega = 0$, $H_o = 50$, and $z_f = 5$ is shown by Spinrad (1986) as providing a good description of the upper envelope of the V-R colours of the 3C galaxies.

Figure 7.5 : Comparison of the data with the R-K and B-R colour evolution of the UV-Cold (solid line) and UV-Hot (dashed line) models, assuming $\Omega = 0$, $H_o = 50$ and formation redshift $z_f = 5$.

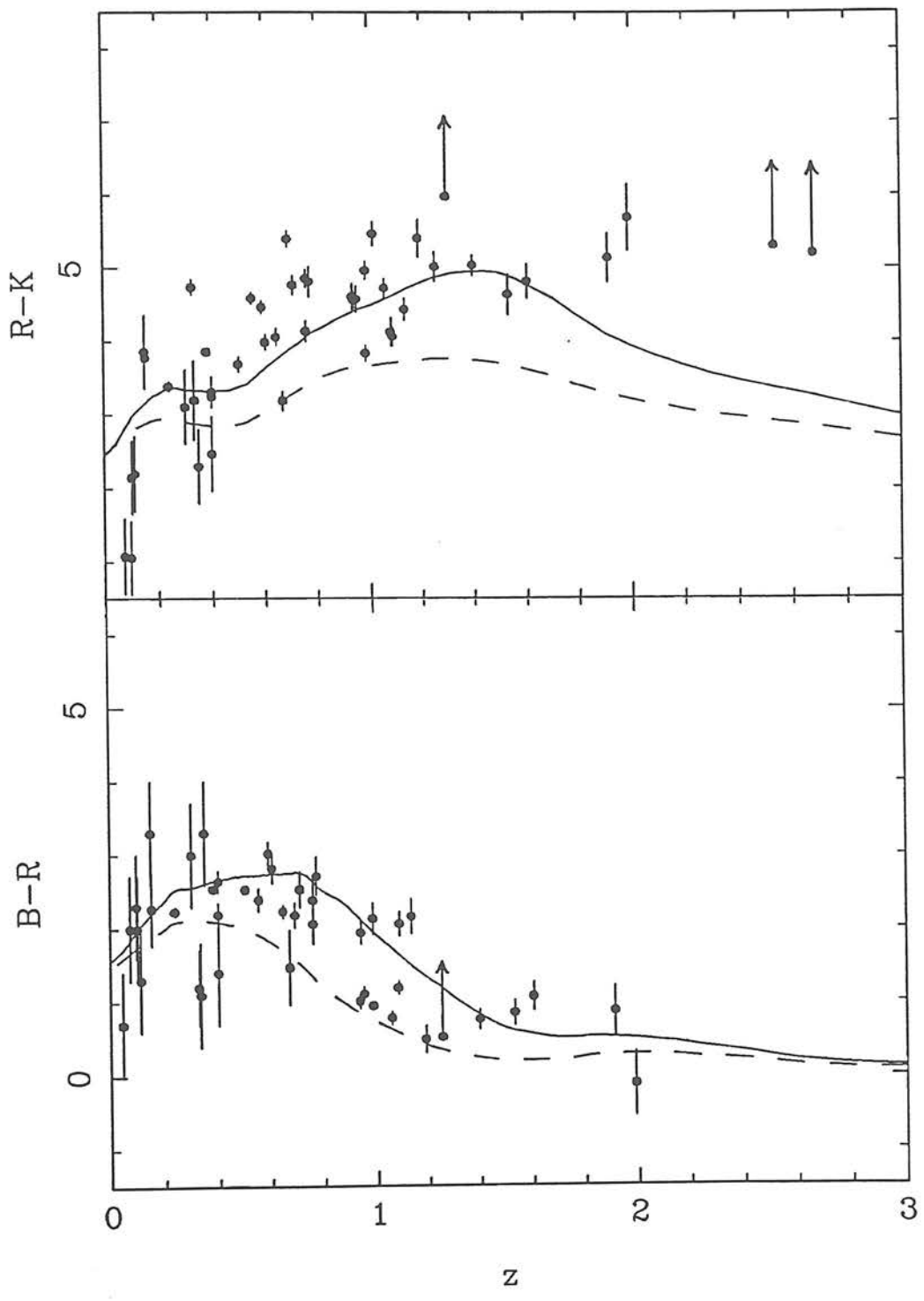

ii) Modelling the red envelope

As mentioned above, older stellar populations are needed in order to produce redder colours. In principle, therefore, the red envelope on the R-K/z diagram should represent the oldest galaxies in the sample and, however the blueward scatter from this envelope is to be interpreted (eg varying levels of star-forming activity or a range of formation redshifts - see Section 7.4c), it is important to find a model which is consistent with these oldest, relatively passive objects. The conflict between the two colour diagrams (described above in i)) means that such a model is unlikely to also be able to describe the upper envelope in B-R, but since the infrared photometry samples the oldest stellar populations in the galaxy it is important to try to fit the envelope in the R-K diagram first - models consistent with both diagrams are discussed below in iii). In Figure 7.6 the R-K colour evolution of the Burst and UV-Cold galaxy models is shown for a range of galaxy formation redshifts, z_f = 3,5,10,20. Ω = 0 and H_o = 50 are assumed. This figure shows that, even with these relatively inactive models, it is a struggle to reproduce the reddest observed galaxy colours at z ~ 1. It is only really achieved with the very oldest models shown - ie z_f = 20 which corresponds to a galaxy age t_{gal} ~ 18Gyr - and even then there are a few unexplained very red points. The corresponding plots for Ω = 1 are shown in Figure 7.7. In a closed Universe a fit to the red envelope in R-K cannot be achieved unless a very low value for the Hubble constant is assumed, because the Universe is simply not old enough to contain galaxies of the required age. A similar problem has been encountered by other workers in trying to fit Bruzual's models to the red envelope of their colour data - Windhorst *et al.* (1986) derives ages of 14 → 16Gyr for the oldest galaxies in his millijansky sample from attempts to fit Bruzual's models to the red envelope of the optical (J-F) colour redshift diagram. The work of Hamilton (1985) on the 4000Å break also implies large ages - he has found galaxies at z ~ 0.8 corresponding to a look-back time of τ = 8.6Gyr (assuming Ω = 0, H_o = 50) which are already 8 → 9Gyr old based on the evolution of the 4000Å break in Bruzual's models. The ages implied by the present study (ie ~ 18Gyr) are even more extreme than the results quoted above, partly because they are based on optical-infrared colours, and

Figure 7.6 : The effect of varying the formation redshift of the Burst (upper diagram) and UV-Cold (lower diagram) models in an attempt to produce old enough models to fit the red envelope of the R-K data. $\Omega = 0$ and $H_o = 50$ are assumed and formation redshifts of $z_f = 3$ (dotted), 5 (dot-dash), 10 (dashed) and 20 (solid) are shown.

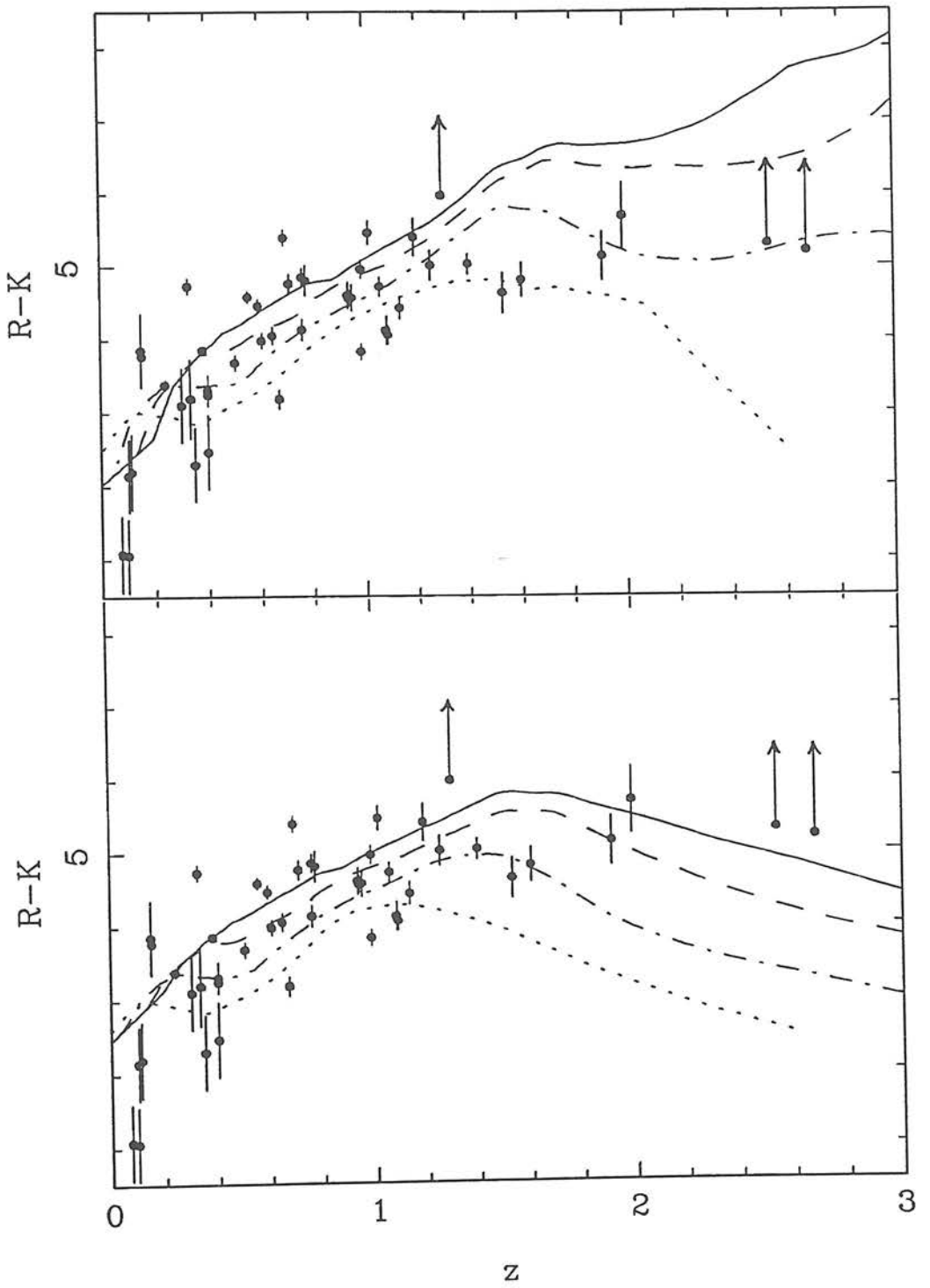

Figure 7.7 : The same as the previous figure, but this time assuming a critical Universe, $\Omega = 1$. With $H_o = 50$ the critical Universe is not old enough to contain models that are sufficiently old to model the reddest R-K colours.

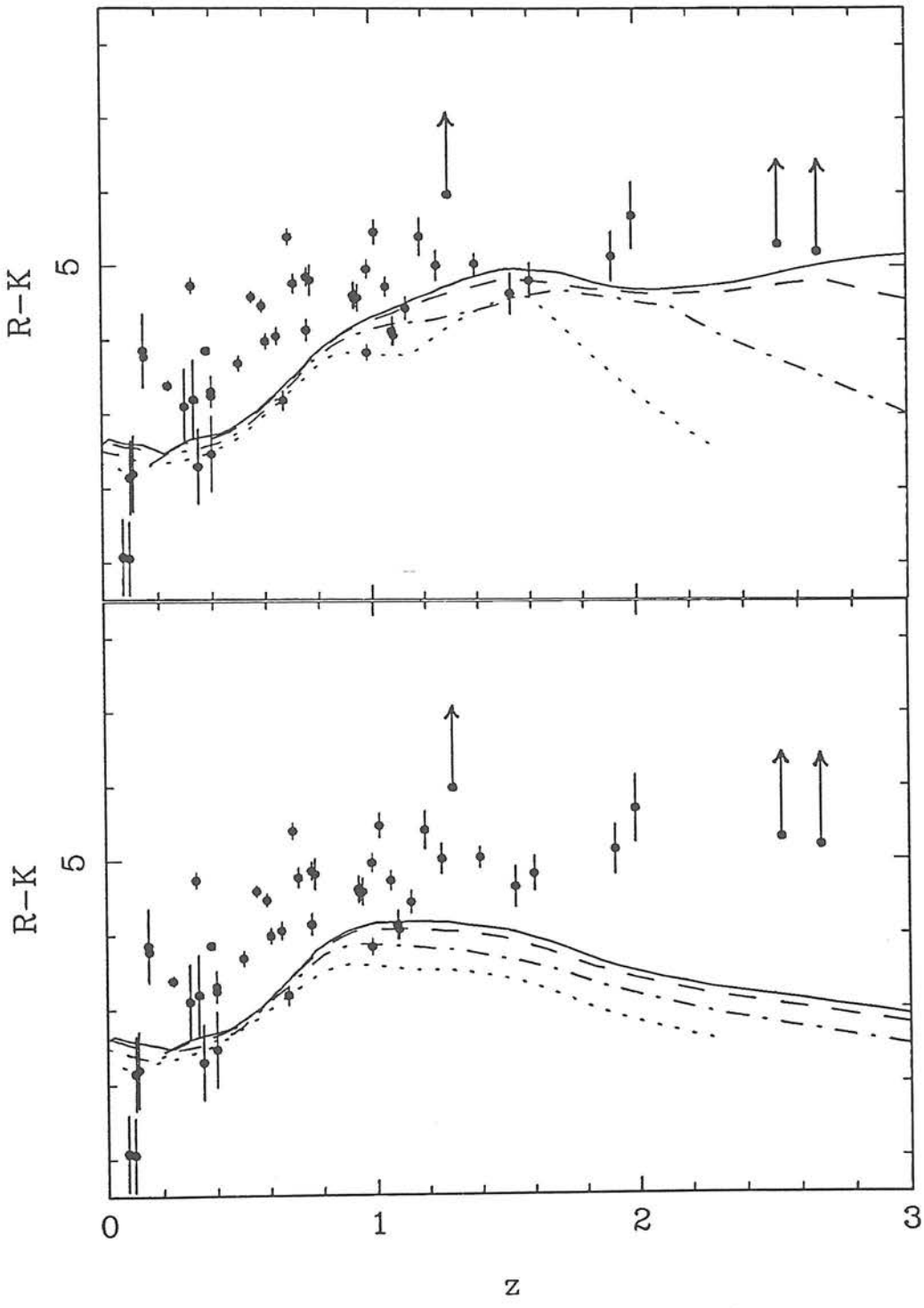

partly because the new models do not produce such red colours at z ~ 1 as do Bruzual's (because of the more sophisticated treatment of the GB in the new models - this difficulty with red colours at low z might cast some doubt as to whether the new GB is really an improvement). Taken literally, the new results suggest

$H_o < 55$ for $\Omega = 0$
$H_o < 35$ for $\Omega = 1$

These results are so extreme that they might suggest some basic problem with the models, such as an IMF which does not produce an adequate number of red giants at z ~ 1. However, it must also be remembered that the age problem in the galaxy models is to some extent an inevitable consequence of the age problem for globular clusters, given that the stellar evolution tracks input to the model have to account for them in the first place. Most recent studies of globular clusters (eg Gratton 1985, Ratcliff 1987) conclude that the ages of Galactic globular clusters are around or in excess of 15Gyr. If a low value of H_o is not desired, then some way of speeding up the stellar evolution models will have to be found.

iii) Consistent models of minimum evolution.

The absolute null hypothesis of zero evolution was rejected in Section 7.4a. It is interesting, therefore, to consider what form of evolutionary model might fulfill the role of a new more realistic null hypothesis (in other words a model of minimum evolution). The requirement of such a model is that it should simultaneously be able to describe the red envelope in both R-K and B-R colour diagrams and therefore reproduce the colours of the least active galaxies in the sample.

Lilly & Longair (1984) showed that the passively evolving C-model was a reasonable null hypothesis model on the r-K diagram for 3C radio galaxies. This is basically in agreement with Figure 7.6 which indicates that on the R-K diagram the Burst, and possibly also the UV-Cold model produce reasonable tracks of minimum evolution, provided that they are old enough. However, in the present work the

null-hypothesis model must also describe the upper envelope of the B–R data. In Figure 7.8 the old (z_f = 20, Ω = 0, H_o = 50) Burst and UV-Cold models are illustrated on both R–K and B–R diagrams – it is clear that the old Burst model is not a reasonable null-hypothesis model in B–R. This result has already been hinted at in i), and in a sense it is reassuring that a pure burst model should be inadequate, given that it is incapable of reproducing the observed spectra of elliptical galaxies at the present day. The UV-Cold model in Figure 7.8 just about qualifies as an acceptable model of minimum evolution, although it is still struggling to be red enough in R–K without losing touch with the B–R locus.

This combined analysis of the R–K and B–R colours therefore enables the following conclusions to be drawn:

a) Based on the reddest R–K colours, the initial epoch of star formation must be very early.

b) Based on the B–R colours, <u>all</u> the galaxies in the sample must have undergone some degree of star-formation activity after the initial formation epoch.

c) If conclusion b) were to be interpreted as a selection effect introduced by the fact that all the galaxies in the present study are <u>radio</u> sources, then this would imply an intimate, and probably direct connection between star-formation and radio-source activity (since ALL the radio galaxies exhibit star-formation activity).

Of course there are various ways of modelling fact b). The UV-cold model which gives an exponentially declining rate of star-formation is one. Another possibility is to decouple the old and young stellar populations and consider a two-component model. Such a model is illustrated in Figure 7.9. This shows the effect of adding to the old Burst model a constant small amount of UV flux at all epochs. The amount of UV flux which has been added is 0.7 × the UV flux of the present day UV-Hot elliptical spectrum. It is clear from the figure that the addition of this small amount of UV flux – which is typical of that seen in many present-day ellipticals – is sufficient

to enable the burst model to fit the red envelope in the B-R diagram without destroying its ability to produce the very red colours in R-K. This composite model may therefore be regarded as an alternative null hypothesis of evolution to the old UV-Cold model, and it seems that this sort of decoupling of the old and new stellar populations may well offer the best chance of reconciling the data at both optical and IR wavelengths.

The "Burst + UV light" model is of interest even if one rejects the view that the UV light in elliptical galaxies is produced by young stars. In this case the more conservative conclusion can still be stated that, by adding an amount of UV light commonly observed in present-day ellipticals (of origin not necessarily determined) an old Burst model can provide an adequate description of both the optical and IR data.

Figure 7.8 : The R-K and B-R evolution of the oldest Burst and UV-Cold models which were shown in Figure 6.6 - ie $\Omega = 0$, $H_o = 50$, and $z_f = 20$. The Burst model (solid line) cannot fit the red envelope on both diagrams, whereas the UV-Cold model (dashed line) almost can.

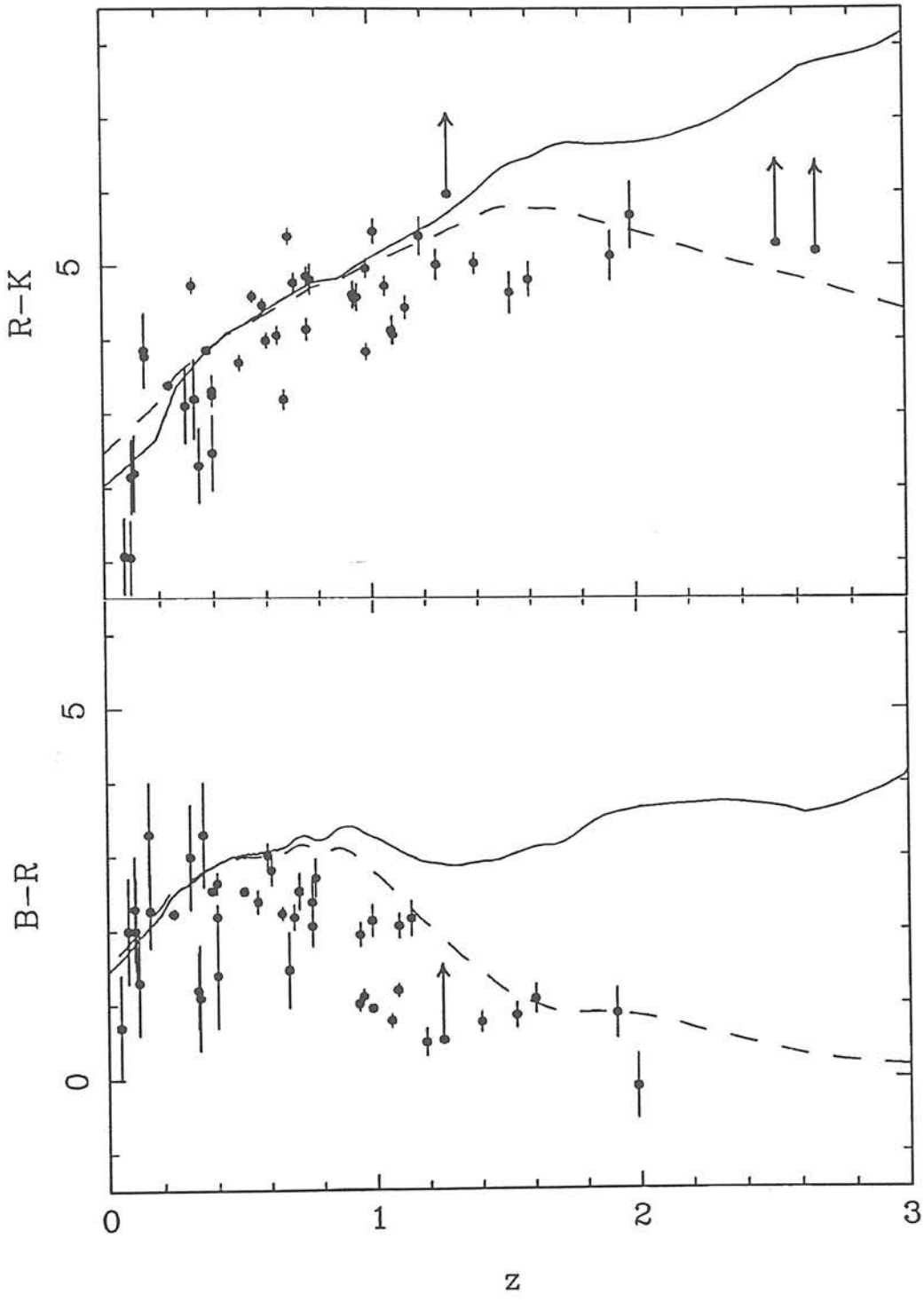

Figure 7.9 : The effect of adding a small amount of UV flux to the Burst model with $z_f = 20$, $\Omega = 0$ and $H_o = 50$. The UV flux added consists of 0.7 × the UV spectrum shortward of 3000Å which is observed in the present-day UV-hot spectrum. This is sufficient to reconcile the Burst model with the upper envelope in both diagrams. The pure Burst model is indicated by a solid line, the Burst+UV model by a dashed line.

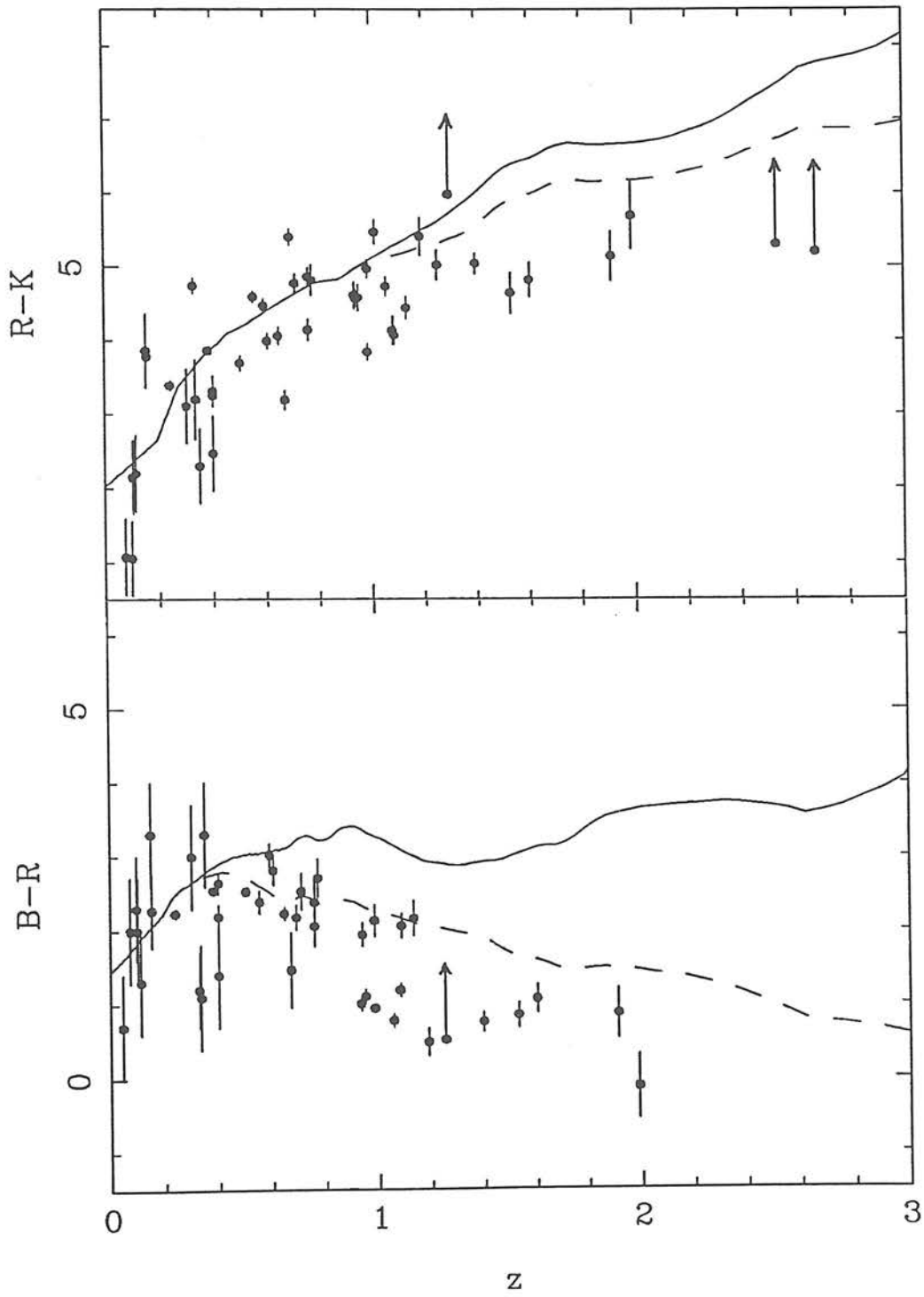

7.4c : The origin of the blueward scatter - different redshifts of formation, or different star-formation histories?

So far in this section the discussion has been confined to the problem of finding models which are capable of describing the red envelope on both colour/redshift diagrams. It therefore still remains to consider the possible origins of the blueward scatter which is so apparent in both R-K and B-R.

The physical origin of the blueward scatter is almost undoubtedly some sort of star-formation activity, but the nature, amount and cause of this activity are as yet undetermined. In reality the situation is likely to be very complex, and a detailed study of each individual galaxy would probably be necessary before a definite answer could be given. However, it is interesting to consider two very different, and probably naively simplistic, ways in which the blueward scatter might arise.

Extreme possibility number one is that all galaxies evolve in the same way, as indicated by the form of evolution required to fit the red envelope, and that the blueward scatter simply results from a range of formation redshifts. This possibility is investigated in Figure 7.10 which shows the effect of varying the formation redshift of the two "successful" models of minimum evolution which were discussed in the previous section. Figure 7.10a shows the colour evolution of the UV-Cold model for a range of formation redshifts, z_f = 1, 2, 4 & 20, assuming Ω = 0, and H_o = 50. Figure 7.10b shows the analogous plots for the Burst+UV model. These diagrams show that it is indeed possible to span the observed range of colours just by varying the formation epoch of these simple galaxy models. It is interesting that in the case of the UV-Cold model (Figure 7.10a), z_f = 2 is sufficiently recent to describe the bluest points at z ~ 1 in B-R, whereas the Burst+UV model requires these galaxies to be effectively newly formed. This means that, whatever the exact interpretation, <u>some level</u> of star formation at epochs later than z ~ 2 is required to reproduce the colours of the bluest galaxies in the sample.

Taken literally, both models indicate that galaxy formation should

Figure 7.10 : The effect on colour evolution of varying the redshift of formation.

a) The R-K and B-R colour evolution of the UV-Cold model for a range of of formation redshifts, z_f = 20 (solid line), 4 (dashed line), 2 (dot-dash line), 1 (dotted line). Ω = 0 and H_o = 50 are assumed.

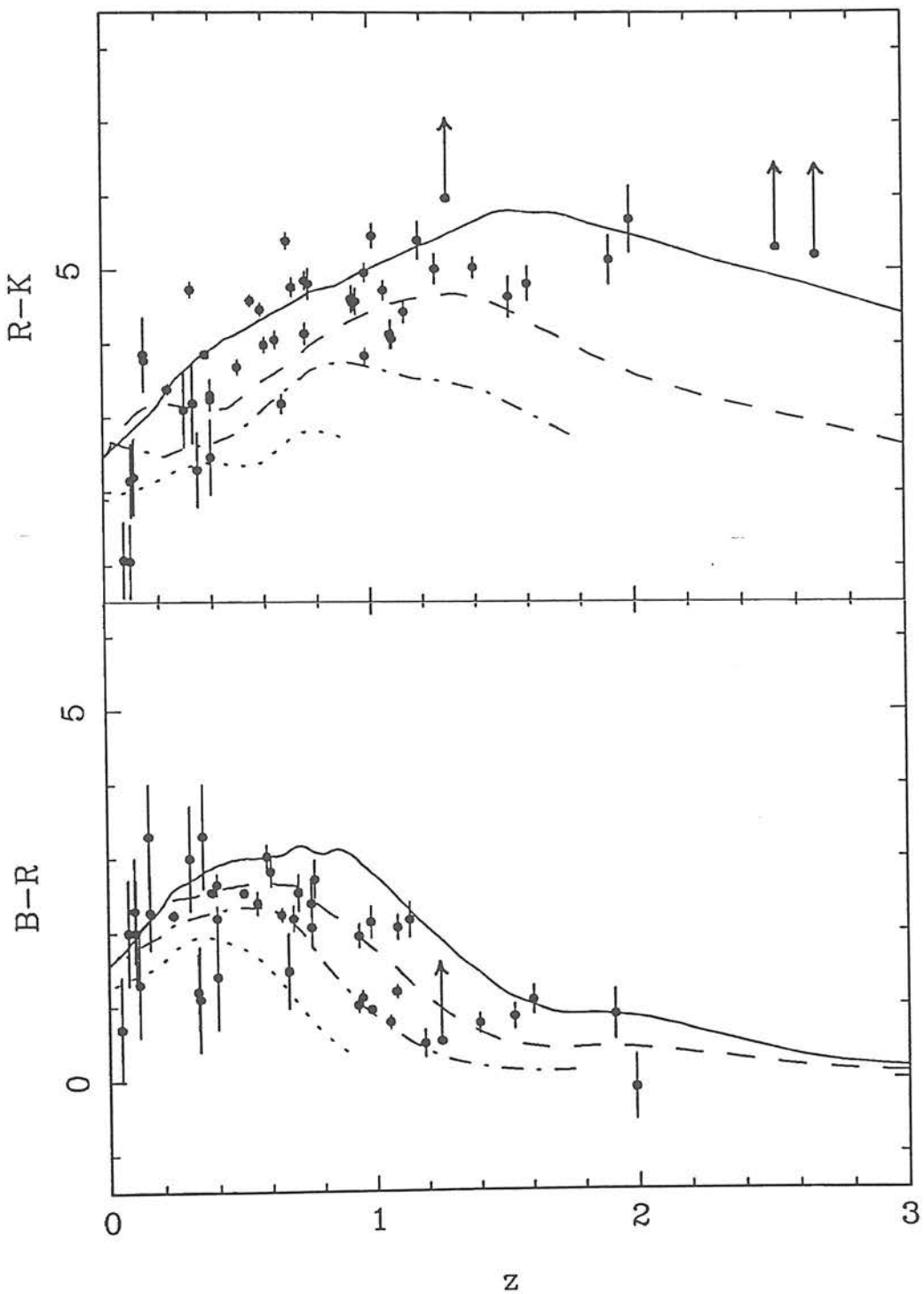

b) The R-K and B-R colour evolution of the Burst+UV model (described in Section 7.4b) for a range of formation redshifts, z_f = 20 (solid line), 4 (dashed line), 2 (dot-dash line), 1 (dotted line). $\Omega = 0$ and $H_o = 50$ are assumed.

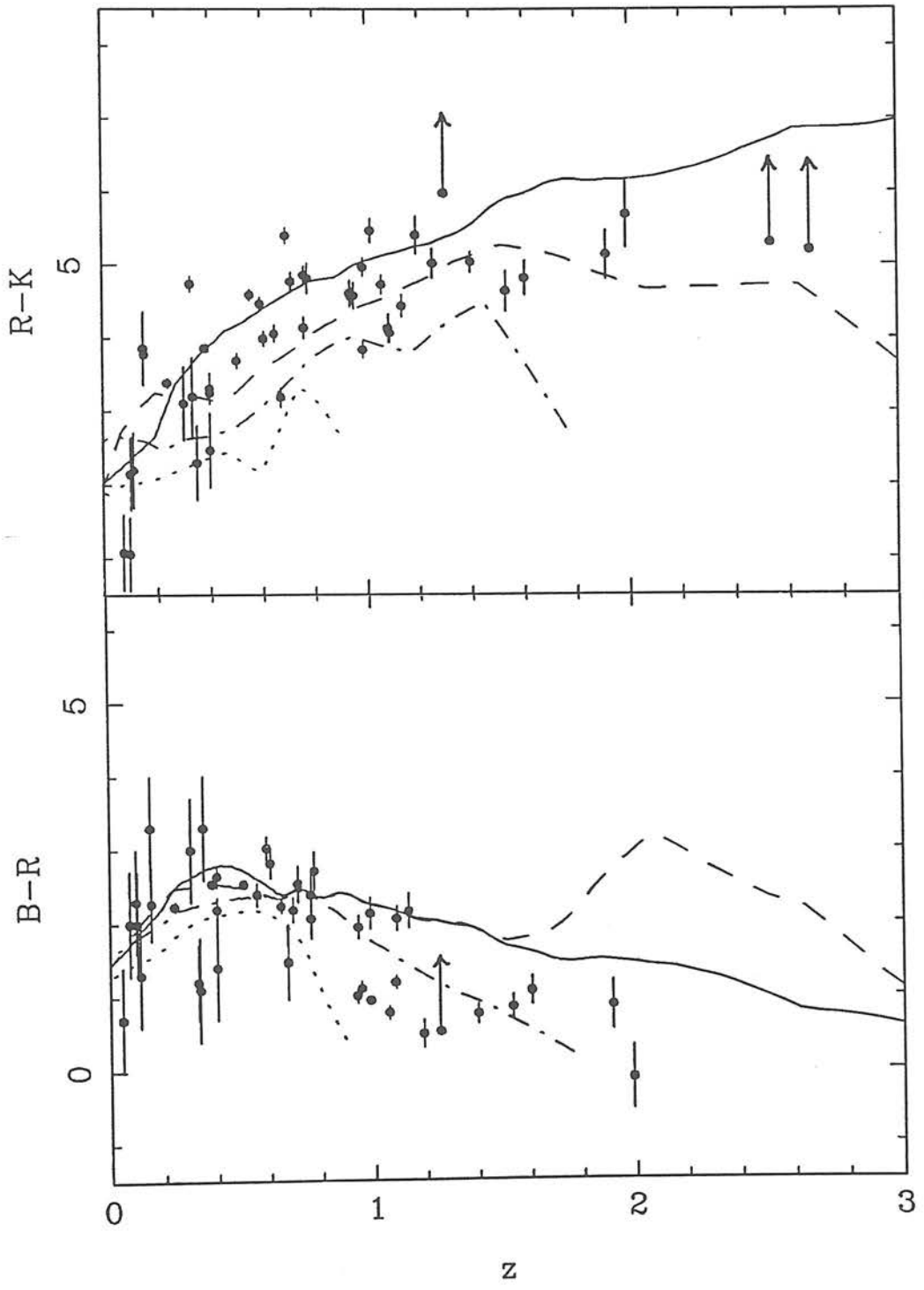

continue up to $z \sim 2$, thus implying a large range of formation redshifts - $z_f = 20$ being required to model the reddest objects. However, it is worth remembering that this range does not seem so large when considered in terms of cosmological time - with $\Omega = 0$ and $H_o = 50$, $z_f = 20$ corresponds to a look-back time of $\tau \sim 18.5$Gyr, while $z_f = 2$ corresponds to $\tau \sim 13$Gyr.

Finally it is important to note that these diagrams are deceptively impressive if the R-K/z and B-R/z plots are viewed individually rather than together. If this very simple explanation of the observed range of colours were to be correct, objects which lie on a particular evolutionary track (for example the $z_f = 2$ track) in the B-R diagram should also lie on the corresponding track in R-K. This is certainly not the case for the Burst+UV model - the $z_f = 2$ track virtually follows the blue envelope in R-K but fails to reproduce the bluest B-R colours. For the UV-Cold model the two diagrams are rather more consistent, but the R-K colours still suggest rather higher formation redshifts than are indicated by the optical colours. Once again it seems difficult to simultaneously explain the two colour diagrams without decoupling the old and the new stellar populations.

The second extreme possibility is to assume that all the galaxies were formed at the same epoch, which must, by necessity, be the epoch required to model the reddest galaxies (ie $z_f = 20$ for the present study). In this picture the blue scatter must then be considered to represent differences in the star-formation histories of individual galaxies. It is therefore interesting to consider the impact of sudden bursts of star-formation activity on the colour evolution of an old, otherwise passively evolving galaxy (ie an old Burst model). Such starbursts could conceivably be triggered by environmental effects such as interactions/mergers, or possibly even directly by the onset of radio activity itself (see Chapter 8). Models to investigate this effect were constructed by superimposing a second burst model onto an old $z_f = 20$ burst model, after an appropriate delay in cosmological time. The two parameters of interest are clearly the size of the second burst relative to the size of the underlying galaxy, and the redshift at which it occurs. Figure 7.11 illustrates the effect of varying the former. The redshift of the burst has been

held constant at z ~ 2 (ie ~ 5.5Gyr after formation of the underlying galaxy) while its size relative to the mass of the existing galaxy is varied from 1 (ie a merger) to 0.001. One interesting feature of this figure is that, immediately after the second burst has occurred, the B-R colour is very insensitive to the size of the starburst, whereas the amount of sudden bluening in R-K is a strong function of the fraction of mass involved. This behaviour is best understood by referring to Figures 7.1 and 7.2. The approximate centroid wavelengths of the B, R and K filters are 4500, 6500 and 22000Å respectively. At z ~ 2 these filters therefore sample the spectrum at rest-frame wavelengths of 1500, 2200 and 7300Å. By this redshift, a Burst model formed at z_f = 20 is ~ 5.5Gyr old and, as is clear from Figure 7.1a, no longer possesses essentially any flux shortward of ~ 3000Å. As can been seen from the shape of the spectrum in the first frame of Figure 7.1a, the sudden occurrence of even a small burst will add a lot of ultraviolet flux to the spectrum of the galaxy and, because of the lack of residual flux from the old galaxy in this region, the resultant shape of the spectrum shortward of 3000Å will be practically independent of the size of the new burst. Since colours are sensitive only to the shape, and not the absolute height, of the spectral energy distribution, it is thus clear why the B-R colour is independent of the size of the burst (at this redshift). In contrast to the situation in the ultraviolet, at 7300Å the old galaxy possesses a large amount of flux, and so the addition of a small burst will have an insignificant effect on the measured K magnitude. This makes the R-K colour a very sensitive measure of the burst size because, at these high redshifts, the R filter is sampling the rest frame ultraviolet light.

The R-K colours can therefore be used to set limits on the permissible size of a starburst, relative to that of the underlying galaxy. If the two datapoints at z ~ 2 are to be explained by a starburst in an old galaxy, their R-K colours constrain the size of that starburst to be ~0.01 × the mass of the galaxy (ie the dashed line in Figure 7.11). However it is then apparent from Figure 7.11 that a starburst at z ~ 2 of this limited size does not affect the colours for very long. Indeed, even the largest burst shown, which represents a doubling of the size of the galaxy, cannot explain the

Figure 7.11 : The effect on the R-K and B-R colour evolution of varying the size of a starburst which occurs at z ~ 2 in an old (z_f = 20) passively evolving elliptical galaxy. The fraction of the final galaxy which is assumed to form at z = 2 is 0.001 (solid line), 0.01 (dashed line), 0.1 (dot-dash line), 0.5 (dotted line). Ω = 0 and H_o = 50 are assumed.

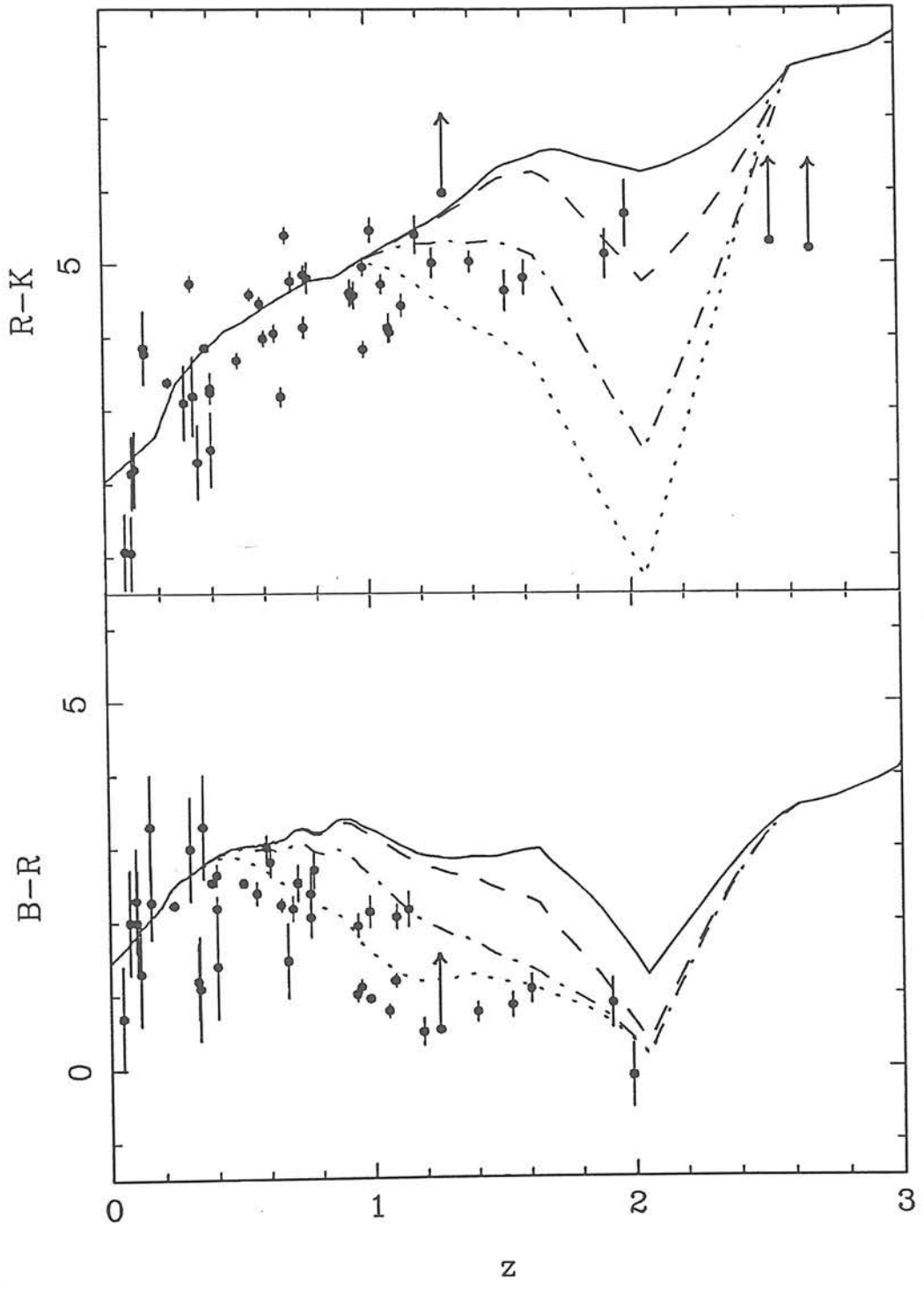

bluest galaxies at z ~ 1 in either R-K or B-R diagrams.

This leads naturally on to the investigation of the second parameter - the epoch at which the second burst occurs. In Figure 7.12 the burst size of 0.01 × the galaxy mass has been taken as a working hypothesis, and the epoch of the burst has been varied - the figure shows the effects of starbursts occurring 5, 7 and 9Gyr after the initial formation epoch (corresponding to redshifts of z ~ 2, 1.3 and 0.9). It is clear from the B-R diagram that bursts of this magnitude are sufficient to account for the full range of optical colours if a suitable burst redshift is chosen for each datapoint. This figure reemphasizes the short recovery time from bursts of this size, implying that the optically bluest galaxies must be being observed at, or very shortly after, the occurrence of the starburst.

Small isolated bursts can therefore account for the blueward scatter in B-R. However it is clear from Figure 7.12 that they do not succeed in R-K. For redshifts less than one both the R and the K magnitudes are relatively insensitive to the new UV flux from a small burst - a fact which is again best understood by referring to Figures 7.1 and 7.2 - and so single small bursts cannot account for the scatter in R-K at low z. One way to reproduce the bluer R-K colours would be to increase the burst sizes at low redshift sufficiently to affect the R magnitude, despite the fact that the R-K colours at high z would only seem to permit small bursts. Another solution is to build up the flux in the near ultraviolet region via a series of small bursts - a situation in effect indistinguishable from a μ model. Whatever the exact details, it is clear that the blue R-K colours at low z can only be explained if a larger mass of the galaxy is involved in recent star-formation activity.

These models serve to illustrate some possible explanations for the observed scatter in colour, and the problems involved. It is probably important first to achieve an adequate description of the optical-infrared data, since it is clearly rather easy to alter the optical colours. Possibly the best solution is to choose a range of μ models, or a range of formation redshifts, to model the scatter in R-K, and then add to these models a small burst whenever some

Figure 7.12 : The effect on the R-K and B-R colour evolution of varying the epoch at which a small starburst (~ 0.01 × the mass of the galaxy) occurs in an old (z_f = 20) passively evolving elliptical galaxy. The starbursts shown occur 5 (solid line), 7 (dashed line) and 9Gyr (dotted line) after the initial formation epoch (corresponding to redshifts of z ~ 2, 1.3, 0.9). Ω = 0 and H_o = 50 are assumed.

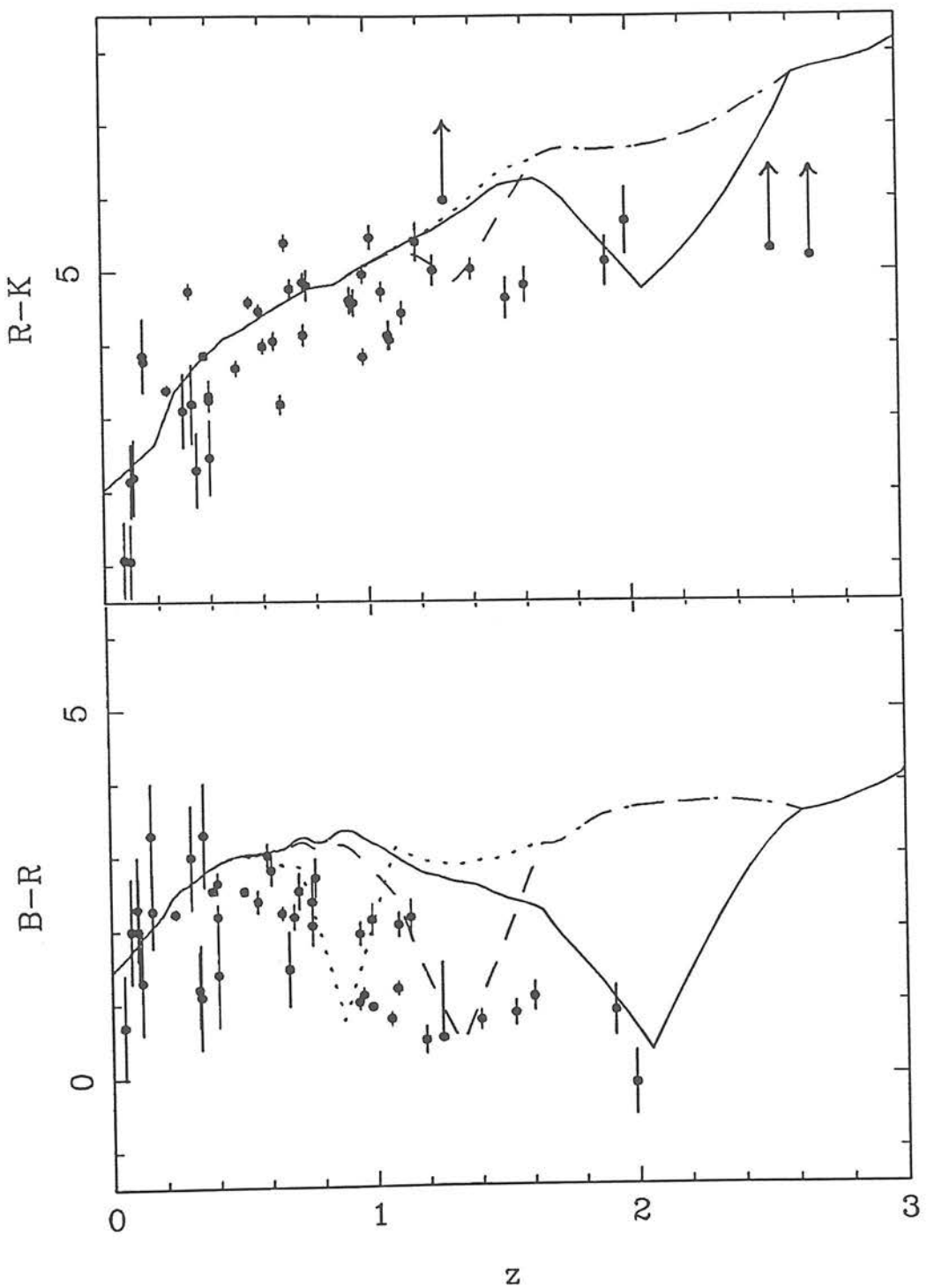

additional far-UV flux is required to produce blue enough B-R colours.

The importance of the infrared data is clear - an optical colour of B-R = 0 at z ~ 2 can be achieved either by formation of the whole galaxy at that redshift, or simply by a small starburst in a much older galaxy. Of course it should in principle be possible to check whether the blue galaxies at z ~ 1 → 2 are genuinely primeval by examination of their optical images, or spectra. This topic is discussed in Chapter 8. Finally, it is worth noting that the burst calculations presented above help to re-emphasize why it is that the infrared Hubble diagram is so much tighter at high redshift than its optical counterpart. The full range of B-R and R-K colours at high z can be reproduced by bursts which are too small to significantly affect the measured K magnitudes, at least up to z ~ 3.

7.4d : Consistency of the models with the estimated redshifts

Finally, it remains to check whether the K-magnitude estimated redshifts used throughout this chapter are consistent with the K-z relations predicted by the models which have been found to fit the colour evolution. The estimated redshifts were derived from the MEAN K-z relation shown in Figure 6.1, which was defined empirically for galaxies brighter than K ~ 17.5. The 3C and 1Jy galaxy data shown in Figure 6.1 are shown again in Figure 7.13, this time with the theoretical K-z relations predicted by two of the new models of spectral evolution. The deviation of the models from the data at low redshift simply results from the fact that aperture corrections have not been applied to the models. The subject of interest is the form of the K-z relation at high redshift. The solid curve is the simplest model which was found to describe the colour data in this chapter - ie the UV-Cold model formed at $z_f = 20$, with $\Omega = 0$, $H_o = 50$ (see Section 7.4b). Comparison with Figure 6.1 shows that the high-redshift form of this K-z relation is very similar to that used to derive the MEAN-z estimates, thus indicating that the modelling of the colour/redshift data is internally consistent. The dashed curve in Figure 7.13 is the K-z relation predicted by the UV-Cold model if it

is formed at z_f = 3.5. The form of this curve at high redshift is, as expected, very similar to the HIGH-z K-z relation shown in Figure 6.1, which was based on a Bruzual C-model with z_f = 3.5. Essentially these young models predict that a galaxy with K ~ 18 should be practically at its formation redshift of 3.5. It is interesting to ask what the implications would be for the analysis of the colour data presented in this chapter if the galaxy redshift estimates were altered to these high values. The answer is that it would be impossible to reconcile the model used to provide the K-z relation, with the resulting colour/redshift data. Use of the HIGH-z estimates would result in the galaxies on the R-K diagram with z > 1.5 all moving out to significantly higher z. Since these galaxies are all fairly red (R-K ~ 5) this would simply strengthen the case for an old model being necessary to fit the optical-infrared colours. This is further evidence that the MEAN-z or LOW-z estimates of Chapter 6 are more likely to be correct than the HIGH-z values because only then is it possible to find a model which is consistent with both the K-z and colour/redshift diagrams.

Figure 7.13 : The empirical K-z relation compared with the curves predicted by the UV-Cold (μ ~ 0.6) model of galaxy evolution. The solid line results from a formation redshift of z_f = 20, the dashed from z_f = 3.5. The filled circles are galaxies from the 3CR sample (Lilly & Longair 1984) while the open circles are galaxies from the 1Jy sample (Lilly *et al.* 1985) The deviation of the models from the data at low-z occurs because aperture corrections have not been applied to the models. The absolute size of the model galaxy is the same for both models - chosen to straddle the pack of data points at z ~ 0.4. The high-redshift form of the z_f = 20 K-z relation is very similar to the MEAN-z relation which was used to estimate the galaxy redshifts (see Figure 6.1).

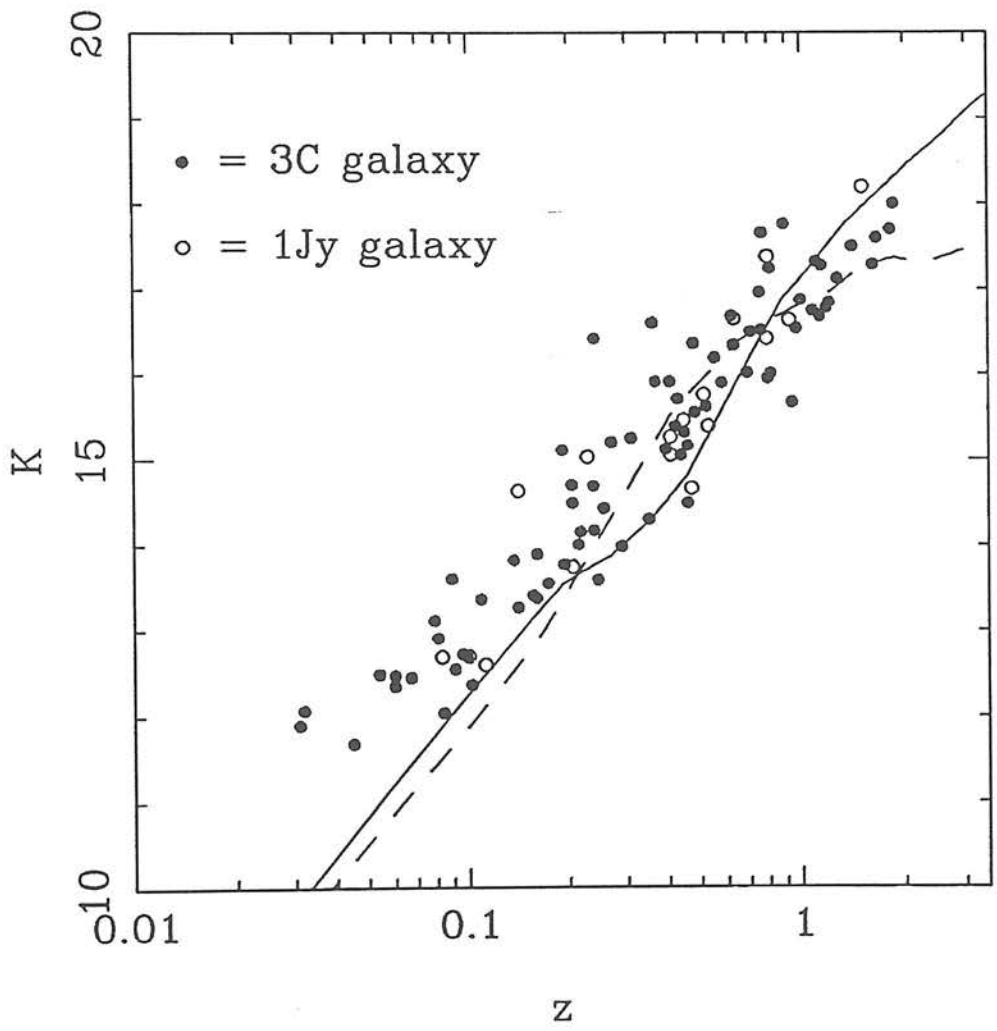

7.5 : SUMMARY OF CONCLUSIONS

The main conclusions from the work described in this chapter may be summarized as follows:

i) ALL the radio galaxies in the sample display at least passive evolution, and a large fraction show signs of more active behaviour. This result is in agreement with that found for the 3C and 1Jy samples by Lilly & Longair (1984) and Lilly *et al.* (1985), but is now found by comparison with more realistic NE models based on the full range of observed present day elliptical spectra. It is not possible to deduce the existence of evolution for the whole sample using only optical data.

ii) It is difficult, with simple models, to reproduce simultaneously both the optical-infrared and optical colour evolution - the former generally implying older and more passive models than the latter. This behaviour is very similar to the problems encountered in trying to fit Bruzual's models to the 3C data (Spinrad & Djorgovski 1987). The new μ-model which best describes the upper envelope of the B-R colours of the Selected Region galaxies is remarkably similar to the Bruzual model which best describes the upper envelope of the 3C optical colours.

iii) To reproduce the reddest R-K colours found in the sample, a formation epoch of $\tau \approx 18.5$Gyr is required. Such ages cannot be accommodated in a closed Universe unless $H_o < 35$, which at present seems highly unlikely. Even in an empty Universe with $H_o = 50$ this implies a formation redshift as large as $z_f = 20$. Other workers have encountered similar age difficulties using Bruzual's models, but not in such a severe form. This problem is intimately connected with the large globular cluster ages at present predicted by stellar evolution theory, since the galaxy models are based on theoretical tracks of stellar evolution. However the especially severe nature of the problem in the present study reflects the difficulty that the new models of Guiderdoni & Rocca-Volmerange have in producing red R-K colours, since the reddest R-K colours in the present sample are no more extreme than were found in the 3C or 1Jy samples. Thus, despite the

attempt of the new models to include a more sophisticated treatment of the GB and post-GB stages, it may well be that problems still remain in the modelling of these phases. There are indications that lower values of metallicity will shift the GB in a way that will result in redder R-K colours. (Guiderdoni, private communication).

iv) An old (z_f = 20) burst model cannot fit the red envelope in the B-R/z diagram, thus implying that ALL the radio galaxies in the sample must experience some star formation activity after the initial formation epoch. This means that, if such star formation were to be peculiar to radio galaxies, the connection between radio activity and star formation would have to be an intimate one. The requirement of star formation after the initial formation epoch can be modelled by a μ-model, μ = 0.6 being just capable of fitting the red envelope in both R-K and B-R colour diagrams. However, this is such a struggle that it suggests that a better solution may be to decouple the old and the new stellar populations and consider a two-component model. A successful fit in both diagrams was achieved by adding the UV flux of a "hottish" present-day elliptical to the old Burst model at all epochs. This result is interesting even if one rejects the idea that the UV flux is produced by young stars. However, in a sense this Burst+UV model is actually the simplest, physically sensible model of minimum evolution - in a real-life galaxy there will always be some gas available for residual star formation, unless the initial burst is perfectly efficient and the subsequent ejecta are blown out of the galaxy. It is worth noting that μ-models, despite their apparently naively simplistic parameterization, may also have a physical basis since they represent the effect of a constant efficiency of star-formation throughout the lifetime of the galaxy. Alternatively they can be considered to represent a series of starbursts of decreasing size, rather than continuous star formation.

v) The blueward scatter in both diagrams can be described by assuming that the galaxies form over the redshift range z_f = 2 → 20, but otherwise evolve in the same manner. However, individual galaxies do not always lie on the corresponding evolution tracks in the two colour diagrams.

vi) The blueward scatter in B-R can be successfully modelled by "small" (~ 0.01 x the galaxy mass) starbursts provided the bluest galaxies are observed very soon after the burst has occurred. The R-K colours at high redshift constrain the possible burst size to be this small, but the R-K colours at low redshift seem to require larger amounts of star formation. The best solution in the context of the present models is to first fit the scatter in R-K via either an appropriate range of μ-models, or a range of formation redshifts, and then add small starbursts to achieve the desired optical colour.

The approach used in this Chapter - ie, existence of evolution → modelling the reddest galaxies → modelling the red envelope in both colours → modelling the blueward scatter - has been adopted simply to try to extract some clear conclusions from what is potentially a very large parameter space. It must be borne in mind that most of the results, except of course the existence of evolution, are inevitably model dependent to some extent. It would therefore be unwise to lay too much weight on, for example, the values of the ages deduced for the oldest galaxies. However there are several factors which provide both confidence and encouragement, not least the fact that the results found by comparing the new data with the new models are so consistent with those which have been found through comparison of the 3C data with Bruzual's models, and this despite the large number of estimated redshifts in the present sample. Given the lower radio luminosity of the galaxies in the Selected Regions, this can be regarded as an encouraging step in the direction of establishing that radio galaxies are indeed unbiassed probes of the evolution of elliptical galaxies at high z. The ultimate confirmation of this belief must of course come from similar studies of radio-quiet elliptical galaxies. Eisenhardt & Lebofsky (1987) (see also Lebofsky & Eisenhardt 1986) have attempted to compare the colour evolution of radio-quiet and radio-loud ellipticals, and have concluded that there is no significant difference between the evolution of the two populations. However, their sample of radio-quiet ellipticals contains only two galaxies with redshifts greater than 0.7. It would therefore be unwise to consider the issue settled, since the dramatic evolution in the radio galaxies is seen at z ~ 1 - at present radio

galaxies remain the only available probes of the "epoch of action". There is probably more reason for confidence in the infrared than in the optical because of the possibility that starbursts are closely connected with radio activity. Radio galaxies are unusual in displaying extended low-ionization line emission - Hamilton (1985) detected no [OII] emission in any of his red, radio-quiet ellipticals. Whether this then implies that radio galaxies are also unusual in displaying star formation is a more difficult question which will be discussed further in Chapter 8.

Chapter 8 : CONCLUSION - THE RELATIONSHIP BETWEEN RADIO SOURCE EVOLUTION AND COSMOLOGICAL EVOLUTION IN GENERAL

8.1 : INTRODUCTION

This thesis has been concerned purely with the evolution of radio sources and their host galaxies. The purpose of this final chapter is to consider how the results presented in Chapters 6 and 7 relate to the evolution of quasars and galaxies in general. Section 8.2 discusses the high-redshift evolution of optically-selected quasars, and in particular whether there is any evidence that radio-quiet quasars suffer a similar redshift cutoff to their radio-loud counterparts. Section 8.3 considers the possibility that the dramatic colour evolution found in Chapter 7 might be peculiar to radio galaxies, and discusses some ways in which radio source and star formation activity could be closely connected. Section 8.4 discusses whether there is any evidence that the redshift cutoff in the radio-source population is closely related to the epoch of galaxy formation - are there any potential primeval galaxies in the Selected Regions sample? Finally, Section 8.5 concludes with some suggestions for future work.

8.2 : THE HIGH-REDSHIFT EVOLUTION OF OPTICALLY-SELECTED QUASARS

Progress in the study of quasar evolution in the optical has been slower than in the radio, simply because of the much greater difficulty in selecting complete samples at optical wavelengths. Nevertheless, in recent years it has proved possible to select large complete samples of quasars on the basis of ultra-violet excess (UVX) (eg Boyle *et al.* 1987a, 1987b). This has enabled the form and evolution of the quasar optical luminosity function to be determined out to a redshift $z \sim 2$, beyond which UVX ceases to be an effective selection criterion. As discussed briefly in Chapter 6, Section 6.5a, this evolving luminosity function can be described as a two power-law function which undergoes pure luminosity evolution ($L(z) \propto$

$(1+z)^k$) and which, if extrapolated to $z = 0$, agrees well with the Seyfert galaxy luminosity function (Marshall 1986, 1987, Boyle *et al.* 1987a, 1987b).

The "low-redshift" evolution of optically-selected quasars is thus now fairly well determined, but at higher redshifts (ie $z > 2$) the problems of selection become much more complex (see Chapter 5, Section 5.4c) and as a result the situation is much less clear. In the past year two groups, using two very different methods, have made a concerted attempt to construct complete samples of quasars with $z > 3$. Warren, Osmer and Hewett have used a multi-colour selection technique (similar to that used by Koo 1986b) to select quasar candidates from UK Schmidt plates using the Automatic Plate Measuring machine at Cambridge (eg Warren *et al.* 1987). In contrast, Schmidt, Schneider and Gunn have attempted to select quasars on the basis of emission lines by using a Grism, coupled with a red-sensitive CCD detector, to obtain large numbers of low-resolution spectra (Schmidt, Schneider & Gunn 1986a, 1986b, 1987a, 1987b). Both these techniques should be capable of selecting quasars with redshifts $z > 4$ (and have indeed done so - Warren *et al.* 1987, Schmidt, Schneider & Gunn 1987b).

The most recent results of these two surveys are shown in Figure 8.1. The Warren, Osmer and Hewett sample now comprises 24 confirmed quasars with $z > 3$ and $R < 20$ in the 30 deg^2 South Galactic Pole (SGP) field (Hewett, private communication), while the Schmidt, Schneider and Gunn survey has now yielded 10 quasars with $z > 3$ in 14 deg^2 (Schmidt, Schneider and Gunn 1987a, 1987b). These two samples are consistent with each other provided that they correspond to similar magnitude limits. This is in fact probably the case - because of the emission-line selection technique the effective limiting magnitude of the Schmidt, Schneider and Gunn survey is redshift dependent, but they quote an approximate limiting magnitude of $B \sim 20.5$ which, for an optical spectral index of $\alpha = 0.5$, is equivalent to $R \sim 20$ (although two of their ten quasars have estimated magnitudes fainter than this).

Because it is larger and its limiting magnitude is more clearly

Figure 8.1 : The most recent results of the two programmes aimed at providing complete samples of faint high-redshift quasars. The Warren, Osmer and Hewett sample contains 24 quasars brighter than R = 20 over an area of 30 deg^2 (Hewett, private communication). The Schmidt, Schneider and Gunn survey has now discovered 10 quasars in an area of 14 deg^2 down to a comparable limiting magnitude.

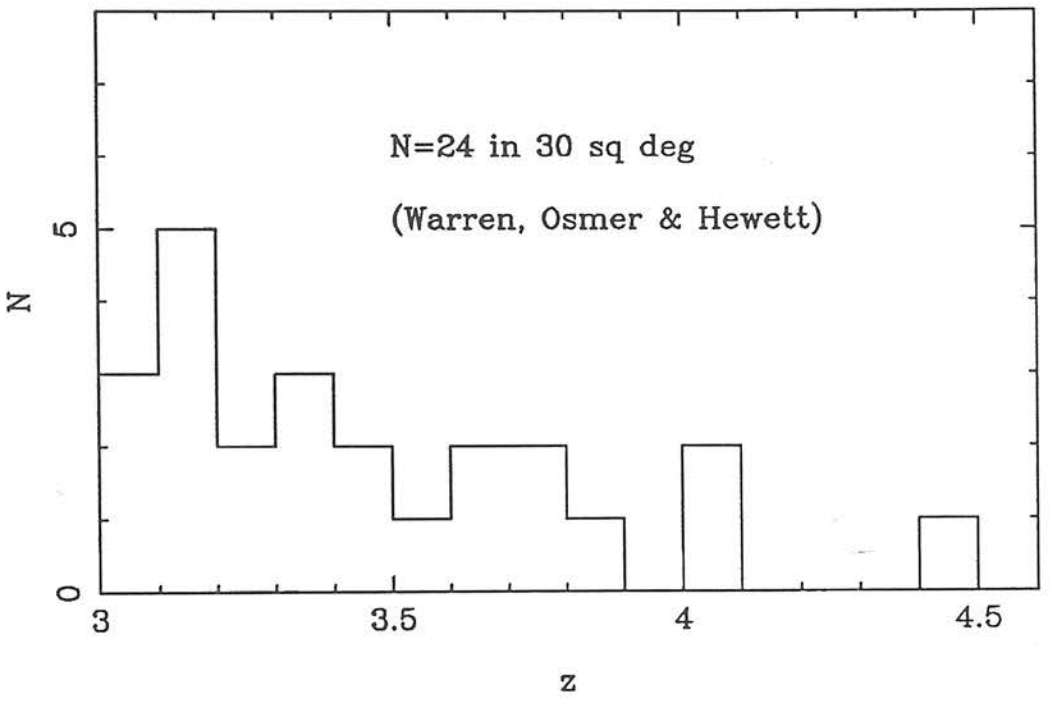

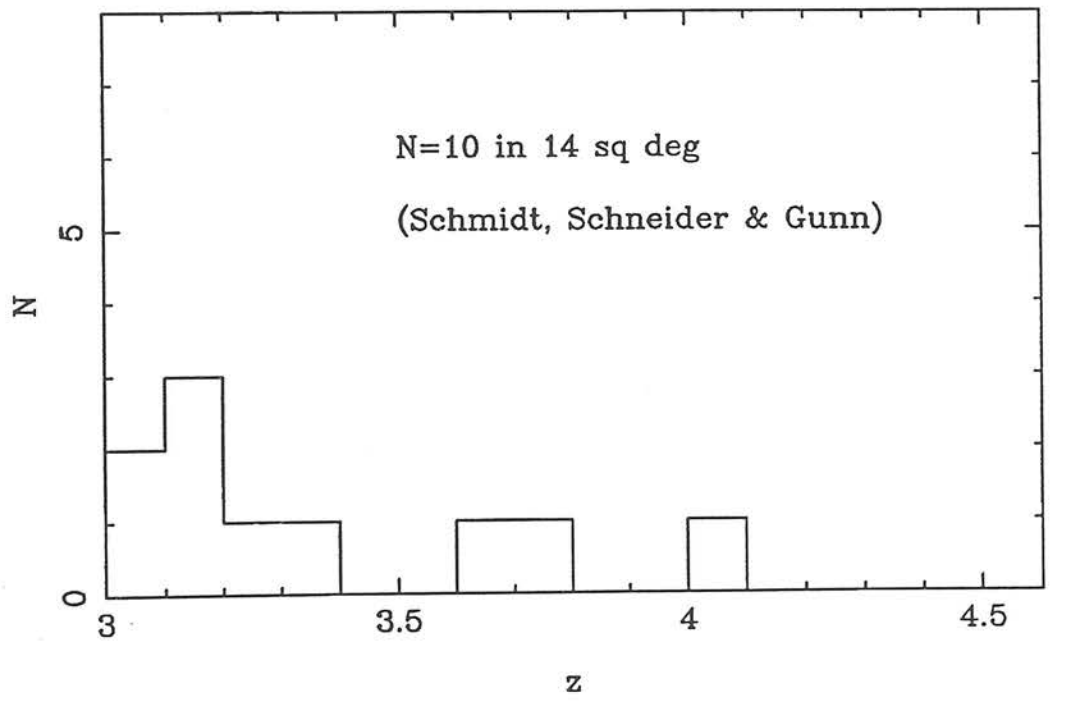

defined, the Warren, Osmer and Hewett sample has been used for comparison with model predictions in the rest of this section. This decision was also made because there remain doubts over the reliability of the Schmidt, Schneider and Gunn results - originally Schmidt *et al.* 1986b found no quasars with $z > 3$ in 7.84 deg^2 of sky, a result which is clearly incompatible with their more recent data described above.

The implications of such results for the high-redshift cutoff have often been confused by a tendency to compare the data with rather extreme extrapolations of the strong positive evolution found at low redshift - there is no doubt that the data are inconsistent with continuing pure luminosity evolution of the form $(1+z)^k$ above $z = 2$, which would predict ~900 quasars between $z = 3$ and $z = 5$ and with $R < 20$ in the 30 deg^2 SGP field! However, a more meaningful null hypothesis is to assume that no further evolution (positive or negative) occurs beyond $z = 2$ (ie taking the $z = 2$ luminosity function to be valid for all higher redshifts). Such a comparison model was therefore constructed, based on the low-redshift luminosity function:

$$\Phi(M_B) = \Phi_o \left[\left[\frac{L}{L_*(1+z)^k} \right]^{2.6} + \left[\frac{L}{L_*(1+z)^k} \right]^{0.25} \right] \qquad (8.1)$$

where Φ is the (differential) comoving density of quasars per magnitude, and L_* is the 'break' luminosity at $z = 0$ which corresponds to an absolute magnitude of $M_B = -21.8$. For $\Omega = 0$, $k = 3.5$ and $\Phi_o = 1331$ Gpc^{-3}, while for $\Omega = 1$, $k = 3.2$ and $\Phi_o = 1512$ Gpc^{-3} (assuming an optical spectral index of $\alpha = 0.5$). This functional form is consistent with the determination given by Marshall (1986, 1987) and the more recent results of Boyle *et al.* (1987a, 1987b).

Figure 8.2 illustrates the result of freezing this luminosity function for $z > 2$, in the form of simulated versions (for $\Omega = 1$ and $\Omega = 0$) of the Warren, Osmer and Hewett sample redshift distribution (ie $z > 3$, $R < 20$, 30 deg^2 - for consistency $\alpha = 0.5$ has again been assumed). The data are shown for comparison. It is clear from this

Figure 8.2 : Comparison of the observed redshift distribution (shown hatched) of $z > 3$ quasars with $R < 20$ in the 30 deg^2 SGP field with the theoretical prediction of a model with zero evolution beyond $z = 2$, shown separately for $\Omega = 1$ and $\Omega = 0$.

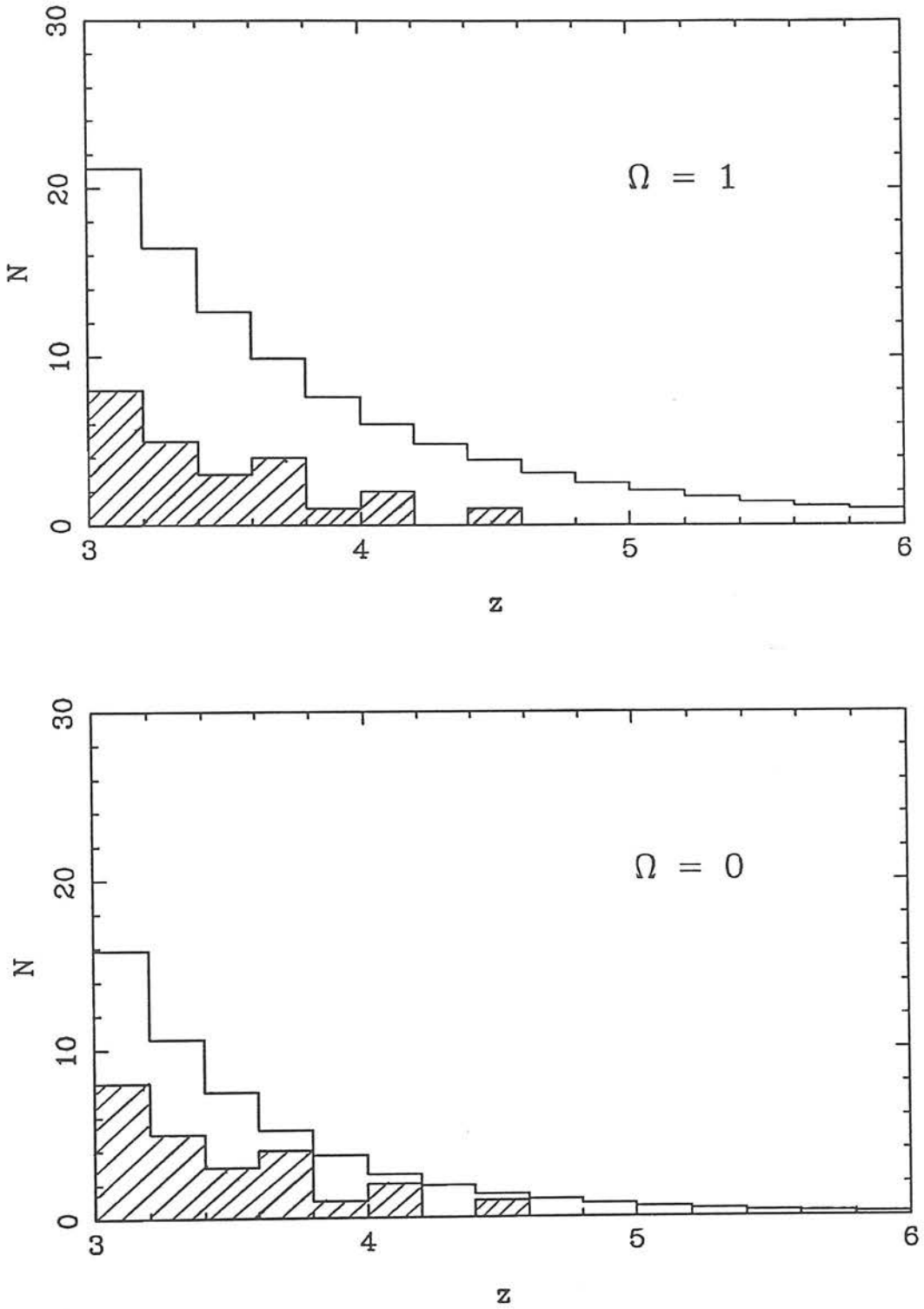

figure that the shape of the predicted and observed distributions are consistent, but that the observed numbers are low by a factor ~ 2 → 3. The straightforward interpretation of this result is that these data do indeed confirm the existence of a redshift cutoff for optically-selected quasars, but one has to be cautious given that the magnitude of the discrepancy is not spectacular. The most obvious worry is the level of completeness of the data - for example the sample is known to be biassed against faint, highly variable objects (ie objects that vary by ~ 0.25 magnitudes on a timescale of a few months) because objects which do not appear on repeated plates are excluded. However, a subset of such excluded objects has been observed and none were found to be quasars. Although the present data have to be regarded as a lower limit to the surface density, it seems unlikely that these numbers could be increased by as much as a factor of two. A second worry is the accuracy of the assumption of $\alpha = 0.5$ used to produce the model predictions, since high-redshift quasars are known to exhibit a wide range of spectra. However, because they are selected at R, the present data are at least free from the uncertain corrections introduced by Lyman damping of the blue continuum, which complicates model predictions for samples selected at faint B magnitudes (such as those of Koo 1986b). In conclusion, there does appear to be tentative evidence for a redshift cutoff but, contrary to many claims in the literature, the issue cannot yet be regarded as settled.

On the assumption that the present sample is indeed reasonably complete, it is interesting to consider the predictions of some alternative models of high-redshift evolution. In particular it is interesting to consider a model with negative luminosity evolution beyond $z \sim 2$ similar to that which was found to give a successful description of the evolving RLF in Chapter 6. In fact, the evolution parameters used to describe the pure luminosity evolution of the RLF come remarkably close to also successfully describing both the high- and low-redshift evolution of the optical luminosity function: evolution of the form $(1+z)^{3.2}$ results in an increase in $\mathrm{Log_{10}L}$ of 1.53 between $z = 0$ and $z = 2$, while the steep-spectrum luminosity evolution model given in Section 6.5b produces a corresponding increase of 1.46. The RLF luminosity evolution model goes on to

successfully predict the observed number of SGP quasars at $z \sim 3$, and only finally fails at the largest redshifts because the sharp cutoff provided by the quadratic form fails to predict the existence of any quasars with $z > 4$. This result suggests the adoption of a model with steady negative luminosity evolution beyond $z = 2$ (above $z \sim 4$ the RLF was not constrained and so the strongly accelerating negative luminosity evolution produced at very high z by the quadratic parameterization is not to be taken seriously). Figure 8.3 compares the SGP data with the predicted redshift distribution produced by such a model (for $\Omega = 1$). The negative luminosity evolution beyond $z = 2$ is parameterized by:

$$\log_{10}L_*(z) = \log_{10}L_*(z=2) - 0.16(z - 2) \qquad (8.2)$$

where the luminosity function at $z = 2$ is given by equation (8.1). The choice of the factor -0.16 produces the observed number of 24 quasars with $z > 3$ and $R < 20$ in 30 deg^2, and it is clear from the figure that the predicted and observed redshift distributions are very similar. The factor -0.16 represents an amount of negative luminosity evolution over the redshift range $z = 2 \rightarrow 3$ which is comparable to that found in the pure luminosity model of the RLF (-0.28 for the flat-spectrum RLF, -0.08 for the steep-spectrum RLF). This suggests that the evolution of radio sources and radio quiet QSOs may indeed be very similar.

An interesting alternative model can be constructed by allowing the positive luminosity evolution seen at low z to continue unabated above $z = 2$, but to offset this with a decrease in number density at high redshift. Such a model produces a luminosity-dependent redshift cutoff, an idea that has grown in popularity as a result of the success of Hazard and his collaborators in discovering high-redshift quasars on UK Schmidt plates of relatively modest limiting magnitude. Figure 8.4 shows the prediction of such a model ($\Omega = 1$), once again compared with the observed redshift distribution in the SGP field. The luminosity evolution has been parameterized as in equation (8.1) (ie $L \propto (1+z)^{3.2}$) for all z, while for $z > 2$ the negative density evolution is given by:

$$\log_{10}\Phi_o(z) = \log_{10}\Phi_o(z=2) - 0.93(z - 2) \qquad (8.3)$$

As in the case of the negative luminosity evolution model considered above, the evolution factor (-0.93) has been chosen so that the model correctly reproduces the observed number of 24 $z > 3$ quasars in the SGP field with $R < 20$. Once again the predicted redshift distribution is clearly consistent with that which is observed, and it is clear that data selected above a single magnitude limit cannot distinguish between these two very different models.

However, at brighter magnitudes these two models produce very different predictions. Figure 8.5 shows the predictions of the two models for the the redshift distribution of quasars with $R < 18.5$ (again, per 30 deg^2), demonstrating how the luminosity-dependent cutoff model predicts a relatively large number of bright high-redshift quasars. The $R < 18.5$ surface density predictions of these two alternative models are given below in Table 8.1 for a range of lower redshift limits.

Table 8.1 : The surface density of quasars brighter than R = 18.5 as predicted by the two alternative models of high redshift evolution described in the text.

	MODEL 1 (-ve luminosity evolution)	MODEL 2 (+ve luminosity evolution + -ve density evolution)
$z > 3.0$	0.025 deg^{-2}	0.096 deg^{-2}
$z > 3.5$	0.008	0.037
$z > 4.0$	0.002	0.014

At present, the testing of such predictions is hampered by the rather poor statistics for high-redshift quasars at such bright magnitudes. Hazard (1987) gives a surface density estimate of 0.1 deg^{-2} with $R < 18.5$ in the redshift range $3.3 < z < 3.8$ which is clearly rather large and favours the idea of continued positive

Figure 8.3 : The observed redshift distribution of $z > 3$ quasars in the $R < 20$, 30 deg^2 SGP sample, compared with that which is predicted by a model involving negative luminosity evolution for $z > 2$ ($\Omega = 1$). The rate of negative luminosity evolution is similar to that required to model the evolving RLF in Chapter 6, Section 6.5b.

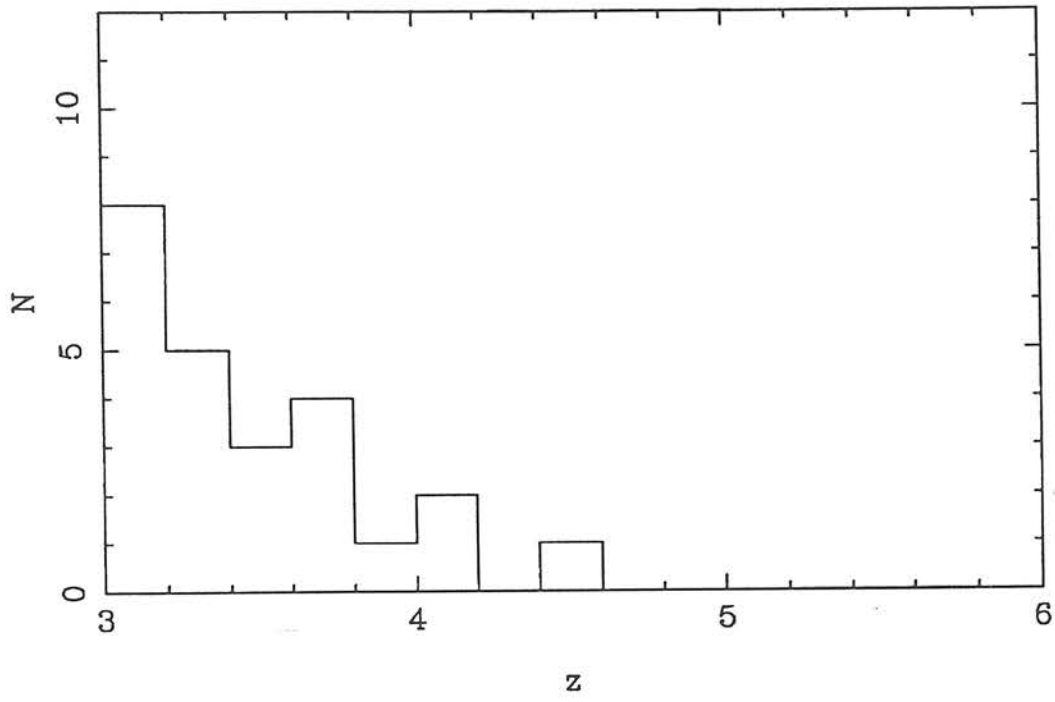

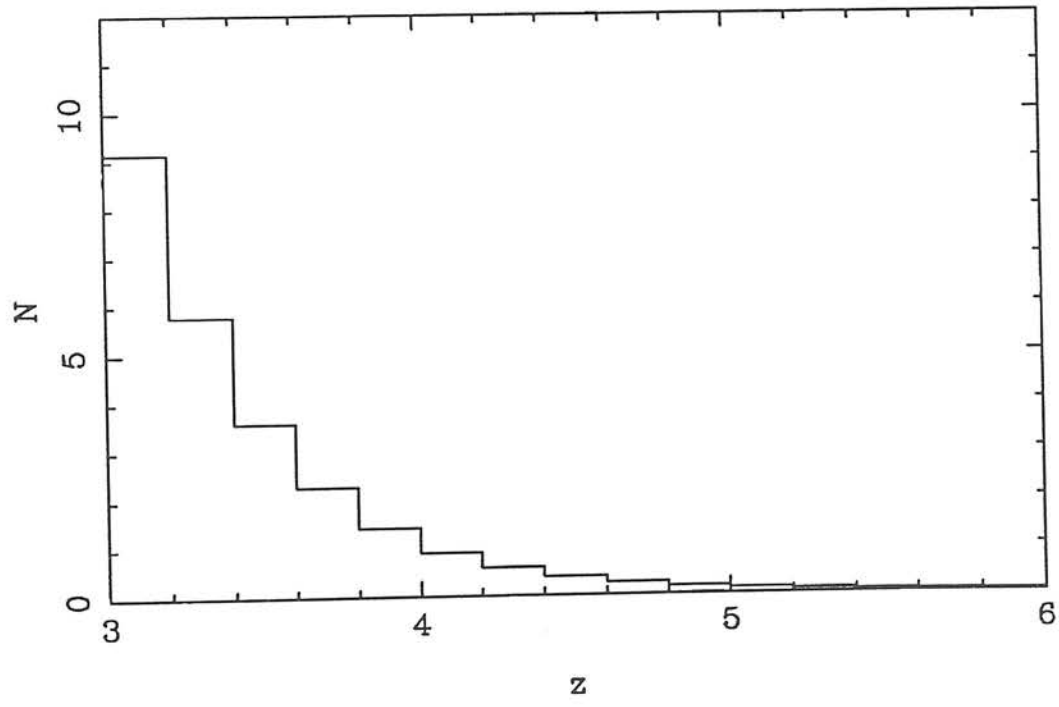

Figure 8.4 : The observed redshift distribution of $z > 3$ quasars in the $R < 20$, 30 deg^2 SGP sample, compared with that which is predicted by a model involving continued positive luminosity evolution coupled with negative density evolution beyond $z = 2$ ($\Omega = 1$).

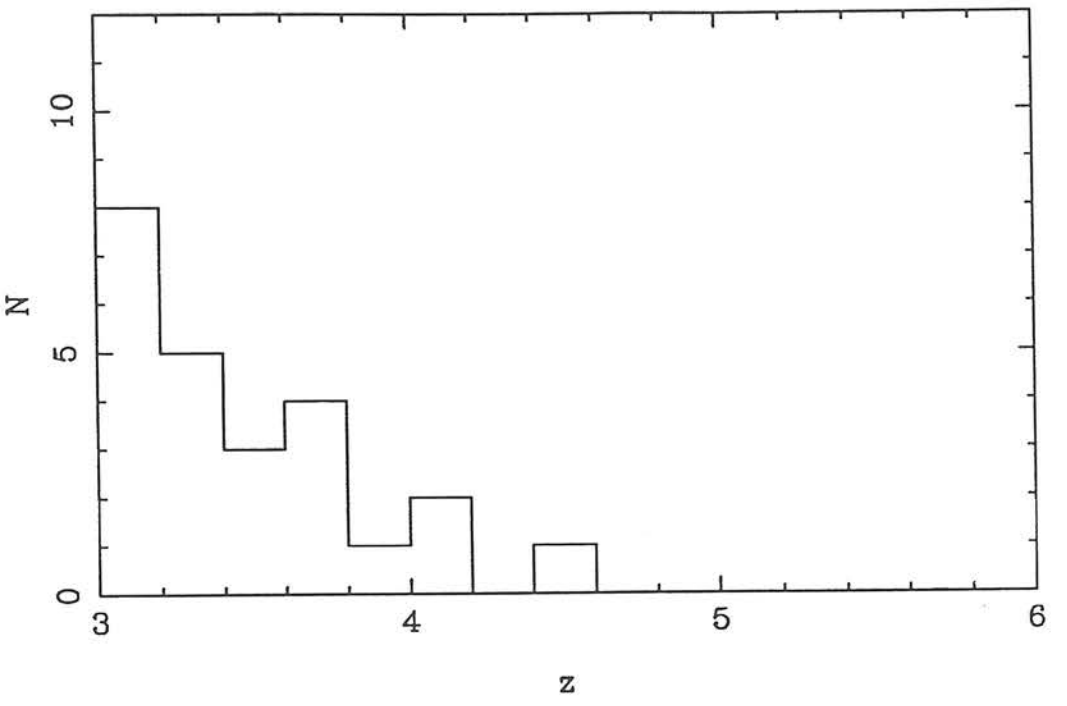

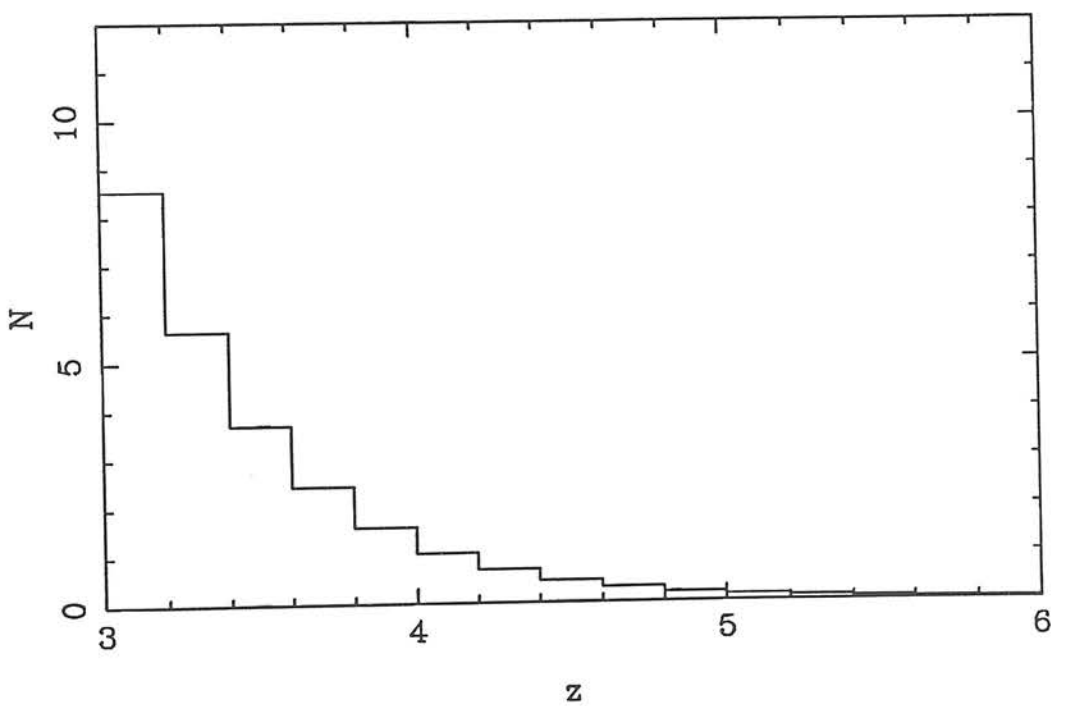

luminosity evolution. However, it should be noted that this result is based on the discovery of 4 objects on 2 Schmidt plates, and ignores the fact that several other plates were examined without success. Clearly a complete, large area survey selected at bright magnitudes is required to settle the issue. Such a survey is at present being produced in Edinburgh by Lance Miller and his collaborators using the same multi-colour selection technique used by Warren, Osmer and Hewett at Cambridge. The combination of these two surveys should provide an effective way of distinguishing between alternative models of the type described above.

In conclusion, it is worth noting that, if the requirement for continuing positive luminosity evolution is definitely confirmed by bright sample results, then an accompanying depression in number density will be essential to avoid violating the constraints at $R < 20$.

Figure 8.5 : The redshift distribution for z > 3 quasars brighter than R = 18.5 in the 30 deg^2 SGP field as predicted by i) the model of negative luminosity evolution (top figure) ii) the model of continuing positive luminosity evolution coupled with negative density evolution (bottom figure). Ω = 1 is again assumed.

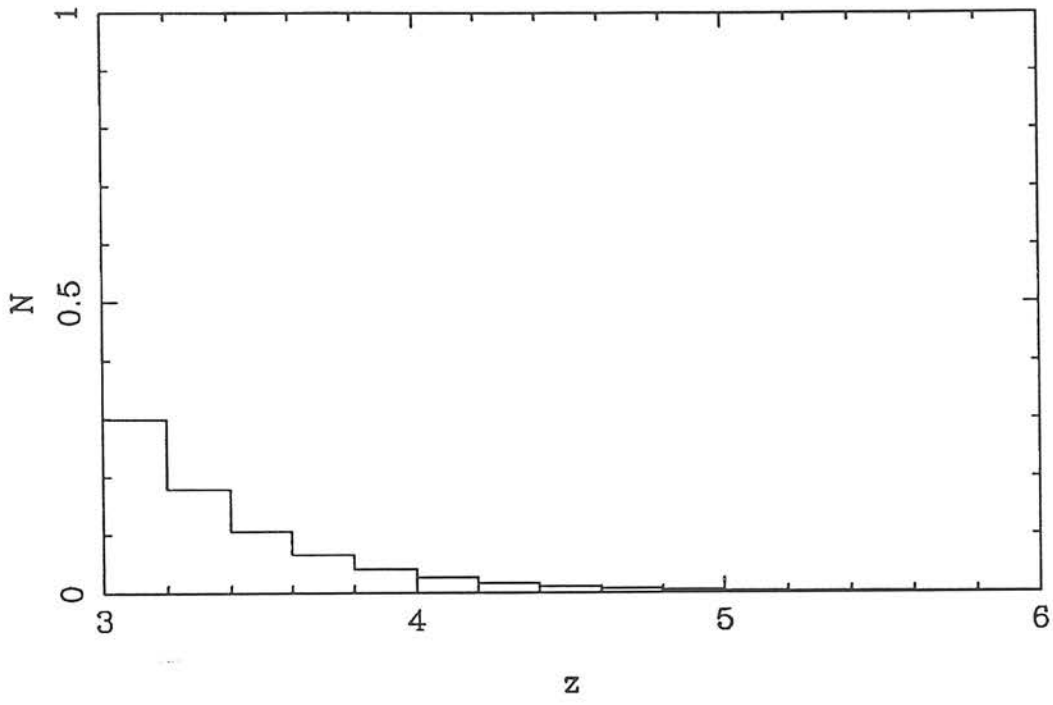

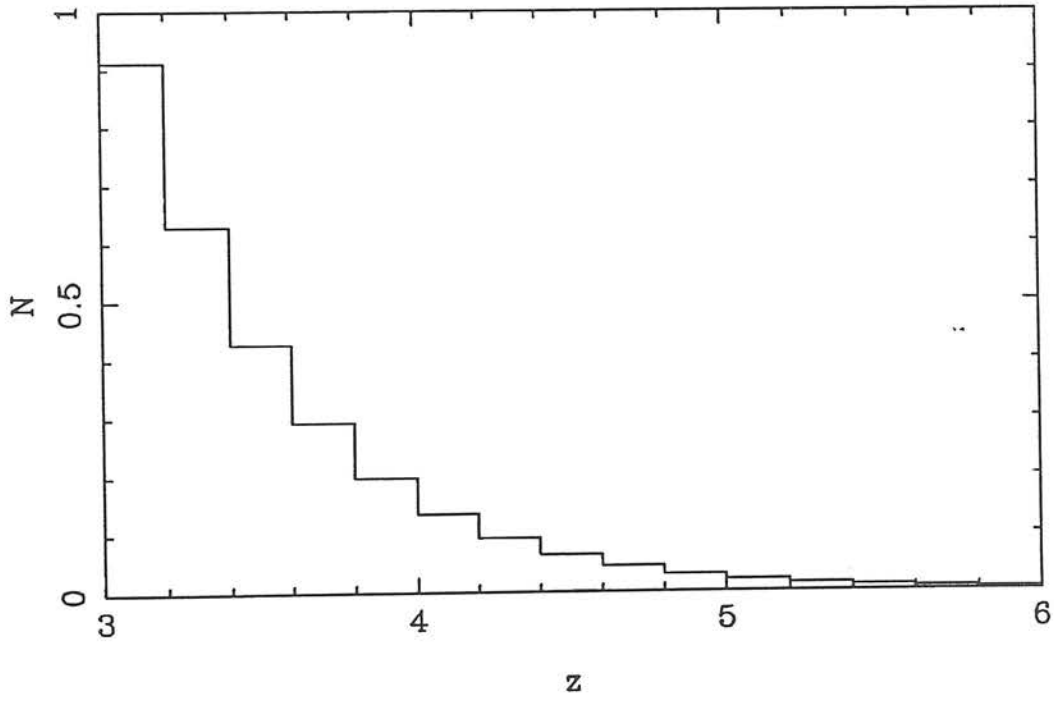

8.3 : RADIO SOURCE ACTIVITY AND STARBURSTS

It is now well established that radio-source activity and star formation often occur together. However, it is not clear whether there is a direct causal connection between the two phenomena. One long standing idea is that both radio source activity and star formation are triggered by the arrival of a new source of fuel as a result of an interaction or merger with another galaxy. Recently, however, evidence has emerged for the existence of an alternative more direct causal connection, in which star-formation activity is triggered by compression of the cool IGM by the radio lobes. Both these possibilities are discussed below.

8.3a : Interactions and mergers

The idea that active galactic nuclei are triggered into action by a galaxy-galaxy interaction is an appealing one because it is a natural way in which a new supply of fuel can be provided for a previously dormant black hole. There is now a growing body of evidence which suggests that the interaction phenomenon may play an important role in the production of quasars and radio sources.

Circumstantial evidence in support of the interaction picture is provided by the observations by Stockton & Mackenty (1987) of extended regions of ionized gas around nearby quasars. Stockton & Mackenty used narrow band filters (set at the appropriate redshifted wavelength) to image the distribution of [OIII] 5007Å emission around each quasar. In ~40% of their quasar sample they found that the line-emitting gas extends over a distance of several kpc (ie considerably further than any starlight from the host galaxy). The distribution of this gas is generally extremely asymmetric and often appears to have the characteristic tidal-tail morphology which is seen in pairs of interacting galaxies. Stockton & Mackenty concluded that the gas could not persist in this disturbed and chaotic state for longer than $\sim 10^8$ yr.

Similar evidence of disruption has been found in nearby radio

galaxies by Heckman *et al.* (1986) and Hutchings (1987). They have found that a large fraction of the host galaxies of powerful ($P_{408} > 10^{25.5}$ $WHz^{-1}sr^{-1}$) radio sources with $z < 0.3$ have peculiar morphologies which are suggestive of interactions or mergers.

Evidence of the occurrence of mergers can also be found after the initial spectacular interaction has subsided. Multiple nuclei are commonly seen in cD galaxies and, although many of these are undoubtedly merely chance superpositions of separate cluster galaxies, some are certainly real physical associations (Tonry 1985). It is thus interesting that the hosts of FRI type radio sources are generally cD galaxies. The host galaxies of FRII radio galaxies tend to be slightly less luminous but still appear to display an optical magnitude - core radius relation which is symptomatic of merging (Lilly & Prestage 1987).

Finally there is the recently acquired evidence that a large fraction of the high-redshift 3CR radio galaxies are elongated and distorted (~50% at $z > 1$). A particularly spectacular example is provided by 3C368 ($z = 1.132$) which was examined in detail by Djorgovski *et al.* (1987a). Djorgovski *et al.* claim that the resolved multi-component morphology (seen in both starlight continuum and [OII] 3727Å emission) and the properties of the ionized velocity field are highly suggestive of a galaxy merger (an alternative explanation suggested by McCarthy *et al.* 1987b is discussed in Section 8.3b). They also propose that, since the galaxy is optically very luminous and blue, this merger must be enhancing the star formation rate throughout the entire galaxy. Given that the morphological and spectroscopic properties of 3C368 are fairly typical of high-redshift 3CR galaxies, it seems feasible that interaction/merging might be the physical origin of both the onset of radio activity and the high degree of colour evolution seen in the 3CR sample. Djorgovski *et al.* therefore go on to speculate that the creation of powerful radio sources may herald an epoch of "secondary formation" of gE/cD galaxies via merging.

In the above picture, the distortion of radio galaxies is seen as a principally epoch dependent effect, presumably widespread at $z > 1$.

However, it is equally possible that these peculiarities are only associated with the extreme radio luminosities of the 3CR sources. Some attempt can be made to investigate this possibility by studying the optical morphologies of the more distant objects in the Parkes Selected Regions (ie the CCD identifications).

The CCD images presented in Chapter 2 are not as deep (relative to the brightness of the ID) as many of the images that have now been obtained of the 3C galaxies, and so a detailed comparison of the distortion statistics in the two samples is neither feasible nor justified at present. Nevertheless, an attempt can still be made to determine how many of the high-redshift Selected Regions sources appear to be interacting. The result of this rather subjective classification procedure is that, of the 71 new CCD identifications 21 appear to be either interacting or possess an extremely close (ie $\leqslant$ two galaxy diameters distant) neighbour. These 21 sources are listed below in Table 8.2.

Table 8.2 : CCD identifications in the Parkes Selected Regions classified as interacting/near neighbour.

2353+010	0045-009	0223-023	1154-019	1331+004	2157-191
2356+033		0232-010	1201-026	1343+011	2158-160
0010+005		0241-012	1205+011	1345+002	2159-215
		0242+028		1352+008	2159-192
					2204-203
					2207-203

Given that many of the CCD identifications are too faint to make any statement about optical morphology, this has to be regarded as a rather high percentage of 'abnormal objects', and therefore further evidence that interactions may play a role in the production of radio sources. However, the present data suggest that distortion is less common and less severe in the Selected Regions sample than in the 3CR. Images of higher quality are clearly required to confirm this.

There does not appear to be any clear correlation between distorted optical morphology and blueness of colour, as might be expected if interactions were the sole cause of bursts of star formation. This fact is demonstrated in Figure 8.6 which plots B-R 'colour excess' versus R-K 'colour excess' for the faint CCD galaxy identifications whose colours were investigated in Chapter 7. In this context 'colour excess' means:

Colour of object - Colour of the red envelope model AT THAT z

and the model chosen to provide the red envelope is the BURST + UV model described in Chapter7, Section 7.4b. In Figure 8.6, the galaxies classified as interacting are indicated by filled symbols and the isolated/normal objects by empty symbols. It is clear from this figure that both classes of object occupy similar regions of this colour/colour plane. Deeper CCD images are required to justify carrying out this analysis in more detail, but the present data suggest that the strong colour evolution found in Chapter 7 is not solely attributable to the effect of interactions. It is important, however, to bear in mind that it is not clear at what stage of an interaction observable colour effects might be produced (an observable bluening due to star-formation activity might only occur once two galaxies have practically merged). One must therefore be cautious in interpreting the results of the above "interacting/near neighbour" classification which clearly will tend to select interactions at a relatively early stage in the encounter.

Finally, in the context of the link between interactions and radio-source activity, it is worth noting that the evidence described above in favour of the frequent occurrence of interactions among radio sources does not automatically imply a close causal connection. After all, radio sources are known to occur in regions of low density as well as in clusters. If certain types of radio source can only arise in the dense environment of a rich cluster (ie FRIs and the most powerful FRIIs, see Chapter 1, Section 1.3) then the corresponding host galaxy will inevitably be exposed to an increased probability of interaction and merging, which might be completely unrelated to radio source activity.

Figure 8.6 : Comparison of the relative blueness of interacting (filled symbols) and non-interacting (empty symbols) galaxies. B-R colour excess is plotted versus R-K colour excess, where excess is measured relative to the colours of the BURST+UV evolutionary model at the relevant redshift (see Chapter 7, Section 7.4b). Only those objects which are CCD galaxy identifications and are contained in the 4-region subsample (ie 0, 1, 2 & 22hr regions) are plotted.

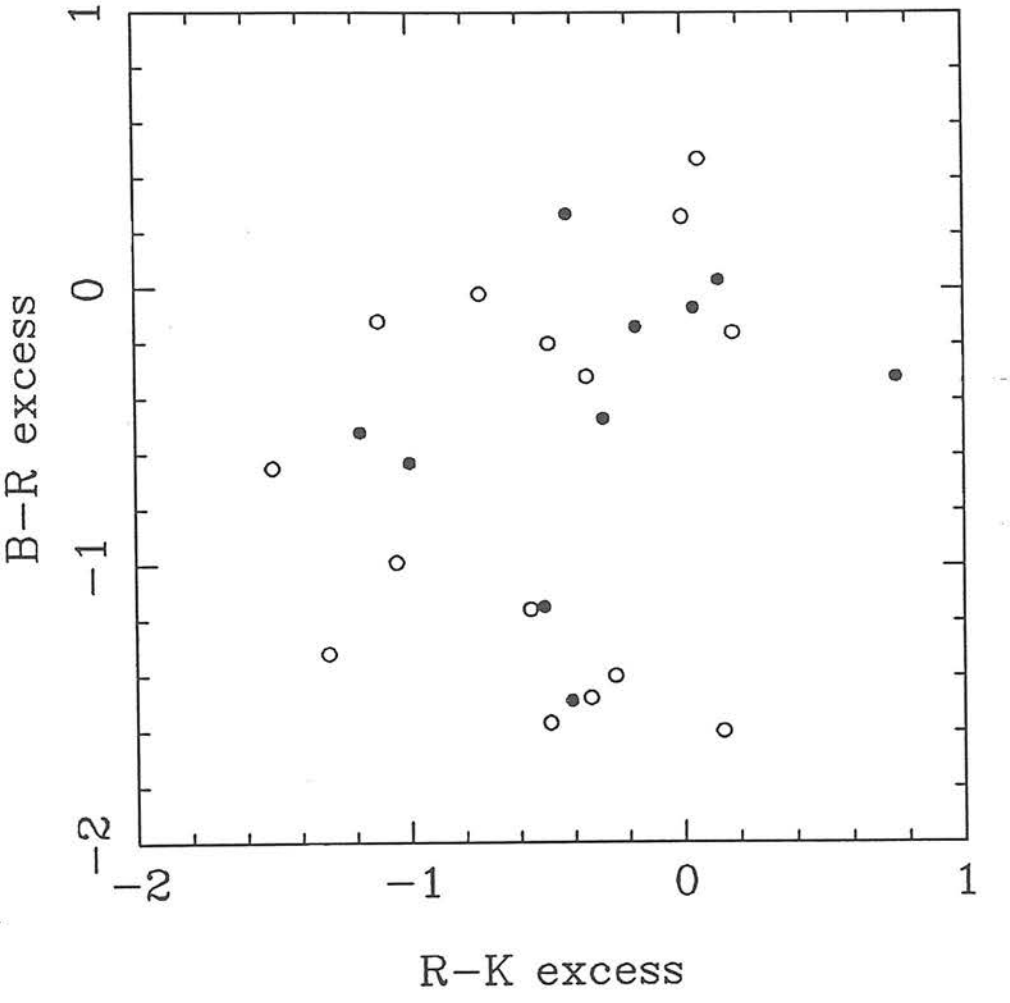

8.3b : Star formation induced by radio source activity

As discussed above, the distorted structures of high-redshift 3CR galaxies have generally been attributed to galaxy/galaxy interactions. Recently, however, evidence has emerged in favour of a different interpretation. McCarthy *et al.* (1987b) have discovered the existence of a strong correlation between the radio and optical morphologies of the distant ($z > 0.6$) 3CR radio galaxies. A similar result has been found for a different sample of radio galaxies by Chambers *et al.* (1987). The correlation is in the sense that the isophotal axes of highly-elongated host galaxies (measured both in stellar continua and extra-nuclear emission lines) show a strong tendency to be aligned with the radio source axes. It is worth noting that this alignment is in the opposite sense to that which has been reported for low-redshift radio galaxies (eg Kapahi & Saikia 1982, Shaver *et al.* 1982 - although the recent study by Sansom *et al.* 1987 suggests that the low-redshift correlation is not statistically significant).

Of their sample of 3CR galaxies, McCarthy *et al.* found that 50% (ie 11) of those with $z > 1$ are unusually elongated (sometimes with axial ratios as large as 4:1) at levels greater that 30% of their peak surface brightness (in the redshift range $0.6 < z < 1$ the figure drops to 30% and the elongation is generally not so dramatic). High spatial resolution images of a few of these galaxies have shown that they consist of several condensations or subunits. Of the 11 asymmetric galaxies with $z > 1$, 10 are aligned with the radio source axis to within 25^{o}. In nearly all cases, despite the elongation of the host galaxies, the radio sources are still larger than their optical counterparts, but there are at least 4 objects in which the [OII] emission appears to be directly associated with one of the radio hotspots - 3C280, 3C277.2, 3C337 and 3C247.

There is no obvious reason why this close correspondence between radio and optical morphology should arise in the interaction interpretation. McCarthy *et al.* therefore suggest that the most likely explanation is that the radio jets (or more probably the backflows from the radio lobes) interact with the interstellar media of the host galaxy and its companions, and thus stimulate starformation around

the radio source. It is important to note that this new interpretation of the distorted structure of high redshift 3CR galaxies in no way invalidates the other evidence cited in Section 8.3a for the importance of interactions. The distortions being discussed here are considerably more dramatic than the low surface brightness features (tidal tails, shells etc) discovered in powerful low-redshift radio galaxies by Heckman *et al.* (1986). They are also quite different from the extended ionized gas regions discovered around low-redshift quasars by Stockton & Mackenty (1987), since these extensions are <u>not</u> associated with any stellar continua.

The results of McCarthy *et al.* clearly raise the possibility that the strong colour evolution exhibited by the 3CR galaxies might be, as feared, a direct consequence of the radio selection criterion. However, it was shown in Chapter 7 that the rather less powerful Selected Regions galaxies exhibit a similar amount of colour evolution. It is therefore interesting to examine the optical images of the high-redshift Selected Region galaxies for evidence of similar, aligned, extended morphologies. In fact, among the 71 CCD identifications there are only two examples of this phenomenon, 1336+020 and 2204-203. Thus, although the present images are not of as high quality as those which have been obtained for some of the 3CR galaxies (and obviously there are as yet no narrow-band images of Selected Region galaxies), the evidence indicates that the extreme, aligned distortions are indeed associated solely with the most extreme radio luminosities. Of course, the possibility cannot be ruled out that the radio jets of the Selected Regions galaxies are still stimulating star formation at some level, but this result suggests that such an effect is not after all the dominant influence on the observed colour evolution.

Finally, it is important to note that, if powerful radio sources at high redshift do stimulate star formation, some explanation will have to be found as to why low-redshift sources of comparable power (eg Cygnus A) do not appear to be doing so. Presumably this explanation would have to be that high-redshift galaxies contain (or are surrounded by) suitable materials for star formation whereas low-redshift ones are not. Perhaps the true answer involves a

combination of the two topics which have been discussed in this Section - ie mergers (and/or recent galaxy formation) to supply the fuel, and interaction with the radio lobes to trigger large-scale star formation.

8.4 : THE REDSHIFT CUTOFF AND GALAXY FORMATION - PRIMEVAL GALAXIES?

Finally it is interesting to consider whether the Selected Regions data provide any evidence in support of the idea that the redshift cutoff in the RLF relates to the epoch of galaxy formation. If radio sources and their host galaxies did in fact form roughly contemporaneously, then it might be expected that at least a few of the more distant galaxies in the Selected Regions should be essentially primeval. The problem with attempting to check this possibility is that there is, as yet, relatively little consensus as to what a primeval galaxy should actually look like. Predictions of their possible appearance range from "extended and red" (eg Partridge & Peebles 1967) to "compact and blue" (eg Meier 1976). A good review of the range of methods which have been used to search for the various predicted forms of primeval galaxy is given by Koo (1986c).

There is, in fact, general agreement over one feature of primeval galaxies, namely that they should possess strong, narrow emission lines with velocity dispersions more typical of galaxies (ie $< 500 kms^{-1}$) rather than the broader lines seen in quasars. However, there is considerable disagreement as to just how visible such lines will actually be to the observer. The presence of even a small amount of dust can result in heavy quenching of Lyα emission, as demonstrated by the rather small Lyα emission line fluxes observed in nearby starburst galaxies (Hartmann *et al.* 1984). This fact provides one possible explanation of the failure of emission-line surveys to detect primeval galaxies (eg the narrow-band imaging search of Pritchett and Hardwick 1987). However, it is important to note that high-redshift Lyα galaxies are known to exist, the best known example being the companion object to the $z = 3.209$ quasar PKS 1614+051 (Djorgovski *et al.* 1985, Djorgovski *et al.* 1987b). The

appearance of this object corresponds closely to that of a primeval galaxy as predicted by the models of Meier (1976) in that it has strong, narrow Lyα emission, a very weak continuum, and is relatively compact. It may not, however, be a typical primeval galaxy since objects of this type do not appear to be very common - only one similar object (a companion of MG 2016+112 at $z = 3.27$, Schneider *et al.* 1986) has been found as a result of narrow-band imaging of some two dozen quasar fields. Nevertheless, the existence of prominent Lyα emission in these objects and also in radio galaxies at $z \sim 2$ (Spinrad 1988) provides encouragement for emission line searches - there are clearly galaxies at high redshift in which the Lyα emission has not been quenched.

An alternative explanation of the failure of emission line surveys to detect primeval galaxies is that most primeval galaxies might be very extended low surface brightness objects. Support for this idea comes from the fact that two such giant (>100kpc) Lyα galaxies have been discovered at moderate redshift, associated with the powerful radio sources 3C 326.1 ($z = 1.825$, McCarthy *et al.* 1987a) and 3C 294 ($z = 1.779$, Spinrad 1988). It is only because of their relatively low redshifts (plus the fact that they contain metals) that one hesitates to call these objects primeval, but, since it is highly probable that galaxy formation extends over a considerable redshift range, they may in fact be such. If one accepts the idea that these giant Lyα clouds are indeed late examples of galaxy formation, then the existence of the radio source indicates that the core must have formed at an earlier epoch. This would be consistent with the standard Cold Dark Matter model of galaxy formation as described by Silk (1987), in which the galaxy core forms at relatively early epochs ($z \sim 5 \rightarrow 10$) and large scale star formation is delayed until the subsequent infall and capture of gas.

Since spectroscopy of the faint Selected Regions galaxies has still to be attempted, it is clearly not yet possible to determine for certain whether any of them might be primeval. However, by examination of the optical images, it should be possible to decide if the Selected Regions contains any very extended, low surface brightness objects similar to 3C326.1 and 3C294. In fact, there appear to be only four candidates - 0051-008, 0100+023, 0105+034 and

0220-023 - and in all cases the images are rather poor. There is thus no clear evidence to support the possibility (which was considered in Chapter 7) that the bluest galaxies at $z \sim 1$ are primeval.

Possibly the best place to look for primeval galaxies in the Selected Regions sample is not among the CCD identifications, but among the remaining optical empty fields. These radio sources are undoubtedly very distant, as evidenced by their small angular sizes (see Chapter 2). It is therefore not unexpected that they should have proved difficult to identify. However this difficulty might also imply that the associated optical objects are actually rather extended and of low surface brightness - ie potential primeval galaxies. Support for this possibility is provided by the difficulty experienced by Windhorst *et al.* (1987) in uncovering the last few optical identifications in the Leiden-Berkley deep survey. These objects (which are also associated with very small double sources) were only discovered after several hours of CCD imaging reaching a depth of r = 26.5 (and even then the reality of the identifications seems questionable). In retrospect Windhorst concluded that the reason they had proved so difficult to discover was that they were very extended (4 → 6 arcsec), low surface brightness objects, which were more easily recognized after convolving the image to an FWHM of 2.5 arcsec. If real, such very distant, extended radio identifications are clearly strong primeval galaxy candidates.

Finally, it is important to note that, although the idea that distant radio galaxies might be primeval is an appealing one, there is as yet no firm evidence in its favour. Indeed, the results of the colour evolution study of Chapter 7 argue in favour of very old underlying stellar populations, and hence that the epoch of galaxy formation occurred some time before the onset of radio activity.

8.5 : SUGGESTIONS FOR FURTHER WORK

It is obviously desirable to further increase the number of measured redshifts in the Parkes Selected Regions. In particular it would be useful if redshifts could be obtained for at least a few of

the faint galaxies in the sample, in order to confirm the form of the K-z relation at faint magnitudes. Such extra redshift information would enable the form of the high-redshift cutoff to be more clearly delineated. However, it has to be accepted that, given the faintness of many of the optical identifications, completion of the redshift content of the sample is at best a long term prospect, although with the redshift measurements of the 3CR sample now essentially completed it is to be hoped that a concerted effort might now be made to tackle this task.

It would be useful (and relatively quick) to complete the infrared photometry for the 2 regions which were not observed because of the persistently bad weather encountered at UKIRT each Easter. This would significantly increase the number of datapoints which can be plotted on the colour-redshift diagrams of Chapter 7. Since infrared array cameras have recently become operational, it would be interesting to complete the K photometry using infrared imaging. In addition to improving the reliability of the photometry, infrared imaging would also allow comparison of the optical and infrared morphologies of the identifications. This would be particularly interesting for objects whose optical morphologies seem somewhat distorted. In the context of infrared imaging, it would be very interesting to obtain infrared images of the optical empty fields which were successfully detected in K using UKT9 (0105+025, 0225+002, 2158-170 & 2357-006 - see Chapter 3). As pointed out above in Section 8.4, these objects are undoubtedly very distant, and possibly primeval galaxies.

Given that the Selected Regions sample is now ~95% identified, optical identification of the few remaining empty fields is not particularly important from a statistical point of view. Nevertheless, it would still be of value to attempt to identify these last few sources, simply because they are potentially very interesting objects in their own right. In particular, it is important to determine whether or not they are very extended, low surface brightness objects, and thus potential primeval galaxies. This possibility suggests an alternative approach to identification other than direct imaging. If these galaxies, like 3C 326.1 and 3C 294, emit most of their light in Lyα emission

then it might be worthwhile attempting identification using narrow-band imaging, systematically adjusting the filter wavelength to cover a likely range of possible redshifts - say, $z = 1.8 \rightarrow 3$ (the lower redshift limit being dictated by the visibility of Lyα for ground-based observations).

In the long term, once considerably more redshifts have been measured, it is to be hoped that the Parkes Selected Regions sample will be considered worthy of the sort of intensive, multi-group study that has recently been devoted to the 3CR sample. Extensive spectroscopy, narrow-band imaging etc would enable a proper investigation of some of the topics which have been raised (possibly somewhat prematurely) in this final chapter.

Finally, it is hoped that the work described in this thesis will act as a stepping stone towards the overall goal of unification which was outlined in the opening section of Chapter 1. The results of Chapter 6 suggest unification of the radio source population, with steep- and flat-spectrum sources displaying very similar evolutionary behaviour. There are also indications that, at least up to $z = 2$ (and possibly beyond), the evolution of the RLF is very similar in form to the evolution of the optical luminosity function of optically-selected quasars. Clarification of the high-redshift evolution of optically-selected quasars is therefore eagerly awaited. The work described in Chapter 7 may be considered a first step towards the removal of the extreme radio bias which has dogged studies of high-redshift galaxy evolution because of the dominance of the 3CR sample. It may however be some time before this radio bias can be completely removed by the study of a high-redshift sample of radio-quiet galaxies.

REFERENCES

References

Allington-Smith, J.R., 1984. *Mon.Not.R.astr.Soc.*, 209, 665.

Anderson, S.F. & Margon, B., 1987. *Nature*, 327, 125.

Arp, H.C. & Sulentic, J.W., 1979. *Astrophys.J.*, 229, 496.

Avni, Y. & Bahcall, J.N., 1980. *Astrophys.J.*, 235, 694.

Avni, Y. & Schiller, N., 1983. *Astrophys.J.*, 267, 1.

Bahcall, N. & Soneira, R., 1983. *Astrophys.J.*, 270, 20.

Barthel, P.D., 1986. In: *Quasars, IAU Symp.No.119,* p.181, eds. Swarup, G. & Kapahi, V.K., Reidel,Dordrecht,Holland.

Bardeen, J., Bond, J.R., Kaiser, N. and Szalay, A., 1986. *Astrophys.J.*, 304, 15.

Bardeen, J., Steinhardt, P. & Turner, M.S., 1983. *Phys.Rev.*, D28, 679.

Barnes, J., Dekel, A., Efstathiou, G. & Frenk, C., 1985. *Astrophys.J.*, 295, 368.

Begelman, M.C., Blandford, R.D. & Rees, M.J., 1984. *Rev.Mod.Phys.*, 56, 255.

Benn, C.R., Wall, J.V., Grueff, G. & Vigotti, M., 1984. *Mon.Not.R.astr.Soc.*, 209, 683.

Bennet, A.S., 1962. *Mem.R.astr.Soc.*, 68, 163.

Bicknell, G.V., 1985. *Proc.Astr.Soc.Aust.*, 6, 310.

Blandford, R.D. & Rees, M.J., 1974. *Mon.Not.R.astr.Soc.*, 169, 395.

Blumenthal, G.R., Faber, S.M., Primack, J.R. & Rees, M.J., 1984. *Nature*, 311, 517.

Bolton, J.G. & Ekers, J.A., 1966a. *Austr.J.Phys.*, 19, 559.

Bolton, J.G. & Ekers, J.A., 1966b. *Austr.J.Phys.*, 19, 713.

Bolton, J.G. & Wall, J.V., 1970. *Austr.J.Phys.*, 23, 789.

Bolton, J.G., Clarke, M.E., Sandage, A.R. & Veron, P., 1965. *Astrophys.J.*, 142, 1289.

Bolton, J.G., Kinman, T.D. & Wall, J.V., 1968. *Astrophys.J.*, 154, L105.

Bosenberger, J. & Gros, M., 1978. *Astr.Astrophys.Suppl.*, 31, 291.

Boyle, B.J., Fong, R. & Shanks, T., 1987a. *Mon.Not.R.astr.Soc.*, 227, 717.

Boyle, B.J., Shanks, T. & Peterson, B.A., 1987b. *Mon.Not.R.astr.Soc.*, in press.

Bridle, A.H., Davis, M.M., Folamont, E.B. & Lequeux, J., 1972. *Astr.J.*, 77, 405.

Browne, I.W.A. & McEwan, N.J., 1972. *Nature*, 239, 101.

Browne, I.W.A. & McEwan, N.J., 1973. *Mon.Not.R.astr.Soc.*, 162, 21P.

Bruzual, G., 1983a. *Astrophys.J.*, 273, 105.

Bruzual, G., 1983b. *Rev.Mexicana.Astron.Astrof.*, 8, 63.

Bruzual, G., 1985. *Rev.Mexicana.Astron.Astrof.*, 10, 55.

Cameron, M.J., 1971. *Mon.Not.R.astr.Soc.*, 152, 429.

Chambers, K.C., Miley, G.K. & van Breugel, W.J.M., 1987.
Nature, 329, 624.

Chokshi, A. & Wright, E.L., 1987. *Astrophys.J.*, 319, 44.

Clarke, M.E., Bolton, J.G. & Shimmins, A.J., 1966.
Austr.J.Phys., 19, 375.

Clements, E.D., 1981. *Mon.Not.R.astr.Soc.*, 197, 829.

Condon, J.J., 1984. *Astrophys.J.*, 287, 461.

Condon, J.J. & Dressel, L., 1978. *Astrophys.J.*, 221, 456.

Condon, J.J. & Ledden, J.G., 1982. *Astr.J.*, 87, 219.

Condon, J.J., Balonek, T.J. & Jauncey, D.L., 1976. *Astr.J.*, 81, 913.

Couchman, H.M.P. & Rees, M.J., 1986. *Mon.Not.R.astr.Soc.*, 221, 53.

de Vaucouleurs, G., de Vaucouleurs, A. & Corwin, H.G.Jr., 1976.
Second Reference Catalogue of Bright Galaxies,
University of Texas press,Austin.

Djorgovski, S., Spinrad, H., McCarthy, P. & Strauss, M.A., 1985.
Astrophys.J., 299, L1.

Djorgovski, S., Spinrad, H., Pedelty, J., Rudnick, L. & Stockton, A.
1987a. *Astr.J.*, 93, 1307.

Djorgovski, S., Strauss, M.A., Perley, R.A., Spinrad, H. & McCarthy, P.,
1987b. *Astrophys.J.*, 93, 1318.

Downes, A.J.B., Peacock, J.A., Savage, A. & Carrie, D.R., 1986.
Mon.Not.R.astr.Soc., 218, 31.

Dressler, A., Faber, S.M., Burstein, D., Davies, R.L., Lynden-Bell, D.,
Terlevich, R.J. & Wegner, G., 1987. *Astrophys.J.*, 313, L37.

Dunlop, J.S., Downes, A.J.B., Peacock, J.A., Savage, A., Lilly, S.J., Watson, F.G. & Longair, M.S., 1986. *Nature*, 319, 564.

Eisenhardt, P.R.M. & Lebofsky, M.J., 1987. *Astrophys.J.*, 316, 70.

Fanaroff, B.L. & Riley, J.M., 1974. *Mon.Not.R.astr.Soc.*, 167, 31P.

Fillipenko, A.V. & Greenstein, J.L., 1984.
Publs astr.Soc.Pacif., 96, 530.

Folamont, E.B., Kellerman, K.I., Wall, J.V. & Weistrop, D., 1984.
Science, 225, 23.

Foltz, C.B. & Chaffee, F.H.Jr., 1987. *Astr.J.*, 93, 529.

Fricke, K.J., Kollatschny, W. & Witzel, A., 1983.
Astr.Astrophys., 177, 60.

Gratton, R.G., 1985. *Astr.Astrophys.*, 147, 169.

Guiderdoni, B. & Rocca-Volmerange, B., 1985.
Astr.Astrophys., 151, 108.

Guiderdoni, B. & Rocca-Volmerange, B., 1987.
Astr.Astrophys., 186, 1.

Gunn, J.E., 1978. In: *Observational Cosmology, Saas-Fee Summer School*, p.1, Geneva Observatory, Switzerland.

Gunn, J.E. & Oke, J.B., 1975. *Astrophys.J.*, 195, 255.

Hall, P. & Mackay, C.D., 1984. *Mon.Not.R.astr.Soc.*, 210, 979.

Hamilton, D., 1985. *Astrophys.J.*, 297, 371.

Hartmann, L.W., Huchra, J.P. & Geller, M.J., 1984. *Astrophys.J.*, 287, 487.

Hayes, D.S. & Latham, D.W., 1975. *Astrophys.J.*, 197, 593.

Hazard, C., 1987. Preprint.

Hazard, C. & McMahon, R., 1985. *Nature*, 314, 238.

Hazard, C., McMahon, R.G. & Sargent, W.L., 1986. *Nature*, 322, 38.

Heckman, T.M., Smith, E.P., van Breugel, W.J.M., Balick, B., Miley, G.K., Bothun, G.D., Illingworth, G.D. & Baum, S.A., 1986. *Astrophys.J.*, 311, 526.

Hine, R.G. & Longair, M.S., 1979. *Mon.Not.R.astr.Soc.*, 188, 111.

Hogbom, J.A., 1974. *Astr.Astrophys.Suppl.*, 15, 417.

Huchra, J.P., 1977. *Astrophys.J.*, 217, 928.

Hutchings, J.B., 1987. *Astrophys.J.*, 320, 122.

Hutchings, J.B., Crampton, D. & Campbell, B., 1984. *Astrophys.J.*, 280, 41.

Kapahi, V.K., 1987. In: *Observational Cosmology, IAU Symp.No.124,* p.251, eds. Hewitt, A., Burbidge, G. & Fang, L.Z., Reidel,Dordrecht, Holland.

Kapahi, V.K. & Saikia, D.J., 1982. *J.Astrophys.Astr.*, 3, 161.

Kellermann, K.I. & Pauliny-Toth, I.K.K., 1981. *Ann.Rev.Astr.Astrophys.*, 19, 373.

Kellermann, K.I. & Wall, J.V., 1983. In: *Early evolution of the Universe and its present structure, IAU Symp.No.104,* p.81, eds. Abell, G.O. & Chincarini, G., Reidel,Dordrecht,Holland.

Kellermann, K.I. & Wall, J.V., 1987. In: *Observational Cosmology, IAU Symp.No.124,* p.545, eds. Hewitt, A., Burbidge, G. & Fang, L.Z., Reidel,Dordrecht,Holland.

King, C.R. & Ellis, R.S., 1985. *Astrophys.J.,* 288, 456.

KPNO, 1983. Kitt Peak National Observatory Newsletter No. 25.

Kjaergaard, P., 1987. *Astr.Astrophys.,* 176, 210.

Koo, D.C., 1983. In: *Quasars and Gravitational Lenses, 24th Liege International Astrophysical Colloquium,* p.240, Liege.

Koo, D.C., 1985. *Astr.J.,* 90, 418.

Koo, D.C., 1986a. *Astrophys.J.,* 311, 651.

Koo, D.C., 1986b. In: *The structure and evolution of Active Galactic Nuclei,* p.317, eds. Giuricin, G., Mardirossian, F., Mezzetti, M. & Ramella, M., Reidel,Dordrecht,Holland.

Koo, D.C., 1986c. In: *The Spectral Evolution of Galaxies,* p.419, eds. Chiosi, C. & Renzini, A., Reidel,Dordrecht,Holland.

Koo, D.C., Kron, R.G. & Cudworth, K.M., 1986. *Publs astr.Soc.Pacif.,* 98, 285.

Krauss, L.M., 1987. *Nature,* 329, 689.

Kuhr, H., 1980. *PhD thesis,* University of Bonn.

Laing, R.A. & Peacock, J.A., 1980. *Mon.Not.R.astr.Soc.,* 190, 903.

Laing, R.A., Riley, J.M. & Longair, M.S., 1983. *Mon.Not.R.astr.Soc.,* 204, 151.

Landolt, A.U., 1983. *Astr.J.,* 88, 439.

Lebofsky, M.J. & Eisenhardt, P.R.M., 1986. *Astrophys.J.*, 300, 151.

Lilly, S.J. & Gunn, J.E., 1985. *Mon.Not.R.astr.Soc.*, 217, 551.

Lilly, S.J. & Longair, M.S., 1984. *Mon.Not.R.astr.Soc.*, 211, 833.

Lilly, S.J. & Prestage, R., 1987. *Mon.Not.R.astr.Soc.*, 225, 531.

Lilly, S.J., Longair, M.S. & Allington-Smith, J.R., 1985. *Mon.Not.R.astr.Soc.*, 215, 37.

Lilly, S.J., McLean, I.S. & Longair, M.S., 1984. *Mon.Not.R.astr.Soc.*, 209, 401.

Longair, M.S., 1966. *Mon.Not.R.astr.Soc.*, 133, 421.

Longair, M.S., 1978. In: *Observational Cosmology, Saas-Fee Summer School*, p.230, Geneva Observatory,Switzerland.

Longair, M.S., 1984. *Theoretical Concepts in Physics*, Cambridge University Press.

Longair, M.S. & Lilly, S.J., 1984. *J.Astrophys.Astr.*, 5, 349.

Longair, M.S. & Seldner, M., 1979. *Mon.Not.R.astr.Soc.*, 189, 433.

Lynds, C.R., 1967. *Astrophys.J.*, 147, 837.

Lynds, C.R., Hill, S.J., Heere, K. & Stockton, A.N., 1966. *Astrophys.J.*, 144, 1244.

MacAlpine, G.M. & Lewis, D.W., 1978. *Astrophys.J.Suppl.*, 36, 587.

Maeder, A., 1981. *Astr.Astrophys.*, 102, 401.

Marshall, H.L., 1986. In: *The structure and evolution of Active Galactic Nuclei*, p.627, eds. Giuricin, G., Mardirossian, F., Mezzetti, M. & Ramella, M., Reidel,Dordrecht,Holland.

Marshall, H.L., 1987. *Astr.J.*, 94, 628.

McCarthy, P.J., Spinrad,H., Djorgovski, S., Strauss, M.A., van Breugel, W. & Liebert, J., 1987a. *Astrophys.J.*, 319, L39.

McCarthy, P.J., van Breugel, W., Spinrad, H. & Djorgovski, S., 1987b. *Astrophys.J.*, 321, L29.

McEwan, N.J., Browne, I.W.A. & Crowther, J.H., 1975. *Mem.R.astr.Soc.*, 80, 1.

McLaren, I., Ellis, R.S. & Couch, W.J., 1987. *Mon.Not.R.astr.Soc.*, in press.

Meier, D.L., 1976. *Astrophys.J.*, 135, 195.

Melnick, J. & Quintana, H., 1981. *Astr.J.*, 86, 1567.

Merkelijn, J.K., 1969. *Austr.J.Phys.*, 22, 237.

Merkelijn, J.K. & Wall, J.V., 1970. *Austr.J.Phys.*, 23, 575.

Mihalas, D., 1972. *NCAR Technical Note* STR76.

Miley, G.K., 1980. *Ann.Rev.Astr.Astrophys.*, 18, 165.

Miley, G.K., 1987. In: *Observational Cosmology, IAU Symp.No.124*, p.267, eds. Hewitt, A., Burbidge, G. & Fang, L.Z., Reidel,Dordrecht, Holland.

Miller, G.E. & Scalo, J.M., 1979. *Astrophys.J.Suppl.*, 41, 513.

Mills, B.Y., Slee, O.B. & Hill, E.R., 1958. *Austr.J.Phys.*, 11, 360.

Morton, D.C. & Tritton, K.P., 1982. *Mon.Not.R.astr.Soc.*, 198, 669.

Mountain, C.M., Leggett, S.K., Selby, M.J., Blackwell, D.E. & Petford, A.D., 1985. *Astr.Astrophys.*, 151, 399.

Norman, M.L., Winkler, K.A. & Smarr, L., 1984. In: *Proc. NRAO Workshop No. 9,* p.150, eds. Bridle, A.H. & Eilek, J.A., Reidel, Dordrecht,Holland.

O'Dea, C. & Owen, F.N., 1985. *Astr.J.,* 90, 927.

Oke, J.B., 1974. *Astrophys.J.*Suppl., 27, 21.

Oke, J.B., 1984. In: *Clusters and Groups of Galaxies,* p.99, eds. Mardirossian, F., Giuricin, G. & Mezetti, M., Reidel,Dordrecht,Holland.

Orr, M.J.L. & Browne, I.W.A., 1982. *Mon.Not.R.astr.Soc.,* 200, 1067.

Osmer, P.S. & Smith, M.G., 1980. *Astrophys.J.Suppl.,* 42, 333.

Ostriker, J.P. & Heisler, J., 1984. *Astrophys.J.,* 278, 1.

Partridge, R.B. & Peebles, P.J.E., 1967. *Astrophys.J.,* 147, 868.

Peacock, J.A., 1983. *Mon.Not.R.astr.Soc.,* 202, 615.

Peacock, J.A., 1985. *Mon.Not.R.astr.Soc.*, 217, 601.

Peacock, J.A. & Gull, S.F., 1981. *Mon.Not.R.astr.Soc.,* 196, 611.

Peacock, J.A. & Wall, J.V., 1981. *Mon.Not.R.astr.Soc.,* 194, 331.

Peacock, J.A., Miller, L. & Longair, M.S., 1986. *Mon.Not.R.astr.Soc.,* 218, 265.

Peacock, J.A., Perryman, M.A.C., Longair, M.S., Gunn, J.E. & Westphal, J.A., 1981. *Mon.Not.R.astr.Soc.,* 194, 601.

Pearson, T.J. & Readhead, A.C.S., 1984. *Ann.Rev.Astr.Astrophys.,* 22, 97.

Peebles, P.J.E., 1983. In: *The Origin and Evolution of Galaxies, NATO Advanced Study Institute Ser.*, p.143, eds. Jones, B.J.T. & Jones, J.E., Reidel,Dordrecht,Holland.

Peebles, P.J.E., 1986. *Nature,* 321, 27.

Peebles, P.J.E. & Dicke, R., 1968. *Astrophys.J.*, 154, 891.

Perryman, M.A.C., Lilly, S.J., Longair, M.S. & Downes, A.J.B., 1984. *Mon.Not.R.astr.Soc.*, 209, 159.

Peterson, B.A., 1987. In: *Quasars, IAU Symp.No.119,* p.555, eds. Swarup, G. & Kapahi, V.K., Reidel,Dordrecht,Holland.

Peterson, B.A., Jauncey, D.L., Wright, A.E. & Condon, J.J., 1976. *Astrophys.J.*, 207, L5.

Peterson, B.A., Savage, A., Jauncey, D.L. & Wright, A.E., 1982. *Astrophys.J.*, 260, L27.

Peterson, B.A., Wright, A.E., Jauncey, D.L. & Condon, J.J., 1979. *Astrophys.J.*, 232, 400.

Prestage, R.M. & Peacock, J.A., 1987. *Mon.Not.R.astr.Soc.*, in press.

Pritchet, C.J. & Hartwick, F.D.A., 1987. *Astrophys.J.*, 320, 464.

Ratcliff, S.J., 1987. *Astrophys.J.*, 318, 196.

Rees, M.J. & Setti, G., 1968. *Nature*, 219, 127.

Renzini, A., 1981. *Ann.Phys.Fr.*, 6, 87.

Renzini, A. & Buzzoni, A., 1986. In: *Spectral evolution of Galaxies,* p.195, eds. Chiosi, C. & Renzini, A., Reidel,Dordrecht,Holland.

Robertson, J.G., 1978. *Mon.Not.R.astr.Soc.*, 182, 617.

Robertson, J.G., 1980. *Mon.Not.R.astr.Soc.*, 190, 143.

Rocca-Volmerange, B. & Guiderdoni, B., 1987a.
Astr.Astrophys., 175, 15.

Rocca-Volmerange, B. & Guiderdoni, B., 1987b.
Astr.Astrophys., in press.

Rocca-Volmerange, B., Lequeux, J. & Maucherat-Joubert, M., 1981.
Astr.Astrophys., 104, 177.

Rowan-Robertson, M.M., 1968. *Mon.Not.R.astr.Soc.*, 138, 445.

Salpeter, E.E., 1955. *Astrophys.J.*, 121, 161.

Sandage, A.R., 1966. *Astrophys.J.*, 145, 1.

Sandage, A.R., 1967. *Astrophys.J.*, 150, L145.

Sandage, A.R., Veron, P. & Wyndham, J.D., 1965.
Astrophys.J., 142, 1307.

Sansom, A.E., Danziger, I.J., Ekers, R.D., Fosbury, R.A.E.,
Goss, W.M., Monk, A.S., Shaver, P.A., Sparks, W.B. & Wall, J.V.,
1987. *Mon.Not.R.astr.Soc.*, 229, 15.

Savage, A. & Bolton, J.G., 1979. *Mon.Not.R.astr.Soc.*, 188, 599.

Savage, A. & Peterson, B.A., 1983. In: *Early evolution of the Universe and its present structure*, *IAU Symp.No.104*, p.57,
eds. Abell, G.O. & Chincarini, G., Reidel,Dordrecht,Holland.

Savage, A., Bolton, J.G. & Trett, J., 1982.
Austr.J.Phys., 35, 207.

Savage, A., Bolton, J.G. & Wall, J.V., 1982.
Mon.Not.R.astr.Soc., 200, 1135.

Savage, A., Browne, I.W.A. & Bolton, J.G., 1976.
Mon.Not.R.astr.Soc., 177, 77P.

Scalo, J.M., 1986. *Fund.Cosm.Phys.*, 11, 1..

Scheuer, P.A.G., 1987. In: *Astrophysical Jets and Their Engines, NATO Advanced Study Institute Ser.*, p.129, ed. Kundt, W., Reidel,Dordrecht,Holland.

Schmidt, M., 1968. *Astrophys.J.*, 151, 393.

Schmidt, M., 1970. *Astrophys.J.*, 162, 371.

Schmidt, M., Schneider, D.P. & Gunn, J.E., 1986a.
Astrophys.J., 306, 411.

Schmidt, M., Schneider, D.P. & Gunn, J.E., 1986b.
Astrophys.J., 310, 518.

Schmidt, M., Schneider, D.P. & Gunn, J.E., 1987a.
Astrophys.J., 316, L1.

Schmidt, M., Schneider, D.P. & Gunn, J.E., 1987b.
Astrophys.J., 321, L7.

Schneider, D.P., Gunn, J.E. & Hoessel, J.G., 1983.
Astrophys.J., 268, 476.

Schneider, D., Gunn, J., Turner, E., Lawrence, C., Hewitt, J., Schmidt, M. & Burke, B., 1986. *Astr.J.*, 91, 991.

Searle, L. & Bolton, J.G., 1968. *Astrophys.J.*, 154, L101.

Shanks, T., Stevenson, P.R.F., Fong, R. & MacGillivary, H.T., 1984.
Mon.Not.R.astr.Soc., 206, 767.

Shanks, T., Fong, R., Boyle, B.J. & Peterson, B.A., 1986.
In: *Quasars, IAU Symp.No.119,* p.37, eds. Swarup, G. & Kapahi, V.K.,
Reidel,Dordrecht,Holland.

Shaver, P.A., Danziger, I.J., Ekers, R.D., Fosbury, R.A.E.,
Goss, W.M., Malin, D., Moorwood, A.F.M. & Wall, J.V. 1982.
In: *Extragalactic Radio Sources, IAU Symp.No.97.,* p.55,
eds. Heeschen, D.S. & Wade, C.M., Reidel,Dordrecht,Holland.

Silk, J., 1986. In: *Inner Space / Outer Space,* p.143.,
eds. Kolb, E.W., Turner, M.S., Lindley, D., Olive, K. & Seckel, D.,
University of Chicago Press.

Silk, J., 1987. In: *Observational Cosmology, IAU Symp.No.124,* p.391,
eds. Hewitt, A., Burbidge, G. & Fang, L.Z.,
Reidel,Dordrecht,Holland.

Smith, E.P., Heckman, T.M., Bothun, G.D., Romanishin, W. & Balick, B.,
1986. *Astrophys.J.,* 306, 64.

Spinrad, H., 1986. *Publs astr.Soc.Pacif.,* 98, 269.

Spinrad, H., 1988. In: *High Redshift and Primeval Galaxies, 3rd IAP meeting*, eds. Bergeron, J. & Rocca-Volmerange, B., in press.

Spinrad, H. & Djorgovski, S., 1984. *Astrophys.J.,* 280, L9.

Spinrad, H. & Djorgovski, S., 1987. In: *Observational Cosmology,*
IAU Symp.No.124, p.129, eds. Hewitt, A., Burbidge, G. & Fang, L.Z.,
Reidel,Dordrecht,Holland.

Stockton, A. & Mackenty, J.W., 1987. *Astrophys.J.,* 316, 584.

Subrahmanya, C.R. & Harnett, J.I., 1987. *Mon.Not.R.astr.Soc.,* 225, 297.

Sweigart, A.V. & Gross, P.G., 1978. *Astrophys.J.Suppl.,* 36, 405.

Tinsley, B.M., 1967. *PhD thesis,* University of Texas.

Tinsley, B.M., 1972. *Astr.Astrophys.*, 20, 383.

Tinsley, B.M., 1980. *Astrophys.J.*, 241, 41.

Tinsley, B.M. & Gunn, J.E., 1976. *Astrophys.J.*, 203, 52.

Toffolati, L., Franceschini, A., De Zotti, G. & Danese, L., 1987. *Astr.Astrophys.*, 184, 7.

Tonry, J.L., 1985. *Astrophys.J.*, 291, 45.

Tritton, K.P., 1972. *Mon.Not.R.astr.Soc.*, 158, 277.

Tritton, K.P., Savage, A. & Morton, D.C., 1984. *Mon.Not.R.astr.Soc.*, 206, 843.

Turner, M.S., 1987. In: *Dark Matter in the Universe, IAU Symp.No.117,* p.445, eds. Kormendy, J. & Knapp, G.R., Reidel,Dordrecht,Holland.

Tyson, J.A., 1986. *Astr.J.*, 92, 691.

Tyson, J.A. & Jarvis, J.F., 1979. *Astrophys.J.*, 230, L153.

Van der Laan, H. & Windhorst, R.A., 1982. In: *Astrophysical Cosmology,* p.383, eds. Bruck, H.A., Coyne, G.V. & Longair, M.S., Pontificia Academia Scientiarum, Vatican City.

Vigroux, L., Audouze, J. & Lequeux, J., 1976. *Astr.Astrophys.*, 52, 1.

Wall, J.V., 1983. In: *The Origin and Evolution of Galaxies, NATO Advanced Study Institute Ser.*, p.295, eds. Jones, B.J.T. & Jones, J.E., Reidel,Dordrecht,Holland.

Wall, J.V. & Peacock, J.A., 1985. *Mon.Not.R.astr.Soc.*, 216, 173.

Wall, J.V., Pearson, T.J. & Longair, M.S., 1980. *Mon.Not.R.astr.Soc.*, 193, 683.

Wall, J.V., Pearson, T.J. & Longair, M.S., 1981.
Mon.Not.R.astr.Soc., 196, 597.

Wall, J.V., Shimmins, A.J. & Merkelijn, K.J., 1971.
Austr.J.Phys.Astrophys.Suppl., 19, 1.

Wampler, E.J., 1987. *Astr.Astrophys.*, 178, 1.

Wampler, E.J., Burke, W.L., Gaskell, C.M. & Baldwin, J.A., 1984.
Astrophys.J., 276, 403.

Warren, S.J., Hewett, P.C., Irwin, M.J., McMahon, R.G.,
Bridgeland, M.J., Bunclark, P.S. & Kibblewhite, E.J., 1987.
Nature, 325, 131.

White, G.L., Jauncey, D.L., Savage, A., Wright, A.E., Batty, M.J.,
Peterson, B.A. & Gulkis, S., 1987. *Astrophys.J.*, in press.

White, S.D.M., 1986. In: *Inner Space / Outer Space*, p.228,
eds. Kolb, E.W., Turner, M.S., Lindley, D., Olive, K. & Seckel, D.,
University of Chicago Press.

Wills, D. & Lynds, R., 1978. *Astrophys.J.Suppl.*, 36, 317.

Wilson, A.S. & Ulvestad, J.S., 1982. *Astrophys.J.*, 263, 576.

Windhorst, R.A., 1984. *PhD thesis*, University of Leiden.

Windhorst, R.A., Dressler, A. & Koo, D.C., 1987. In: *Observational Cosmology, IAU Symp.No.124*, p.575, eds. Hewitt, A., Burbidge, G. & Fang, L.Z., Reidel,Dordrecht,Holland.

Windhorst, R.A., Koo, D.C. & Spinrad, H., 1986. In: *Galaxy distances and Deviation from Universal Expansion, NATO Advanced Research Workshop*, p.197, eds. Madore, B.F. & Tully, R.B.,
Reidel,Dordrecht,Holland.

Wright, A.E., 1983. In: *Quasars and Gravitational Lenses, 24th Liege Astrophysical Colloquium,* p.240, Liege.

Wright, A.E., Jauncey, D.L., Bolton, J.G. & Savage, A., 1982. *Aust.J.Phys.,* 35, 77.

Wright, A.E., Jauncey, D.L., Peterson, B.A. & Condon, J.J., 1977. *Astrophys.J.,* 211, L115.

Wu, C.C., Faber, S.M., Gallagher, J.S., Peck, M. & Tinsley, B.M., 1980. *Astrophys.J.,* 237, 290.

Wyndham, J.D., 1965. *Astr.J.,* 70, 384.

Wynne, C., 1982. *Optica.Acta.*, 29, 1557.

Yates, M.G., Miller, L. & Peacock J.A., 1986. *Mon.Not.R.astr.Soc.*, 221, 311.

Yoshii, Y. & Takahara, F., 1987. *Astrophys.J.,* in press.

APPENDIX

Appendix A : THE COMPLETE SAMPLE DATA AT 2.7GHz

This appendix provides updated versions of the 4 samples which comprise the complete database at 2.7GHz. The Tables are as follows:

Table A.1 : The $S_{2.7} > 0.1$Jy, 0.075sr Parkes Selected Regions sample, revised and expanded from Downes *et al.* (1986) to incorporate the new observational results described in Chapters 2, 3 & 4.

Table A.2 : The $S_{2.7} > 0.5$Jy, 0.584sr flat-spectrum sample selected by Peacock (1985) from the Parkes $\pm 4^{o}$ zone (Wright *et al.* 1982).

Table A.3 : The $S_{2.7} > 1.5$Jy, 4.05sr 'Northern-Sky' survey of Peacock & Wall (1981).

Table A.4 : The $S_{2.7} > 2$Jy, 9.81sr 'All-Sky' survey of Wall & Peacock (1985).

Note that there are regions of overlap between these 4 samples and therefore that they have certain sources in common.

Layout of Table A.1

Column (1) PKS source number, followed by an asterisk * if the first interferometer observation of the source was made by Downes *et al.* (1986).

Columns (2) and (3) The Right ascension α and Declination δ (1950.0) of the expected position for the optical identification. For unresolved or partly resolved sources this is the position of the peak. For doubles with central components the position of the central component has been used, while for doubles without central components the (unweighted) midpoint of the outer components is given. In D2 sources the flat-spectrum component has been used. Sources which were revealed by the observations of Downes *et al.* to consist of several distinct sources have been labelled A,B,.... in order of increasing RA. For sources marked ** the positions were taken from the list of VLA calibrators, or from various other references which are detailed in Downes *et al.* (1986).

Column (4) The flux density at 2.7GHz from the original survey. Values in brackets were corrected by Downes *et al.* (1986) to allow for confusion.

Column (5) The radio spectral index α (where $S_\nu \propto \nu^{-\alpha}$) over the frequency range 1.4 → 5GHz.

Column (6) A brief description of the radio structure:

- U Unresolved. The flux density decreases by less than 10% on the longest baselines (d ~ 25km).
- P Partially resolved. The flux density decreases by more than 10% on the longest baselines, but no details of the structure are available.
- Do Double.
- CC Central component.

Di Diffuse emission.

V Variable. (1) indicates that variability was detected by Condon *et al.* (1976).

D2 D2 (flat-spectrum core and extended emission on one side only.

H Diffuse halo.

HT Head-tail structure.

I/II Classification of the structure according to the scheme by Fanaroff & Riley (1974) in which type II sources have hotspots separated by more than half the length of the source while type II sources do not.

Columns (7) and (8) The position of the optical identification. The positions are only given in last unit (s in RA and arcsec in Dec). The larger units (h, m in RA and ^{o}, ' in Dec) are generally as in columns (2) and (3). The coordinates refer to equinox 1950.0.

Column (9) The offset of the radio and optical positions in arcsec.

Column (10) Optical classification:

Q Quasi-stellar, confirmed by spectroscopy, variability or colour (see Chapter 5 of this thesis and Section 5 of Downes *et al.* 1986).

Q? Stellar object on position, with colour classification suggesting it is probably a quasar.

G Galaxy confirmed by image or colour.

G? Faint object, possibly extended with colour classification suggesting it is probably a galaxy.

EF Empty field (ie undetected at optical wavelengths and not observed at K - see Chapter 3, Section 3.3b).

? Uncertain optical classification.

Columns (11) and (12) The apparent B magnitude and associated uncertainty (see Chapter 2)

Columns (13) and (14) The apparent R magnitude and associated uncertainty (see Chapter 2)

Columns (15) and (16) The apparent K magnitude and associated uncertainty. The presence of an asterisk * indicates that the measurement was made through the 7.8" diameter aperture, rather than the 12.4" aperture which was used for the bulk of the infrared measurements (see Chapter 3).

Column (17) The redshift z.

Column (18) The references for (respectively) the optical position (C denotes COSMOS measurement by Downes *et al.*), the identification, the finding chart, and the redshift. The abbreviations are:

0 Present work
1 Downes *et al.* (1986)
2 Condon *et al.* (1976)
3 Sandage *et al.* (1965)
4 Lynds (1967)
5 Perryman, Downes, Lilly & Longair (private comm.)
6 McEwan *et al.* (1975)
7 Browne & McEwan (1973)
8 Wills & Lynds (1978)
9 Bolton & Wall (1970)
10 O'Dea & Owen (1985)
11 Merkelijn & Wall (1970)
12 Melnick & Quintana (1981)
13 Peterson *et al.* (1976)
14 Bolton & Ekers (1966b)
15 Sandage (1967)
16 Bolton & Ekers (1966a)
17 Savage, Bolton & Trett (1982)
18 Wampler *et al.* (1984)
19 Browne & McEwan (1972)
20 MacAlpine & Lewis (1978)
21 Wright *et al.* (1977)
22 Bolton *et al.* (1968)
23 Merkelijn (1969)
24 Fricke *et al.* (1983)
25 Clements (1981)
26 Mills *et al.* (1958)
27 Wilson & Ulvestad (1982)
28 de Vaucouleurs *et al.* (1976)
29 Savage (private comm.)
30 Bolton *et al.* (1965)
31 Lynds *et al.* (1966)
32 Clarke *et al.* (1966)
33 Sandage (1966)
34 Peterson *et al.* (1979)
35 Condon & Dressel (1978)
36 Searle & Bolton (1968)
37 Savage, Bolton & Wall (1982)
38 Savage & Bolton (1979)
39 Jauncey (private comm.)
40 Savage *et al.* (1976)
41 Morton & Tritton (1982)
42 Wyndham (1965)
43 Fosbury (private comm.)
44 Tritton (1972)
45 Arp & Sulentic (1979)
46 Allington-Smith & Peacock (private comm.)
47 Spinrad (private comm.)

Late alterations to Table A.1

Two of the original sky-survey identifications of Downes *et al.* (1986) have recently been discovered (spectroscopically) to be galactic stars - 0059+017 and 2215-185 - and have therefore been revised in Table A.1.

In the case of 0059+017 the possibility was raised in Chapter 2 that the original Q? identification might well be incorrect (ie a star) and, since a CCD image had been taken of the field (see Plate 2.3), it proved possible to suggest an alternative ID in case spectroscopy should prove this to be the case. A spectrum of the original ID has recently been obtained by Jeremy Allington-Smith at the William Herschel Telescope, showing that it is indeed a star. Table A.1 has therefore been updated to show the revised identification - ie the faint G? identification situated 5" east and 18" south of the object marked in Figure 2.1 and Plate 2.3.

The original Q? ID of 2215-185 has also been shown to be a star by the spectrum given in Chapter 4. Despite the large angular size of the radio source, the validity of the original ID was not strongly suspected because it appeared to be associated with a (rather dubious) compact radio component. However, a CCD image was taken of the field (see Plate 2.3) and now that the original ID has been shown to be incorrect, this image provides an alternative faint G? identification, situated 9" north and 7" east of the object marked in Figure 2.1 and Plate 2.3 (very close to a similar faint object some 4" further north east). In the light of this new information Table A.1 has been updated to give the position of the new ID and the radio position has been altered to represent the mid-point of a double source which is no longer indicated as possessing a central component.

Since both the above radio sources are Do,II sources without a compact core, the new faint galaxy identifications are more consistent with the expected type of identification than were the original quasi-stellar IDs.

Table A.1 : Radio sources with $S_{2.7} > 0.1$ Jy in the Parkes Selected Regions.

(1)	(2)	(3)	(4)	(5)	(6)	(7)	(8)	(9)	(10)	(11)	(12)	(13)	(14)	(15)	(16)	(17)	(18)
IAU	α_{rad} (1950)	δ_{rad} (1950)	$S_{2.7}$	$\alpha_{2.7}^{1.4}$	Structure	α_{opt}	δ_{opt}	$\Delta/''$	ID	B	±	R	±	K	±	z	refs.
0000−006	00 00 23.41	−00 41 29.2	0.236	(0.34)	U+Di,V(1)	23.38	29.3	0.5	G	20.70	0.50	18.90?	0.50	14.71	0.20	0.07?	1C 2 2 0
0000+035	00 00 37.71	03 33 36.9	0.146	1.41	P	37.68	36.4	0.7	G	23.01	0.07	21.27	0.13	>19.00*		0.363	0 0 0 46
0000−022*	00 00 50.60	−02 13 36.4	0.156	0.90	P	50.51	36.6	1.4	G	23.70	0.22	22.36	0.09	17.30*	0.17		0 0 0
0003+006	00 03 32.21	00 37 19.9	0.248	0.97	Do,II	32.11	18.0	2.4	G			22.57	0.11	16.84	0.12		0 0 0
0003−003	00 03 48.84	−00 21 06.0	2.410	0.72	D2	48.86	06.4	0.5	Q	20.20	0.50	19.30	0.50	16.50	0.13	1.037	1C 3 3 4
0005+021	00 05 10.00	02 09 50.6	0.117	0.36	U,V	10.05	49.7	1.2	Q?	24.40	0.26	>23.00					0 0 0
0007+016	00 07 24.81	01 41 13.7	0.160	0.84	P	24.80	13.8	0.2	Q	19.60	0.50	18.70	0.50	15.56	0.08	2.900	1C 2 2 46
0008−006	00 08 18.76	−00 36 48.1	0.106	0.43	U,V	18.77	47.8	0.3	Q?	23.95	0.21	22.88	0.15	18.94*	0.49		0 0 0
0010+005	00 10 36.87	00 34 55.2	0.950	0.92	Do,II	36.71	51.1	4.8	G	23.06	0.20	20.24	0.02	15.99	0.10	0.606	0 0 0 47
0011−023*	00 11 51.93	−02 22 36.2	0.243	0.74	P	51.92	36.2	0.2	G?	23.53	0.12	22.37	0.11	17.53*	0.18		0 0 0
0012−008	00 12 29.68	−00 51 39.8	0.120	0.42	U	29.62	40.0	0.8	G	18.40	0.50	17.15	0.03	15.12	0.05	0.171	1C 2 2 5
0013−005	00 13 37.27	−00 31 52.8	0.870	0.21	U	37.37	53.6	1.7	Q	20.20	0.50	18.40	0.50			1.575	1C 6 6 0
0017+026	00 17 12.48	02 41 30.0	0.142	0.00	U,V	12.41	29.2	1.3	G?			21.99	0.08	16.72*	0.10		0 0 0
0038−019	00 38 52.67	−01 59 42.6	0.650	1.22	Do+CC,II	52.57	42.6	1.5	Q	16.80	0.50	17.60	0.50	14.80	0.06	1.679	1 7 7 8
0040+017	00 40 13.94	01 46 00.0	0.117	0.66	Do+CC,II	13.91	00.4	0.6	G	17.90	0.50	16.50	0.50	14.03	0.03		1 2 2
0041+007*	00 41 30.72	00 45 28.2	0.212	1.24	Do+CC,II	30.66	29.0	1.2	G	17.30	0.50	16.00	0.50	13.80	0.10	0.112	1 1 1 0
0043+000	00 43 08.30	00 04 42.0	0.269	1.03	Do,II	08.17	39.9	2.9	G	24.17	0.21	21.46	0.15	16.38	0.14		0 0 0
0043−010	00 43 33.17	−01 00 05.0	0.188	0.82	P	33.14	04.7	0.5	G	>23.00		23.04	0.22	17.64	0.30		0 0 0
0043−003	00 43 56.99	−00 21 54.1	0.100	1.07	Do,II				EF	>23.50		>23.00					
0045−009	00 45 30.12	−00 59 04.0	0.144	1.13	Do,II	30.19	03.0	1.5	G	23.85	0.30	21.47	0.04	16.35	0.11		0 0 0
0045−000	00 45 45.33	−00 01 24.0	0.110	0.24	U	45.35	23.3	0.8	Q	19.60	0.50	19.50	0.50	18.01	0.32	1.536	1C 9 9 8
0045−024*	00 45 47.47	−02 29 32.3	0.157	0.85	Do+CC,II	47.42	31.5	1.1	G	22.63	0.08	20.40	0.02	16.08	0.11	0.535	0 0 0 46
0047+023	00 47 08.86	02 20 44.0	0.319	0.23	U,V	08.88	44.3	0.4	Q	19.00	0.50	18.20?	0.50	17.78	0.25		1C 2 2
0049+019	00 49 05.34	01 59 24.1	0.111	0.25	U	05.34	23.2	0.9	G	>23.50		21.79	0.06	17.12	0.19		0 0 0
0051−008	00 51 49.30	−00 49 31.8	0.137	0.82	Do,II	49.34	30.2	1.7	G?	>23.00		22.48	0.11	17.20	0.17		0 0 0
0053−016	00 53 29.19	−01 36 16.7	0.709	0.74	HT,I	29.31	16.9	1.8	G	12.50	0.50	11.40	0.50	11.81	0.05	0.044	10 11 11 12
0053−015	00 53 52.53	−01 31 55.2	0.781	0.81	HT,I	52.08	57.1	7.0	G	11.50	0.50	10.90	0.50	11.32	0.03	0.044	10 10 10 12
0054−006	00 54 43.39	−00 40 45.7	0.113	−0.43	U,V	43.41	45.1	0.7	Q	18.60	0.50	18.90	0.50	17.76	0.20	2.795	1C 2 2 13
0054+018	00 54 53.53	01 53 22.9	0.274	0.95	Do,I	53.53	22.6	0.3	G	20.90	0.50	17.60	0.50	13.74	0.05	0.291	1C 2 2 46
0055−016	00 55 01.54	−01 39 52.0	3.358	0.63	Do+CC,I	01.41	50.6	2.4	G	11.60	0.50	10.90	0.50	11.61	0.03	0.045	10 14 14 15
0055+015A	00 55 07.15	01 34 20.7	0.158	0.60	P	07.19	21.4	0.9	G	23.49	0.11	22.54	0.13	16.16	0.10		0 0 0
0056−001	00 56 31.76	−00 09 18.8	1.960	0.49	U	31.76	18.4	0.4	Q	16.60	0.50	16.50	0.50	14.86	0.03	0.717	1C 16 16 4
0056+020	00 56 43.80	02 04 33.0	0.127	0.99	Do,II	43.75	27.5	5.6	G	23.06	0.15	20.67	0.02	15.82*	0.07		0 0 0
0059+017	00 59 40.91	01 47 07.1	0.400	1.06	Do,II	41.11	1.5	6.4	G?								0 0 0
0059+027	00 59 55.20	02 46 32.6	0.151	1.06	Do+CC,II	55.21	32.5	0.2	G	23.27	0.09	22.78	0.16	17.11	0.20		0 0 0

Table A.1 Continued

(1)	(2)	(3)	(4)	(5)	(6)	(7)	(8)	(9)	(10)	(11)	(12)	(13)	(14)	(15)	(16)	(17)	(18)
IAU	α_{rad} (1950)	δ_{rad} (1950)	$S_{2.7}$	$\alpha_{2.7}^{1.4}$	Structure	α_{opt}	δ_{opt}	Δ/"	ID	B	±	R	±	K	±	z	refs.
0100+023	01 00 55.99	02 19 45.6	0.128	0.80	P	55.71	44.9	4.3	G	>23.00		22.06	0.06	17.22*	0.25		0 0 0
0101−025	01 01 44.24	−02 31 42.0	(0.184)	0.76	P	44.24	43.1	1.1	Q	18.80	0.50	18.70	0.50			2.05?	1 17 17 17
0101+023	01 01 49.52	02 23 44.0	0.105	1.33	Do,II	49.40	38.1	6.2	G	22.06	0.13	19.42	0.06	15.85	0.20	0.390	1 1 1 46
0103−021	01 03 49.91	−02 11 40.5	0.420	0.47	D2	49.86	39.7	1.1	Q	19.00	0.50	19.00	0.50			2.201	1 9 9 18
0105+034	01 05 49.84	03 25 33.7	0.181	0.64	U	49.93	34.1	1.4	?	24.18	0.23			18.59*	0.33		0 0 0
0105+025	01 05 50.09	02 33 50.0	0.122	0.87	Do,II/D2?				G?	>24.00		>23.50		17.26	0.22		
0105−008	01 05 53.33	−00 53 23.7	0.730	0.26	P	53.34	23.9	0.3	Q	17.20	0.50	17.00	0.50	15.17	0.09	0.318	1 19 20 8
0220−023*	02 20 40.78	−02 18 44.0	0.112	0.24	P,V?	40.81	44.8	0.9	G	23.76	0.20	22.15	0.12	16.73	0.19		0 0 0
0222+000	02 22 34.21	00 03 36.0	0.142	0.90	P	34.24	36.1	0.5	Q	19.80	0.50	18.30	0.50	15.13	0.06	0.523	1C 9 9 13
0222−008	02 22 34.64	−00 49 03.6	0.660	0.79	Do,II	34.72	03.8	1.2	Q	19.40	0.50	18.10	0.50	15.45	0.08	0.687	1C 6 6 21
0223−023*	02 23 02.03	−02 23 47.0	0.225	0.93	P	02.10	47.8	1.3	G?	>23.50		22.61	0.07	17.32*	0.14		0 0 0
0223+035	02 23 19.48	03 33 51.3	0.142	1.09	Do,II	19.48	51.3	0.0	G?	23.30	0.12	22.45	0.12	17.55	0.25		0 0 0
0223+012	02 23 34.98	01 15 59.4	0.240	0.76	Do+CC,II	35.04	00.6	1.5	Q	19.90	0.50	18.80	0.50	18.14	0.28	1.369	1C 9 9 0
0223+018	02 23 40.17	01 51 44.8	0.220	0.45	Do,II	39.86	48.2	5.8	Q?	21.68	0.10	21.11	0.20				1C 1 1
—						40.37	45.2	3.1	G	22.81	0.22	20.81	0.12				1C 1 1
0225+002	02 25 31.94	00 17 54.4	0.141	1.15	Do,II				G?	>24.00		>24.00		18.54*	0.36		
0225−014	02 25 35.05	−01 29 03.8	0.300	0.75	Do+CC,II	35.07	03.8	0.1	Q	17.50	0.50	17.60	0.50	16.01	0.04	2.037	1C 22 22 8
0227+001	02 27 04.43	00 11 58.2	0.131	1.15	Do+CC,II	04.19	56.2	4.1	?	23.16	0.30			17.98	0.36		0 0 0
0229+034	02 29 43.73	03 25 26.2	0.106	0.66	Do+CC,II	43.72	24.9	1.3	G	21.00	0.50	18.00	0.50	14.89	0.05	0.278	1 2 2 46
0230−027*	02 30 11.84	−02 46 55.9	0.330	0.83	Do,II	11.30	45.4	13.3	G	20.41	0.05	18.18	0.04	14.53	0.05	0.239	1C 1 1 0
0230−022*	02 30 58.19	−02 16 31.5	0.173	0.75	P	58.28	31.2	1.4	G	21.40	0.50	19.50	0.50	15.77	0.06	0.794	1C 17 17 46
0232−010	02 32 12.81	−01 03 30.3	0.109	1.19	Do,II	12.85	29.9	0.7	G	24.15	0.20	22.02	0.08	16.79*	0.09		0 0 0
0233−025	02 33 00.61	−02 32 35.1	0.580	0.78	Do,II	00.61	35.5	0.4	Q	19.40	0.50	19.30	0.50	17.10	0.14	1.321	1C 23 23 8
0235+017	02 35 06.61	01 45 40.0	(0.135)	(0.51)	U+Di	06.6	33.0	7.0	G	10.90	0.50	10.50	0.50				2 2 2
0235−019	02 35 24.96	−01 58 08.9	0.224	0.89	Do,II	24.79	07.1	3.1	G	22.68	0.07	21.57	0.06	16.73	0.17	0.840	0 0 0 46
0235+023*	02 35 57.09	02 20 53.7	0.293	0.72	Do+CC?,II	57.14	53.7	0.8	Q	17.70	0.50	17.10	0.50	13.44	0.02	0.209	1C 1 1 0
0236−015*	02 36 40.88	−01 31 09.6	0.147	1.08	Do,II	40.87	09.3	0.3	Q	18.80	0.50	18.90	0.50	16.64	0.12	1.794	1C 1 1 0
0237−027	02 37 13.72	−02 47 32.9	0.400	−0.41	U	13.64	33.8	1.5	Q	18.50	0.50	17.90	0.50	17.43	0.20	1.116	1C 9 9 24
0238−018*	02 38 21.61	−01 50 56.8	0.102	1.19	Do,II	21.67	57.8	1.3	Q	19.10	0.50	19.60	0.50	16.29	0.10		1C 1 1
0239+002	02 39 11.19	00 13 51.0	0.147	1.06	U+Di	09.70	07.0	36.5	G	11.40	0.50	12.20	0.50			0.003	2 11 11 28
0239−016*	02 39 35.56	−01 41 21.1	0.128	0.76	Do+CC,II	35.24	18.3	5.6	G	22.81	0.25	20.75	0.11	16.35*	0.09		1 1 1
0240−002	02 40 07.06	−00 13 31.3	3.130	0.83	I	07.08	31.5	0.4	G	9.50	0.50	8.80	0.50			0.004	25 26 27 28
0240−021*	02 40 15.44	−02 10 33.2	0.122	0.95	U+Di	15.44	33.3	0.1	Q	19.69	0.04	18.87	0.05	16.03	0.12	0.617	1C 1 1 0
0240−027*	02 40 59.58	−02 45 38.0	0.207	1.28	P				OBS								
0241+011*	02 41 04.90	01 08 30.8	0.122	1.03	Do+CC,II	04.83	29.7	1.5	Q	19.00	0.50	19.50	0.50			1.400	35 35 35 45
0241−012*	02 41 16.57	−01 15 41.4	0.107	0.26	Do,II	16.57	42.5	1.1	G?	>23.50		23.58	0.30				0 0 0

Table A.1 Continued

(1)	(2)	(3)	(4)	(5)	(6)	(7)	(8)	(9)	(10)	(11)	(12)	(13)	(14)	(15)	(16)	(17)	(18)
IAU	α_{rad} (1950)	δ_{rad} (1950)	$S_{2.7}$	$\alpha_{2.7}^{1.4}$	Structure	α_{opt}	δ_{opt}	Δ/"	ID	B	±	R	±	K	±	z	refs.
0242+028	02 42 50.51	02 49 43.2	0.285	0.95	Do,II	50.44	43.1	1.1	G	23.48	0.15	21.54	0.05	16.71*	0.11		0 0 0
0242+009	02 42 59.52	00 55 38.0	0.164	0.91	Do+CC,II	59.52	38.3	0.3	Q	19.60	0.50	18.20	0.50	16.16	0.07	1.520	1C 2 2 0
0245+013	02 45 12.58	01 18 52.7	0.153	1.01	Do,II	12.62	54.2	1.6	G	23.84	0.16	23.96	0.40	18.01*	0.22		0 0 0
1154−019*	11 54 04.27	−01 56 10.1	0.112	0.93	Do+CC,II	04.48	05.0	6.0	G	23.62	0.13	21.73	0.07				0 0 0
—						04.74	10.0	7.1	G	22.81	0.06	22.06	0.09				0 0 0
1154−011	11 54 37.23	−01 07 28.4	0.106	0.88	Do,II?	37.19	28.5	0.6	G	22.38	0.08	21.23	0.07	17.10*	0.30		0 0 0
1155−029*	11 55 16.41	−02 55 41.6	0.233	0.56	Do,II?	16.46	42.3	1.0	G	21.90	0.50	19.00	0.50				1 1 1
1157+026	11 57 01.49	02 36 52.5	0.133	0.23	U	01.59	49.5	3.4	G?	24.05	0.19	>23.50		17.20	0.50		0 0 0
1157+014	11 57 11.07	01 28 48.9	0.143	0.55	U	11.10	49.4	0.7	Q	18.07	0.03	17.20	0.03	14.79	0.04	1.986	1C 2 2 21
1158+007	11 58 49.51	00 45 10.4	0.257	0.26	D2	49.52	10.6	0.3	Q	18.94	0.04	18.33	0.04	17.12	0.10	1.367	1C 9 9 8
1159−036*	11 59 38.93	−03 37 53.7	0.118	1.12	Do+CC,II	38.94	51.7	2.0	Q	20.30	0.50	20.30	0.50			1.102	1 9 9 8
1159−023	11 59 58.51	−02 23 21.4	0.430	1.03	P				EF	>24.00		>23.50					
1200−033*	12 00 17.52	−03 19 44.0	0.116	0.95	Do,II	17.54	41.9	2.1	G	21.10	0.50	18.30	0.50				1 1 1
1201−026*	12 01 08.28	−02 38 27.9	0.143	1.07	Do,II	08.27	27.2	0.7	G?	23.11	0.08	22.87	0.21				0 0 0
1201−002	12 01 31.93	−00 13 11.5	0.193	0.79	Do+CC,I	31.88	10.9	1.0	G	21.40	0.50	17.80	0.50	14.62*	0.05		1C 2 2
1203+011	12 03 14.76	01 10 25.8	0.126	−0.07	U	14.78	26.2	0.5	Q	18.20	0.50	17.30	0.50			0.104	1C 9 9 21
1205−008	12 05 07.89	−00 49 55.0	0.138	0.26	D2,V(1)	07.94	55.6	1.0	Q	19.50	0.50	18.20	0.50			1.002	1C 2 2 21
1205+011	12 05 59.93	01 11 03.5	0.231	−0.18	U	59.94	03.8	0.3	G?	23.59?	0.16	21.64	0.09	17.20*	0.20		0 0 0
1206−026	12 06 32.95	−02 41 04.5	0.143	0.87	Do,II	32.87	04.9	1.4	?	20.50	0.50	19.50	0.50				1C 1 1
—						33.28	08.3	6.2	Fl?			22.50	0.50				1C 1 1
1207−013	12 07 57.49	−01 20 08.3	0.370	0.70	Do,II	57.49	07.6	0.7	G	21.80	0.50	18.80	0.50				1C 11 11
1211+000	12 11 23.25	00 03 31.8	0.233	1.08	Do,II	23.16	28.2	3.8	G	21.06	0.08	18.56	0.04	14.80	0.20		1C 2 2
1212−007	12 12 15.00	−00 43 36.0	0.510	1.00	Do,II	14.96	35.7	0.7	G?	23.25	0.18			17.87*	0.19		0 0 0
1212+005	12 12 49.50	00 35 33.3	0.285	0.89	Do,II	49.42	34.5	1.7	G	21.84	0.12	19.54	0.05	15.40	0.20		1C 2 2
1214−029*	12 14 31.46	−02 54 53.0	(0.131)	1.06	HT,I	31.97	57.0	8.6	?	22.07	0.10	21.05	0.09				0 0 0
1215−033*	12 15 21.31	−03 20 44.2	0.108	0.88	D2	21.26	43.4	1.1	G	19.87	0.05	17.90	0.03	14.35	0.01	0.184	1 1 1 0
1215−002	12 15 24.94	−00 13 06.9	0.286	0.33	U+H,V?/HT	24.99	06.8	0.8	G	18.40	0.50	17.50	0.50			0.417	1C 2 2 0
1215+013	12 15 54.12	01 19 16.6	0.104	−0.15	U,V	54.10	16.8	0.4	G	19.03	0.04	17.21	0.03	13.65	0.03	0.118	1 2 2 21
1216−010	12 16 01.07	−01 03 15.1	0.189	−0.28	U,V	01.12	14.8	0.8	Q	17.80	0.50	16.90	0.50			0.415	1 2 2 29
1217+023	12 17 38.34	02 20 20.9	0.470	−0.45	D2	38.39	21.2	0.8	Q	15.30	0.50	15.10	0.50			0.240	1 30 30 31
1328−034*	13 28 53.80	−03 25 48.6	0.257	0.16	P,V?	53.90	48.2	1.6	Q	18.30	0.50	18.50	0.50			1.352	1 9 9 8
1329+012	13 29 43.04	01 17 10.9	0.210	0.95	Do,II	43.34	12.4	4.7	G	24.60	0.30	22.00	0.09	17.10*	0.30		0 0 0
1330+022	13 30 20.46	02 16 07.7	1.911	0.59	Do+CC,II	20.48	08.2	0.6	G	19.42	0.05	17.82	0.03	14.00	0.10	0.216	1 32 32 33
1331+004	13 31 07.38	00 26 23.4	0.140	1.44	Do,II	07.24	21.5	2.8	G?	23.14	0.08	22.06	0.16				0 0 0
1331+025	13 31 12.43	02 34 33.9	0.145	1.19	Do,II	12.43	33.0	0.9	G	21.29	0.09	18.97	0.05	15.40	0.10		1 2 2
1334+008	13 34 58.02	00 50 43.9	0.101	−0.10	U	57.96	44.1	0.9	G	20.25	0.05	18.39	0.04	14.52	0.03	0.299	1C 2 1 0
1335+023	13 35 06.94	02 22 12.2	0.104	0.41	U,V?	06.88	12.1	0.9	Q	17.10	0.50	17.10	0.50			1.356	1 9 9 34

Table A.1 Continued

(1)	(2)	(3)	(4)	(5)	(6)	(7)	(8)	(9)	(10)	(11)	(12)	(13)	(14)	(15)	(16)	(17)	(18)
IAU	α_{rad} (1950)	δ_{rad} (1950)	$S_{2.7}$	$\alpha_{2.7}^{1.4}$	Structure	α_{opt}	δ_{opt}	Δ/"	ID	B	±	R	±	K	±	z	refs.
1336+003	13 36 07.53	00 18 00.6	0.117	1.05	Do+CC,II	07.50	00.6	0.5	G?	24.09	0.19	23.13	0.22				0 0 0
1336−030*	13 36 57.37	−03 01 54.8	0.190	0.51	P	57.38	54.6	0.3	Q	18.90	0.50	18.00	0.50			2.313	1C 17 17 0
1336+020	13 36 59.59	02 00 34.4	0.380	1.02	Do,II	59.65	34.4	0.9	G	22.05	0.05	19.99	0.02	16.72	0.10		0 0 0
1337−000	13 37 00.40	−00 01 24.1	0.132	0.95	Do,I	00.43	24.6	0.7	G	16.00	0.50	13.50	0.50			0.144	1C 1 1 34
1337−013*	13 37 30.11	−01 22 36.1	0.192	−0.44	P,V	30.18	35.1	1.4	Q	18.60	0.50	17.80	0.50			1.619	1C 9 9 8
1337−033	13 37 37.85	−03 20 10.6	0.580	0.84	U	37.96	09.2	2.2	G?	22.90	0.07	21.68	0.07				0 0 0
1339+015	13 39 44.02	01 32 23.2	0.172	0.86	U	44.04	24.1	0.9	?	24.97	0.44	24.09	0.50				0 0 0
1340+022	13 40 15.66	02 13 15.0	0.540	0.91	Do,II	15.63	14.7	0.5	G	22.66	0.08	20.49	0.04	15.91*	0.08		0 0 0
1342−016*	13 42 42.17	−01 41 24.8	0.224	0.87	Do+CC,II	42.19	24.6	0.4	G	17.80	0.50	15.80	0.50	13.62*	0.03	0.167	1C 11 11 0
1343−007	13 43 03.09	−00 42 06.3	0.620	0.69	Do,II	03.03	06.8	1.0	G	22.30	0.06	20.24	0.03	15.71	0.04		0 0 0
1343−026*	13 43 16.80	−02 37 31.8	0.245	0.93	Do+CC?,II	17.00	30.4	3.3	G	21.84	0.13	19.81	0.06	15.19	0.05		1C 1 1
1343+011	13 43 50.68	01 10 35.8	0.101	1.08	Do,II	50.68	37.0	1.2	G	23.07	0.11	20.45	0.04				0 0 0
1345+008	13 45 06.85	00 49 58.0	0.139	1.21	Do,II	06.70	54.2	4.4	G?	24.23	0.22	23.70	0.38				0 0 0
1345+002	13 45 11.42	00 14 07.7	0.103	1.06	Do,II	11.47	07.5	0.8	G	22.12	0.05	19.82	0.02				0 0 0
1346+018	13 46 57.16	01 49 30.9	0.147	0.84	Do,II	57.15	31.9	1.0	G	21.73	0.11	20.37	0.07	16.29*	0.09		1C 1 1
1348−012	13 48 18.64	−01 13 48.5	0.107	0.57	D2?	18.62	48.0	0.6	Q	19.40	0.50	19.20	0.50			1.482	1C 2 2 0
1348+007	13 48 31.01	00 46 08.8	(0.132)	0.37	U	31.02	08.4	0.4	Q	21.92	0.04	21.40	0.10	16.12	0.07	2.084	0 0 0 0
1349−019*	13 49 22.98	−01 55 10.6	0.139	1.11	Do,II				EF	>24.00		>24.00					
1349−017*	13 49 48.71	−01 42 01.7	0.310	0.88	Do,II	48.71	01.7	0.0	G	19.54	0.05	18.39	0.04	14.50	0.10		1C 11 11
1349−008	13 49 52.66	−00 52 48.6	0.137	0.93	Do,II	52.53	49.3	2.1	G	23.31	0.09	22.02	0.08				0 0 0
1351+021	13 51 18.90	02 06 37.4	0.500	0.38	D2	18.87	37.6	0.5	Q	18.30	0.50	20.10	0.50			1.606	1 6 6 8
1351−018	13 51 32.03	−01 51 20.1	1.000	−0.08	U	32.00	20.1	0.4	Q	20.90	0.03	19.30	0.10	17.26	0.19	3.709	1C 17 17 0
1352+008*	13 52 34.26	00 55 24.3	0.400	0.85	U	34.20	24.9	1.1	G?	23.77	0.14	22.64	0.14	17.00*	0.50		0 0 0
2150−202*	21 50 56.08	−20 15 26.9	0.310	0.95	Do,II	56.15	19.0	8.1	G?	22.96	0.30	22.45	0.40				1 1 1
2152−218*	21 52 26.07	−21 51 16.6	0.270	(1.48)	U,V?	26.08	16.7	0.2	G	20.60	0.50	19.16	0.05	16.08*	0.09	0.306	1C 1 1 0
2153−219*	21 53 12.50	−21 59 00.7	0.114	1.24	Do,II	12.60	49.6	11.4	G	16.40	0.50	14.10	0.50	13.04	0.02	0.097	1C 11 11 0
2153−188*	21 53 21.83	−18 51 56.9	0.141	0.99	Do,I?	21.70	57.2	1.9	G	21.87	0.03	19.33	0.01	15.21*	0.05		0 0 0
2153−204*	21 53 47.16	−20 26 48.0	0.220	0.20	U	47.11	49.0	1.2	Q	17.00	0.50	16.40	0.50	15.23	0.06	1.310	1C 1 1 36
2154−184*	21 54 12.13	−18 28 03.7	1.108	1.17	Do+CC,II	12.11	04.8	1.1	Q	19.80	0.50	19.43	0.08	15.20	0.06	0.668	1C 37 37 0
2154−183*	21 54 44.02	−18 21 21.8	1.001	0.79	U	43.93	21.8	1.6	Q	20.60	0.50	21.41	0.25	16.46	0.10	1.423	1C 38 38 0
2155−202*	21 55 03.17	−20 12 10.2	0.217	1.24	Do,II	02.54	09.1	9.0	G	21.86	0.15	19.67	0.05	16.16	0.11		1C 1 1
2156−192*	21 56 26.16	−19 12 57.3	0.103	0.74	Do,II	26.09	56.4	1.3	G	20.90	0.50	19.96	0.08	14.96	0.06		1C 1 1
2157−214*	21 57 10.13	−21 25 05.0	0.167	0.96	Do,II	10.08	05.6	0.9	?	21.20	0.50	20.51	0.10	16.79	0.13		1C 1 1
2157−200*	21 57 21.79	−20 00 12.7	0.133	−0.09	U,V?	21.85	11.3	1.6	Q	19.40	0.50	18.90	0.50			1.198	1C 9 1 40
2157−191*	21 57 55.70	−19 10 06.7	0.133	0.97	Do,II	55.75	06.6	0.7	G	23.78	0.15	22.71	0.12	17.63*	0.20		0 0 0

Table A.1 Continued

(1)	(2)	(3)	(4)	(5)	(6)	(7)	(8)	(9)	(10)	(11)	(12)	(13)	(14)	(15)	(16)	(17)	(18)
IAU	α_{rad} (1950)	δ_{rad} (1950)	$S_{2.7}$	$\alpha_{2.7}^{1.4}$	Structure	α_{opt}	δ_{opt}	Δ/"	ID	B	±	R	±	K	±	z	refs.
2158−160*	21 58 02.78	−16 01 44.1	0.140	0.74	Do+CC?,II	02.81	43.7	0.6	G	23.45	0.11	22.69	0.07	17.39*	0.12		0 0 0
2158−167*	21 58 11.07	−16 46 59.7	0.147	0.12	Do+CC,I	11.07	59.5	0.2	?	20.70	0.50	20.64	0.10	16.60	0.13		1C 1 1
2158−206*	21 58 40.78	−20 40 03.4	0.235	0.67	P	40.77	04.3	0.9	Q	19.90	0.50	20.00	0.50	17.17*	0.13	0.370	1C 37 37 37
2158−170*	21 58 53.13	−17 03 02.0	0.178	1.12	D2				G?	>24.50		>24.00		18.44*	0.28		
2158−177*	21 58 54.19	−17 47 35.7	0.294	0.93	Do,II	54.50	35.0	4.5	G	23.89	0.23	21.73	0.06	17.03*	0.14		0 0 0
2159−215*	21 59 03.35	−21 32 34.0	0.130	1.15	P	03.34	34.0	0.1	G	23.50	0.11	22.25	0.09	18.21*	0.33		0 0 0
2159−187*	21 59 04.70	−18 47 36.1	0.183	1.33	D2	04.70	35.7	0.4	G	19.40	0.50	18.30	0.50	15.10	0.20	0.334	1C 37 37 0
2159−192*	21 59 27.26	−19 17 22.6	0.169	1.07	Do,II	27.27	21.3	1.3	G	24.21	0.21	23.34	0.26	17.94*	0.21		0 0 0
2159−201*	21 59 55.98	−20 09 40.3	0.200	1.66	Do,II/D2?	56.05	40.3	1.0	G?	>24.50		23.20	0.16				0 0 0
2200−189*	22 00 06.84	−18 54 24.7	0.167	0.68	U	06.80	24.7	0.6	?	>23.00		22.07	0.10	18.55*	0.36		0 0 0
2201−216*	22 01 15.71	−21 41 26.4	0.146	0.71	Do,I?	15.67	27.8	1.5	G	16.50	0.50	14.50	0.50	12.35	0.01		1C 1 1
2202−179*	22 02 14.42	−17 57 09.1	0.340	1.11	Do,II	14.50	08.7	1.2	G?	21.84	0.03	20.89	0.03	16.79*	0.10		0 0 0
2203−188	22 03 25.72	−18 50 17.0	5.200	0.32	U	25.77	17.2	0.7	Q	18.50	0.50	17.60	0.50	15.15	0.08	0.618	1C 16 41 41
2203−215*	22 03 55.01	−21 34 19.8	0.158	−0.19	U	55.05	21.9	2.2	Q	17.70	0.50	17.90	0.50	15.09	0.09	0.577	1C 38 38 0
2204−182*	22 04 11.38	−18 15 28.4	0.340	0.83	Do,II	11.88	27.2	7.2	G?	>24.00		23.82	0.45	>19.00*			0 0 0
2204−203*	22 04 30.58	−20 18 07.5	0.350	1.20	Do,II	30.56	07.2	0.4	G	22.68	0.06	21.90	0.07	16.91*	0.11		0 0 0
2204−208*	22 04 48.12	−20 53 17.0	0.145	0.05	U,V	48.08	17.6	0.8	Q	20.26	0.05	19.81	0.05			1.923	1C 1 1 0
2205−178*	22 05 21.47	−17 52 12.3	0.152	1.21	Do+CC,II	21.48	11.8	0.5	?	23.63	0.15	22.30	0.11	>19.00*			0 0 0
2207−203*	22 07 31.44	−20 22 32.1	0.111	1.13	P	31.58	33.8	2.6	G	23.86	0.19	21.54	0.08	17.40*	0.18		0 0 0
2211−172*	22 11 42.54	−17 16 38.3	4.515	1.17	Do,II	42.56	32.1	6.2	G	19.70	0.50	17.69	0.04	13.65	0.02	0.153	1C 42 1 43
2213−167*	22 13 31.06	−16 46 47.0	0.198	0.85	Do+CC,II	31.08	43.8	3.2	G	16.10	0.50	14.10	0.50	13.02	0.12	0.074	1C 1 1 0
2213−156*	22 13 51.96	−15 39 14.0	0.281	0.80	Do+CC,II	51.94	11.1	2.9	?	21.20	0.07	21.22	0.13	17.03	0.15		1C 1 1
2214−206*	22 14 58.55	−20 37 51.7	0.125	0.97	P	58.64	52.9	1.8	Q	20.60	0.50	20.16	0.09	16.07	0.09	2.316	1C 1 1 0
2215−179*	22 15 20.31	−17 58 15.0	0.234	1.26	Do,II	20.29	12.7	2.3	G	23.68	0.16	20.66	0.02	15.93*	0.08		0 0 0
2215−185*	22 15 37.45	−18 35 06.9	0.104	1.10	Do,II	37.47	4.7	2.2	G?								0 0 0
2353−003	23 53 02.08	−00 19 29.3	0.163	1.20	Do,II	02.28	29.9	3.1	G	21.30	0.50	18.00	0.50	15.70	0.08	0.198	1C 2 2 46
2353−018*	23 53 32.51	−01 48 33.5	0.118	1.35	Do+CC,II	32.59	33.4	1.2	G	22.53	0.08	21.34	0.04	16.95	0.19	1.028	0 0 0 46
2353+010	23 53 34.24	01 02 44.0	0.104	1.10	Do,II	33.67	40.2	9.4	G	24.03	0.16	21.85	0.06	16.19*	0.09		0 0 0
2354+008	23 54 38.72	00 49 53.1	0.157	1.04	Do,II	38.25	54.4	7.2	G	22.58	0.08	21.57	0.05	16.70?	0.17		0 0 0
2354−021*	23 54 51.46	−02 08 57.5	0.287	0.07	P,V	51.31	57.4	2.3	Q?	21.16	0.08	20.20	0.10	15.81*	0.10		1C 1 1
2355−024*	23 55 27.56	−02 27 28.7	0.151	0.80	P,V	27.29	26.6	4.6	Q?	22.93	0.15	22.37	0.10	>19.00*			0 0 0
2355−010	23 55 51.19	−01 01 20.1	0.423	1.02	Do,II	51.22	22.4	2.3	G	23.35	0.16	21.29	0.04	16.96*	0.12		0 0 0
2356+033	23 56 08.88	03 20 21.8	0.209	0.90	Do+CC?,II	08.86	21.4	0.5	G	23.80	0.24	21.27	0.04	16.24	0.12		0 0 0
2356+018	23 56 41.86	01 50 12.1	0.156	0.85	Do,II	41.94	13.1	1.6	G?	20.80	0.50	19.59	0.08	16.14	0.10		1C 1 1
2357−007	23 57 03.04	−00 47 54.9	0.101	−0.13	U,V	03.04	54.4	0.5	Q	21.27	0.02	19.89	0.02	16.74*	0.11	1.107	0 0 0 47
2357+004	23 57 25.04	00 25 24.2	0.275	0.54	Do+CC,I	24.81	24.8	3.5	G	15.60	0.50	14.30	0.50			0.084	1C 2 2 44
2357−006*	23 57 27.97	−00 38 52.2	0.147	0.66	P				G?	>24.00		>23.50		17.97*	0.23		
2359+018*	23 59 21.07	01 48 07.3	(0.120)	1.33	Do,II	21.01	07.9	1.1	G	22.14	0.05	19.61	0.01	15.66	0.10		0 0 0

Layout of Tables A.2 → A.4

Column (1) IAU name

Column (2) Other name

Column (3) Right ascension, α (1950)

Column (4) Declination, δ (1950)

Column (5) Positional uncertainty in arcsec

Column (6) Flux density at 2.7GHz

Column (7) The radio spectral index α (where $S_\nu \propto \nu^{-\alpha}$) over the frequency range 1.4 → 5GHz.

Column (8) Optical classification:

- Q QSO confirmed by spectrum or variability (and including BLlacs)
- Q? Stellar object on position
- G Galaxy confirmed by extended image
- G? Very faint object; presumed galaxy
- EF Empty field

Column (9) Apparent V magnitude.

Column (10) Redshift z. An asterisk * indicates an estimate (see Wall & Peacock 1985).

All full, updated list of references for the positions, identifications, finding charts and redshifts of the sources in the following 3 samples will be provided by Peacock, Prestage and Wall (in preparation).

Table A.2 : The 0.5-Jy Sample

(1)	(2)	(3)	(4)	(5)	(6)	(7)	(8)	(9)	(10)
IAU	Name	α (1950)	δ (1950)	$\pm$(")	$S_{2.7}$	$\alpha^5_{2.7}$	ID	V	z
0013−005		00 13 37.40	−00 31 50.4	1.7	0.80	0.34	Q	20.1	1.575
0038−020		00 38 23.80	−02 02 54.0	1.7	0.72	0.41	Q	18.5	1.176
0111+021		01 11 08.61	02 06 25.5	1.7	0.63	−0.05	G	15.9	0.047
0112−017		01 12 43.75	−01 42 53.2	1.7	0.94	−0.26	Q	18.2	1.365
0115−016	4C-1.07	01 15 42.27	−01 36 14.9	1.3	0.64	0.22	EF		1.000*
0122−003		01 22 55.17	−00 21 31.4	1.7	1.19	−0.13	Q	16.9	1.085
0213−026	4C-2.09	02 13 09.84	−02 36 49.9	0.8	0.54	−0.58	EF		1.000*
0215+015		02 15 14.06	01 30 57.9	1.7	0.73	−0.61	Q	18.8	1.649
0216+011		02 16 32.32	01 07 14.7	1.7	0.62	−0.27	Q	20.7	1.611
0226−038	4C-3.07	02 26 22.00	−03 51 00.4	1.7	0.77	0.13	Q	17.4	2.064
0237−027		02 37 13.88	−02 47 36.2	1.7	0.68	−0.87	Q	20.1	1.116
0421+019		04 21 32.74	01 57 31.6	1.7	0.83	0.21	Q	16.6	2.048
0422+004		04 22 12.61	00 29 17.1	1.7	1.28	−0.36	Q	16.3	0.354*
0440−003		04 40 05.27	−00 23 20.0	1.7	1.85	0.45	Q	18.7	0.850
0458−020	4C-2.19	04 58 41.48	−02 03 32.4	1.7	1.89	−0.24	Q	19.2	2.286
0823+033		08 23 13.41	03 19 16.7	1.7	1.03	0.15	Q?	17.5	0.668*
0837+035		08 37 12.39	03 30 32.7	1.7	0.69	0.28	Q?	20.5	3.273*
0906+015	4C1.24	09 06 35.16	01 33 48.0	1.7	0.97	−0.35	Q	17.6	1.018
0907−023		09 07 13.11	−02 19 16.8	1.7	0.52	0.43	Q	18.8	0.957
0922+005		09 22 33.67	00 32 12.4	1.7	0.82	0.26	Q	18.2	1.720
1004−018		10 04 31.75	−01 52 33.4	1.7	0.59	0.17	Q	19.5	1.212
1008−017	4C-1.21	10 08 18.20	−01 46 42.0	7.0	0.95	0.41	G?	20.0	0.631*
1103−006	4C-1.24	11 03 58.16	−00 36 39.0	1.7	0.59	0.48	Q	15.7	0.427
1217+023		12 17 38.35	02 20 20.9	1.7	0.51	0.24	Q	15.7	0.240
1218−024	4C-2.53	12 18 51.00	−02 25 12.0	1.7	0.57	0.42	Q	19.0	0.668
1222+037	4C3.23	12 22 19.16	03 47 27.1	1.7	1.08	0.09	Q	19.0	0.957
1229−021	4C-2.54	12 29 25.88	−02 07 31.9	1.7	1.19	0.45	Q	17.2	1.041
1302−034		13 02 08.77	−03 29 59.0	1.7	0.60	0.17	Q	19.8	1.250
1317+019		13 17 53.80	01 56 19.0	1.7	0.59	0.00	G?	20.4	0.603*
1351−018		13 51 32.00	−01 51 20.1	1.7	0.80	−0.04	Q	20.1	3.709
1356+022		13 56 54.60	02 14 26.3	1.7	0.75	0.16	Q	18.5	1.329
1402−012		14 02 11.37	−01 15 58.7	1.7	0.73	0.32	Q	18.8	2.518
2012−017		20 12 39.73	−01 46 45.6	1.7	0.78	0.35	Q	17.2	0.570*
2047+039		20 47 35.90	03 56 36.7	1.7	0.57	−0.16	Q	19.5	1.928*
2059+034		20 59 08.04	03 29 42.9	1.7	0.50	0.14	Q	17.5	1.013
2215+020		22 15 15.56	02 05 08.8	0.6	0.65	0.05	G?	21.5	0.871*
2224+006	4C0.81	22 24 13.08	00 36 53.5	0.6	0.52	0.10	G?	21.8	1.148*
2245+029		22 45 25.99	02 54 55.6	1.7	0.73	0.29	Q?	20.1	2.649*
2320−035		23 20 57.54	−03 33 33.5	1.7	0.89	0.17	Q	18.9	1.410
2332−017		23 32 46.20	−01 47 43.8	1.7	0.56	−0.03	Q	18.8	1.185
2335−027		23 35 23.19	−02 47 35.2	1.7	0.63	0.11	Q	19.0	1.072

Table A.3 : The 1.5-Jy Sample

(1)	(2)	(3)	(4)	(5)	(6)	(7)	(8)	(9)	(10)
IAU	Name	α (1950)	δ (1950)	$\pm$(")	$S_{2.7}$	$\alpha^5_{2.7}$	ID	V	z
0013+79	3C6.1	00 13 34.40	79 00 10.0	0.4	1.87	0.93	G	22.0	0.840
0016+73	S5	00 16 54.20	73 10 51.4	0.2	1.52	−0.15	Q	19.5	1.788
0026+34	OB343	00 26 34.81	34 39 57.8	0.4	1.53	0.28	G	20.4	0.603*
0038+32	3C19	00 38 13.83	32 53 41.2	0.6	1.90	0.65	G	20.5	0.482
0040+51	3C20	00 40 19.70	51 47 07.2	1.1	6.50	0.70	G	19.0	0.174
0104+32	3C31	01 04 39.17	32 08 44.3	0.6	3.53	0.82	G	12.1	0.017
0106+72	3C33.1	01 06 03.00	72 55 50.0	8.0	1.75	1.13	G	19.5	0.181
0106+13	3C33	01 06 14.54	13 04 14.6	0.5	8.01	0.73	G	15.2	0.060
0116+31	4C31.04	01 16 47.24	31 55 05.8	0.1	2.11	0.58	G	14.5	0.059
0123+32	3C41	01 23 54.86	32 57 35.6	0.4	2.25	0.69	G	22.0	0.794
0125+28	3C42	01 25 42.89	28 47 29.3	1.8	1.61	1.03	G	20.0	0.395
0127+23	3C43	01 27 15.08	23 22 52.7	0.4	1.70	0.70	Q	20.0	1.470
0133+20	3C47	01 33 40.42	20 42 10.6	0.5	2.08	1.02	Q	18.1	0.425
0133+47	OC457	01 33 55.13	47 36 13.0	0.3	2.21	−0.64	Q	18.0	0.860
0134+32	3C48	01 34 49.83	32 54 20.5	0.1	9.07	0.83	Q	16.2	0.367
0138+13	3C49	01 38 28.46	13 38 20.1	0.4	1.53	0.77	G	21.0	0.621
0153+74	S5	01 53 04.31	74 28 05.6	0.2	1.88	0.34	Q	18.0	2.339
0202+14	4C15.05	02 02 07.40	14 59 51.3	0.9	3.03	0.45	G?	22.1	1.318*
0210+86	3C61.1	02 10 40.00	86 05 20.0	8.0	3.76	1.08	G	19.0	0.186
0212+73	S5	02 12 49.93	73 35 40.1	0.2	2.39	0.11	Q	19.5	2.370
0220+42	3C66B	02 20 01.73	42 45 54.6	0.5	5.23	0.97	G	12.9	0.022
0220+39	3C65	02 20 36.80	39 47 20.0	1.0	1.61	1.17	G	23.5	1.176
0221+27	3C67	02 21 18.06	27 36 38.2	0.4	1.70	0.99	G	18.0	0.310
0223+34	4C34.07	02 23 09.72	34 08 01.3	0.4	1.80	0.53	Q?	20.5	3.273*
0235+16	OD160	02 35 52.62	16 24 04.0	0.2	1.94	−0.61	Q	17.0	0.851
0300+16	3C76.1	03 00 27.50	16 14 30.0	5.0	1.96	0.64	G	14.9	0.032
0307+16	3C79	03 07 11.35	16 54 36.8	1.0	2.48	1.01	G	18.6	0.256
0314+41	3C83.1B	03 14 56.79	41 40 32.6	0.3	4.65	0.51	G	12.5	0.026
0316+16	4C16.09	03 16 09.21	16 17 41.1	0.4	5.01	0.89	G?	22.0	1.259*
0316+41	3C84	03 16 29.57	41 19 51.9	0.1	9.63	−1.09	G	11.9	0.017
0319+12	OE131	03 19 08.21	12 10 31.7	1.1	1.60	0.59	G?	19.0	2.670
0356+10	3C98	03 56 09.90	10 16 58.7	1.0	7.09	0.56	G	14.5	0.031
0400+25	OF200	04 00 03.60	25 51 46.7	0.5	1.80	−0.01	Q	18.8	2.109
0404+76	4C76.03	04 04 00.13	76 48 52.5	0.2	4.04	0.58	G	21.2	0.871*
0407+74	4C74.08	04 07 06.00	74 43 24.0	5.0	1.69	0.90	G?	20.5	0.631*
0410+11	3C109	04 10 54.85	11 04 39.5	0.5	2.46	0.64	G	17.8	0.306
0411+14	4C14.11	04 11 40.94	14 08 48.3	5.0	1.50	0.83	G	19.3	0.207
0428+20	OF247	04 28 06.86	20 31 09.2	0.1	3.19	0.50	G?	20.0	0.219
0433+29	3C123	04 33 55.19	29 34 12.7	0.3	27.54	0.83	G	19.9	0.218
0453+22	3C132	04 53 42.72	22 44 49.0	2.4	1.96	0.99	G	18.5	0.214
0518+16	3C138	05 18 16.53	16 35 26.8	0.1	6.06	0.59	Q	18.8	0.759
0528+13	OG147	05 28 06.72	13 29 42.2	1.0	2.96	−0.44	Q?	19.5	2.060
0538+49	3C147	05 38 43.51	49 49 42.8	0.1	13.12	0.75	Q	17.8	0.545
0605+48	3C153	06 05 44.46	48 04 49.0	0.4	2.33	0.86	G	18.5	0.277
0651+54	3C171	06 51 11.05	54 12 50.4	0.4	2.02	0.80	G	18.8	0.238
0703+42	4C42.23	07 03 12.39	42 35 17.0	0.4	1.69	0.85	G	14.4	0.038*
0710+43	OI417	07 10 03.33	43 54 26.2	0.3	1.93	0.23	G	19.9	0.517
0711+35	OI318	07 11 05.62	35 39 52.6	0.4	1.85	0.31	Q	19.0	1.260
0723+67	3C179	07 23 04.29	67 54 52.7	0.4	1.60	0.30	Q	18.0	0.846
0734+80	3C184.1	07 34 25.10	80 33 24.6	0.3	1.90	0.67	G	17.0	0.118

Table A3 continued

(1)	(2)	(3)	(4)	(5)	(6)	(7)	(8)	(9)	(10)
IAU	Name	α (1950)	δ (1950)	$\pm$(")	$S_{2.7}$	$\alpha^5_{2.7}$	ID	V	z
0735+17	OI158	07 35 14.12	17 49 09.0	0.2	1.93	−0.05	Q	15.5	0.424
0738+31	OI363	07 38 00.18	31 19 02.0	0.1	1.96	−0.40	Q	17.0	0.630
0742+10	OI471	07 42 48.45	10 18 32.4	0.1	3.74	−0.06	EF		2.000*
0744+55	DA240	07 44 34.82	55 56 28.3	0.6	2.84	0.78	G	14.2	0.036
0748+12	OI280	07 48 05.07	12 38 45.0	1.0	1.69	−0.45	Q	18.8	0.880
0755+37	4C37.21	07 55 09.08	37 55 20.6	0.5	1.79	0.55	G	14.9	0.043
0802+24	3C192	08 02 34.50	24 18 30.0	5.0	3.20	0.70	G	15.5	0.060
0804+49	OJ508	08 04 58.40	49 59 23.0	0.3	1.55	−0.49	Q?	19.0	1.433
0809+48	3C196	08 09 59.42	48 22 07.2	0.4	7.75	0.91	Q	17.6	0.871
0814+42	OJ425	08 14 51.67	42 32 07.7	0.1	2.23	0.44	Q	16.9	0.486*
0831+55	4C55.16	08 31 04.37	55 44 41.4	0.1	7.53	0.46	G	17.5	0.242
0836+71	4C71.07	08 36 21.57	71 04 22.5	0.2	3.14	0.31	Q?	16.5	2.190
0838+13	3C207	08 38 01.84	13 23 06.1	0.4	1.80	0.34	Q	18.2	0.684
0851+20	OJ287	08 51 57.25	20 17 58.6	0.1	3.42	0.42	Q	14.0	0.306
0859+47	4C47.29	08 59 39.97	47 02 56.9	0.3	1.89	0.08	Q	18.7	1.462
0906+43	3C216	09 06 17.25	43 05 59.4	0.4	2.42	0.45	Q	18.5	0.668
0917+45	3C219	09 17 50.67	45 51 36.8	0.1	4.40	1.04	G	17.2	0.174
0923+39	4C39.25	09 23 55.31	39 15 23.6	0.1	4.59	−0.83	Q	17.9	0.699
0936+36	3C223	09 36 50.86	36 07 34.7	0.7	2.08	0.76	G	17.1	0.137
0939+14	3C225B	09 39 32.20	13 59 33.0	2.0	1.52	0.96	G	19.0	0.580
0945+73		09 45 10.30	73 28 22.8	0.5	1.70	0.80	G	14.7	0.058
0945+66	4C66.09	09 45 14.84	66 28 58.2	0.2	1.64	0.46	G	21.8	1.148*
0947+14	3C228	09 47 27.65	14 34 00.0	3.0	2.00	0.89	G	20.5	0.550
0951+69	3C231	09 51 41.95	69 54 57.5	0.1	5.65	0.57	G	8.4	.0014
0954+55	4C55.17	09 54 14.34	55 37 16.4	0.2	2.63	0.22	Q	17.7	0.909
0958+29	3C234	09 58 57.38	29 01 37.4	0.2	2.95	1.04	G	17.3	0.185
1003+35	3C236	10 03 05.39	35 08 48.0	0.2	2.03	0.66	G	16.0	0.099
1030+58	3C244.1	10 30 19.50	58 30 06.0	4.0	1.97	0.90	G	19.0	0.428
1031+56	OL553	10 31 56.00	56 44 18.1	0.5	1.60	0.30	Q?	19.5	0.459
1040+12	3C245	10 40 06.00	12 19 15.1	0.4	2.11	0.66	Q	17.3	1.029
1055+20	4C20.24	10 55 37.55	20 07 54.8	1.0	1.90	0.85	Q	17.1	1.110
1056+43	3C247	10 56 08.08	43 17 27.8	2.0	1.65	0.87	G	20.0	0.749
1116+12	4C12.39	11 16 20.81	12 51 06.8	0.4	1.83	0.16	Q	19.3	2.118
1137+66	3C263	11 37 09.30	66 04 27.1	0.2	1.75	0.82	Q	16.3	0.656
1140+22	3C263.1	11 40 49.16	22 23 34.8	0.4	1.61	1.15	G	20.0	0.824
1142+19	3C264	11 42 29.58	19 53 02.7	0.4	3.27	0.78	G	12.7	0.020
1150+49	4C49.22	11 50 47.98	49 47 50.1	0.1	1.58	0.55	Q	16.1	0.334
1153+31	4C31.38	11 53 44.09	31 44 45.7	0.9	1.70	0.92	Q	19.0	1.557
1157+73	3C268.1	11 57 48.00	73 17 27.0	1.0	4.04	0.68	EF		0.970
1203+64	3C268.3	12 03 54.08	64 30 18.5	0.1	2.00	0.97	G	20.0	0.371
1218+33	3C270.1	12 18 03.90	33 59 48.2	0.5	1.51	0.87	Q	18.6	1.519
1222+13	3C272.1	12 22 31.58	13 09 50.7	1.5	3.95	0.51	G	9.4	.0028
1225+36	ON343	12 25 30.78	36 51 46.9	0.3	1.60	1.17	G?	21.9	1.202*
1228+12	3C274	12 28 17.56	12 40 12.0	0.3	119.6	0.80	G	8.7	.0038
1241+16	3C275.1	12 41 27.54	16 39 17.2	1.6	1.58	0.87	Q	19.0	0.557
1250+56	3C277.1	12 50 15.19	56 50 37.0	0.5	1.55	0.61	Q	17.9	0.321
1251+27	3C277.3	12 51 46.02	27 53 47.5	2.5	1.95	0.72	G	15.9	0.086
1254+47	3C280	12 54 41.05	47 36 32.1	0.3	2.86	1.00	G	20.0	0.996
1323+32	4C32.44	13 23 57.96	32 09 43.8	1.5	3.35	0.58	G?	19.0	0.362
1328+30	3C286	13 28 49.65	30 45 58.7	0.1	10.37	0.51	Q	17.3	0.846

Table A3 continued

(1)	(2)	(3)	(4)	(5)	(6)	(7)	(8)	(9)	(10)
IAU	Name	α (1950)	δ (1950)	$\pm$(")	$S_{2.7}$	$\alpha^5_{2.7}$	ID	V	z
1328+25	3C287	13 28 15.92	25 24 37.6	0.1	4.65	0.56	Q	17.7	1.055
1336+39	3C288	13 36 38.36	39 06 22.3	1.5	1.78	0.93	G	18.3	0.246
1345+12	4C12.50	13 45 06.17	12 32 21.3	1.1	3.75	0.51	G	17.0	0.122
1350+31	3C293	13 50 03.23	31 41 32.6	0.4	2.92	0.70	G	14.3	0.045
1354+19	4C19.44	13 54 42.06	19 33 43.8	1.0	1.70	0.12	Q	16.0	0.720
1358+62	4C62.22	13 58 58.32	62 25 06.7	0.2	2.69	0.66	G	20.1	0.429
1404+28	OQ208	14 04 45.62	28 41 29.3	0.1	1.81	−0.78	G	14.0	0.077
1409+52	3C295	14 09 33.50	52 26 13.0	0.4	11.96	0.96	G	20.1	0.461
1413+34	OQ323	14 13 56.27	34 58 29.5	0.4	1.72	0.60	EF		2.000*
1414+11	3C296	14 14 26.36	11 02 18.6	1.2	2.73	0.74	G	12.2	0.024
1419+41	3C299	14 19 06.41	41 58 30.0	0.4	1.61	0.92	G	19.4	0.367
1420+19	3C300	14 20 39.93	19 49 13.3	0.6	1.94	0.90	G	18.0	0.270
1441+52	3C303	14 41 23.60	52 14 19.2	1.6	1.57	0.81	G	17.3	0.141
1442+10	OQ172	14 42 50.48	10 11 11.9	0.2	1.77	0.68	Q	17.6	3.530
1448+63	3C305	14 48 17.16	63 28 37.0	1.7	1.66	0.94	G	13.7	0.042
1458+71	3C309.1	14 58 56.64	71 52 11.2	0.1	5.36	0.56	Q	16.8	0.904
1502+26	3C310	15 02 46.88	26 12 35.4	0.7	3.13	1.43	G	15.3	0.054
1502+10	4C10.39	15 02 00.15	10 41 17.6	0.2	1.74	−0.63	Q	19.5	1.833
1511+26	3C315	15 11 30.81	26 18 39.4	0.4	2.39	1.00	G	16.8	0.108
1529+24	3C321	15 29 33.50	24 14 26.5	1.0	2.05	0.82	G	16.0	0.096
1538+14	4C14.60	15 38 30.21	14 57 22.4	0.9	1.98	0.01	Q?	16.4	0.373*
1549+62	3C325	15 49 14.10	62 50 21.5	1.7	1.86	1.29	G	20.0	0.860
1557+70	4C70.19	15 57 41.24	70 49 50.7	0.4	1.78	0.88	G	14.0	0.032*
1600+33	0S300	16 00 11.94	33 35 09.6	0.5	2.25	0.63	EF		2.000*
1607+26	OS111	16 07 09.27	26 49 18.6	0.5	2.92	0.89	G?	21.0	0.794*
1609+66	3C330	16 09 16.16	66 04 30.0	0.2	3.80	0.76	G	20.3	0.549
1611+34	OS319	16 11 47.91	34 20 19.8	0.1	2.45	−0.16	Q	17.5	1.401
1624+41	4C41.32	16 24 18.22	41 41 23.4	0.3	1.60	0.30	G?	23.0	2.550
1627+44	3C337	16 27 19.73	44 25 37.4	1.5	1.59	0.88	G	20.0	0.635
1633+38	4C38.41	16 33 30.63	38 14 09.9	0.3	2.53	−0.79	Q	18.0	1.814
1634+62	3C343	16 34 01.06	62 51 41.8	0.1	2.71	0.95	Q	20.6	0.988
1637+62	3C343.1	16 37 55.29	62 40 34.2	0.1	2.25	1.00	G	20.7	0.750
1637+82	NGC6251	16 37 56.95	82 38 18.5	0.1	2.17	0.70	G	13.0	0.024
1641+17	3C346	16 41 34.55	17 21 20.6	0.5	2.36	0.58	G	17.0	0.161
1641+39	3C345	16 41 17.60	39 54 10.8	0.1	6.08	0.10	Q	16.0	0.594
1658+47	3C349	16 58 05.74	47 07 09.1	4.0	1.90	0.81	G	19.0	0.205
1704+60	3C351	17 04 03.55	60 48 31.2	0.2	2.05	0.84	Q	15.3	0.371
1726+31	3C357	17 26 27.83	31 48 17.9	5.0	1.82	0.95	G	15.5	0.167
1739+52	4C51.37	17 39 29.00	52 13 10.3	0.3	1.95	−0.05	Q	18.5	1.375
1749+70	S4	17 49 03.41	70 06 39.6	0.2	1.91	0.89	Q	17.0	0.760
1803+78	S5	18 03 39.15	78 27 54.3	0.2	2.36	−0.20	Q	13.8	0.690
1807+69	3C371	18 07 18.54	69 48 57.1	0.1	1.94	0.16	G	14.8	0.050
1819+39	4C39.56	18 19 42.33	39 41 15.0	0.3	1.80	0.98	G?	19.5	0.398*
1823+56	4C56.27	18 23 14.93	56 49 18.1	0.3	1.53	−0.16	Q	18.9	0.660
1828+48	3C380	18 28 13.54	48 42 40.5	0.4	9.99	0.45	Q	16.8	0.691
1829+29	4C29.56	18 29 17.93	29 04 58.3	2.4	1.91	0.80	G?	20.0	0.501*
1832+47	3C381	18 32 24.38	47 24 34.9	0.3	2.33	0.94	G	17.2	0.160
1842+45	3C388	18 42 35.45	45 30 21.6	0.2	3.14	0.91	G	15.3	0.090
1845+79	3C390.3	18 45 37.57	79 43 06.4	0.1	6.63	0.62	G	14.5	0.056
1928+73	4C73.18	19 28 49.33	73 51 44.9	0.2	3.42	0.02	Q	15.5	0.360

Table A3 continued

(1)	(2)	(3)	(4)	(5)	(6)	(7)	(8)	(9)	(10)
IAU	Name	α (1950)	δ (1950)	$\pm$(")	$S_{2.7}$	$\alpha^5_{2.7}$	ID	V	z
1939+60	3C401	19 39 38.84	60 34 32.6	0.5	2.79	1.13	G	18.0	0.201
1954+51	OV591	19 54 22.46	51 23 46.3	0.3	1.59	0.15	Q	18.5	1.230
2021+61	OW637	20 21 13.31	61 27 18.1	0.1	2.19	−0.10	G	19.5	0.227
2104+76	3C427.1	21 04 45.00	76 21 10.0	5.0	1.91	1.10	G	21.0	0.572
2121+24	3C433	21 21 30.69	24 51 22.7	1.3	6.56	0.89	G	16.2	0.102
2141+27	3C436	21 41 58.34	27 56 32.2	4.3	1.84	0.99	G	18.2	0.215
2145+15	3C437	21 45 01.25	15 06 42.1	9.0	1.53	0.87	G	22.0	1.480
2153+37	3C438	21 53 45.49	37 46 12.9	0.6	3.26	1.19	G	19.2	0.290
2200+42	OY401	22 00 39.36	42 02 08.6	0.1	5.21	0.13	Q	14.5	0.068
2203+29	3C441	22 03 49.54	29 14 45.6	2.5	1.53	0.80	G	22.0	0.707
2229+39	3C449	22 29 07.60	39 06 03.4	0.6	2.50	0.93	G	13.2	0.017
2230+11	4C11.69	22 30 07.79	11 28 22.4	0.1	4.98	0.50	Q	17.5	1.037
2243+39	3C452	22 43 32.81	39 25 27.6	0.2	5.94	0.95	G	16.0	0.081
2247+14	4C14.82	22 47 56.72	14 03 57.2	0.9	1.53	0.62	Q	17.0	0.237
2251+15	3C454.3	22 51 29.51	15 52 54.2	0.1	10.82	−0.99	Q	16.1	0.860
2252+12	3C455	22 52 34.48	12 57 33.3	0.4	1.50	0.75	Q	19.7	0.543
2324+40	3C462	23 24 30.59	40 31 39.2	5.0	1.53	0.48	G?	20.5	0.631*
2335+26	3C465	23 35 58.95	26 45 16.4	0.1	4.26	0.66	G	13.3	0.029
2342+82	S5	23 42 06.50	82 10 01.3	0.2	2.33	0.92	EF		0.735
2351+45	4C45.51	23 51 49.96	45 36 22.9	0.3	1.50	0.08	G?	20.6	2.000
2352+49	OZ488	23 52 37.78	49 33 26.8	0.1	2.20	0.34	G	19.0	0.237

Table A.4 : The 2-Jy Sample

(1)	(2)	(3)	(4)	(5)	(6)	(7)	(8)	(9)	(10)
IAU	Name	α (1950)	δ (1950)	$\pm$(")	$S_{2.7}$	$\alpha^5_{2.7}$	ID	V	z
0003−00	3C2	00 03 48.84	−00 21 06.0	0.4	2.40	0.86	Q	19.4	1.037
0008−42		00 08 21.30	−42 09 50.6	0.1	2.47	1.03	EF		1.600*
0022−42		00 22 15.42	−42 18 40.7	0.1	2.84	0.77	G?	20.6	0.661*
0023−26	OB-238	00 23 18.91	−26 18 49.3	0.1	5.80	0.70	G	19.5	0.398*
0034−01	3C15	00 34 30.56	−01 25 37.8	0.4	2.56	0.79	G	15.3	0.073
0035−02	3C17	00 35 47.18	−02 24 09.5	0.3	4.04	0.72	G	18.0	0.220
0038+09	3C18	00 38 14.57	09 46 56.1	4.1	3.00	1.00	G	18.5	0.188
0039−44		00 39 46.86	−44 30 28.6	2.4	2.08	0.93	G	18.5	0.251*
0040+51	3C20	00 40 19.99	51 47 08.1	5.0	6.51	0.72	G	19.0	0.350
0043−42		00 43 54.50	−42 24 01.0	3.0	5.00	0.87	G	16.0	0.053
0045−25	NGC253	00 45 05.60	−25 33 37.0	3.0	3.52	0.62	G	7.0	.0010
0055−01	3C29	00 55 01.57	−01 39 39.4	0.3	3.46	0.76	G	14.1	0.045
0104+32	3C31	01 04 39.17	32 08 44.3	0.6	3.53	0.84	G	12.2	0.017
0105−16	3C32	01 05 48.78	−16 20 21.1	1.2	2.25	1.10	G	20.1	0.525*
0106+13	3C33	01 06 14.94	13 04 26.4	24.0	8.02	0.76	G	15.2	0.060
0114−21	OC-224	01 14 25.95	−21 07 55.0	0.1	2.23	0.95	EF		1.600*
0116+31	4C31.04	01 16 47.25	31 55 05.8	0.1	2.12	0.61	G	14.5	0.059
0117−15	3C38	01 17 59.84	−15 35 57.3	2.1	2.72	0.90	G?	21.0	0.794*
0123−01	3C40	01 23 27.41	−01 36 16.7	0.3	3.29	0.91	G	12.3	0.018
0123+32	3C41	01 23 54.70	32 57 38.7	2.3	2.26	0.71	G	22.0	0.794
0131−36		01 31 43.54	−36 44 57.2	1.3	5.60	0.51	G	13.0	0.030
0133+20	3C47	01 33 40.42	20 42 10.6	0.5	2.00	0.88	Q	18.1	0.425
0133+47	OC457	01 33 55.11	47 36 12.8	0.1	2.22	−0.62	Q	18.0	0.860
0134+32	3C48	01 34 49.83	32 54 20.5	0.1	9.08	0.85	Q	16.2	0.367
0157−31	OC-397	01 57 58.51	−31 07 50.6	1.5	2.37	0.81	Q?	19.6	2.032*
0159−11	3C57	01 59 30.27	−11 47 00.2	1.3	2.00	0.64	Q	16.4	0.669
0202+14	4C15.05	02 02 07.40	14 59 51.0	0.1	3.00	0.43	G?	22.1	1.202*
0208−51		02 08 56.97	−51 15 07.5	0.2	3.56	0.17	Q	17.5	1.003
0210+86	3C61.1	02 10 45.20	86 05 08.2	18.0	3.77	1.31	G	19.0	0.186
0212+73		02 12 49.94	73 35 40.1	0.1	2.39	0.13	Q?	19.5	2.370
0213−13	3C62	02 13 11.61	−13 13 24.0	3.6	2.79	0.74	G	18.0	0.140
0220+42	3C66B	02 20 01.73	42 45 54.6	0.3	5.23	0.54	G	12.8	0.022
0235−19	OD-159	02 35 24.90	−19 45 29.3	1.2	2.41	0.87	G?	20.3	0.575*
0237−23	OD-263	02 37 52.79	−23 22 06.3	0.1	4.90	0.64	Q	16.6	2.223
0240−00	NGC1068	02 40 07.09	−00 13 30.7	0.6	3.13	0.78	G	9.0	.0041
0252−71		02 52 26.50	−71 16 43.0	4.0	3.10	1.14	G	18.0	0.200*
0255+05	3C75	02 55 05.10	05 50 44.0	8.0	3.30	0.86	G	13.6	0.024
0305+03	3C78	03 05 49.05	03 55 13.1	0.1	5.34	0.64	G	12.8	0.029
0307+16	3C79	03 07 11.35	16 54 36.8	1.0	2.50	0.93	G	18.5	0.256
0314+41	3C83.1B	03 14 56.79	41 40 32.6	0.3	4.92	0.54	G	13.3	0.026
0316+16	CTA21	03 16 09.14	16 17 40.4	0.1	4.77	0.79	G?	22.0	1.259*
0316+41	3C84	03 16 29.56	41 19 51.9	0.1	9.64	−2.58	G	11.9	0.017
0320−37	For A	03 20 46.80	−37 23 06.0	4.0	98.00	0.52	G	5.1	.0057
0325+02	3C88	03 25 18.90	02 23 22.0	0.4	3.18	0.79	G	14.0	0.030
0336−01	CTA26	03 36 58.95	−01 56 16.9	0.1	2.02	−0.21	Q	18.4	0.852
0347+05	4C05.16	03 47 06.97	05 42 35.2	2.6	2.00	0.78	G?	20.9	0.759*
0349−27	OE-283	03 49 36.90	−27 52 50.0	30.0	2.89	0.59	G	15.8	0.066
0356+10	3C98	03 56 10.49	10 17 16.4	25.0	5.80	0.92	G	14.4	0.031
0403−13	OF-105	04 03 14.20	−13 16 21.0	3.0	3.15	−0.05	Q	17.2	0.571
0404+76	4C76.03	04 04 00.13	76 48 52.5	0.2	4.05	0.60	G	22.2	1.380*

Table A4 continued

(1)	(2)	(3)	(4)	(5)	(6)	(7)	(8)	(9)	(10)
IAU	Name	α (1950)	δ (1950)	$\pm$(")	$S_{2.7}$	$\alpha^5_{2.7}$	ID	V	z
0404+03	3C105	04 04 48.07	03 32 49.7	0.6	3.54	0.64	G	18.5	0.089
0405−12	OF-109	04 05 27.45	−12 19 32.4	0.7	2.35	0.42	Q	17.1	0.574
0407−65		04 07 58.09	−65 52 49.2	1.3	6.50	1.11	Q?	18.0	0.871*
0409−75		04 09 58.94	−75 14 57.1	2.0	7.23	0.86	G?	21.5	1.000*
0410+11	3C109	04 10 54.85	11 04 39.5	0.5	2.50	0.56	G	17.9	0.306
0420−01		04 20 43.54	−01 27 28.8	0.1	2.15	0.01	Q	17.8	0.915
0428−53		04 28 00.00	−53 56 00.0	20.0	3.84	0.20	G	13.2	0.039
0428+20	OF247	04 28 06.86	20 31 09.1	0.1	3.18	0.53	G	20.0	0.219
0430+05	3C120	04 30 31.60	05 14 59.5	0.1	3.00	−1.71	G	14.1	0.033
0433+29	3C123	04 33 55.30	29 34 18.8	2.0	27.57	0.86	G	19.9	0.218
0438−43		04 38 43.18	−43 38 53.1	0.1	6.20	−0.20	Q	18.8	2.852
0440−00	OF-67	04 40 05.29	−00 23 20.6	0.1	3.73	0.28	Q	18.5	0.844
0442−28	OF-271	04 42 37.40	−28 15 18.0	7.0	3.84	0.93	G	17.4	0.151*
0451−28	OF-285	04 51 15.13	−28 12 29.3	0.1	2.38	−0.08	Q	18.5	2.564
0453−20	OF-289	04 53 14.13	−20 38 56.4	2.0	2.79	0.73	G	13.0	0.035
0453+22	3C132	04 53 42.05	22 44 43.4	1.0	2.10	1.01	G	19.0	0.214
0454−46		04 54 24.19	−46 20 38.5	0.2	2.36	0.24	Q	18.0	0.858
0500+01	OG3	05 00 45.18	01 58 53.8	0.1	2.47	0.47	G?	21.4	0.995*
0518+16	3C138	05 18 16.53	16 35 26.9	0.1	7.10	0.92	Q	17.9	0.759
0518−45	Pic A	05 18 23.00	−45 49 44.0	6.0	29.00	1.07	G	16.0	0.035
0521−36		05 21 12.90	−36 30 16.5	1.1	12.50	0.49	G	16.8	0.062
0528+13	OG147	05 28 06.76	13 29 42.2	0.1	2.97	−0.43	Q?	19.5	2.060
0537−44		05 37 21.00	−44 06 46.8	0.1	3.84	0.02	Q	15.5	0.894
0538+49	3C147	05 38 43.51	49 49 42.8	0.1	13.14	0.77	Q	16.9	0.545
0605−08	OH-10	06 05 36.03	−08 34 20.3	0.1	2.70	−0.37	Q?	18.0	0.871*
0605+48	3C153	06 05 44.46	48 04 49.0	0.4	2.33	0.89	G	18.5	0.277
0620−52		06 20 34.30	−52 39 42.0	4.0	2.10	0.87	G	14.5	0.051
0625−53		06 25 19.23	−53 39 25.5	1.6	3.70	1.17	G	13.0	0.054
0625−35	OH-342	06 25 20.80	−35 27 20.0	3.0	2.90	0.53	G	14.0	0.055
0637−75		06 37 23.42	−75 13 37.4	0.2	4.51	−0.32	Q	15.8	0.651
0651+54	3C171	06 51 11.05	54 12 50.4	0.4	2.02	0.90	G	18.8	0.238
0735+17	OI158	07 35 14.13	17 49 09.3	0.1	2.00	−0.04	Q	14.9	0.424
0736+01	OI61	07 36 42.51	01 44 00.2	0.1	2.30	0.18	Q	16.5	0.191
0742+10	OI471	07 42 48.47	10 18 32.5	0.1	3.74	0.08	EF		2.000*
0743−67		07 43 22.19	−67 19 09.1	0.3	2.74	0.97	Q	16.4	0.395
0744+55	DA240	07 44 34.82	55 56 28.3	0.6	2.84	0.78	G	14.2	0.036
0802+24	3C192	08 02 32.31	24 18 54.9	10.0	3.30	0.71	G	15.5	0.060
0806−10	3C195	08 06 29.90	−10 19 09.7	1.4	2.49	0.72	G	17.8	0.182*
0809+48	3C196	08 09 59.42	48 22 07.2	0.4	7.75	0.94	Q	17.6	0.871
0814+42	OJ425	08 14 51.67	42 32 07.7	0.1	2.24	0.47	Q	16.9	0.486*
0825−20	OJ-242	08 25 03.49	−20 16 25.9	1.0	2.10	0.94	Q	18.0	0.871*
0831+55	4C55.16	08 31 04.38	55 44 41.4	0.1	7.54	0.48	G	17.5	0.242
0834−20	OJ-257.5	08 34 24.60	−20 06 30.4	0.1	4.15	0.31	Q	19.0	2.752
0834−19	OJ-158.1	08 34 56.15	−19 41 25.4	0.4	2.50	0.82	G?	20.7	0.692*
0836+71	4C71.07	08 36 21.56	71 04 22.5	0.1	3.15	0.33	Q?	16.5	2.190
0842−75		08 42 10.73	−75 29 36.3	1.6	2.15	0.72	Q	18.9	0.524
0851+20	OJ287	08 51 57.25	20 17 58.4	0.1	3.42	0.44	Q	14.0	0.306
0858−27	OJ-297	08 58 31.70	−27 56 33.0	4.0	2.00	0.60	Q?	16.2	0.336*
0859−25	OJ-299	08 59 36.63	−25 43 38.8	1.7	3.30	1.08	G	21.0	0.794*
0859−14	OJ-199	08 59 54.94	−14 03 38.9	0.1	2.93	0.40	Q	16.6	1.327

Table A4 continued

(1)	(2)	(3)	(4)	(5)	(6)	(7)	(8)	(9)	(10)
IAU	Name	α (1950)	δ (1950)	$\pm$(")	$S_{2.7}$	$\alpha^5_{2.7}$	ID	V	z
0906+43	3C216	09 06 17.25	43 05 59.4	0.4	2.42	0.50	Q	18.5	0.668
0915−11	Hyd A	09 15 41.50	−11 53 06.0	7.0	23.50	0.90	G	14.8	0.052
0917+45	3C219	09 17 50.70	45 51 44.2	0.1	4.40	1.06	G	17.3	0.174
0923+39	4C39.25	09 23 55.32	39 15 23.5	0.1	4.60	−1.07	Q	17.9	0.699
0936+36	3C223	09 36 50.86	36 07 34.7	0.7	2.09	0.78	G	17.1	0.137
0945+07	3C227	09 45 07.80	07 39 09.0	5.0	4.30	0.82	G	16.3	0.086
0951+69	M82	09 51 41.95	69 54 57.5	0.1	5.66	0.59	G	8.4	.0014
0954+55	4C55.17	09 54 14.36	55 37 16.4	0.1	2.63	0.24	Q	17.7	0.909
0958+29	3C234	09 58 57.38	29 01 37.4	0.2	2.96	1.06	G	17.1	0.185
1003+35	3C236	10 03 05.39	35 08 48.0	0.2	2.03	0.70	G	16.0	0.099
1005+07	3C237	10 05 22.02	07 44 58.6	0.4	3.50	0.97	G?	21.3	0.912*
1015−31	OL-327	10 15 53.39	−31 29 11.3	0.1	2.22	0.84	G?	20.2	0.550*
1017−42		10 17 56.23	−42 36 21.9	1.3	2.33	1.08	Q	19.0	1.280
1040+12	3C245	10 40 06.00	12 19 15.1	0.4	2.00	0.57	Q	17.3	1.029
1055+01	4C01.28	10 55 55.32	01 50 03.5	0.1	3.02	−0.03	Q	17.7	0.888
1127−14	OM-146	11 27 35.67	−14 32 54.4	0.1	6.50	−0.18	Q	16.9	1.187
1136−13	OM-161	11 36 38.51	−13 34 05.4	1.1	2.80	0.65	Q	17.8	0.554
1142+19	3C264	11 42 29.58	19 53 02.7	0.4	3.27	0.53	G	12.8	0.021
1148−00	4C-00.47	11 48 10.13	−00 07 13.3	0.1	2.58	0.45	Q	17.6	1.982
1151−34	OM-386	11 51 49.44	−34 48 47.2	0.1	4.18	0.69	Q	17.5	0.258
1157+73	3C268.1	11 57 49.30	73 17 26.5	4.0	4.05	0.70	G	22.0	0.970*
1203+64	3C268.3	12 03 54.08	64 30 18.5	0.1	2.00	0.88	G	19.0	0.371
1216+06	3C270	12 16 51.20	06 06 13.0	6.0	12.80	0.56	G	10.4	.0069
1222+13	M84	12 22 31.58	13 09 50.7	1.5	4.30	0.74	G	8.7	.0028
1226+02	3C273	12 26 33.25	02 19 43.3	0.1	38.90	−0.05	Q	12.8	0.158
1228+12	Vir A	12 28 17.56	12 40 02.0	0.3	120.00	0.93	G	8.7	.0038
1245−19	ON-176.2	12 45 45.22	−19 42 57.5	0.1	3.94	0.76	G?	19.5	0.398*
1246−41	NGC4696	12 46 03.27	−41 02 21.4	1.7	2.21	0.82	G	11.2	.0090
1251−12	3C278	12 51 59.60	−12 17 08.0	6.0	4.50	0.93	G	13.5	0.015
1253−05	3C279	12 53 35.84	−05 31 08.0	0.1	11.20	−0.59	Q	17.8	0.538
1254+47	3C280	12 54 41.36	47 36 32.1	1.3	2.86	1.02	G	22.0	0.996
1306−09	OP-10	13 06 02.20	−09 34 33.0	3.0	2.80	0.65	G?	20.5	0.631*
1308−22	3C283	13 08 57.40	−22 00 46.7	0.4	2.43	1.30	G?	21.5	1.000*
1318−43	NGC5090	13 18 14.00	−43 26 57.0	30.0	3.09	0.96	G	14.5	0.011
1322−42	Cen A	13 22 32.23	−42 45 25.0	40.0	128.00	1.20	G	7.0	.0008
1323+32	4C32.44	13 23 57.92	32 09 43.0	0.1	3.35	0.60	G?	19.0	0.362
1328+25	3C287	13 28 15.93	25 24 37.4	0.1	4.60	0.65	Q	17.7	1.055
1328+30	3C286	13 28 49.66	30 45 58.6	0.1	10.38	0.53	Q	17.3	0.849
1333−33	IC4296	13 33 47.18	−33 42 39.8	0.9	10.06	0.79	G	11.1	0.013
1345+12	4C12.50	13 45 06.17	12 32 20.3	0.1	3.80	0.44	G	17.0	0.122
1350+31	3C293	13 50 03.23	31 41 32.6	0.4	2.93	0.73	G	14.4	0.045
1355−41		13 55 56.83	−41 38 16.7	1.5	2.49	0.93	Q	16.0	0.313
1358+62	4C62.22	13 58 58.36	62 25 06.7	0.1	2.69	0.68	G	20.2	0.429
1409+52	3C295	14 09 33.50	52 26 13.0	0.4	11.94	0.99	G	20.1	0.461
1414+11	3C296	14 14 26.36	11 02 18.6	1.2	2.73	0.76	G	12.2	0.024
1416+06	3C298	14 16 38.77	06 42 20.9	0.4	2.70	0.93	Q	16.8	1.439
1424−41		14 24 46.73	−41 52 54.4	1.0	2.63	0.35	Q	17.5	1.522
1453−10	OQ-190	14 53 12.32	−10 56 51.0	1.5	2.50	0.93	Q	17.4	0.940
1458+71	3C309.1	14 58 56.64	71 52 11.2	0.1	5.36	0.77	Q	16.8	0.904
1502+26	3C310	15 02 46.88	26 12 35.4	0.7	3.10	1.46	G	15.3	0.054

Table A4 continued

(1)	(2)	(3)	(4)	(5)	(6)	(7)	(8)	(9)	(10)
IAU	Name	α (1950)	δ (1950)	$\pm$(")	$S_{2.7}$	$\alpha^5_{2.7}$	ID	V	z
1504−16	OR-107	15 04 16.42	−16 40 59.3	0.1	2.30	0.26	Q	18.5	0.876
1508−05	4C-05.64	15 08 14.98	−05 31 49.0	0.1	2.50	0.11	Q	17.0	1.191
1510−08	OR-107	15 10 08.90	−08 54 47.6	0.1	3.00	−0.13	Q	16.3	0.361
1511+26	3C315	15 11 30.81	26 18 39.4	0.4	2.10	0.77	G	16.8	0.108
1514+07	3C317	15 14 17.08	07 12 16.2	1.9	2.20	1.40	G	13.5	0.035
1514−24	Ap Lib	15 14 45.28	−24 11 22.6	0.1	2.10	0.13	Q	15.0	0.049
1518+04	4C04.51	15 18 44.73	04 41 05.5	0.4	2.20	1.28	G?	22.8	1.820*
1529+24	3C321	15 29 33.50	24 14 26.5	1.0	2.20	1.14	G	16.0	0.096
1547−79		15 47 39.15	−79 31 42.4	2.1	2.28	0.85	G	18.0	0.200*
1549−79		15 49 28.38	−79 05 17.8	0.3	4.02	−0.18	G	18.8	0.288*
1559+02	3C327	15 59 58.60	02 06 24.0	30.0	5.04	0.95	G	15.9	0.104
1600+33	4C33.38	16 00 11.91	33 35 09.6	0.1	2.26	0.65	EF		2.000*
1602+01	3C327.1	16 02 12.96	01 25 58.7	0.3	2.14	1.07	G	20.5	0.480*
1607+26	CTD93	16 07 09.29	26 49 18.6	0.1	3.04	1.08	G?	21.0	0.794*
1609+66	3C330	16 09 13.90	66 04 22.8	6.0	3.76	0.76	G	20.3	0.549
1610−77		16 10 51.75	−77 09 52.6	0.3	3.37	−0.81	Q	19.0	1.710
1611+34	OS319	16 11 47.92	34 20 19.8	0.1	2.45	−0.14	Q	17.5	1.401
1622−25	OS-237.8	16 22 44.11	−25 20 51.5	0.1	2.27	0.19	G?	21.9	1.202*
1633+38	4C38.41	16 33 30.63	38 14 10.1	0.1	2.53	−0.78	Q	18.0	1.814
1634+62	3C343	16 34 01.08	62 51 41.6	0.1	2.71	0.96	Q	20.6	0.988
1637−77		16 37 05.50	−77 09 55.0	4.0	3.77	0.62	G	16.0	0.043
1637+62	3C343.1	16 37 55.31	62 40 34.3	0.1	2.26	1.03	G	20.7	0.750
1637+82	NGC6251	16 37 56.95	82 38 18.5	0.1	2.17	0.70	G	13.0	0.024
1641+39	3C345	16 41 17.61	39 54 10.8	0.1	6.08	−0.95	Q	16.0	0.594
1641+17	3C346	16 41 34.55	17 21 20.6	0.5	2.20	0.80	G	17.2	0.161
1648+05	Her A	16 48 40.10	05 04 28.0	5.0	24.60	1.11	G	16.9	0.154
1704+60	3C351	17 04 03.51	60 48 31.3	0.6	2.05	0.86	Q	15.3	0.371
1717−00	3C353	17 17 56.80	−00 55 49.0	4.0	33.80	0.84	G	15.4	0.030
1733−56		17 33 20.40	−56 32 26.0	10.0	5.20	0.73	G?	17.0	0.126*
1740−51		17 40 27.00	−51 43 25.0	2.0	4.60	0.72	G	19.2	0.347*
1741−03	OT-68	17 41 20.62	−03 48 48.9	0.1	3.05	−0.28	Q	18.5	1.054
1803+78		18 03 39.18	78 27 54.3	0.1	2.36	−0.18	Q	13.8	0.690
1814−63		18 14 46.13	−63 47 00.9	1.6	7.50	0.91	G	16.0	0.063
1828+48	3C380	18 28 13.54	48 42 40.5	0.4	10.00	0.78	Q	16.8	0.691
1832+47	3C381	18 32 24.40	47 24 36.5	7.0	2.33	0.96	G	17.5	0.161
1839−48		18 39 27.10	−48 39 39.0	3.0	2.00	0.75	G	16.5	0.100*
1842+45	3C388	18 42 35.45	45 30 21.6	0.2	3.15	0.94	G	15.7	0.091
1845+79	3C390.3	18 45 37.57	79 43 06.4	0.1	6.64	0.70	G	14.4	0.057
1928+73	4C73.18	19 28 49.35	73 51 44.9	0.1	3.42	0.04	Q	15.5	0.360
1932−46		19 32 18.91	−46 27 23.9	1.2	6.54	1.03	G	18.9	0.302*
1934−63		19 34 47.65	−63 49 34.7	1.6	11.10	0.88	G	18.4	0.183
1938−15	OV-164	19 38 24.80	−15 31 34.0	4.0	3.80	0.82	G?	21.5	1.000*
1939+60	3C401	19 39 38.84	60 34 32.6	0.5	2.79	0.99	G	19.1	0.201
1949+02	3C403	19 49 44.13	02 22 41.5	2.1	3.68	0.73	G	15.4	0.059
1954−55		19 54 18.90	−55 17 42.0	4.0	3.74	0.78	G	16.3	0.060
1954−38		19 54 39.06	−38 53 13.3	0.1	2.00	0.00	Q	17.5	0.630
2008−06	OW-15	20 08 33.70	−06 53 01.8	0.1	2.20	0.82	G?	21.6	1.047*
2021+61	OW637	20 21 13.30	61 27 18.1	0.1	2.17	−0.10	G	19.5	0.227
2032−35	OW-354	20 32 37.20	−35 04 29.6	1.4	3.70	1.10	G?	21.5	1.000*
2052−47		20 52 50.13	−47 26 19.6	0.2	2.20	−0.17	Q	17.8	1.491

Table A4 continued

(1)	(2)	(3)	(4)	(5)	(6)	(7)	(8)	(9)	(10)
IAU	Name	α (1950)	δ (1950)	$\pm$(")	$S_{2.7}$	$\alpha^5_{2.7}$	ID	V	z
2058−28	OW-297.8	20 58 39.50	−28 13 15.0	30.0	3.10	0.74	G	14.6	0.038
2104−25	OX-208	21 04 25.30	−25 37 58.0	30.0	7.30	0.89	G	15.8	0.037
2106−41		21 06 19.39	−41 22 33.4	0.1	2.11	−0.13	Q	20.0	1.055
2121+24	3C433	21 21 31.00	24 51 36.0	10.0	7.00	1.07	G	15.5	0.102
2128+04	OX46	21 28 02.61	04 49 04.3	0.1	3.12	0.67	G	23.6	3.311*
2128−12	OX-148	21 28 52.67	−12 20 20.6	0.1	2.00	0.00	Q	16.0	0.501
2134+00	OX57	21 34 05.21	00 28 25.1	0.1	7.60	−0.79	Q	18.0	1.936
2135−14	OX-158	21 35 00.10	−14 46 27.0	4.0	2.00	0.63	Q	15.5	0.200
2135−20	OX-258	21 35 01.32	−20 56 03.7	0.1	2.49	0.82	G	19.4	0.380*
2145+06	4C06.69	21 45 36.08	06 43 40.9	0.1	3.10	−0.63	Q	16.5	0.990
2150−52		21 50 48.17	−52 04 23.9	1.8	2.10	0.95	G?	22.2	1.380*
2152−69		21 52 58.60	−69 55 50.0	8.0	19.27	0.71	G	14.0	0.027
2153+37	3C438	21 53 45.42	37 46 13.1	2.0	3.26	1.22	G	19.2	0.290
2200+42	Bl Lac	22 00 39.36	42 02 08.6	0.1	5.21	0.15	Q	14.5	0.069
2203−18	OY-106	22 03 25.73	−18 50 17.1	0.1	5.20	0.33	Q	19.0	0.618
2211−17	3C444	22 11 42.51	−17 16 33.7	1.2	4.52	1.26	G	18.0	0.153
2221−02	3C445	22 21 15.50	−02 21 16.0	30.0	3.46	0.70	G	15.8	0.056
2223−05	3C446	22 23 11.05	−05 12 17.4	0.7	4.40	0.03	Q	18.4	1.404
2229+39	3C449	22 29 07.60	39 06 03.4	0.6	2.50	0.95	G	13.2	0.017
2230+11	CTA102	22 30 07.80	11 28 22.8	0.1	5.30	0.67	Q	17.5	1.037
2243+39	3C452	22 43 32.81	39 25 27.6	0.2	5.94	0.97	G	16.0	0.081
2243−12	OY-172.6	22 43 39.80	−12 22 40.3	0.1	2.74	0.23	Q	17.3	0.630
2245−32	OY-376	22 45 51.53	−32 51 42.2	0.1	2.01	0.18	Q	18.6	2.268
2250−41		22 50 12.25	−41 13 44.4	1.7	2.34	0.99	G	19.0	0.316*
2251+15	3C454.3	22 51 29.52	15 52 54.3	0.1	10.00	−1.37	Q	16.1	0.860
2314+03	3C459	23 14 02.27	03 48 55.2	0.4	2.36	0.97	G	17.6	0.220
2326−47		23 26 33.72	−47 46 51.8	0.2	2.34	−0.08	Q	16.0	1.299
2331−41		23 31 45.37	−41 42 02.5	1.3	2.66	0.91	G	18.0	0.200*
2335+26	3C465	23 35 58.95	26 45 16.4	0.1	4.00	1.03	G	13.2	0.029
2342+82		23 42 06.35	82 10 01.3	0.1	2.33	0.95	EF		0.735
2345−16	OZ-176	23 45 27.69	−16 47 52.6	0.1	4.08	0.26	Q	18.0	0.600
2352+49	OZ488	23 52 37.79	49 33 26.8	0.1	2.21	0.36	G	19.0	0.237
2356−61		23 56 30.00	−61 11 30.0	36.0	10.22	1.36	G	16.0	0.096

Appendix B : THE FREE-FORM MODEL RLF EXPANSION COEFFICIENTS

This appendix gives the expansion coefficients of the free-form model radio luminosity functions described in Chapter 6.

Three separate Tables are given. Table B.1 gives the expansion coefficients for the 5 models in the ensemble which were derived using the data involving the MEAN-z estimated redshifts for faint galaxies (see Chapter 6). Table B.2 gives the corresponding coefficients for the model ensemble based on the LOW-z dataset, while Table B.3 presents the HIGH-z results.

Table B.1 : RLF expansion coefficients for models 1 - 5, MEAN-z data.

order of term		Steep-spectrum				
x	y	RLF1	RLF2	RLF3	RLF4	RLF5
0	0	-2.64	-2.50	-2.40	-2.49	-2.46
1	0	-6.44	-5.44	-5.81	-5.76	-5.87
0	1	4.57	18.99	-7.14	11.07	5.15
2	0	-21.13	-20.75	-30.04	-23.68	-25.15
1	1	135.77	114.59	19.52	69.66	69.35
0	2	319.10	-36.91	146.33	-29.07	165.21
3	0	10.28	-53.98	25.35	-0.66	9.82
2	1	-977.91	-1589.29	59.39	-640.83	-359.58
1	2	-625.64	2100.14	-309.97	1555.91	892.53
0	3	-1427.48	-1440.04	-475.85	-2623.26	-5013.23
4	0	198.37	520.87	208.60	256.59	217.19
3	1	2326.26	4413.19	-567.29	1251.27	225.84
2	2	-781.97	-8717.47	589.55	-2294.80	-600.71
1	3	3189.11	8261.38	1563.89	640.91	8259.89
0	4	1086.04	-1829.42	-572.48	6351.20	1585.11
5	0	-477.14	-1060.38	-417.00	-533.41	-444.97
4	1	-1694.96	-3368.98	877.29	-533.90	490.73
3	2	1718.47	8127.80	-1082.02	-558.24	-3056.57
2	3	-2881.57	-9005.28	-987.67	5689.42	2575.66
1	4	10.82	2980.42	1059.08	-9402.58	-6579.32
0	5	-602.32	-161.04	-256.28	-831.59	959.06
6	0	302.54	654.31	145.87	293.21	216.72

order of term		Flat-spectrum				
x	y	RLF1	RLF2	RLF3	RLF4	RLF5
0	0	-3.71	-3.71	-3.76	-3.75	-3.75
1	0	-9.27	-9.41	-8.18	-8.60	-8.78
0	1	3.15	2.36	0.35	2.95	3.45
2	0	6.95	7.99	3.91	5.66	7.26
1	1	52.41	55.96	-8.93	-0.26	-4.81
0	2	-291.73	-273.67	4.21	-120.22	-126.16
3	0	-16.47	-19.19	-14.67	-16.09	-21.06
2	1	49.04	46.12	90.38	229.78	257.46
1	2	187.06	87.38	-56.56	-523.94	-537.88
0	3	558.58	633.58	-4.73	925.15	870.69
4	0	2.67	4.77	3.53	1.04	6.25
3	1	-92.19	-88.78	-98.80	-202.84	-253.38
2	2	31.83	110.61	114.76	432.49	609.01
1	3	-409.64	-446.39	-73.00	-236.29	-624.79
0	4	-212.71	-275.62	30.44	-833.97	-281.91

Table B.2 : RLF expansion coefficients for models 1 - 5, LOW-z data.

order of term		Steep-spectrum				
x	y	RLF1	RLF2	RLF3	RLF4	RLF5
0	0	-2.48	-2.52	-2.43	-2.49	-2.48
1	0	-6.06	-5.25	-5.51	-5.65	-5.72
0	1	3.91	17.07	-7.74	11.37	5.29
2	0	-22.36	-22.11	-30.08	-23.78	-24.72
1	1	113.65	87.23	18.94	58.93	62.58
0	2	434.52	33.51	160.41	7.37	207.89
3	0	5.68	-43.43	17.17	-1.01	5.14
2	1	-851.95	-1295.37	69.04	-557.79	-382.42
1	2	-1117.11	1381.38	-304.19	1428.47	1158.16
0	3	-1693.49	-1187.73	-565.10	-2995.76	-6135.78
4	0	223.31	474.84	237.80	250.88	229.03
3	1	2076.50	3734.81	-634.49	1012.37	359.76
2	2	103.90	-6990.44	567.94	-1513.01	-1606.01
1	3	3498.57	7436.07	1843.03	-73.59	11188.55
0	4	1357.80	-1796.06	-658.59	7503.23	1531.16
5	0	-510.75	-978.74	-446.87	-512.69	-460.62
4	1	-1520.99	-2919.15	987.67	-373.32	348.72
3	2	1103.73	6961.06	-1212.97	-1184.82	-2250.39
2	3	-2803.23	-8430.34	-1039.18	6426.79	1048.10
1	4	-319.59	3013.38	1095.86	-9865.30	-8071.03
0	5	-628.55	-185.53	-258.39	-1178.46	2486.27
6	0	315.12	606.11	147.30	278.45	227.50

order of term		Flat-spectrum				
x	y	RLF1	RLF2	RFL3	RLF4	RLF5
0	0	-3.71	-3.71	-3.75	-3.75	-3.75
1	0	-9.27	-9.40	-8.25	-8.70	-8.80
0	1	3.23	2.47	0.32	2.87	2.99
2	0	6.93	8.13	4.32	6.10	7.50
1	1	51.51	53.40	-8.65	0.00	-6.16
0	2	-291.81	-265.83	3.46	-120.06	-112.02
3	0	-16.42	-19.79	-15.59	-16.77	-21.64
2	1	51.41	53.34	90.17	229.20	261.00
1	2	185.84	63.86	-54.83	-523.55	-558.54
0	3	560.28	635.21	-4.39	124.02	844.94
4	0	2.62	5.33	4.24	1.36	6.60
3	1	-93.89	-94.11	-99.22	-202.14	-252.83
2	2	33.28	126.64	114.30	431.09	598.51
1	3	-410.98	-443.43	-73.90	-234.48	-559.38
0	4	-213.65	-281.09	30.58	-833.44	-305.94

Table B.3 : RLF expansion coefficients for models 1 - 5, HIGH-z data.

order of term		Steep-spectrum				
x	y	RLF1	RLF2	RLF3	RLF4	RLF5
0	0	-2.47	-2.51	-2.44	-2.50	-2.49
1	0	-6.43	-5.61	-5.51	-5.49	-5.36
0	1	5.49	13.48	-4.77	9.62	1.45
2	0	-20.78	-21.02	-29.01	-23.06	-25.41
1	1	160.69	119.19	21.28	80.10	27.05
0	2	242.68	87.15	102.65	26.12	297.29
3	0	3.70	-34.31	13.03	-18.14	2.66
2	1	-1036.61	-1377.45	16.05	-686.85	8.03
1	2	-521.24	938.92	-170.71	1536.17	225.70
0	3	-1321.02	-1016.82	-376.57	-3169.32	-5440.69
4	0	222.48	425.63	240.02	321.57	221.36
3	1	2272.10	3862.69	-474.78	1279.74	-534.30
2	2	-567.83	-6320.74	749.62	-2485.25	514.23
1	3	3287.81	7381.24	393.13	1380.93	8562.66
0	4	734.18	-2012.14	92.52	8342.61	3927.19
5	0	-504.75	-903.20	-452.28	-615.95	-414.30
4	1	-1544.77	-3018.71	740.84	-452.10	923.56
3	2	1180.93	6717.93	-1127.87	-567.28	-3218.21
2	3	-2507.27	-8472.28	-155.42	5138.46	892.32
1	4	-298.50	3026.77	606.53	-9234.07	-5888.03
0	5	-308.07	-78.45	-373.45	-3730.88	-1434.92
6	0	308.91	570.66	171.02	320.52	185.21

order of term		Flat-spectrum				
x	y	RLF1	RLF2	RLF3	RLF4	RLF5
0	0	-3.71	-3.72	-3.76	-3.75	-3.75
1	0	-9.25	-9.29	-8.20	-8.62	-8.85
0	1	2.74	2.84	0.29	2.84	2.90
2	0	6.87	8.00	4.09	5.73	7.88
1	1	49.00	47.49	-9.15	0.88	-5.12
0	2	-270.98	-253.72	4.47	-122.33	-115.52
3	0	-16.10	-20.32	-15.25	-16.15	-22.71
2	1	62.67	69.80	91.83	227.82	261.64
1	2	106.02	28.55	-57.66	-520.92	-558.21
0	3	600.13	631.96	-4.68	930.00	853.11
4	0	1.98	6.19	4.09	1.10	7.56
3	1	-99.18	-107.37	-100.46	-201.86	-257.12
2	2	80.47	154.17	116.04	431.17	614.08
1	3	-412.60	-438.90	-73.15	-240.08	-591.11
0	4	-256.81	-283.70	30.42	-836.97	-290.78